APS SCIENCE 2003

The annual report of the
Advanced Photon Source at
Argonne National Laboratory

May 2004 • ANL-04/07

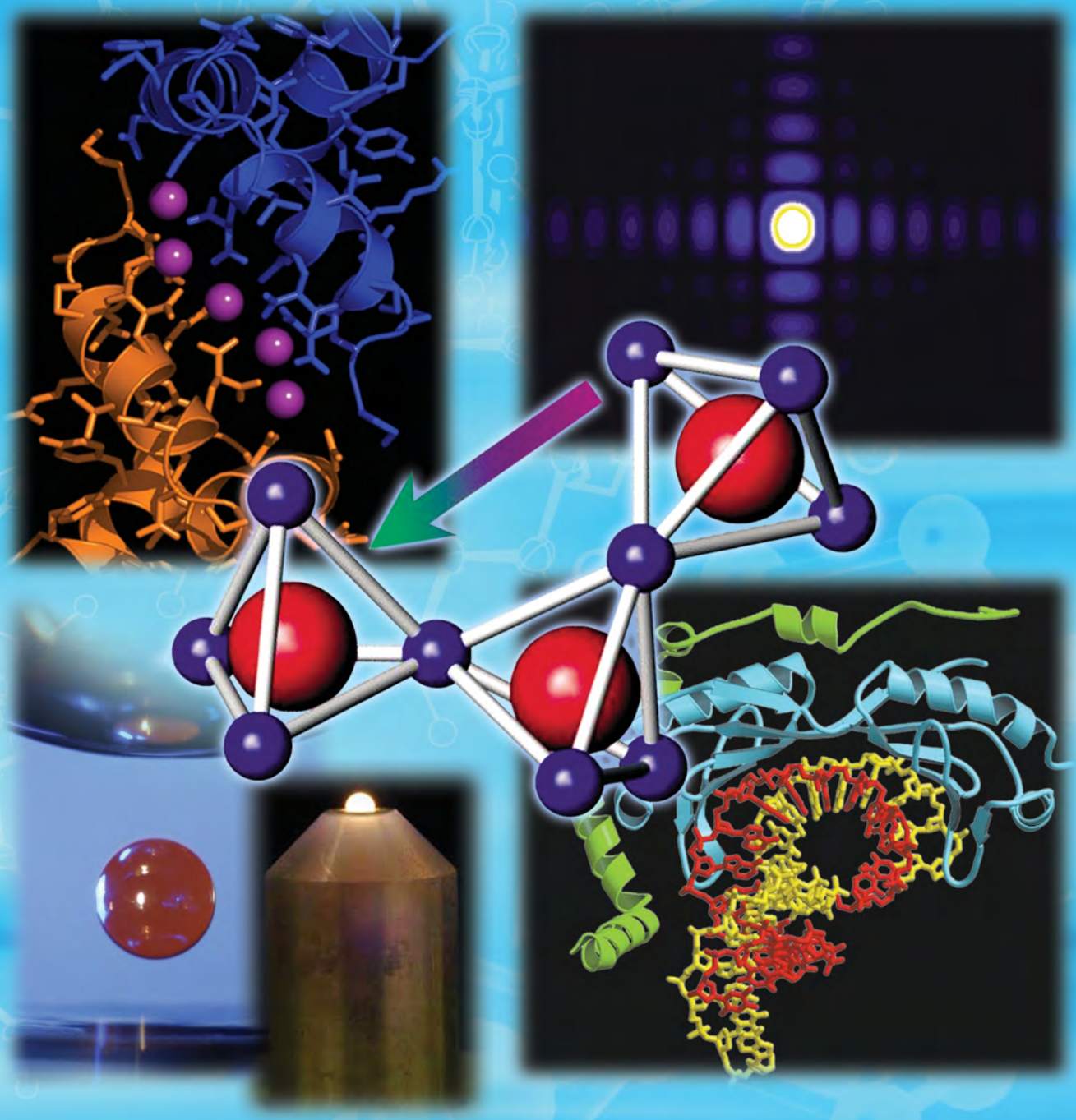

Office of Science
U.S. Department of Energy

APS SCIENCE 2003

The annual report of the
Advanced Photon Source at
Argonne National Laboratory

May 2004 • ANL-04/07

Available electronically at http://www.osti.gov/bridge/. Available for a processing fee to U.S. Department of Energy and its contractors, in paper, from: U.S. Department of Energy Office of Scientific and Technical Information, P.O. Box 62, Oak Ridge, TN 37831-0062, phone: (865) 576-8401, fax: (865) 576-5728, email: reports@adonis.osti.gov

Argonne National Laboratory, a U.S. Department of Energy Office of Science laboratory,
is operated by The University of Chicago under contract W-31-109-Eng-38.

The Advanced Photon Source is funded by the U.S. Department of Energy,
Office of Science, Office of Basic Energy Sciences.

Office of Science
U.S. Department of Energy

Welcome

J. Murray Gibson...

... is Associate Laboratory Director of Argonne National Laboratory and Director of the Advanced Photon Source.

The year 2003 was a landmark for the Advanced Photon Source (APS). The number of users who did an APS experiment at least once in 2003 increased by 20% over 2002, to reach 2,747*. This made us, for the first time, the largest scientific user facility in the Western Hemisphere. And we're not done growing! Other metrics reflected the same trend; for example, the APS became the world's most prodigious depositor of structures into the Protein Data Bank. This annual report demonstrates the real product of our facility through a rich variety of scientific highlights in areas from soil science to condensed matter physics.

In 2003, we were reviewed by a committee, appointed by The University of Chicago and chaired by Yves Petroff, former Director of the European Synchrotron Radiation Facility. The review was very positive about the performance of the APS accelerator complex; the orbit stability was described as "state-of-the-art," and top-up mode as a "resounding success." We are also very proud of the level of availability and reliability, which we work very hard to attain—over 96% availability with over 42 h mean time between faults in calendar year 2003. It remains a significant challenge for us to sustain this level of performance in the years to come, as we deal with aging equipment and strive to make continuing performance improvements. Innovations in machine performance last year described in this report include implementation of real-time orbit feedback and the first light from hard x-ray canted undulator sources at sector 23.

It is exciting to see the many new beamlines being developed at the APS. Three new structural biology sectors are under construction—the General Medicine and Cancer Institutes Collaborative Access Team (CAT, sector 23), Northeastern CAT (24), and Life Sciences CAT (21). In the physical sciences, the Inelastic X-ray Scattering Collaborative Development Team (CDT, sector 30), the hard x-ray Nanoprobe-CDT (26), and a bending magnet powder diffraction beamline (11-BM) are all under development. The Nanoprobe beamline will be intimately coupled with the Center for Nanoscale Materials, which will sprout up at the south wall of the APS in the summer of 2004. The building was generously provided by the State of Illinois, and the equipment and operating budget will be funded by the Department of Energy (DOE).

In 2003 we submitted to the DOE Basic Energy Sciences Advisory Committee (BESAC) a four-phased plan for upgrades to the APS over the next 20 years, which would deliver over three orders of magnitude performance improvement to our users. The first two phases, constructing the remaining beamlines and tailoring insertion devices for the science of each sector, were strongly endorsed by BESAC. We are engaged in a study to identify "New Scientific Directions for the APS," sponsored by the APS Scientific Advisory Committee and co-chaired by Gopal Shenoy (Senior Scientific Advisor, Argonne National Laboratory) and Sunil Sinha (Professor, University of California, San Diego). The study has identified a number of key areas and will host workshops, culminating in a strategic planning meeting to be held August 29–September 1, 2004 (http://www.dev.aps.anl.gov/News/Conferences/2004/apsspm/asfsd.htm). From that meeting, we aim, among other things, to identify the strongest scientific proposals for the four uncommitted sectors.

The later phases of our upgrade plan include rebuilding the storage ring to reduce the emittance by an order of magnitude. The upgrade, more than 10 years from today, would deliver improved beam to existing ports and might allow our users to access fourth-generation capabilities. The new super storage ring, which we are calling APS^2, was listed in the long-term priorities for new facilities by the DOE Office of Science (http://www.er.doe.gov/Sub/Facilities_for_future/facilities_future.htm). Dennis Mills (Deputy Associate Laboratory Director for the APS) and Kwang-Je Kim (Senior Accelerator Physicist) are in charge of strategic planning for APS^2, and they will be

Cont'd. on page 6

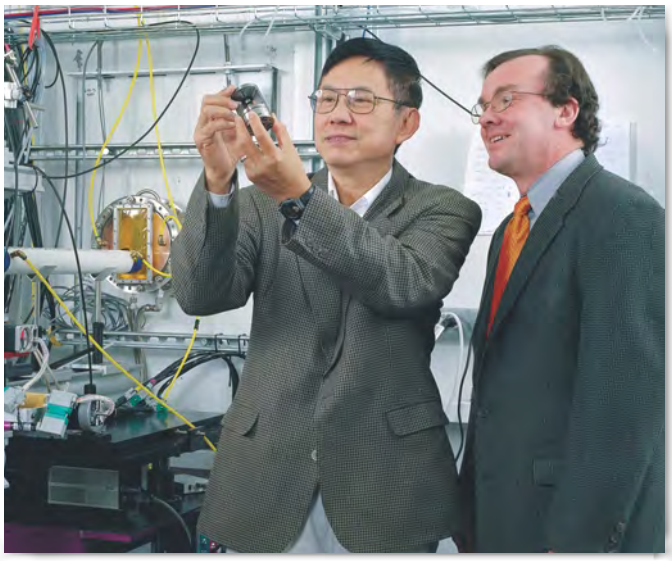

David H. Mao (left, Director of the High Pressure Collaborative Access Team, or HP-CAT) showing a panoramic high-pressure diamond-anvil cell to Murray Gibson, inside the beamline 16-ID-D research station. The HP-CAT is one of the most recent APS sectors to pass through commissioning and into operations. The integrated high-pressure facility at HP-CAT is opening myriad new research frontiers in multidisciplinary physical sciences.

*This was in part due to increases in the allocation of beam time on APS-operated sectors and to the increase in the number of beamlines accepting general users (22 vs. 25 insertion device beamlines and 8 vs. 10 bending magnet beamlines in 2002 and 2003, respectively).

Report from the APS Users Organization—2003

Stephen M. Durbin...

... (Chair, APS Users Organization) is Professor of Physics at Purdue University and a user with X-ray Operations and Research.

The highlight of the year was the Twelfth Users Meeting for the Advanced Photon Source on April 19-May 1, where nearly 500 APS users set a new attendance record. They were rewarded with an outstanding collection of scientific talks and workshops that ranged from imaging insect respiration to the latest in nanoscience and proteomics. Special presentations were given by Paul Doucette, chief aide to U.S. Representative Judy Biggert (R-IL13), who represents the Argonne area in Congress and is a leader in promoting funding for the Department of Energy (DOE) Office of Science, and by Susan Ginsberg of the American Physical Society, who provided a Capitol Hill-view of the merits of user outreach to their elected representatives. The meeting itself generated over 100 letters sent by users to their senators and representatives, and clearly motivated the APS user community to be more active in educating our federal government about the value of synchrotron science at the APS.

Erin Miller (left), a student from the University of Washington, chats with Steve Durbin, APSUO Chair, in front of the Advanced Photon Source exhibit at the 2004 American Physical Society March Meeting.

Washington outreach was a recurring theme for the Advanced Photon Source Users Organization (APSUO) in 2003. In April, a team of user-group chairs from the APS as well as from our sister DOE labs, the National Synchrotron Light Source, the Advanced Light Source, and the Stanford Synchrotron Radiation Laboratory, traveled to Washington, D.C., to expound on the importance of the DOE investment in synchrotron science. In addition to meetings at the Office of Science & Technology Policy that included an unscheduled session with its director, Dr. Jack Marburger, we met with officials from the Office of Management and Budget (OMB) as well as staff of the House Science Committee, the House Appropriations Committee, the Senate Committee on Energy and Natural Resources, and the Senate Appropriations Committee.

In the fall of 2003, the users of the APS submitted electronic letters to Congress and OMB: nearly 400 APSUO members generated over 1,000 letters to Washington, a total nearly ten times higher than from any other DOE user group! The APSUO has set a standard for Washington outreach that is the envy of our colleagues, and one that we should strive to surpass in 2004. The APSUO also initiated the first joint letter to Congress from the "Consortium of Science User Groups," consisting of the elected chairs of 15 different user organizations associated with DOE Office of Science facilities.

At the quarterly meetings throughout the year, the APSUO Steering Committee has been called upon to advise APS management on issues including the University of Chicago Review of the APS in September, the APS 20-year plan, the centralized General User Proposal system, the call for partner user proposals, non-resident user access issues, and the transfer of Office of Basic Energy Sciences (BES) sectors to APS operations support. A new policy was implemented to help keep the Steering Committee up to date on new developments among users. This was accomplished by inviting user group representatives to join the Committee for lunch and give short presentations. In the course of the year, all APS user groups have this opportunity to share issues and concerns with the Steering Committee.

Finally, the Steering Committee initiated a special workshop to focus attention on an area of importance to a large fraction of the users, the "Technical Workshop for Protein Crystallography CATs" held on January 13, 2004. Presentations were made by representatives from nearly all of the life-science CATs on three critical subjects: future developments in common user interfaces, implementation and development of robotics, and the future of telepresence. Consensus was achieved that telepresence in particular is an especially promising area in which to invest now, in order to achieve the highest level of productivity and standardization. These issues are being pursued further at workshops associated with the 2004 Users Meeting for the Advanced Photon Source, sponsored as always by the APSUO. ❍

APS Scientific Advisory Committee Meeting, January 20-22, 2004

J. Michael Rowe...

... (Chair, APS Scientific Advisory Committee) is the Director of the Center for Neutron Research at the National Institute of Standards and Technology.

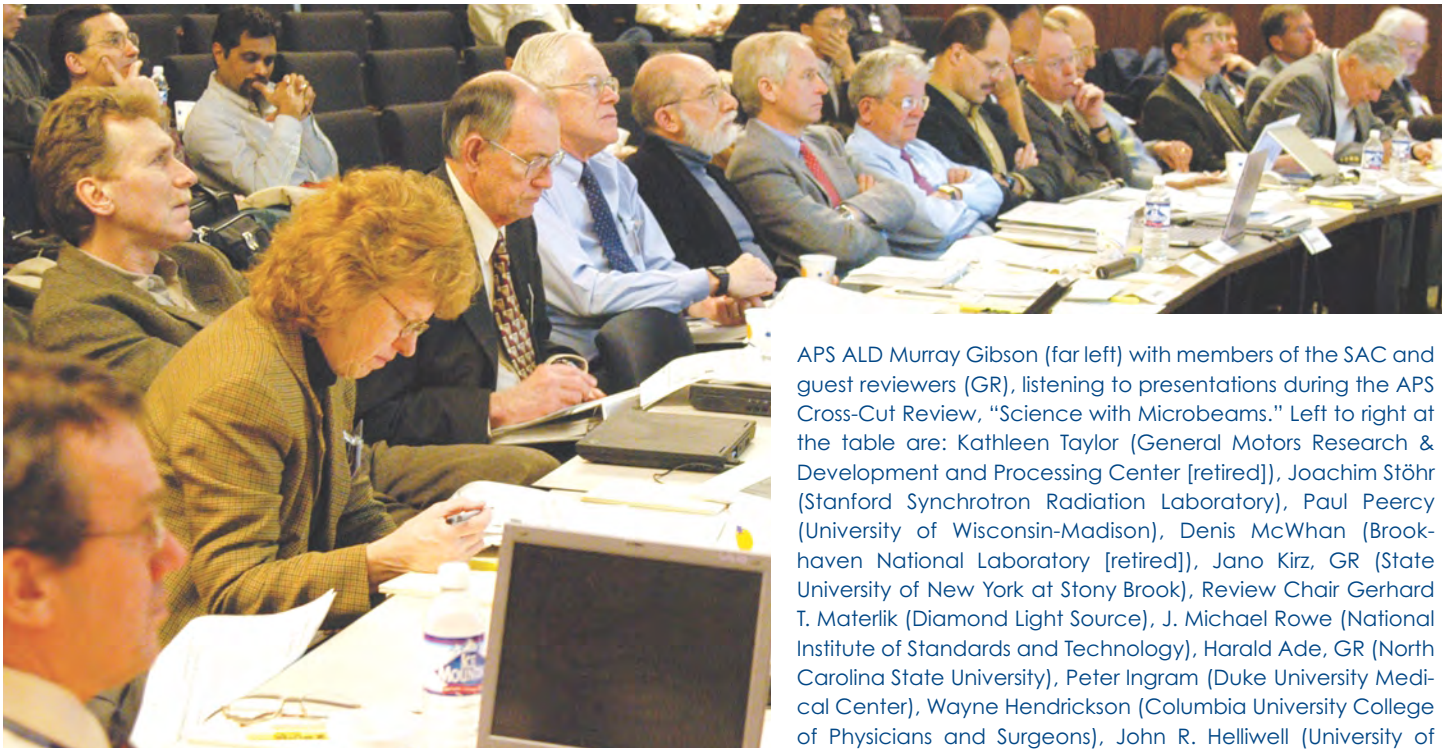

APS ALD Murray Gibson (far left) with members of the SAC and guest reviewers (GR), listening to presentations during the APS Cross-Cut Review, "Science with Microbeams." Left to right at the table are: Kathleen Taylor (General Motors Research & Development and Processing Center [retired]), Joachim Stöhr (Stanford Synchrotron Radiation Laboratory), Paul Peercy (University of Wisconsin-Madison), Denis McWhan (Brookhaven National Laboratory [retired]), Jano Kirz, GR (State University of New York at Stony Brook), Review Chair Gerhard T. Materlik (Diamond Light Source), J. Michael Rowe (National Institute of Standards and Technology), Harald Ade, GR (North Carolina State University), Peter Ingram (Duke University Medical Center), Wayne Hendrickson (Columbia University College of Physicians and Surgeons), John R. Helliwell (University of Manchester), Stephen Durbin, *ex officio* SAC member (Purdue University), Howard Birnbaum (University of Illinois at Urbana-Champaign [retired]), Paul Bertsch (Savannah River Ecological Laboratory), and William Bassett (Cornell University). A complete list of SAC members can be found in the appendices to this report.

The second meeting of the APS Scientific Advisory Committee (SAC) was held on January 20-22, 2003, at Argonne. Once again, the SAC spent much time on the reports of the sector review panels (SRPs) that met in 2003 to review APS sectors 8, 10, 14, 15, 17, 19, 20, and 22. The SRP membership included SAC members in every case, and in every case, a SAC member was chair. The chair of each SRP delivered an oral report in addition to the written reports, and the full committee discussed each report and formulated recommendations. We thank all of you for your cooperation in this process, which we understand is burdensome. However, it is a critical part of the never-ending assessment of the performance of the APS, which in turn is the key to continuing and increasing funding for operations. In addition, the SAC reviewed the responses to the prior round of sector reviews and developed additional requests for actions where appropriate.

Another task before the APS and the SAC is determination of optimal staffing levels for different sectors, and Gabrielle Long (Experimental Facilities Division) presented the results of her preliminary analysis of this problem. The SAC encourages the Partner User Council, the APS Users' Organization, and other interested parties to send us their thoughts, as this is a difficult area and additional input will be helpful. Finally, Partner User Proposals were reviewed, and recommendations given to the Director.

As a way of developing a broader view of the APS, the SAC has decided to perform cross-cutting reviews during its meetings. The first such review was a one-day review of microbeam capabilities and plans around the ring. This was a success in many ways, not only for the committee, but also for the APS staff and users (who were welcomed to the talks). It provided a snapshot of activities at a much broader scale than we normally can get from sector reviews, which is a necessary part of optimizing utilization of the country's brightest x-ray source. We intend to continue with these reviews and have tentatively agreed that the next such review will be centered on science that requires and exploits the time structure of the ring.

Among many other topics, the SAC also discussed metrics for industrial users, the "20-Year Plan for the APS," The University of Chicago review of the APS, and the Department of Energy roadmap for future facilities. In all, it was a very full meeting, and the committee ended exhausted but confident that the APS is doing great science. ❍

THE APS PARTNER USER COUNCIL

P. JAMES VICCARO...

... (Chair, APS Partner User Council) is the Executive Director of the Consortium for Advanced Radiation Sources (CARS) at The University of Chicago and ChemMatCARS Principal Investigator.

The formation of the APS Partner User Council (PUC) was one of the last acts of the APS Research Directorate (RD), which had been the forum for discussion of management issues involving the APS and the collaborative access teams (CATs). In the last meeting of the RD and the first meeting of the PUC, the Chair, Jim Viccaro, was elected. His first act was to request that John Quintana, Director of DND-CAT, become the Deputy Chair. Quintana accepted, and the new forum was initiated

From the outset, the PUC was not intended to be the Research Directorate with only a change in name. There are substantial differences in the way business is now conducted. The PUC is composed of a member representative from each APS sector; the representative is appointed by the partner user management responsible for the development and operation of the sector. These PUC members are non-APS employees; however the APS may also appoint *ex-officio* members, who may be APS employees at sectors not otherwise represented. Additional standing members of the Council include the chairs of the Technical Working Group (TWG), Reinhard Pahl (The University of Chicago/CARS) and Eric Dufresne (APS/MHATT/XOR); and a representative of the APSUO, Mark Rivers (The University of Chicago/CARS).

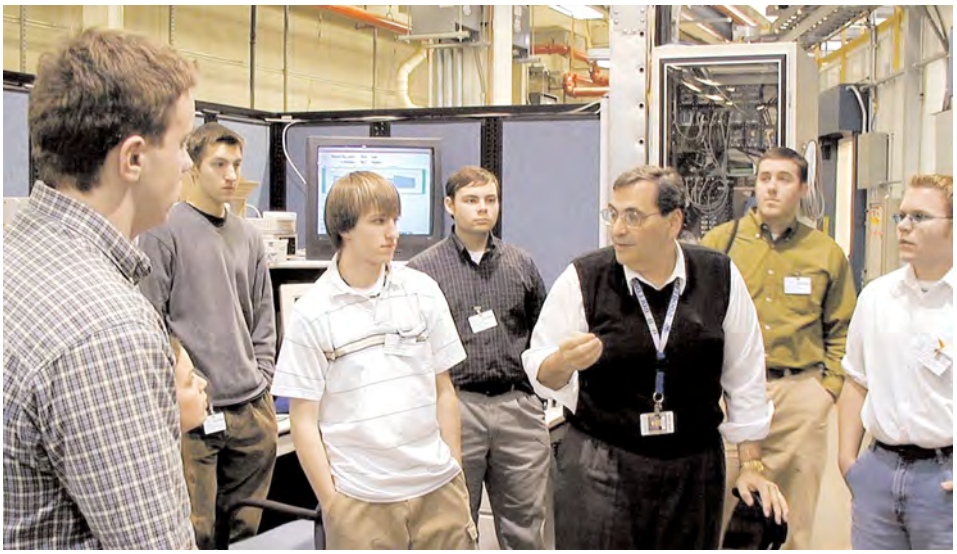

Jim Viccaro (third from right) with some of the advanced placement physics students from Riverside-Brookfield High School, in Illinois, who spent a day at the ChemMatCARS sector 15 beamlines in the APS experiment hall (see Murray Gibson's "Welcome"). ChemMatCARS and APS staff members guided the students through an intensive curriculum that ranged from basic scientific principles to the finer points of experimentation.

The PUC sets the agenda with input from the members and in consultation with APS management. The principal thrust of the meetings is to discuss issues related to current and future beamline operations, APS facility development, and APS/partner user relationships. The main objective is to provide advice and recommendations to the APS management. Towards this end, the Council may appoint *ad hoc* committees to focus on specific issues.

Three meetings were held in 2003, including the inaugural one. The meetings, which are preceded by an executive session, have been well attended with lively discussion. APS management has readily adopted the new format and been forthcoming and responsive to issues raised by Council members.

As a result of the change in operational paradigm, the partner users have quite a bit more responsibility as participants in APS committees related to operations and user issues. For example, John Quintana regularly attends the weekly APS Operations Meeting as the Council representative. The Council Chair is an *ex officio* member of the APS Scientific Advisory Committee (SAC), and the Council also has representation on the SAC panels that review APS sectors. The PUC Chair and Deputy Chair also participate in setting the agenda for the monthly APS/User Operations Meetings.

In addition to these standing responsibilities, input on several issues has been requested by the APS. In some cases, the Council has formed *ad hoc* committees to meet the APS operations and CAT/partner user issues. In others, the requests have been forwarded to the TWG for discussion. In order to provide user input on current and future operational modes of the APS storage ring, a standing committee has been formed. Discussion is ongoing in an attempt to mitigate the apparently conflicting operational requirements of different user groups. Representation in this group will be expanded in 2004, and an impact statement to the APS is planned.

The Council has proven to be an effective forum for focusing on user concerns related to operations, etc. The initial Partner User Council forum to discuss user questions about a new insertion device front end developed by the APS helped clarify the relevant issues for both the user community and APS management. Subsequent mitigation by the APS was effective, and Council input was included during the process.

The year 2003 has been a learning experience for the user groups that participate in the Council. The new responsibility placed on the users to define and pursue to closure issues that are relevant to effective scientific productivity at the sectors is sometimes a daunting challenge. We look forward to an even more effective forum in 2004. ❍

Cont'd. from page 2

Fig. 1. Participants in the fifth year of the highly successful National School on Neutron and X-ray Scattering (NSNXS). This year's NSNXS, whose Scientific Directors were Dean Haeffner (XFD) and Raymond Osborn (MSD), welcomed 60 graduate students pursuing doctorate degrees at U.S. universities while majoring in physics, chemistry, materials science, or related fields. The school gives students tutorial lectures on scattering theory, neutron and synchrotron x-ray source characteristics, and scattering methods for condensed matter research; lectures by prominent scientists; and hands-on experiments at both the IPNS and APS.

organizing seminars, workshops, and feasibility studies over the next couple of years to narrow the design choices for this exciting upgrade.

The APS is a key partner in the major DOE project to construct the first x-ray laser (the fourth-generation x-ray facility) at the Stanford Linear Accelerator Center (see p. 160). We are also seeking external funding to develop our own fourth-generation free-electron laser into a source for vacuum ultraviolet radiation (see p. 159).

We have moved forward significantly in our efforts to support user sectors that were previously receiving operational support from the DOE Office of Basic Energy Sciences. Sectors 1, 2, 3, 4, 11, and 12 are now fully supported by the APS; sectors 7, 8, and 20 receive significant support; and sector 9 receives some support. Today we have 25 more beamline scientific staff within the X-ray Operations and Research (XOR) group than we had three years ago. We are delighted that Gabrielle Long has joined us as the Associate Division Director in the Experimental Facilities Division. She is responsible for all our beamline operations and research. Gabrielle will have the primary role of attracting outstanding new beamline staff as we expand in the future and of overseeing the evolution of focused, dedicated capabilities amongst our beamlines. The latter was identified by The University of Chicago review committee as the most significant challenge for APS to address in increasing the scientific impact of our users.

The APS Operations Division (AOD) has also increased support to users, in areas such as beamline controls and data acquisition, computer support, experimental safety review, and the detector pool. We were very pleased in 2003 to welcome Bill Ruzicka as Division Director for AOD. The University of Chicago review of the APS was very supportive of the changes we are making in XOR and AOD to maximize the scientific impact of users, and identified some areas where we could further leverage success, especially in the structural biology area.

Of course, the future of x-ray science is really in the hands of the next generation of x-ray scientists. The APS is committed to providing the opportunities and environment for young people who are interested in an up-close encounter with this exciting field of research. The National School on Neutron and X-ray Scattering, organized each year by Argonne's (ANL's) Intense Pulsed Neutron Source (IPNS), the APS, and the ANL divisions of Materials Science and Education (Fig. 1); the program for advanced placement high school students hosted by the Chemistry and Materials beamlines of the Consortium for Advanced Radiation Sources Collaborative Access Team (ChemMatCARS-CAT) at APS sector 15; the group of undergraduate engineering students participating in a National Science Foundation Research Experience for Undergraduates program, who performed a series of synchrotron x-ray tomography experiments at GeoSoilEnviroCARS-CAT (GSECARS, APS sector 13) (Fig. 2); and the American Crystallographic Association Summer School in Crystallography, which brings students to the Industrial Macromolecular Crystallography Association (sector 17) and BiologyCARS-CAT (sector 14) beamlines, are a few examples of the community's commitment to science education.

I hope that you enjoy the information in this annual report. We at the APS are proud of the success of our users. Whether you are a present or prospective user, we hope that you will be a satisfied user in the future. The outlook for APS science is bright, although we face the challenge of securing the resources needed to achieve our vision. We are grateful to the DOE for its continuing support of our facility. ❍

Fig. 2. Amy Grove, a senior Civil Engineering major at Cornell University, shown in the GSECARS 13-BM tomography station aligning a sediment/barrier core prior to collecting images of several sediment/reactive barrier systems. Her work is part of a pilot-scale study conducted at the University of New Hampshire and funded by the Cooperative Institute for Coastal and Estuarine Environmental Technology and the Hazardous Substance Research Center South/Southwest.

The APS facility occupies an 80-acre site on the Argonne National Laboratory campus, about 25 miles from downtown Chicago, Illinois.
For maps of the Argonne/Chicago area, see http://www.aps.anl.gov/user/maps/maps.html.
For directions to Argonne, see http://www.anl.gov/OPA/anlil.html.

Access to Beam Time at the APS

There are two ways to obtain beam time at the APS: as a general user (a researcher not associated with a particular beamline) or as a partner user, e.g., a member of a collaborative access team (CAT). If you are a CAT member, contact your CAT for instructions on applying for CAT beam time. All operating beamlines at the APS reserve at least 25% of their available beam time for general users.beam time.

How general users can apply for beam time at the APS:
1) New users should read the information for new users found on on our Web site at http://www.aps.anl.gov/user/new_users.html before applying for beam time. Also, certain administrative requirements must be completed. In particular, a user agreement between the APS and each research-sponsoring institution must be in place.

2) To choose the appropriate beamlines, consult the APS techniques directory (http://beam.aps.anl.gov/pls/apsweb/bd_display_pkg.technique_dir). Detailed beamline specifications (http://www.aps.anl.gov/aps/beamtime-nav.html) are also available.

3) Submit a proposal via the Web-based system. Proposals are evaluated before each user run. For more information and the current proposal schedule, see the proposal system overview (http://www.aps.anl.gov/user/beamtime/prop_submission.html).

Table of Contents

APS Research Highlights

APS Research Highlights

APS Research Groups:

XOR—sectors 1-4
X-ray Operations and Research

DND-CAT—sector 5
DuPont-Northwestern-Dow Collaborative Access Team

MU-CAT—sector 6
Midwest Universities Collaborative Access Team

MHATT/XOR—sector 7
Center for Real-Time X-ray Studies Collaborative Access Team

IMMY/XOR—beamline 8-ID
IBM-McGill-MIT-Yale Collaborative Access Team

CMC-CAT—sector 9
Complex Materials Consortium Collaborative Access Team

MR-CAT—sector 10
Materials Research Collaborative Access Team

BESSRC/XOR—sectors 11 & 12
Basic Energy Sciences Synchrotron Radiation Center

CARS-CAT
Consortium for Advanced Radiation Sources
Collaborative Access Team
GeoSoilEnviroCARS—sector 13
BioCARS—sector 14
ChemMatCARS—sector 15

HP-CAT—sector 16
High Pressure Collaborative Access Team

IMCA-CAT—sector 17
Industrial Macromolecular Crystallography Association
Collaborative Access Team

Bio-CAT—sector 18
Biophysics Collaborative Access Team

SBC-CAT—sector 19
Structural Biology Center Collaborative Access Team

PNC/XOR—sector 20
Pacific Northwest Consortium Collaborative Access Team

LS-CAT—sector 21
Life Sciences Collaborative Access Team

SER-CAT—sector 22
South East Regional Collaborative Access Team

GM/CA-CAT—sector 23
General Medicine and Cancer Institutes Collaborative Access Team

NE-CAT—sector 24 & beamline 8-BM
Northeastern Collaborative Access Team

Nanoprobe-CDT—sector 26
Nanoprobe Beamline Collaborative Development Team

IXS-CDT—sector 30
Inelastic X-ray Scattering Collaborative Development Team

SGX-CAT—sector 31
Structural GenomiX Collaborative Access Team

COM-CAT—sector 32
Commercial Collaborative Access Team

UNI-CAT—sectors 33 & 34
A University-National Laboratory-Industry Collaborative Access Team

THE ADVANCED PHOTON SOURCE

Sector Allocations & Disciplines

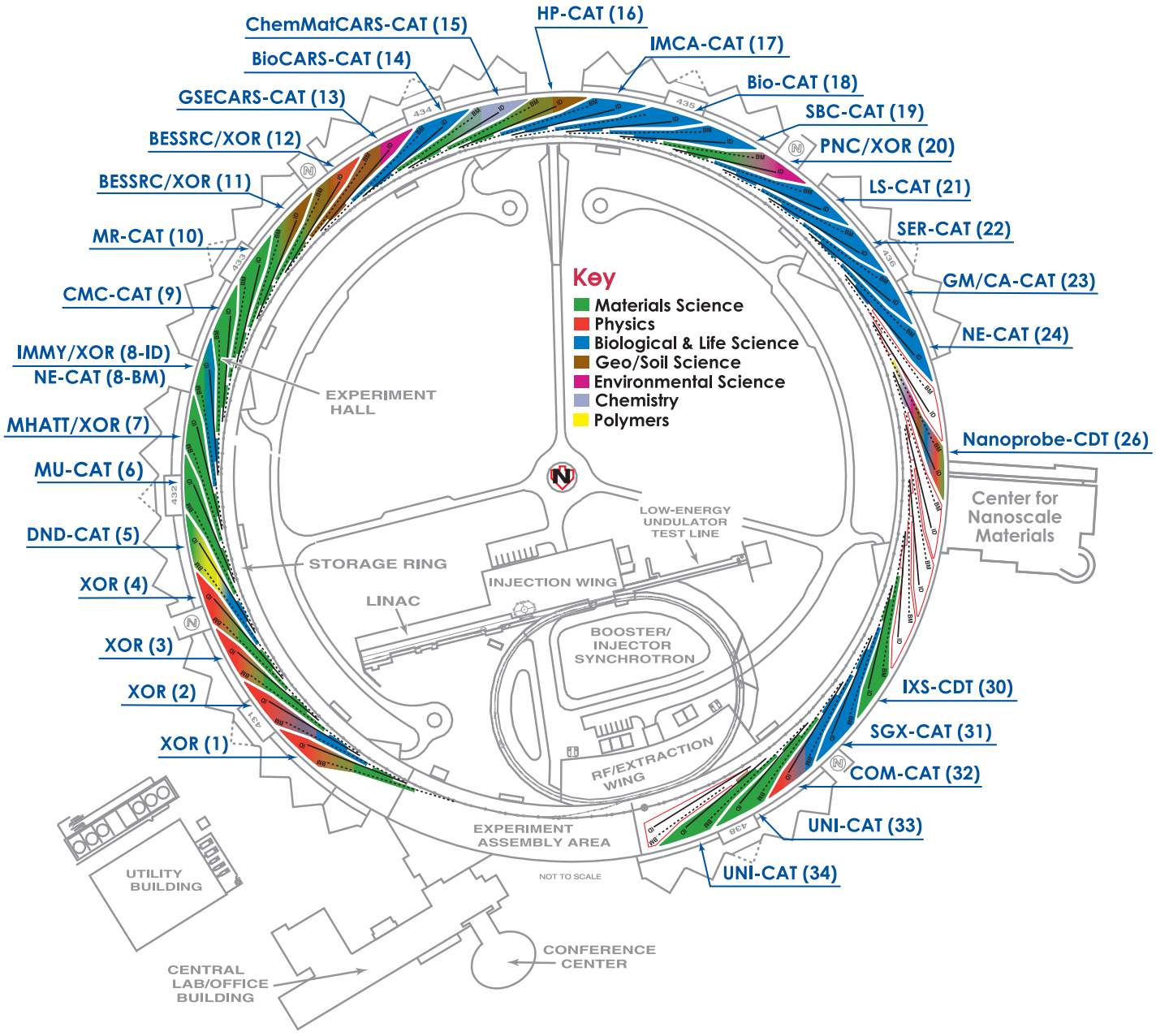

MAPPING IMPURITY ATOMS WITH X-RAY STANDING WAVES

X-ray and neutron diffraction have long been powerful techniques in crystallography, but they suffer from a serious drawback. Although scattering amplitudes can be measured with precision, information about the phase of the scattered radiation is lost. This phase ambiguity means that the scattering data cannot be simply Fourier transformed into a map of atom locations. Instead, complex statistical methods must be used to retrieve the phase information and extract the crystal structure. Atomic fluorescence emitted during excitation of an x-ray standing wave provides a powerful alternative because phase information can be retained. Recently, researchers at Argonne National Laboratory, Northwestern University, and the University of Illinois at Chicago used this technique to locate impurity atoms in the crystal lattice of muscovite.

X-ray standing waves are created in a crystal when an incoming beam is reflected by Bragg planes in the lattice, much like the standing wave in an organ pipe. Atoms in this standing wave field will then emit characteristic fluorescence radiation that allows identification. Because this characteristic emission signals both phase and amplitude, these data can be Fourier transformed back to a real-space atomic distribution. For the present experiment, the research team examined the distribution of manganese, iron, titanium, and barium impurities in a sample of muscovite mica, whose native atomic constituents are potassium, silicon, and aluminum.

The research team used x-rays from the BESSRC/XOR beamline 12-ID-D at the APS. A silicon monochromator selected the beam's energy to 7.44 keV, and additional beam conditioning was provided by two postmonochromators. Characteristic atomic fluorescence was collected at a grazing angle above the sample surface plane and analyzed with a solid-state detector. X-ray standing wave data were taken for the first eight orders of Bragg reflection. For each Bragg order, the sample was rotated through the Bragg reflection to shift the standing wave pattern to modulate the atomic emission yield. In this experiment, phase data were obtained via dynamical diffraction theory and known structure factors for muscovite. The amplitude and phase data could then Fourier inverted to create the real space representation.

The researchers found that the distributions of lattice cations obtained by the standing wave method quantitatively reproduced the known structure of muscovite (Fig. 1). In this study, the known muscovite scattering structure factors were used in analysis of the fluorescence yield. But even if the bulk structure is not available, it should be possible to make use of the precision reflectivity measurements to iteratively invert the data without reference to *a priori* structural information. Although more complex, such an inversion would produce a completely model-independent distribution of lattice atoms.

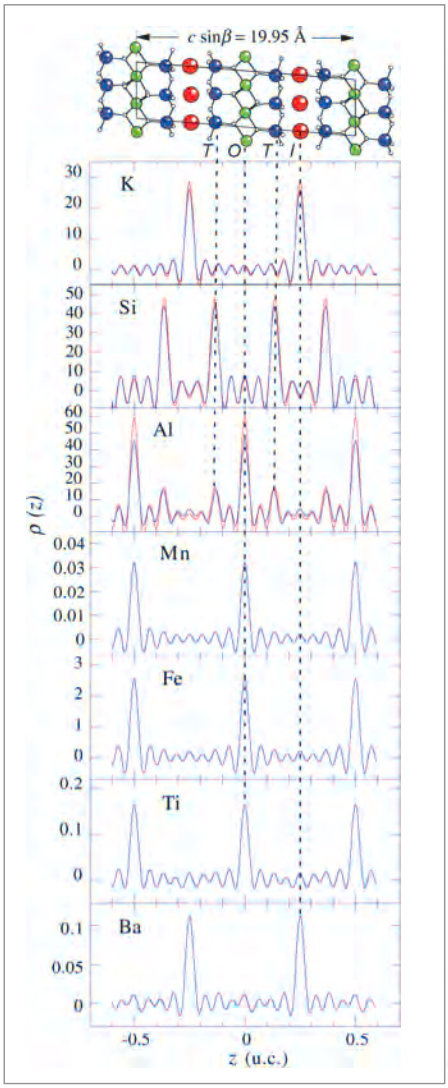

Fig. 1. Distributions of lattice atoms (K, Si, Al) and impurity atoms (Mn, Fe, Ti, Ba) in the muscovite unit cell. Blue lines show distributions based on Fourier solution of x-ray standing wave data. Red lines indicate lattice atom distributions similarly derived from crystallographic data. Diagram at top shows unit cell model on same scale as distribution data. Interlayer, tetrahedral, and octahedral sites are red, blue, and green, respectively.

To demonstrate the feasibility of the model-dependent approach, the research team obtained the density distributions of the impurity atoms Mn, Fe, Ti, and Ba. The results show that while Mn, Fe, and Ti occupy octahedral (Al) sites, the Ba impurities are found at interlayer positions (K sites).

X-ray standing wave methods such as those demonstrated in this work provide an alternative to conventional diffraction techniques, particularly if element-specific density distributions are desired. In the future, x-ray standing wave structural data are expected to be especially useful in complex bulk-impurity measurements and surface chemistry studies. Moreover, these results indicate the value of high-brightness facilities, such as the APS synchrotron, in successfully carrying out x-ray standing wave measurements. ❍

See: L. Cheng[1], P. Fenter[1], M.J. Bedzyk[1,2], and N.C. Sturchio[1,3], "Fourier-Expansion Solution of Atom Distributions in a Crystal Using X-ray Standing Waves," Phys. Rev. Lett. **90**(25), 255503-1 to 255503-4 (27 June 2003).

Author affiliations: [1]Argonne National Laboratory, [2]Northwestern University, [3]University of Illinois at Chicago

This work was supported by the Geosciences Research Program of the U.S. Department of Energy, Office of Science, Office of Basic Energy Sciences, through Contract No. W-31-109-Eng-38, and was conducted at the BESSRC/XOR beamlines at the APS and at the X-ray Diffraction Facility at Northwestern University (supported by National Science Foundation Contracts No. DMR-0076097 and No. CHE-9810378). Use of the Advanced Photon Source was supported by the U.S. Department of Energy, Office of Science, Office of Basic Energy Sciences, under Contract No. W-31-109-Eng-38.

REVEALING FINE DETAILS OF GOLD NANOPARTICLES

A major challenge in the study of nanometer-scale particles is their tendency to behave unpredictably: they aggregate, or clump together, and nucleate, or disperse. One way to achieve a degree of stability and homogeneity is to cap the particles with a molecular agent that acts at the surface of the particle to control the size. This allows more precise exploration of the structure and electronic properties of nanoparticles.

By using an array of probes, including high-energy spectroscopy at the PNC/XOR 20-BM and 20-ID beamlines at the APS, and the Canadian Synchrotron Radiation Facility (CSRF) at the Synchrotron Radiation Center (SRC), University of Wisconsin-Madison, researchers from the University of Western Ontario conducted a systematic study of the structural and electronic characteristics of gold nanoparticles. In these studies, the capping agent thiol was used to manipulate and control the size of the nanoparticle, and high-beam probes measured changes in the surface electronic charge and crystal structure of the particles as the size decreased.

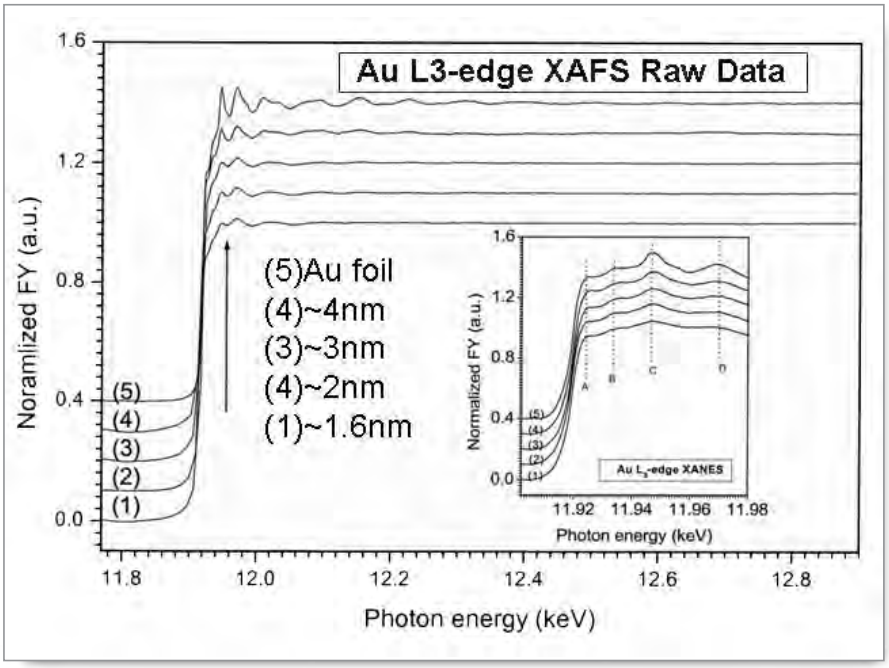

Fig. 1. Raw data obtained at the APS show the trend of the absorption spectrum as a function of size. The arrow indicates the similarities of spectra as size increases. As the particles become larger, the features are better defined. The inset shows the threshold of absorption where the x-ray has sufficient energy to take one electron from a $2p_{3/2}$ to a higher level of gold 5 d character above the Fermi level.

First, by manipulating the ratio of the gold salt and the capping agent at 0°C, a degree of control was achieved in synthesizing gold nanoparticles ranging in size from 1.6 to 4.0 nanometers.

Extended x-ray absorption fine structure (EXAFS) analysis revealed that the structure of the gold nanoparticles did indeed change as size varied. In the smaller nanoparticles, the atoms in the lattice contracted relative to bulk as the size decreased. This confirms and further refines the results of electron microscopy probes. Measurements of the x-ray absorption coefficient of the particles also revealed that as the size decreased, the EXAFS oscillations were broader and less intense, though the pattern remained intact, suggesting that the smaller particles become more disordered and the nanoparticle remains crystalline.

Probes of the electronic characteristics of the nanoparticles by using x-ray absorption near-edge structure (XANES) analysis showed that the electronic charge of the thiol-capped nanoparticles was depleted in the smaller particles (Fig. 1).

The capping molecule alkanethiolate also affected the electronic properties of the nanoparticles. Naked or weakly capped nanoparticles generally contract relative to the bulk. However, analysis with x-ray absorption fine structure (XAFS) detected a slight reduction in the contraction of thiol-capped particles.

XANES analysis supported a previous observation, inferred from measuring the intensity of the x-ray whiteline, that there is some transfer of electronic charge from the gold nanoparticle to the thiol capping agent. XANES analysis also was used to determine whether the interaction of the bonding agent sulfur/thiol was sensitive to size. Previous studies had suggested a weak correlation with size, and this analysis supported that finding, revealing only a slight increase in bonding strength for the smallest 1.6-nanometer nanoparticles.

This systematic study of the properties of gold nanoparticles demonstrates that it is possible to gain a degree of control over the size and stability of nanoparticles and, with the help of high-intensity x-ray beams, obtain a more detailed understanding of the fundamental properties of these building blocks for the next generation of nanotechnologies. ❍

See: P. Zhang and T.K. Sham, "X-ray studies of the structure and electronic behavior of alkanethiolate-capped gold nanoparticles: The electronic interplay of size and surface effects," Phys. Rev. Lett. **90**(24), 245502-1 to 245002-4 (2003).
Author affiliations: University of Western Ontario

Research at the University of Western Ontario and CSRF supported by NSERC of Canada. XAFS were obtained at PNC/XOR (supported by U.S. DOE under Contract No. DE-AC02-98CH10886) and at SRC, University of Wisconsin-Madison (supported by U.S. NSF, Grant No. DMR-0084402). Use of the Advanced Photon Source was supported by the U.S. Department of Energy, Office of Science, Office of Basic Energy Sciences, under Contract No. W-31-109-Eng-38.

CRACKING OPEN A GLASS PUZZLE

With the right stimulus, some materials can make a transition from a low-density amorphous form to a higher density one. Though long known, this phenomenon of polyamorphism is not well understood. Part of the solution to this mystery lies in untangling the changes in atomic order over various length scales. Glasses, for example, can exhibit short-range order, which involves correlations between nearest neighbors. But ordered correlations beyond this can also exist, especially in network-forming glasses, and are generally known as intermediate-range order correlations. During transitions among amorphous forms, changes occur in both short-range and intermediate-range order. The former tend to be more straightforward, while the latter have become the subject of intense debate. Recently, a collaboration of researchers from the University of Wyoming, Argonne National Laboratory, Arizona State University, and the Centre de Recherche sur les Matériaux à Haute Température, in Orléans, France, has used x-ray and neutron diffraction to reveal the mechanism by which important structural changes occur in the glassy network before a polyamorphic transition in GeO_2.

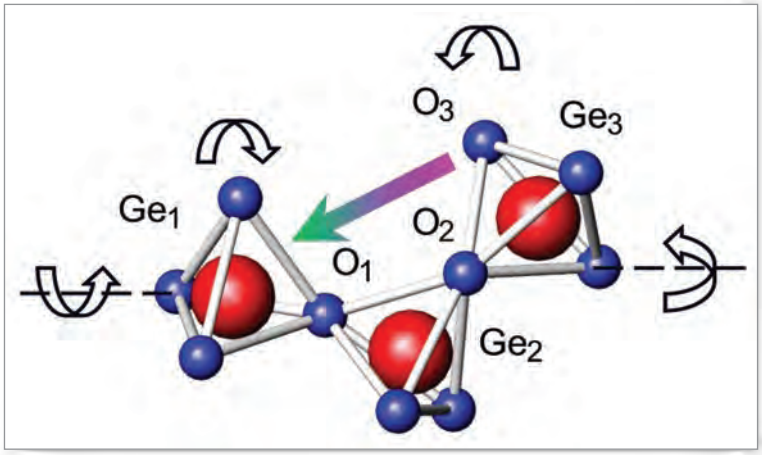

Fig. 1. Mechanism for GeO_2 densification proposed on the basis of combined neutron and x-ray diffraction studies. (Oxygen atoms are blue, germanium atoms are red.) Oxygen-oxygen correlations were found to be the most important factor in the changes in intermediate range order accompanying densification. The decrease in next-nearest neighbor oxygen distance is likely the result of rotation of the GeO_4 tetrahedra around the Ge-O-Ge bonds.

Canonical network glasses, such as GeO_2 and SiO_2, both consist of corner-shared tetrahedra that link together to form cage structures. Likewise, both these systems undergo a polyamorphic transition under pressure. The structure of these materials becomes more compact as the coordination gradually changes from fourfold to sixfold. When pressure is removed, the coordination returns to fourfold but the density of the glass is found to be permanently increased, giving important clues to the mechanism of densification. Compaction results in a decrease of intermediate-range order and reduction in size of the network cages. In glassy GeO_2 this is also associated with a decrease in Ge-O-Ge bond angle with only a slight elongation of the Ge-O bond length. Previous neutron studies are subject to the problem of overlapping correlations, making it impossible to obtain exact details on the Ge-Ge distances. With a combination of neutron and x-ray scattering, new experiments at the APS have been able to highlight the salient structural transformations in densified GeO_2.

In the current work, samples of GeO_2 were synthesized by a sol-gel process and annealed at 1400ºC for 12 hours. The resulting glass was densified at room temperature in a 10-gps diamond anvil cell at Arizona State University. The sample's density increased by 11% and was observed to be stable during the two-year study. Neutron diffraction measurements were performed at the Intense Pulsed Neutron Source at Argonne National Laboratory, and the x-ray scattering was carried out at the BESSRC/XOR beamline ID-11-C at the APS. Taken together, the neutron and x-ray data make it possible to obtain difference structure factors, with each partial structure factor (Ge-Ge, O-O, and Ge-O) eliminated.

From previous studies, it has been long believed that the cation-cation correlations (Ge-Ge) were primarily responsible for the changes in intermediate-range order observed after densification. But the difference structure factors obtained here show that the structural changes are greatest when the Ge-Ge correlations are eliminated and least when O-O correlations are factored out. Given the accepted picture of a network of corner-shared GeO_4 tetrahedra, the most likely explanation is that the tetrahedral units are rotated about the Ge-O-Ge bonds during densification and undergo slight distortion at the same time (Fig. 1).

These results have resolved the complex puzzle of how the network collapses, leading up to a polyamorphic transition in a classic network glass. Because the experiments required accurate data across a wide range of momentum transfers only achievable with high-energy x-rays, they also demonstrate the importance of third-generation synchrotron sources in making such studies feasible. In future, it should be possible to do *in situ* measurements on an absolute scale and follow the details of changes in glass structure all the way through the amorphous transitions. ❍

See: S. Sampath[1,2], C.J. Benmore[2], K.M. Lantzky[1], J. Neuefeind[2], K. Leinenweber[3], D.L. Price[2,4], and J.L. Yarger[1], "Intermediate-Range Order in Permanently Densified GeO_2 Glass," Phys. Rev. Lett. **90**(11), 115502-1 to 115502-4 (21 March 2003).

Author affiliations: [1]University of Wyoming, [2]Argonne National Laboratory, [3]Arizona State University, [4]CNRT-CRMHT

This work was funded in part by the DOE, DOD-ARO, and NSF under Contracts No. DOE-DE-FG-2- 00ER45836, No. NSF-CHE-0094202, and No. DODARO-DAAD19-01-1-0433. Use of the Advanced Photon Source was supported by the U.S. Department of Energy, Office of Science, Office of Basic Energy Sciences, under Contract No. W-31-109-Eng-38.

A DASH OF TELLURIUM SMOOTHES THE WAY TO MORE ORDERLY FILMS OF GERMANIUM ON SILICON

Sandwich a little germanium between layers of silicon, and you've got yourself the heart of a high frequency transistor—if you can keep the germanium film smooth and regular on atomic scales. That's tricky because germanium and silicon atoms naturally arrange themselves in crystal lattices with slightly different spacings. However, as materials scientists from Northwestern University recently found, a dash of tellurium promotes orderly growth.

The atoms in both silicon and germanium fit into diamond structure lattices, and, in principle, it's possible to put down layers of germanium atoms that line up perfectly with the atoms in the silicon substrate, a process called epitaxial growth. However, germanium atoms naturally space themselves about 4% farther apart than silicon atoms, so the atoms in the germanium film are squeezed together horizontally. To compensate, they push farther apart vertically. After just a few layers of growth, the germanium atoms begin to rearrange to relieve the strain, and such "relaxation" creates defects in the film and can even cause the germanium to collect in little islands. The germanium and the silicon from the cap layer may also diffuse into each other, blurring the material interface, which, for most device applications, should be sharply defined.

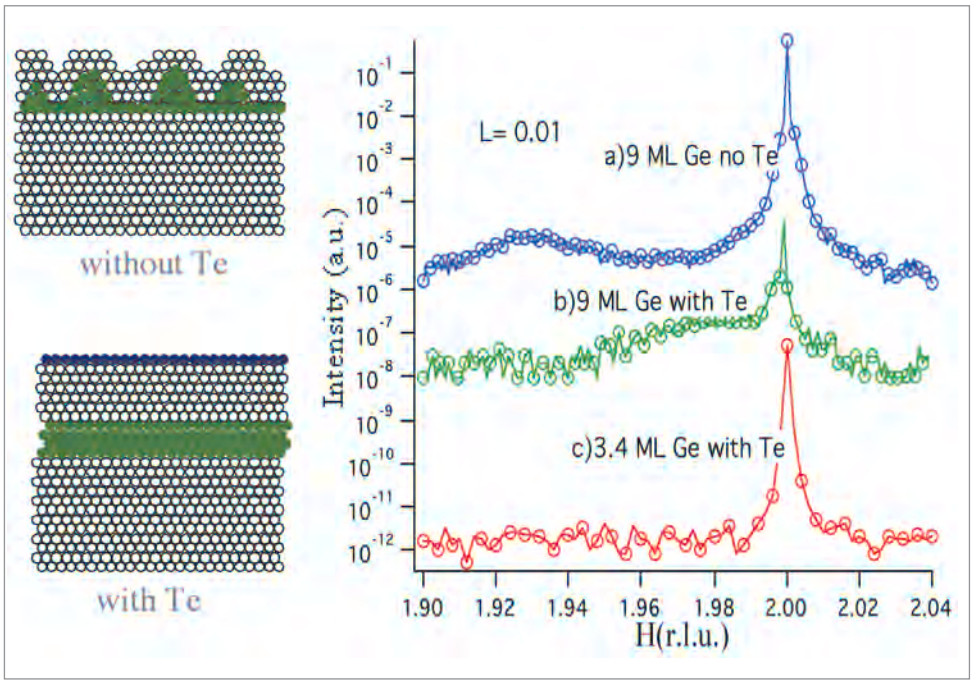

Fig. 1. Grazing incidence x-ray scattering data for a 70-Å Si/9 monolayer (ML) Ge/Si(001) heterolayer structure grown by molecular beam epitaxy with and without a Te atomic layer being used as a surfactant. These are HK scans at H = K and L = 0.01, at which the probed depth should be approximately 100 Å. The peak at H = K = 2.00 corresponds to the Si(220) Bragg peak. a) For the 9 ML Ge/ no-Te GIXD scan, there is evidence of fully relaxed Ge with the peak showing up at H = K = 1.92. b and c) This does not appear when Te is used as a surfactant. (Each set of data is vertically offset for reasons of clarity.) The left side depicts the side view of the resultant morphology for heterolayer structure. Ge/Si intermixing and islanding occur when Te is not used as a surfactant.

Mixing in traces of arsenic, antimony, bismuth, or tellurium helps quell the unruliness by tying up the dangling chemical bonds on the surface as the film grows. For example, a little tellurium inhibits island formation and makes it possible to lay down hundreds of atomic layers of germanium one at a time, although such thick films are still riddled with defects. Now the Northwestern team has shown that tellurium also promotes the growth of strained, defect-free films up to nine layers thick. The tellurium atoms also inhibit the germanium atoms from migrating into the silicon cap, thus creating an atomically sharp interface. To prove it, the researchers employed a pair of x-ray techniques that revealed the atomic-scale structure of germanium films grown on a silicon (001) surface and capped with more silicon.

The team studied the vertical distribution of germanium by using x-ray standing waves in experiments at the DND-CAT beamline 5-ID-C at the APS and the National Synchrotron Light Source beamline X15A. Monochromatic x-rays diffracted off lattice planes in the silicon substrate, and the incident and diffracted beams interfered to create a standing wave that permeated the germanium above and caused it to fluoresce. Researchers scanned the angle of the incident x-rays through the diffraction condition, which moved the planes of maximum intensity through the germanium and revealed the distribution of the material. Measurements around several diffraction peaks showed that for films grown in the presence of tellurium, germanium up to nine layers thick remained defect free. Without the tellurium, films just 3.7 layers thick relaxed and formed defects.

The researchers next studied the horizontal distribution of the germanium at the DND-CAT beamline by using a technique known as grazing incidence x-ray diffraction (GIXD). A beam of x-rays struck the sample at an angle so glancing that it could not penetrate deep into the silicon but was almost completely reflected. The beam could still probe the surface of the sample, however, and diffract off lattice planes lying perpendicular to it like a dominoes standing on end. The diffraction measurements showed that for films as thick as nine layers grown with

tellurium, the germanium atoms had the same horizontal spacing as the silicon atoms. But in a nine-layer film grown without tellurium, some of the germanium had relaxed to its usual, looser spacing.

The results show that tellurium impedes the movement of germanium atoms in the accumulating film, inhibiting relaxation and promoting the growth of orderly films. In theory, tellurium should be more effective than arsenic, antimony, or bismuth in smoothing germanium growth, as a single tellurium atom will tie up all the loose bonds from a silicon or germanium atom. It takes a pair of arsenic, antimony, or bismuth atoms to do the same thing. Bolstered by their smooth progress so far, the researchers hope to use tellurium to make thicker defect-free films. ❍

See: B.P. Tinkham, D.M. Goodner, D.A. Walko, and M.J. Bedzyk, "X-ray studies of Si/Ge/Si(001) epitaxial growth with Te as a surfactant," Phys. Rev. B **67**(3), 035404-1 to 035404-6 (15 January 2003).

Author affiliation: Northwestern University

This work was supported by the National Science Foundation's Division of Materials Research under contract numbers DMR-9973436 and DMR-0076097 to Northwestern University and by the Department of Energy under contract number DE-AC02-98CH10886 to Brookhaven National Laboratory, and by the State of Illinois under contract number IBHE-HECA-NWU-96 to Northwestern University. Use of the Advanced Photon Source was supported by the U.S. Department of Energy, Office of Science, Office of Basic Energy Sciences, under Contract No. W-31-109-Eng-38.

QUANTUM LAYERING IN THIN METAL FILMS

Advances in nanotechnology critically depend on understanding the behavior of matter on an atomic scale. As the size of a structure decreases, its properties are increasingly influenced by the nonclassical rules of quantum mechanics. Of particular interest is the question of how thin films grow during atomic deposition onto a substrate. Theory predicts that quantum effects will control the morphology and thickness of the thin films as they grow, but experimental observations of this process have been difficult to obtain. Recently, researchers from the University of Illinois at Urbana-Champaign have used UNI-CAT beamline 33-ID at the APS to form a detailed picture of the growth of thin films of lead.

In metal films, electronic effects are important, and for thicknesses of one to several monolayers, quantum size effects are expected to play a dominant role. One direct manifestation of these effects will be variations in the atomic interlayer spacing as a function of the number of layers. Previous studies have attempted to measure step heights by means of scanning tunneling microscopy and helium atom scattering, but such methods are sensitive only to the topmost layer of the metal films. In the present work, x-ray specular reflection was used to precisely measure changes in the film structure for a wide range of thicknesses.

The samples were prepared by depositing lead vapor from an effusion cell onto a freshly prepared Pb/Si(111)-($\sqrt{3} \times \sqrt{3}$) reconstructed surface maintained at a temperature of 110K. Films were built up incrementally, and their structures were analyzed with each full completion of a new atomic layer. The extended x-ray reflectivity was measured at the 33-ID surface x-ray diffraction station. The incident beam energy was 19.9 keV, and the scattered x-rays were collected with a scintillation point detector. The background-subtracted integrated intensity for coverages of 6 to 18 monolayers are shown in Fig. 1.

Multilayer interference fringes appear in the reflectivity plots between the large silicon (111) and (333) Bragg peaks at reciprocal lattice units 3 and 9, respectively, and the smaller lead (111), (222), and (333) Bragg peaks at l = 3.3, 6.6, and 9.9, respectively. In the figure, inverted triangles mark the positions of prominent fringes at l = 4.8 and 8.1, which are half-

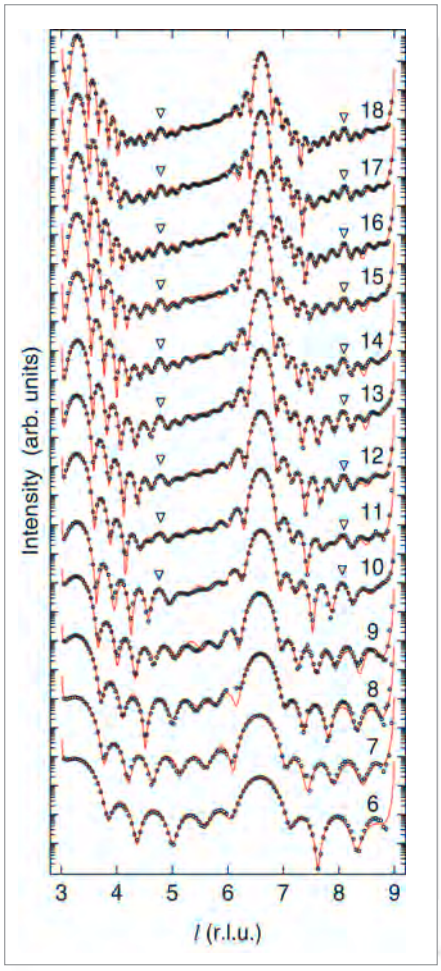

Fig. 1. Extended x-ray reflectivity for lead thin films with thicknesses from 6 to 18 monolayers. Open circles are the measured data. Solid red lines are fits to calculated reflectivity patterns based on lattice distortions derived from charge density variations in a quantum well. Inverted triangles indicate positions of prominent half-order features originating from quasibilayer periodicity. (r.l.u. = reciprocal lattice unit).

order features arising from a quasibilayer periodicity in the layer structure. These features are a direct consequence of quantum confinement of the electrons in the lead film, and they are accurately reproduced by a model of charge density variations in a one-dimensional quantum well structure. Charge imbalances cause the atomic layers to be shifted from their ideal bulk positions in an alternating fashion, leading to an effective near-doubling of the unit cell periodicity and the prominent interference fringes halfway between the lead Bragg peaks. As a further test, the researchers found that these results are also consistent with previous scanning tunneling microscopy and atomic scattering data.

A key finding of this work is that quantum confinement on an atomic layer scale can cause structural alterations that extend throughout a film, a phenomenon that must be understood in the application of metal films to nanotechnology. In addition, the ability to obtain these kinds of details of nanolayered materials at atomic resolution also shows the power of third-generation synchrotron facilities such as the APS. Future studies will investigate the effects that quantum confinement can have on other film properties, including stability and relative surface energy. ❍

See: P. Czoschke, H. Hong, L. Basile, and T.-C. Chiang, "Quantum Oscillations in the Layer Structure of Thin Metal Films," Phys. Rev. Lett. **91**(22), 226801-1 to 226801-4 (28 November 2003).

Author affiliation: University of Illinois at Urbana-Champaign

This work is supported by the U.S. Department of Energy Grant No. DEFG02-91ER45439) The UNI-CAT facility at the APS is supported by the University of Illinois at Urbana-Champaign, Frederick Seitz Materials Research Laboratory (U.S. DOE, and the State of Illinois-IBHEHECA); the Oak Ridge National Laboratory (U.S. DOE under contract with UT-Battelle LLC); the National Institute of Standards and Technology (U.S. Department of Commerce); and UOP LLC. Partial equipment and personnel support from the Petroleum Research Fund, administered by the American Chemical Society, and the U.S. National Science Foundation (Grant No. DMR-02-03003). Use of the Advanced Photon Source was supported by the U.S. Department of Energy, Office of Science, Office of Basic Energy Sciences, under Contract No. W-31-109-Eng-38.

SOFT GRAPHITE BECOMES SUPERHARD UNDER HIGH PRESSURE

Carbon exhibits a rich structural chemistry because of its ability to form linear (sp), trigonal (sp^2), and tetrahedral (sp^3) hybridized bonds. Recent successes in synthesizing new forms of carbon have stimulated considerable theoretical and experimental interest in synthesizing new allotropes. The processes that initiate and govern these transformations are only beginning to be understood, despite their great scientific and technological importance.

In the transformation of graphite under cold compression, there is a marked increase in electrical resistivity above 15 GPa, a sharp drop in optical reflectivity, broadening of the pure-graphite E_{2g} Raman line from 9 to 15 GPa, an increase in optical transmittance above 18 GPa, and changes in x-ray diffraction patterns beginning at 14 GPa. These observations have led to speculations that the high-pressure phase may be a hexagonal diamond phase, an intermediate phase between graphite and diamond, or an amorphous phase.

Researchers from The University of Chicago, the Carnegie Institution of Washington, Brookhaven National Laboratory, Argonne National Laboratory, and the University of Alaska performed a direct characterization of the π and σ bonding of compressed graphite by using synchrotron-based inelastic x-ray scattering (IXS) spectroscopy. They ground a single-crystal graphite sample into a fine polycrystalline aggregate and loaded it into a diamond anvil cell (DAC). Under uniaxial com-

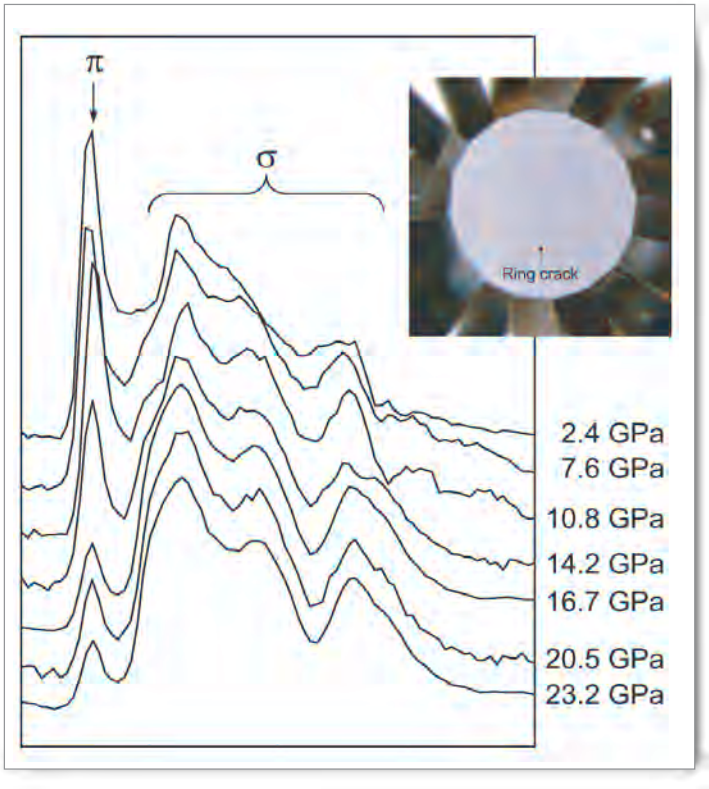

Fig. 1. IXS spectra for compressed graphite plotted as normalized intensity (i.e., scattered intensity normalized to the incoming intensity) versus energy loss (incident energy minus analyzer energy). The spectra were taken in the vertical direction, which probes the c plane. The lower energy peak corresponds to transitions associated with π bonding and the higher energy portion corresponds to transitions associated with σ bonding. After the transition at ~17 GPa, the σ bonds increase at the expense of the π bonds. The insert shows a photomicrograph of the indentation of a diamond anvil by the compressed, superhard graphite sample.

pression, the polycrystalline graphite sample quickly developed a strong preferred orientation, so IXS spectra for specific crystallographic directions were obtained by repeatedly reorienting the DAC.

To investigate structural changes in the sample while avoiding the complication of a strong preferred orientation and peak broadening due to uniaxial stress, the researchers conducted an x-ray diffraction study to 24 GPa by using a helium hydrostatic medium. Monochromatic x-radiation at 37.45 keV gave rise to diffraction patterns that were collected with a charge-coupled device detector at the GSECARS 13-BMD beamline; the results were subsequently confirmed at the HP-CAT 16-ID-B beamline at the APS.

Graphite was found to undergo a transition at ~17 GPa when compressed under ambient temperature. The near-K-edge spectroscopy of carbon using synchrotron-based IXS revealed that half of the π bonds between the graphite layers converted to σ bonds, whereas the other half remained as π bonds in the high-pressure form (Fig. 1). The x-ray diffraction pattern of the high-pressure form was consistent with a distorted graphite structure in which bridging carbon atoms between graphite layers pair and form σ bonds, while non-bridging carbon atoms remain unpaired with π bonds.

The new phase exhibited exceptional hardness (see insert in Fig. 1). After releasing the pressure on the high-pressure phase (without the helium pressure medium), the researchers found that the graphite sample had left a ring crack indentation on the diamond anvils that traced the original boundary of the sample. In normal DAC operation, ring cracks have been observed only when a diamond anvil is indented by another superhard material, such as an opposing beveled diamond anvil. The reversible, orders of-magnitude change in strength from very soft graphite to a superhard material offers the possibility of intriguing applications, such as uses as a pressure-dependent structural component (for instance, a composite gasket for a high-pressure apparatus). ❍

See: W.L. Mao[1,3], H.-k. Mao[1,3], P.J. Eng[1,2], T.P. Trainor[2,6], M. Newville[2], C.-c. Kao[4], D.L. Heinz[1], J. Shu[3], Y. Meng[5], and R.J. Hemley[3], "Bonding Changes in Compressed Superhard Graphite," Science **302**(17), 425-427 (October 2003).

Author affiliations: [1]The University of Chicago, [2]GSECARS, The University of Chicago, [3]Carnegie Institution of Washington, [4]Brookhaven National Laboratory, [5]HP-CAT, Argonne National Laboratory, [6]University of Alaska

Use of the HP-CAT facility was supported by the U.S. Department of Energy (DOE), Basic Energy Sciences; DOE National Nuclear Security Administration; the NSF; the Department of Defense, Tank-Automotive and Armaments Command; and the W.M. Keck Foundation.Use of the Advanced Photon Source was supported by the U.S. Department of Energy, Office of Science, Office of Basic Energy Sciences, under Contract No. W-31-109-Eng-38.

New Opportunities for Actinide Science

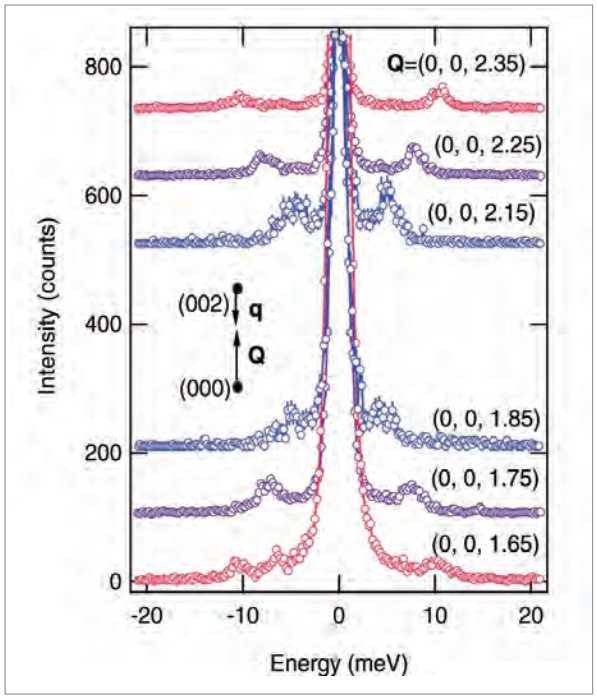

Although first known for its unique nuclear properties, uranium also exhibits several unusual solid-state properties that may be studied in terms of quantized lattice vibrations (phonons). Despite the development of inelastic neutron scattering techniques in the 1950s and 1960s, there remains little phonon-dispersion data for many actinides, including uranium. This is because many isotopes have large neutron absorption cross sections, and, even in cases where a suitable isotope exists, crystals large enough for neutron scattering (>0.1 cm^3) were rarely grown successfully.

Researchers from the Institute for Transuranium Elements and Los Alamos and Argonne National Laboratories have begun changing this situation by taking advantage of the development of high-resolution inelastic x-ray scattering (IXS) at the APS. Synchrotron-based IXS offers a great opportunity because uranium crystals can be much smaller and, unlike with neutrons, the technique IXS has no special isotope requirements.

In a demonstration experiment, high-purity uranium crystals were grown at Argonne and mounted in a small vacuum chamber at the XOR 3-ID beamline. The researchers obtained phonon-dispersion curves at room temperature with an incident energy of 21.657 keV (λ= 0.57 Å). This energy was chosen to give a maximum flux at a resolution of ~2 meV but was unfortunately just 700 eV *above* the L_2 edge of uranium at

Fig. 1. Raw data, counted 60 seconds per point, showing the dispersion of the [00ζ] longitudinal-optic phonon mode through the (002) zone center. The scattering vector, Q, is on the c-axis. The phonon wave vector, q, conserves momentum according to Q = G + q, where G is a reciprocal lattice vector pointing to the nearest reciprocal lattice point.

20.95 keV. Since the crystal thickness of ~1 mm was far larger than the penetration depth, all measurements had to be performed in reflection. This requirement represents the most significant disadvantage of IXS for heavy elements in comparison to traditional neutron scattering, since the latter can operate in transmission without the complications involved in thinning crystals.

Nevertheless, the test experiment was a considerable success. Phonon count rates of ~1 count/s were obtained from a scattering volume of only ~2×10^{-3} mm^3, which translates to an equivalent scattering mass of ~40 µg. Modes displacing atoms along [00ζ] and propagating in all three high-symmetry directions were measured. Whereas the acoustic modes agreed with corresponding neutron-scattering measurements, the longitudinal-optic branch frequencies (Fig. 1) were about 10% higher in energy, yet were consistent with the higher cutoff energies observed in phonon density-of-states measurements involving polycrystals.

This experiment demonstrates the feasibility of a number of experiments, such as uranium phonon dispersion, as a function of temperature and pressure. These experiments are now being planned. ❍

See: M.E. Manley[1], G.H. Lander[1,2], H. Sinn[3], A. Alatas[3], W.L. Hults[1], R.J. McQueeney[1], J.L. Smith[1], and J. Willit[3], "Phonon dispersion in uranium measured using inelastic x-ray scattering," Phys. Rev. B **67**, 052302-052304 (27 February 2003).

Author affiliations: [1]Los Alamos National Laboratory, [2]Institute for Transuranium Elements, [3]Argonne National Laboratory

Use of the Advanced Photon Source was supported by the U.S. Department of Energy, Office of Science, Office of Basic Energy Sciences, under Contract No. W-31-109-Eng-38.

REVEALING THE KINETICS OF PHASE TRANSFORMATIONS IN BULK METALLIC GLASS

For the first time, researchers, using the APS, have applied simultaneous diffraction and small-angle x-ray scattering (SAXS) with high-energy x-rays. They used this technique to investigate the kinetics of the amorphous-to-crystalline phase transformation in $Zr_{52.5}Cu_{17.9}Ni_{14.6}Al_{10}Ti_5$ bulk metallic glass (BMG). Key benefits of this new technique are that (1) it simultaneously probes transformation behavior at two different length scales and (2) the significant penetration power of high-energy x-rays ensures that the measurements are representative of bulk behavior.

Investigating phase transformation kinetics is important because phase transformations are a promising way of making nanostructured materials in large quantities. Potential benefits of increasing the production of nanostructured materials include lower cost and greater market penetration of products that incorporate nanostructured materials. Phase transformations involving nanostructured materials usually occur under conditions far from equilibrium. Although thermodynamics ultimately determines the equilibrium phase for a given set of conditions, whether—and how—the nanostructured phase is produced from the meta-stable precursor depends on kinetic processes.

The *in situ* annealing study was carried out at the XOR 1-ID beamline by using 81-keV x-rays (Fig. 1). Researchers used bulk metallic glass BAM-11, the composition of which was $Zr_{52.5}Cu_{17.9}Ni_{14.6}Al_{10}Ti_5$. The samples were 1-mm-thick disks with a diameter of 8 mm. The glass and crystallization temperatures, T_g and T_x, were 628K and 714K, as determined from differential scattering calorimetry at a heating rate of 10 K/min. Annealing at 681K–713K leads to 2–10 nm crystalline particles based on x-ray diffraction and transmission electron microscopy studies. Samples were measured in transmission geometry, yielding a probe volume of $0.1 \times 0.1 \times 1$ mm^3, and heated by using a furnace constructed at XOR sector 1 at the

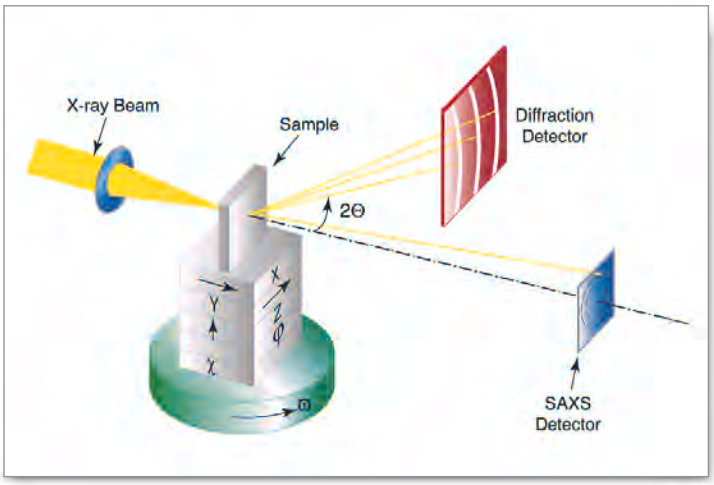

Fig. 1. Schematic diagram of the experiment set-up. Diffraction and small-angle scattering data were recorded simultaneously by using two area detectors. The diffraction detector was mounted on one side to capture a greater range of Q. The samples were 1-mm-thick discs with a diameter of 8 mm. High-energy x-rays (80.7 keV) easily penetrated the sample thickness, ensuring that the measurements were representative of the bulk. Note that the dimensions are not drawn to scale.

APS. Researchers using beamline 1-ID have recently developed a pinhole-based SAXS camera using high-energy x-rays with a Q range of 0.008–0.2 Å^{-1}, where Q is the magnitude of the momentum transfer. To determine the kinetics of both phase separation and crystallization, researchers simultaneously recorded the diffraction and SAXS intensities using two area detectors.

A key finding is that nucleation and growth of the crystalline phase in $Zr_{52.5}Cu_{17.9}Ni_{14.6}Al_{10}Ti_5$ BMG occur in separate stages, with different kinetics. Phase separation occurred first, setting the stage for crystallization. The crystalline phase obtained by

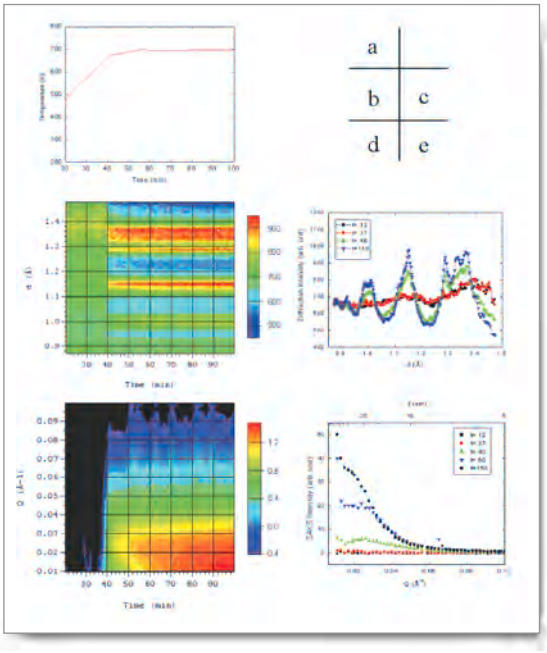

Fig. 2. Simultaneous diffraction and SAXS data obtained with high-energy synchrotron x-rays. (a) Temperature of the sample for 20<t<100 min. (b) Kinetic diffraction diagram for 20<t<100 min. (c) Diffraction patterns at selected annealing times; prominent diffraction peaks appeared at t = 40 min. (d) Kinetic diagram of SAXS intensity for 20<t<100 min (in log scale). (e) SAXS profiles at selected annealing times. The top axis gives the corresponding length scale $\left[d=\frac{2\pi}{Q}\right]$ that is being probed.

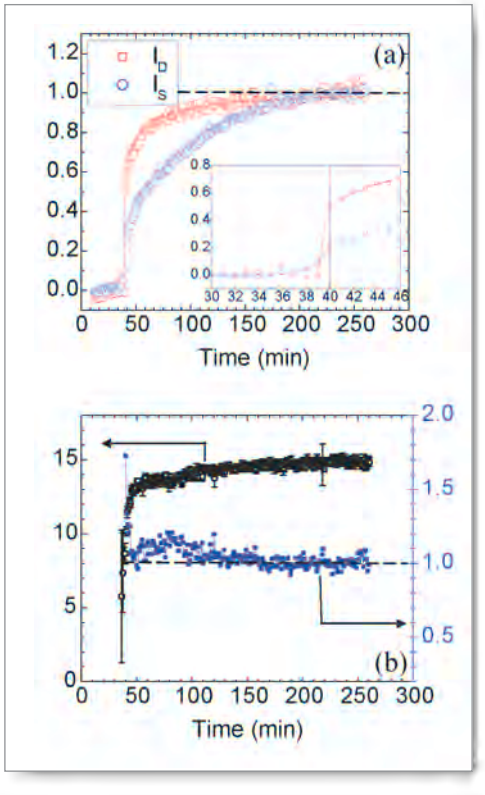

Fig. 3. (a) Integrated diffraction (I_D) and small angle scattering (I_S) intensities as a function of time. (b) Evolution of D_g and $\frac{I_D}{D_g^3}$. D_g is a representative particle size determined from a Guinier analysis of the SAXS data. For a system consisting of uniform-sized particles, $\frac{I_D}{D_g^3} \propto N$, where N is the number of particles. The flat profile seen for $\frac{I_D}{D_g^3}$ indicates that N is held constant during growth. The values of I_D, I_S, and have been normalized to unity (dashed lines) at equilibrium (t>200 min).

annealing at T ~ 700K is primarily Zr_2Ni, suggesting that Ni and/or Zr atoms are involved in nucleation. How is nucleation of the crystalline phase possible? Researchers believe that the mechanism of nucleation is the homogenous formulation of Ni-rich clusters resulting from the local exchange of atoms. The experimental results support such a mechanism: the first appearance of the SAXS intensity was captured during heating at T = 630K, just above T_g.

Figure 2 shows the simultaneous diffraction and SAXS data. A remarkable feature shown in Fig. 2c is the abrupt change at t = 40 min., when prominent diffraction peaks suddenly appeared. . Figure 3(b) shows the evolution of D_g, which is a representative particle size determined from a Guinier analysis of SAXS data. The Guinier analysis yields a representative particle size, D_g, of about 15.0±0.3 nm in final equilibrium. By measuring the diffraction and SAXS data simultaneously, the researchers were able to uncover how the BMG material transforms by exploring the kinetics at two different length scales.

The research is not only the first of its kind, but it also has significant implications in terms of applying scattering technology in other ways. For example, researchers found that scattering instruments that can simultaneously measure diffraction and small-angle scattering provide a unique tool for studying phase transformation behaviors and kinetics under non-equilibrium conditions. Also, researchers expect to gain a better understanding of the development of nanostructures as a result of their research. In fact, several instruments under construction at the Spallation Neutron Source have been designed on the basis of anticipated advances in nanostructure technology resulting from these studies.

In summary, APS researchers were able to probe the kinetics of phase transformations at different length scales. The results of the experimental work show that partial crystallization in $Zr_{52.5}Cu_{17.9}Ni_{14.6}Al_{10}Ti_5$ BMG proceeds in two separate stages—nucleation and growth—with distinctively different kinetics. In addition to providing valuable insight into kinetic mechanisms in this material, the implications of the research are significant in that they may help influence the degree to which nanotechnology will advance in the marketplace. ❍

See: X.-L. Wang[1,2], J. Almer[3], C.T. Liu[2], Y.D. Wang[1], J.K. Zhao[1], A.D. Stoica[1], D.R. Haeffner[3], and W.H. Wang[4], "*In situ* Synchrotron Study of Phase Transformation Behaviors in Bulk Metallic Glass by Simultaneous Diffraction and Small Angle Scattering," Phys. Rev. Lett. **91**(26), 265501-1 to 265501-4 (31 December 2003).

Author affiliations: [1]Oak Ridge National Laboratory, [2]Oak Ridge National Laboratory, [3]Argonne National Laboratory, [4]Chinese Academy of Sciences

This research was supported by Division of Materials Sciences and Engineering, Office of Basic Energy Sciences, U.S. Department of Energy under Contract No. DE-AC05-00OR22725 with UT-Battelle, LLC.Use of the Advanced Photon Source was supported by the U.S. Department of Energy, Office of Science, Office of Basic Energy Sciences, under Contract No. W-31-109-Eng-38.

USING X-RAY SCATTERING TO CHARACTERIZE THE NANOSTRUCTURES OF DOT ARRAYS

Nanodot systems (periodic arrays of nanostructured dots) are drawing great interest for their potential use in future high-density optical and magnetic media storage devices. Researchers at the APS have demonstrated that x-ray scattering can be used to precisely characterize these deep nanostructures to a degree of accuracy that has been unattainable with microscopy techniques.

The novel electrical, magnetic, and photonic properties of nanodot systems are based on their structural parameters. Quantitative analysis of an x-ray diffraction pattern from a mesoscopic two-dimensional array of nanofabricated dots is challenging because its reciprocal space density is many orders of magnitude higher than those of typical solid-state or biological crystals.

Researchers from Argonne National Laboratory; The University of California, San Diego, Los Alamos National Laboratory, the University of Illinois at Chicago; and Cornell University have overcome that challenge: they found that the diffraction pattern exhibits characteristic features because of the highly anisotropic nature of the instrumental resolution function, which can be understood as analogs of Kossel lines—or pseudo-Kossel lines. Although such an unusual diffraction pattern had already been observed [1], researchers at the APS have gone beyond previous research to explain this unique pattern by using a clear, simple resolution function.

The sample for analysis was prepared by using a standard lithography and lift-off process to fabricate a square array of circular disk-shaped dots with a period of 750 nm and a diameter of 340 nm. E-beam lithography was used to prepare the required pattern in a single poly(methyl-methacrylate) layer, and e-beam evaporation was used to deposit a 50-nm-thick Gd film. An area of 0.5 x 0.5 mm^2 was patterned on a 10 x 10-mm^2 Si/SiO_2 wafer. Researchers then took x-ray diffraction measurements using 9-keV monochromatic x-rays at the XOR beamlines 1-BM, 2-BM, and 4-ID-D at the APS. In contrast to scanning electron microscopy (SEM) or atomic force microscopy (AFM)—which are highly effective microscopy tools for topical measurements—the primary benefit of x-ray scattering is that the measurements take the structural average of the entire sample.

By using their technique, researchers can characterize the "deep" nanostructures that can be difficult to characterize by using SEM or AFM (Fig. 1). Moreover, once researchers combined their technique and analysis concept with magnetization-sensitive x-ray or neutron measurements, they found that the diffraction measurements from the mesoscopic magnetic dot (or pattern) arrays could be explained without a failure, and excellent results were finally obtained [2, 3].

The research at the APS demonstrates that x-ray scattering augments the capabilities of SEM and AFM, since it can be used to characterize the structural details of deep nanostructures and measure the buried interfaces. Ultimately, the work at the APS may help to advance nanofabrication technology. ❍

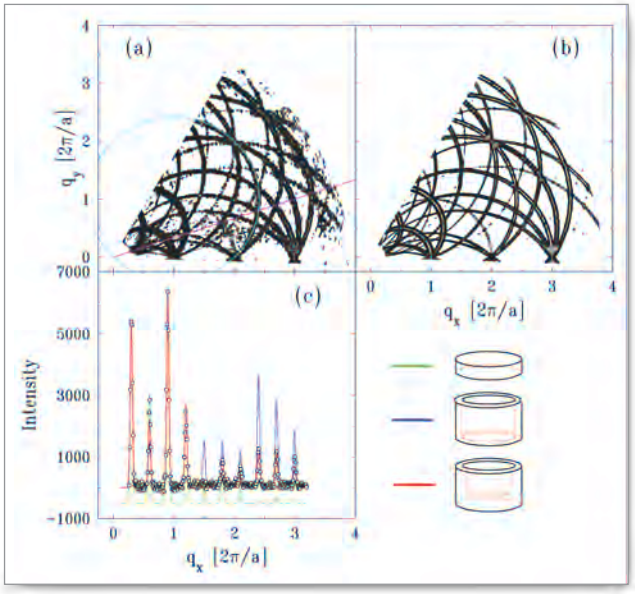

Fig. 1. Contour map of intensity distribution in the q_x–q_y reciprocal plane: (a) measurements and (b) calculations with horizontal resolution width of 2.75 x 10^{-3} $Å^{-1}$. For reference, 2π/a corresponds to 8.37 x 10^{-4} $Å^{-1}$. The circle in (a) shows a pseudo-Kossel circle. Pseudo-Kossel lines, like real Kossel lines in crystalline samples, can be used for precise characterization of the nanostructures of the dot array. (c) Diffraction intensities of the radial scan along the (3 1) direction, the trajectory of which is indicated by the line in (a). Circles represent measurements, and lines represent the calculations with different models: circular disks (green), ring cylinders (blue), and crowns (red), as shown in the inset. For clarity, the green line is shifted.

References

[1] D. Rafaja, V. Valvoda, J. Kub, K. Temst, M.J. Van Bael, and Y. Bruynseraede, Phys. Rev. B 61, 16144 (2000).

[2] D.R. Lee, G. Srajer, M.R. Fitzsimmons, V. Metlushko, and S. K. Sinha, Appl. Phys. Lett. 82(1), 82 (2003).

[3] D.R. Lee, J.W. Freeland, G. Srajer, S.K. Sinha, V. Metlushko, and B. Ilic, submitted to Phys. Rev. B; (available at http://xxx.lanl.gov/abs/cond-mat/0309672).

See: D.R. Lee [1], Y.S. Chu [1], Y. Choi [1], J.C. Lang [1], G. Srajer [1], S.K. Sinha [2], V. Metlushko [3], and B. Ilic [4], "Characterization of the nanostructures of a lithographically patterned dot array by x-ray pseudo-Kossel lines," Appl. Phys. Lett. **82**(6), 982-984 (10 February 2003).

Author affiliations: [1]Argonne National Laboratory, [2]University of California, San Diego, and Los Alamos National Laboratory, [3]University of Illinois at Chicago, [4]Cornell University

V.M. is supported by NSF Grant No. ECS-0202780. S.K.S. is supported by the U.S. Department of Energy (DOE), Office of Science, Office of Basic Energy Sciences (BES)-Materials Sciences and Engineering Division under contract No. W-7405-Eng-36. Use of the APS supported by the U.S. DOE, Office of Science, BES, under Contract No. W-31-109-Eng-38.

EVALUATING THE FORCED OXIDATION OF FERROMAGNETIC CONTACTS IN MAGNETIC TUNNEL JUNCTIONS

Magnetic tunnel junction (MTJ) devices are broadly used because of the ability attain high values of tunneling magnetoresistance (TMR). However, the role of interface structure is key to the performance of these devices. To understand this issue, researchers need to determine how best to form a high-quality insulating oxide spacer without influencing the quality of neighboring ferromagnetic contacts. At the APS, researchers studied forced oxidation of ferromagnetic contacts in magnetic tunnel junctions. As a result of their research, they concluded that microstructure plays an important role in determining the impact of the oxidation process on the layers.

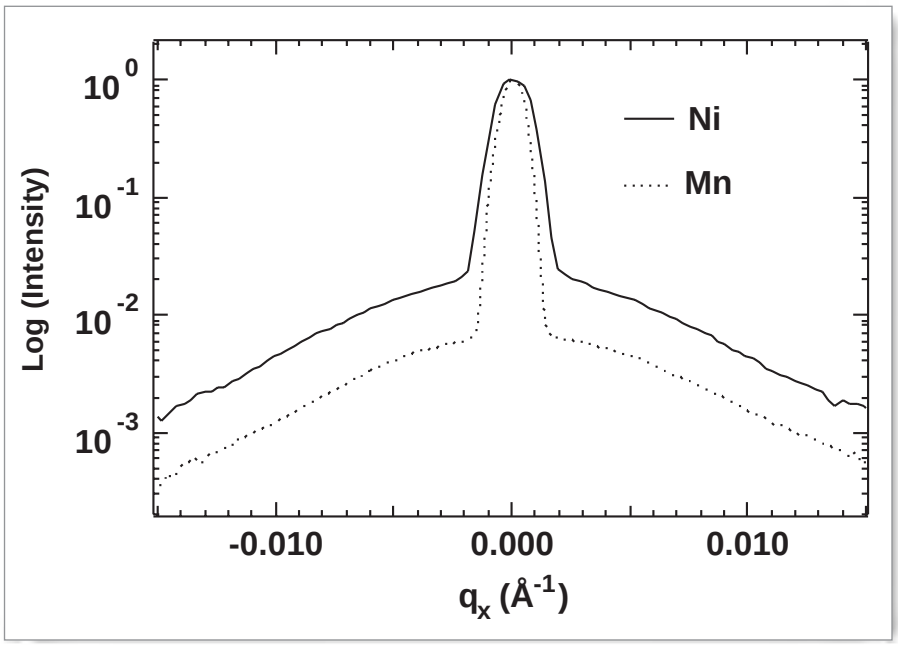

Fig. 1. X-ray resonant rocking curves at the Ni and Mn L_3 edges measured after field annealing.

Experiments were performed at XOR sector 4 of the APS by using the intermediate energy beam line (4-ID-C). Researchers used samples consisting of an MTJ with a wedge-shaped Al oxide-insulating layer. The full structure was SiO_2/IrMn/CoFe (30 Å)/Al_2O_3(x Å)/NiFeCo(30 Å), where x ranges from 5–20 Å. Polarization-dependent X-ray absorption and scattering—which is element-selective and therefore layer-selective—was used to provide detailed information about the chemical and magnetic state of the separate layers.

Although the absorption provides insight into a large portion of the CoFe layer, the TMR is still strongly sensitive to the oxidation at the Al_2O_3/CoFe interface. By using x-ray reflectivity at the Co L_3 resonance, which is sensitive to the top 2–3 Å of CoFe, researchers can directly probe the chemical state at the boundary. If the oxide is present first in the grain boundary, it will show clearly in the absorption. However, the grain boundary comprises a small fraction of the interface, and so the interface signal will be dominated by the Al_2O_3/metal CoFe signature. This is also consistent with nonzero MR in the overoxidized region. Until the aluminum thickness is reduced to around 6 Å, there are still regions of metallic CoFe in contact with Al_2O_3. The MR decreases in this region because the density/area of metal/Al_2O_3 is decreasing.

Another major issue to address is the change in the structure after annealing in applied field to 200°C, which is required for attaining the highest TMR values. Are changes in the magnetic response due to structural or magnetic changes? Measurements of the x-ray resonant diffuse scattering allow the chemical and magnetic interface structure to be determined in a layer-by-layer fashion. Scattering at the Mn, Co, and Ni L3 edges provides element- (and, therefore, layer-) specific information. Figure 1 shows a set of rocking curves measured at the Mn and Ni L edges. By analyzing the rocking curves, researchers found that the preanneal structure is characterized by a conformal roughness (perpendicular roughness = 3 Å and in-plane roughness = 300 Å) propagating through the whole structure. After the anneal, there is no change, indicating that the structure is stable under these conditions and all magnetic changes are due solely to dipolar fields from the alignment of the random domains on the IrMn exchange bias layer. This finding confirms that the origin of changes in the TMR must be magnetic, not structural.

Overoxidizing the layers of a magnetic tunnel junction provided new insights into the impact of unwanted oxidation. APS researchers concluded that, from the evidence of grain boundary diffusion, the microstructure plays and important role in determining the impact of the oxidation process. From the perspective of TMR, they found that the main contribution to the change with field annealing appeared to be due to change in the layer-dependent switching after field annealing. ❍

See: J.W. Freeland[1], D.J. Keavney[1], R. Winarski[1], P. Ryan[1], J.M. Slaughter[2], R.W. Dave[2], and J. Janesky[2], "Grain boundary mediated oxidation and interlayer dipolar coupling in a magnetic tunnel junction structure," Phys. Rev. B **67**, 134411-1 to 143311-4 (17 January 2003).

Author affiliations: [1]Argonne National Laboratory, [2]Motorola Labs

Work at Motorola Labs was supported in part by DARPA. Use of the Advanced Photon Source was supported by the U.S. Department of Energy, Office of Science, Office of Basic Energy Sciences, under Contract No. W-31-109-Eng-38.

NEW INFORMATION ON MAGNETIC SEMICONDUCTORS

Manipulation of electron spin, as well as charge, in electronic devices may allow researchers to examine and control spin under very well controlled environments and to develop new functions in future magnetic semiconductor-based devices. A key question is resolving the details of the electronic structure and the origin of the states that participate in the magnetic coupling. To fully realize the potential of this technology, APS researchers sought to fully understand the origin of ferromagnetic ordering in Mn-doped GaAs. By using x-ray magnetic circular dichroism at the Mn, Ga, and As $L_{3,2}$ edges, researchers using the XOR 4-ID-C soft x-ray beamline at the APS have detected induced Ga and As moments in ferromagnetic $Ga_{1-x}Mn_xAs$.

Mn-doped GaAs is ideal for exploring the origins of ferromagnetic ordering in this class of materials. Polarized holes that are primarily derived from As 4p valence band states are generally thought to mediate the coupling between Mn. Recent calculations of the band structure for Mn-doped GaAs predict an induced magnetic moment on the As atoms that is antiparallel to the Mn 3*d* moments and a smaller parallel Ga moment. Soft x-ray magnetic circular dichroism (XMCD) provides element-specific magnetic information, so it is a powerful technique to test for the presence of these moments.

APS researchers found an As magnetic moment antiparallel to the Mn and a very small parallel Ga moment by using XMCD at the Mn, Ga, and As $L_{3,2}$ edges in molecular beam epitaxy (MBE) -grown films of $Ga_{1-x}Mn_xAs$ (with x = 0.039, 0.049, 0.059, 0.07, and 0.081). The 4-ID-C soft x-ray beamline was used to make the XMCD measurements. Researchers used total electron yield to measure x-ray absorption and dichroism. Dichroism scans were taken at fixed photon polarization by reversing the magnetization of the sample at each energy.

Figure 1 shows a plot of the Mn, Ga, and As L edge dichroism taken from the x = 0.07 sample. As shown in the figure, both the As and Ga L_3 data display a weak dichroism at the onset of the absorption edge jump, indicating a magnetic moment on each. By applying selection rules to these transitions, researchers determined that the orientations of the induced host moments are antiparallel to the Mn for As and parallel for Ga. Figure 2 shows the field and temperature dependence of the Ga and Mn signals. This figure shows that the Ga dichroism signal follows very closely that of the Mn and is clearly associated with the ordering of the Mn. These results are consistent with the notion that polarized As valence band holes mediate the ferromagnetic coupling between Mn ions in $Ga_{1-x}Mn_xAs$. By comparing the areas under the As and Ga L_3 dichroism curves, researchers obtained an estimate of the relative sizes of the As and Ga *s* spin moment per hole.

By using soft x-ray magnetic circular dichroism, APS researchers detected induced moments on both Ga and As in the ferromagnetic semiconductor $Ga_{1-x}Mn_xAs$ and determined the relative spin orientations of each atomic species. They found, for example, that the As average moment is aligned antiparallel to that of the Mn, while the Ga is parallel. The results show that the hole states that mediate the ferromagnetic ordering are derived primarily from As, and that these As valence band states are antiferromagnetically coupled to the Mn 3*d* moments.

These results support the hole-mediated model of coupling in magnetic semiconductors and identify the electronic states that are involved. This investigation will help other researchers design new materials with enhanced magnetic properties. A principal goal is a room-temperature

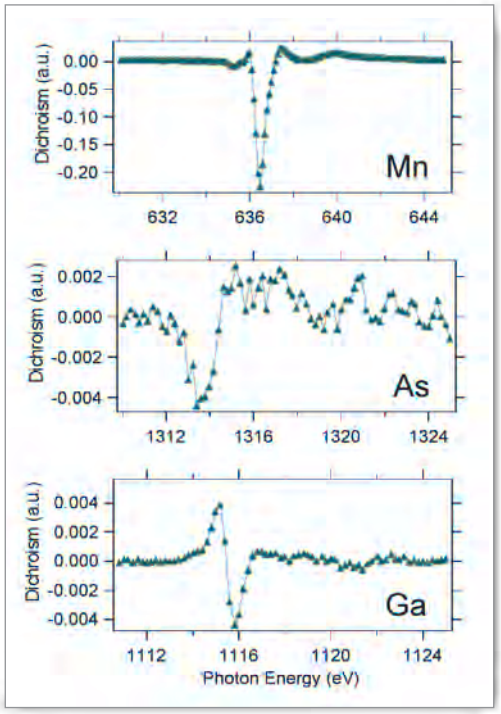

Fig. 1. X-ray magnetic circular dichroism observed at the Mn, As, and Ga L_3 edges for the x = 0.07 sample.

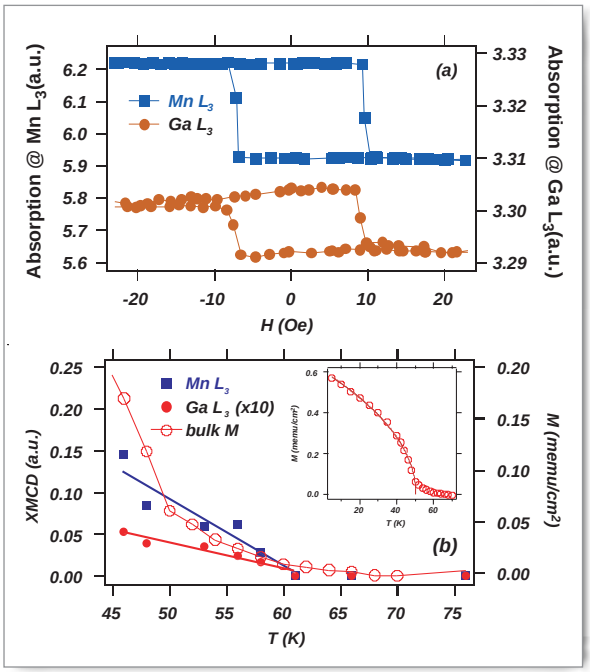

Fig. 2. Magnetic field (a) and temperature (b) dependence of the dichroism signals seen at the Mn and Ga L edges for x = 0.049. Field dependence data were taken at 44K, and temperature dependence at zero field. Inset in (b) shows bulk magnetization (M) data for the same sample.

magnetic semiconductor that is compatible with the existing semiconductor fabrication technology, which is important for the realization of spin-based devices. Researchers are now using the APS to examine similar issues in other Mn-doped semiconductors, such as GaN and InAs. Further experiments are planned on $Ga_{1-x}Mn_xAs$ to examine in greater detail the locations of the Mn ions within the GaAs lattice. ❍

See: D.J. Keavney[1], D. Wu[2], J.W. Freeland[1], E. Johnston-Halperin[3], D.D. Awschalom[3], and J. Shi[2], "Element Resolved Spin Configuration in Ferromagnetic Manganese-Doped Gallium Arsenide," Phys. Rev. Lett. **91**(18), 187203-1 to 187203-4 (31 October 2003).

Author affiliations: [1]Argonne National Laboratory, [2]University of Utah, [3]University of California, Santa Barbara

Work at the University of Utah was supported by the ONR/DARPA under Grant No. N00014-02-10595, and at UCSB by ONR/DARPA under Grant No. N00014-99-1-1096 and AFOSR F49620-02-10036. Use of the Advanced Photon Source was supported by the U.S. Department of Energy, Office of Science, Office of Basic Energy Sciences, under Contract No. W-31-109-Eng-38.

A Quantitative Picture of Strain Generation Due to Dense Electron-hole Plasmas

Researchers from the University of Michigan; the University of California, Berkeley; Kansas State University; the University of Oxford; and University College in Cork, Ireland, are pioneering a new technique for studying strain generation and propagation in crystalline solids. The APS's high-brightness, short-pulse, hard x-rays permit probing of coherent strain generation and propagation in both the frequency and time domains through the use of time-resolved x-ray anomalous transmission, which, unlike other methods, can provide quantitative structural information.

X-rays establish two standing waves upon propagating along a particular direction through a periodic medium. These consist of an anomalous transmission wave (α-wave), which is minimally absorbed, and a β-wave, which is strongly absorbed. In thick crystals, the β-wave is absorbed almost completely, so what exits the crystal is mainly the anomalous wave, which propagates as two x-ray beams, one in the direction of the incident beam and the other in a deflected direction. The researchers have shown that a short acoustic pulse directed at the x-ray exit face of the crystal can coherently transfer energy between the α and β beams. Following an initial transient, the diffracted x-ray intensities oscillate in time as the pulse travels into the crystal. The relative phase of the oscillations and the amplitude of the transient provide information about the strain generation process at times shorter than the duration of the x-ray probe.

The researchers recently used the new technique as a bulk-sensitive structural probe in studying the propagation and lattice coupling of dense electron-hole plasmas produced by a subpicosecond laser. The experiments were performed at the MHATT/XOR 7-ID beamline, where the x-ray energy was set to 10 keV using a cryogenically cooled Si(111) double-crystal monochromator. Coherent strain pulses were produced on the x-ray exit face of a 280-μm thick germanium (Ge) single crystal by sub-100-fs, 800-nm laser pulses focused to a 1.5 mm^2 spot on the crystal surface. A fast silicon avalanche photodiode (APD) and a picosecond x-ray streak camera were used as the time-resolved detectors of the two exiting x-ray beams; the APD sampled the deflected-diffracted beam intensity while the streak camera sampled the forward-diffracted beam. X-ray bunch separation was about 152 ns, which is large enough to allow electronic gating and measurement of single x-ray pulses. This is critical for ultrafast experiments where the laser repetition rate is typically considerably less than that of the x-ray pulses.

Following laser excitation, high-contrast oscillations were observed in the time-resolved x-ray data over a large span of excitation densities. The transient behavior is due to a perturbation in the lattice that reached a depth of more than 1.5 μm within 40 ps. Conceptualizing the strain as a moving interface that couples the α and β waves, the researchers concluded that the excitation must initially propagate into the bulk at speeds greater than 37,000 m/s, which is more than seven times the longitudinal speed of sound. The results are consistent with a picture in which electron-phonon coupling modified by carrier diffusion is the dominant mechanism for energy transport in laser-excited Ge. This research can be extended to study how the elastic response of the material can modify the electronic transport properties of semiconductors. ❍

See: M.F. DeCamp[1], D.A. Reis[1], A. Cavalieri[1], P.H. Bucksbaum[1], R. Clarke[1], R. Merlin[1], E.M. Dufresne[1], D.A. Arms[1], A.M. Lindenberg[2], A.G. MacPhee[2], Z. Chang[3], B. Lings[4], J.S. Wark[4], and S. Fahy[5], "Transient Strain Driven by a Dense Electron-Hole Plasma," Phys. Rev. Lett. **91**(16), 165502-1 to 165502-4 (17 October 2003).

Author affiliations: [1]University of Michigan, [2]University of California, Berkeley, [3]Kansas State University, [4]University of Oxford, [5]University College

This work was supported in part by the U.S. Department of Energy, Grants No. DE-FG02-03ER46023 and No. DE-FG02-00ER15031; by the AFOSR under Contract No. F49620-00-1-0328 through the MURI program, and from the NSF FOCUS physics frontier center. S. F. acknowledges the financial support of the Science Foundation Ireland. Use of the Advanced Photon Source was supported by the U.S. Department of Energy, Office of Science, Office of Basic Energy Sciences, under Contract No. W-31-109-Eng-38.

LOCAL STRUCTURE OF MAGNETORESISTIVE OXIDES

Manganese-based magnetoresistive oxides are receiving increased attention because they show promise in a wide variety of applications, particularly spin-based electronics, or "spintronics." The properties of magnetoresistive oxides depend sensitively on the structure of the MnO_6 octahedral building blocks that make up the crystal lattice. A deeper understanding of local structure—often studied using pair distribution function (PDF) analysis or x-ray absorption fine structure (XAFS)—is important because in many alloys it often differs from the average crystal structure probed by x-ray or neutron diffraction. Such diffraction studies have shown that in $LaMnO_3$, the four short and two long bonds of the MnO_6 octahedra exhibit a Jahn-Teller distortion that is removed by Sr doping ($La_{1-x}Sr_xMnO_3$). At an Sr composition of x ~0.175, no long-range Jahn-Teller distortion exists at room temperature in the average structure. Previous studies of the local MnO_6 structure used the PDF of $La_{1-x}Sr_xMnO_3$ (LMSO) as a function of x at 10K and near room temperature to show that the local MnO_6 structure does differ from the average structure. The lengths of both the short and long Mn-O bonds changed little until local distortion disappeared, possibly forming localized three-site polarons though additional work produced conflicting results.

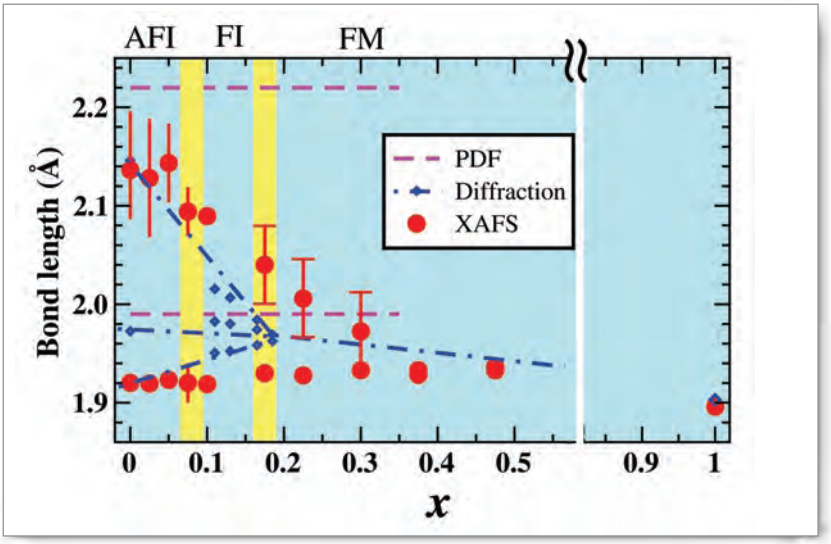

Fig. 1. Mn-O bond lengths as a function of x at 10K, Dots show low-temperature average structure from diffraction experiments. Hatched line is phase boundary: AFI (antiferromagnetic insulator), FI (ferromagnetic insulator), FM (ferromagnetic metal).

Using data collected at the MR-CAT 10-ID beamline at the APS, investigators from the University of Notre Dame and Argonne National Laboratory provided a more detailed picture of local structure by measuring Mn K-edge XAFS at T ≈ 10K and room temperature (290K) for various alloy compositions in the region x <0.475, thereby establishing the local MnO_6 structure as a function of x. They discovered some distortion in the metallic phase, where x varied between 0.175 and 0.3, but found the bond length-splitting to be substantially smaller than the PDF results and the local distortion of MnO_6 strongly correlated with the electronic phase diagram.

Samples for the Mn K-edge XAFS experiments were those previously used for La K-edge and Sr K-edge XAFS studies. The Mn K-edge XAFS spectra were measured at sample holder temperatures of T ≈ 10K and 290K in transmission mode at the MR-CAT beamline at the APS. Duplicate or triplicate measurement of each sample allowed a check on the repeatability and noise level of the spectra, and a Fourier transform was fit to a model built with theoretical scattering paths.

Several different fit methods were used to deal with parameter correlations among the Mn-O bond lengths, the Debye Waller Factor (DWF), and the population of short and long bonds. For example, the number of long bonds (N_L) and the DWF are strongly correlated. N_L was thus constrained according to four models among which N_L varied.

The first coordination shell carries six oxygen atoms with 8 La/Sr second neighbors and 6 third neighbors around Mn ions. A systematic edge-energy shift with Sr composition is consistent with the LSMO or other manganite systems, was observed. The long bond peak—a distinct feature for the $LaMnO_3$—appears in samples with low Sr doping and shifts with doping for x <0.175, nearly disappearing for x >0.175 (Fig. 1). The largest deviation from the PDF results exists in the low-x region (x <0.35). More detailed examination of these parameters shows either the absence of the bond at distances above 2.08 Å or a large length distribution, suggesting a maximum possible long bond length of about 2.08 Å, much shorter than that of $LaMnO_3$ (2.15 Å) or PDF results (2.22 Å). Room temperature results were similar to those at low temperature.

The finding that $LaMnO_3$ had three different bond lengths in average structure corroborates the previous PDF finding of three different bond lengths in local structure. The residual distortion found in the ferromagnetic metallic phase x >0.175 is less than the PDF results. The XAFS results suggest that the structure does change with doping. Taken together, the data allow a detailed view of the Mn-O bonds. ❍

See: T. Shibata[1], B.A. Bunker[1], and J.F. Mitchell[2], "Local distortion of MnO_6 clusters in the metallic phase of $La_{1-x}Sr_xMnO_3$," Phys. Rev. B **68**, 024103-024112 (2003).

Author affiliations: [1]University of Notre Dame, [2]Argonne National Laboratory

The MR-CAT is supported by the U.S. Department of Energy (DOE), DE-FG02-94-ER45525 and the member institutions. Use of the Advanced Photon Source was supported by the U.S. Department of Energy, Office of Science, Office of Basic Energy Sciences, under Contract No. W-31-109-Eng-38.

Probing Picosecond Domain Dynamics in Ferroelectrics by Using Synchrotron X-ray Beams

Synchrotron x-rays open new doors for studying materials: researchers are now able to investigate much faster processes, analyze much weaker interactions among materials, and go much deeper into a material's interior—all at much better spatial resolution than before. In fact, the systematic use of synchrotron radiation for materials characterization has led to breakthroughs in many aspects of materials science. A good example is time-resolved x-ray diffraction measurements of very fast switching processes in ferroelectric thin films.

Researchers from the Technion-Israel Institute of Technology, and Northwestern University used the DND-CAT 5-BM-D beamline at the APS to carry out stroboscopic diffraction measurements with ferroelectric films subjected to strong periodic electric fields. The group found that the electric-field-induced variations of lattice parameters, as a function of delay time between the x-ray and electric signals, are well described by damped periodic functions, with the periodicity defined by the electric field frequency. They also found that the damping parameter is directly related to the system's attenuation time. They attribute the latter finding to the hindering of domain walls during domain switching as a result of their interaction with the arising deformation waves. This information may be important to the operation of devices based on ferroelectric films.

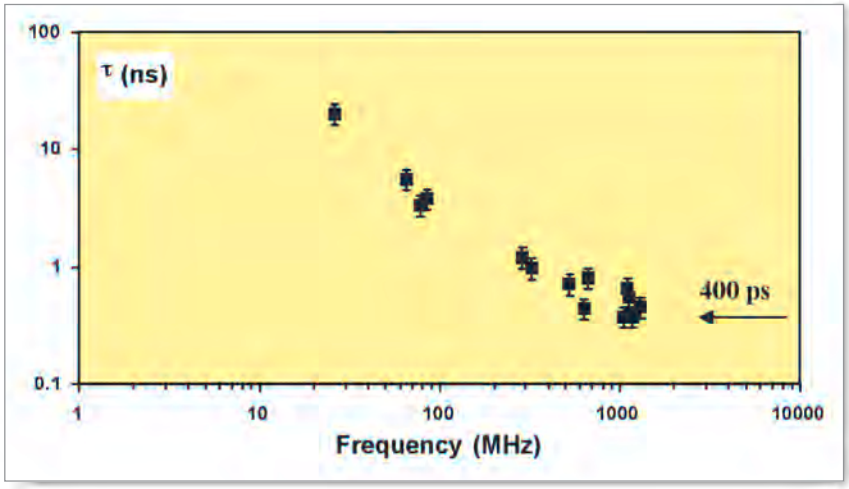

Fig. 1. Attenuation times, τ, of domain motions stroboscopically measured in a wide range of electric field frequencies between 25 MHz and 1.3 GHz.

Ferroelectric materials have built-in electric dipoles, which produce net electric polarization without an external electric field (as magnetization in magnetic materials). Ferroelectric thin films are very promising for next-generation random access memories (RAM), since, in principle, these memory elements can be "trained" and used like in neural networks. As is the case for magnetic memories, the major factor that will determine the speed of future device operation will be the dynamics of ferroelectric domains in the ns to ps time scale. Today, researchers do not know how fast the ferroelectric memory could be and what the sources of limiting factors are. Complexity is increasing as domain size is reduced, which, in thin films, ranges from a few tens to a few hundreds of a nanometers. Probing fast-domain dynamics under an applied electric field in such nanostructures requires the development of novel experimental techniques.

The research at the APS is significant in that a novel experimental technique—stroboscopic x-ray diffraction on synchrotron beamlines—has now been used to characterize domain motion. This technique utilizes in-time synchronization between synchrotron x-ray bursts and periodic external field (in this case, an electric field) applied to the sample. In the stroboscopic mode of measurement, the phase difference between the periodic electric signal and the x-ray burst periodicity is kept constant during a single measurement run. After that, the phase shift is changed by means of a programmable delay unit, and measurements are continued. Changes in lattice parameters, measured as a function of the delay time, make domain dynamics "visible," providing spectral characteristics of domain motion.

In this research, 200-nm-thick $BaTiO_3$ films, epitaxially grown on 500-μm-thick (100) MgO substrates, served as samples. Researchers used the stroboscopic registration of 25-keV x-rays diffracted from the ferroelectric films under an alternating current electric field with an amplitude of a few MV/m. For this purpose, electric pulses with a frequency of 6.517 MHz from a bunch clock generator of the APS storage ring were passed through a programmable delay unit (the minimal step was 18 ps) and applied to the input of a frequency synthesizer. The latter generated sinusoidal signals of multiple frequencies between 25 MHz and 1.3 GHz, which were phase-locked to the x-ray burst periodicity. After amplification, the sinusoidal signals were applied to the ferroelectric films via interdigital electrodes deposited on top of them.

The measured attenuation times revealed rapid reduction with the electric field frequency (see Fig.1). Shorter attenuation time means heavier damping of domain motion. In these experiments, researchers were able to measure extremely short attenuation times (down to 400 ps), which demonstrates the capabilities of the developed technique. On the basis of the collected experimental data, researchers concluded that, despite heavy damping, ferroelectric domains in $BaTiO_3$ films can be effectively switched by the applied electric field at least up to 1.3 GHz.

Further experimental and theoretical studies of domain damping are required in order to clarify the particular mechanisms, which are responsible for the observed relationship between attenuation time and frequency. ❍

See: E. Zolotoyabko[1], J.P. Quintana[2], D.J. Towner[2], B.H. Hoerman[2], and B.W. Wessels[2], "Nanosecond-Scale Domain Dynamics in $BaTi0_3$ Probed by Time-Resolved X-ray Diffraction," Ferroelectrics **290**, 115-124, (2003).

Author affiliations: [1]Technion-Israel Institute of Technology, [2]Northwestern University

DND-CAT is supported by the E. I. DuPont de Nemours & Co., the Dow Chemical Company, the U.S. NSF through grants DMR-9304725 and the State of Illinois through the Department of Commerce and the Board of Higher Education grant IBHE HECA NWU 96. Additional financial support from NSF under grant DMR-0076077 and ECS-0123469. Use of the Advanced Photon Source was supported by the U.S. Department of Energy, Office of Science, Office of Basic Energy Sciences, under Contract No. W-31-109-Eng-38.

ROOM-TEMPERATURE FERROMAGNETIC SEMICONDUCTORS: A CLOSER LOOK AT A PROMISING CANDIDATE

Ferromagnetic semiconductors that remain magnetic at and above room temperature are critical to the development of spintronics. Co-doped TiO_2 anatase is an oxide semiconductor that exhibits ferromagnetism well above room temperature. The thermally robust ferromagnetism is thought to be mediated by electrons from oxygen vacancies, but the mechanism has been elusive. Knowledge of the local structure of the magnetic dopant is critical to determining whether the magnetism is caused by elemental Co nanocrystals, or whether Co is a magnetic dopant in the host lattice. The latter is a necessary but insufficient condition for the material being a magnetic semiconductor. Investigators from the Pacific Northwest National Laboratory (PNNL) in Richland, Washington, used the APS to produce data showing that Co-doped TiO_2 anatase has a structure favorable for ferromagnetic semiconductor formation.

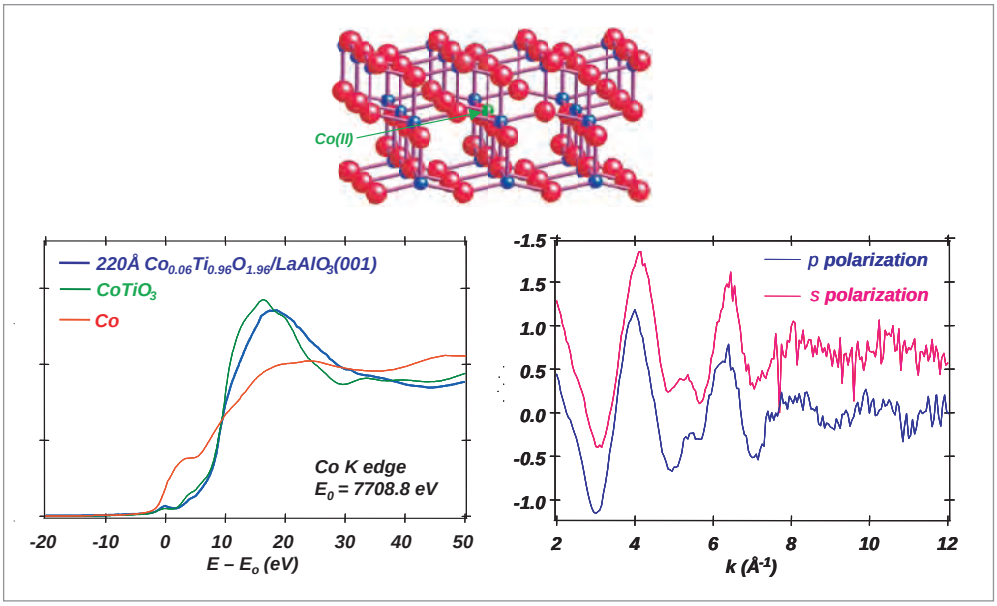

Fig. 1. Left: K-shell XANES for a 22-nm-thick $Co_{0.06}Ti_{0.94}O_{1.94}$ epitaxial film on $LaAlO_3(001)$ and appropriate standards. These spectra establish that the formal oxidation state of the Co is +2. Right: Co K-shell EXAFS for the same specimen in both s- and p-polarizations. The crystal model shows Co(II) substituting for Ti(IV) in the lattice, with an O vacancy adjacent to the Co(II). The O vacancy is required to maintain local charge neutrality.

Based on extensive previous research focused on the nucleation and growth of this material, the PNNL team used oxygen-plasma-assisted molecular beam epitaxy (OPAMBE) to grow epitaxial $Co_xTi_{1-x}O_2$ on $LaAlO_3(001)$ to produce either semiconducting or insulating films. Co K-shell x-ray absorption spectra for two representative films were used to determine the local structure around the Co dopant. One film, grown under oxygen-rich conditions, was insulating and atomically flat. A second film, grown under slightly oxygen-poor conditions, was semiconducting, but consisted of two phases—a continuous epitaxial anatase phase with very little Co, and smaller epitaxial particles of Co-enriched anatase that formed on the surface of the continuous film.

Co K-shell x-ray absorption near-edge structure (XANES) and extended x-ray absorption fine structure (EXAFS) were measured at the APS using the PNC/XOR beamlines 20-ID and 20-BM.

The Co K-edge XANES (Fig. 1, left panel) are virtually identical for the two films and show that Co is in the +2 formal oxidation state. The spectra also reveal that the local structure resembles that of Co in $CoTiO_3$ more than CoO. There is no evidence for Co metal in either film. The Co K-edge is more sensitive to charge state and local structure than Co L-edge XANES, which was used in previous studies. Co L-edge XANES does not discriminate among Co, CoO, and $CoTiO_3$ as effectively.

Co K-shell EXAFS (Fig. 1, right panel) was used to determine the detailed structure of Co(II) in $Co_xTi_{1-x}O_2$. The two specimens exhibited similar oscillations and thus similar local structural environments for the Co. Fourier transforms and multiple scattering analyses for two x-ray polarizations showed bond lengths intermediate between those in pure anatase and the larger Co-O bond lengths in $CoTiO_3$, suggesting local strain fields at substitution sites. The Debye-Waller factors were also higher than expected for room-temperature Co-O bonds, presumably resulting from disorder at Co sites. The

spherically averaged effective coordination number was less than 6, indicating the presence of an oxygen vacancy in the vicinity of substitutional Co ions.

Expelling oxygen from the lattice produces strain relief and allows local charge neutrality to be maintained. Indeed, one O vacancy is required for each substitutional Co(II). The resulting empirical formula for Co-doped TiO_2 is $Co_xTi_{1-x}O_{2-x}$. There is a significant but incomplete structural correlation between oxygen vacancies and substitutional Co(II). These oxygen vacancies do not, however, contribute to electrical conductivity, since the two electrons per vacancy are effectively bound to the nearby Co(II). In order to make the material semiconducting, oxygen vacancies greater than those needed to compensate substitutional Co(II) in $Co_xTi_{1-x}O_{2-x}$ anatase are required.

These results establish that there is no detectable Co metal in OPAMBE-grown doped TiO_2 anatase. The magnetism is correlated with the presence of substitutional Co(II) in the anatase lattice and free carriers resulting from excess O vacancies These results support, but do not prove, that Co-doped TiO_2 anatase is a true ferromagnetic semiconductor. Work on this and other magnetically doped oxide semiconductors is ongoing. ❍

See: S.A. Chambers, S.M. Heald, and T. Droubay, "Local Co structure in epitaxial $Co_xTi_{1-x}O_{2-x}$ anatase," Phys. Rev. B **67**, 100401-1 to 100401-4 (2003).
Author affiliation: Pacific Northwest National Laboratory

See also: S.A. Chambers and R.F.C. Farrow, "New Possibilities for Ferromagnetic Semiconductors," MRS Bulletin **28**, 729 (2003).

The film growth and *in situ* materials characterization described in this paper were performed in the Environmental Molecular Sciences Laboratory, a national scientific user facility sponsored by the DOE's Office of Biological and Environmental Research and located at PNNL. This work was supported by the PNNL Nanoscience and Technology Initiative, the U.S. DOE, Office of Science, Office of Basic Energy Sciences, Division of Materials Science, and the DARPA Spins in Semiconductors Initiative. The PNC/XOR is supported by funding from the U.S. DOE, Basic Energy Sciences, the NSF, the University of Washington, the Natural Sciences and Engineering Research Council in Canada, and Simon Fraser University. Use of the Advanced Photon Source was supported by the U.S. DOE, Office of Science, Office of Basic Energy Sciences, under Contract No. W-31-109-Eng-38.

FERROELECTRIC BONDING REVEALED BY X-RAY SCATTERING

Ferroelectric materials—substances that possess a permanent electric polarization—are of interest for a variety of potential technological applications, from sensors and displays to nonvolatile data storage. Although researchers have made significant progress in the theoretical understanding of these materials, some aspects of their behavior remain puzzling. In particular, the orbital symmetry of the bonds that are associated with the ferroelectric ordering has eluded detailed measurement. Recently, a team of researchers from the University of Pennsylvania and Argonne National Laboratory has used resonant x-ray scattering to observe the details of orbital ordering in a canonical ferroelectric, potassium niobate.

$KNbO_3$ was chosen for the present work in part because the nature of the niobium-oxygen bonds in this material is well understood and the computational results for the band structure are reliable. The ferroelectric properties of $KNbO_3$ arise from the highly directional bonding between the niobium and oxygen atoms (Fig. 1). Techniques such as x-ray absorption near-edge spectroscopy (XANES) have been used in the past to observe the directional bonding, but details of the orbital structure of these bonds are not revealed by these methods. Here, resonant x-ray scattering was used to observe the orbital symmetry in the ferroelectric ordering. Such studies could be extended to other materials, especially Pb- and Nb-based relaxor ferroelectrics.

A beam of polarized x-rays tuned near the niobium K edge at 18.987 keV is incident on a single crystal of $KNbO_3$, which can be rotated to probe either the bonding or the nonbonding direction. Thermal diffuse x-ray scattering is collected near the Bragg peak positions with a solid-state detector, and these data

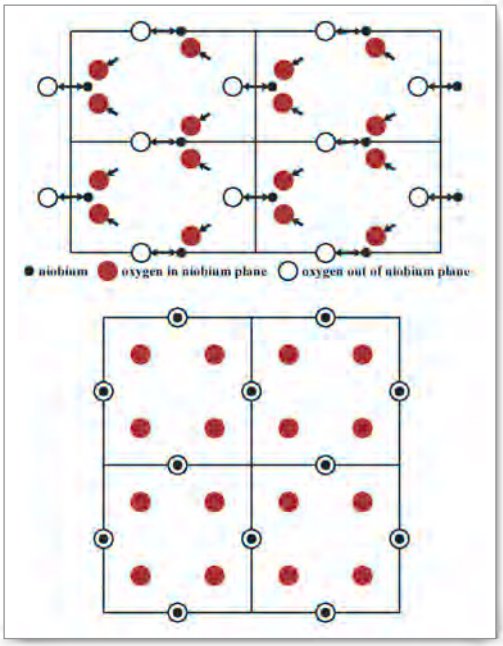

Fig. 1. The structure of niobium and oxygen in potassium niobate. At room temperature, $KNbO_3$ is orthorhombic (top), and displacement of the niobium and oxygen atoms produces a ferroelectric polarization. Above the Curie temperature, the structure is cubic and non-ferroelectric (bottom).

are used to construct x-ray dispersion curves. The anisotropy of the dispersion curves with respect to crystal orientation can be used to deduce the character of the niobium-oxygen bonds. Preliminary data were collected at beamline X25 at the National Synchrotron Light Source (NSLS), Brookhaven National

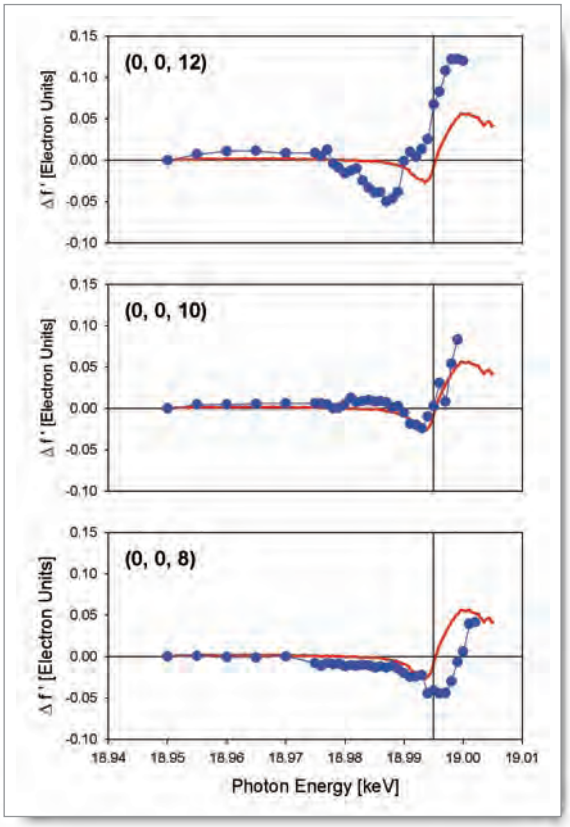

Fig. 2. Difference plots for the real part of the dispersion near the niobium K edge for three scattering momentum transfer vectors Q's. The curves are obtained by subtracting the thermal diffuse scattering collected with x-ray polarization parallel to the lattice b axis from that collected with polarization parallel to the a axis (filled circles). Anisotropy of f' measured by XANES with no momentum resolution is shown as a solid line. The shift of the characteristic features toward lower energy with increasing Q is the result of increased involvement of d states in the bonding orbitals.

Laboratory, while the main set of experiments was carried out at the CMC-CAT beamline 9-ID at the APS.

From the collected data, difference plots of the anomalous dispersion curves are obtained that show the shifts in characteristic features as a function of Q, the momentum transfer vector (Fig. 2). Dipolar transitions involving states of p character are not dependent on Q, whereas the contribution of quadrupolar transition involving d states grows with increasing Q. Thus, the shift toward lower energy indicates that the lowest unoccupied states in the valance band probed by the resonant x-ray scattering are predominantly of d orbital symmetry.

The results show that resonant x-ray scattering can be a useful complement to XANES measurements in studying ferroelectric materials, particularly the details of the bonding that gives rise to their polarization properties. Moreover, given the subtlety of the shifts in anomalous dispersion, the high incident energy resolution offered by the monochromator crystals and third generation synchrotron at APS was essential in carrying out these experiments. Building on these results, the researchers now expect to be able to study even more complex ferroelectrics where the theoretical picture needs to be better understood. ❍

See: E. Mamontov[1], T. Egami[1], W. Dmowski[1], T. Gog[2], and C. Venkataraman[2], "Anisotropic covalent bonds in $KNbO_3$ observed by resonant x-ray scattering," Phys. Rev. B **66**, 224105-1 to 224105-6 (10 December 2002).

Author affiliations: [1]University of Pennsylvania, [2]CMC-CAT

The work at the University of Pennsylvania was supported by the Office of Naval Research through N000-14-01-10860. The NSLS is supported by the U.S. Department of Energy (DOE) Contract No. DE-AC02-98CH10866.Use of the Advanced Photon Source was supported by the DOE Office of Science, Office of Basic Energy Sciences, under Contract No. W-31-109-Eng-38.

UNUSUAL TOPOLOGICAL CHARGE FLUCTUATIONS IN AN ANTIFERROMAGNETIC COPPER OXIDE MATERIAL

High-temperature superconductivity in cuprate materials, colossal magnetoresistance in the manganates, and unusually intense nonlinear optical response in nickelates are all phenomena thought to result from very strong interactions among electrons in these materials. According to theory, some of these compounds should also exhibit other unusual physical properties, such as the separation of charge and spin fluctuations in the form of exotic quanta called holons and spinons. Researchers have been turning to inelastic x-ray scattering as a way of probing the details of electronic structure. Recently, a team of researchers from Princeton University, Argonne National Laboratory, Lawrence Berkeley National Laboratory, the Nano-electronic Research Center in Tsu-kuba, Japan, and the University of Tokyo used resonant x-ray scattering to obtain direct evidence of holons in a strontium copper oxide antiferromagnet.

The strontium copper oxide compounds Sr_2CuO_3 and $SrCuO_2$ are one-dimensional (1-D) quantum antiferromagnets and thus believed to support spin-charge separation. To examine this phenomenon, some method that is sensitive to valence band excitations must be employed. Although x-ray scattering is a useful tool for probing bulk electronic structure, excitations of valence electrons yield a far weaker signal. In earlier work, the research team demonstrated that by tuning the incident x-ray energy near an absorption edge, a large enhancement of the valence band scattering could be observed, making possible detailed momentum-resolved studies of high-Z materials. In addition, because of the high brightness of third-generation synchrotrons such as the APS, scattering studies over the entire Brillouin zone were feasible.

Single-crystal samples of $SrCuO_2$ were grown and characterized for this study by established techniques and found to be

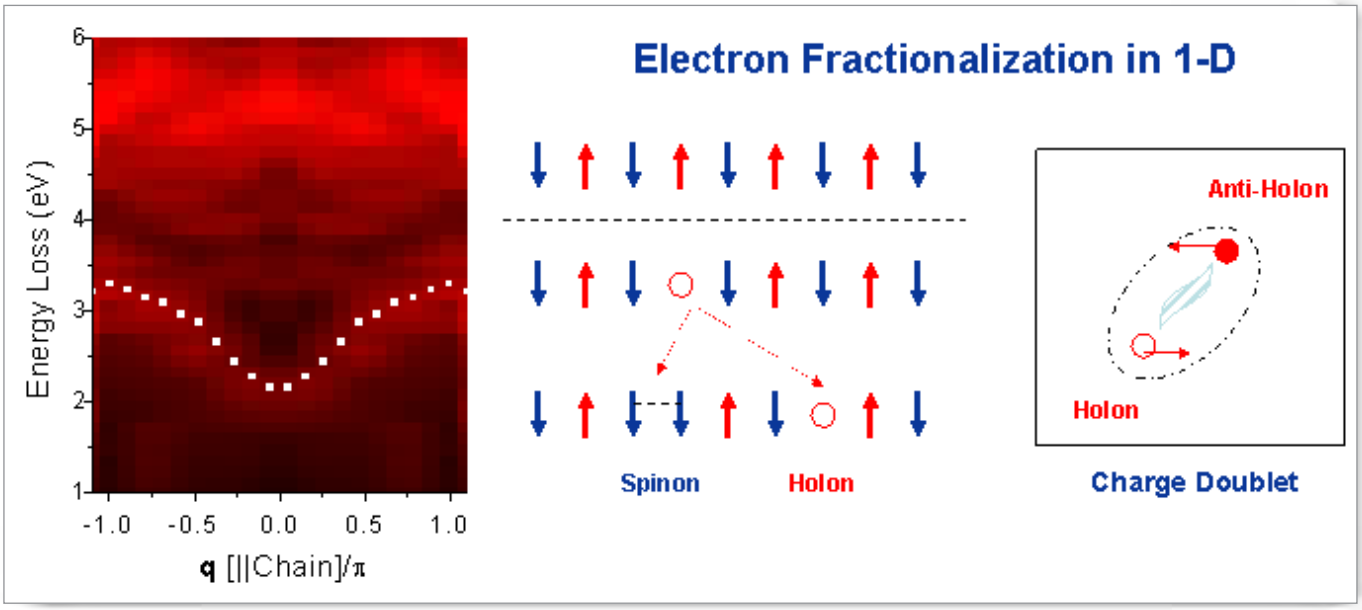

Fig. 1. Left: Dispersion plot of experimental inelastic x-ray scattering features as a function of q (red indicates high spectral intensity). Right: A cartoon view of electron fractionalization in 1-D. X-ray scattering couples to the charge part of the excitations and traces out holon excitation (holon-antiholon) spectrum. The necklace feature in the left figure corresponds to the holon-antiholon spectrum.

1-D spin chain materials at room temperature. The inelastic x-ray scattering data were obtained at the CMC-CAT beamline 9-ID and BESSRC/XOR beamline 12-ID at the APS. The incident beam energy was selected to be near the copper K edge at 8.997 keV to produce resonant scattering. The scattered beam was passed through a germanium spectrometer and measured with a solid-state detector. The overall energy resolution for the experiment was 350 meV. Scans over a range of *q* values were obtained by rotating the spectrometer about the scattering point on the sample. Data were also obtained for scans in energy through the Cu K edge.

Two features are seen in the inelastic x-ray scattering spectra as a function of *q*. One of these is approximately fixed at about 5.6 eV. The other is a lower-energy excitation, which can be interpreted as a particle-hole excitation across the Mott gap in the cuprate spin chain. In particular, the dispersion of this feature parallels the dispersion of the Mott gap itself. Moreover, the *q*-dependence in this 1-D material is stronger than that seen in previous measurements of two-dimensional materials, which is expected for spin-charge separation. A comparison with numerical studies also shows good agreement with holon formation in a half-filled spin-1/2 Hubbard model with charge fluctuations. Considered together, these observations are consistent with the observation of spin-charge separation and the formation of holons and antiholons in this cuprate (Fig. 1).

The data in the present experiment are, by their nature, sensitive primarily to the charge (holon) portion of the excitation. Single spin excitations are much weaker and would appear at a much lower energy than observable in this work. Future efforts, perhaps feasible at high-brightness facilities, such as the Inelastic X-ray Scattering sector 30 at the APS, may allow much higher-resolution experiments that can capture the full range of spin-charge behavior in these interesting materials. ❍

References

[1] M.Z. Hasan[1,2], Y-D. Chuang[3], Y. Li[1], P. Montano[4], M. Beno[4], Z. Hussain[3], H. Eisaki[15], S. Uchida[6], T. Gog[7], and D.M. Casa[7], "Direct Spectroscopic Evidence of Holons in a Quantum Antiferromagnetic Spin-1/2 Chain," Intl. J. of Mod. Phys. B **17**(18, 19, 20), 3479-3483 (2003).

[2] M.Z. Hasan, P.A. Montano, E.D. Isaacs, Z.-X. Shen, H. Eisaki, S.K. Sinha, Z. Islam, N. Motoyama, and S. Uchida, "Momentum-Resolved Charge Excitations in a Prototype One-Dimensional Mott Insulator," Phys. Rev. Lett. **88**, 177403 (2002).

See: Reference [1] above is the source of this article.

Author affiliations: [1]Princeton University, [2]Princeton Materials Institute, [3]Advanced Light Source, [4]Argonne National Laboratory, [5]National Center for Advanced Industrial Science and Technology (Tsukuba, Japan), [6]University of Tokyo, [7]CMC-CAT

This work was partially supported by National Science Foundation grant DMR-0213706. Use of the Advanced Photon Source was supported by the U.S. Department of Energy, Office of Science, Office of Basic Energy Sciences, under Contract No. W-31-109-Eng-38.

X-RAY SCATTERING REVEALS UNUSUAL GROWTH OF LEAD ON SILICON

Most thin films grow on substrates in only three ways: layer by layer, formation of atomic islands, or layers followed by islands. The particular growth mode that a given material will follow crucially depends on the relative magnitudes of the surface energy of the film versus the interfacial energy of the film on the substrate. Recently, a team of researchers from the University of Illinois, Academica Sinica in Taiwan, Georgia Institute of Technology, and the City University of Hong Kong has discovered a remarkable anomaly. By means of real-time x-ray scattering measurements, the researchers found that lead films grown on silicon adopt a completely novel pattern of growth.

Earlier studies of lead films on silicon with scanning tunneling microscopy and electron diffraction revealed hints that certain island heights above the substrate were preferred over others. These "magic" dimensions suggest that quantum size effects play a strong role in the formation of the films. Yet, the magic numbers do not seem to bear any relation to characteristic dimensions or length scales of the films themselves. In order to unravel this puzzle, the researchers also performed first-principles density functional calculations to understand their experimental results.

Real-time x-ray scattering measurements of the film structure were obtained with a growth chamber placed at the UNICAT beamline 33-ID at the APS. Lead vapor from an effusion cell was deposited at a rate of 0.0044 monolayers per second onto silicon substrates prepared to expose the (111)-7X7 surface. A CCD camera captured the scattered 26.05-keV x-rays from the APS undulator beam (Fig. 1) in order to measure reflectivity and truncation rod scattering at regular intervals. Film growth was monitored *in situ* with a vibrating quartz thickness gauge and the temperature of the sample was monitored with a thermocouple.

Truncation rod profiles obtained from the CCD images give a detailed picture of the film evolution during growth. From the interference fringes, information about island height and film thickness is deduced. At first, there is an increase in the intensity of the silicon surface diffraction, indicating that a lead wetting layer is forming, commensurate with the underlying substrate lattice. After a thickness of about 1.1 monolayer, the silicon diffraction intensity decreases, followed by a rise in lead intensity and island formation at a deposition of 1.5 monolayer. At this stage, the islands begin growing up to a height of 5 monolayers above the wetting layer (a net island height of 6 monolayers). Then, in an unusual departure from typical growth modes, the islands remain locked at this height but begin growing horizontally until all of the islands have filled in to form a single 6-monolayer film. Now the growth switches completely from island growth to layer-by-layer growth for the rest of the film's evolution.

Two characteristic thicknesses emerge from this analysis: the 1-monolayer wetting layer, which gives way to island for-

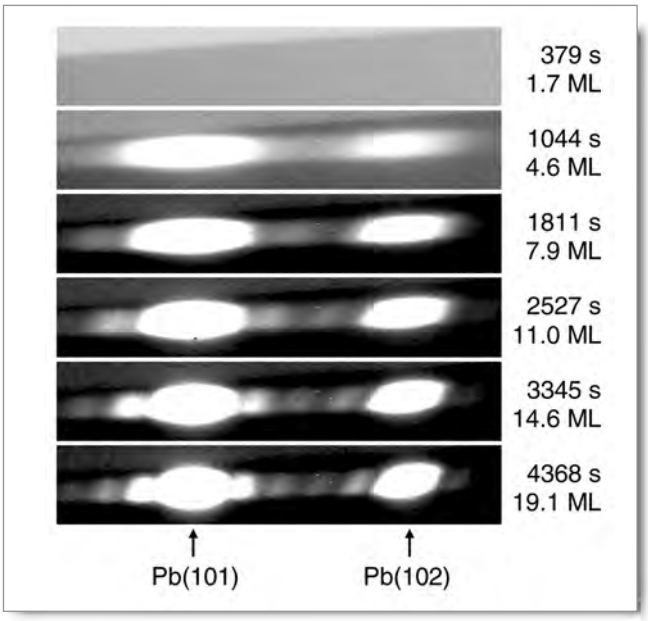

Fig. 1. X-ray diffraction images taken with a CCD camera during growth of Pb films on Si(111). The interference fringes yield information about island height and layer thickness.

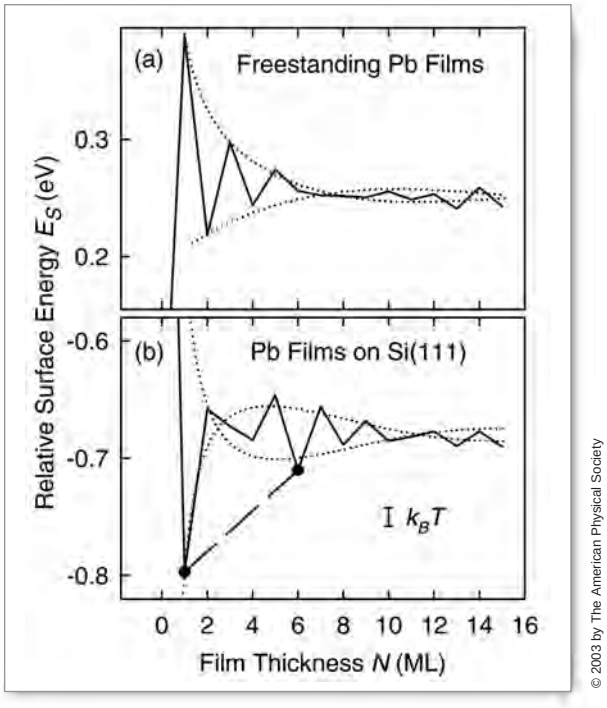

Fig. 2. First-principles calculations of (a) a free-standing Pb film and (b) Pb film on silicon substrate. The altered Friedel oscillations in (b) give rise to energy minima, which account for the magic island height and wetting layer.

mation, and the 6-monolayer magic island height. To make sense of these critical thicknesses, the researchers performed first-principles calculations of the relative surface energy per surface atom of the films (Fig. 2). For free-standing lead films, the energy follows a typical damped Friedel oscillation pattern with a period of 1.8 monolayer. When the calculation is done for lead atoms on a silicon substrate, however, the altered boundary condition produces a phase shift in the envelope function, resulting in deep minima at 1 monolayer and 6 monolayers.

The absolute energy minimum at 1 monolayer explains the wetting layer, while the minimum at 6 monolayers accounts for the magic island height. For coverages between these two values, the system would be expected to phase separate into a linear combination of the two, in excellent agreement with the behavior observed in the island formation. As shown by this work, taking into the consideration the global energy picture and not just the local energy landscape is essential in understanding the complete story of thin-film growth. ❍

See: H. Hong [1], C.-M. Wei [2,3], M.Y. Chou [3], Z. Wu [1], L. Basile [1], H. Chen [6], M. Holt [1], and T.-C. Chiang [1], Phys. Rev. Lett ***90*** (7), 076104-1 to 076104-4 (21 February 2003).

Author affiliations: [1]University of Illinois at Urbana-Champaign, [2]Academia Sinica, [3]Georgia Institute of Technology, [4]City University of Hong Kong

This work was supported by the U.S. Department of Energy (Grants No. DEFG02-91ER45439 and No. DEFG02-97ER45632), the R.O.C. National Science Council (Grant No. 90-2112-M-001-062), the U.S. National Science Foundation (Grants No. DMR-02-03003 and No. SBE-01-23532), and the Petroleum Research Fund administered by the American Chemical Society. The UNI-CAT facility at the APS is supported by the University of Illinois Frederick Seitz Materials Research Laboratory (U.S. Department of Energy and the State of Illinois-IBHE-HECA), the Oak Ridge National Laboratory (U.S. Department of Energy under contract with Lockheed Martin Energy Research), the National Institute of Standards and Technology (U.S. Department of Commerce), and UOP LLC. The APS is supported by the U.S. Department of Energy (Grant No. W-31-109-Eng-38).

Revealing the Nature of Inhomogeneous Magnetic States in Artificial Ferrimagnets

Artificial magnetic layered structures are widely used for applications in information storage (*i.e.*, magnetic memory). Current devices use homogeneous magnetic states, in which the layers' magnetization aligns parallel or antiparallel to an applied magnetic field. Parallel or antiparallel relative alignment of alternate layers results in significantly different electrical resistance, which makes the 0's and 1's of a binary logic base for storage and computation. Inhomogeneous magnetic states, in which the layers' magnetization can be made to orient at a variety of angles with respect to the applied field direction, could be used as a basis for a more complex but efficient logic scheme. The intermediate, inhomogeneous magnetic states also exhibit varying degrees of electrical resistance, which could provide the necessary signatures for higher speed storage and computation.

For years, science has tried to experimentally resolve the mechanism of nucleation of magnetic inhomogeneous states in artificial multilayers. By using grazing incidence x-ray magnetic circular dichroism (XMCD) at the XOR beamline 4-ID at the APS, experimenters from Argonne National Laboratory have successfully measured the low-field surface nucleation and evolution of the inhomogeneous magnetic state in strongly coupled Fe/Gd ferrimagnetic multilayers. The results of their research help explain the effect of surface termination upon nucleation of inhomogeneous magnetic states in magnetic multilayers.

The studies show that at nucleation, the magnetic surface state extends tens of interatomic distances into the bulk (approximately 200 Å) — a direct consequence of the strong antiferromagnetic interlayer coupling between the Fe (35 Å) and Gd (50 Å) layers. In this state, the magnetization deviates from the applied field direction in the near-surface region while it remains field-aligned in the bulk. Tuning the sample temperature to near the compensation temperature, T_0 (at which the sublattice magnetizations are equal but opposite) causes the inhomogeneous state to penetrate throughout the bulk. Homogeneous magnetic states occur far below and above T_0. Surface termination has a dramatic effect on the nature of the inhomogeneous state.

Before the work at APS, several techniques have been used to gather experimental evidence for a magnetic inhomogeneous state. The work at the APS is unique in that researchers took direct, real-space measurements of the low-field nucleation of an inhomogeneous magnetic state near the surface of an Fe-terminated ferrimagnetic multilayer.

For several years, it has been predicted that a phase transition into an inhomogeneous magnetic state would nucleate at the surface of a strongly coupled artificial ferromagnetic multilayer, if the multilayer was terminated by the minority magnetic component. In this “surface-twisted” phase, the magnetization deviates from the applied field direction near the surface, while the bulk remains field-aligned. Unfortunately, probing surface and bulk states in the same measurement has not been possible, making experimental detection of this inhomogeneous phase difficult. The challenge is to observe both the existence of a surface-twisted phase and the absence of a bulk twist.

This challenge was overcome through the use of the brilliant x-ray beams from the APS, which enable the collection of direct, real-space data on the near-surface and bulk magnetic states in the same measurement. This was achieved by exploiting the penetration depth tunability of the x-rays at grazing- and larger-incidence angles to alternately probe the surface and bulk magnetic states.

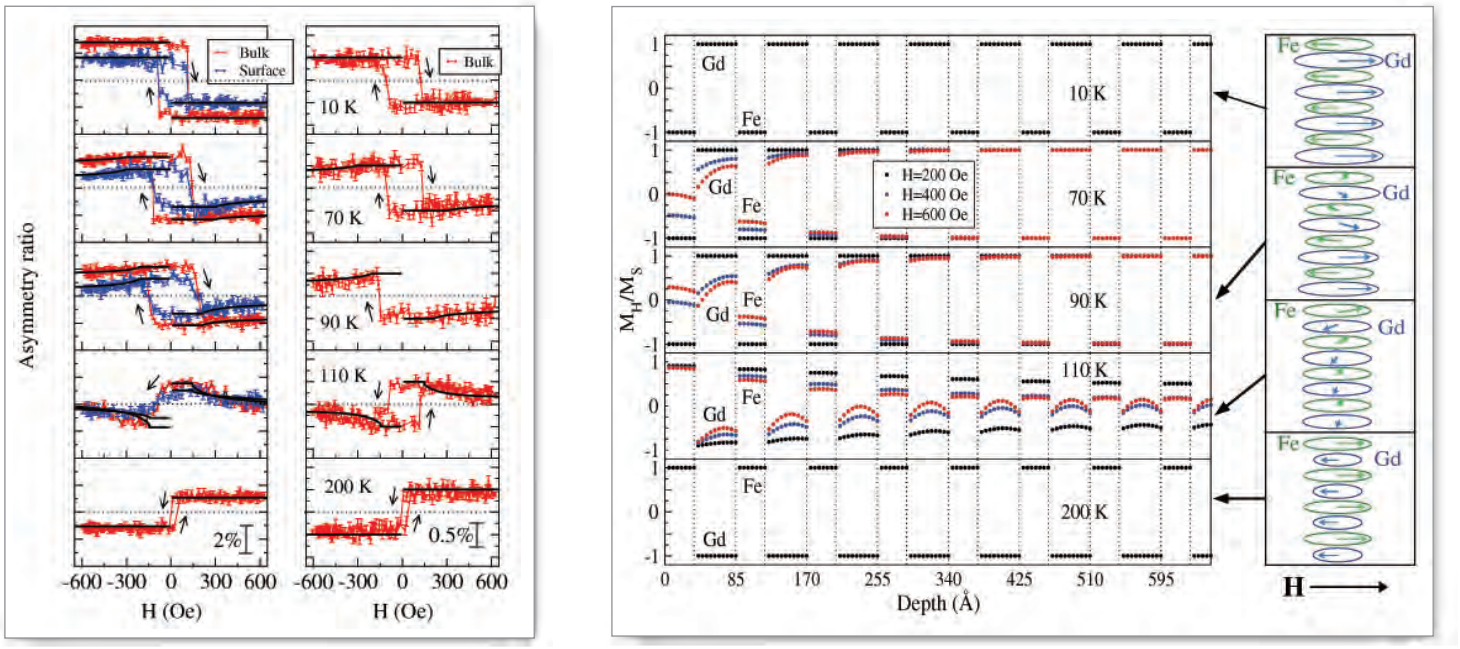

Fig. 1. Left panel: Gd (left) and Fe (right) hysteresis loops (points). Surface loops are scaled down for clarity. Right panel: Theoretical calculations of magnetization depth profiles, shown for half of the multilayer structure (other half is mirror symmetric). Profiles are normalized to saturation magnetization at each temperature. The schematic diagram (far right) represents the magnetization in the upper four bilayers (intralayer averaged) at H = 600 Oe. Calculated hysteresis loops are given by the solid lines superimposed on the data points of the left panel. "Flat" loops correspond to homogeneous magnetic states, while "tilted" loops indicate deviations of the magnetization from the applied field direction.

The unique experimental setup enabled the researchers to simultaneously measure specular reflectivity and XMCD in fluorescence geometry. Element-specific hysteresis loops were then measured at the resonant energies for which the magnetic contrast is the largest by reversing the x-ray helicity at each applied field value and measuring the asymmetry ratio *i.e.*, the difference in the absorption of opposite helicities of circularly polarized x-rays divided by its sum. To accurately determine the x-ray incidence angle, the specularly reflected signal was used. Despite constraints set by a Nb capping layer, researchers were able to retrieve surface-enhanced magnetic information from Gd layers. These constraints, however, led to reduced surface sensitivity at the Fe resonance. A fit to the specular reflectivity data (modified to include roughness) confirmed the nominal structural parameters of the multilayer.

Comparing the experimental results with theoretical calculations of the static magnetization profile validated the accuracy of this approach. Researchers found that the calculations were in good agreement with the experimental results and supported the conclusion of the extent of the penetration depth at nucleation. By contrast, the results of previous attempts to determine the penetration depth at nucleation indicated that it was several thousand angstroms—a significant difference. The results at the APS are the first to directly confirm the long-ago predicted inhomogeneous magnetic phase in the strongly coupled model system. The method also promises to open new doors for distinguishing surface from bulk states in other inhomogeneous magnetic systems. ❍

See: D. Haskel, G. Srajer, Y. Choi, D.R. Lee, J.C. Lang, J. Meersschaut, J.S. Jiang, and S.D. Bader, "Nature of inhomogeneous magnetic state in artificial Fe/Gd ferrimagnetic multilayers," Phys. Rev. B **67**, 180406-1 (R) to 180406-4 (R) (2003).
Author affiliations: Argonne National Laboratory

J.M. was supported by the Belgian Science Foundation (F.W.O.-Vlaanderen). Use of the Advanced Photon Source was supported by the U.S. Department of Energy, Office of Science, Office of Basic Energy Sciences, under Contract No. W-31-109-Eng-38.

PEERING INTO THE FORMATION AND DEVITRIFICATION OF METALLIC GLASSES

Metallic glasses are an important class of materials, because of their many unique properties and because their devitrification characteristics can reveal a great deal about how the formation of such materials may be controlled. Devitrification involves gradually heating a metallic glass until thermal energy becomes sufficient to allow for atomic realignments into a more ordered crystalline state. Controlling devitrification is important, for example, to the formation of nanoscale materials, such as rare-earth permanent magnets, which are often produced by rapidly solidifying and heat treating amorphous alloys to obtain optimal magnetic properties.

Researchers from Ames Laboratory and Argonne National Laboratory used high-temperature x-ray diffraction (HTXRD) to investigate the devitrification pathways of two related zirconium-based metallic glasses: $Zr_{70}Pd_{30}$ and $Zr_{70}Pd_{20}Cu_{10}$. Charges of $Zr_{70}Pd_{30}$ and $Zr_{70}Pd_{20}Cu_{10}$ were inductively melted to about 1500K and ejected onto a Cu wheel rotating at a tangential wheel speed of 25 m/s. Long, continuous ribbons of very uniform thickness (0.03 mm) and width (2 mm) were produced and cut into ~8-mm lengths for HTXRD measurements at the APS.

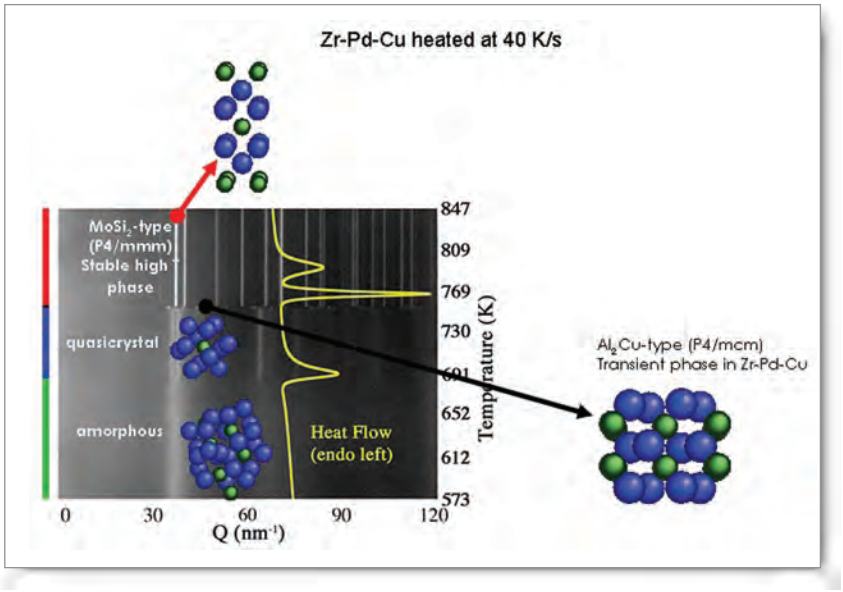

Fig. 1 The $Zr_{70}Pd_{20}Cu_{10}$ alloy shows a rapid transition from the icosahedral phase to the Al_2Cu-type structure, which undergoes a polymorphic transition to the $MoSi_2$-type structure at high temperature.

Time-resolved synchrotron x-ray studies were performed using energies of 80.73 and 124.63 keV at the XOR 1-ID-C and MU-CAT 6-ID-D beamlines, respectively. Thermal analysis was conducted on as-quenched samples to assess heats of formation and nucleation kinetics, by using differential scanning calorimetry at scanning rates of 5–40°C/min.

The studies demonstrated that the $Zr_{70}Pd_{30}$ and $Zr_{70}Pd_{20}Cu_{10}$ alloys have similar as-quenched structures and show a transition from the amorphous to an icosahedral phase over a narrow temperature range, the onset temperature for the $ZZr_{70}Pd_{30}$ alloy being about 30 K higher than that for $Zr_{70}Pd_{20}Cu_{10}$. Isothermal HTXRD suggests that devitrification occurs by nucleation and growth of the icosahedral phase. The $Zr_{70}Pd_{20}Cu_{10}$ alloy shows a rapid transition from the icosahedral phase to the Al_2Cu-type structure and then undergoes a polymorphic transition to the $MoSi_2$-type structure, which is the stable phase at high temperature (Fig. 1). The $Zr_{70}Pd_{30}$ alloy clearly shows coexistence of the quasicrystalline and $MoSi_2$-type structures.

While many transition metal alloys can be quenched to form amorphous alloys, few form icosahedral phases during devitrification. The Zr-based alloys are interesting because many compositions form icosahedral order during devitrification from the glass phase. To establish if there exists any relationship between the structure of the liquid and icosahedral order in the solid, a number of questions need to be addressed: What is the short-range order (SRO) of the as-quenched alloy, and how is it altered by the starting chemistry? What role, if any, does the SRO have on the devitrification products, particularly the formation of the icosahedral phase? Moreover, how does composition affect the stability of the icosahedral phase and subsequent crystallization pathways?

This study shows that HTXRD, using high-energy synchrotron radiation, is a promising tool for helping to answer these questions, since it provides high signal-to-noise diffraction data over a long reciprocal distance with collection times having the same timescale as the reaction kinetics. Because of their excellent signal-to-noise characteristics over short counting times and high spatial resolution, the high-flux high-energy photons derived from third-generation synchrotron sources, such as the APS, are ideal for studying the SRO of metallic glasses and the nanoscale structures formed during devitrification. ❍

See: M.J. Kramer[1], M.F. Besser[1], N. Yang[1], E. Rozhkova[1], D.J. Sordelet[1], Y. Zhang[2], and P.L. Lee[2], "Devitrification studies of Zr–Pd and Zr–Pd–Cu metallic glasses," J. Non-Cryst. Solids 317, 62–70 (2003).

Author affiliations: [1]Iowa State University, [2]Argonne National Laboratory

The MU-CAT sector at the APS is supported by the U.S. Department of Energy, Office of Science, Office of Basic Energy Sciences, through the Ames Laboratory under Contract No. W-7405-Eng-82. Use of the APS and XOR was supported by the U.S. Department of Energy, Officece of Science, Office of Basic Energy Sciences, under Contract No. W-31-109-Eng-38.

INELASTIC X-RAY SCATTERING MEASUREMENTS AND *AB INITIO* DENSITY-RESPONSE CALCULATIONS REVEAL MANY-BODY ELECTRONIC CORRELATIONS

Electron-electron interactions play a central role in determining the physical properties of materials, including all transport-related phenomena. Although short-range exchange-correlation effects have long been studied theoretically, a full description of them with regard to solids remains a significant challenge. Fortunately, the availability of third-generation synchrotron sources and high-resolution inelastic-scattering facilities now permits detailed experimental investigations of large wave-vector processes associated with short-range many-body effects in materials with relatively high and low atomic number. This new experimental capability has emerged concurrently with advances in *ab initio* electron density-response calculation methods for periodic crystals. The confluence of these developments has enabled the exploitation of the direct, absolute intensity linkage between dynamical electronic response calculations and inelastic x-ray scattering (IXS) spectra through the dynamical structure factor, yielding a means of achieving a fundamental understanding of electron correlations.

Researchers from Oak Ridge National Laboratory, the University of Illinois at Urbana-Champaign, Universität Würzburg, and the University of Tennessee have shown that the dynamical structure factor per unit volume (rather than per unit cell) provides a natural connection to first-principles density-response calculations, including all-electron methods. They used pseudo-potential dynamical response calculations make it possible to augment first-moment absolute normalizations beyond semi-core absorption edges for *f*-sum rule evaluations in free-electron materials. In addition, a method was provided for transferring absolute IXS calibrations to arbitrary materials, such as the transition-metal oxides, as part of a fundamental investigation of dynamical electronic correlations in aluminum.

Figure 1 shows measurements, made on the UNI-CAT ID-33 beamline at the APS, that were used in connection with a theoretical extension of first-moment intensity determinations for free electrons beyond the 72-eV semi-core absorption edge in aluminum. This procedure provided an accurate, absolute normalization for dynamical structure factor measurements made at the Fermi wave vector, k_F, in aluminum, which was used to analyze IXS measurements performed on ⟨001⟩- and ⟨013⟩-oriented aluminum single crystals on the X-21 beamline at the National Synchrotron Light Source. Quantitative evaluation of the measurements was carried with *ab initio*, time-dependent density-functional theory (TDDFT) calculations of electron-hole excitation spectra that included the band structure and many-body kernels based on the local-density approximation and dynamical exchange decoupling techniques. Dynamical electronic response calculations of the dynamical structure factor made using the many-body kernel obtained within the adiabatic extension of the local-density approximation (ALDA) yielded good agreement with the IXS energy-loss spectra for energies up to about 30 eV and momentum transfers up to k_F. For energy losses above 15 eV, the complex, frequency-dependent, dynamical exchange decoupling-based many-body kernel of Devreese et al. [1] was shown to lead to a description of the IXS data that was comparable or better than that provided by the ALDA. For low energies, though, the ALDA worked better, presumably because of the absence of correlations in the dynamical exchange kernel.

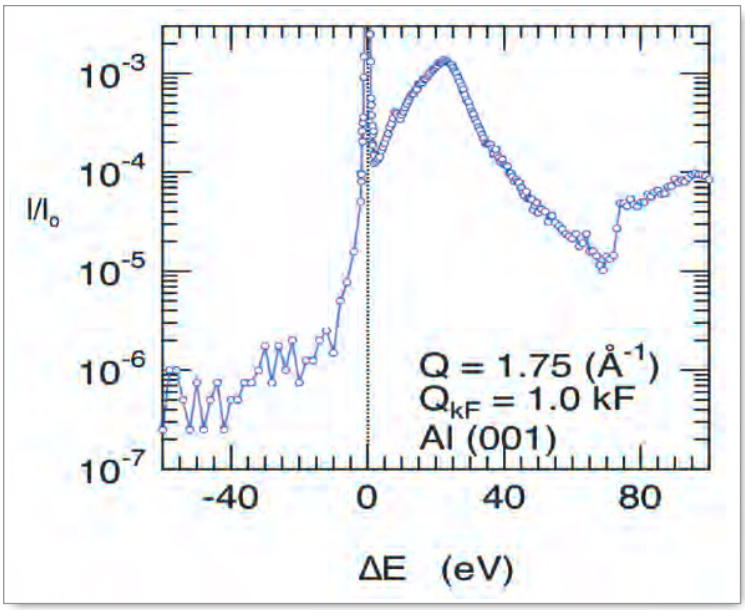

Fig. 1. Logarithmic-scale plot of the IXS measured energy-loss spectrum at the Fermi wave vector, k_F, in the [001] direction in Al. Measurements at negative ΔE provide an estimate of the background for corresponding positive ΔE values, indicating that first moment *f* sum-rule integrations for free electrons must be extended beyond the 72-eV L-absorption edge using theoretical response calculations.

The work provides a general method for the absolute calibration of IXS measurements on arbitrary materials. It suggests that high-precision IXS measurements, in combination with state-of-the-art TDDFT calculations for periodic crystals, offer a promising framework for benchmark development toward the goal of fundamental treatments of dynamical correlations in real materials. ❍

References

[1] J.T. Devreese, F. Brosens, and L.F. Lemmens, Phys. Rev. B **21**, 1349 (1980).

See: J.Z. Tischler[1], B.C. Larson[1], P. Zschack[2], A. Fleszar[3], and A.G. Eguiluz[4], "Interplay between inelastic X-ray scattering and *ab initio* density-response calculations: Insight into the elec-

tronic correlations in aluminum," Phys. Stat. Sol. (b) **237**(1), 280–288 (2003).

Author affiliations: [1]Oak Ridge National Laboratory, [2]University of Illinois at Urbana-Champaign, [3]Universität Würzburg, [4]University of Tennessee and Oak Ridge National Laboratory

This research was sponsored in part (A.G.E.) through NSF Grant ITR DMR-0219332 and in part by the U.S. Department of Energy, Basic Energy Sciences, Division of Materials Sciences under Contract No. DE-AC05-00OR22725 with Oak Ridge National Laboratory, managed by UT-Battelle, LLC. UNI-CAT is supported by the University of Illinois Materials Research Laboratory, Oak Ridge National Lab, the National Institute for Standards and Technology, and UOP, Inc. Use of the UNI-CAT beamline at the Advanced Photon Source and the X-21 beamline at the NSLS was supported by the U.S. Department of Energy, Office of Science, Office of Basic Energy Sciences. Use of the Advanced Photon Source was supported by the U.S. Department of Energy, Office of Science, Office of Basic Energy Sciences, under Contract No. W-31-109-Eng-38.

X-ray-Induced Fluorescence Enables Detailed Study of High-pressure Arc Plasmas

Metal-halide arc lamps are among the most energy-efficient sources of white light, which is why they are frequently used to illuminate large stadiums, malls, warehouses, and roadways. With further improvements in efficiency, produced by scientific and engineering advances, they could also see use in applications currently dominated by fluorescent and incandescent lamps.

A typical metal-halide arc lamp consists of a sealed evacuated tube containing two electrodes, several milligrams of Hg, smaller amounts of argon and various metal-halide salts. When a sufficient electrical potential is placed between the electrodes, an argon glow discharge is initially ignited. As the tube heats up, Hg evaporates, raising the pressure in the tube. At sufficiently high pressures, the discharge transitions from a glow to an arc. Further heating causes the metal-halide salts to evaporate and then dissociate as they move into the arc. The resulting free metal atoms and their ions become the most important source of visible light.

The plasma arcs responsible for visible light production by metal-halide lamps pose a daunting challenge to researchers seeking to observe and understand phenomena occurring in these arcs. Besides being chemically complex, metal-halide lighting arcs are opaque in many portions of the optical spectrum, hindering traditional optical diagnostics. The tubes encasing the arcs also scatter optical wavelengths, even when the tubes are transparent. This limitation has become more severe with the recent introduction of high-temperature polycrystalline alumina (PCA) arc tubes, which are translucent instead of transparent. Optical emission by the arc is also scattered strongly by PCA. Such scattering effectively negates any attempt at determining spatially resolved distributions of the contributing atoms, ions, and molecules.

It has long been recognized that the technique of x-ray-induced fluorescence could overcome these difficulties because x-rays are virtually unaffected by arc opacity or arc-tube scattering. Although this technique was initially tried elsewhere, it was first demonstrated successfully in arc lamps at the XOR 1-ID beamline at the APS, because of the beamline's high-energy, high-brightness, and monochromatic radiation, all of which are necessary to make x-ray-induced fluorescence practical for measurements in high-pressure metal-halide arcs.

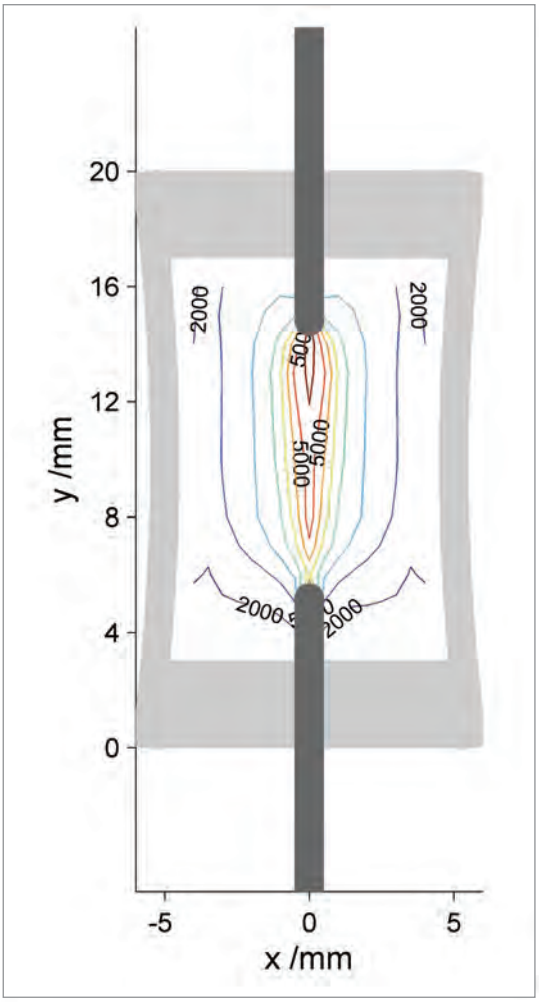

Fig. 1. Temperature contours in a 150 W ceramic metal-halide lamp containing a Hg/DyI_3/CsI mixture. Temperature values are in Kelvin with contours separated by 500K. The light gray regions represent the translucent ceramic arc tube, and the dark gray regions represent tungsten electrodes.

In x-ray-induced fluorescence, high-energy synchrotron radiation induces K-shell fluorescence in the components of a high-pressure plasma arc. The detected fluorescence is spectrally resolved, so that multiple elemental species are observed simultaneously. The penetrating nature of the high-energy photons allowed researchers from the National Institute of Standards and Technology, OSRAM SYLVANIA, and Argonne National Laboratory to make these measurements *in situ*, while the arc remained contained by an optically translucent PCA arc tube and a glass vacuum jacket. Absolute densities of Hg, the metal additives, and iodine were measured with an absolute calibration obtained by comparison with observed fluorescence from cells containing a known density of Dy in solution.

The gas density, equivalent to the Hg density (along with a knowledge of the lamp pressure), allowed the researchers to establish the gas temperature distribution in the arc (Fig. 1). The elemental densities and gas temperature then allowed them to derive the distributions of light-emitting and light-absorbing atomic and molecular species in the arc. Spatial distributions extending from one end of the arc tube to the other and from the arc core all the way to the wall were obtained for all of the principal elements in the arc (Fig. 2). These parameters are essential to developing a clearer scientific understanding of these high-pressure arc systems, and they cannot be obtained in any other way.

In the experiment, the arc saw a millimeter-size beam of monochromatic x-rays, the energy of which was tuned in the range of 70 to 85 keV, depending on the species to be observed. The energy resolution was ~1 part in 10^3, and photon flux densities were on the order of 10^{12} s^{-1} mm^{-2}.

Besides being useful for research into high-pressure lighting arcs, the technique of x-ray-induced fluorescence could also be applied to the study of a variety of other arc plasma systems, including arcs without arc-tube enclosures and arcs that must be accessed through an x-ray window. ❍

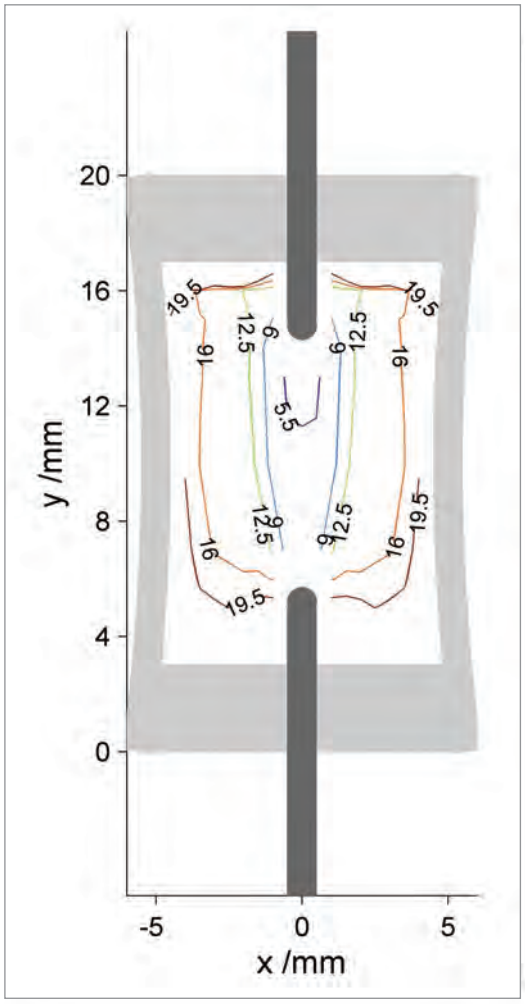

Fig. 2. Dy density contours in a 150-W ceramic metal-halide lamp containing a $Hg/DyI_3/CsI$ mixture. Density values are in 10^{16} cm^{-3} with contours separated by 3.5 x 10^{16} cm^{-3}. Dy produces most of the visible light emitted by the arc. These contours represent the total elemental Dy densities. The light gray regions represent the translucent ceramic arc tube, and the dark gray regions represent tungsten electrodes.

See: J.J. Curry [1], H.G. Adler [2], S.D. Shastri [3], and W.-K. Lee [3], "X-ray induced fluorescence measurement of density distributions in a metal–halide lighting arc," J. Appl. Phys. **93**(5), 2359-2368 (1 March 2003).

Author affiliations: [1]National Institute of Standards and Technology, [2]OSRAM SYLVANIA, [3]Argonne National Laboratory

Work at the University of Wisconsin was supported by OSRAM SYLVANIA and by National Science Foundation Grant No. ECS 99-88282. Use of the Advanced Photon Source was supported by the U. S. Department of Energy, Office of Science, Office of Basic Energy Sciences, under Contract No. W-31-109-Eng-38.

TWO GROWTH MODES FOR OXIDE FILMS ON TEXTURED METAL SUBSTRATES

Most crystalline materials are composed of small single-crystal grains that are packed together to form complicated networks of phase and grain boundaries. Although local three-dimensional grain-by-grain interactions ultimately determine the structural and electronic behavior of such materials, these interactions have long been virtually impossible to observe directly. Thanks, however, to enormous increases in x-ray brilliance provided by third-generation synchrotron sources and advances in x-ray mirrors, Fresnel zone plates, and refractive lenses, x-ray microbeam studies of individual grains in polycrystalline matrices can now simultaneously characterize the local structure, orientation, and strain tensor of different heteroepitaxial layers with submicrometer resolution in three dimensions.

These capabilities were demonstrated by researchers from Oak Ridge National Laboratory, the Advanced Light Source, the University of Florida, Soongsil University, and the Korea Electrotechnology Research Institute. The measurements were performed at the UNI-CAT 34-ID and MHATT/XOR 7-ID beamlines at the APS.

The researchers used polychromatic synchrotron radiation in an investigation of the epitaxial growth of cerium oxide (CeO_2) films on textured nickel (Ni) substrates deposited by pulsed laser deposition. Understanding the microstructure of these and similar materials is crucial to the development of deposited-superconductor technology. The focused polychromatic beam was diffracted from a submicrometer-diameter area within a single grain of the CeO_2/Ni sample, producing complete diffraction patterns from each layer on a charge-coupled-device area detector. Quantitative analysis of the Laue patterns yielded the local lattice orientation (resolution ~0.01°) and deviatoric strain tensor (resolution ~10^{-4}) for each layer.

Grain-by-grain microstructural studies of the cerium oxide films revealed two distinct kinetic growth regimes: ledge growth at elevated temperatures and island growth at lower temperatures. In addition, a combinatorial approach showed that crystallographic tilting associated with these complex interfaces is qualitatively described by a simple geometrical model applicable to brittle films on ductile substrates.

As indicated in Fig. 1, large-area orientation mapping also revealed that the tilting gave rise to enhanced texture and thus greater percolation distances in the oxide film. With regard to practical applications, these results suggest that significant enhancements can be achieved in heteroepitaxial systems with large lattice mismatch, in contrast to conventional growth approaches where lattice mismatch is typically minimized.

The tilt mechanisms studied should be relevant to many oxide/metal systems, including thermal barrier coatings, solar cells, and corrosion and interfaces in electronic devices. Thus, the benefits of intentionally enhanced texture should be achievable for many coated materials. Additional experiments examining more localized microstructures, such as grain-boundary grooves and crack propagation, are now possible with microbeams, and are in progress. ❍

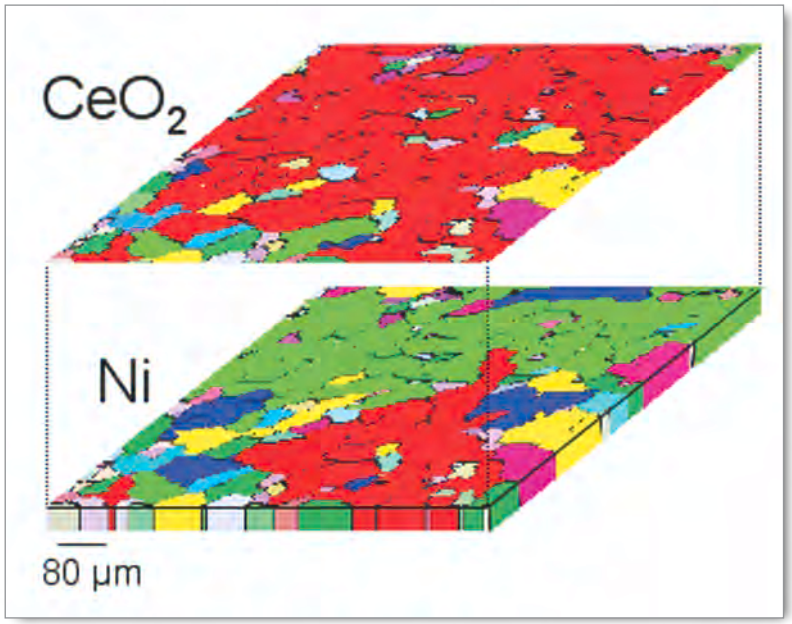

Fig. 1. Orientation maps from a deposited oxide film and a textured Ni substrate obtained by using x-ray Laue microdiffraction. Black lines within each map indicate boundaries where the total misorientation is greater than 5°. Each colored area shows a percolative region connected by boundaries of less than 5°. The oxide film exhibits larger percolation distances than the substrate, due to crystallographic tilts induced during epitaxial growth.

See: J.D. Budai[1], W. Yang[1], N. Tamura[2], J.-S. Chung[3], J.Z. Tischler[1], B.C. Larson[1], G.E. Ice[1], C. Park[4], and D.P. Norton[5], "X-ray microdiffraction study of growth modes and crystallographic tilts in oxide films on metal substrates," Nat. Mater. **2**, 487-492 (July 2003).

Author affiliations: [1]Oak Ridge National Laboratory, [2]Lawrence Berkeley National Laboratory, [3]Soongsil University, [4]Korea Electrotechnology Research Institute, [5]University of Florida

This research was sponsored by the U.S. Department of Energy Office of Basic Energy Sciences, Division of Materials Sciences, under contract with Oak Ridge National Laboratory, managed by UT-Battelle, LLC. Use of the Advanced Photon Source was supported by the U.S. Department of Energy, Office of Science, Office of Basic Energy Sciences, under Contract No. W-31-109-Eng-38.

With Nanoparticles, A Little Water on the Outside Can Rearrange the Atoms on the Inside

Sometimes, it is what's on the outside that counts. Within a nanometer-sized particle of a given material, the arrangement of atoms may depend on the particle size and the conditions during growth. But that internal organization can change when a nanoparticle is coated with a little water, a team from the University of California, Berkeley, recently found in experiments at the APS. The observation suggests that the structure of nanoparticles can be controllably altered after the particles are synthesized and that their behavior may depend on the chemistry of their surroundings.

Thermodynamically, a nanoparticle is distinct from a tiny dollop of a bulk material. The free energy of a nanoparticle includes a hefty surface term, and that term can determine the arrangement of atoms within the nanoparticle as it minimizes its free energy. Moreover, chemical interactions on the surface can alter the free-energy balance and, hence, the internal structure of the particle.

That is what the Berkeley team demonstrated in work at the BESSRC/XOR beamline 11 ID-C. The researchers synthesized nanoparticles of zinc sulfide in anhydrous methanol in a special vial compatible with x-ray scattering experiments. Using wide-angle x-ray scattering (WAXS), they studied *in situ* the structure of the nanoparticles, both before and after seasoning the methanol with a soupçon of water, which was anticipated to interact strongly with the nanoparticles. The high energies available at the beamline—up to 115 keV—enabled the researchers to probe a wide range in x-ray diffraction vector. With this high-quality diffraction data, they then deduced the real-space pair distribution function for atoms within the nanoparticles.

The WAXS data clearly showed that the water caused the atoms within the nanoparticles to rearrange. Additional measurements showed that the water changed the structure of the nanoparticles but did not make them grow or shrink. According to transmission electron microscopy and ultraviolet light absorption studies, the average nanoparticle diameter was 3 nm both before and after the addition of water.

To obtain detailed views of the nanoparticle structures, the team employed molecular dynamics simulations. For the nanoparticles in pure methanol, the simulations indicated that the zinc and sulfur atoms were highly disordered; only near the very center of the nanoparticle did they form a regular cubic zinc blende structure. When the simulation included a sub-monolayer coating of water molecules, however, the cubic phase filled the entire particle, and only the surface remained disordered. The simulated structures were in good agreement with the experimental observations, reinforcing the conclusion that the transformation was caused by the interaction of water molecules with the nanoparticle surface.

The researchers were not able to remove the water because it bonded too tightly to the zinc sulfide. However, other experiments by the team indicate that such structural transitions are reversible. X-ray absorption fine structure measurements at the DCM beamline of the University of Wisconsin-Madison's Synchrotron Radiation Center (SRC) in Stoughton showed that dried zinc sulfide nanoparticles changed structure when they were heated to drive off residual methanol. The structure reverted to its original form when the methanol was replaced.

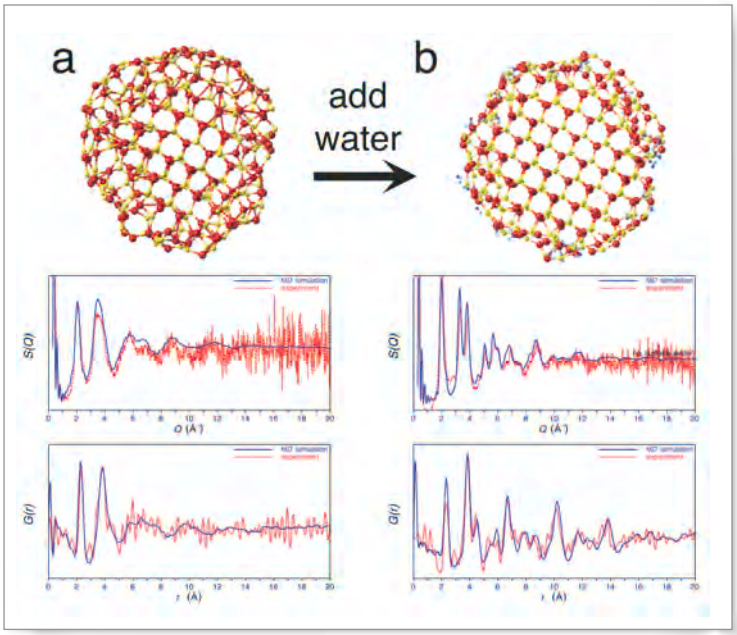

Fig. 1 Water binds to the surface of zinc sulfide nanoparticles in methanol and drives a transition from structural disorder (a) to order (b). From wide angle x-ray scattering data acquired versus diffraction vector, Q, the researchers calculate the structure factors, S(Q), and the real-space pair distribution functions, G(r) of the nanoparticles before and after the transformation. Molecular dynamics simulations reproduce the x-ray scattering data and provide specific predictions of the nanoparticle structure.

The results demonstrate that nanoparticles are not kinetically trapped in one structure or another but can respond to environmental changes and surface interactions. They suggest that coatings might induce and stabilize uncommon structures even after the particles are synthesized. Moreover, the findings indicate that the properties of nanoparticles depend not just on what the particles are made of and how they're created, but on their surroundings as well. As with people, nanoparticles will be judged by the company they keep. ❍

See: Z.H. Zhang, B. Gilbert, F. Huang, and J.F. Banfield, "Water-driven transformation of nanoparticle structure at room temperature," Nature **424**, 1025-1029 (23 August 2003)

Author affiliation: University of California, Berkeley

Work supported by the US DOE, a Lawrence Berkeley National Laboratory LDRD, and the U.S. NSF. The SRC is supported by the Division of Materials Research of the U.S. NSF. Use of the Advanced Photon Source was supported by the U.S. Department of Energy, Office of Science, Office of Basic Energy Sciences, under Contract No. W-31-109-Eng-38.

Revealing the Microscopic Transport Properties of Molten Aluminum Oxide

Levitated liquid-aluminum-oxide sample in a super-cooled state at ~1800° C. The sample is levitated by an oxygen gas stream and heated by a 270-W CO_2 laser. The article reports on inelastic x-ray measurements performed on this sample.

The transport properties of high-temperature oxide melts are of considerable interest for a variety of applications, including modeling the Earth's mantle, optimizing aluminum production, confining nuclear waste, and investigating the use of aluminum in aerospace propulsion. Information on melt viscosities and the speed of sound through liquid oxides is essential for testing the validity of theories used in predicting the geophysical behavior of the Earth's mantle as well as mathematical models of aluminum combustion. The experimental techniques described here supply fundamental insights into the behavior of liquid oxides that help provide a basis for these and other advanced applications.

Kinematic restrictions on neutron scattering make it impossible to reach acoustic modes in liquid oxides, and the high-temperature regime is inaccessible by light scattering because of black body radiation. Another factor making it difficult to obtain data on microscopic transport properties with conventional techniques is the chemical reactivity of oxide melts at high temperatures. Aluminum oxide, for example, melts at about 2327K and is an exceptionally aggressive material in the liquid state, which precludes the use of traditional containers for the material while measurements are being made.

Researchers from three French research centers, Centre de la Recherche sur la Matière Divisée, Institut de Science et de Génie des Materiaux et Procédés, and Centre de la Recherche sur la Matériaux à Haute Température; Spain's University of the Basque Country; and from Argonne National Laboratory sought to circumvent these limitations by studying molten aluminum oxide using high-resolution inelastic x-ray scattering (IXS) at XOR beamline 3-ID-C at the APS. The measurements were performed in a containerless environment. Aluminum oxide spheres 3 to 4 mm in diameter were suspended in an oxygen gas jet and heated with a 270-W CO_2 laser beam to temperatures between 2300 and 3100K. A carefully adjusted gas flow through a conical nozzle maintained the levitated sample at a position that was stable to within ±20 µm above the plane of the top edge of the nozzle, allowing a clear path for the incident and diffracted x-ray beams. Sample temperature was measured by a pyrometer directed at the point illuminated by the x-ray beam.

The x-ray energy was 21.657 keV, and the energy resolution was determined to be 1.8 meV, full width at half maximum. Data were collected at six values of the wave vector Q (over the energy transfer range of –30 to 60 meV), covering the Q value range of 1.09 to 6.09 nm^{-1}, and over a more restricted range (–30 to 30 meV), covering values of Q out to 28 nm^{-1}.

The excitation spectra showed a well-defined triplet peak structure at lower Q values (1 to 6 nm^{-1}) (Fig. 1). and a single quasi-elastic peak at higher Q. The high-Q spectra were well described by kinetic theory, but the low-Q spectra diverged significantly from predictions based on hydrodynamic theory.

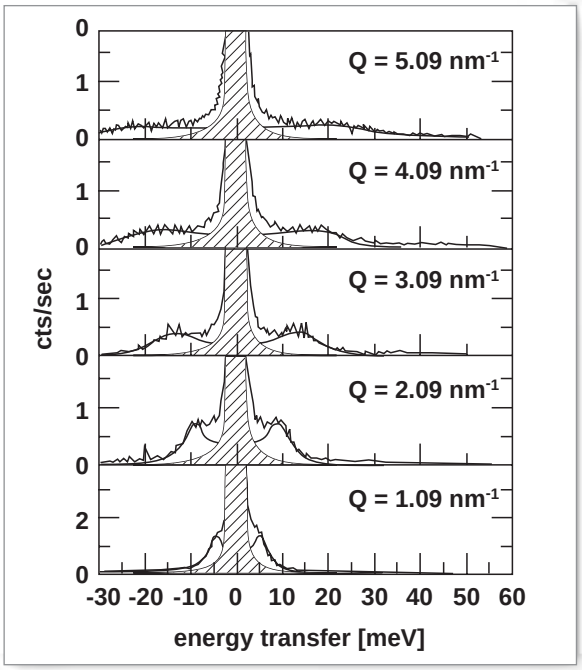

Fig. 1. Excitation spectra in liquid aluminum oxide at 2323K measured with inelastic x-ray scattering for different Q.

When the IXS spectra measured at the lowest six wave vectors at 2323K were fit to the hydrodynamic equation for the scattering function, it was found unexpectedly that the Brillouin modes remained underdamped out to Q=6 nm^{-1} (Fig. 2). Furthermore, the observed Brillouin line width increased with temperature, whereas it was expected that the viscosity would decrease in the hydrodynamic limit. Other discrepancies were discovered as well. The researchers found that an extension of hydrodynamic theory that allows for frequency dependence of the transport coefficients, such as the viscosity, yielded reasonable fits to the low-Q data up to 6.09 nm^{-1}. This provides a description of the liquid dynamics in the relatively uncharted regions between hydrodynamics and kinetic theory (Fig. 3). ❍

See: H. Sinn [1], B. Glorieux [2], L. Hennet [3], A. Alatas [1], M. Hu [1], E.E. Alp [1], F.J. Bermejo [4], D.L. Price [3], and M.-L. Saboungi [5], Science **299**, 2047-2049 (28 March 2003).

Author affiliations: [1]Argonne National Laboratory, [2]Institut de Science et de Génie des Materiaux et Procédés, [3]Centre Nationalde la Recherche Scientifique (CNRS), [4]University of the Basque Country, [5]CNRS, Université d' Orléans

This work, and use of the Advanced Photon Source, was supported by the U.S. Department of Energy, Office of Science, under contract W-31-109-Eng-38; the CNRS, and the Universitié d' Orléans.

Demonstration of the Influence of Local Icosahedral Order on the Nucleation Barrier of Metallic Liquids

For over 50 years, it has been known that, under carefully controlled conditions, metallic liquids can be cooled far below their equilibrium melting temperatures (undercooled) before crystallization takes place. This suggests that the homogeneous nucleation mechanism responsible for formation of the solid phase must present a large barrier to phase change. To explain this surprising result, F. C. Frank [1] theorized that as metallic liquids cool, (1) local structures develop in the liquid phase containing icosahedral short-range order (ISRO), which is incompatible with the long-range periodicity of the crystalline phase, and that (2) this incompatibility creates a barrier to the formation of the crystalline phase.

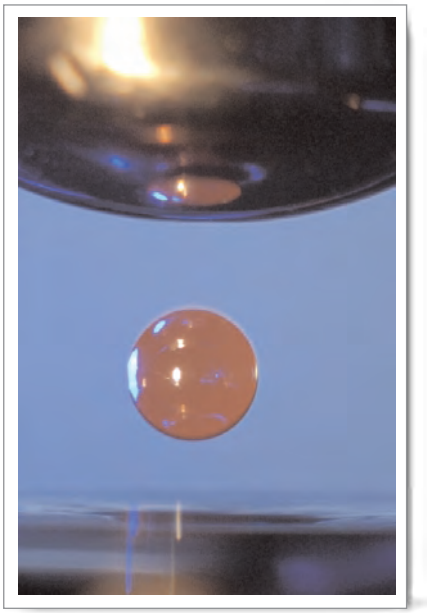

Fig. 1. Electrostatically levitated 2.5-mm-diameter droplet of molten $Ti_{39.5}Zr_{39.5}Ni_{21}$, held near the liquidus temperature (1083K).

Several experimental studies have supported this hypothesis, but have shopped short of providing direct proof of it. It has been found, for example, that an increase in the maximum undercooling before crystallization is associated with decreasing ISRO of the crystallized phases of Al-Cu-Fe, Al-Cu-Co, and Ti-Zr-Ni liquids. Direct observations of ISRO in the undercooled liquids, however, were not made. Similarly, ISRO was recently found in undercooled Ni, Fe, and Zr liquids, but these results did not establish a link between the ISRO and the nucleation barrier for the solid phase.

The first direct experimental confirmation of Frank's hypothesis took place at the MU-CAT 6-ID-D beamline at the APS [2]. Using the recently developed Beamline Electrostatic Levitation technique, which allows *in situ* x-ray diffraction experiments on electrostatically levitated droplets (Fig. 1), researchers from Washington University, NASA Marshall Space Flight Center, and MU-CAT studied the undercooling behavior of $Ti_{39.5}Zr_{39.5}Ni_{21}$. Electrostatic levitation in vacuum (~10^{-7} Torr) was used to create a containerless environment, which was needed to avoid the masking effects of heterogeneous nucleation. The levitated droplets were ≈2.5 mm in diameter and were positively charged by induction. The charge was maintained through the photoelectric effect by using intense ultraviolet light. Samples were melted with a fiber-coupled diode laser and then allowed to drop in temperature through free radiation cooling. Optical pyrometers measured sample temperature, and high-energy x-rays (125 keV, 0.099 Å) provided a scattering range of $0 \le q \le 9$ $Å^{-1}$.

The researchers measured an increasing ISRO in the Ti-Zr-Ni liquid with undercooling, finding that this increasing ISRO in the liquid phase is responsible for the nucleation of a metastable Ti-Zr-Ni icosahedral quasicrystal phase (*i* phase) instead of the stable polytetrahedral C14 Laves phase, which also tends to nucleate easily over a wide composition range. Two recalescence events were observed (see Fig. 2): in the first, the temperature rose from 953K to 1058K, followed within a few seconds by a second rise in temperature to 1083K. *In situ* x-ray diffraction analysis showed that the metastable *i* phase nucleates and grows during the primary recalescence from 953K, releasing evolved heat of fusion, which causes sample temperature to rise. This *i* phase subsequently transforms within a few seconds to the stable C14 Laves phase during the second recalescence event from 1058 to 1083K, which is the equilibrium solidus temperature.

In summary, the researchers demonstrated an enhanced icosahedral short-range order with undercooling in Ti-Zr-Ni liquids that decreases the barrier for the nucleation of a metastable *i* phase to below that for the formation of stable polytetrahedral crystal phases. In this way, the data demonstrate the connection between the local order of the liquid and the nucleation barrier. This verifies Frank's hypothesis that the origin of the barrier to nucleation of crystallographic phases is the formation of local icosahedral order in the liquid.

The data demonstrate that local order in the liquid phase strongly influences the nucleation of specific phases even in metallic liquids, in which atomic interactions are weak and relatively isotropic. This indicates that the influence of preexisting local order in the liquid is an important ingredient in the liquid/solid phase transition that should be considered in theoretical treatments of nucleation. ❍

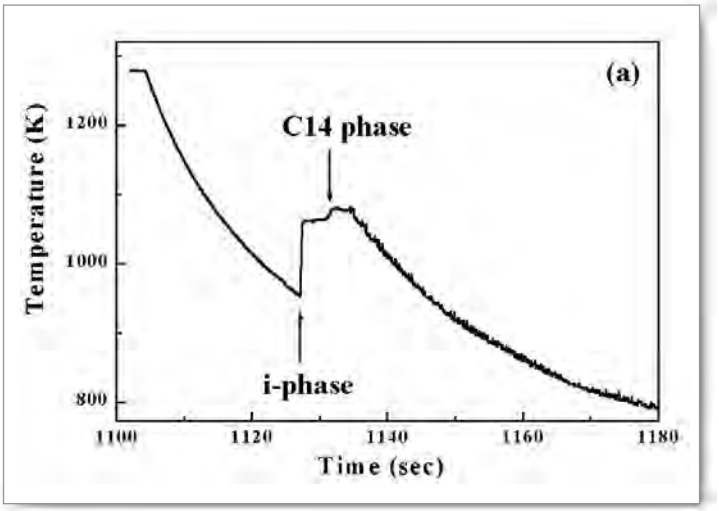

Fig. 2. Cooling curves for electrostatically levitated 2.5-mm droplet of $Ti_{39.5}Zr_{39.5}Ni_{21}$ as a function of temperature, showing two recalescence events (indicated by arrows). The first event corresponds to the nucleation and rapid growth of a metastable icosahedral quasicrystal; the second event indicates the transformation to the stable C14 crystal phase.

References

[1] F.C. Frank, Proc. R. Soc. London A **215**, 43 (1952).
[2] K.F. Kelton[1], G.W. Lee[1], A.K. Gangopadhyay[1], R.W. Hyers[2], T.J. Rathz[3], J.R. Rogers[3], M.B. Robinson[3], and D.S. Robinson[4], Phys. Rev. Lett. **90**(19), 195504-1 to 195504-4 (16 May 2003).

See: Reference [2] is the source for this article.

Author affiliations: [1]Washington University, [2]University of Massachusetts, [3]NASA Marshall Space Flight Center, [4]Ames Laboratory

The work at Washington University was supported by the National Aeronautics and Space Administration under Contract No. NCC 8-85 and the National Science Foundation under Grant No. DMR 00-72787. Use of the Advanced Photon Source was supported by the U.S. DOE, Basic Energy Sciences, Office of Science, under Contract No. W-31-109-Eng-38, and MU-CAT by Contract No.W-7405-Eng-82 through the Ames Laboratory.

Exploring Puzzling Properties of Polystyrene Films

Studies of thin polymer films provide a glimpse into their intrinsic properties and also help determine surface characteristics that could be useful in designing new technologies, from biocompatible medical implants to next-generation computer disk drives, adhesives, and optical coatings.

In simple bulk liquids, such as water and helium, thermally excited capillary waves are a primary determinant of the roughness at the surface/vapor interface. In thin, viscous polymer films on a substrate, however, other forces—including molecular interactions between the film and the substrate, the molecular structure of the polymer, surface tension, and viscosity—can alter surface roughness. These effects make it more difficult to predict surface roughness and tension by using capillary wave theory.

Previous studies of surface roughness in highly viscous liquids, an oil-water-surfactant interface, and very thin polymer films found that the surface roughness was lower than expected from capillary wave theory. The discrepancies are poorly understood.

In this study, researchers from Northern Illinois University; Argonne National Laboratory; the University of California, San Diego; the Massachusetts Institute of Technology; and Yale University used high-brilliance synchrotron x-rays to characterize polystyrene films of varying thinness on silicon substrates. When comparing the results of the measured x-ray scattering with capillary wave theory, the research team found that the variation of the measured intensity with with wave-vector agreed with theory over a wide range of wave-vectors. In addition, the surface tension was found to be only slightly higher than expected from theory, which was in contrast with previous studies which had claimed very large values for the surface tension (Fig. 1).

The research team prepared the films by spin-casting onto silicon substrates. The solvent was removed by annealing the samples at 150° for 12 h, and the thinness of the films was manipulated by varying the concentration of polystyrene in the toluene to achieve a range of thickness from 84 to 359 nanometers.

The 8-ID beamline at IMMY/XOR, APS sector 8, was used to measure the samples. The x-ray beam was generated by an APS undulator A. A germanium channel-cut double-bounce monochromator was used to select a narrow slice of energy from the harmonic. The beam was aligned vertically and horizontally, and stray scattering was intercepted by a beamstop

placed in front of a Princeton Instruments charge coupled device camera. By adjusting the angle of incidence, the team was able to deliver a glancing beam that penetrated the films by only 9 nm.

The study found that the surface tension of the supported polymer films was slightly greater, 20%, than that measured in bulk material. At capillary wavelength scales of 2 nm, the team also found slightly greater roughness than predicted by capillary wave theory. In addition, surface roughness was found to increase at higher temperatures and in thinner films.

Surface x-ray scattering can measure total surface roughness and can also determine the extent to which surface roughness depends on capillary wavelength. This study found that surface tension properties were in better agreement with values predicted for bulk materials than was found in previous studies. These observations provide a more accurate description of surface roughness and tension of supported polymer films, which correspond better with capillary wave theory. ❍

See: L. Lurio[1], H. Kim[2], A. Rühm[3], J. Basu[1], J. Lal[4], S. Sinha[2], and S.G.J. Mochrie[5], "Surface Tension and Surface Roughness of Supported Polystyrene Films," Macromolecules **36**, 5704-5709 (2003).

Author affiliations: [1]Northern Illinois University, [2]University of California, San Diego, [3]Massachusetts Institute of Technology, [4]Argonne National Laboratory [5]Yale University

Work at MIT and Yale was supported by the NSF (DMR 0071755). J.K.B. was supported by the DOE (DEFG02-91ER45439). IMM/YXOR 8-ID is supported by the DOE Facilities Initiative Program DE-FG02-96ER45593 and NSERC. Use of the Advanced Photon Source was supported by the U.S. Department of Energy, Office of Science, Office of Basic Energy Sciences, under Contract No. W-31-109-Eng-38.

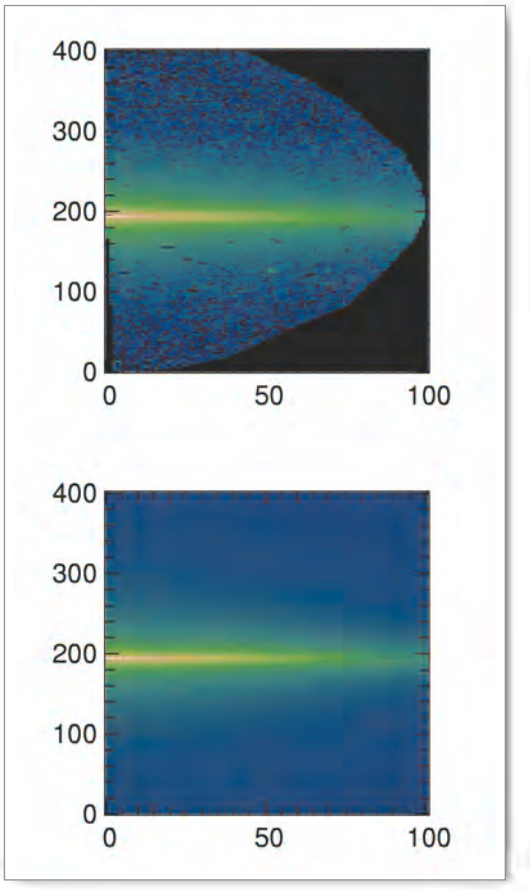

Fig.1. The top figure depicts static diffuse scattering measured from a 359 nanometer polystyrene film. The bottom figure shows a theoretical calculation of the diffuse scattering based on thermally driven capillary waves.

Collective Structure of Nanoparticle Fluids and Gels

From biotechnology to microelectronics fabrication, the behavior of dense colloidal and nanoparticle suspensions is of immense technological importance. Depending on the effective interactions between particles, a suspension may undergo a dramatic transition from a fluid to a gel state, which strongly influences how these materials are used. Control of the microstructural and mechanical properties of gels, therefore, is of great current interest but is poorly understood. Recently, researchers from the University of Illinois at Urbana-Champaign carried out a systematic study [1] at the UNI-CAT 33-ID beamline at the APS to determine the structural changes that take place during the approach to the gel transition and in the soft gel state, and they compared the results with theoretical calculations.

A widely used experimental system for studying particle gelation is a suspension to which small nanometer-size (radius of gyration, R_g) nonadsorbing polymers are added. The polymers induce exquisitely controllable, short-range "depletion attractions" between the particles that increase in strength with polymer concentration. Their initial effect is to induce equilibrium nanoparticle clustering over many length scales, and they ultimately trigger an abrupt nonequilibrium transition to a gel state where long-range diffusive motion is absent.

The researchers synthesized silica nanoparticles with radii of 59 ± 3 nm that behave as model hard spheres when dispersed in the solvent decalin. Polystyrene with R_g of ~3-4 nm was added to induce attraction between the nanoparticles. The collective colloid structure at a high particle volume fraction of ϕ ~40% was experimentally measured as a function of polymer concentration from zero up to, and well beyond, values that induce gelation.

Structural determinations were carried out using ultra-small-angle x-ray scattering. The measurements were made with the facility's Bonse-Hart camera operated at 10-keV photon energy and a q range of 2×10^{-4} to 2×10^{-1} A^{-1} (resolution $\Delta q = 2 \times 10^{-4}$ A^{-1}). The scattered x-rays were analyzed with a rotating Si crystal and solid-state detector. The colloidal structure factor $S(q)$ was determined from the measured scattering

intensity of the colloid-polymer mixture *I(q)* and the polymer-free, dilute colloid scattering intensity *P(q)*. *S(q)* yields information about the mean spacing of nanoparticles, the coherence of the local (cage) order, and suspension compressibility.

As the polymer concentration was increased in the fluid phase, particle concentration fluctuations increased in the low-angle scattering region, the length scale of the local cage structure decreased, and the intensity of the wide-angle peak that quantifies local cage coherence varied nonmonotonically, first decreasing at a low polymer concentration (weak attractions) and then increasing up to the gel transition (see Fig. 1). These equilibrium structural reorganizations on multiple length scales were shown to be in excellent agreement with no-adjustable-parameter theoretical calculations based on a novel version of the Polymer Reference Interaction Site Model (PRISM) theory for polymer-particle suspensions of Fuchs and Schweizer [2]. In the gel, multiple nonequilibrium structural reorganizations occurred, including local particle densification, enhancement of cage order, and suppression of intermediate scale compressibility. In addition, large amplitude scattering intensity emerged at relatively small wave vectors. Detailed analysis implies the formation of narrow interfaces and a characteristic cluster size or quenched heterogeneity length scale of roughly 4-5 nanoparticle diameters. By combining all the experimental and theoretical results, a consistent picture of the colloid microstructure has been constructed (see Fig. 1).

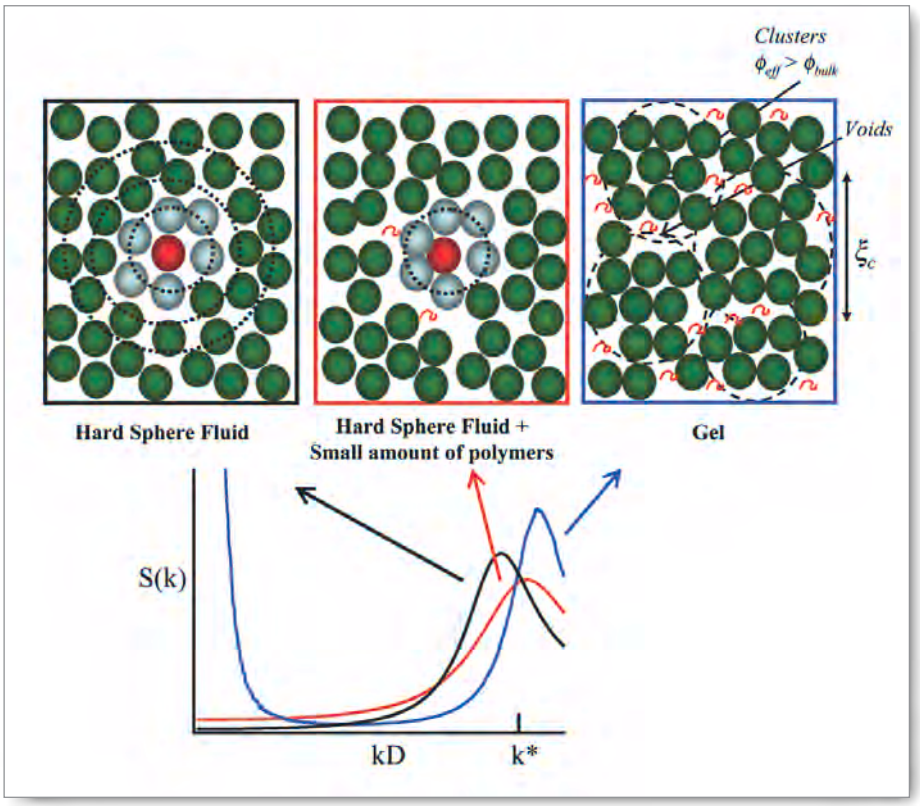

Fig. 1. Illustration (left to right) of particle organization in a hard sphere fluid, weakly clustered nanoparticle fluid, and a gel composed of dense percolated clusters with a locally increased effective volume fraction and an average size ξ_c. Also shown is a schematic illustrating changes in the structural correlations as equilibrium fluids transform to dense gels.

Ultrasmall-angle x-ray scattering (USAXS) has been shown in this work to be a powerful tool for identifying the onset of colloidal gelation and for quantitatively testing predictive theories of the structure and thermodynamics of nanoparticle-polymer suspensions. Such studies are possible because of the high brightness of the third-generation synchrotron at the APS. Ongoing and future work is focused on systematically characterizing the gel microstructure as a function of colloid volume fraction and polymer concentration and size [3]. The structural studies have provided a foundation for experimentally and theoretically understanding and controlling the elasticity and bulk mechanical properties of nanoparticle gels [3,4]. ❍

References

[1] S.A. Shah, Y.L. Chen, S. Ramakrishnan, K.S. Schweizer, and C.F. Zukoski, "Microstructure of Dense Colloid-Polymer Suspensions and Gels," J.Phys. Condens. Matter **15**, 4751-4778, (2003).

[2] M. Fuchs and K.S. Schweizer, "Structure of Polymer-Colloid Suspensions," J. Phys. Condens. Matter **14**, R239-R269 (2002).

[3] S. Ramakrishnan, Y.L. Chen, K.S. Schweizer, and C.F. Zukoski, "Elasticity and Collective Structure in Concentrated Depletion Gels," Phys. Rev. Lett. (submitted February 2004).

[4] S.A. Shah, Y.L. Chen, K.S. Schweizer, and C.F. Zukoski, "Viscoelasticity and Rheology of Depletion Flocculated Gels and Fluids," J. Chem. Phys. **119**, 8747-8760 (2003).

See: Reference [1] above is the source for this article.

Author affiliations: University of Illinois at Urbana-Champaign

This work was supported by the Nanoscale Science and Engineering Initiative of the National Science Foundation under Grant No. DMR-0117792 and the U.S. Department of Energy, Division of Materials Sciences, under Award No. DEFG02-91ER45439 through the Frederick Seitz Materials Research Laboratory at the University of Illinois at Urbana-Champaign. USAXS measurements were performed at the UNI-CAT facility at the Advanced Photon. Use of the Advanced Photon Source was supported by the U.S. Department of Energy, Office of Science, Office of Basic Energy Sciences, under Contract No. W-31-109-Eng-38.

Detailed Characterization of Two Distinct Phase Transitions at the Surface of Poly(*n*-Alkyl Acrylates)

X-ray reflectometry (XR), grazing incidence x-ray diffraction (GIXD), and infrared-visible sum-frequency generation spectroscopy (SFG) were all used to unambiguously delineate the two distinct surface phase transitions that poly(*n*-alkyl acrylate) comb polymers with alkyl side chains undergo when heated above the bulk melting temperature T_m. Researchers from the University of Akron, Kent State University, and Iowa State University used synchrotron x-rays produced at the MU-CAT 6-ID beamline at the APS for the XR and GIXD measurements.

Previous research performed at the University of Akron by this group had already demonstrated a two-step transition from order to disorder for short alkyl chains chemically linked to a flexible polymer backbone. That particular research was limited to surface-sensitive SFG spectroscopy alone. In this technique, the SFG intensity is proportional to the direction of the alkyl side chains; therefore, the measured SFG intensities were used to determine the side-chain orientations. Depending on the size of the alkyl side chain, the first transition was found to occur at 1-2ºC above T_m. The second surface transition was found to take place at 10-20ºC above T_m. (Again, the variation in phase transition temperature depended on the length of the particular alkyl side chain present.)

While SFG spectroscopy established the existence and temperature ranges of the phase transitions for the material studied, it was, by itself, inadequate for describing the structure in different phase regimes. The XR, GIXD, and SFG techniques together provided the data necessary to determine the changes in the polymer's surface structure associated with its two-phase transitions.

For this study, poly(*n*-alkyl acrylate) comb polymers with varying alkyl side-chain lengths were synthesized and probed. However, this paper mainly discusses results for the comb polymer having 21 methylene and 1 methyl unit side chains (n = 22). Differential scanning calorimetry (DSC)—with heating and cooling rates of 0.3ºC/min—was used to determine this material's bulk melting temperature of 64.9ºC, while its temperature of crystallization (T_f) was found to be 60.8ºC.

At 60ºC (4.9ºC below T_m), and at an incident angle of 0.5 times the critical angle (the angle of total external reflection), the GIXD measurements showed the presence of a crystalline surface layer with a lattice spacing of 4.2 Å (Fig. 1). That lattice spacing translates to a side-chain-to-chain spacing of 4.85 Å and an area per side chain of 20.4 Å^2 per chain. All these quantities reveal that the crystallized alkyl chains are oriented normal to the surface.

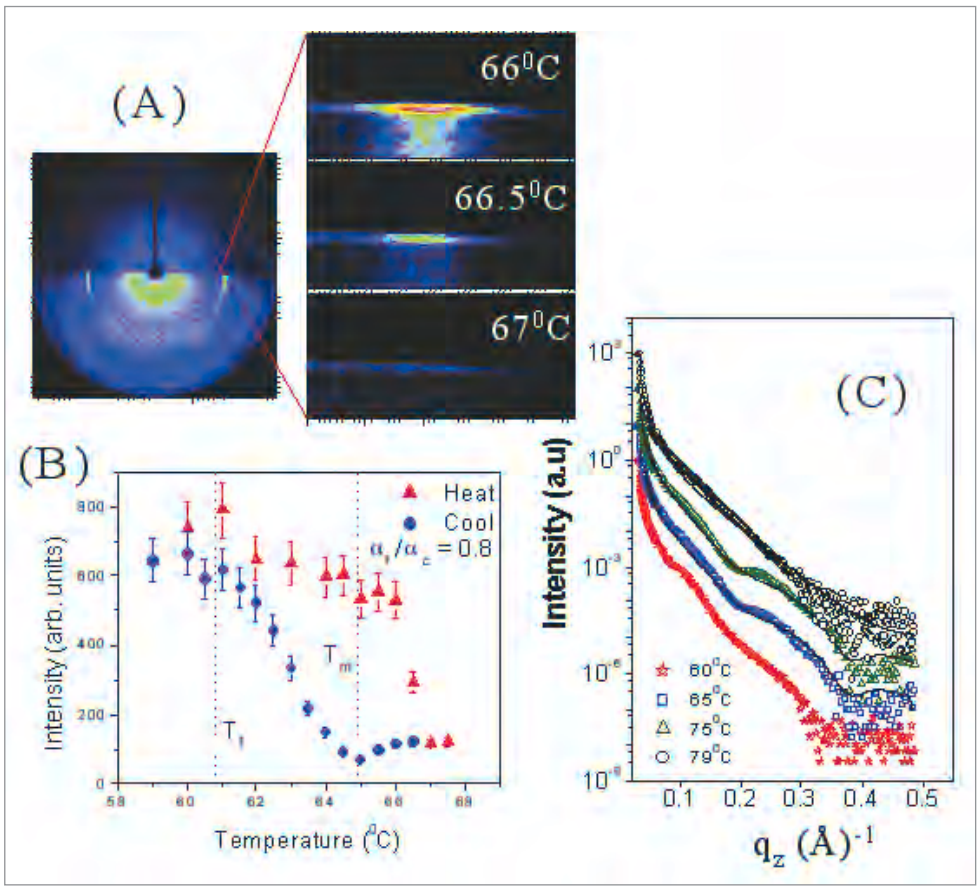

Fig. 1. (A) Image of the diffraction patterns on the plate detector at 60°C, and expanded views of the diffraction patterns obtained above the bulk-melting temperature T_m (64.9°C). (B) X-ray intensity as a function of temperature at a fixed value of α_f(diffraction angle)/α_c = 0.8 in the heating (triangles) and cooling (circles) cycles. The dashed lines are bulk transition temperatures measured by using DSC at a heating and a cooling rate of 0.3°C/min. (C) X-ray intensity plotted as a function of q_z (Å)$^{-1}$ for four different temperatures. These measurements were done in the cooling cycle. The Kiessig fringes, above the first transition, correspond to a 33-Å high-density ordered monolayer on the surface.

An abrupt change in measured GIXD intensity at 66.5ºC (1.6ºC above T_m) indicated the melting of surface alkyl side chains. This temperature marked the first phase transition. Beyond 67ºC (2.1ºC above T_m), GIXD measurements indicated the loss of the long-range crystalline order. But XR analysis showed the presence of a higher density surface layer above 67ºC, indicating that the material—even though it was no

longer in a crystalline form—still possessed at least some sort of molecular ordering. At 74.9ºC (10ºC above T_m), the second phase transition occurred, and the surface layer became completely disordered.

The SFG data verified and complemented the results from the GIXD and XR measurements. The SFG data for the first phase transition, associated with melting of the surface chains, was consistent with the GIXD results. Further heating above the first transition temperature indicated the presence of ordered alkyl side chains at the surface, which was consistent with the XR results above T_m. At 10° above T_m, however, a pronounced drop in SFG intensity showed the transition (i.e., the second phase transition) from a noncrystalline, smectic-like state to a disordered surface layer. When the process was reversed (that is, when the material was cooled), the transitions from the disordered to "semi-ordered," to crystalline state occurred in the expected sequence, but a hysteresis effect was encountered. In other words, the temperatures marking the transition from one phase to another were slightly lower when the material was being cooled than when it was being heated.

A detailed understanding of the surface structure and transition temperatures of the type of material examined in this study has important potential applications in the design of heat-responsive surface adhesives, as well as ramifications in other areas of research. ❍

See: K.S. Gautam[1], S. Kumar[2], D. Wermeille[3], D. Robinson[3], and A. Dhinojwala[1], "Observation of Novel Liquid-Crystalline Phase above the Bulk-Melting Temperature," Phys. Rev. Lett. **90**, 215501-1 to 215501-4 (30 May 2003).

Author affiliations: [1]The University of Akron, [2]Kent State University, [3]Iowa State University

This work was supported by the NSF-DMR-9984996 (A. D.) and Petroleum Research Funds. Use of the Advanced Photon Source was supported by the U.S. Department of Energy, Office of Science, Office of Basic Energy Sciences, under Contract No. W-31-109-Eng-38.

Unusual Structure in Thin Alkane Films

A microscopic theory of lubrication requires a detailed understanding of the physical configuration of the thin films that make up the lubricating coat—how their molecules are configured in each layer of a film. Alkane molecules are particularly attractive for such studies, not only because they are the principal constituents of commercial lubricants but also because they are a simpler molecule that serves as a prototype of the more complex polymers that are used in coatings, adhesives, and electronic devices.

There have been intriguing hints about the peculiarities of how alkanes configure themselves at boundaries and interfaces. An alkane fluid-air interface was discovered in which a solid alkane phase immediately adjacent to the air not only persists a few degrees above the bulk melting point, but in which the rod-like alkane molecules align themselves perpendicular to the interface, standing on end.

Subsequent studies of an alkane film adsorbed onto silicon dioxide (SiO_2)-coated substrates found an unusual growth mode. Next to the substrate, the long alkane molecules (chemical formula $C_{32}H_{66}$, denoted "C32" and known as dotriacontane) lay down parallel to the surface, in a film one or two molecular layers thick. Just above this parallel layer, though, is an alkane layer in which the molecules are aligned perpendicular to the substrate, standing up on end, one molecular layer thick. Above this perpendicular phase, alkane molecules are observed to nucleate in bulk particles.

This novel growth mode of alkane on silicon dioxide was inferred using the optical method of high-resolution ellipsometry—experiments that use the change in the polarization state of visible laser light to measure optical thickness—but it had not received direct microscopic confirmation. Using x-ray specular scattering measurements conducted at the MU-CAT 6-ID-B beamline at the APS, a team from the University of Missouri-Columbia, Pontificia Universidad Católica de Chile, Brookhaven National Laboratory, Technical University of Denmark, and the University of Wisconsin-Milwaukee determined the thickness of the parallel and perpendicular alkane film phases. In addition, they showed that the coexisting bulk phase consists of two different structures, both of which are preferentially oriented with respect to the film.

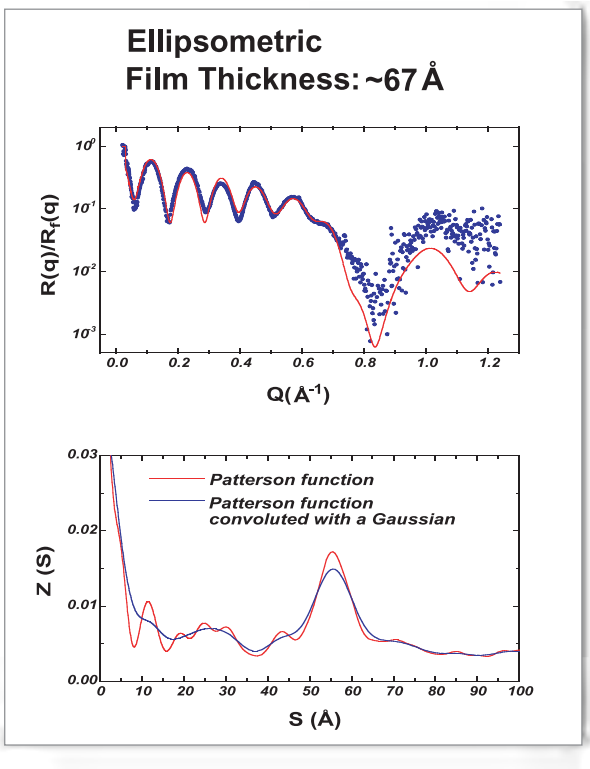

Fig. 1. Top: Representation of a normalized x-ray reflectivity, as a function of photon momentum transfer, for C_{32}/SiO_2 sample with a C_{32} thickness of 67 Å. Bottom graph represents a transformation of the reflectivity curve showing the thickness of the dominant layers in the C_{32} film.

The x-ray beam was scattered off the C32 film, and its reflectivity was scanned and plotted as a function of the incident angle. Peaks and valleys in the reflectivity spectrum are used to infer the thicknesses of the parallel and perpendicular films. A thickness of 11.7 Å was inferred for the parallel-phase film, about twice the width of the C32 molecule, corresponding to a molecular bilayer. (Other samples yielded a parallel film only one molecular layer thick.) The perpendicular-phase film was determined to be 43.2 Å thick, which is about the length of the C32 molecule. In no case was the perpendicular-phase film found to be in direct contact with the silicon dioxide substrate. The coexisting bulk phase was found to exist atop the perpendicular phase in two different structures: an orthorhombic phase and a monoclinic phase.

The present results show that thin films can grow on substrates in novel, unexpected ways, while raising questions about whether a minimum molecular length is required to stabilize the perpendicular monolayer phase and whether the type of substrate, and the nature of the alkane deposition, matters.❍

See: H. Mo[1], H. Taub[1], U.G. Volkmann[2], M. Pino[2], S.N. Ehrlich[3], F.Y. Hansen[4], E. Lu[5], P. Miceli[1], "A novel growth mode of alkane films on an SiO_2 surface," Chem. Phys. Lett. **377**, 99-105 (2003).
Author affiliations: [1]University of Missouri-Columbia, [2]Pontificia Universidad Católica de Chile, [3]Brookhaven National Laboratory, [4]Technical University of Denmark, [5]University of Wisconsin-Milwaukee

This work was supported by the US NSF under Grant Nos. INT-9605227, DMR-9802476, and DMR-0109057 and by the Chilean government under CONICYT Grant No. 018/AT/005NSF and FONDECYT Grant Nos. 1010548 and 7010548. The MU-CAT sector at the APS is supported by the US Department of Energy, Office of Science, Office of Basic Energy Sciences, through the Ames Laboratory under Contract No. W-7405-Eng-82. Use of the Advanced Photon Source was supported by the U.S. Department of Energy, Office of Science, Office of Basic Energy Sciences, under Contract No. W-31-109-Eng-38.

Shear Effects on Interfacial Structure in Liquids

The effect of shear flow on interfacial structures is a relatively unexplored phenomenon, particularly at nanoscale dimensions. While x-ray scattering is a useful technique in the study of liquid structure near interfaces, it is difficult to study shear effects with this means because of the necessity of enclosing the liquid under study within solid substrates and the resultant attenuation and scattering of the x-ray beam caused by the substrates. Under such limitations, only strong signals from bulk liquid structure are normally detectable, rather than weaker signals from interfacial boundaries. A team from Northwestern University managed to overcome these difficulties in order to study shear flow effects on the interfacial structures of two nonpolar liquids, tetrakis (2-ethylhexoxy)silane (TEHOS) and poly(dimethylsiloxane) (PDMS), using the using the MR-CAT 10-ID beamline at the APS and the MATRIX beamline X18-A at the National Synchrotron Light Source.

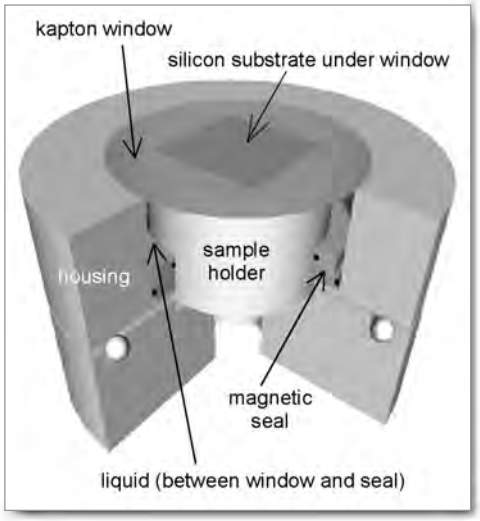

Fig. 1. Schematic diagram of experimental setup. The outer housing and attached kapton window are rotated to apply shear.

The Northwestern team created a sample chamber consisting of a stainless steel liquid sample holder encased in a circular housing with a Kapton window allowing access by the x-ray beam (Fig. 1). A silicon substrate protruded slightly above the top of the sample holder, permitting x-rays to encounter the sample at small incidence angles. To apply shear, the outer housing of the sample chamber was rotated, with the sample liquid confined between the Kapton window and a magnetic seal.

X-ray scattering data from unsheared TEHOS shows a scattering maximum at 0.63 A^{-1}, which indicates layering of the interfacial TEHOS with an approximately 10 angstrom spacing between individual layers. After shear stress is applied at a rate of 0.17 turns per second for 1 minute, and reflectivity is measured at various distances from the center in regions with different shear rates, the diffraction peak diminishes, while maintaining the same shape and position as observed without shear. This suggests that the number of ordered layers is not reduced but an increasing part of the substrate surface is covered by disordered rather than layered TEHOS. The peak takes several hours to recover following the removal of shear stress.

These effects are quite distinct from those observed by the Northwestern researches in PDMS, a polymeric liquid of long and flexible molecules. Without the application of shear stress, PDMS displays no diffraction peak attributable to layering. Only at very high shear rates, approximately 104 s^{-1}, does a change occur, demonstrating molecular layering at a thickness of approximately 30 angstroms in the ordered region of the interface. Because the layered PDMS region returned to a disordered state in approximately 3 hours, the experimenters suggest that the layering observed under shear stress is due to the disentanglement of the polymeric chains.

The Northwestern/MR-CAT sector 10 results provide a clear demonstration of the usefulness of shear effects in the observation and study of interfacial molecular structure. Shear effects can be applied in order to manipulate molecules at interfacial regions to provide direct evidence of microscopic structure under x-ray reflectivity observation. ❍

See: C. Yu, G. Evmenenko, J. Kmetko, and P. Dutta, "Effects of Shear Flow on Interfacial Ordering in Liquids: X-ray Scattering Studies," Langmuir **19**, 9558-9561 (2003).
Author affiliation: Northwestern University

This work was supported by the National Science Foundation under Grant DMR-0305494. Use of the National Synchrotron Light Source was supported by the U.S. Department of Energy, Office of Science, Office of Basic Energy Sciences. Use of the Advanced Photon Source was supported by the U.S. Department of Energy, Office of Science, Office of Basic Energy Sciences, under Contract No. W-31-109-Eng-38.

Phase Transitions in Suspensions of Colloidal *fd* Virus

Whether of biological or technological origin, liquid crystals are composed of elongated rod-like molecules that undergo phase transitions in which the molecules spontaneously rearrange themselves, not unlike the phase transition when liquid water transforms into crystalline ice. In the simplest of these phase transitions, the rods change from an "isotropic" phase, where each rod points in a random direction, to a "nematic phase" where all rods point more or less in the same direction.

What drives this phase transition? Molecules in a liquid both attract and repel one another. Repulsive interactions tend to dominate in fluids, as molecules bounce off that hard-core potential that exists. Long rod-like viruses are particularly interesting for the study of such phase transitions, because they're so large that the underlying repulsive interactions dominate over quantum mechanical interactions and van der Waals (attractive) forces. Consequently, the free energy is dominated by entropy, which counterintuitively implies that the low-symmetry liquid crystalline nematic phase is actually more disordered than the high-symmetry isotropic phase. In the 1940s, Onsager developed a theory of such phase transitions, modeling the isotropic to nematic phase transition via a tour de force of statistical mechanics.

Testing Onsager's theory is possible by using the *fd* virus in solution. One must measure a central quantity in his theory: the probability that a molecule points at a certain angle, called the angular distribution function. *fd* viruses, discovered in the sewers of New York City in the 1970s, have a high aspect ratio, with a length-to-diameter ratio of 130:1, and importantly, they are monodispersed—all of the same length. Until this experiment, these two qualities had never before been realized in a physical system, making this the most complete test of Onsager's theory. (Polymer chemists are yet unable to produce polymers all of the same length, something nature has been doing for three billion years.) Unlike some science today, where physicists are turning to biological questions, here biology has come to the aid of physics.

In order to measure the angular distribution function, x-ray diffraction was done at the small-angle x-ray scattering (SAXS) station on the IMMY/XOR 8-ID beamline at the APS by experimenters from Brandeis University, Massachusetts Institute of Technology, Northern Illinois University, and Yale University.

Insofar as the assumptions of Onsager hold—that electrostatic repulsions are minimized, a condition obtained by adding the *fd* virus to a high salt solution—his theory was found to be quite accurate. (The salt serves to screen the long-range attractions.) However, as electrostatic interactions become stronger (that is, as salt concentrations become weaker, or virus concentrations become high), Onsager's theory begins to fail, indicating a need for further theory in terms of charged macromolecules. Thus, in order to understand biopolymers, such as actin or neurofilaments or even DNA, which in their biological milieu are highly concentrated and aligned in liquid crystalline states, additional theory is needed. ❍

See: K.R. Purdy[1], Z. Dogic[1], S. Fraden[1], A. Ruhm[2], L. Lurio[3], S.G.J. Mochrie[4], Phys. Rev. E **67**, 031708-1 to 031708-12 (2003).
Author affiliations: [1]Brandeis University, [2]Massachusetts Institute of Technology, [3]Northern Illinois University, [4]Yale University.

Work at Brandeis was supported by the NSF (Grant No. DMR-0088008). Work at Yale was supported by the NSF (Grant No. DMR-0071755). The 8-ID beam line at the Advanced Photon Source is supported by the U.S. Department of Energy (Grant No. DE-FG02-96ER45593) and NSERC. Use of the APS supported by the U.S. Department of Energy, Office of Science, Office of Basic Energy Sciences, under Contract No. W-31-109-Eng-38.

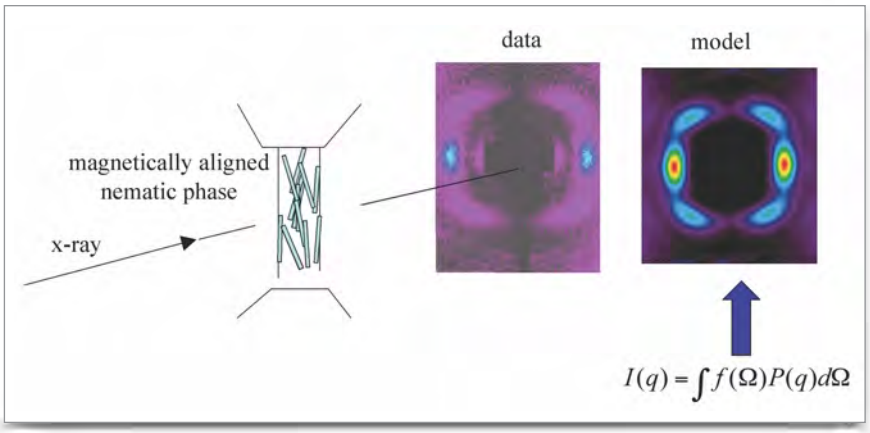

Fig. 1. The *fd* virus consists of about 2700 copies of a single protein helically arranged to form a hollow cylinder into which is stuffed the viral DNA. The periodic arrangement of the proteins causes x-rays to be scattered as distinct spots arranged in layers perpendicular to the virus axis. The x-ray scattering pattern from a perfectly aligned virus shows peaks that are very sharp and are confined to horizontal planes. Shown is an example of scattered x-rays from a nematic sample compared with the calculated data. Different angular distribution functions are used to model the data, and the one that best fits the data is used to calculate the phase transition order parameter.

Surface Dynamics of Polymer Films

Thin polymer films are attracting considerable attention because they have a wide variety of technological applications, ranging from the creation of bio-compatible surfaces for medical implants to expanding the limits of computer disk drive technology.

Recent theoretical work has raised questions about whether thermal effects could cause polymer thin films to stratify such that their viscosity varies with depth. Clearly, such an effect would present a challenge—or an opportunity—for applications that depend on surface properties of such films. However, it is not clear how well the theory holds for films with a thickness on the same order as the length of the polymer chains.

The first experiments testing the theoretical premise behind this predicted effect have been conducted at IMMY/XOR beamline 8-ID. The emerging technique of x-ray photon correlation spectroscopy (XPCS) was used to measure random thermal fluctuations in the surface height of a thin polystyrene film as a function of lateral length scale. The results support the theory in question: namely, that the surface dynamics of a polymer film take the form of overdamped thermal capillary waves. Such waves are something like the ripples spreading from a pebble dropped in water.

The method used, XPCS, extends a well-established laser technique to the smaller length scales accessible with x-rays. It exploits the coherence of synchrotron x-rays to generate a speckle pattern that reflects spatial inhomogeneity. The method is particularly well suited to studying spatial dynamics on relatively slow time scales (seconds to minutes).

The goal of the initial experiment was to determine how fast the surface disturbances relax, or smooth out, and also whether this relaxation time varies depending on the wavelength (or wave vector) of the disturbance. The XPCS method allows simultaneous measurement of features at several length scales. In this case, the relaxation times were measured for wave vectors ranging from 10^{-3} to 10^{-2} nm^{-1}.

The samples studied were polystyrene films (M_W = 123,000 g/mol) with thicknesses ranging from 84 to 333 nm, prepared by spin-casting on silicon substrates. Measurements were taken at temperatures ranging from 150 to 170°C (above the polystyrene glass transition temperature). Effects of interaction between the film and substrate were excluded by choosing an incident beam angle that limited the depth of penetration to ~9 nm. The off-specular diffuse scattering from the polymer surface was recorded with a direct-illumination CCD camera.

Figure 1 shows a CCD image and a fit to the capillary wave model for an 84-nm film. The good agreement between the data and the model confirms that the surface morphology of the film is governed by capillary waves. The results also showed that the surface tension and viscosity are consistent with that of bulk polystyrene and that the overall film viscosity is independent of both film thickness and the length scale of the disturbance. The data also confirm the expected relationship between the wave vector and the relaxation time and film thickness: long-wavelength ripples damp out more slowly than small ones, and all relaxation times are faster in the thicker films.

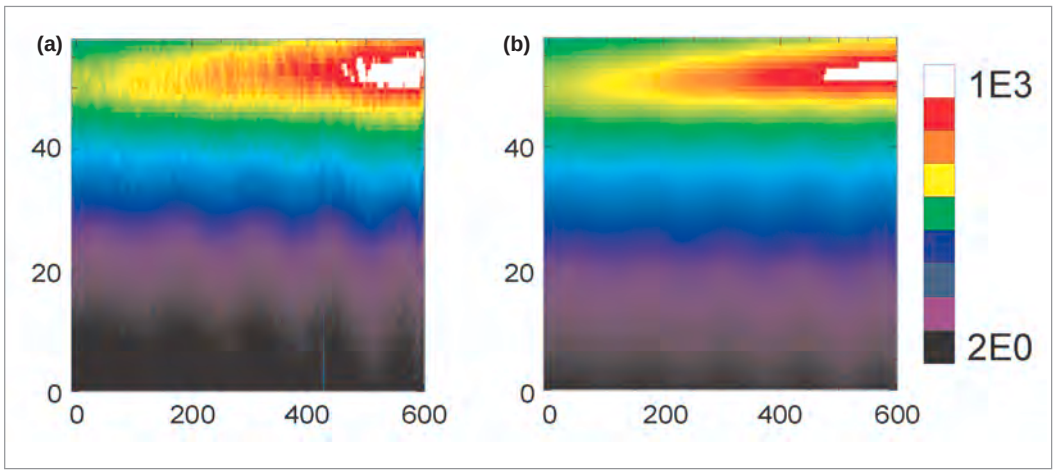

Fig.1. (a) Time-averaged thermal diffuse scattering from the surface of an 84-nm-thick polystyrene film at 160°C. (b) Results of capillary wave model for same film thickness and temperature. The close agreement with (a) shows that this model holds for polymer films.

These initial results were used in a preliminary analysis of the potential for viscosity to vary with depth in the film. The calculations show that if a high-mobility surface layer were present, it would not be more than 10 nm thick. This layer might cause the viscosity of the thin film to differ from that of the bulk, but only in films thinner than ~20 nm. Further experiments are in progress to explore such effects. ❍

See: H. Kim[1,2,3], A. Rühm[4,5], L.B. Lurio[4,6], J.K. Basu[1,7], J. Lal[1], D. Lumma[4], S.G.J. Mochrie[8], and S.K. Sinha[1,2], "Surface Dynamics of Polymer Films," Phys. Rev. Lett. **90**(6), 068302-1 to 068302-4 (14 February 2003).

Author affiliations: [1]Argonne National Laboratory, [2]University of California, San Diego, and Los Alamos National Laboratory, [3]Sogang University, [4]Massachusetts Institute of Technology, [5]Max-Planck-Institut für Metallforschung, [6]Northern Illinois University, [7]University of Illinois at Urbana-Champaign, [8]Yale University

Work at MIT and Yale was supported by the NSF (DMR 0071755). J.K.B. was supported by the DOE (DEFG02-91ER45439). IMMY/XOR 8-ID is supported by the DOE Facilities Initiative Program DE-FG02-96ER45593 and NSERC. Use of the Advanced Photon Source was supported by the U.S. Department of Energy, Office of Science, Office of Basic Energy Sciences, under Contract No. W-31-109-Eng-38.

CAPTURING THE CONTORTIONS OF EXCITED MOLECULES

Give a complex molecule a little extra energy, and it tends to get bent out of shape. The structure of an excited molecule may differ from that of the molecule in its ground state, and the distortions can greatly affect the molecule's chemical reactivity and other properties. Reversible shape changes are fleeting, however, lasting only millionths or billionths of a second. To measure them, researchers from the State University of New York at Buffalo and The University of Chicago are developing a technique called "photocrystallography" that essentially provides snapshots of excited molecules within a molecular crystal.

The method adds a new dimension—time—to traditional x-ray crystallography. In a standard technique, monochromatic x-rays diffract off the various planes of symmetry within a slowly rotating single-domain crystal, and the trajectories of the scattered x-rays reveal the arrangement of molecules within the crystal and atoms within the molecules. However, the molecules are generally not excited, and the measurements make no use of timing. Such measurements provide a good long look at the ground state structure of the molecules but yield little insight into the shapes of excited molecules.

To detect reversible shape changes, the researchers hit a molecular crystal with a one-two punch: a nanosecond pulse of intense laser light followed almost immediately by a microsecond burst of x-rays. The pulse of laser light excites many of the molecules in the crystal, and the x-rays diffract off them before they have a chance to relax to their ground state. The deformed molecules alter the intensities of the x-rays diffracted in various directions, and from such intensity changes researchers can deduce the precise shape of the excited molecules. The photons in each laser pulse must outnumber the molecules in the crystal to ensure that a detectable fraction of the molecules—5% to 10 %—are excited; the x-rays must be intense enough to determine the crystal structure before the repeated laser pulses damage the crystal. And to keep the laser from vaporizing the tiny sample, the crystal must be cooled with helium gas.

A user facility for time resolved measurements is being commissioned on the ChemMatCARS insertion device beamline at the APS [1]. While preliminary experiments were performed at Brookhaven National Laboratory, ChemMatCARS effort has concentrated on instrumentation development appropriate for a high-brilliance undulator source and data acquisition/analysis packages which promote efficient use of this new capability.

The first experiments at ChemMatCARS used a sample of a photosensitive metalloorganic dye containing a copper atom between phosphorous and nitrogenous ligands. The two ligands are roughly planar and are nearly perpendicular in the molecule's ground state. But when the molecule is excited, an electron hops from the copper to the nitrogenous ligand. That causes the molecule to flatten, the measurements showed, and the angle between the planes of the ligands decreases by several degrees. The distortion was smaller than density functional theory calculations had predicted. However, the calculations had analyzed an isolated molecule, instead of a molecule within a crystal, which would be confined by its neighbors.

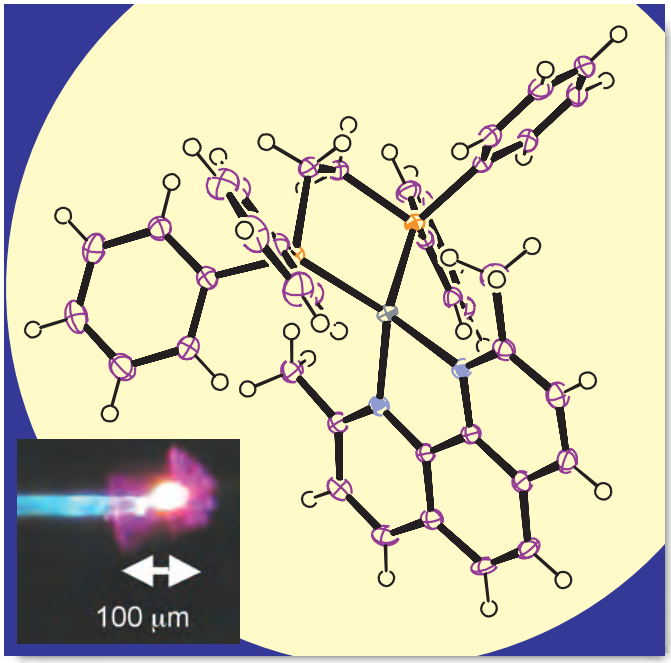

The ground state structure of the photosensitive metalloorganic dye known as Cu(I)(dmp)(diphos)+. The molecule's excited-state structure was determined by photocrystallography at the APS. Inset: Photograph of laser-illuminated crystal emitting light during photocrystallographic data collection.

These first measurements demonstrate the potential of the technique to capture structural changes caused by any light-induced reversible process. They open the way to myriad applications, and the researchers are hoping that the ChemMatCARS 15-ID beamline can serve as a national user facility for photocrystallography. In the meantime, they are hoping to achieve picosecond x-ray pulses by synchronizing their laser with the circulating particle bunches within the synchrotron. Such x-ray pulses would enable them to resolve even shorter-lived excitation. ❍

Reference

[1] P. Coppens, T. Graber, and P.J. Viccaro, Synchrotron Radiation News 16 (4), 27-28 (2003)

See: P. Coppens, Chem. Commun. **12**, 1317-1320 (2003).

Author affiliation: State University of New York at Buffalo

This work made possible with support from NSF grants CHE9981864 CHE0236317, DOE grants DEFG02-86ER45231, DEFG02-02ER15372. The ChemMatCARS 15-ID beamline at the APS is supported by NSF0087817. Research carried out in part at the National Synchrotron Light Source at Brookhaven National Laboratory, which is supported by the U.S. Department of Energy, Office of Science, Office of Basic Energy Sciences, Division of Material Sciences and Division of Chemical Sciences. Use of the Advanced Photon Source is supported by the U.S. Department of Energy, Office of Science, Office of Basic Energy Sciences, under Contract No. W-31-109-Eng-38.

REFINING THE WAY CATALYSTS ARE MADE

Platinum supported on alumina catalysts are important for production of high-octane gasoline in the petroleum industry and exhaust gas abatement in the automotive industry. A better understanding of how these catalysts are produced is crucial for the preparation of more effective catalysts in the future. The Revised Physical Adsorption (RPA) model simulates the uptake of Pt versus pH onto alumina but is simplistic in that only the doubly valent $[PtCl_6]^{-2}$ complex is considered. Because previous studies suggested that other Pt complexes might be present in the preparative solutions, investigators from the University of Illinois at Chicago, BP Research Center in Naperville, Illinois, and Argonne National Laboratory collaborated to refine the RPA model. By characterizing the molecular changes that occur when Pt complexes are adsorbed onto alumina, a better understanding of Pt adsorption is expected to lead to better control of the composition and performance of these catalysts.

The high sensitivity of the undulator beamline at MR-CAT, APS sector 10, was used to determine, via extended x-ray adsorption fine structure (EXAFS) measurements, the structures of Pt complexes in dilute solution and adsorbed on alumina. The exact structures of the aqueous Pt species were highly dependent on the Pt and Cl concentration, pH, and age of the solutions. For example, aqueous solutions of H_2PtCl_6, which are commonly used to prepare catalysts, were observed to undergo rapid hydrolysis, giving Pt (IV) complexes with 3 Cl and 3 O ligands (Fig. 1). Although EXAFS cannot distinguish between OH and H_2O ligands, a proton balance indicated that the initial O ligands were H_2O. After about 24 h, as the solutions age, the H_2O ligands are exchanged by OH^- ions. The number of hydroxide ligands also increases as the pH increases.

In aqueous solution, γ-alumina with a surface area of about 200 m^2/g becomes positively charged. A "double layer" theory is the kernel of the RPA model, which predicts that there is a Coulombic attraction between the negatively charged Pt complexes and the positive surface charge on alumina. Pt complexes, which initially contain H_2O ligands, are positively charged and not readily adsorbed. Aged solutions with hydroxide ligands, however, are readily adsorbed and lead to the formation of small particles upon reduction. EXAFS analysis (Fig. 1) also indicates that the Pt species undergo additional changes upon adsorption. These structural changes are due to the influence of the surface pH of the alumina. Proper control of the support, pH of the preparative solutions, and the charge on the metal complex, leads to monolayer coverage of the support and smaller metal particles upon reduction.

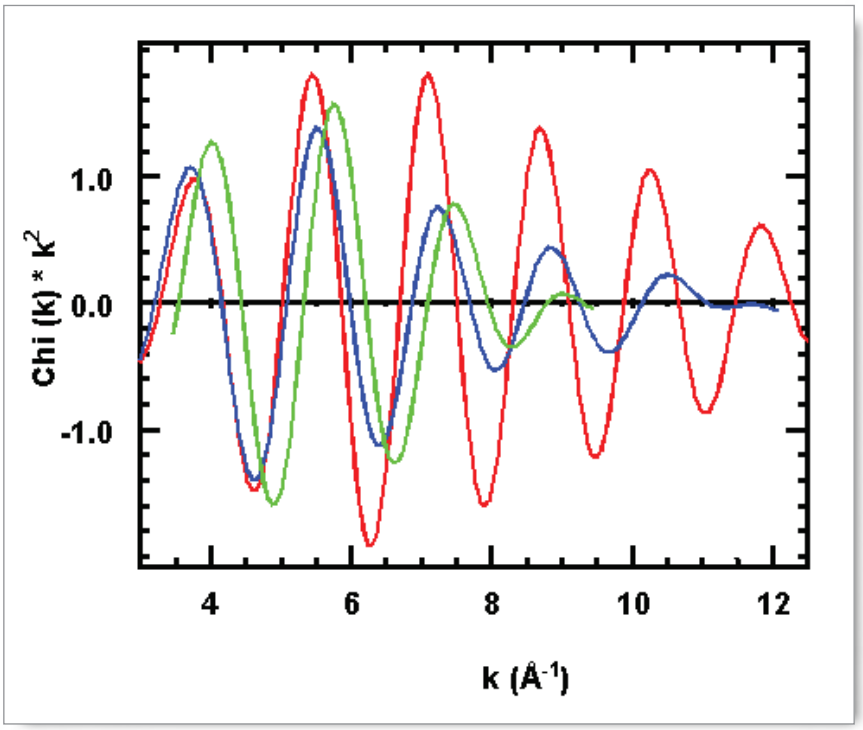

Fig. 1. k^2-weighted EXAFS of solid H_2PtCl_6 (6 Pt-Cl at 2.32 Å in red); 200 ppm H_2PtCl_6 at pH = 2.5 (2.7 Pt-Cl at 2.32 Å and 3.3 Pt-O at 2.05 Å) in blue ; 200 ppm H_2PtCl_6 at pH = 2.5 adsorbed on alumina (1.7 Pt-Cl at 2.32 Å and 4.3 Pt-O at 2.05 Å) in green.

From this and similar studies, a general understanding has been developed that makes it possible to make superior catalysts with nearly any metal on any support. By using these advances, a simple method for production of a new generation of fuel cell electrodes, which has a very high Pt loading and very small metallic particles, has been recently developed. This work has attracted the interest of several catalyst manufacturers and is currently under development. ❍

See: W.A. Spieker[1], J. Liu[1], X. Hao[1], J.T. Miller[2], A.J. Kropf[3], and J.R. Regalbuto[1], "An EXAFS study of the coordination chemistry of hydrogen hexachloroplatinate (IV) 2. Speciation of complexes adsorbed onto alumina," Appl. Catal. A **243**, 53-66, (2003).
Author affiliations: [1]University of Illinois at Chicago, [2]BP Research Center, [3]Argonne National Laboratory

Work performed at MR-CAT supported, in part, by funding from the US DOE under Grant No. DEFG0200ER45811. J.R. Regalbuto gratefully acknowledges the support of the National Science Foundation (Grant No. CTS-9908181). Use of the Advanced Photon Source was supported by the US Department of Energy, Basic Energy Sciences, Office of Science (DOE-BES-SC), under Contract No. W-31-109-Eng-38.

ANOMALOUS X-RAY REFLECTIVITY DETERMINES ION-SPECIFIC PROFILE AT MEMBRANES

Ions bound to the surfaces of biological membranes can dramatically affect processes and behaviors of molecules located on or near those membranes. Collaborators from Iowa State University's Ames Laboratory, the Institute of Experimental Physics (Leipzig University, Germany), and The Johns Hopkins University developed anomalous x-ray reflectivity techniques to probe, in detail, the distribution of such ions at a surface that mimics a biological membrane, formally called a biomimetic surface. A biological membrane consists of two lipid-protein (a variety of lipids, cholesterol, and proteins) leaflets bound together at the hydrophobic surface of the lipids, exposing the hydrophilic surfaces to the interior and exterior fluids of a cell or an organelle (Fig. 1). In this case, the biomimetic surface was a lipid monomolecular leaflet (Langmuir monolayer) formed at the gas-water (Ba-solution) interface. To investigate these biomimetic membranes, the researchers used a newly commissioned liquid surface diffractometer at the MU-CAT 6-ID beamline at the APS. The synchrotron x-ray beam at this beamline is both highly monochromatic (i.e., very narrow bandwidth) and tunable (variable x-ray energy).

Several related x-ray fluorescence methods had been developed in the past to probe adsorbed ions at solid and liquid interfaces. The researchers of this study employed the anomalous reflectivity to obtain the location and density of the adsorbed ionic layer near a Langmuir monolayer by collecting x-ray reflectivities at different energies at the absorption edge (resonance) of these ions and away from it.

The basic experimental setup for x-ray reflection involves the detection of a highly monochromatic beam that is mirror-reflected from the biomimetic surface at various angles of incidence. The special diffractometer at the 6-ID beamline enables *in situ* studies of liquid surfaces and monomolecular layers at a liquid interface. A typical reflectivity curve is measured over a relatively narrow range of incident angles (0° to 5°, depending on the x-ray energy). From a measured reflectivity curve, the average electron-density profile of the film across the interface is determined and can be interpreted in terms of molecular arrangements at the surface.

At energies away from any resonance (absorption edge), the electron density corresponds to the total electrons in the film. On the other hand, for x-ray energies at a resonance of a specific ion, heuristically, fewer electrons of these ions contribute to the reflection process; the effective electron-density at the location of these ions is thereby reduced. Figure 2a shows the effective number of electrons for some of the ions present in the film; whereas, for Cl^- and H_2O this number is practically constant, it varies dramatically for Ba ions in the vicinity of a resonance (E = 5.247 keV, for instance).

To form a biomimetic surface, the researchers spread DMPA (1,2-dimyristoyl-*sn*-glycero-3-phosphatidic acid) as a monolayer on dilute aqueous barium chloride ($BaCl_2$) solutions kept inside a Teflon® Langmuir trough. Their objective was to detect if ions from the solution bind to the charged biomimetic surface and to determine the distribution of these ions in relation to the molecular structure. They collected reflectivities at three distinct x-ray beam energies (E, measured in thousands of electron-volts): 5.1, 5.247, and 8.0 keV. The 5.1 and 8.0 levels were away from an absorption edge, while the 5.247 level

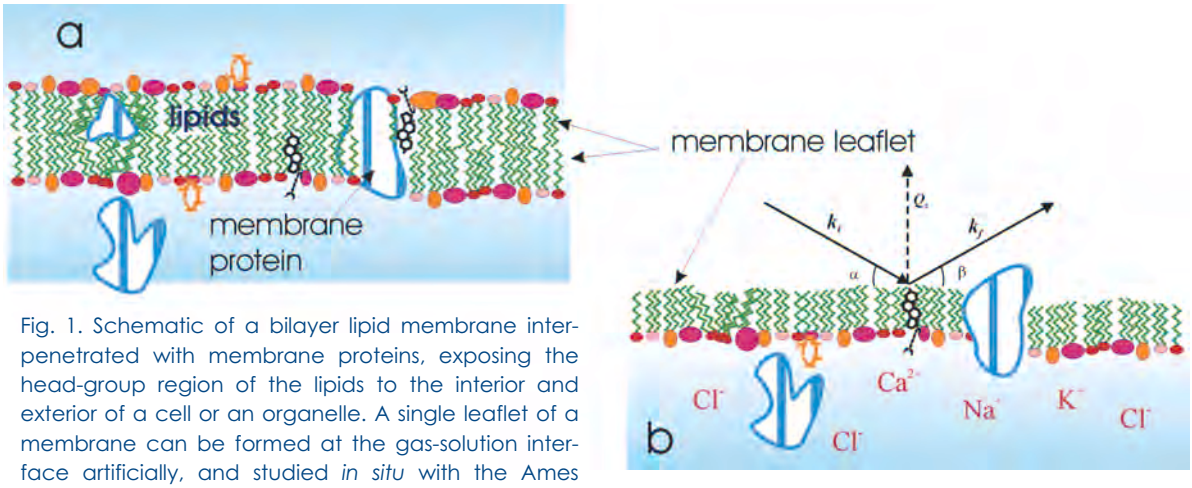

Fig. 1. Schematic of a bilayer lipid membrane interpenetrated with membrane proteins, exposing the head-group region of the lipids to the interior and exterior of a cell or an organelle. A single leaflet of a membrane can be formed at the gas-solution interface artificially, and studied *in situ* with the Ames Laboratory liquid surface diffractometer at the MU-CAT 6-ID beamline. X-ray diffraction from a leaflet system can yield the structure of the film and monitor interfacial phenomena (protein recognition processes, ionic accumulations, and others) relevant to biological processes at membrane surfaces. Note: The above graphic illustrates generic experimental arrangements and does not depict the actual membrane leaflet used in this study. (In this study, only DMPA was present in the membrane leaflet. No membrane proteins were used.)

was located at an absorption edge. Figure 2b shows three reflectivities normalized to the reflectivity of the bare surface water (shifted for clarity). The electron-density (ED) profiles that were determined from those measurements show variations at the head group region of the monolayer, and, from these differences, the distribution and concentration of the Ba ions were extracted. (Ba was chosen to replace Ca, which is abundant in biological solutions, in order to enhance the anomalous scattering effect in this model system study.)

The results pointed to a higher ratio of barium ions present at the surface than would be expected from the stoichiometric ratio alone (i.e., the stoichiometric ratio of 0.5 Ba^{2+} to $DMPA^{-}$). Previously, lower-resolution x-ray research had hinted at the barium ion overabundance on the monomolecular layer. But with the definitive ion profile that anomalous x-ray reflection provided, the researchers in this instance were able to construct a detailed picture of not only the barium ion profile on the Langmuir monolayer, but also the most likely nature of the chemical species at and near that layer. The picture that emerged was one in which the total barium ion distribution was quite asymmetric in nature, incorporating a bound Stern layer (most likely composed of $BaOH^{+}$ cations) in conjunction with a diffuse cloud of barium cations (Ba^{2+}).

Follow-up studies will increase knowledge of the detailed chemistry involved in ion binding to LM layers, including Ca. But this particular research has already demonstrated the power of anomalous x-ray reflection to yield a detailed profile of ion distribution at surfaces. With that profile, detailed chemical information about the surface layer can subsequently be deduced. ❍

See: D. Vaknin[1], P. Krüger[2], and M. Lösche[2,3], "Anomalous X-ray Reflectivity Characterization of Ion Distribution at Biomimetic Membranes," Phys. Rev. Lett. **90**, 178102-1 to 178102-4 (2 May 2003).

Author affiliations: [1]Iowa State University, [2]Leipzig University, [3]The Johns Hopkins University

Use of the Advanced Photon Source was supported by the U.S. Department of Energy, Office of Science, Office of Basic Energy Sciences, under Contract No. W-31-109-Eng-38.

ZINC ENZYME CAUGHT IN THE ACT OF CATALYSIS

New x-ray spectroscopy data is helping to resolve a 20-year debate on the catalytic mechanism of a common zinc-containing metabolic enzyme. A group performed the first millisecond-resolution x-ray absorption study on a biological reaction to investigate the way alcohol dehydrogenase removes hydrogen from alcohols. The results suggest that the zinc atom forms two different catalytic intermediates.

Alcohol dehydrogenase (ADH) removes two hydrogen atoms from one of an alcohol's carbon atoms, turning the molecule into an aldehyde or ketone (which contain a carbon-oxygen double bond). Researchers have proposed two basic mechanisms for hydrogen removal. In the traditional mechanism, the alcohol displaces a water molecule bound to a zinc atom, which serves primarily to orient the alcohol. In the alternative scenario, the water molecule stays bound to zinc during catalysis and serves as a temporary site for hydrogen transfer. A key feature distinguishing the two mechanisms is the number of atoms zinc is bound to—four if water is displaced; five if not. Researchers have had a tough time figuring out what zinc is doing, however, in part because it resists analysis by conventional forms of spectroscopy.

One way of scanning ADH (and other metal-containing proteins) is to bombard it with x-rays that vary in frequency over time and measure the resulting fluorescence spectrum, which provides information on bond length and number of atoms near zinc and is sensitive to zinc's charge and bonding geometry. Varying the x-ray frequency usually takes 50 milliseconds (ms) or longer, however, while the ADH reaction itself takes less than 100 ms. Now a group from the Weizmann Institute of Science in Rehovot, Israel, and Yeshiva University in New York has improved two methods well enough to get around that obstacle.

In one experiment, performed on the National Synchrotron Light Source beamline X9B at Brookhaven National Laboratory, they successively froze the reaction in its tracks to observe it at

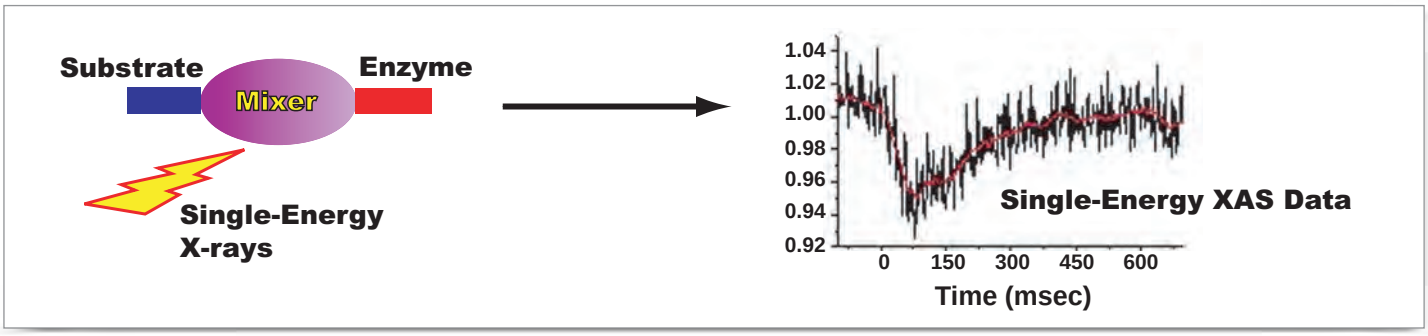

Fig. 1. Kinetic x-ray absorption spectroscopy experiments are used to follow real-time electronic changes, which are related to the structure of the catalytic site. X-ray fluorescence photons are recorded at single X-ray energy by synchronizing X-ray beam, rapid mixer, and fast data acquisition system.

elapsed times ranging from around 2 ms to 110 ms. Enzyme from bacteria and substrate were rapidly mixed and injected into a bath of liquid isopentane, which halts or "quenches" the reaction. Although the quenched molecules are actually in a mix of states, sophisticated mathematical analysis of the fluorescence data indicated the zinc formed two successive five-bond transition states in the first 70 ms after the reactants came together. They proposed that the first transition state forms when water binds to zinc, which then breaks its bond with the protein and binds to the alcohol, forming the second transition state. Water remains bound until the reaction is finished.

In a second experiment, performed on the Bio-CAT beamline 18-ID at the APS, they measured fluorescence at a single x-ray energy over time, down to the millisecond (see Fig. 1). Changes in absorption at that energy correspond to changes in zinc's charge. They observed a rapid buildup of partial positive charge on zinc, followed by a slow return to neutrality beginning around 70 ms. They interpret the partial positive charge as a sign of the second five-bond zinc transition state, in which the attached alcohol pulls zinc's electrons away from it. Theoretical calculations supported the conclusion.

The result suggests the ADH mechanism is more complicated than previously thought, but further experiments will be needed to test the proposed mechanism, and bacterial ADH may behave differently than the mammalian enzyme. The spectroscopic techniques may also prove useful in analyzing other metal-containing enzymes. ❍

See: O. Kleifeld [1], A. Frenkel [2], J.M.L. Martin [1], and I. Sagi [1], "Active site electronic structure and dynamics during metalloenzyme catalysis," Nat. Struct. Bio. **10**, 98-103 (1 February 2003).

Author affiliations: [1]The Weizmann Institute of Science, [2]Yeshiva University

I.S. was supported by the Israeli Science Foundation. J.M.L.M. was supported by the Minerva Foundation. Use of the Advanced Photon Source was supported by the U.S. Department of Energy, Office of Science, Office of Basic Energy Sciences, under Contract No. W-31-109-Eng-38.

STUDIES OF INSECT RESPIRATION USING PHASE-ENHANCED, TIME-RESOLVED X-RAY IMAGING

Many types of bugs breathe in much the same way that we do. This surprising discovery was made by scientists from Chicago's Field Museum of Natural History and Argonne National Laboratory, who studied living, breathing insects at the XOR 1-ID beamline of the APS. The investigation revealed the existence of a previously unknown breathing mechanism that is similar to the inflation and deflation of lungs in vertebrate animals.

Scientists had long known that bugs breathe by means of a complex network of gas-filled tubes, called tracheae, that carry oxygen to various parts of their bodies, but it was felt that breathing took place mainly through passive gas diffusion or through changes in internal pressure produced by body motion or hemolymph circulation. The breakthrough came as a result of the ability to take high-resolution x-ray videos of the internal workings of insects in real time as they breathed.

The researchers employed phase-enhanced, time-resolved x-ray imaging, which was enabled by the high flux and partial coherence of the x-ray beams at the APS. The technique produced edge enhancement of the images, with the APS x-ray beams permitting video rates of 30 frames per second. x-ray videos were recorded for the anterior thorax and head regions of ground beetles (*Platynus decentis*), carpenter ants (*Camponotus pennsylvanicus*), house crickets (*Achaeta domesticus*), and other insects.

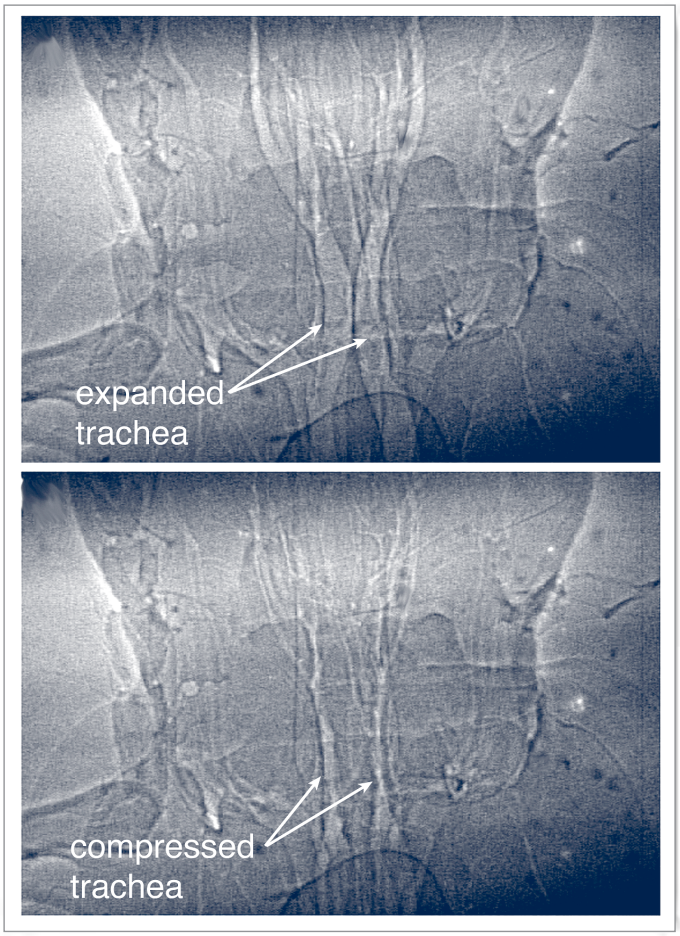

Fig. 1. Ground beetle tracheal images about 0.5 s apart. Upper image shows beetle tracheal tubes fully expanded; in the lower image, they are fully compressed. (Images: Mark W. Westneat)

The tracheal systems were clearly visible as bright branching patterns on the x-ray videos. The tracheae were seen to be inflated at rest (see Fig. 1). They then became squeezed progressively over the course of 300 to 500 msec and subsequently expanded over a similar time period. The tracheae were compressed primarily in one direction so that the roughly circular cross section of a trachea at rest was compressed into an ellipse. Narrowing of the tracheae was often synchronous throughout the head and thorax regions, but local tracheal compression was also observed. The data indicated interspecies variability in both exhalation-inhalation duration and cycle frequency. The researchers also observed other respiratory mechanisms, such as abdominal pumping, autoventilation, and circulatory fluid motion.

Further development of the x-ray imaging technique used in this study could lead to an increased understanding of the basic principles of mammalian, fish, and insect physiology, which could have important implications for humans and their health care. This is because many aspects of human physiology have their counterparts in lower animal orders. For example, studying how larval fish move their backbones could provide information on human backbones, which may provide clues for treating spinal cord injuries in humans. Likewise, studying the walls of blood vessels in mice and the tiny hearts in beetles (each beetle has multiple "hearts") may possibly shed light on how to treat high blood pressure.

The imaging technique itself may have medical applications, as turned out to be true of many imaging advances in the past (magnetic resonance imaging, computed axial tomography computed tomography . The tool also has the potential for a wide variety of other applications, including detecting and studying cracks, voids, and other boundaries inside optically opaque structures; studying fluid flow in rocks and soils for oil exploration and recovery; and characterizing advanced materials, such as ceramics and fiber-reinforced composites. ❍

See: M.W. Westneat [1], O. Betz [1,2], R.W. Blob [1,3], K. Fezzaa [4], W. J. Cooper [1,5], W.-K. Lee [4], "Tracheal respiration in insects visualized with synchrotron x-ray imaging," Science **299**, 558-560 (24 January 2003).

Author affiliations: [1]Field Museum of Natural History, [2]University of Kiel, [3]Clemson University, [4]Argonne National Laboratory, [5]The University of Chicago

Use of the APS is supported by the DOE Office of Science, Office of Basic Energy Sciences, under Contract no. W-31-109-Eng-38. This research was also funded by grants ONR N000149910184 and NSF DEB-9815614.

SYNTHESIS AND ANALYSIS OF TiO_2-OLIGONUCLEOTIDE HYBRID NANOPARTICLES

New developments in nanotechnology offer the creation of chemical-biological hybrid nanocomposites, which can be introduced into cells to initiate intracellular processes or biochemical reactions. Researchers from Northwestern University Medical Center and Argonne National Laboratory synthesized TiO_2-oligonucleotide nanocomposites made of DNA oligonucleotides attached to 45-Å TiO_2 nanoparticles and tested them by using the XOR 2-ID-E beamline at the APS. A key benefit of nanocomposites is that they could advance medical biotechnology and open new doors in chemistry and materials sciences.

The research goal was to develop the TiO_2-oligonucleotide nanocomposites into nanodevices that could be introduced into cells and function in vivo and in situ. To accomplish that goal, researchers first determined that the nanocomposites could successfully hybridize with long DNA molecules. One concern was that the nanocomposites would "clump" and not be able to withstand an incubation temperature of 95°C, the temperature required for annealing and polymerase chain reaction (PCR). Using atomic force spectroscopy, researchers visualized a

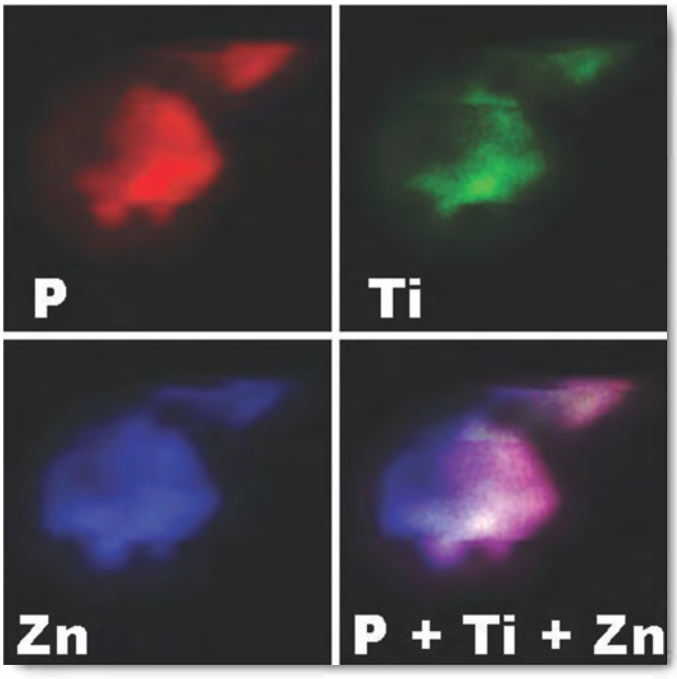

Fig. 1. Scan of a 21 x 21-μm area with a single nucleus containing 3.6 x 10^6 nanoparticles. Scanning was done in 0.2-μm x 0.2-μm steps, and this nucleus was isolated from cells infected by SuperFect reagent with 80 pmol of R18Ss-TiO_2 hybrid nanocomposite and 160 pmol of "free" R18Sas oligonucleotide, applied onto 4 x 10^6 cells and incubated for two hours. Nuclei were isolated according to the published procedure. [1] Co-localization of phosphorus (red), titanium (green), and zinc (blue) signals is presented as the overlap of these three colors.

hybridization mixture that had been annealed. The nanocomposite did not clump and withstood the annealing process, paving the way for further research.

Mammalian cells were "infected" in vitro with TiO_2-oligonucleotide nanocomposites by conventional methods. Researchers mapped the location of the titanium in the cells by using titanium-specific Kα x-ray fluorescence induced at the APS. In total, researchers used 514 cultured cells from 24 different samples infected with seven different nanocomposites. Depending on the experiment, 20–50% of the cells were found to have accepted and retained titanium nanoparticles. To confirm that the nanocomposites were, indeed, able to enter the cell nucleus, researchers then isolated nuclei from cells infected with a TiO_2 nanocomposite and a "free" oligonucleotide.

Scans revealed titanium in 6 out of 13 sampled nuclei, demonstrating that the TiO_2-DNA nanocomposites reached the nucleus of the mammalian cells. Figure 1 shows that signals of phosphorus and zinc overlap and that the titanium signal showed the highest density in a circular subregion of the nucleus. Given its size and shape, this nuclear subregion is likely to be the nucleolus — the subregion of the interphase nucleus where rDNA is located — and would therefore be the most likely nuclear location for retention of an oligonucleotide-TiO_2 nanocomposite with rDNA sequences attached.

In another experiment, researchers tested the hypothesis that oligonucleotide-TiO_2 nanocomposites are capable of photoinduced endonuclease activity. They showed that DNA oligonucleotides covalently attached to TiO_2 nanoparticles anneal/hybridize to target DNA with specificity dependent on the sequence of the oligonucleotide and participate in PCR reactions. With subsequent illumination, the completed PCR products containing the TiO_2 nanoparticles induced DNA strand breaks in a short distance from the TiO_2.

To gather PCR band cleavage data, researchers used standard PCR reactions. After a reaction, PCR products were divided equally; white light was then used to illuminate one-half of each reaction for 2 min. Polymerase chain reaction products from non-illuminated and illuminated portions were separated by agarose gel electrophoresis, blotted to Gene-Screen membranes, and hybridized with a radiolabelled probe. Researchers found that, as in the experiments establishing cleavage of oligonucleotides, DNA linked to a TiO_2 nanoparticle did not migrate through the gel. After illumination, however, the same PCR products (primed by the nanocomposite) were cleaved away from the TiO_2 nanoparticle at a random short distance (up to 50 base pairs) and entered the gel, forming a short, diffuse band.

Researchers concluded that even the simple TiO_2-oligonucleotide hybrid nanoparticles synthesized in this project can perform many chemical and biological tasks, including a light-induced site-specific (within 50 nucleotides) nucleic acid endonuclease activity. The nanocomposites analyzed at the APS can perform a multitude of chemical-biological tasks, indicating that other types of TiO_2-biomolecule nanocomposites can be engineered to be nanodevices for medical biotechnology. ❍

References

[1] B. Pichon and D. Christophe, Anal. Biochem. 261, 233 (1998).

See: T. Paunesku[1,2], T. Rajh[2], G. Wiederrecht[2], J. Maser[2], S. Vogt[2], N. Stojićevic´[1,2], M. Protić[2], B. Lai[2], J. Oryhon[2], M. Thurnauer[2], and G. Woloschak[1,2], Nat. Mat. 2, 343-346 (May 2003).

Author affiliations: [1]Northwestern University Mredical Center, [2]Argonne National Laboratory

T.P., N.S., M.P., J.O. and G.W.were supported by National Institute of Health grants CA81375, CA73042, and NS21442; T.P., T.R.,G.W., J.M., S.V., N.S., B.L., M.T., G.W., and use of the APS, were supported by the US Department of Energy, Office of Basic Energy Sciences under contract No.W-31-109-Eng-38.

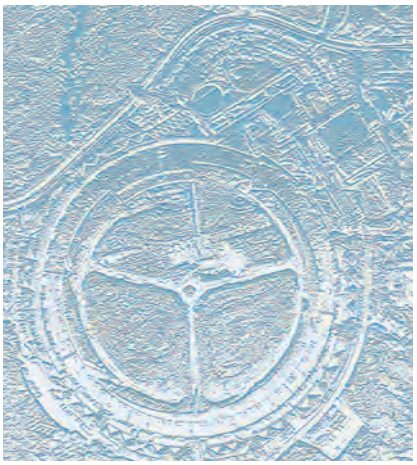

GRASPING THE STRUCTURE OF INSECT MUSCLE POISED TO CONTRACT

Researchers have achieved the first detailed view of resting muscle filaments poised to contract, a long sought window into the biochemical cycle that causes muscle contraction. The group determined the overall structure of insect muscle fibers from x-ray diffraction patterns and performed computer modelling to analyze the data. The resulting structure, reported in August 2003, suggests a specific mechanism for insect muscle activation.

Muscle cells (fibers) contain two parallel, overlapping sets of protein filaments, made of myosin and actin, respectively, that align with the direction of contraction. The myosin and actin filaments have fixed length individually, but they slide past each other like telescope segments to stretch or shorten the overall muscle. The shortening motion is driven by comma-shaped myosin "heads," which radiate out from the myosin filaments and cyclically bind to, bend against, and then release adjacent actin filaments. The bind-and-bend phase of each cycle is called a powerstroke. Comparing bound and resting head structures and positions can help researchers deduce the powerstroke mechanism. Researchers had previously viewed the end state of the powerstroke, in which myosin heads have bent and are strongly bound to actin (Fig. 1). No one had reported the orientation of the unbound heads in myosin's relaxed initial state until August 2003, however.

Researchers from Imperial College London, Duke University, and the Illinois Institute of Technology decided that improved synchrotron technologies and data analysis tools offered the prospect of modelling the relaxed structure. They recorded so-called low-angle x-ray diffraction patterns from flight muscle fibers of giant waterbugs on the Bio-CAT beamline 18-ID at the APS, which gave them new and sharper details of the large-scale myosin filament structure. A single recording cannot produce both large- and fine-scale data because large structural elements are encoded in low-angle features of the diffraction pattern and vice versa; cameras can resolve one or the other, but not both. So the group computed thousands of different ways of fitting existing high-resolution atomic models of head structure into the overall model, on the basis of the assumption that each head could pivot at two points, and identified the best fit to the observed low-angle x-ray pattern. The model confirmed that resting myosin filaments have stacked rings or "crowns" of eight heads each — two heads per myosin molecule. One head of each myosin projects about 90° from the filament axis; the other tucks inward against the filament's circumference.

Comparing the results of modeling against actual post-powerstroke myosin head conformations in waterbug and many other species suggests the changes that take place during a powerstroke cycle (Fig. 1). Each of the four projecting heads rotates slightly about the "neck," which connects to a pivot on the myosin filament. The rotation positions the head to bind tightly to the actin filament and tilt forcefully by 45° relative to the

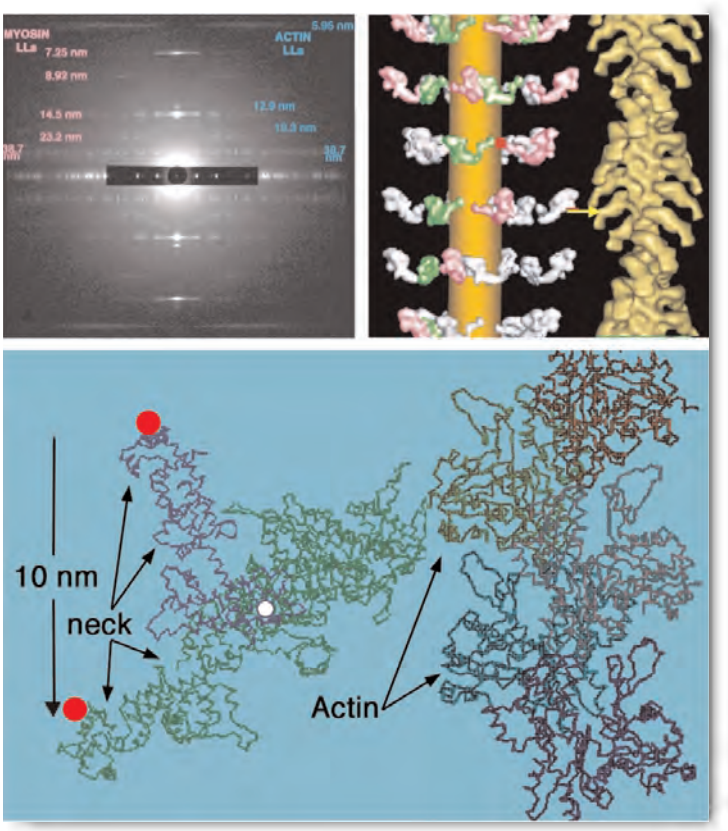

Fig. 1. Top left: Low-angle x-ray diffraction pattern from relaxed insect flight muscle. (Pink and blue numbers represent spacings between repeating structural elements as calculated from the pattern.) Top right: Structure (left) of the modelled myosin heads (pink/white/green) in their relaxed, pre-powerstroke state and (right) in their "rigor" or post-powerstroke state. Bottom: Transition from the head shape in relaxed insect muscle (blue) to rigor-like final shape (green), showing the pivots needed (red on thick filament, white within head) to let the neck swing from one form to the other when bound to actin.

axis of the filament. Such a powerstroke would move the head and bound actin filament 10 nanometers down the axis. The four inward-pointing heads each touch an adjacent projecting head. These contacts may restrain both myosin heads from cleaving high-energy ATP molecules—the powerstroke fuel—until the right moment.

Insect flight muscles must contract rapidly and precisely to keep the insect aloft. As if optimized to do so, the relaxed outward myosin heads seem poised to bind actin and begin powerstroking. The researchers speculate that the increased calcium in stimulated muscle cells may loosen the heads and modify actin filaments to facilitate binding. Stretching flight muscle triggers concerted powerstrokes, perhaps by perturbing the ring of contacts between inward and outward heads to fully enable ATP splitting and actin binding. ❍

See: H.A. Al-Khayat[1], L. Hudson[1], M.K. Reedy[2], T.C. Irving[3], and J.M. Squire[1], "Myosin Head Configuration in Relaxed Insect Flight

Muscle: X-ray Modeled Resting Cross-Bridges in a Pre-power-stroke State Are Poised for Actin Binding," Biophys. J. **85**, 1063–1079 (August 2003).

Author affiliations: [1]Imperial College London, [2]Duke University, [3]Bio-CAT/Illinois Institute of Technology

J.M.S. was supported from a UK Biotechnology and Biological Sciences Research Council (BBSRC) project grant (28/S10891). M.K.R. was supported by National Institutes of Health AR-14317. CCP13 software was developed as part of UK BBSRC/Engineering and Physical Sciences Research Council (EPSRC) funded projects (e.g., 28/B10368 and 28/B15281). Use of the Advanced Photon Source was supported by the U.S. Department of Energy, Basic Energy Sciences, Office of Energy Research, under Contract No. W-31-109-Eng-38. BioCAT is a U.S. National Institutes of Health-supported Research Center RR08630.

METAL SENSOR KEEPS COPPER IN CHECK

How's this for a hair trigger? A metal-sensitive molecular switch found in *E. coli* bacteria trips at a zeptomolar concentration of free copper—equivalent to one free copper ion in every 10^{11} cells. Researchers determined the three-dimensional structure of the protein switch, which helps maintain copper levels in the cell, and found that an unusual binding pocket allows it to distinguish copper from other metal ions with such spectacular sensitivity.

Metal ions are crucial to many enzymes, but too much metal floating around in a cell may weaken or kill it. A family of proteins sensitive to zinc, mercury, and other metal ions therefore monitors the cell interior and turns on ion pumps, detoxifying enzymes and other cellular machinery if metal concentrations get too high. If more than a few thousand copper ions accumulate in a cell, for example, the CueR protein senses the change and takes action. To test the sensitivity of CueR, researchers from Northwestern University added decreasing amounts of copper to a mixture of this sensor protein and one of the genes it activates, called copA. Active, copper-bound CueR binds to the copA DNA and recruits enzymes to copy the gene into molecules of RNA. The mixture began producing RNA at a tiny concentration of copper, corresponding to one free ion in a volume the size of 10^{11} *E. coli* cells.

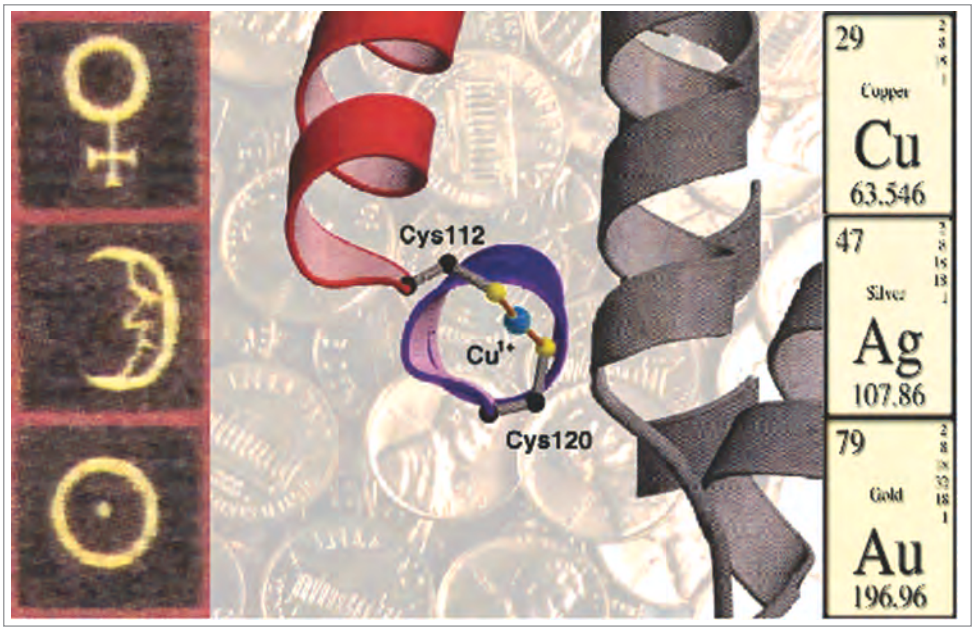

Fig. 1. The CueR protein is spectacularly sensitive and specific to metal ions with one unit of positive charge—including copper, silver and gold—despite a relatively simple linear binding geometry. Here two sulfur atoms (yellow) hold a copper ion (blue) in place.

CueR achieves its sensitivity and specificity by burying a copper ion away from solution and spearing it between two sulfur atoms (Fig. 1). The group compared the structure of CueR, which recognizes metal ions that have only a single unit of positive charge, to that of the zinc sensor ZntR, which recognizes only ions that have two units of charge, such as zinc . The researchers crystallized both metal sensors and solved their structures from x-ray diffraction patterns, obtained at the DND-CAT 5-ID beamline at the APS, and the Stanford Synchrotron Radiation Laboratory in Stanford, California. To confirm that the copper ion and sulfur atoms are arranged in a line, the Northwestern researchers and a group from the University of Michigan in Ann Arbor scattered x-rays of increasing energy off the protein. The energy of the resulting photons emitted from the copper-sulfur complex were consistent with a linear geometry.

The structure reveals several reasons for the specificity of CueR. Ions with less charge prefer to form fewer bonds with adjacent atoms. The cramped metal binding pocket of CueR is structured to offer an ion only the two sulfur atoms for bonding, whereas ZntR holds two zinc atoms in a web of four bonds each. CueR also stabilizes the copper-sulfur complex by neutralizing its net negative charge. Each sulfur atom is negatively charged. The copper ion neutralizes one negative charge, and an adjacent protein dipole offsets the other. A greater local charge would upset that balance in the greasy interior of the protein.

The surprisingly simple linear arrangement suggests that the sensitivity of CueR rises from the charge neutralization and additional weak bonding between copper and the surrounding pocket of amino acids, the researchers say. The linear copper-sulfur geometry has been reported in only a few copper-transporting proteins related to copA. The high sensitivity of CueR

also implies that the internal space (cytosol) of *E. coli* is typically starved for copper, which raises the question of how the cell supplies other molecules with the metal. One possible explanation is that copper ions are not tolerated in the cytosol, but when they overflow into it, they are transported out to the cell envelope, where all of *E. coli*'s known copper-dependent molecules are located. ❍

See: A. Changela, K. Chen, Y. Xue, J. Holschen, C.E. Outten, T.V. O'Halloran, and A. Mondragón, "Molecular Basis of Metal-Ion Selectivity and Zeptomolar Sensitivity by CueR," Science **301**, 1383-1387 (5 September 2003).
Author affiliation: Northwestern University

See also: K. Chen et al., "An Atypical Linear Cu(I)-S_2 Center Constitutes the High-Affinity Metal-Sensing Site in the CueR Metalloregulatory Protein," J. Am. Chem. Soc. **125**, 12088-12089 (2003).

Supported by NIH GM51350 (to A.M.), NIH GM38784 (T.V.O.), NIH F32 DK61868 (K.C.), and the National Research Service Award Institutional Training Grant in Molecular Biophysics (NIH GM08382) (A.C. and C.E.O.). Use of instruments in the Keck Biophysics Facility at Northwestern University is acknowledged. Support from the R.H. Lurie Comprehensive Cancer Center of Northwestern University to the Structural Biology Facility is acknowledged. Portions of this work were performed at the DuPont-Northwestern-Dow Collaborative Access Team (DND-CAT) Synchrotron Research Center at the Advanced Photon Source (APS) and at the Stanford Synchrotron Radiation Laboratory (SSRL). DND-CAT is supported by DuPont, Dow, the state of Illinois, and the NSF. SSRL is operated by the DOE, Of•ce of Basic Energy Sciences. The SSRL Biotechnology Program is supported by the NIH and the DOE. Coordinates and structure factors have been deposited in the Protein Data Bank with accession numbers 1Q05, 1Q06, 1Q07, 1Q08, 1Q09, and 1Q0A.Use of the Advanced Photon Source was supported by the U.S. Department of Energy, Office of Science, Office of Basic Energy Sciences, under Contract No. W-31-109-Eng-38.

SAXS Studies Reveal Metals in the Jaws of Marine Worms

What makes our hard tissues—especially our teeth and jaws—so hard? In higher-order organisms, particularly in vertebrates (like us), it's calcium, but in some invertebrates, such as insects and worms, the fangs and mandibles contain high levels of the transition metals zinc, copper, iron, and manganese. Using the x-ray absorption spectroscopy(XAS) station on the PNC/XOR beamline 20-ID at the APS, collaborators from the University of California, Santa Barbara; Vienna University of Technology; the Austrian Academy of Sciences; Helsinki University of Technology; and Argonne National Laboratory studied the detailed composition of worm jaws, delineating the location of metal and elucidating the fundamental underpinnings of jaw strength.

In particular, two invertebrates were studied in detail: clam worms (*Nereis limbata*) and bloodworms *(Glycera dibranchiata*), both the size of a typical earthworm (about 20 cm in length). Jaws dissected from the worms were about 5 mm long or less and mainly proteinaceous, containing significant amounts of the amino acids glycine and histidine with a few weight percent metal concentrated at the tip of the jaw. The type of transition metal depends on the species: the jaws of the raptorial bloodworm contain predominately copper as the major inorganic constituent, whereas its scavenger cousin the clam worm apparently prefers zinc.

Intact worm jaws were subjected to synchrotron microbeam analysis—x-ray diffraction and x-ray absorption

Fig.1. The jaw of a *Nereis limbata worm*. The jaw is about 5 mm long, hollow at the base and solid at the tip. Higher x-ray absorption is found at the tip, indicating that that area has higher local electron density. All of the zinc is concentrated in the tip region of the jaw, with no or very low levels of zinc at the base.

experiments, done at the APS, as well as small-angle x-ray scattering.

The zinc in the *Nereis* jaw was found to be in nonmineralized form: noncrystalline, distributed in the proteineous jaw matrix, yet still hardening the structure. Nanoindentation was carried out to examine the local mechanical properties of the jaw materials and to relate the hardness and stiffness to the local metal content. A small diamond tip in the shape of an inverted pyramid was used to press on the surface of the (typically dried) jaw tissue, rendering a displacement point typically one micrometer in size. Recording of a load-displacement curve provided for the calculation of local jaw stiffness.

The presence of zinc and chlorine in *Nereis* jaws was found to correlate strongly with the local hardness and stiffness of the material. Despite the co-localization of the two elements, no simple zinc-chlorine compound was found. Instead, it is proposed that both zinc and chlorine bind directly to the protein, thus cross-linking the protein molecules and adding strength to the jaw. This idea gets extra support from the fact that the jaw protein contains a significant amount of the amino acid histidine, which prefers to coordinate with metals.

In general, jaws of *Nereis* worms were considerably softer than those of their relatives *Glycera*. The difference appears to be due to a difference of functionality: *Glycera* is a venomous species that must grasp tightly in order to inject venom, while *Nereis* jaws serve mainly to grasp small pieces of food. Form, once again, follows function. ❍

See: H.C. Lichtenegger[1,2], T. Schoberl[3], J.T. Ruokolainen[4], J.O. Cross[5], S.M. Heald[5], H. Birkedal[1], J.H. Waite[1], G.D. Stucky[1], "Zinc and mechanical prowess in the jaws of *Nereis*, a marine worm," Proc. Natl. Acad. Sci. U.S.A. **100** (16), 9144-9149 (5 August 2003).

Author affiliations: [1]University of California, Santa Barbara, [2]Vienna University of Technology, [3]Austrian Academy of Sciences, [4]Helsinki University of Technology, [5]PNC/XOR

Support was provided by the Office of Naval Research; and the Biomaterials Program at the National Institute of Dental and Craniofacial Research, National Institutes of Health. This work was supported by Fonds zur Förderung der Wissenschaftlichen Forschung (Austria) Award J2184 (to H.C.L.) and the Danish Natural Sciences Research Council (H.B.) and made use of the Central Facilities, Materials Research Laboratory at University of California, Santa Barbara, supported by National Science Foundation Award DMR 00-80034. Use of the Advanced Photon Source was supported by the U.S. Department of Energy, Office of Science, Office of Basic Energy Sciences, under Contract No. W-31-109-Eng-38.

MAPPING THE UPTAKE OF PLATINUM ANTICANCER AGENTS IN INDIVIDUAL HUMAN OVARIAN ADENOCARCINOMA CELLS

Cisplatin, a platinum-based chemotherapeutic drug, has been a boon to physicians in treating testicular and ovarian cancer. The cisplatin analogue Pt103 is even better, because it remains active long after such tumors develop a resistance to cisplatin. This advantage has prompted research into finding the reasons why. The most critical aspect of this work involves establishing whether Pt103 differs significantly from its parent drug in cellular uptake and intracellular distribution.

Researchers from five Australian research centers—La Trobe University, the Peter MacCallum Cancer Institute, the University of Melbourne, Monash University, and the Australian Nuclear Science and Technology Organisation—explored this issue by using the state-of-the-art hard x-ray microprobe (XMP) at the XOR 2-ID-D beamline of the APS. The study aimed to determine whether the XMP is capable of quantifying the uptake and intracellular distribution of potential anticancer agents within individual adenocarcinoma cells. This capability would be a great improvement over current techniques, which obtain such information only as averages over millions of cells, because of the minute amounts of optical fluorescence marker material that become distributed within each cell.

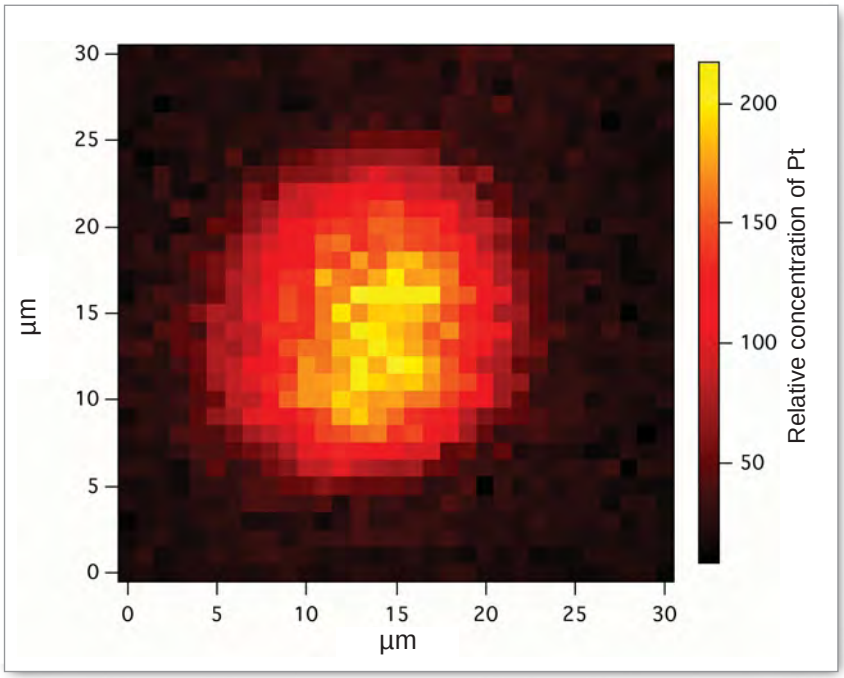

Fig. 1. The elemental distribution of platinum in a human ovarian 2008 cell that was dosed with 10 µm Pt103 over an 8-h period.

Human ovarian 2008 cells and cisplatin-resistant 2008/CDDP cells were treated with cisplatin or Pt103, snap frozen in isopentane, and then freeze-dried before being mounted on an X-Y translation stage at 2-ID-D. The samples were scanned across a microfocused x-ray spot, yielding spatially resolved fluorescence maps of many different elements simultaneously. This work mainly concentrated on the presence of platinum (Pt). An incident x-ray energy of 11.7 keV was used to excite the Pt L fluorescence lines. At this energy, x-rays penetrate biological cells without significant absorption; thus, no specimen thinning is required, and the fluorescence map of an element represents a two-dimensional projection of its volumetric distribution within the specimen.

Uptake of cisplatin in cancer cells that are resistant to the drug was found to be reduced by ~50%, compared with uptake in normal cancer cells over a 24-h period. In contrast, resistant cells showed an increased uptake of the Pt103 derivative by up to an order of magnitude. The researchers speculate that the enhanced uptake of Pt103 may allow the drug to overcome the resistance mechanism induced by long-term exposure to cisplatin. Interestingly, Pt103 uptake was found to be largest in resistant cells (over a 24-h period), which was contrary to findings from previous bulk measurements. This result highlights the difference between measurements performed on millions of cells as opposed to those performed on individual cells, as it appears from this work that measurable variation in uptake can occur within cell batches.

This experiment successfully demonstrates the feasibility of using the XMP for single-cell analysis, even for clinical doses of anticancer agents, which has not been possible previously with other analytical techniques. The XMP technique was shown to provide a minimum detectable limit of 20 attograms (2×10^{-17} grams or 6×10^{4} atoms) for platinum.

In this study, a step size of 1 µm was chosen to map out the Pt distribution in the whole cell (see Fig. 1). The XMP, however, is capable of achieving a spatial resolution of ~100 nm and may therefore be used for subcellular imaging in future studies when cell sections are used. This high spatial resolution combined with an ultimate elemental sensitivity at the parts-per-billion level pave the way for quantitative submicron three-dimensional mapping of elemental distributions within individual cells. The spatial and elemental resolution would allow for direct quantification of drug uptake in the nuclear and mitochondrial components. Such subcellular information may one day allow the detailed mechanisms of drug uptake to be studied directly, which could lead to more effective drug designs. ❍

See: P. Ilinski[1], B. Lai[1], Z. Cai[1], W. Yun[1], D. Legnini[1], T. Talarico[2,3], M. Cholewa[4], L.K. Webster[3], G.B. Deacon[5], S. Rainone[3], D.R. Phillips[2], and A.P.J. Stampfl[1,6], "The Direct Mapping of the Uptake of Platinum Anticancer Agents in Individual Human Ovarian Adenocarcinoma Cells Using a Hard X-ray Microprobe," Can. Res. **63**(8), 1776-1779, (15 April 2003).

Author affiliations: [1]Argonne National Laboratory, [2]La Trobe University, [3]Peter MacCallum Cancer Institute, [4]University of Melbourne, [5]Monash University, [6]Australian Nuclear Science and Technology Organisation

This research was supported by the Australian Synchrotron Research Program, funded by the Commonwealth of Australia under the Major National Research Facilities Program; the U. S. Department of Energy, under Contract W-31-109-Eng-38; and a grant from the Clive and Vera Ramaciotti Foundation (T. T., M. C., and D. R. P.). Use of the Advanced Photon Source was supported by the U.S. Department of Energy, Office of Science, Office of Basic Energy Sciences, under Contract No. W-31-109-Eng-38.

HOW UBIQUITIN TAKES ITS CUE

Proteins often just cannot get away from ubiquitin, a versatile protein tag that might mark them for destruction, sorting, or enlistment into gene repair or cell division. Now researchers have determined how a ubiquitin-binding component of several proteins, called CUE, recognizes that tag. They solved the crystal structure of CUE and found that it groups in pairs capable of binding single ubiquitins, and that multiple pairs can team up to form a series of pockets for binding multiple ubiquitin molecules.

Researchers originally discovered ubiquitin, named for its nearly identical form in cells from yeast to human, as a tag marking other proteins for destruction. Some-times the tag is a single ubiquitin; other times it is a string of them. They have since learned that these tags help regulate a range of basic cellular processes by attracting different proteins that recognize and bind to ubiquitin. The discovery of new ubiquitin-binding modules brought to light additional functions for ubiquitin in the recent past, but researchers still know little about how such modules work. One mystery is how they can tell a single ubiquitin molecule from a string of them. Hoping to shed light on that ability, a group from the National Institutes of Health and the Mayo Clinic crystallized and solved the structure of a yeast protein's CUE domain, which recognizes single ubiquitin tags.

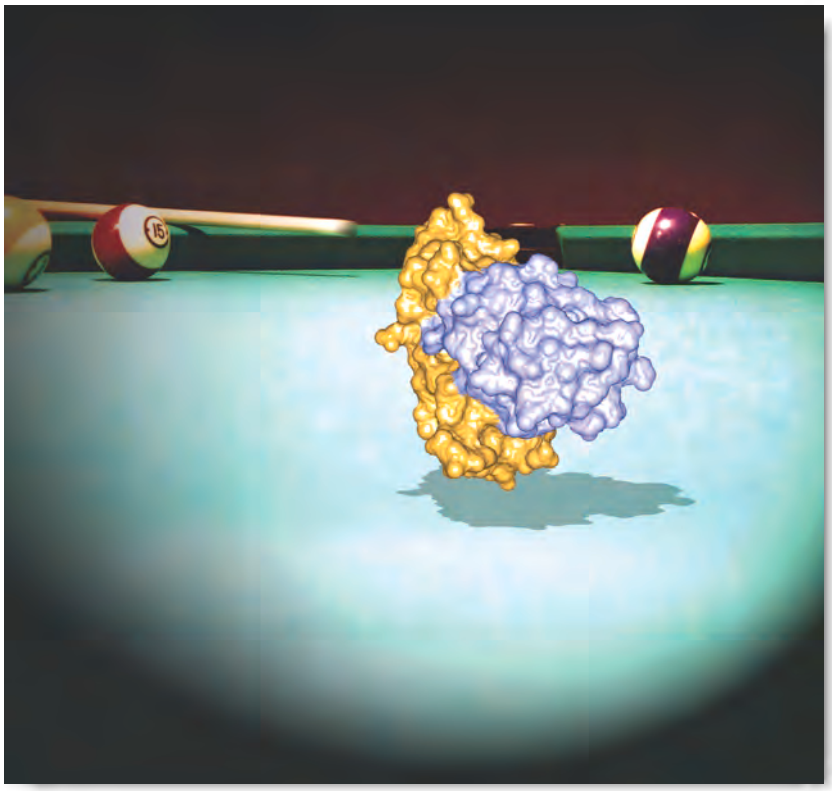

Fig. 1. The CUE domain (gold) joins in pairs to form a basket-like pocket that cups the ubiquitin protein (blue). (Image by G. Prag.)

Based on x-ray diffraction data obtained at the SBC-CAT 19-ID beamline and the SER-CAT 22-ID beamline at the APS, the group found that CUE has a short, rod-like structure consisting of three helices, very similar to another ubiquitin-binding domain called UBA. They were surprised to find that CUE domains pair up to bind ubiquitin. Individual CUE molecules, or monomers, join together by swapping one helix for the identical one from their partner. The researchers found that such a pair, or dimer, undergoes a dramatic structural shift upon binding, flexing into a basket shape that cups the protein tag (Fig. 1). CUE can also dimerize in real cellular conditions as part of a full-length protein, they found.

To understand why the dimer is responsible for binding ubiquitin, the group constructed mutant proteins whose key binding amino acids were swapped for amino acids that interfere with binding. The first and last helices of the CUE monomer nestle against ubiquitin, whereas the middle helix faces away. In the dimer, however, the middle helix of each monomer snuggles closer to ubiquitin. The group mutated either the middle helix or the flanking helices of the dimer and found that both kinds of mutation made CUE much less sticky to ubiquitin, indicating that the middle and flanking helices both take part in binding. Because the monomer can bind only with the flanking helices, the group conclude that this interaction is not enough to cause tight binding.

Surprisingly, each dimer was joined to two ubiquitin molecules in the crystal structure, despite forming a basket designed to hold just one. Because of the way the dimer forms, the same amino acids in one monomer that bind to ubiquitin on the inner, concave surface of the basket are also present in the other monomer, but on the outer, convex surface. If two baskets are side by side, their outer surfaces complement each other and form essentially the same binding pocket as the inner basket does. Two CUE dimers would therefore have three basket-like pockets and be able to bind three ubiquitin molecules. The researchers say that the existence of such a binding pattern could allow domains like CUE to bind individual ubiquitin molecules or strings of them, depending on its state—monomer or dimer. ❍

See: G. Prag[1], S. Misra[1], E.A. Jones[1], R. Ghirlando[1], B.A. Davies[2], B.F. Horazdovsky[2], and J.H. Hurley[1], "Mechanism of Ubiquitin Recognition by the CUE Domain of Vps9p," Cell **113**, 609–620 (30 May 2003).

Author affiliations: [1]National Institutes of Health, [2]The Mayo Clinic Cancer Center

This study was supported in part by NIH grant number GM55301 to B.F.H. and a predoctoral fellowship from the HHMI to B.A.D. Use of the Advanced Photon Source was supported by the U.S. Department of Energy, Office of Science, Office of Basic Energy Sciences, under Contract No. W-31-109-Eng-38.

How a Promiscuous Enzyme Recognizes Cocaine and Heroin

The first three-dimensional structure of a human protein bound to chemicals that mimic cocaine and heroin has been determined by researchers from the University of North Carolina in Chapel Hill and St. Jude Children's Hospital. The enzyme, called hCE1, cleaves apart both narcotics and detoxifies the nerve gas sarin and similar chemical weapons. The structure reveals that hCE1 is capable of acting on structurally diverse chemicals because it has both specific and indiscriminate binding pockets. The enzyme might be used to treat drug overdose and defend against chemical weapon exposure.

Human carboxylesterase (hCE1, also called egasyn), which is found in the liver and several other tissues, metabolizes foreign chemicals—from narcotics to clinical drugs to poisons—by surgically removing small carbon-oxygen chemical groups. The United States military is working to develop the protein into a defense against chemical weapons such as sarin, soman, tabun and VX gas. Not only does the enzyme recognize a wide range of chemicals, it also rejects molecules with subtly different structures, called isomers. To understand how the enzyme could be so general yet so specific, and how it could be improved, the group crystallized mixtures of hCE1 with analogs of cocaine and heroin, called homatropine and naloxone (Fig. 1). They solved the resulting structures from x-ray diffraction patterns obtained at the SER-CAT beamline 22-ID at the APS and beamline 9-1 at the Stanford Synchrotron Radiation Laboratory.

The protein works its magic by juxtaposing a large, flexible binding pocket to a small, rigid one. These are buried deep in the middle of the molecule, in a gorge called the "active site." The small pocket prefers slender chemical linkages, making the protein selective, whereas the larger one can accommodate a variety of bulky chemical groups, making it promiscuous. The enzyme's binding pocket is unique compared to other known proteins that bind cocaine, so it may serve as a model for understanding how the drug binds to targets in the brain and other tissues.

The researchers modeled the orientations of cocaine and heroin in the enzyme's active site based on the positions of their analogs. Cocaine would be positioned to have one of its chemical bonds dissolved by amino acids in the rigid pocket, whereas the corresponding chemical group in one of its isomers (similar to a mirror image of the drug) would clash with the surrounding amino acids. The heroin analog naloxone bound to the active site in two different orientations but preferred one orientation over the other, which explains why hCE1 can metabolize heroin into either of two compounds but carries out one reaction more efficiently than the other. hCE1 is also responsible for creating an especially toxic derivative of cocaine, called cocaethylene, in the presence of alcohol. The researchers propose that ethanol in the blood accesses the protein's active site through a side-door on the surface of the enzyme that opens up into a secondary pore.

Two other human enzymes metabolize cocaine, but one of these prefers the drug's mirror image isomer, and only hCE1 converts it into a compound that is easily removed from the body in urine. A bacterial enzyme proposed to treat cocaine overdose deteriorates rapidly in the blood and may cause an allergic reaction, which hCE1 would be unlikely to do because it is native to humans. The group observed that hCE1 partially clusters into symmetric groups of six (Fig. 1) in the presence of naloxone. Encouraging such clustering may make the purified protein stable enough to provide days worth of protection against chemical weapons. The researchers are now trying to develop a more selective and efficient form of the protein. ❍

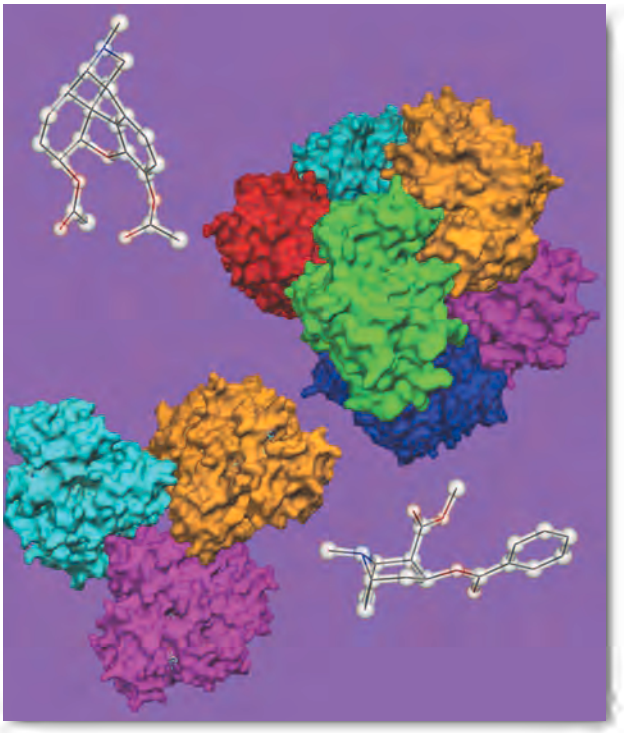

Fig. 1. The "promiscuous" human drug-processing enzyme carboxylesterase 1 (hCE1), which exists as both a three-membered form (lower left) and a six-membered form (upper right), catalyzes the metabolism of the dangerous narcotics heroin (upper left) and cocaine (lower right).

See: S. Bencharit[1], C.L. Morton[2], Y. Xue[1], P.M. Potter[2], and M.R. Redinbo[1], "Structural basis of heroin and cocaine metabolism by a promiscuous human drug-processing enzyme," Nat. Struct. Biol. **10**(5), 349-366 (May 2003).
Author affiliations: [1]University of North Carolina at Chapel Hill, [2]St. Jude Children's Hospital

This research was supported by the NIH (including a Core Grant), a Burroughs Wellcome Career Award in the Biomedical Sciences, and by the American Lebanese Syrian Associated Charities. Use of the Advanced Photon Source was supported by the U.S. Department of Energy, Office of Science, Office of Basic Energy Sciences, under Contract No. W-31-109-Eng-38.

A CLEAR PICTURE OF THE SARS MAIN PROTEASE STRUCTURE

Severe Acute Respiratory Syndrome (SARS) achieved global notoriety as the first new epidemic of the 21st century. Three months after this new coronavirus was identified and characterized, the disease was declared contained, but only after it had infected over 8,400 people from 30 countries and killed more than 800. SGX (Structural GenomiX, Inc.), in collaboration with the Genome Institute of Singapore, determined the crystal structure of the SARS-CoV main protease to 1.86 Å resolution as a first step toward developing an antiviral therapeutic using structure-based drug discovery.

Residues 1-304 were expressed in *E. coli* as a fusion protein. After purification and cleavage of the fusion partner, the protein was crystallized by hanging drop vapor diffusion. Diffraction data were collected at the SGX-CAT beamline 31-ID at the APS, and the structure was determined via molecular replacement with the program EPMR at SGX, San Diego. The structure was deposited in the Protein Data Bank with accession ID 1Q2W and was released to the public immediately.

In the SARS-CoV M^{pro} dimer, the chain terminus of one molecule falls near the active site of the dimeric partner. Geometric constraints do not allow autoproteolysis. Dimer formation is, therefore, absolutely necessary for trans intradimer cleavage of the opposing molecule from the viral polyprotein.

The natural SARS-CoV M^{pro} substrate is a peptide corresponding to the consensus sequence immediately N-terminal to each one of the mature viral proteins (including the protease itself): TSAVLQ. Specificity for substrate glutamine in the P1 peptide recognition pocket and the presence of a hydrophobic residue in the P2 pocket are features conserved in all coronaviruses. The glutamine sidechain in the P1 position could make hydrogen-bonding interactions with the Phe140 carbonyl oxygen and the His163 imidazole sidechain, both of which occur in the P1 pocket of the enzyme. ❍

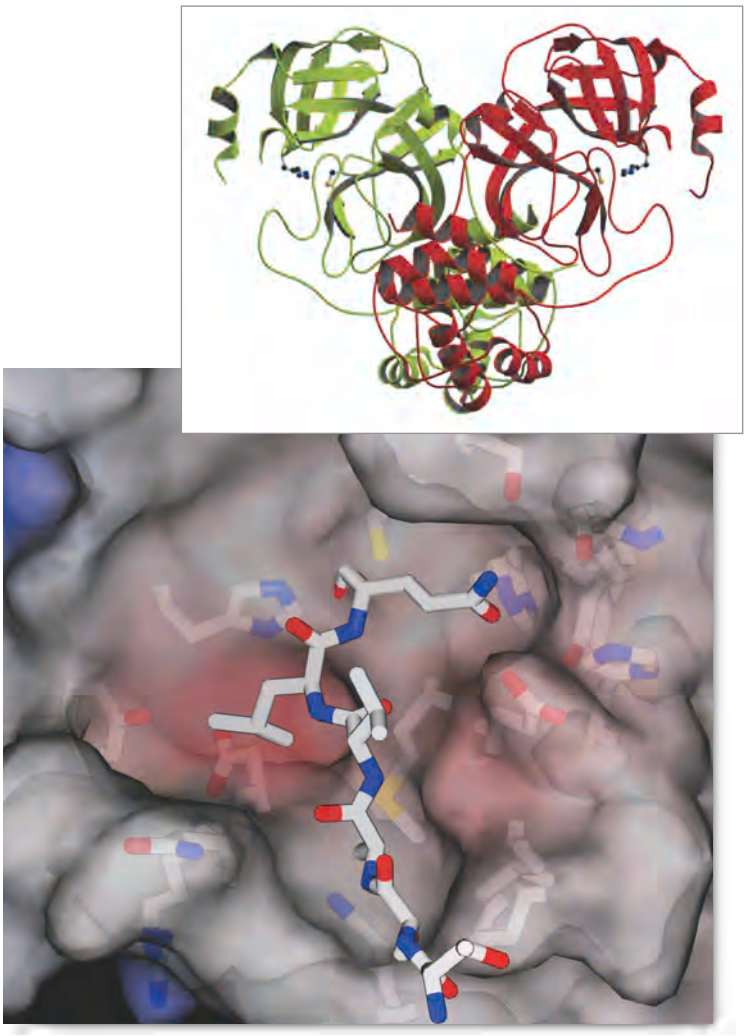

Fig. 1. Top: Ribbon representation of the SARS main protease dimer. Catalytic residues are displayed in ball and stick Bottom: Surface representation of active site with overlaid model of the consensus peptide.

J.M. Sauder[1], J.B. Bonanno[1], D. Lorimer[1], R. Fowler[1], R. Romero[1], J. Hendle[1], S. Gupta[2], C.-L. Wei[2], E.T. Liu[2], S.K. Burley[1], T. Harris[1]
[1]Structural GenomiX, Inc., [2]Genome Institute of Singapore

Relevant Literature: K. Anand, G.J. Palm, J.R. Mesters, S.G. Siddell, J. Ziebuhr, and R. Hilgenfeld, "Structure of coronavirus main proteinase reveals combination of a chymotrypsin fold with an extra alpha-helical domain," EMBO J. **21**, 3213-3224 (2002).

K. Anand, J. Ziebuhr, P. Wadhwani, J.R. Mester, and R. Hilgenfeld, "Coronavirus main proteinase (3CLpro) structure: Basis for design of anti-SARS drugs," Science **300**, 1763-1767 (2003).

M.A. Marra et al., "The genome sequence of the SARS-associated coronavirus," Science **300**, 1399-1404 (2003).

P.A. Rota et al., "Characterization of a novel coronavirus associated with severe acute respiratory syndrome," Science **300**, 1394-1399 (2003).

Y.J. Ruan et al., "Comparative full-length genome sequence analysis of 14 SARS coronavirus isolates and common mutations associated with putative origins of infection," Lancet **361**, 1779-1785 (2003).

E.J. Snijder et al., "Unique and conserved features of genome and proteome of SARS-coronavirus, an early split-off from the coronavirus group 2 lineage," J. Mol. Biol. **331**, 991-1004 (2003).

Use of the Advanced Photon source was supported by the U.S. Department of Energy, Office of Science, Office of Basic Energy Sciences, under Contract No. W-31-109-Eng-38.

THE MOLECULES BEHIND TAY-SACHS DISEASE

Using the BioCARS beamline 14-BM at the APS, a group of researchers from the University of Alberta, the Hospital for Sick Children, the University of Toronto, and Rutgers University have determined how changes in a pair of proteins lead to the family of neurological disorders that includes Tay-Sachs disease. They solved the three-dimensional structure of one protein essential to Tay-Sachs and modeled the structure of a second key protein based on the first. The results help explain why different mutations lead to different forms of the same class of neurological disorder, and may help in developing treatments against them.

Tay-Sachs is caused by an inherited deficiency of the enzyme Hex A, which removes a sugar residue from fatty molecules found in brain cells. Without it, fat builds up in the cells and kills them in a still mysterious way. Three genes must interact to remove the sugar properly: HEXA and HEXB, which produce the α- and β-subunits of Hex A, respectively; and GM2A, whose protein product, GM2A, activates Hex A. Mutations that significantly reduce the activity of these genes can cause one of several related disorders, including Tay-Sachs and Sandhoff disease. One in 35 Ashkenazi Jews carries the mutation that causes Tay-Sachs, and 1 in 300 individuals in general carries it. Understanding the structures of the proteins involved might enable researchers to design drugs to activate or replace them. However, researchers had, to date, only determined the structure of the GM2A protein.

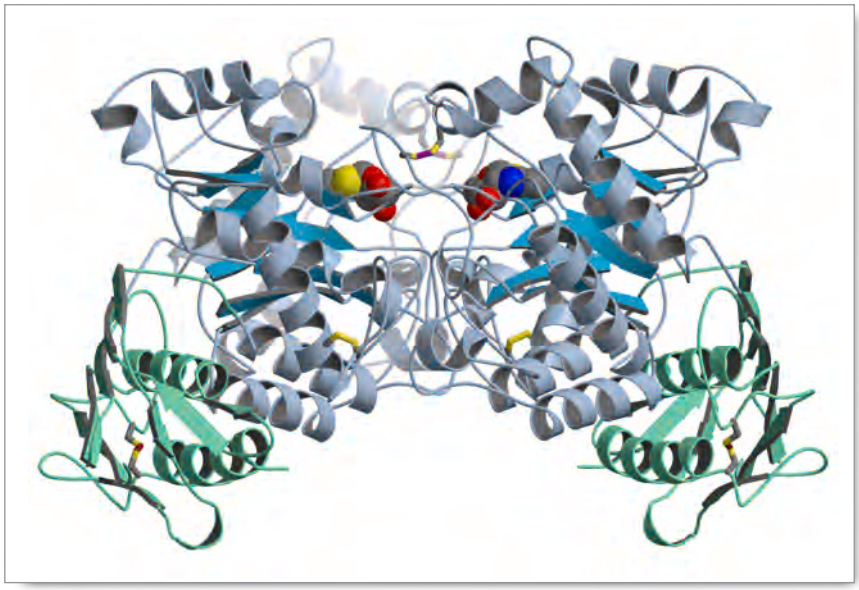

Fig. 1. Schematic image of Hex B showing its two identical, rotationally symmetric subunits. Small molecule inhibitors are shown as black, red, blue, and yellow space-filling models. The enzyme active sites, which contain the inhibitors, are offset perpendicularly to the plane of the image.

The researchers solved two structural problems at once—Hex A and the closely related Hex B. They first crystallized Hex B, made of two β-subunits, and determined its structure by analyzing its x-ray diffraction pattern. In Hex B, which is easier to crystallize than Hex A, two kidney-shaped β-subunits come together so their active sites, or catalytic regions, face each other but are offset (Fig. 1). Previous studies had indicated that each type of Hex subunit has an active site capable of performing a slightly different type of sugar removal, but that two subunits must come together for either one to be active. To determine how the β-subunit active site binds its substrate, the researchers soaked a Hex B inhibitor that mimics the substrate into the crystallized enzyme. They found that the active sites work cooperatively because several of the amino acids that make up each subunit's active site come from the other subunit. People who have mutations in these amino acids experience a mild, chronic form of Sandhoff disease, or a variant or acute form of Tay-Sachs, depending on which amino acid is mutated. Soaking the crystal with a different inhibitor also confirmed that Hex B uses a similar catalytic mechanism to related enzymes.

Next they modeled the α-subunit based on the β-subunit, which has 60% of the same amino acids. In support of the modeling approach, much of the amino acid similarity occurs in the regions implicated in subunit joining or catalysis, suggesting that the β-subunit binds the a in the same way it binds itself; Hex A would probably need a similar overall shape to that of Hex B to support the same type of subunit binding. The model indicates that three amino acids in the α-subunit are responsible for the ability of Hex A to bind substrates with a negative charge at one end. Biochemical studies of the enzyme's reaction rate when these amino acids are mutated support the conclusion. The predicted subunit interface also forms a large groove suitable for binding the cup-shaped activator protein Gm2A. Shape and electrostatic complementarities suggest that the activator positions itself over the α-subunit active site. ❍

See: B.L. Mark[1], D.J. Mahuran[2,3], M.M. Cherney[1], D. Zhao[4], S. Knapp[4], and M.N.G. James[1], "Crystal Structure of Human β-Hexosaminidase B: Understanding the Molecular Basis of Sandhoff and Tay–Sachs Disease," J. Mol. Biol. **327**, 1093–1109 (2003).

Author affiliations: [1]University of Alberta, [2]The Hospital for Sick Children, [3]University of Toronto, [4]Rutgers University

This work supported by Canadian Institutes of Health Research grants (to D.M. and M.N.G.J.). B.L.M. is supported by scholarships from the C.I.H.R., the Alberta Heritage Foundation for Medical Research, and the University of Alberta. M.N.G.J. holds a Canada Research Chair in Protein Structure and Function at the University of Alberta. Use of the BioCARS beamline was supported by the National Institutes of Health, National Center for Research Resources, under grant number RR07707. Use of the Advanced Photon Source was supported by the U.S. Department of Energy, Office of Science, Office of Basic Energy Sciences, under Contract No. W-31-109-Eng-38.

BINDING OF TWO YEAST TRANSCRIPTION FACTORS

The RNA polymerase enzyme transcribes DNA sequences (genes) into matching RNA molecules. RNA polymerase III produces small RNAs that aid in protein synthesis. Researchers have now determined the three-dimensional (3-D) structure of fragments of two proteins that recruit yeast polymerase III to DNA. The research reveals how these proteins assemble and bind together, despite one of them having a seemingly loose structure. Similar structural features may exist in other recruiting factors for RNA polymerases across the eukaryotes, which include everything from amoeba to humans.

Transcription factor IIIB recruits polymerase III to a region of DNA at the beginning of every gene called the promoter and helps separate the strands of DNA there. It consists of three proteins: a DNA-binding protein called TBP and two connector proteins called Brf1 and Bdp1. Half of Brf1 is very similar to an analogous protein that helps recruit RNA polymerase II, but the other half, especially a region called homology domain II, is more responsible for binding TBP. To understand the structural basis of this binding, a group of experimenters from Yale University and the University of California, San Diego, has crystallized Brf1's homology domain II and the key portion of TBP bound to a short stretch of promoter DNA. They determined the complex's 3-D structure from its x-ray diffraction pattern, which was measured at the SBC-CAT beamline 19-ID at the APS and at the National Synchrotron Light Source beamlines X4A and X25.

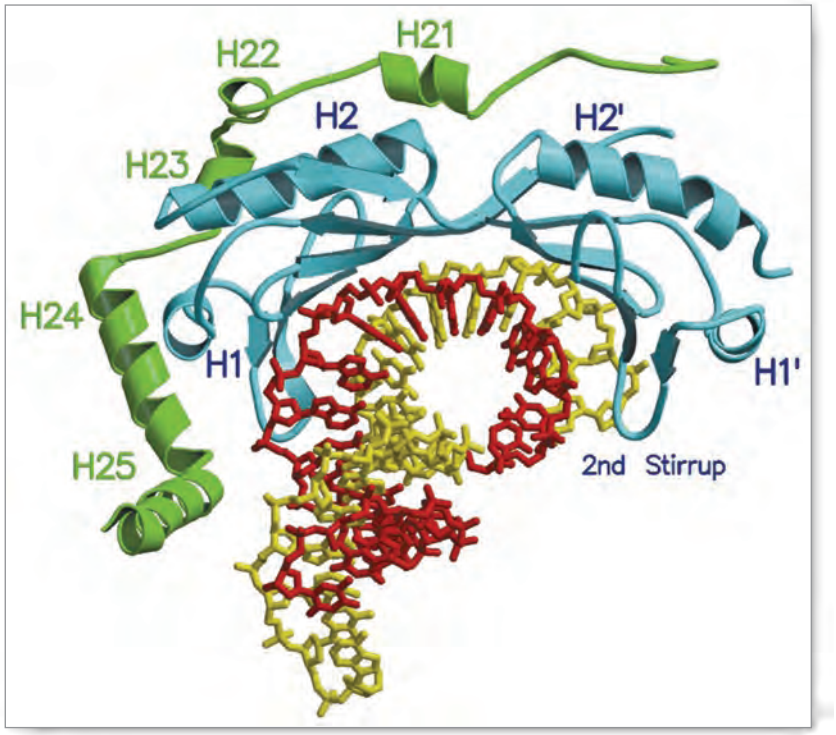

Fig. 1. Image of yeast transcription factor Brf1 (green) bound to the DNA-binding factor TBP (blue). DNA is shown in yellow and red. Brf1 helices H21-23 and their connecting loops surround helix H2 of TBP. Helices H24 and H25 of Brf1 make contact with helix H1 and the first "stirrup" (blue loop, obscured by DNA in red) of TBP.

The crystal structure shows the symmetric, saddle shaped TBP wedged into the groove between strands of the DNA double helix, straddling the molecule at an angle. Part of Brf1 forms an elongated structure running along the convex outer surface of TBP; the rest forms a bent helix that curls around one of TBP's "stirrups" (Fig. 1). The researchers compare Brf1's fold to that of a vine on a tree, which is markedly different from known structures of polymerase II transcription complexes consisting of TBP and DNA. Brf1 and TBP interact at about 30 locations, which is three to five times more than in the analogous polymerase II complex.

Brf1 is unusually extended along the surface of TBP, nothing like the regular structural domains proteins normally fold into. The researchers found that free Brf1 resists digestion by protein-chewing enzymes (which is only possible if it folds into a more compact, stable structure), and suggest that Brf1 unfolds to grasp TBP. The bent helix may form part of a DNA-binding element, according to earlier research. Researchers suggest its orientation probably positions it for optimal interaction with DNA, Bdp1, and other polymerase III subunits.

Brf1 makes extensive contact with two regions of TBP: a helix on the convex outer surface and a helix and stirrup region on the side. At the first region, Brf1 extensively complements the charge and shape of TBP, forming 17 hydrogen bonds. The second region contains medium-strength hydrogen bonds formed mostly between the backbones of the two proteins. Proteins normally recognize each other through interactions between amino acid side chains, so the second location probably helps preserve the overall shape of the complex.

Human Brf1 may bind TBP like its yeast counterpart does. On the basis of an amino acid sequence comparison, 28 of 31 hydrogen bonds in the yeast Brf1-TBP complex would exist in the human complex. Yeast Brf1 also has a similar sequence to yeast TAF1, a polymerase II transcription factor (28/31 hydrogen bonds), and human TAF1 (24/31 hydrogen bonds). ❍

See: Z.S. Juo[1], G.A. Kassavetis[2], J. Wang[1], E.P. Geiduschek[2], and P.B. Sigler[1(‡)], "Crystal structure of a transcription factor IIIB core interface ternary complex," Nature **422**, 534-539 (3 April 2003).

Author affiliations: [1]Yale University, [2]University of California, San Diego ([‡]Deceased)

This work was supported in part by the Howard Hughes Medical Institute and by the National Institutes of Health (E.P.G., P.B.S., and T. Steitz). Use of the Advanced Photon Source was funded by the U.S. Department of Energy, Office of Science, Office of Basic Energy Sciences, under Contract No. W-31-109-Eng-38.

STRUCTURE OF A BACTERIAL PROTEIN TRANSPORTER

The three-dimensional (3-D) structure of a protein essential for the tuberculosis bacterium's ability to secrete proteins into its environment has been determined by a team of researchers using the BioCARS 14-BM and 14-ID and SBC-CAT 19-ID beamlines at the APS. The protein, called SecA, may serve as a molecular ratchet, using energy from the breaking of high-energy chemical bonds to physically push other proteins out of a pore in the bacterium's external membrane. The research provides a framework for understanding the protein secretion machinery important for a variety of processes, including transport of membrane proteins and proteins that make tuberculosis infectious. It may also help lead to drugs against the disease, which kills three million people every year.

The system for protein secretion, or translocation, is similar in all types of cells, whether from bacteria or humans. Proteins destined to cross the cell membrane are synthesized with an additional section of protein at one end that alerts the cell to their intended fate. In bacteria, the minimum requirements for translocation are a protein pore, which extends through the membrane, and a membrane enzyme that breaks down ATP, the high-energy molecule that fuels most cellular processes. It is known that SecA binds to other proteins destined for translocation by recognizing the additional piece of protein. Some have proposed that it moves a protein through the pore system by repeatedly inserting and releasing it. A shape change caused by ATP binding would drive the process.

To see if structural data corroborate the hypothesis, the researchers from the Institute of Biosciences and Technology, Texas A&M University, the University of North Carolina, and the Albert Einstein College of Medicine crystallized *Mycobacterium tuberculosis* SecA alone and bound to ADP, the spent form of ATP. They then analyzed its x-ray diffraction pattern, from which they determined its structure. The protein is made of two identical subunits, each of which contains more than 900 amino acids folded into a "motor" domain and a translocation domain (Fig. 1). It is convex on one side and concave on the other, with an elliptical pore running between the two sides. The researchers believe concave surface of SecA, which contains the translocation domain, docks with the membrane pore to form a continuous channel through both proteins.

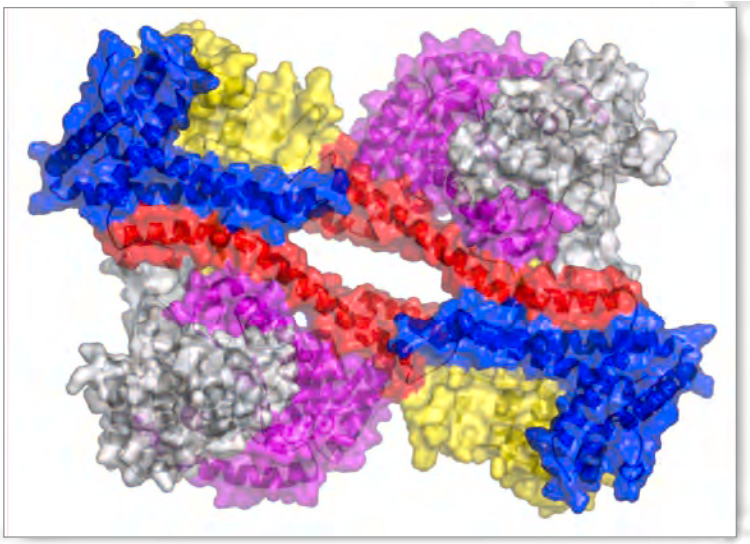

Fig. 1. SecA, made of two identical subunits, is shown here in a schematic representation of its protein fold (ribbons) underneath a translucent image of its molecular surface. The motor domain (purple, gray), translocation domain (blue, yellow), and long "pump handle" (red) surround an elliptical pore.

The group compared the structure of the ADP-bound SecA's motor domain to the very similar domain of a protein that unwinds DNA helices. The motor domain's structure closely matched the "off" state of the unwinding protein (whose mode of action researchers have modeled), implying that SecA undergoes a similar small rotation when switching on or off. The motor domain is composed of two parallel wheel-shaped pieces, which would rotate about 10° relative to one another. The group believes this small motion would transform into a much larger motion of the translocation domain relative to the motor through a hand-pump-like mechanism. The small rotation would move a long, bent stretch of protein (Fig. 1) up and down like a pump handle, which would then twist the translocation domain back and forth along the direction set of the pore axis. The group speculates that a ratchet effect, resulting from pore contraction or interaction with the membrane channel, would keep translocated proteins moving forward.

The group plans to crystallize the bacterium's other SecA protein, SecA2, which transports proteins that make tuberculosis virulent. Comparing its structure with that of SecA may help to better understand the disease and aid in the design of new pharmacueticals. ❍

See: V. Sharma [1, 2], A. Arockiasamy [2], D.R. Ronning [2], C.G. Savva[2], A. Holzenburg [2], M. Braunstein [3], W.R. Jacobs, Jr. [4], and J.C. Sacchettini [1,2], "Crystal structure of *Mycobacterium tuberculosis* SecA, a preprotein translocating ATPase," Proc. Nat. Acad. Sci. U.S.A. **100** (5), 2243–2248 (4 March 2003).

Author affiliations: [1]Institute of Biosciences and Technology, [2]Texas A&M University, [3]University of North Carolina, [4]Albert Einstein College of Medicine

Use of the Argonne National Laboratory Structural Biology Center beamlines at the Advanced Photon Source was supported by the U.S. Department of Energy, Office of Energy Research, under Contract W-31-109-Eng-38. Use of the BioCARS beamline was supported by the National Institutes of Health, National Center for Research Resources, under grant number RR07707. This work was supported by the Robert A. Welch Foundation and National Institutes of Health Grant GM62410. Use of the Advanced Photon Source was supported by the U.S. Department of Energy, Office of Science, Office of Basic Energy Sciences, under Contract No. W-31-109-Eng-38.

STRUCTURE OF A VIRAL DNA-UNWINDING PROTEIN

The three-dimensional structure of a virus protein that plays a key role in DNA replication has been solved by a group of researchers from the University of Colorado Health Science Center, School of Medicine; Argonne National Laboratory; and the Dana-Farber Cancer Institute at Vanderbilt University. Simian virus 40 produces a protein called large tumor antigen (LTag), which disrupts host cells' anti-tumor machinery and begins the viral DNA replication process. Studying LTag's structure could help elucidate the mechanism behind DNA replication in human and other cells. The research helps explain how LTag forms a six-membered complex and contacts host anti-tumor proteins and suggests that it uses an "iris" effect to separate DNA.

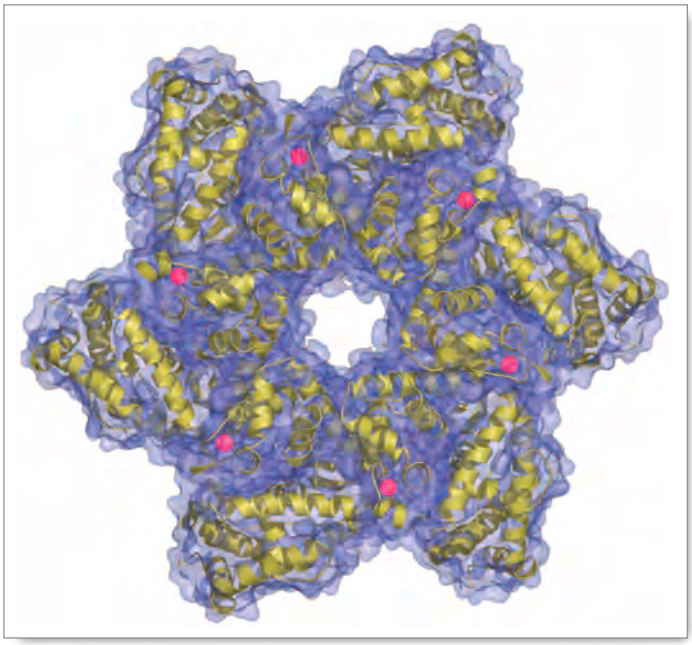

Fig. 1. Top view of the LTag hexamer showing the central channel. Each pointed arm in the star-like shape represents one monomer. Zinc atoms are in red.

During viral DNA replication, LTag forms a double six-membered complex around DNA, opens gaps in the two DNA strands, and unwinds them so the replication machinery can copy them. A protein in archaeal cells has the same function and also seems to form a double hexamer, so the two proteins may use a similar mechanism. Now, this group of experimenters have isolated the smallest LTag fragment that acts as a DNA-unwinder (helicase) and determined its structure from the x-ray diffraction pattern. They collected structural data at the SBC-CAT beamline 19-ID at the APS.

Viewed from the side, six LTag proteins combine to form two stacked tiers, a smaller one on top of a larger one, with a central channel running from top to bottom. From the top the hexamer looks like a six-pointed gear or star (see Fig. 1). In the top tier, each monomer reaches over counterclockwise to touch its neighbor. A cleft between each pair of monomers in the bottom tier might provide room for an energy-dependent conformational change to drive DNA remodeling.

Each monomer consists of three domains, D1-D3. A zinc atom holds the five helices of domain D1 in place. D2 folds into a sheet sandwiched by helices. D3 consists of two interlocked rings composed of three and four helices, respectively. Hydrophobic interactions between D1 domains and hydrogen and ionic bonds between D2 domains cause adjacent monomers to stick together. D3 domains form the triangular points radiating outward in the bottom tier.

The position of the zinc-binding region suggested it might be important for hexamerization. To test the idea, the group deleted part of the region and passed solutions of the complete fragment and deletion mutant through a gel chromatograph. The complete fragment formed mostly or all hexamers, whereas the deletion mutant seemed to form only monomers, supporting the hypothesis.

Researchers had previously identified several mutations that disrupt LTag's ability to bind the anti-tumor protein p53. Four of the amino acids altered in these mutations form a patch on the outer surface of the hexamer, suggesting they contact p53 or lie where LTag and p53 meet.

The central channel of Hexameric LTag is strongly positively charged and has six similarly charged, smaller channels radiating out from it, perfect for manipulating negatively charged DNA. The opening in the larger tier initially appears wide enough for just single-stranded (ss) DNA. But the same opening in LTag crystals formed at different pH or salt concentrations varies in width, suggesting the opening can open and close. The researchers suggest the hexamer operates like the iris (diaphragm) of a camera by flexing the helices that connect the two tiers.

They propose two linked hexamers bind DNA along the inner channel surface and use the iris effect to pull apart the twin strands of DNA at two locations. LTag repeats the iris motion again and again, extruding the strands as ssDNA loops through side channels on opposite sides of the protein complex. The hypothesis is consistent with electron microscope images showing DNA "rabbit ears' connected to the complex. ❍

See: D. Li[1], R. Zhao[1], W. Lilyestrom[1], D. Gai[1], R. Zhang[2], J.A. DeCaprio[3], E. Fanning[4], A. Jochimiak[2], G. Szakonyi[1], and X.S. Chen[1], "Structure of the replicative helicase of the oncoprotein SV40 large tumor antigen," Nature **423**, 512-518 (29 May 2003).

Author affiliations: [1]University of Colorado Health Science Center, School of Medicine, [2]Argonne National Laboratory, [3]Dana-Farber Cancer Institute, [4]Vanderbilt University

This work is supported in part by start-up and cancer-centre funds from University of Colorado Health Sciences Center to X.C. and NIH-R01 to X.C., J.A.D. and E.F., and a DOE grant to R.Z. and A.J. Use of the Advanced Photon Source was supported by the US Department of Energy, Office of Science, Office of Basic Energy Sciences under Contract No.W-31-109-Eng-38.

CAPTURING AN ENZYME'S UNSTABLE INTERMEDIATE

Researchers from the Boston University School of Medicine and the University of New Mexico have determined the structure of the first high-energy intermediate of an enzymatic reaction. Enzymes sometimes accelerate chemical reactions by stabilizing such states, allowing the reaction to proceed with less energy input. The group crystallized a mixture of an enzyme and its substrates, capturing the enzyme in the act of catalysis. The result provides direct evidence of a key enzymatic strategy.

Without an enzyme around, reactions happen by chance. Substrates must bump into each other at just the right angle and with enough energy to form a short-lived structure, called a transition state, which resolves itself into the products. Enzymes carefully orchestrate reactions to place substrates automatically in the optimal positions. To lower the energy barrier, they stabilize the transition state, sometimes proceeding via a high-energy intermediate that is unique to the enzyme-catalyzed reaction. Structural biologists perform various experimental tricks to observe or infer the structure of intermediates and transition states. They introduce enzyme inhibitors believed to mimic the transition state, alter the enzyme to make the intermediate build up, or, in rare cases, perform time-resolved crystallography on a cold sample to extend the intermediate's lifespan. Until March 2003, however, nobody had determined the structure of a high-energy intermediate in its natural environment.

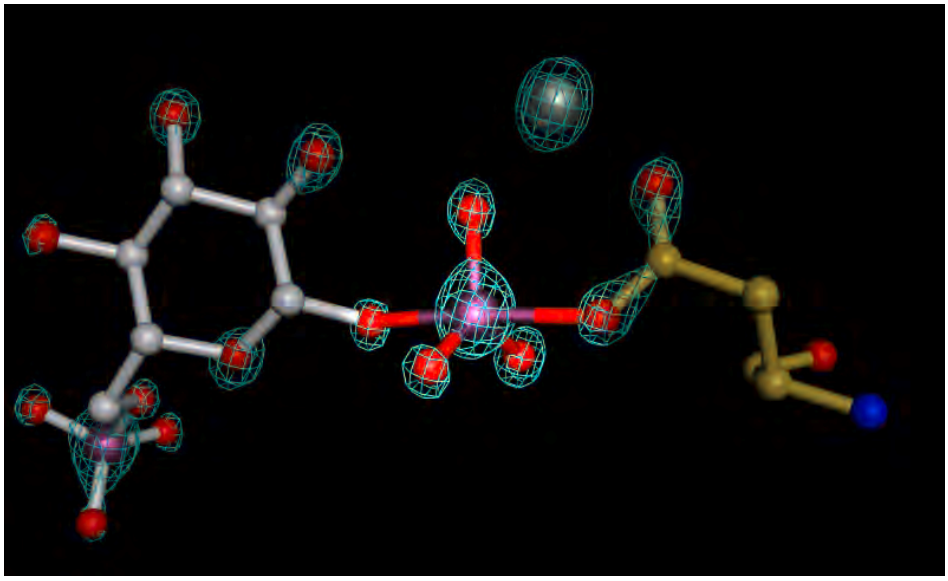

Fig. 1. The high-energy intermediate formed by the enzyme ß-PGM as it rearranges a phosphate group on a glucose molecule. Five oxygen atoms (red) are oriented around a phosphorous atom (purple) in a so-called trigonal bipyramid. The two outer atoms can be viewed as the apices of two triangular pyramids, which share a common base in the three middle oxygen atoms.

The group chose the enzyme ß-phosphoglucomutase (ß-PGM) to fill this gap because it crystallizes in a closed form that traps its high-energy intermediate in place. ß -PGM can switch the location of a phosphate group back and forth between two positions on a glucose molecule. In the process, it forms an intermediate state in which a phosphorous atom is bound to five oxygen molecules—one from the enzyme, one from glucose, and three of its own—which are arranged as the points of a "trigonal-bipyramidal" structure (Fig. 1), reports the group. They combined the enzyme with either of its substrates and allowed the mixture to come to equilibrium, in which each enzyme molecule is in either the substrate-bound ground state or the intermediate state. By crystallizing the mixture and analyzing its x-ray diffraction pattern, they were able to reconstruct the elusive intermediate. High-intensity x-rays from the BioCARS beamline 14-BM at the APS allowed them to resolve the intermediate structure. (Additional work was done at the HHMI beamline X4A at Brookhaven National Laboratory.)

The research indicates that ß-PGM stabilizes the intermediate in two ways. It anchors the substrate by forcing it to bond precisely with a magnesium ion, water molecules, and amino acids. The anchoring prevents a large loss of entropy, which would make the reaction unfavorable in solution. The enzyme also forms strong bonds with the oxygen atoms at either end of the trigonal bipyramid; otherwise they would be unstable and likely to break away. Both kinds of interaction make the intermediate more thermodynamically stable, giving the reaction a better chance of proceeding. Researchers had suspected that similar structures are involved in several phosphorous transfer reactions that occur with or without enzyme catalysis but had never observed such an intermediate. ❍

See: S.D. Lahiri [1], G. Zhang [2], D. Dunaway-Mariano, [2], and K.N. Allen [1], "The Pentacovalent Phosphorus Intermediate of a Phosphoryl Transfer Reaction," Science **299**, 2067-2071 (28 March 2003).

Author affiliations: [1]Boston University School of Medicine, [2]University of New Mexico

Supported by a grant from NIH (grant GM16099) (to K.N.A and D.D.M). Use of the BioCARS Sector 14 was supported by NIH, National Center for Research Resources, under grant number RR07707. Research was carried out (in part) at the HHMI beamline X4A at the National Synchrotron Light Source, Brookhaven National Laboratory. Coordinates have been deposited in the Protein Data Bank (accession codes 1O08 and 1O03, for G1P and G6P cocrystals, respectively). Use of the BioCARS beamline was supported by the National Institutes of Health, National Center for Research Resources, under grant number RR07707. Use of the Advanced Photon Source was supported by the U.S. Department of Energy, Office of Science, Office of Basic Energy Sciences, under Contract No. W-31-109-Eng-38.

How an Immune System Protein Binds its Receptors

Mice expressing too much of the protein TALL-1 experience symptoms that mimic the human autoimmune disease systemic lupus erythematosus. TALL-1 seems to bind receptors in a novel way. Studying that interaction may increase our understanding of autoimmune disease and aid in designing drugs to counteract it. Researchers have now determined the crystal structure of the functional section of TALL-1 bound to the key sections of two of its receptors. Their research, carried out at the SBC-CAT beamline 19-ID at the APS reveals why one receptor binds TALL-1 instead of a closely related protein.

Mice deficient in TALL-1 (called a ligand) or its receptor BAFF-R cannot grow mature B cells, which produce antibodies. At low pH, functional TALL-1 fragments form threesomes and fold into the same shape as other proteins in the same family: a "jellyroll," which looks like a bent paper clip. At high pH, the fragments cluster together and acquire their biological function (Fig. 1). The binding regions of BAFF-R and the related receptor BCMA have many fewer cysteines (sulphur-containing amino acids) than proteins of the same family do. Such amino acids often form bonds within proteins to hold the three-dimensional (3-D) structure in shape. The receptors still bind TAFF-1 strongly, however, suggesting a unique binding mechanism. To test the hypothesis, researchers from the National Jewish Medical and Research Center, Howard Hughes Medical Institute, The University of Colorado Health Science Center, Peking University, and Argonne National Laboratory diffused fragments of either BCMA or BAFF-R into crystallized TALL-1 and reconstructed their 3-D shapes from x-ray diffraction patterns.

The overall structure resembles a sunflower, with receptors as the petals and 60 TALL-1 ligands assembled into the seedbed. Each receptor fragment consists of two domains and folds into a saddle-like shape. BCMA has a helical section positioned like a "rider" on the saddle. BAFF-R has a lone extended coil in place of the helix. Both structures are unique among proteins of the same family.

Each saddle sits slightly askew on a "horseback"-like surface formed by four loops of a TALL-1 fragment. In related proteins, one elongated receptor binds the cleft formed by two ligands. Both receptors bind TALL-1 through a combination of ionic bonds and two so-called hydrophobic cores, in which nonpolar amino acid side chains cluster together. Nonpolar or hydrophobic side chains create disorder among water molecules. Proteins become more energetically stable by burying hydrophobic side chains away from water. The major difference between the two fragments is in BAFF-R, which distinguishes it from typical proteins of the same family. The coil makes several additional ionic and hydrogen bonds with TAFF-1.

Mice lacking April, the protein that most resembles TALL-1, die as embryos. The researchers have speculated previously that April may compete with excess TALL-1, offsetting the latter's ability to cause symptoms of autoimmune disease symptoms. BCMA binds April as strongly as it does TALL-1, but the structurally similar BAFF-R does not. To figure out why, the researchers mutated BAFF-R in several ways, removing or altering different sections. When they mutated either of two cysteines in the middle of BAFF-R, the protein could suddenly bind April strongly. The researchers conclude that one of BAFF-R's two natural cysteine-cysteine bonds makes the protein rigid and unable to conform to April's shape. ❍

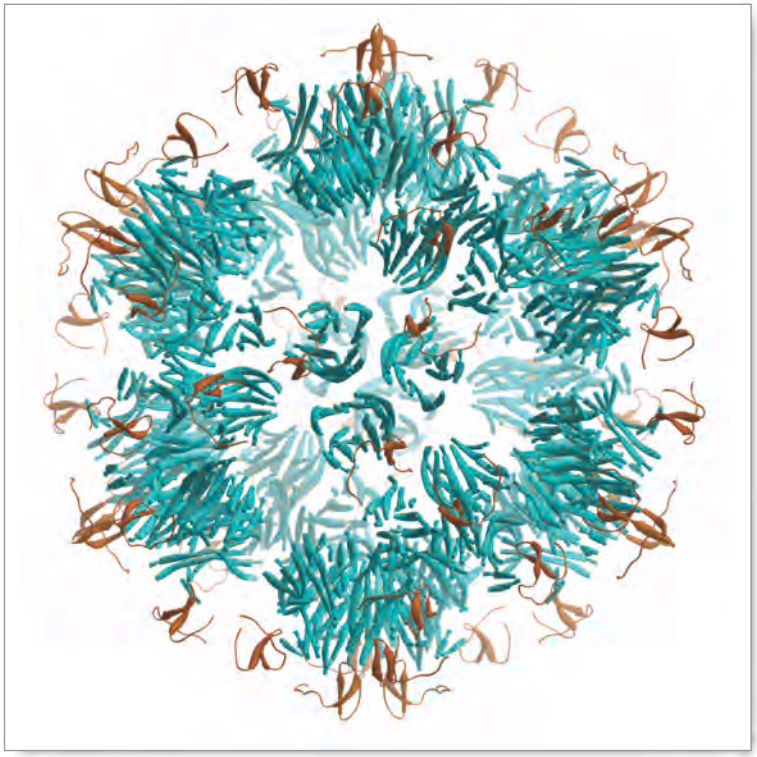

Fig. 1. Crystalline structure of 60 monomers of TALL-1 (blue) complexed with 60 monomers of eBAFF-R (orange).

See: Y. Liu [1], X. Hong [1], J. Kappler [1,2,3], L. Jiang [1], R. Zhang [5], L. Xu [1], C.-H. Pan [1], W. E. Martin [1], R. C. Murphy [1], H.-B. Shu [1,4], S. Dai [1,2], and G. Zhang [1,3], "Ligand–receptor binding revealed by the TNF family member TALL-1," Nature **423**, 49-56 (1 May 2003).

Author affiliations: [1]National Jewish Medical and Research Center, [2]Howard Hughes Medical Institute, [3]University of Colorado Health Science Center, [4]Peking University, [5]Argonne National Laboratory

S.H.B. is supported by an NIH grant and the Arthritis Foundation; Y.L. is supported partly by a Priscilla Campbell Memorial Fellowship; X.H. is supported partly by a Janet S. Lewald fellowship; G.Z. is supported by a PEW Scholar Award, a start-up fund from National Jewish Medical and Research Center and the Cancer League of Colorado, Inc.; P.M. and G.Z. are supported by NIH grants. Use of the APS is supported by the U.S. Department of Energy (Grant No. W-31-109-Eng-38).

IN SEARCH OF NEW ANTIBIOTICS

The antibiotic vancomycin is often the last resort for life-threatening infections of the wounds or blood of hospital patients, but bacteria are becoming increasingly resistant to the drug. In an early step toward developing new antibiotics on the same model, researchers have solved the structure of an enzyme that synthesizes a derivative of vancomycin. Changing the enzyme's structure on the basis of such information could lead to new antibiotics.

Vancomycin consists of a short series of amino acids, which form the "peptide core," with sugars projecting from it. Researchers have found that changing the sugars on the core can overcome bacterial resistance, but such derivatives are complicated to synthesize, which has prevented drug companies from manufacturing them. If researchers could reprogram enzymes that naturally produce vancomycin and related antibiotics to form new products, companies could use the enzymes in developing or producing new drugs. Researchers would need detailed structural information about how the enzymes recognize different substrates to enact such a scheme, however.

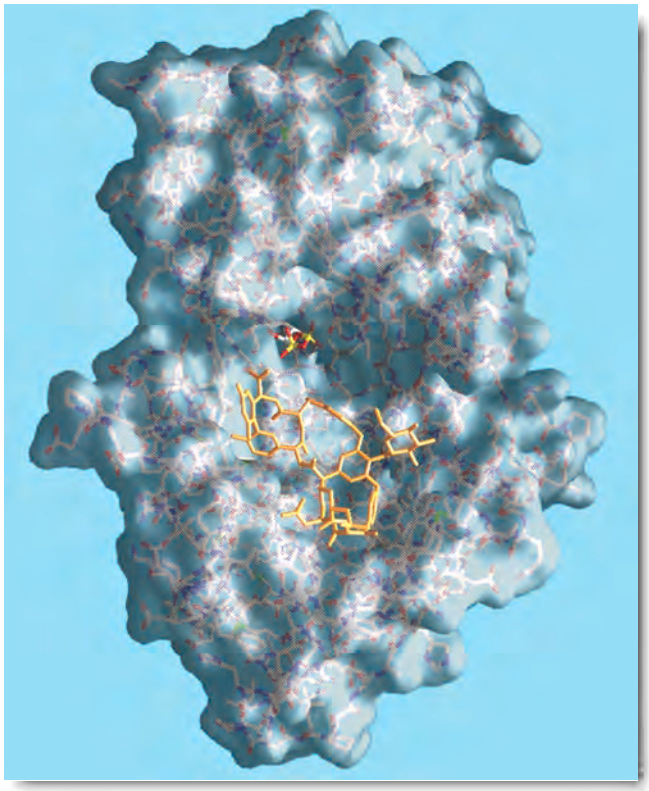

Fig. 1. The molecular surface (and underlying atoms) of the GtfA enzyme, with the antibiotic precursor DVV (gold) bound to the so-called active site, and TDP (red and yellow) buried between the two protein domains.

Add an extra sugar to a specific spot on vancomycin and the antibiotic chloroeremomycin results. Researchers from Michigan State University, Harvard University, and DND-CAT have solved the structure of the bacterial enzyme that adds the extra sugar, called GtfA. The enzyme, which swaps a sugar from a nucleotide anchor to a vancomycin precursor, snaps from an open to closed form when the nucleotide-sugar molecule binds to it. To determine the structure, they crystallized mixtures of the enzyme and vancomycin or its precursor DVV, then analyzed the x-ray diffraction pattern, collected at the SBC-CAT beamline 19-ID and the DND-CAT beamline 5-ID at the APS.

GtfA, like related enzymes, is made of two domains, each of which recognizes and binds a different substrate. The reaction joining the two substrates takes place in a deep cleft between the two domains (Fig. 1). A shallow pocket on the outer surface of one domain holds the cup-shaped vancomycin or DVV molecule, accommodating their different sugar attachments by slight shifts in structure. The nucleotide-sugar molecule would bind to the other domain along the cleft. Although the sugar to be swapped was not included in the structure, comparison with other enzymes suggests it would project further into the cleft. The structure revealed two forms of the enzyme: an open form in which the nucleotide anchor is absent, and a closed form with a smaller cleft when the nucleotide anchor is present. The result indicates that binding of the nucleotide triggers the cleft to close, allowing the molecule to interact with both domains. A small rotation of the two domains about a flexible link is responsible for the closure.

The result marks the first direct observation of a sugar acceptor (DVV or vancomycin) bound to a member of this family of enzymes and provides hints at how different members accomplish their specific reactions. GtfA seems to prefer DVV because vancomycin's extra sugar would interfere with cleft closure. A structurally similar enzyme transfers the same sugar to a different spot on DVV, and the authors suggest that variability in the antibiotic binding site makes the difference. How such differences reprogram the enzyme is unclear, but swapping domains between different enzymes could be one way to generate novel antibiotics. ❍

See: A.M. Mulichak[1], H.C. Losey[2], W. Lu[2], Z. Wawrzak[3], C.T. Walsh[2], and R.M. Garavito[1], "Structure of the TDP-epivancosaminyltransferase GtfA from the chloroeremomycin biosynthetic pathway," Proc. Natl. Acad. Sci. USA **100**(16), 9238–9243 (5 August 2003).

Author affiliatons: [1]Michigan State University, [2]Harvard Medical School, [3]DND-CAT

Portions of this research were carried out at the National Synchrotron Light Source at Brookhaven National Laboratory (supported by U.S. DOE Contract DE-AC02-98CH10886), DND-CAT Synchrotron Research Center at the APS, and the Argonne National Laboratory Structural Biology Center (supported by U.S. DOE Contract W-31-109-Eng-38) at the APS. DND-CAT is supported by E.I. DuPont de Nemours, Dow Chemical Company, NSF Grant DMR-9304725, and the State of Illinois (IBHE HECA NWU 96). This work was supported by National Institutes of Health Grant No. 49338 (to C.T.W.) and the Michigan Life Sciences Corridor (R.M.G.). Use of the Advanced Photon Source was supported by the U.S. DOE, Office of Science, Office of Basic Energy Sciences, under Contract No. W-31-109-Eng-38.

A FIRST LOOK AT THE STRUCTURE OF CFTR NBD1

Cystic fibrosis (CF) is a life-threatening, autosomal-recessive genetic disease, most common among Caucasians, affecting tens of thousands of people worldwide. Defects in the cystic fibrosis transmembrane conductance regulator (CFTR) protein are the root cause of CF. Cystic fibrosis transmembrane conductance regulator is a member of the ABC transporter family of proteins that typically conduct various ions and small molecules through the cell membrane and consist primarily of two membrane-spanning domains (MSD1 and MSD2) and two nucleotide binding domains (NBD1 and NBD2). CFTR acts as a chloride channel and is important for maintaining proper mucus viscosity in the lungs and other vital organs. Most frequently, CF results from a genetically inherited deletion of a single amino acid in NBD1: phenylalanine at position 508 in the protein chain referred to as ΔF508.

Fig. 1. X-ray structure of the NBD1 domain of mouse CFTR. The protein is drawn in cartoon style, where purple cylinders represent alpha helices and yellow arrows represent beta strands. Atoms of the ATP molecule, with coordinated magnesium ion, are shown as spheres (lower right).

SGX (Structural GenomiX, Inc.) and Cystic Fibrosis Foundation Therapeutics (CFFT), the nonprofit drug discovery and development affiliate of the Cystic Fibrosis Foundation, are collaborating to use x-ray crystallography to determine the structure of CFTR with the goals of explaining disease etiology and supporting drug discovery efforts. At SGX, an intense effort to determine the structure of the most important globular domain of CFTR, NBD1, has spanned two years and involved molecular biology efforts with cDNAs from 10 different organisms. After characterizing more than 500 different versions of NBD1, a truncated form of mouse CFTR containing NBD1 was crystallized. SGX, San Diego, determined the structure of NBD1 using diffraction data collected at the SGX-CAT beamline 31-ID at the APS (Fig. 1).

It was expected that NBD1 of CFTR would possess strong similarities to the known structures of NBDs from other ABC transporters. While overall similar in fold to the bacterial NBD structures, there are significant differences that distinguish mammalian NBDs from their bacterial counterparts. These structural differences include an unexpected domain definition where both the N- and C-termini of the domain are more extended than would be predicted from sequence alone. In addition, the protein was crystallized and analyzed in several different liganded states including adenosine triphosphate (ATP) bound, adenosine diphosphate (ADP) bound, and with no ligand present (apo) and surprisingly showed no conformation change. ATP was found bound to the domain, as expected, but no hydrolysis of the nucleotide was observed, either in the structure or in accompanying biochemical tests, in contrast to the known ATPase functions of NBDs in other ABC transporters. Residue Phe508 falls in a surface-exposed short loop or turn region of the NBD1 fold. It is not apparent from the structure how its deletion would affect CFTR function. Further studies with this important mutation will be required.

In summary, the structure of NBD1 from mouse CFTR has raised many new questions relating to CFTR function and the role of ΔF508 in the development of CF. Ongoing and future projects to help answer these questions include the determination of a structure or structures of forms of NBD1 bearing the DF508 mutation; the determination of the structure of human NBD1 structure to support drug discovery efforts the crystallization and structure determination of the other nucleotide-binding domain in CFTR, NBD2; and ultimately, the co-crystallization of NBD1 with NBD2 to provide a direct look at how these two important domains may interact. ❍

See: H.A. Lewis[1], S.G. Buchanan[1], S.K. Burley[1], K. Conners[1], M. Dickey[1], M. Dorwart[2], R. Fowler[1], X. Gao[1], W.B. Guggino[3], W.A. Hendrickson[4], J.F. Hunt[5], M.C. Kearins[1], D. Lorimer[1], P.C. Maloney[3], K.W. Post[1], K.R. Rajashankar[1], M.E. Rutter[1], J.M. Sauder[1], S. Shriver[1], P.H. Thibodeau[2], P.J. Thomas[2], M. Zhang[1], X. Zhao[1], and S. Emtage[1], "Structure of nucleotide-binding domain 1 of the cystic fibrosis transmembrane conductance regulator," EMBO J. **23**(2), 282-293 (2004).

Author affiliations: [1]Structural GenomiX Inc; [2]University of Texas Southwestern Medical Center; [3]The Johns Hopkins University; [4]Howard Hughes Medical Institute, Columbia University; [5]Columbia University

This work was supported by a research contract from Cystic Fibrosis Foundation Therapeutics. Use of the Advanced Photon Source was supported by the U.S. Department of Energy, Office of Science, Office of Basic Energy Sciences, under Contract No. W-31-109-Eng-38.

AN APPETITE FOR APATITE

The three-dimensional (3-D) structure of the second most abundant protein in bone after collagen has been solved by a group of researchers from the Illinois Institute of Technology, Microstar Biotech, Inc., Mount Sinai Hospital, and the University of Toronto, led by experimenters from McMaster University. Called osteocalcin, the protein binds to the calcium-containing mineral hydroxyapatite and thereby helps regulate the amount of calcium in bone. The group crystallized the protein and used x-rays to determine its structure. The result shows that osteocalcin's binding site complements the crystal structure of the mineral.

The body constantly builds up bone and tears it down. The net balance of these two processes determines the amount of calcium in bone and thus the overall health of the skeletal system. Because osteocalcin plays an important role in regulating bone growth, its blood level can serve as a marker for skeletal health. Researchers would like to better understand how the protein interacts with hydroxyapatite and other molecules to aid in designing drugs to combat osteoporosis, for example. Previous structural studies had found that it has a globular structure made of many helices packed together, but researchers had not ascertained its precise mechanism of action on the molecular scale.

To determine how the protein recognizes hydroxyapatite, the group crystallized pig osteocalcin (all vertebrates share a very similar form of the protein) and analyzed the crystal's x-ray diffraction pattern, measured at the IMCA-CAT beamline 17-ID at the APS. Osteocalcin has a novel, roughly pyramidal shape built from three helices. One helix contains an elongated negatively charged region, including three amino acids that researchers had already implicated in hydroxyapatite binding. The negatively charged areas on two adjacent osteocalcin molecules are capable of holding five positively charged calcium ions in place through a network of ionic bonds (Fig. 1). The researchers were surprised to observe that the calcium ions have a periodic arrangement reminiscent of a crystal lattice, so they performed a computer search to identify corresponding calcium arrangements in hydroxyapatite. The best match was found in the most common surface presented by natural and synthetic versions of the mineral. Evidence for the structure of hydroxyapatite in bone is inconclusive but consistent with the best match surface.

The group, which includes members from Microstar Biotech, Inc., the Samuel Lunenfeld Research Institute of Mount Sinai Hospital, the University of Toronto, and the Illinois Institute of Technology, speculates that osteocalcin binds hydroxyapatite in a way that is analogous to the way antifreeze proteins recognize ice crystals and inhibit their growth. Antifreeze proteins have different shapes that complement, and thus bind specifically to, different planes of ice crystals, allowing the protein to modify their structure. The high complementarity between osteocalcin and hydroxyapatite suggests the protein may likewise directly modify crystal growth and structure. The remaining portions of the protein would then be well positioned to transmit signals to and from the surrounding cellular environment. ❍

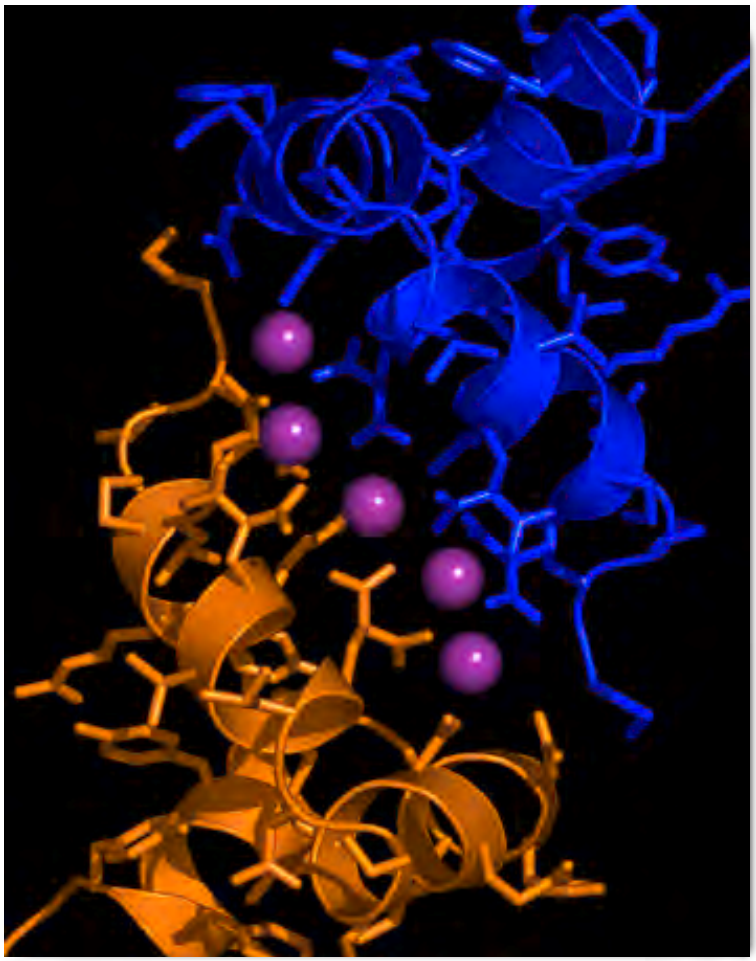

Fig. 1. Crystal structure of two osteocalcin molecules bound to five calcium ions (purple).

See: Q.Q. Hoang[1,2], F. Sicheri[3,4], A. J. Howard[5], and D.S.C. Yang[1], "Bone recognition mechanism of porcine osteocalcin from crystal structure," Nature **425**(30), 977-980 (October 2003).

Author affiliations: [1]McMaster University, [2]Microstar Biotech, Inc., [3]Samuel Lunenfeld Research Institute, Mount Sinai Hospital, [4]University of Toronto, [5]Illinois Institute of Technology

This work was supported by the Natural Sciences and Engineering Research Council (NSERC) of Canada. Use of the IMCA-CAT beamline 17-ID at the APS was supported by the companies of the Industrial Macromolecular Crystallography Association through a contract with Illinois Institute of Technology. Use of the Advanced Photon Source was supported by the U.S. Department of Energy, Office of Science, Office of Basic Energy Sciences, under Contract No. W-31-109-Eng-38.

COLLECTING PROTEIN STRUCTURAL INFORMATION WITHOUT CRYSTALS

The most common method of determining protein structure is to crystallize a protein and collect its x-ray diffraction pattern, but researchers have been able to crystallize only a few percent of all proteins. Some have therefore turned to another method: measuring x-ray scattering from proteins in solution—without crystallizing them. The intense power of third-generation synchrotron sources, such as the APS, should allow researchers to obtain high-quality structural information from scattering experiments, but one of their key concerns has been the effect of radiation damage on the observed scattering. The results reported here indicate that such protein damage is measurable and avoidable.

Scattering data provide less-detailed structural information than crystallography because individual protein molecules are oriented randomly in solution instead of locked into the fixed, repetitive arrangement of a crystal. But the technique complements crystallography by providing information about proteins that either do not crystallize or undergo large structural changes that would be confined in a crystalline lattice. Researchers flash-freeze crystallized proteins to liquid nitrogen temperatures; otherwise, x-rays can disrupt their structure and chemistry by splitting important structural bonds, cleaving chemical groups from amino acids, and even distorting the crystal geometry. But flash-freezing causes additional experimental problems for scattering experiments, so a group of researchers from Argonne National Laboratory and the Illinois Institute of Technology scattered increasing doses of x-rays off proteins in solution to observe and quantify radiation damage at room temperature.

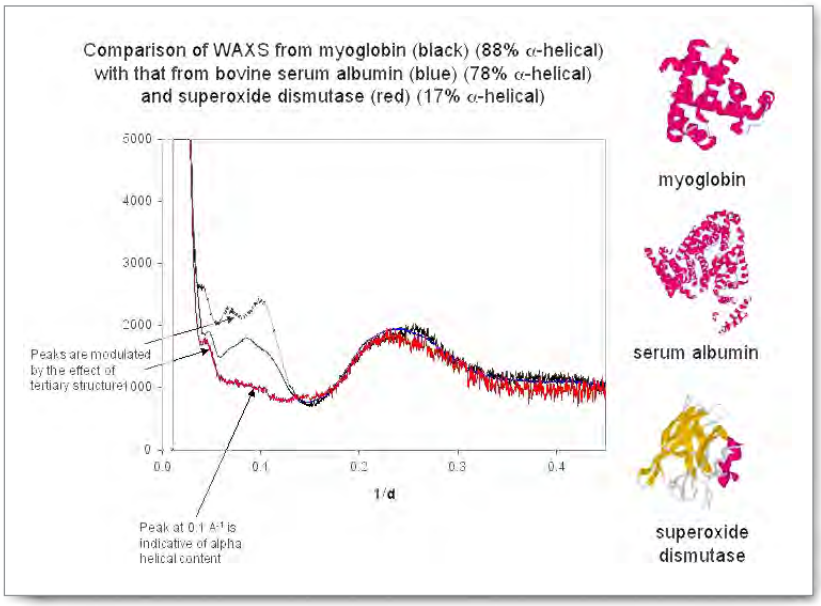

Fig.1. Wide-angle x-ray scattering data from three proteins with decreasing helical content show progressive flattening of the scattering peak at 0.1 $Å^{-1}$. Myoglobin (88% helical) is in black; serum albumin (78%) in blue; superoxide dismutase (17%) in red.

Working at the Bio-CAT beamline 18-ID at the APS, the group is studying the protein fold-dependence of the wide-angle x-ray scattering (WAXS) pattern (FIg. 1). Specific peaks within the pattern correlate with the secondary and tertiary features formed by the amino acid residues of protein molecules such as helices and sheets. To assess radiation damage, the group went on to resolve medium-scale features of hemoglobin and myoglobin, two oxygen-carrying proteins found in blood, and cytochrome C, a metabolic enzyme. They examined each protein by using three protocols with different exposure times. First, samples were made to flow through a quartz capillary such that no part of the sample was exposed longer than 100 ms, which is a typical exposure time for WAXS experiments. Secondly, samples were oscillated slowly in a capillary during an 8-s exposure. Third, samples remained stationary during a 0.7-s exposure. The group found that scattering from the stationary hemoglobin showed signs of protein degradation compared to that of the flowing samples. Hemoglobin consists of four protein chains, and the scattering experiments demonstrated that these chains fall apart after repeated stationary exposures. Myoglobin and cytochrome C showed much less sign of breakdown, even in the stationary samples.

To demonstrate the potential of WAXS to detect structural changes in proteins, scattering experiments were also performed on hemoglobin exposed to increasing concentrations of a denaturing salt — a salt that is known to unfold proteins. The resulting scattering patterns showed a progressive loss of structural features as the concentration of the salt increased. The group concluded that WAXS experiments can (1) provide accurate and informative data about the structure of a protein in solution; (2) can observe changes in protein structure; and (3) can be carried out in a way to minimize radiation damage to the protein. ❍

See: R.F. Fischetti[1,2], D.J. Rodi[1], A. Mirza[3], T.C. Irving[3,4], E. Kondrashkina[4], and L. Makowski[1], "High-resolution wide-angle x-ray scattering of protein solutions: effect of beam dose on protein integrity," J. Synchrotron Rad. **10**, 398–404 (2003).

Author affiliations: [1]Argonne National Laboratory, [2]GM/CA-CAT, [3]Illinois Institute of Technology, [4]Bio-CAT

Bio-CAT is a National Institutes of Health-supported Research Center RR-08630. Use of the Advanced Photon Source was supported by the U.S. Department of Energy, Office of Science, Office of Basic Energy Sciences, under Contract No. W-31-109-Eng-38.

TOGGLING A NUCLEAR RECEPTOR

Science is beginning to understand how chemicals in cells spur on and rein in a major hormone receptor. The human glucocorticoid receptor is biologists' primary source of basic knowledge about the function and mechanism of action of nuclear receptors, which turn genes on and the off. Now, researchers from Karo Bio company in Sweden and Abbott Laboratories has solved the three-dimensional (3-D) structure of the protein bound to drugs that stimulate and suppress its activity. By comparing the two, they found that the position of a short stretch of protein determines whether the protein will be highly active or sluggish.

Human glucocorticoid receptor (GR) waits in the cell for the arrival of steroid hormones such as cortisol, a stress hormone, or progestin, a reproductive hormone. The receptor latches onto them and burrows into the cell nucleus, where it activates some genes and deactivates others. As a result, the body may begin accumulating fat or (in women) ovulating, depending on the hormone. Drugs and other chemicals in the body can make it easier or harder for GR and similar receptors to do their jobs. Although researchers began studying GR before most other nuclear receptors, whose 3-D structures are now known, they only recently determined the structure of one of its key pieces. The so-called ligand-binding domain (LBD) is where the receptor grabs hormones and recognizes other chemical signals.

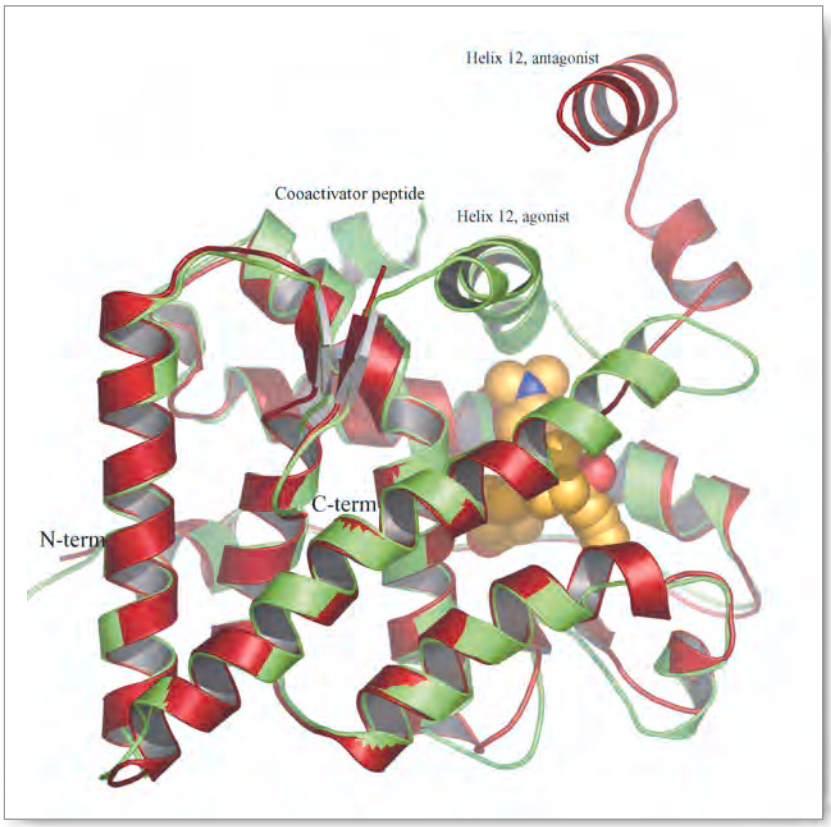

Fig. 1. Comparison of GR with bound agonist (green) or antagonist (red). A chemical group on the side of mifepristone (RU-486) displaces helix 12.

The researchers decided to compare the structure of the LBD when bound to the agonist, or stimulator, dexamethasone and the antagonist, or suppressor, mifepristone (RU-486), which counteracts the effects of progestin in a related receptor. They crystallized two different forms of the complete mifepristone-bound protein. Mifepristone deactivates GR by nudging a stretch of protein called helix 12 over a cavity the protein uses to bind a so-called co-activator protein (Fig. 1), the group reported in the June 20, 2003 issue of the Journal of Biological Chemistry, based on x-ray diffraction patterns recorded at the IMCA-CAT beamline 17-ID at the APS, and beamline ID14-4 at the European Synchrotron Radiation Facility in Grenoble, France. In the presence of dexamethasone, helix 12 bends away from the cavity (Fig. 1), giving the co-activator access to GR. Other nuclear receptors have a similar mechanism of inhibition.

The second form of GR crystallizes in units made of symmetric pairs of receptors, as opposed to asymmetric groups. In this crystal form, each protein helps antagonize the other. Helix 12 of one member of the pair extends out and covers the activating cavity of the other. The researchers say this structure is unusual and may be an artifact of crystallization. If not, it indicates that GR is quite flexible and open to antagonism in more than one way. The group says the structural comparisons reveal how a single protein can exert different biological functions based on its contacts with stimulating and suppressing factors. Researchers can now begin interpreting biochemical data from an assortment of GR mutants based on these structures, they add. ❍

See: B. Kauppi[1], C. Jakob[2], M. Färnegårdh[1], J. Yang[2], H. Ahola[1], M. Alarcon[1], K. Calles[1], O. Engström[1], J. Harlan[2], S. Muchmore[2], A.-K. Ramqvist[1], S. Thorell[1], L. Öhman[1], J. Greer[2], J.-Å. Gustafsson[3], J. Carlstedt-Duke[3], and M. Carlquist[1], "The Three-dimensional Structures of Antagonistic and Agonistic Forms of the Glucocorticoid Receptor Ligand-binding Domain," J. Biol. Chem. **278**(25), 22748-22754 (2003).

Author affiliations: [1]Karo Bio AB, [2]Abbott Laboratories, [3]Karolinska Institute

The facilities of the Industrial Macromolecular Crystallography Association Collaborative Access Team at the Advanced Photon Source are supported by the companies of the Industrial Macromolecular Crystallography Association through a contract with Illinois Institute of Technology (IIT), executed through the IIT Center for Synchrotron Radiation Research and Instrumentation. Use of the Advanced Photon Source was supported by the U.S. Department of Energy, Office of Science, Office of Basic Energy Sciences, under Contract No. W-31-109-Eng-38.

NEW CRYSTAL STRUCTURE FOR NICKEL-RESPONSIVE TRANSCRIPTION FACTOR

Many bacteria require nickel for anaerobic metabolism. The transcription factor NikR regulates nickel uptake in such a way that sufficient amounts, but not too much, of the potentially toxic metal are obtained. NikR, a member of the ribbon-helix-helix family of transcription factors, requires nickel to bind DNA, and there is some evidence to suggest that the binding of DNA changes the geometry of NikR. Using an array of data sets, including some collected at the NE-CAT 8-BM beamline at the APS, investigators from the Massachusetts Institute of Technology determined the crystal structures of two forms of *E. coli* NikR (the full-length apo-repressor at a resolution of 2.3 Å, and the nickel-bound C-terminal regulatory domain at a resolution of 1.4 Å) that establish a better understanding of the mechanism of nickel binding.

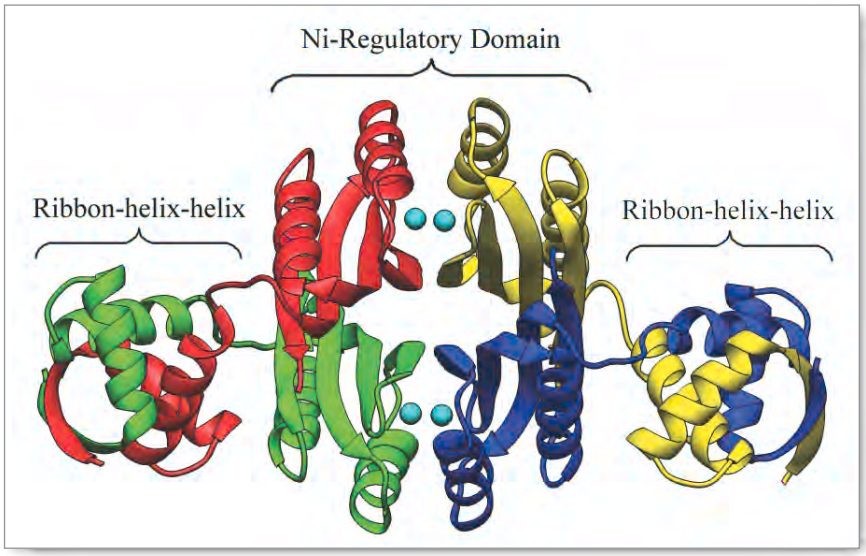

Fig. 1. Model of Ni-NikR, highlighting the modular domain organization. This model was produced from structures of Apo-NikR and the isolated Ni-bound regulatory domain. The NikR tetramer is displayed as a ribbon diagram, colored by the NikR monomer. Nickel ions are displayed as cyan spheres.

Overexpressed full-length NikR and the C-terminal regulatory domain were each purified by nickel-affinity followed by size-exclusion chromatography. Cells grown in a medium supplemented with selenomethionine (SeMet) were used to produce full length SeMet NikR. Crystals were obtained by hanging-drop vapor diffusion and flash-cooled in gaseous N_2 at 100K, the temperature at which all data were collected.

X-ray wavelengths near the N, K-edge and far from the edge were used to determine the structure of the nickel-bound C-domain, using multiwavelength anomalous diffraction (MAD) techniques. Several rounds of iterative manual building and refining by using SHELXL resulted in a model of the nickel-bound C-terminal regulatory domain of NikR. Single-wavelength anomalous dispersion was used to calculate experimental electron density maps for apo-NikR. The C-domain tetramer and two DNA-binding domains were then built into this map. A high-resolution native data set was used to refine the model, which was compared to electron density maps calculated in CNS for manual adjustment.

The basic structure of NikR proves to be a homotetramer: two ribbon-helix-helix DNA binding domains attached at each end of the tetrameric C-terminal regulatory domain (Fig. 1). Two NikR monomers intertwine at their N-termini to each form a two-fold symmetric ribbon-helix-helix domain. A core dimer is formed by the C-terminal regulatory domains of two NikR monomers. Together, the dimers form a tetramer with approximate D2 symmetry, stabilized by a hydrophobic cluster and hydrogen bonding. At the high-affinity nickel-binding sites at the tetramer interface, the nickel ligands show a square-planar coordination, which may account for the specificity of binding nickel at this site rather than other metal ions that do not take on this geometry.

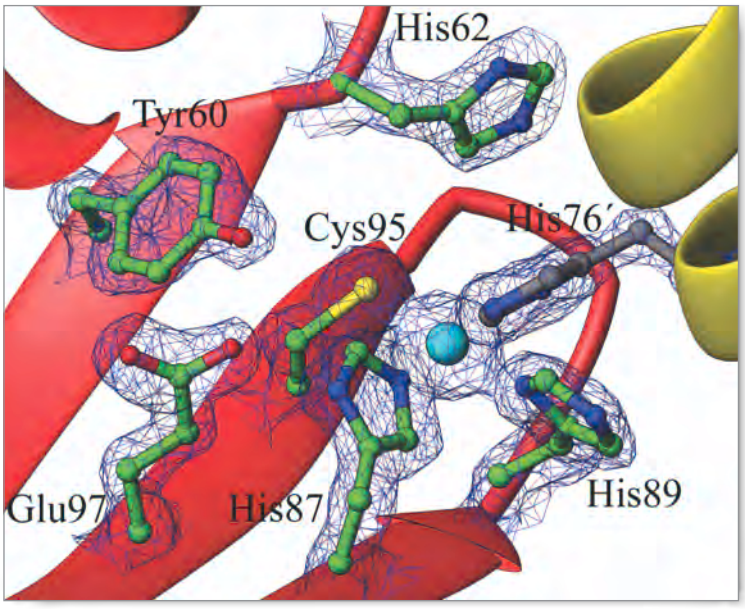

Fig. 2. The high-affinity nickel-binding site in NikR. Strictly conserved amino-acid sidechains are shown with a ribbon diagram of the protein backbone. Note the square-planar coordination of a nickel ion and the contribution to nickel binding from two NikR monomers. The electron density map around the amino-acid sidechains is a $2F_o$-F_c map contoured at 1.2 sigma.

The C-domain structures are similar either with and without nickel, though some differences are related to the movement of nickel ligands and adjacent residues (Fig. 2). NikR exhibits a C-domain most similar to the regulatory domains of enzymes such as phosphoglycerate dehydrogenase (PGDH), ATP phosphoribosyltransferase (ATP-PRTase) and phenylalanine hydroxylase (PheOH), suggesting a common mechanism for propagating ligand-binding signals to adjacent protein domains. Though NikR has a dimeric structure similar to other proteins in the ribbon-helix-helix family, such as Mnt, Arc, and MetJ, it is the only such transcriptional repressor known to be metal-responsive.

Several models for nickel-binding regulation of NikR can be inferred from the established structures. Nickel could be used to induce a conformational change in the protein to make it capable of binding DNA; it could affect transcription by its role in formation or stabilization of the NikR tetramer; or it could make an interaction with DNA electrostatically favorable by decreasing the net negative charge of the regulatory C-domain tetramer. All three mechanisms may be operating in activating NikR for operator binding. ❍

See: E.R. Schreiter, M.D. Sintchak, Y. Guo, P.T. Chivers, R.T. Sauer, and C.L. Drennan, "Crystal structure of the nickel-responsive transcription factor NikR," Nature Struct. Biol. **10**(10), 794-799 (October 2003).

Author affiliation: Massachusetts Institute of Technology

This research supported in part by the U.S. National Institutes of Health (NIH), Searle Scholars Program, Cecil and Ida Green Career Development Fund, Lester Wolfe Predoctoral Fellowship, and the Gray Fund for Undergraduate Research. Data were collected at the Advanced Photon Source, National Synchrotron Light Source, Advanced Light Source, and Stanford Synchrotron Radiation Laboratory synchrotrons. Synchrotron facilities are funded by the U.S. DOE, NIH National Center of Research Resources, and the U.S. National Institute of General Medical Sciences. Use of the Advanced Photon Source was supported by the U.S. Department of Energy, Office of Science, Office of Basic Energy Sciences, under Contract No. W-31-109-Eng-38.

PICKING A PICKY INHIBITOR

Why do some potential drugs specifically target an enzyme that plays a key role in type II diabetes and obesity?

A team of researchers from the Merck Frosst Center for Therapeutic Research and the Merck Research Laboratory has solved the three-dimensional structure of an enzyme bound to several compounds that inhibit its activity as much or more than a similar enzyme. The results may provide a framework for designing potent and selective drugs against diabetes and obesity.

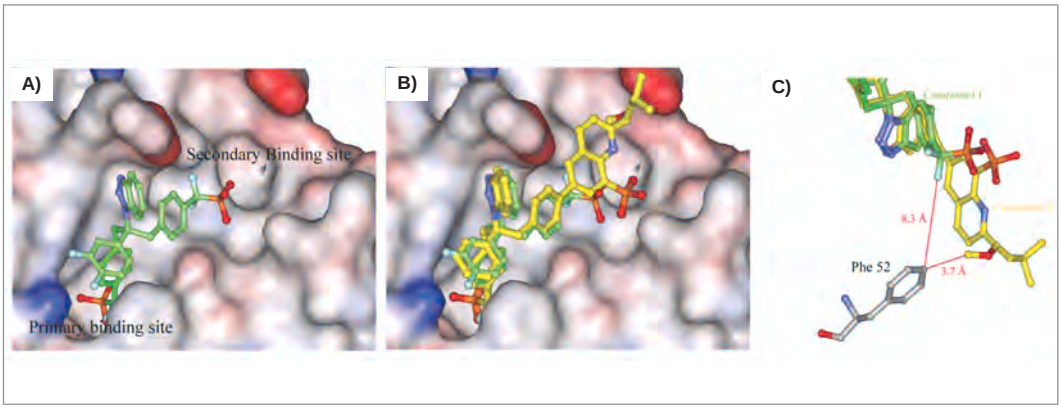

Fig. 1. A) Surface of the substrate binding site of PTP1B. A first-generation, non-selective inhibitor (compound 1) binds in the primary binding site, but does not reach into the secondary binding site. B) A second-generation, more selective inhibitor (compound 2) has been overlaid onto compound 1: compound 2 reaches into and interacts with the secondary binding site. C) The moderate selectivity observed for compound 2 is consistent with its proximity (3.7 Å) to the amino acid phenylalanine (Phe 52).

Chemical signals circulating in the blood tell cells when to grow, divide, etc. When a signal reaches an individual cell, the cell often responds by turning on enzymes that add or remove phosphorous groups from proteins inside it, which turns those proteins on or off. Mice lacking a specific phosphorous-removing enzyme, called protein tyrosine phosphatase 1B (PTP1B), become resistant to weight gain and more sensitive to insulin, a hormone that tells cells to burn fuel. In humans, researchers have observed that obese people gradually lose sensitivity to insulin and develop adult onset or type II diabetes. Pharmaceutical companies would like to develop drugs that turn off PTP1B in hopes of counteracting those diseases.

The group synthesized a set of compounds that inhibit PTP1B but ran into a common problem: the compounds also inhibit a T-cell phosphatase that is required for a healthy immune system. With the help of existing 3D structures for the two phosphatases, the group designed a second set of inhibitors to take advantage of the slightly different shape of the secondary site in each enzyme, and indeed some of the resulting compounds prefer PTP1B moderately over the T-cell phosphatase. To confirm the validity of their approach, the group solved the structure of the enzyme bound to members of both sets of inhibitors. They crystallized a mix of enzyme and inhibitor and determined the resulting structure by analyzing the crystal's x-ray diffraction pattern, measured at the IMCA-CAT beamline 17-ID at the APS.

Each phosphatase has a shallow, elongated crevice on its surface for binding substrates (Fig. 1A,B). Inhibitors block that crevice, which is divided into a primary and secondary site. The more an inhibitor occupies the secondary binding site, the more specific it is for PTP1B. The only difference between the two sec-

ondary binding sites is that two of the amino acids lining PTP1B's pocket—phenylalanine and alanine—are replaced by bulkier amino acids in the T-cell phosphatase. Compounds from the earlier, non-specific set of inhibitors fill the primary binding site, which gives them their potency, but don't extend far enough into the second to make contact with the amino acids that distinguish the two phosphatases (Fig. 1A). With no way to differentiate the two enzymes, the inhibitors bind them both with essentially equal strength.

The group looked at three second-generation inhibitors. The crystal structures confirm that the least specific inhibitor, containing the smallest arm projecting into the secondary binding site, does not make contact with the key amino acids. The other two inhibitors have arms that extend further across the binding site and are both selective for PTP1B. The inhibitor that gets closer to the crucial phenylalanine is also the more selective one (Fig. 1B,C).

The compounds take advantage of most of the available binding sites for potency and selectivity, the researchers conclude. They suggest that possible ways to improve compound design would be to simplify the molecules while trying to retain the interactions with the primary binding site, which determine potency, or anchor them better in the secondary binding site. ❍

See: G. Scapin[1], S. B. Patel[1], J.W. Becker[1], Q. Wang[2], C. Desponts[2], D. Waddleton[2], K. Skorey[2], W. Cromlish[2], C. Bayly[2], M. Therien[2], J.Y. Gauthier[2], C.S. Li[2], C.K. Lau[2], C. Ramachandran[2], B.P. Kennedy[2], and E. Asante-Appiah[2] "The Structural Basis for the Selectivity of Benzotriazole Inhibitors of PTP1B," Biochem. **42**, 11451-11459 (2003).

Author affiliations: [1]Merck Research Laboratory, [2]Merck Frosst Center for Therapeutic Research

The facilities at IMCA-CAT are supported by the companies of the Industrial Macromolecular Crystallography Association through a contract with Illinois Institute of Technology (IIT), executed through IIT's Center for Synchrotron Radiation Research and Instrumentation.Use of the Advanced Photon Source was supported by the U.S. Department of Energy, Office of Science, Office of Basic Energy Sciences, under Contract No. W-31-109-Eng-38.

PLANT VIRUS DEFENDS ITSELF WITH TINY CALIPER

In the long arms race against viruses and other parasitic bits of genetic material, plants have evolved a mechanism for chopping up foreign genes called RNA silencing. Some viruses have retaliated with proteins that negate RNA silencing, and researchers have now discovered how one of these suppressor proteins recognizes and interacts with the silencing signal. They solved the three-dimensional structure of the plant virus protein and found that it acts like a tiny caliper, measuring lengths of nucleic acid and binding preferentially to nucleic acid of the right length. The result may give researchers a new tool for studying RNA silencing in other organisms.

Certain viruses and other genetic "freeloaders," seeking only to reproduce or insert themselves into a host's genome, spend part of their lives as a double-stranded molecule of RNA (a variant of DNA). The host responds by chopping up these RNA double helices into short pieces. Specialized proteins each nab a small fragment of the diced RNA and use the fragments to recognize and destroy (or silence) RNAs from molecular parasites. Some plant viruses produce a protein called p19, which researchers believe interferes with RNA silencing by scouring up all the small RNA fragments of a specific length. To understand how p19 recognizes those molecules, researchers from the National Institutes of Health and the Agricultural Biotechnology Center of Hungary, crystallized and solved the structure of p19 from Carnation Italian Ringspot Virus (CIRV) bound to an RNA fragment.

Based on x-ray diffraction studies performed at the SER-CAT beamline 22-ID at the APS and additional biochemical studies, the group concluded that p19 protein can select the

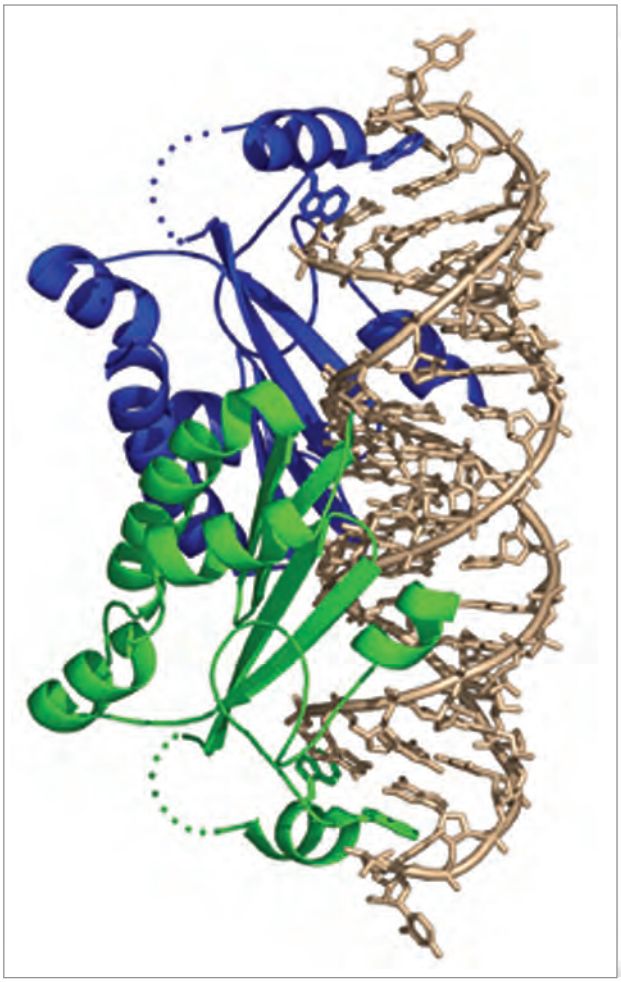

Fig. 1. Two viral p19 protein molecules (green, blue) join to form a long groove for binding RNA fragments that would destroy the virus if left alone.

size class of small RNA fragment that it prefers. Two p19 molecules join together to form an elongated concave surface, and the double-stranded RNA molecule rests in this groove (Fig. 1). The protein binds to atoms along the edge of the RNA that are the same for every RNA molecule but does not bind to the bases in the core of the helix, so the protein can't recognize the specific sequence of those bases. Instead, two amino acids at either end of the protein stick to the bases at either end of the RNA. Replacing one or both amino acids with different ones made CIRV less potent in plant cells, indicating that they are needed for p19 to function properly. One could imagine that the distance between the two amino acids determines the size of the RNA molecule the protein will recognize, namely 21 bases. Shorter segments wouldn't be anchored at the ends and longer ones would kink, missing out on some of the generic bonding along their edges. Consistent with this possibility, the group measured the binding strength of RNAs ranging from 19 to 26 bases long and found that binding strength decreased for each base added to or subtracted from 21.

It is known that p19 suppresses fruit fly RNA silencing and binds short, artificial RNAs in test tubes, so the protein may be useful as a tool in studying the silencing process in animals as well as plants. Animals exploit a version of it to turn their own genes off. ❍

See: J.M. Vargason[1], G. Szittya[2], J. Burgyán[2], and T.M. Tanaka Hall[1], "Size Selective Recognition of siRNA by an RNA Silencing Suppressor," Cell **115**, 799–811 (26 December 2003).
Author affiliations: [1]National Institutes of Health, [2]Agricultural Biotechnology Center

This research supported by grants from the Hungarian Ministry of Education (NKFP 4/023/2001) and "VIS" EU project (QLG2-CT-2002-01673) and the intramural program of the National Institute of Environmental Health Sciences. Use of the Advanced Photon Source was supported by the U.S. Department of Energy, Office of Science, Office of Basic Energy Sciences, under Contract No. W-31-109-Eng-38.

STRUCTURE OF UNUSUAL PROTEIN PROVIDES INSIGHT INTO DEVELOPMENT OF NEURONS

The semaphorins are extracellular proteins that play important roles in growing neurons. These molecules provide chemical signals that guide axonal growth cones. The process begins with the initial stages of axon outgrowth and ends with the formation of a functioning synapse. Many parts of these signaling events, however, are not well understood. Experimentalists from the Memorial Sloan-Kettering Cancer Center, Brookhaven National Laboratory, Cornell University, and Westfälische Wilhelms Universität used data collected at the NE-CAT 8-BM beamline at the APS and the Cornell High Energy Synchrotron Source F2 beamline to determine the crystal structure of one form of a semaphorin, identified the site at which it binds one of its receptors, and may have found the site where it binds a coreceptor. They developed a model describing how the signaling starts and suggested that this model could also explain how signaling is initiated by other molecules with similar structures.

Semaphorin 3A (Sema3A) is particularly interesting because it is a potent repulsive molecule inhibiting or repelling neurite outgrowth. It may also be important for growing blood supplies, which makes it of interest to cancer researchers looking for ways to block the growth of blood vessels around tumors. Ultimately, the researchers want to understand the molecular mechanisms of semaphorin-mediated signaling.

As a small part of that goal, they need to understand how Sema3A interacts with its two coreceptors. Sema3A is unusual in that it needs two receptors (Plexin-A1 and Neuropilin-1) in order to function. Plexin-A1 acts as the signal-transducing unit, but Sema3A cannot bind directly to it. Another receptor, Neuropilin-1 (Nrp-1), brings the two together.

In order to investigate the structure of the protein, they used the techniques of x-ray crystallography to study a func-

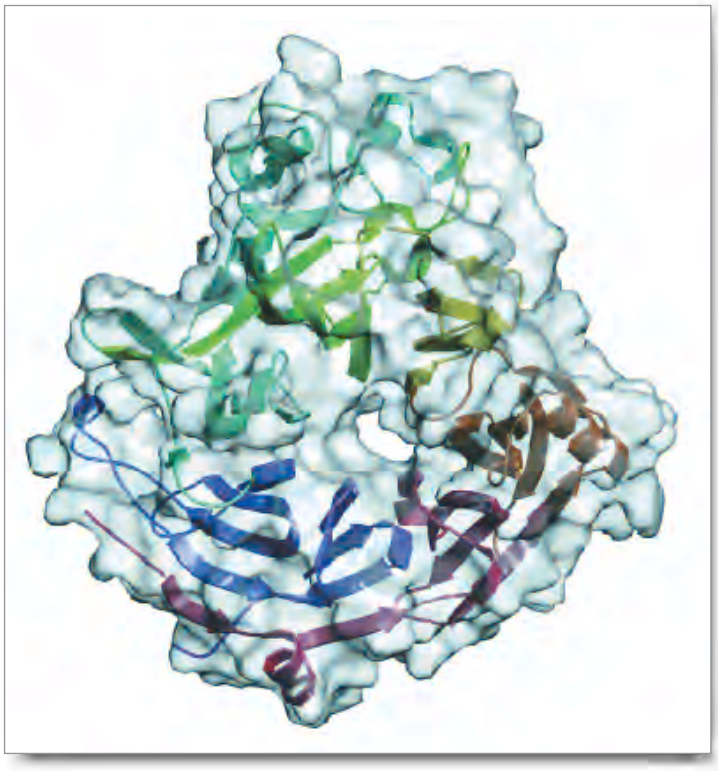

Fig 1. Structure of semaphorin Sema3A-65K contains seven propeller blades. Starting at the N-terminal end of the protein, each of the seven blades is assigned a color (red, orange, yellow, green, cyan, blue, and magenta) before reaching the C-terminal end of the molecule.

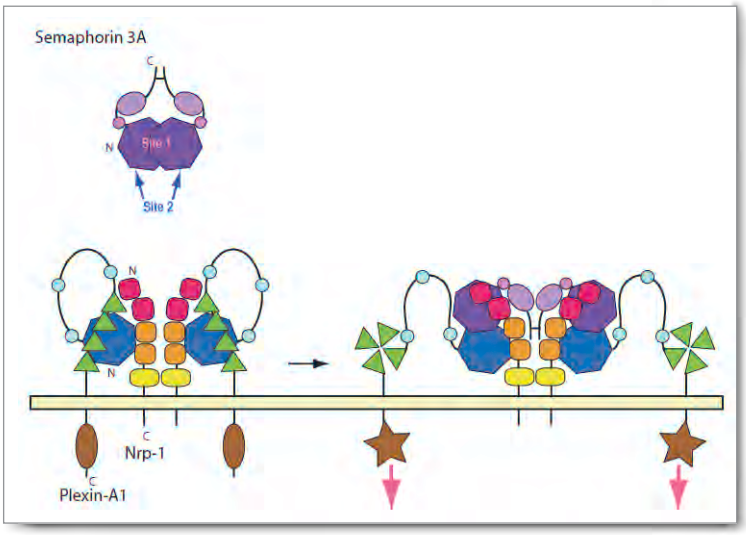

Fig. 2. A model for semaphorin-initiated signaling. The authors suggest that (left) in the absence Sema3A, the Nrp-1/Plexin-A1 complex is both stable and inactive. When Sema3a binds to the two receptors, it releases a part of the plexin molecule that was previously bound by Nrp-1, allowing it to adopt an active conformation. Plexin is shown in dark blue, light blue, green, and brown. NRP-1 shown in red, orange, and yellow. Semaphorin shown in purple, lavender, and pink.

tional 65-kDa Sema3A form (Sema3A-65K). It contains the entire semaphorin domain (the roughly 500 amino acids that define semaphorins). Nikolov's group used two-wavelength multiple anomalous diffraction (MAD) phasing, a method that requires changing the wavelength—a requirement that is beyond the capability of many x-ray sources but possible using the APS. The high-intensity source also aided the researchers by providing a good signal from weakly diffracting crystals. The data obtained at APS allowed them to build a semaphorin model, which they refined at 2.8-Å resolution.

They found that the protein is shaped like an elongated disc and measures about $60 \times 70 \times 45$ Å. To their surprise, the group also found that the protein folds in a propeller-like fashion, a variation of the so-called beta propeller topology, in which seven blades are arranged radially around a central axis (Fig. 1). Interestingly, most of the blades contain a larger than usual number of amino acids. Some of the extra secondary structure elements are likely to have important biological functions, including the four protruding loops that form the proposed neuropilin-binding site.

The researchers were able to compile clues about the way neuropilins and semaphorins interact with each other to identify their potential binding sites. Because neuropilin binding competes with semaphorin dimer formation, they surmised that the binding spot is probably near the dimerization interface. Also, since some semaphorins do not bind neuropilin-1, they must lack some binding site features that are present in Sema3A. As an additional indication that they'd found the right site, analysis of the electrostatic potential at the molecular surface showed that the binding sites are oppositely charged and therefore attractive. To test their theory, they created two Sema3A-65K variants with alterations in the proposed binding site: neither would bind to Nrp-1.

Given the structural information and previously published data, the researchers propose a series of molecular events that occur at the beginning of semaphorin signaling (see Fig. 2.) In the absence of ligands, the plexins remain in an inactive (autoinhibited) state. Nrp-1 interacts with the extracellular region of Plexin-A1, stabilizing this inactive form of the molecule. When Sema3A binds to the Nrp-1/PlexinA1 complex, however, the shape of Plexin-A1 changes both outside and inside the cell. This process releases the plexin from inaction, allowing it to begin signaling.

This signal-initiation sequence could be similar to that of other cell surface receptors (such as integrins and the LDL receptor) with the same beta propeller topology.

See: A. Antipenko[1], J.-P. Himanen[1], K. van Leyen[1], V. Nardi-Dei[1], J. Lesniak[1], W. A. Barton[1], K.R. Rajashankar[2], M. Lu[3], C. Hoemme[4], A. W. Püschel[4], and D.B. Nikolov[1], "Structure of the Semaphorin-3A Receptor Binding Module," Neuron **39**, 589–598 (14 August 2003).

Author affiliations: [1]Memorial Sloan-Kettering Cancer Center, [2]Brookhaven National Laboratory, [3]Weill Medical College of Cornell University, [4]Westfälische Wilhelms Universität

This work was supported by the New York State Spinal Cord Injury Research Program (D.B.N) and by DFG and Fonds der Chemischen Industrie (A.W.P.). D.B.N. is a Bressler Scholar. Use of the Advanced Photon Source was supported by the U.S. Department of Energy, Office of Science, Office of Basic Energy Sciences, under Contract No. W-31-109-Eng-38.

THE MORE, THE MERRIER: MULTIPLE PRECIPITANTS ARE BETTER THAN ONE

X-ray crystallography studies to determine a protein's structure are notoriously limited by many proteins' stubborn refusal to crystallize. Experimentalists from the National Institutes of Health and Columbia University have found that combining several types of precipitants, or chemicals that nudge molecules out of solution, can work better than adding just a single type. They screened 64 precipitant mixtures and reported that mixtures increased the chance of crystallization and the quality of crystals formed.

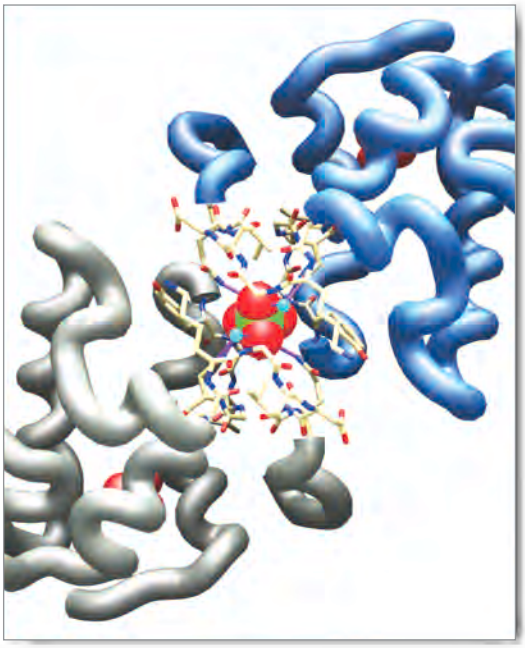

Fig. 1. A never-before-seen type of egg white lysozyme—the first new crystal lattice of lysozyme to be reported since 1967. Pairs of lysozyme molecules (silver, blue) are held together by sulfate ions (red, green).

Although researchers have dramatically increased the number of protein structures determined by X-ray diffraction over the last decade, the crystallization process is still somewhat mysterious and finicky. Precipitating agents, used to force proteins out of solution and possibly into crystal form, have become key ingredients. Researchers often resort to screening a range of solution conditions when trying to crystallize a protein, but typically treat the precipitant as a single variable, even though precipitants come in a number of distinct flavors: Salts make water repel oil more strongly, forcing the greasy parts of proteins together; organic solvents prevent water from shielding charged parts of proteins, allowing complementary charges to stick; and high molecular weight polymers crowd the dissolved molecules, forcing them to cluster together. Previous researchers had discovered that fortuitous mixtures of precipitants sometimes give crystals, but no one had systematically tested the effect of precipitant mixtures on crystallization.

The group devised a 64-member screen varying along five dimensions: pH, the presence of an additive (positive or negative ion, detergent, etc), and the choice of three dissimilar precipitants. Many combinations didn't mix, but those that did often lowered the concentration of protein required for precipitation. Compared to a commercially available screen, the so-called precipitant synergy (PS) screen covered a wider and denser range of possible precipitation conditions. They tested the two screens on ten HIV proteins whose long flexible loops make them extremely difficult to crystallize. Although both screens produced the same number of initial crystals, the PS produced three times as many crystals large and ordered enough for structural analysis--six in total--based on x-ray studies on the SER-CAT 22-ID beamline at the APS. (Several of the structures were recently published.*) The experimental screen also crystallized three proteins that the commercial screen couldn't, but failed to crystallize two proteins the commercial screen could. Many of the commercial screen's successes were from mixtures of precipitants, though, and when the initial crystals were optimized to find the best crystallization conditions, all formed the best crystals in precipitant mixtures.

The group also tested the PS screen on hen egg white lysozyme, a protein studied for over 50 years and commonly used to evaluate screens. 29 out of 64 combinations supported crystal growth, and one combination even produced a novel crystal structure that hadn't been reported previously. The crystal was built out of symmetric pairs of protein molecules, held together electrostatically by sulfate ions (Fig. 1) with adjacent pairs joined by hydrophobic (water-excluding, non-electrostatic) interactions.The researchers speculate that the interactions holding the crystal together reflect the mixture of precipitants responsible for crystallization. Researchers believe crystal formation may begin from a small number of contacts. Precipitants stabilize different types of protein interactions, which may enhance the probability of forming specific types of contacts.

The results suggest that existing robotic technology should be able to search through significant regions of “crystallization space,” the sum of all possible precipitant combinations. Pharmaceutical and biotech companies would like to assemble as complete a library of structures of proteins in the human genome as possible, the researchers point out, and even doubling the average probability of crystallization would have a big effect. ❍

*Huang et al. 2004 PNAS 101:2706-2711

See: S. Majeed[1,2], G. Ofek[1], A. Belachew[2], C.-c. Huang[1], T. Zhou[1], and P.D. Kwong[1,2], “Enhancing Protein Crystallization through Precipitant Synergy,” Structure **11**, 1061-1070 (September 2003).

Author affiliations: [1]National Institutes of Health, [2]Columbia University

These studies were supported by the National Institutes of Health. P.D.K. was a recipient of a Burroughs Wellcome Career Development award. Beamline X4A at the National Synchrotron Light Source, a Department of Energy facility was supported by the Howard Hughes Medical Institute. Use of SER-CAT at the Advanced Photon Source was supported by the U.S. Department of Energy, Office of Science, Office of Basic Energy Sciences, under Contract No. W-31-109-Eng-38.

RARE TWO-PHOTON EMISSION AIDS IN ATOMIC CALCULATIONS

In most cases, electronically excited atoms decay by emitting a single photon with an energy equal to the excitation energy. One of the exceptions is two-photon decay, where the electronic energy is released with the emission of two photons, the total energy of which equals that of the excitation. Because the individual photon energies in the twosome can vary, the emission appears as continuum radiation below the energy of the single photon transition. Despite its extreme rarity, two-photon decay provides a powerful window into the details of atomic structure. Using the APS, collaborators from Argonne and the Gesellschaft für Schwerionenforschung (GSI) in Darmstadt, Germany, have measured two-photon emission from gold atoms and compared the results with theoretical calculations.

Early measurements of two-photon decay in heavy atoms were achieved by creating a K electron vacancy via photoionization, but most of the previous studies of two-photon processes in atoms relied on radioactive sources where the K hole was produced by nuclear electron capture. While this leads to clean results, it places a severe restriction on the atomic elements that can be studied. The high brightness and high photon energy x-ray beams available from third-generation synchrotrons, such as the APS, now make it possible to produce K shell vacancies on a wider range of heavy elements.

To create the K shell holes, the Argonne/GSI team used x-rays from BESSRC/XOR beamline 12-BM at the APS. A silicon monochromator and germanium 220 crystal were employed to select the third-order x-rays at 85.5 keV, with first-order energy being further reduced by an aluminum filter plate. This filtered x-ray beam was directed at a 2-mg/cm^2 gold foil target at normal incidence.

Two-photon events were analyzed by means of a pair of shielded germanium detectors arranged 90 degrees to each other and operated in coincidence detection mode. Tantalum shields were used to suppress cross-talk events that could be generated when an atomic fluorescence photon from the target is Compton scattered in one detector and detected in the other. All decays in which a coincidence within 5 μs were recorded, along with single photon events in order to assess the K vacancy production rate.

The sum-energy fluorescence spectrum for gold, corrected for random coincidences, shows two distinct peaks, corresponding to two groups of lines dominated by the 3d-1s and 2s-1s two-photon transitions, respectively (Fig. 1). The event data were then fit to an expression for two-photon decay rate for each of the transitions, taking into account the K hole production rate and detector characteristics.

Although no theoretical calculations have yet been done for two-photon decay from excited inner shell vacancies in gold, it is worthwhile to compare the results with calculations for neutral lower Z and hydrogen-like atoms. Experimentally, the gold (Z = 79) results appear to follow a roughly flat trend for decay rate versus Z when added to data for other species, such as silver (Z = 47), xenon (Z = 54), and hafnium (Z = 72). Calculations for the neutral atoms appear to give appropriate values for the lower Z elements but show an increasing trend not matched by the gold data. On the other hand, a nonrelativistic calculation for highly ionized hydrogen-like atoms exhibits the flat trend, but the magnitude of the decay rate does not agree.

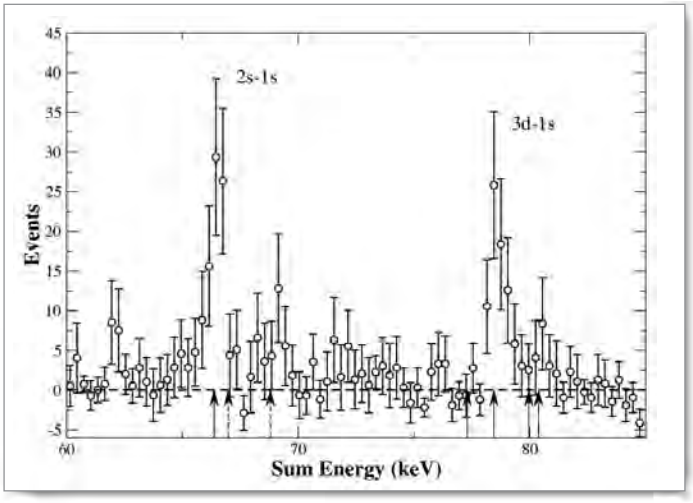

Fig. 1. Spectrum of two-photon decay events in gold atoms showing peaks at 2s-1s and 3d-1s transitions. Horizontal axis is sum energy of the two photons. Events are counted when measured by coincidence detection and random coincidences have been subtracted out. Solid arrows show possible two-photon transitions for atoms with single K shell vacancy, while dashed arrows indicate $K\alpha_1$ and $K\alpha_2$ transition energies.

The present results show the usefulness of high-output synchrotron sources in detecting and analyzing unusual atomic processes, such as two-photon decay. Moreover, the results for gold atoms dramatically highlight the need for improved atomic calculations. By enhancing the experimental setup, especially in reducing spurious events, it will be possible to probe the character of the continuum spectrum and thus enable more thorough tests of the theoretical calculations. ❍

See: R.W. Dunford[1], E.P. Kanter[1], B. Krässig[1], S.H. Southworth[1], L. Young[1], P.H. Mokler[2], and Th. Stöhlker[2], "Two-photon decay in gold atoms following photoionization with synchrotron radiation," Phys. Rev. A **67**, 054501-1 to 054501-4 (2003).

Author affiliations: [1]Argonne National Laboratory, [2]GSI

This work was supported by the Chemical Sciences, Geosciences, and Biosciences divisions of the Office of Basic Energy Sciences, Office of Science, U.S. Department of Energy, under Contract No. W-31-109-Eng-38. P.H.M. and T.S. were supported by GSI and a NATO travel grant.

Distribution of Chromium Contamination and Microbial Activity in Soil Aggregates

As a by-product of numerous industries, from wood preservatives to metal plating, chromium is an environmental carcinogen often found in some contaminated soils. Ideally, it can be fixed in place through a reaction that reduces a soluble form of chromium to an insoluble form. These processes have typically been analyzed by assuming microbial and chromium distributions are homogeneous within the soil. However, biogeochemical conditions within soils become heterogeneous at the scale where chemical transport is slow. This heterogeneity occurs in soil aggregates, millimeter-scale cohesive units comprised of many additional soil particles. Using an x-ray microprobe and micro-x-ray absorption near-edge structure (micro-XANES) mapping to examine soil aggregates at microscales, researchers from Lawrence Berkeley National Laboratory, The University of California, Berkeley, The University of Chicago, and the University of Georgia have shown that the heterogeneity of a complex system in nature will affect the efficiency of the chromium reduction: microenvironments exposed to oxygen and low in available organic carbon are oxidizing and therefore slow chromium reduction rates. These studies show that to understand the fate of chromium contamination can require analyzing chemical and microbiological distributions with microscale (micrometer to millimeter) spatial resolution.

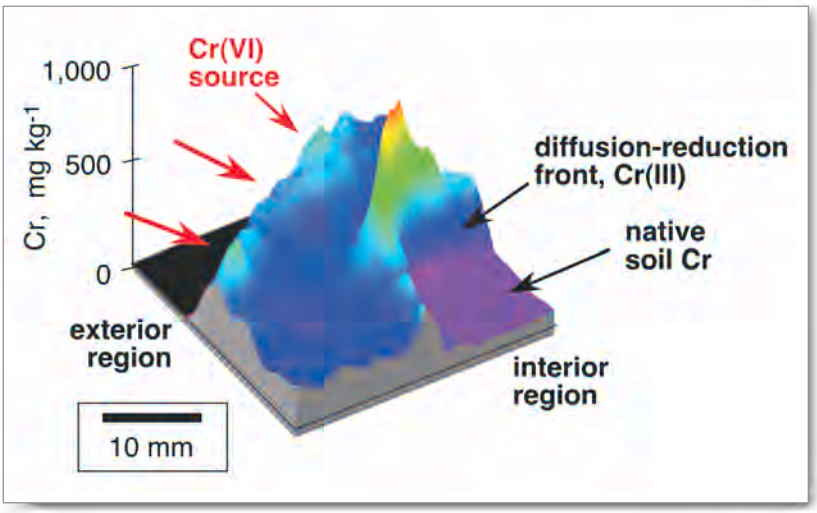

Fig. 1. Chromium distribution in a quarter-section slice through a natural soil aggregate, 31 days after exposure. Chromium occurs primarily as Cr(VI) along the exterior , and primarily as Cr(III) at the diffusion-reduction front.

Chromium VI (Cr(VI)) is soluble and easily transported through the environment. However, the natural soil microbial community can transform it to chromium III (Cr(III)) both directly, by enzymatic reduction, and indirectly, by depleting oxygen concentrations and increasing availability of iron II (Fe(II)), an important reductant in the soil. To analyze the efficiency of the microbial activity in reducing chromium, synthetic soil columns were examined, as were natural soil aggregates (both used Altamont clay, from Altamont Pass in Alameda County, CA). For the synthetic soil columns, the clay was homogenized and repacked into columns. The natural aggregates were simply collected as-is from the soil, in roughly spherical shapes, 90 to 150 mm across. Both columns and aggregates were permeated with a solution of Cr(VI) before fixing the aggregates by freezing, freeze-drying, and encasing in resin. (Half of the aggregates were fixed immediately after being exposed to the chromium; the other half were fixed 28 days later in order to study the soil after a month of microbial activity.)

The samples were mapped to obtain profiles of their chromium distributions. The synthetic columns were mapped over the course of a month by using x-ray microprobe and micro-x-ray absorption near edge structure techniques at the GSECARS beamline 13-ID at the APS. The natural aggregates were examined at Beamline X26A of the National Synchrotron Light Source, Brookhaven National Laboratory. Chromium reduction efficiency depended on the level of organic carbon available to the sample. Those samples that were enriched with carbon supported higher microbial activity and consequently very active reduction—organic carbon-rich, microbially active soils showed all the Cr(VI) reduced and immobilized as Cr(III). The distribution of oxygen had an effect as well, as oxygen inhibits chromium reduction. The maps showed that there was only Cr(III) on the inside of the samples with greater reduction, while only Cr(VI) was seen in the surface region, to depths of about a millimeter. The delineation between the two areas—a thin band where both types of chromium were present—was sharp, no greater than 0.2 mm in more microbially active soils. Such distributions of the two types of chromium could be seen within the first few days of the soil's first contact with the chromium solution; they were firmly established by the end of a month (Fig. 1). The heterogeneous nature of chemical and microbial composition of soil, therefore, has an obvious effect on immobilizing chromium that cannot be analyzed properly simply by averaging across the bulk samples.

The natural and synthetic samples showed surprisingly similar results, suggesting that synthetic columns are an effective laboratory tool, providing a good model for the natural system. Columns are useful since the window along the side of the container allows one to analyze the soil over time as the microbes are working, which cannot be done with natural aggregates.

Bulk analysis of contaminated soil systems — as well as any other samples — would simply show a mixture of Cr(VI) and Cr(III). This study shows, however, that this is not due sim-

ply to lack of complete reduction, but rather that the chromium is distributed in sharply differentiated areas, depending on microbial and chemical composition of the soil, thus still providing distinct areas of insoluble and immobilized Cr(III) and the more toxic Cr(VI). ❍

See: T.K. Tokunaga[1], J. Wan[1], T.C. Hazen[1], E. Schwartz[2], M.K. Firestone[2], S.R. Sutton[3], M. Newville[3], K.R. Olson[1], A. Lanzirotti[3], and W. Rao[4], "Distribution of Chromium Contamination and Microbial Activity in Soil Aggregates," J. Environ. Qual. **32**, 541-549 (March-April 2003).

Author affiliations: [1]Lawrence Berkeley National Laboratory, [2]University of California, Berkeley, [3]GSECARS, The University of Chicago, [4]University of Georgia

Funding provided through the U.S. Department of Energy Basic Energy Sciences, Geosciences Program, under Contract No. DE-AC03-76SF00098. The National Synchrotron Light Source, Brookhaven National Laboratory, is supported by the U.S. Department of Energy, Division of Materials Sciences and Division of Chemical Sciences. GSECARS is funded by the NSF (Earth Sciences Division) and by DOE (Geosciences Program). Use of the Advanced Photon Source was supported by the U.S. Department of Energy, Office of Science, Office of Basic Energy Sciences, under Contract No. W-31-109-Eng-38.

Properties of Iron Alloys Deep Inside the Earth

Understanding the composition of the Earth's core is one of the main challenges facing geophysicists today. From geochemical and planetary formation models it is believed that the main constituent of the core is an iron alloy with about 5% nickel by weight. Yet the density of the Earth's outer core is 10% lighter than pure iron at core temperatures and pressures. In addition, the velocity of sound waves in the outer core is 3% higher than in iron alone. These discrepancies are consistent with the presence of other chemical elements in the core structure. It is essential, therefore, that the effects of alloying on the physical properties or iron be measured in order to gather an accurate picture of the deepest parts of our planet. Recently, researchers from the Carnegie Institution of Washington, Argonne National Laboratory, and Academia Sinica in Taiwan used inelastic x-ray scattering (IXS) at the APS to measure the physical properties of iron-nickel and iron-silicon alloys at pressures comparable to Earth's core.

Among the elements that could be alloyed with iron in the core besides nickel, silicon stands out as a prime candidate light element. Other light elements, such as sulfur and oxygen, do not form solid solutions with iron in the relevant pressure and temperature ranges. Silicon, on the other hand, easily combines with iron to form alloys. To observe the effects of nickel and silicon on iron alloys, the researchers used nuclear resonant inelastic x-ray scattering (NRIXS) to measure the phonon density of states under high pressure. From the density of states, the velocity of sound waves—an important geophysical parameter directly measured by seismic wave study—can be derived.

Iron-57 was used in the creation of the test samples to single out the resonant x-ray absorption line for NRIXS. Samples of Fe-Ni were synthesized by reducing the starting elements in a hydrogen atmosphere at high temperature, followed by melting and annealing; the Fe-Si alloy samples were synthesized by arc melting. To conduct the measurements, alloy specimens together with a few ruby chips (an internal pressure calibrant) were placed in a hole drilled into a beryllium gasket which was put into a diamond anvil cell. The NRIXS measurements were carried out at X-ray Operations and Research beamline 3-ID at the APS in collaboration with staff from HP-CAT (APS sector 16).

Density-of-states profiles were calculated from the spectra at pressures up to 106 GPa for the iron-nickel alloy and up to 70 GPa for the iron-silicon alloy. To extract sound velocities, a parabolic fit was made to the low energy slope of the density of states curve. This yields a good approximation to the bulk Debye sound velocity of the samples containing iron-57. A correction factor was applied to obtain the sound velocities for the natural isotopic abundance. Aggregate compressional and shear velocities were then calculated with previously obtained equations of state for iron-rich nickel and silicon alloys as a function of density.

The results indicate that adding nickel to iron slightly lowers the compressional and shear velocities, whereas addition of silicon raises them, which is consistent with silicon being a major light element in the Earth's core. The results also indicate the importance of applying *in situ* x-ray microanalysis of this kind to geophysical problems, an application made feasible by the high brightness of third-generation synchrotron facilities such as the APS. The researchers have launched new experiments to understand the sound velocities and physical properties of iron and its alloys under extremely high pressures and temperatures by combining the NRIXS with the laser-heated diamond anvil cell technique. These state-of-the-art experiments will enable us to better understand geophysical and geochemical models of our planet's deepest part. ❍

See: J.-F. Lin[1], V.V. Struzhkin[1], W. Sturhahn[2], E. Huang[3], J. Zhao[2], M.Y Hu[4], E.E. Alp[2], H.-k. Mao[1], N. Boctor[1], and R.J. Hemley[1], "Sound velocities of iron-nickel and iron-silicon alloys at high pressures," Geophys. Res. Lett. **30**(21), 2112 (2003).

Author affiliations: [1]Carnegie Institution of Washington, [2]Argonne National Laboratory, [3]Academia Sinica, [4]HP-CAT and the Carnegie Institution of Washington

This work supported by tthe State of Illinois under HECA. We thank GSECARS and HPCAT, APS for the use of the ruby fluorescence system. Work at Carnegie was supported by DOE/ BES, DOE/NNSA (CDAC), NSF, and the W. M. Keck Foundation. Use of the Advanced Photon Source supported by the U.S. DOE, Office of Science, Office of Basic Energy Sciences, under Contract No. W-31-109-Eng-38.

Measuring Deformation Mechanisms at Pressures of the Lower Mantle

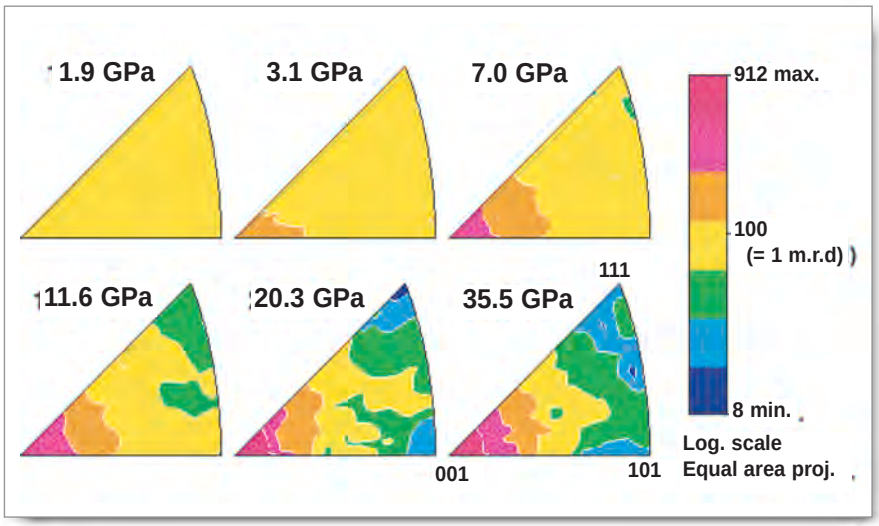

Fig. 1. Experimental inverse pole figures illustrating the development of lattice-preferred orientations in MgO over increasing pressures.

A deeper understanding the rheology of the Earth's mantle is important for understanding mantle convection and seismic anisotropy, but these studies are difficult to carry out in a laboratory setting due to the intense pressures needed. In addition, there are no good analogs for the minerals in question. Recent advances have been made, however, by using diamond anvils to put minerals under extreme pressures while performing x-ray diffraction. These methods have here been further improved by analyzing samples of polycrystalline MgO, commonly known as periclase. The data, collected by a group of researchers from École normale supérieure de Lyon, the Carnegie Institute of Washington, The University of California, Berkeley, and The University of Chicago, show the feasibility of analyzing elastic moduli, shear strength, and deformation mechanisms under pressures relevant to the Earth's lower mantle.

MgO was used in the samples because it is a common mineral, accounting for some 20% of the Earth's lower mantle. The MgO was ground down to particle sizes of about 1 µm and then pressed into platelets between two large diamonds. To pressurize the samples, a diamond anvil cell with a 300-µm-diameter tip was used, with a 65-µm hole drilled into the gasket to form a chamber for the sample. The chamber was filled with a layer of MgO powder, then a platelet of iron, then another platelet of MgO. Diffraction experiments were conducted by using angle-dispersive synchrotron x-ray diffraction at the GSECARS beamline 13-ID at the APS.

Samples were compressed from ambient pressure up to 47 GPa, at room temperature. As the pressure increased, the macroscopic deformation of the sample could be seen. The uniaxial stress component increased sharply from 0 to 7 GPa as the sample was raised from ambient pressure to 10 GPa. Above 10 GPa, the uniaxial stress component remained approximately constant at 8 GPa. For one set of samples in which the iron was not evenly placed, the uniaxial stress component then decreased as the iron underwent a phase transition at 12 GPa. The elastic moduli that were deduced were largely consistent with those derived from Brillouin spectroscopy. We observed progressive development of a sharp texture in the samples above 1.90 GPa, from which the calculated preferred lattice orientations were calculated and the active deformation mechanisms in the experiment were deduced.

In the context of the Earth's mantle itself, the data suggested that the single-crystal elastic anisotropy tends to decrease with pressure—although this effect is also countered by competing effects from increases in temperature. As such, the anisotropy factor decreases from 0.115 at 670-km depth to 0.050 at 1050-km depth, and then increases again to 0.180 at 1660-km depth. Results also suggest that polycrystalline MgO deforms by slip along the {110} system in cold compression up to the pressures found in the lower mantle.

While further study needs to be done on MgO to understand its behavior in the planet's interior, these raw results were in good agreement with results employing other techniques, which gives confidence that diamond anvil cells are an efficient way to analyze elasticity, strength, and deformation mechanisms in materials at extreme pressures. This is one of the first demonstrations that measurements of deformation mechanisms can be successfully done at pressures above 10 GPa. The transparency and immense pressure capabilities of the diamond anvil cells has opened new doors for studying minerals *in situ*, allowing for more realistic geodynamic models. ❍

See: S. Merkel[1,2], H.R. Wenk[3], J. Shu[2], G. Shen[4], P. Gillet[1], H.-k. Mao[2], and R.J. Hemley[2], "Deformation of polycrystalline MgO at pressures of the lower mantle," J. Geophys. Res. **107**(B11), 2271, 3-1 to 3-17 (2002).

Author affiliations: [1]École normale supérieure de Lyon, [2]Carnegie Institute of Washington, [3]University of California, Berkeley, [4]GSECARS, the university of Chicago

This work was supported by the National Science Foundation, the U.S. Department of Energy (DOE), the Center for High Pressure Research, the W.M. Keck Foundation, and the Centre National de la Recherche Scientifique-Institut National des Sciences de l'Univers program "Intérieur de la Terre." H.R.W. acknowledges support from NSF (EAR 99-02866), IGPP-LANL, the University of Chicago Education Abroad Program, and the A. von Humboldt Foundation. GSECARS is funded by the NSF (Earth Sciences Division) and by DOE (Geosciences Program). Use of the Advanced Photon Source was supported by the DOE Office of Science, Office of Basic Energy Sciences, under Contract No. W-31-109-Eng-38.

Measuring the Velocity of Sound in Diverse Materials

Measuring the velocity of sound through natural and fabricated compounds can reveal the composition and structure of materials at unprecedented detail. The challenge is to develop a method that can be used to determine sound velocity in condensed matter having a diverse structure. To overcome that challenge, researchers from the Carnegie Institution of Washington, Argonne National Laboratory, the University of Connecticut, and Northern Illinois University have applied nuclear resonant inelastic x-ray scattering — or NRIXS — at the XOR beamline 3-ID of the APS. Using NRIXS, they have successfully measured the velocity of sound in samples that represent both crystalline and noncrystalline materials [1]. Now that this method has been demonstrated successfully, researchers expect that it could significantly accelerate developments in high-pressure research and yield benefits in geophysics and other fields, like nanoscience.

NRIXS is used to study lattice dynamics of materials by means of low-energy nuclear resonances. Signals from nuclear resonance absorption are specific to the resonant isotope. Because the probe nuclei "see" the phonon excitation spectrum, researchers can extract the partial vibrational frequency distribution, which is a function often referred to as the partial phonon density of states (PDOS). NRIXS has been applied to diverse materials, including thin films and multilayers, nanoparticles, crystals with impurities, organic molecules, proteins, samples under high pressures, and geophysical samples. Most of these samples are compounds, and while the obtained PDOS gives only part of the lattice dynamics, the low-energy portion of the PDOS provides the Debye sound velocity of the whole sample.

In studies at the APS, researchers showed that, because of universal features of acoustic modes of harmonic solids, the low-energy portion of the PDOS is related to the Debye sound velocity. Specifically, they used NRIXS to measure the PDOS of a variety of samples. By averaging the PDOS of the samples, which were obtained from measured data from the PDOS in the region from 0 to 5 meV, researchers extracted numerical values for the velocities of sound (Fig.1). The results from NRIXS measurements of iron and palladium were within the range of sound velocities that were obtained by other means. But for hematite, the mean sound velocity, or vD, obtained by using NRXIS was lower than that obtained from measured elastic constants. One explanation for this difference may be that at the high frequencies used to derive sound velocity, phonon dispersion may be nonlinear, which could result in a lower vD. Improving energy resolution could make smaller phonon energies accessible, which would potentially provide a better measure of sound velocity. The technique is currently applicable to specific isotopes of Kr, Fe, Eu, Sn, and Dy, which can be present as an essential ingredient or doped as an impurity.

NRXIS is now poised to open new doors of scientific inquiry. Given its effectiveness—even for very low concentrations of nuclear resonant isotope — additional refinements are certain to lead to key developments in physical science. Not only does probing nuclei provide information about the host lattice, but strategically placing resonant nuclei in artificial structures may provide insight into local atomic motion, which at low energies is thought to influence the electronic noise in nanostructure devices. The NRIXS method is also promising in that it can complement other methods—or even replace established methods that are becoming too difficult to use. ❍

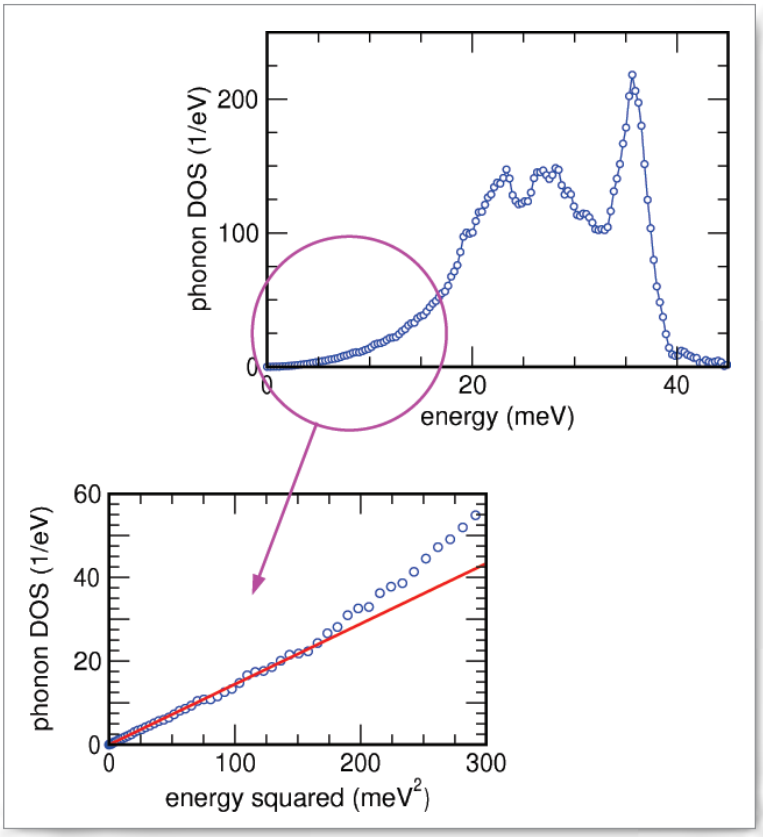

Fig. 1. Sound velocity can be derived from the low-energy part of the phonon densities of states. The quadratic behavior of the DOS in this region is usually a good approximation, which is demonstrated in the replot in the above figure.

Reference

[1] See below.

See: M.Y. Hu[1], W. Sturhahn[2], T.S. Toellner[2], P.D. Mannheim[3], D.E. Brown[4], J. Zhao[2], and E.E. Alp[2], "Measuring velocity of sound with nuclear resonant inelastic x-ray scattering," Phys. Rev. B **67**, 094304-1 to 094304-5 (2003).

Author affiliations: [1]HP-CAT and Carnegie Institution of Washington, [2]Argonne National Laboratory, [3]University of Connecticut, [4]Northern Illinois University

Use of the Advanced Photon Source was supported by the U.S. Department of Energy, Office of Science, Basic Energy Sciences, under Contract No. W-31-109-Eng-38.

Mapping Impurities in Synthetic Diamond

With the advent of new growth methods, synthetic diamond has increasingly become an important technological material. As a result, a better understanding of the influence of impurities on the physical and chemical properties of diamond is essential. Impurities in natural diamond are of equal interest, because they can provide a record of gem growth and past environmental conditions. Among known impurities, metal atoms such as iron, nickel, and cobalt are the most common in synthetic diamonds. Over the past few decades, several experimental techniques have been brought to bear on the problem; however, these previous studies left unsettled questions owing to the limited capabilities of the experimental techniques used. Recently, a team of researchers from the Carnegie Institution of Washington, The University of Chicago, and Miami University used synchrotron x-ray fluorescence and absorption spectroscopy to study the behavior of iron and nickel impurities in synthetic diamond.

Commercial methods of diamond synthesis usually involve a high-pressure high-temperature (HPHT) process that employs iron and nickel as catalysts; hence their appearance as impurities in the finished material. Study of these impurities has been hampered by difficulties in preparing suitable samples. Because of the extreme hardness of diamond, creating a standard thin section of this material is problematic, and the necessary machining often causes high heat, which may alter the nature and distribution of metal impurities. In current work, GSECARS and HP-CAT researchers used the x-ray microprobe facility at GSECARS sector 13 at the APS to analyze impurities in as-grown synthetic HPHT diamond without the complications of post-synthesis processing.

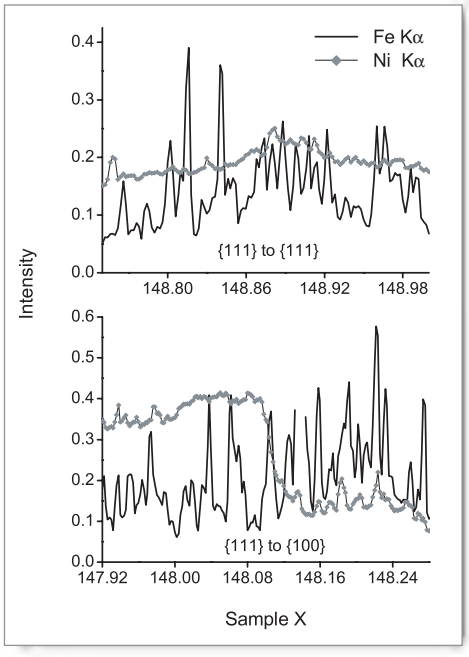

Fig. 1. XRF intensity of iron and nickel as a function of sample position. Top: Line scan with incident x-ray beam moved from a {111} sector to an adjacent {111} sector. Bottom: Line scan with beam moved across the boundary between a {111} sector and the adjacent {100} sector.

Fig. 2. Transmission and fluorescence tomograms. From the transmission data, the density of diamond (top) displays the orientation of the analyzed horizontal plane with four {111} faces and two {100} faces. Reconstructed iron and nickel fluorescence virtual slices are shown as labeled.

Diamond samples were selected from a commercial grit product of the General Electric Company. The grit was synthesized with iron and nickel catalysts under HPHT conditions, generally in the range from 1200˚C to 2000˚C and 5 to 7 GPa. Three crystals, each approximately 700 µm in diameter, were chosen for the study. X-ray fluorescence (XRF), x-ray tomography, and x-ray absorption near-edge structure (XANES) were used to analyze the diamond samples at 13-ID-C. In the XRF work, an incident beam energy of 8.6 keV was used, and Ka fluorescence lines from iron and nickel were collected with a multielement, energy-dispersive germanium detector. XANES scans were taken from 7040 to 7260 eV across the Fe K edge.

The XRF analysis showed a dramatic difference in the behavior of the iron and nickel impurities. The intensity pattern of the nickel Ka line indicates a dispersed distribution of nickel varying by sector throughout the sample, whereas the iron fluorescence shows sharp peaks as a function of position, consistent with aggregates or clusters of iron with no sector zoning (Fig. 1). The sector zoning of nickel is also clearly observed in the virtual slices reconstructed from the set of angular dependent line-scans (Fig. 2). In addition, it is possible from the XANES data to measure the oxidation state of the iron impurities in the diamond samples. Comparison with known iron compounds indicates that the iron in diamond has a valence of +2 in an octahedral coordination with FeO bonding.

Detailed atomic impurity studies such as these are made possible by the high brightness of the third-generation synchrotrons such as the APS, and by the energy and spatial resolutions of the spectroscopic instruments available at the GSECARS sector 13 at the APS. This advanced capability should be of special interest for future studies in a wide range of research fields, including geoscience, environmental science, gemology, materials science, and physical chemistry. ❍

See: Y. Meng[1], M. Newville[2], S. Sutton[2], J. Rakovan[3], and H.-k. Mao[1], "Fe and Ni impurities in synthetic diamond," Am. Mineral. **88**, 1555-1559 (2003).

Author affiliations: [1]HP-CAT and Carnegie Institution of Washington, [2]GSECARS, The University of Chicago [3]The University of Chicago

This work was supported byNSF, DOE, EAR-9814691, and the W.M. Keck Foundation. GSECARS is funded by the NSF (Earth Sciences Division) and by DOE (Geosciences Program). Use of the Advanced Photon Source was supported by the U.S. Department of Energy, Office of Science, Office of Basic Energy Sciences, under Contract No. W-31-109-Eng-38.

Phase Diagram of Tantalum at High Pressure

In materials science and geophysics, it is essential to understand how elements undergo the transition between solid and liquid phases at high pressures. For example, an accurate picture of materials performance under extreme conditions and detailed models of planetary interiors both depend on this knowledge. The element tantalum is especially interesting in this regard because it has one of the highest melting points at ambient pressure of any metal. At ambient temperatures, tantalum remains in a stable body-centered cubic (bcc) structure up to extremely high pressures. Tantalum therefore is a valuable test case for studying how materials melt. Despite a large number of experimental and theoretical efforts, however, agreement on the melting behavior of tantalum at high pressure has been elusive. Recently, researchers from the Carnegie Institution of Washington and the University of Valencia (Spain) have used the facilities of HP-CAT (sector 16) at the APS to obtain the phase diagram of tantalum at high pressure and temperature.

A number of previous experimental studies were carried out with the use of shock-wave measurements and laser-heated diamond anvil cells (DACs). Likewise, theoretical studies attempted to predict the melting curve of various materials. Unfortunately, substantial variation exists in the results of these earlier efforts, owing to the use of different experimental and theoretical techniques. Using the APS synchrotron and a laser-heated DAC, the researchers in the present study have gathered comprehensive melting data on tantalum over a wide range of pressures.

Commercial tantalum powder was used in the experiments. It was loaded into the pressure cell with sodium chloride as the pressure-transmitting and thermally insulating medium. Fluorescence from a ruby chip and the shifts in the sodium chloride x-ray diffraction lines were used to determine the cell pressure. The samples were heated on both sides of the cell by means of two infrared Nd:YLF lasers, and the temperature distribution was measured by spectroscopic imaging of the thermal radiation from the hot cell. X-ray diffraction measurements of the samples in this cell were made at the HP-CAT beamline 16-ID-B. The beam was filtered with a double-crystal monochromator to a wavelength of 0.3738 Å having an energy resolution of 10^{-3}. Diffraction patterns were recorded with a charge coupled device array and corrected for distortion.

The research team successfully performed experiments at pressures up to 52 GPa and temperatures as high as 3800K. Pressure-temperature data were obtained by compressing the samples to a desired pressure and then heating them. The melting point was ascertained by the disappearance of the tantalum diffraction lines (Fig. 1) and the appearance of a diffuse broad scattering for nine different pressure values. Thermally induced pressure changes were estimated by the shifts in the NaCl diffraction lines. The P-T measurements (Fig. 2) agree well with earlier DAC experiments but differ with previous observations performed with a piston-cylinder pressure chamber. Moreover, the present results do not follow an empirical Lindemann relation but rather can be understood with the help

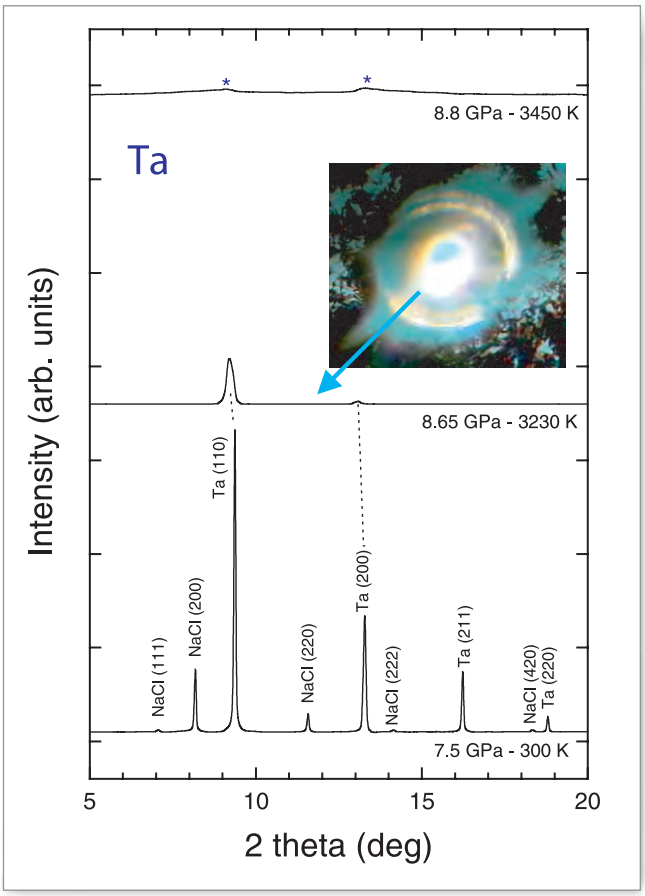

Fig. 1. X-ray diffraction patterns (λ = 0.3738 Å) in a tantalum sample at different temperatures around 8 GPa. P and T are indicated in the figure, and the diffraction peaks are identified. Stars depict the broad scattering characteristic of the onset of melting. The inset shows a hot tantalum sample from which the 8.65 GPa, 3230K pattern was measured.

of a vacancy generation model of melting. From these measurements, a pressure-volume-temperature (P-V-T) equation of state for tantalum was obtained.

These results indicate the importance of microstructural analysis and careful temperature mapping in obtaining accurate P-T data at high temperatures and pressures. In part, this type of measurement is made possible by the high brightness and precise energy resolution available at the APS. Currently, research in this area concentrates on extending the studies on Ta and other bcc transition metals (e.g., Mo and W) to the megabar (100 GPa) pressure range searching for the existence of a predicted unknown high P-T phase. ❍

See: D. Errandonea[1,2], M. Somayazulu[1], D. Häusermann[1], and H. K. Mao[3], "Melting of tantalum at high pressure determined by angle dispersive x-ray diffraction in a double-sided laser-heated diamond-anvil cell," J. Phys. Condens. Matter **15**(45), 7635-7649 (2003).

Author affiliations: [1]HP-CAT/Carnegie Institution of Washington, [2]Universitat de València, [3]Carnegie Institution of Washington

This work was supported by the NSF, the DOE, and the W M Keck Foundation. D.E. acknowledges the financial support from the MCYT of Spain and the Universitat of València through the 'Ramón y Cajal' program for young scientists. Use of the Advanced Photon Source was supported by the U.S. Department of Energy, Office of Science, Office of Basic Energy Sciences, under Contract No. W-31-109-Eng-38.

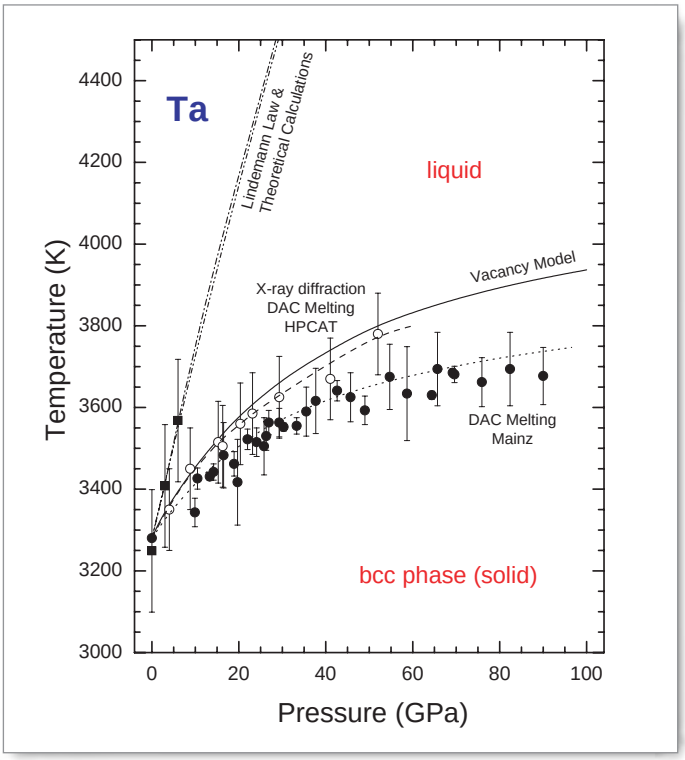

Fig. 2. P-T phase diagram of tantalum. Present synchrotron data (open circles) and previous data (solid circles and squares) are shown together with theoretical estimations. The dashed and dotted lines are fits to the experimental data. The solid line is the melting calculated by Errandonea et al. by assuming a vacancy-mediated melting model.

GETTING THE LEAD OUT: SORPTION VS. BIOMINERALIZATION IN *B. CEPACIA* BIOFILMS

Lead is one of the most common toxic heavy metals found in contaminated soil sites, but it can be fixed in place through sorption to metal oxide surfaces, as well as through biomineralization because of the microbial community. Using x-ray spectroscopy methods, researchers from Stanford University, The University of Chicago; Pacific Northwest National Laboratory, and the Stanford Synchrotron Radiation Laboratory studied biofilms of *Burkholderia cepacia*, a ubiquitous bacteria, to examine its mode of Pb (II) uptake — important information because the chemical form of Pb in the soil affects its solubility, bioavailability, and toxicity. For example, Pb that has been biomineralized will be more firmly fixed in place than that which is solely sorbed, since environmental changes, such as changes in pH, can lead sorbed metals to be re-released into the soil. These studies showed that biomineralization accounts for 90% of the total Pb immobilization below pH 4.5, but only 45-60% at near-neutral PH.

Several kinds of samples were studied, both suspensions and biofilms. The *B. cepacia* suspensions were introduced to Pb solutions at various pH levels, while a single-celled layer of *B. cepacia* on a substrate of α-Al_2O_3 (commonly known as sapphire) was grown for the biofilms. In addition to being a well-understood material, aluminum oxides are often found in contaminated soil and are highly reactive with heavy metals, making them an integral component of remediation. Researchers then either immersed the biofilm directly into a solution containing Pb or submitted the film to five minutes of x-rays to stop metabolic activity, and then introduced the Pb solution. The biofilms underwent x-ray fluorescence mapping at the GSE-CARS beamline 13-ID at the APS. X-ray absorption fine structure experiments were done on both the biofilms and the suspensions at the Stanford Synchrotron Radiation Laboratory.

Mapping of the biofilms that were x-ray treated showed a fairly homogeneous distribution of Pb uptake across the sample. The biofilms that had been allowed to retain metabolic activity, however, showed variations of up to an order of magnitude, with larger amounts of Pb collecting at various "hotspots" within the microcolonies (Fig. 1.).

Turning to the suspensions in order to better understand what was happening with the biofilms, x-ray absorption fine

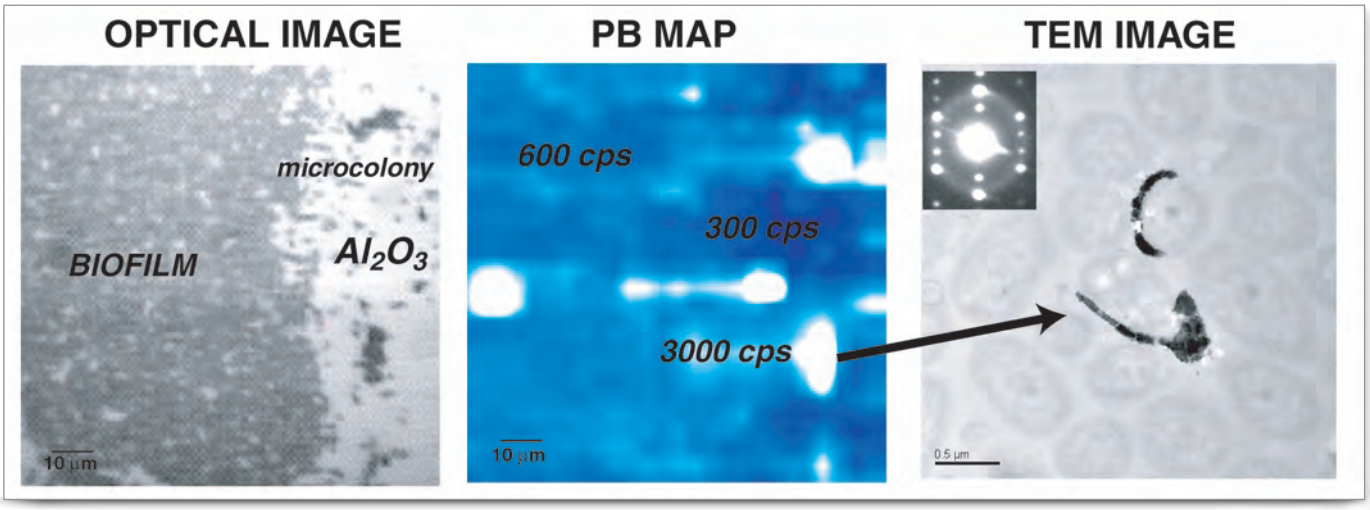

Fig. 1. Optical image and coupled Pb L_{III} x-ray fluorescence map (5 x 5-μm spot size) for a *B. cepacia* biofilm on α-Al_2O_3 incubated with 60-μm $Pb(NO_3)_2$ at pH 6. The false color scale from blue (300-cps Pb FY) to white (3000-cps Pb FY) shows the formation of Pb "hot-spots" in the biofilms. These hot-spots have been identified as Pb-phosphates (*e.g.*, pyromorphite) forming on the bacterial cell surfaces from TEM images (right) and GI-EXAFS spectra (data not shown).

structure (EXAFS) data showed that levels of adsorption and precipitation depend on pH. At low pH values, *e.g.*, pH 4, the EXAFS spectra matched those of the lead phosphate mineral pyromorphite ($Pb_5(PO_4)_3(OH)$), suggesting that the uptake is due to the formation of a precipitated form of Pb that is, at the very least, similar to pyromorphite. Subsequent transmission electron microscopy data showed that there was, indeed, pyromorphite present in the outer membrane of the *B. cepacia*. At low pH, the formation of pyromorphite accounts for 90% of the total Pb uptake. At higher pH, *e.g.,* pH 6, however, there is a mixture of sorbed Pb (42%) and biomineralized Pb (58%).

It is therefore hypothesized that similar adsorption and precipitation rates occurred within the biofilms. The films in which metabolic activity had ceased led solely to sorbed Pb, which was distributed evenly across the plate. In the remaining films, however, the "hotspots" were areas in which cells were substantially more biomineralized. These cells actively produce pyromorphite, incorporating the soluble form of Pb(II) as they do so, thus fixing it into place.

In the field, various characteristics affect the immobilization of toxic heavy metals. Different pHs, for one, affect sorption rates for different metals, and environmental chemists would like to predict which materials will provide the major repository for Pb at any given pH. This study shows that Pb binds to bacterial surfaces to a much greater extent at higher pH — and that such binding is all the more potent since it is through biomineralization, in addition to sorption. ❍

See: A.S. Templeton[1], T.P. Trainor[1,2], A.M. Spormann[1], M. Newville[2], S.R. Sutton[2], A. Dohnalkova[3], Y. Gorby[3], and G.E. Brown, Jr.[1,4], "Sorption versus Biomineralization of Pb(II) within *Burkholderia cepacia* Biofilms," Environ. Sci. Technol. **37**, 300-307 (2003).

Author affiliations: [1]Stanford University, [2]GSECARS, The University of Chicago [3]Pacific Northwest National Laboratory, [4]Stanford Synchrotron Radiation Laboratory

This work was supported by National Science Foundation (NSF) grants NSF-EAR-9905755 and NSF-CHE-0089215 and by the Eugene Holman Stanford Graduate Fellowship (A.S.T.). SSRL and the W.R. Wiley Environmental Molecular Sciences Laboratory (PNNL) are funded by the U.S. Department of Energy (Offices of Basic Energy Sciences and Biological and Environmental Research). SSRL is also funded by the National Institutes of Health. GSECARS is funded by the NSF (Earth Sciences Division) and by DOE (Geosciences Program). Use of the Advanced Photon Source was supported by the U.S. Department of Energy, Office of Science, Office of Basic Energy Sciences, under Contract No. W-31-109-Eng-38.

Novel X-ray Techniques & Instrumentation

Pushing the Limits of Coherent X-ray Diffraction: Imaging Single Submicrometer Silver Nanocubes

X-ray crystallography has been proven to be an extremely efficient investigation method for solving the structure of matter at the atomic scale. Although several methods have been employed to circumvent the intrinsic phase problem, other limitations do exist for classical x-ray crystallographic methods. In particular, disordered materials, single nanostructures, or noncrystalline and/or nonrepetitive biological structures (e.g., some important viruses or proteins) cannot be accessed by this approach.

A combination of coherent x-ray diffraction with a so-called oversampling phasing method can overcome these limitations. In a first demonstration experiment, that method was used to invert the soft x-ray forward-scattering pattern measured from a fabricated object. More recently, the reconstruction of two-dimensional and three-dimensional (3-D) crystalline and noncrystalline (!) structures has been reported. In particular, the latest results, where the complete 3-D phase and shape information of a micrometer-sized gold crystal could be retrieved, impressively demonstrate the high potential of this nondestructive method.

The experiment described here focused on applying that technique to even smaller nanocrystals in order to investigate the feasibility of pushing the limits of imaging by using coherent x-ray diffraction into the nanometer range.

Chemically synthesized, crystalline silver nanocubes were used as demonstration samples, with a typical size of 90–150 nm. The coherent x-ray diffraction experiments were carried out at the UNI-CAT 34-ID beamline by using monochromatic x-rays with an energy of 8.5 keV.

In order to have both sufficient flux and the opportunity to select single nanocrystals, a Kirkpatrick-Baez (K-B) mirror system was used to focus the x-ray beam to typically 1.0 x 1.5 μm^2 at the position of the sample. The diffraction data were recorded using a charge-coupled-device detector placed at a position corresponding to the 111 Bragg reflection of the silver crystal lattice.

The following major conclusions could be drawn from the experimental results. First and most important, the high-resolution reciprocal diffraction patterns clearly demonstrate the feasibility of carrying out such measurements on single nanocrystals at sizes in the 100-nm range (Fig. 1). Depending on the orientation of the individual nanocrystals, the measured diffraction patterns showed nice three- and four-fold symmetry and up to, typically, 5-10 high-contrast interference fringes in directions corresponding to the facets of the cubic structure. Furthermore, no negative effects on the transverse coherence were found by using the experimentally crucially important K-B focusing optics. Finally, the obtained results agree well with some model calculations based on a simple Fourier transform of a two-dimensionally projected single silver nanocube (Fig. 2).

Encouraged by this successful first demonstration experiment of coherent x-ray diffraction on submicrometer single crystalline nano-objects, researchers are currently working on

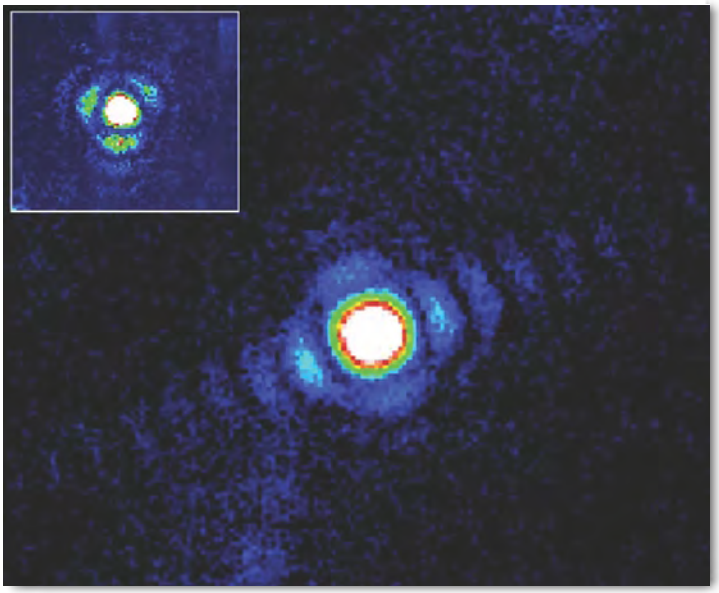

Fig. 1. Charge coupled device image of the measured single crystal coherent diffraction pattern around the 111 Bragg peak of a silver nanocube (8.5 keV x-rays). The two diffraction images are taken for slightly different Q-values and correspond to the Fourier transform of different projections of the cubic crystal.

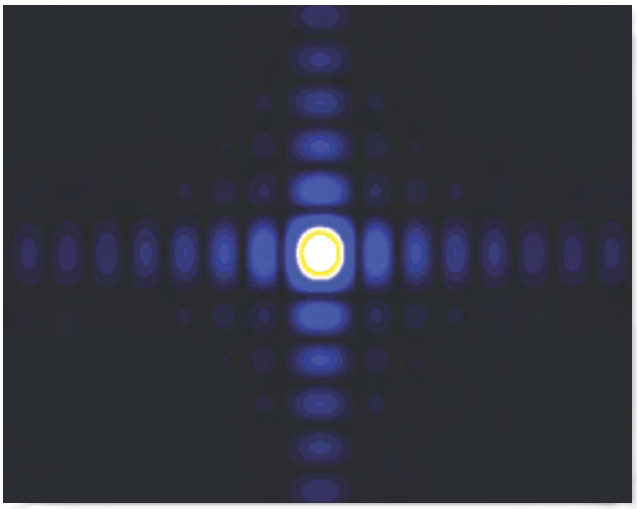

Fig. 2. Calculated coherent diffraction pattern of a single nanocube assuming the simplest possible diffraction geometry (detector plane perpendicular to the surface normal of one the cubes facets).

the direct reconstruction of full 3-D diffraction data using the oversampling phasing method. ❍

See: I. Robinson[1], F. Pfeiffer[1,2], I. Vartanyants[1], Y. Sun[3], Y. Xia[3], "Enhancement of coherent X-ray diffraction from nanocrystals by introduction of X-ray optics," Opt. Express **11**(19), 2329-2334 (September 2003).

Author affiliations: [1]University of Illinois at Urbana-Champaign, [2]Paul Scherrer Institut, [3]University of Washington

Work supported by the NSF under grant DMR 03-08660. The 34-ID-C Coherent Xray Diffraction facility was built with funds from NSF DMR 97-24294. The UNI-CAT facility is supported by the University of Illinois Materials Research Laboratory, funded by U.S. DOE under DEFG02-91ER45439, Oak Ridge National Laboratory,NIST, and UOP Research & Development. Use of the Advanced Photon Source was supported by the U.S. Department of Energy, Office of Science, Office of Basic Energy Sciences, under Contract No. W-31-109-Eng-38.

Coherent X-ray Diffraction Imaging Details the 3-D Microstructure of Au Nanocrystals

Coherent x-ray diffraction (CXD) is an emerging technique that has considerable potential for revealing many structural and dynamic characteristics of nanocrystalline materials. The method is enabled by high-brilliance third-generation x-ray sources because the technique depends entirely on the coherence volume of the x-ray beam being large enough to enclose the crystal under study; the coherence volume is directly proportional to source brilliance.

The penetrating power of a hard x-ray beam allows scientists to look below the surface of materials, while the ability to distinguish the diffraction patterns from neighboring nanocrystalline grains is retained, making it possible to image the full volume of a grain with negligible absorption effects. In principle, even three-dimensional (3-D) real-space strain maps of the interiors of materials should be feasible. This prospect was advanced by researchers from the University of Illinois at Champaign-Urbana (UIUC), who used CXD to obtain 3-D images of the interiors of gold (Au) nanocrystals that were formed by high-temperature coalescence from an evaporated polycrystalline thin film (Fig. 1).

In an x-ray crystallographic experiment, x-rays interact with electrons in a crystal to produce a diffraction pattern that is the Fourier transform of the desired electron density distribution. A Fourier transform can be reversed to reconstruct the 3-D distribution of the electrons (and, hence, the atoms) in the crystal, but to do this, one needs not only the amplitudes of the diffracted waves, which are obtained from the intensity distribution of the diffraction pattern, but also their relative phase shifts, which cannot be measured directly. Generally one gets phase data from supplementary information of some sort. The UIUC researchers obtained the needed information by oversampling the diffraction patterns, which is possible with small crystals because they generate continuous patterns.

The CXD experiment was conducted at the UNICAT 33-ID undulator beamline at the APS, where the transverse coherence length was greater than 5 µm and the longitudinal coherence length was determined to be

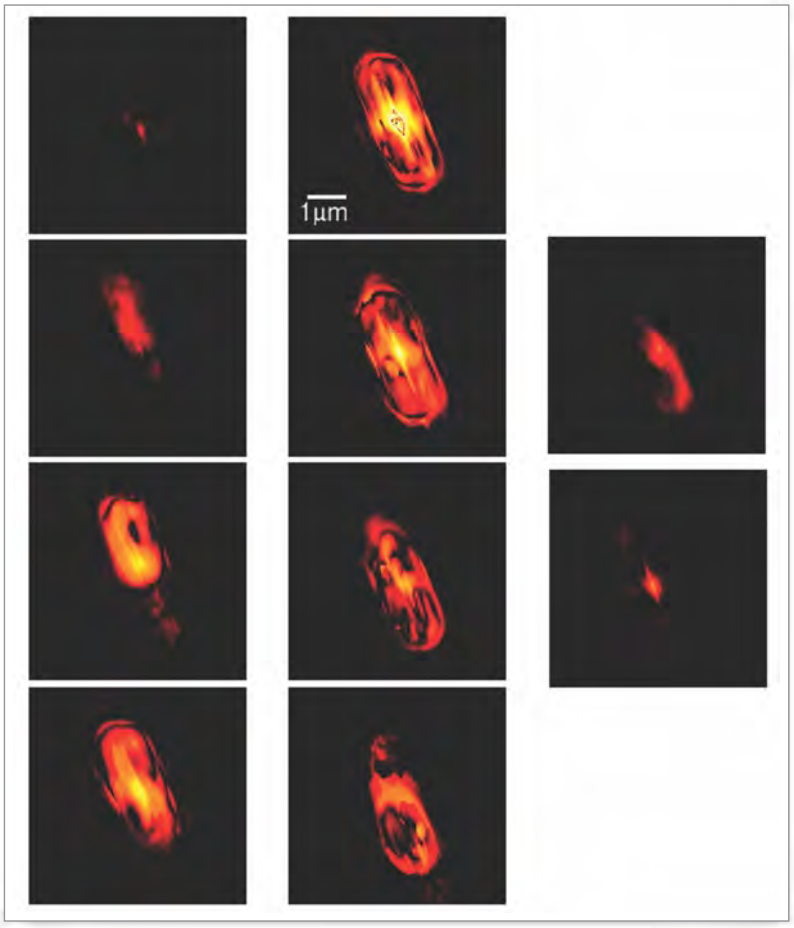

Fig. 1. Slices through a 3-D reconstruction of the internal density for a micron-sized gold nanocrystal, measured with the new CXD method. The striping effects, which follow the crystallographic directions, indicate the presence of internal microstructure in the crystal.

6 µm by a Si(333) monochromator at 9.5 keV. Two-dimensional diffraction patterns were collected with a direct-reading charge-coupled device. To construct full 3-D patterns, each sample was rotated through the Bragg condition in steps of 0.002°, thus acquiring a sequence of nearly parallel 2-D slices, which were then stacked to obtain the sampled 3-D patterns.

It proved possible to draw some conclusions about the size and shape of the Au grains directly from the CXD patterns before they were phased. The flares in reciprocal space were seen to correspond to facets of the crystal, while the modulation of these flares indicated the spacing of parallel facets. Phasing of the oversampled diffraction patterns was accomplished through the use of an iterative method, utilizing known information to find a set of phases consistent with the measured data. This cycle was repeated until the search converged to a solution.

The 3-D images of the interiors of the Au nanocrystals showed 50-nm-wide bands of contrast with {111} orientation that probably arose from internal twinning by dynamic recrystallization during their formation at high temperature. In the method used by the researchers, entire patterns were measured directly. Because Bragg diffraction was involved, all artifacts due to air or slit scattering and the presence of other grains were avoided, and a strong sensitivity to strain was manifested. ❍

See: G.J. Williams, M.A. Pfeifer, I.A. Vartanyants, and I.K. Robinson, "Three-Dimensional Imaging of Microstructure in Au Nanocrystals," Phys. Rev. Lett. **90**(17), 175501-1 to 175501-4 (2 May 2003).

Author affiliations: University of Illinois at Urbana-Champaign

This research was supported by the NSF under Grant No. DMR98-76610. The UNICAT facility at the APS is supported by the University of Illinois, Materials Research Laboratory (DOE Contract No. DEFG02-91ER45439, the State of Illinois-IBHE-HECA, and the NSF), the ORNL, NIST, and UOP LLC. SEM work was carried out in the Center for Microanalysis of Materials, University of Illinois. Use of the Advanced Photon Source was supported by the U.S. Department of Energy, Office of Science, Office of Basic Energy Sciences, under Contract No. W-31-109-Eng-38.

A High-repetition-rate Laser System for Time-resolved X-ray Absorption Fine Structure

X-ray absorption fine structure (XAFS) is a valuable technique for probing materials dynamics, because (in contrast to x-ray diffraction), with XAFS, one can determine the behavior of a sample directly without dependence on long-range order. The dynamics of heating and phase changes induced by laser excitation may, therefore, be directly monitored by XAFS regardless of a material's state. In addition, the near-edge portion of the XAFS (the XANES) contains electronic information about the material, and it is, for example, sensitive to the shielding between the core hole and photoelectron, which can be modified by the laser pulse in a semiconductor, since the excited carrier density can be initially similar to that of a metal. As a result, XANES has the potential for use in studies of dynamics of this type of phenomenon, regardless of material state.

Researchers from the University of Washington and the Pacific Northwest National Laboratory, using the PNC/XOR facility at sector 20, have developed a high-repetition-rate laser system for time-resolved pump-probe XAFS studies on sub-nanosecond to microsecond time scales. A schematic diagram of the timing electronics and laser system is shown in Fig. 1. The 800-nm Ti:sapphire pulsed-laser system repeats at the APS P0 frequency of 272 kHz with ~4µJ/pulse, allowing researchers using the PNC/XOR apparatus to collect data from a given bunch at each appearance. This provides an increase in data-collection efficiency of more than an order of magnitude when compared to typical pulsed-laser systems and data collection times similar to those of typical non-time-resolved

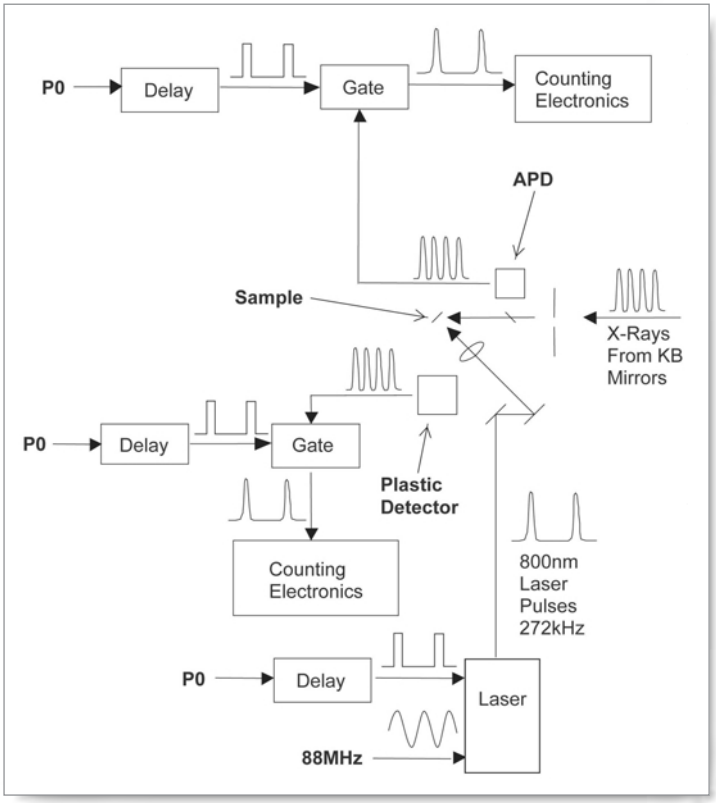

Fig. 1. Schematic of system timing electronics and laser.

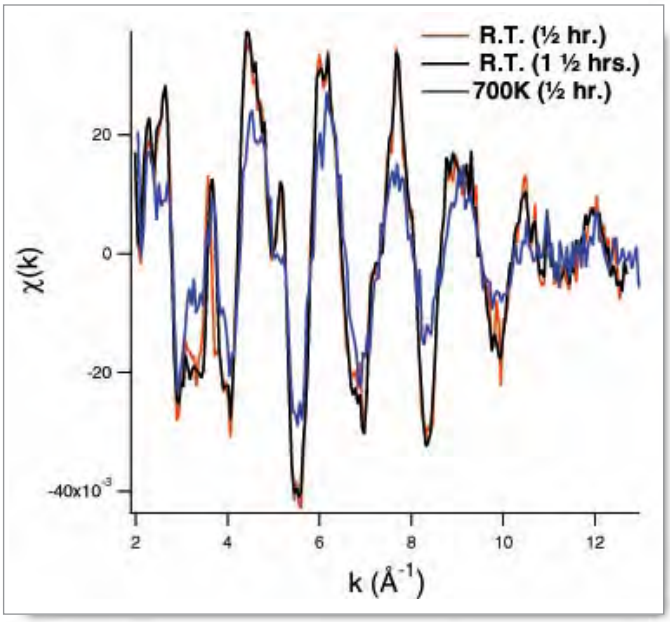

Fig. 2. Single EXAFS spectrum from a sample at room temperature, with the average of three similar scans, and data collected from the same sample while laser-heated to ~700K.

experiments. Diffraction measurements can also be made concurrently with the same time resolution.

The PNC/XOR laser system is used in conjunction with Kirkpatrick-Baez x-ray focusing mirrors to enable time-resolved micro-XAFS on a 10-µm scale. Focusing both the x-rays and the laser also provides the ability to perform experiments not inherently microscopic in nature but requiring extremely large fluences. The current timing resolution is limited by the finite electron-bunch width to ~90 ps. To date, the PNC/XOR team has utilized the laser system to investigate the time-resolved extended x-ray absorption fine structure (EXAFS) of laser-heated germanium, but it could be utilized in a wide range of time-resolved pump-probe experiments that are currently impractical due to the long data collection time required by lower-repetition-rate systems.

Experiments have been performed using a 10-µm x-ray beam to obtain micro-EXAFS from a 200-nm-thick Ge film that was initially amorphous and crystallized by heating with the laser beam. Micro-EXAFS was obtained from the heated film after crystallization. Figure 2 shows a single EXAFS spectrum from the sample at room temperature, along with the average of three similar scans, and data collected from the same sample as it was heated by the laser to ~700K. The temperature of the heated film was measured by determining the vibration amplitude of the Ge-Ge bond revealed in the EXAFS. The vibrations cause the amplitude of the EXAFS oscillations to decrease with increasing temperature, as seen for the 700K plot. A comparison of the single room-temperature spectrum with the averaged spectra illustrates the excellent noise level and reproducibility for a data collection time of ~1/2 hour, from a sample with very small absorption (~2%). The spectra in the figure were collected in pulse-counting mode, which required a reduction of the potentially available signal to avoid saturation caused by pulse pile-up. The addition of radio-frequency-derived lock-in detection of the gated signal should allow use of the entire available flux, an increase over the current configuration by a factor of at least five. Use of an avalanche photodiode array for the fluorescence signal would provide an alternative approach for increasing data quality, by keeping the signal on each element low enough to remain within the pulse-counting regime, with a much larger total collected signal.

Figure 3 shows preliminary results for the time dependence of the EXAFS from the laser-heated film for times within a few ns of the laser excitation. Future plans call for an increase of the laser fluence to heat the Ge film to the melting point and a study of the dynamics of the transition from the four-fold coordinated solid to the six-fold coordinated liquid by directly monitoring the EXAFS, thus using the ability of this probe to look at local atomic structure independent of the material state. ❍

See: E.A. Stern, D.L. Brewe, K.M. Beck, S.M. Heald, Y. Feng, "Sub-nanosecond time-resolved XAFS of laser excited thin Ge films', invited paper at XAFS 12, June 2003.

PNC/XOR facilities and research at these facilities is supported by the U.S. DOE Office of Science grant no. DE-FG03-97ER45628. Additional support was provided by Battelle-Pacific Northwest National Laboratory's (PNNL) Laboratory Directed Research Directorate.

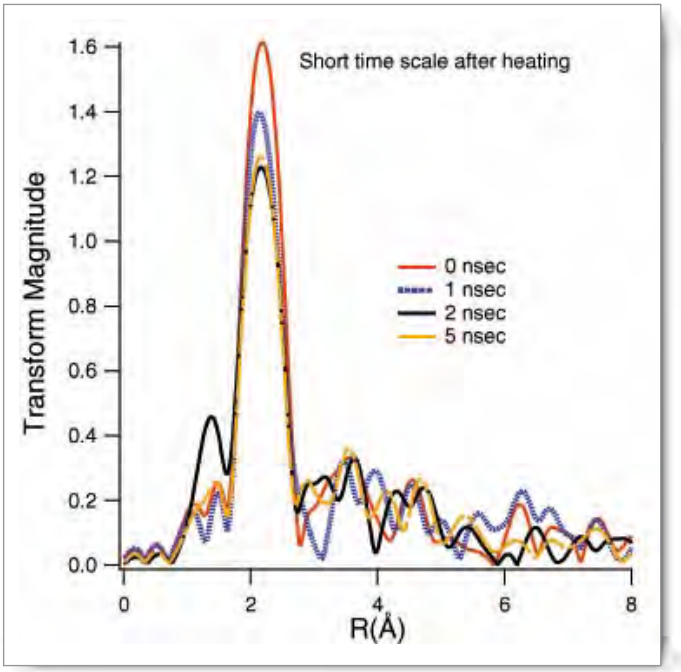

Fig. 3. Preliminary results for the time dependence of the EXAFS from the laser-heated film for times within a few ns of the laser excitation.

Upgrade of the Inelastic Spectrometer at 3-ID-C

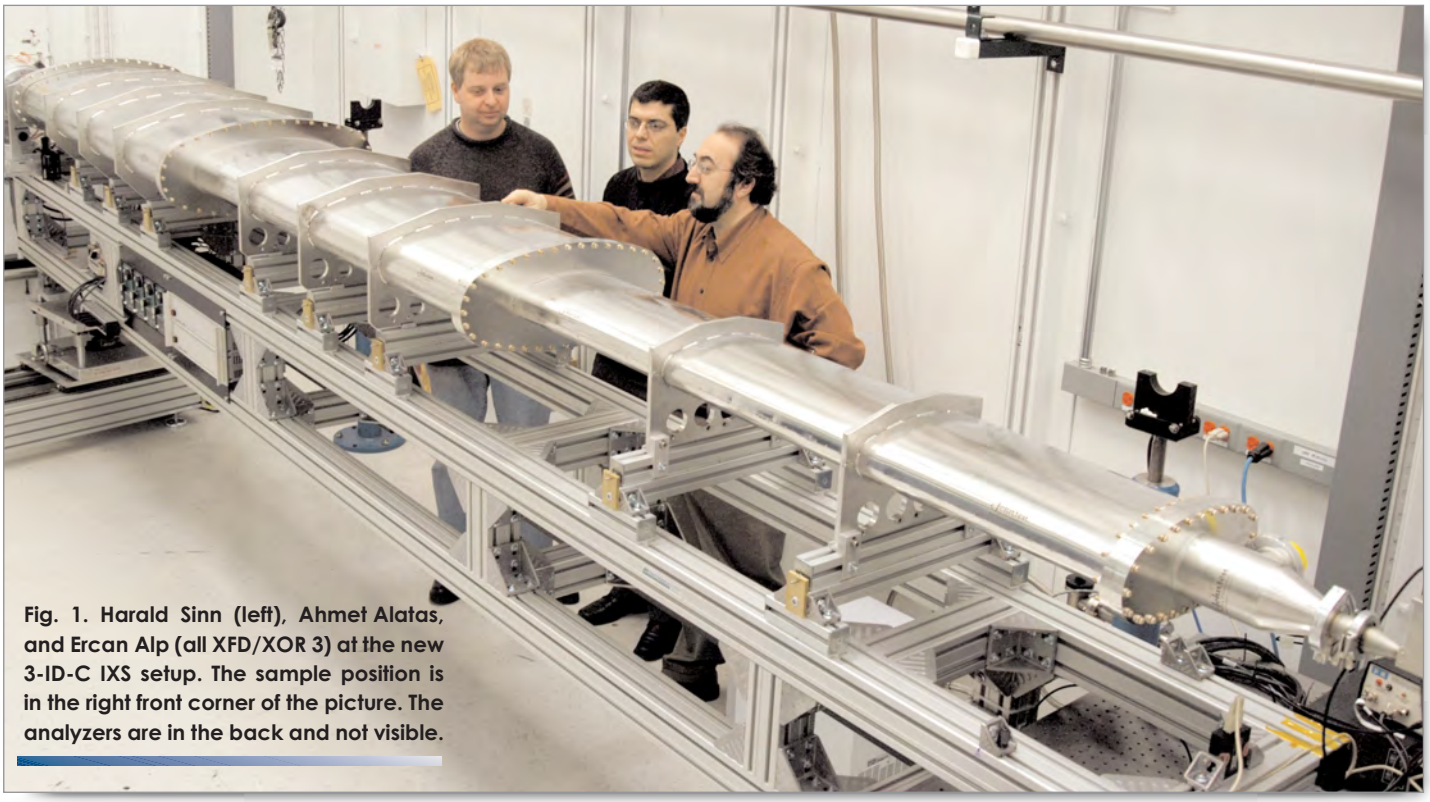

Fig. 1. Harald Sinn (left), Ahmet Alatas, and Ercan Alp (all XFD/XOR 3) at the new 3-ID-C IXS setup. The sample position is in the right front corner of the picture. The analyzers are in the back and not visible.

During the last decade, inelastic x-ray scattering (IXS) with an energy resolution of a few meV became a very successful spectroscopic method on third-generation synchrotron sources. At x-ray energies of about 20 keV, monochromatization of x-rays can be achieved either by multiple bounce inline monochromators or—in the case of the analyzer—by high-order silicon reflections in backscattering geometry.

At the APS, an inelastic spectrometer with 2 meV resolution was built at XOR beamline 3-ID-C with, initially, one analyzer. However, with count rates often less than 0.1 Hz at the phonon position, many experiments would benefit from a multiple analyzer setup. Currently, the instrument is being upgraded to four analyzers, which will work simultaneously, enabling faster data collection for liquid and disordered samples.

Upgrade Details

The four analyzers are located 6 m from the sample. each analyzer has an active diameter of 100 mm, and there is a lateral distance of 180 mm between two analyzers.

The four analyzers, and a 5.4-m-long vacuum chamber that connects to the backscattering detector, are on a common 2-theta arm, which can be moved in the horizontal plane (Fig. 1). The maximum angle of the 2-theta-arm is 17.6° and is limited only by the dimensions of the station.

The four analyzers were built as adjustable, two-dimensional bending devices (Fig. 2). Each analyzer is temperature controlled by Peltier elements stable to about 10 mK over nine days.

A four-element detector, developed in collaboration with AMPTEK, allows for collection of the radiation from the four analyzers individually. Each CdTe element is 3 mm × 3 mm and is cooled by a peltier cooler. The center-to-center distance between elements is 6 mm. The quantum efficiency of the CdTe elements is close to 100%, while the noise rate is about 0.001 Hz per channel. *(Contact E. Alp, eea@aps.anl.gov)* ❍

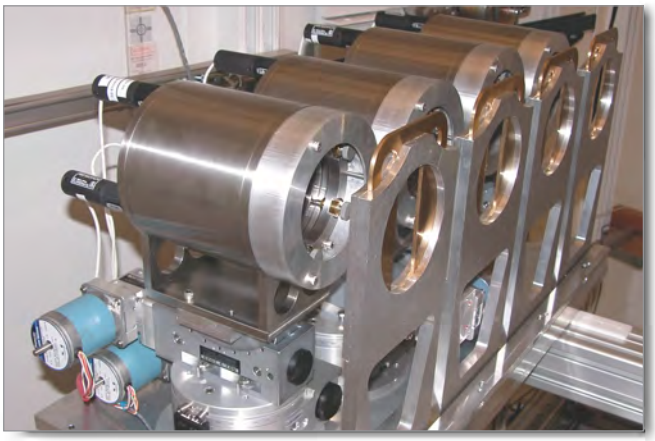

Fig. 2. Four-analyzer setup in the back of the 2-theta arm.

Time-dependent Spectroscopy

At BESSRC/XOR, the time-dependent spectroscopy program has been significantly broadened by the development of a time-dependent resonant inelastic scattering technique (RIXS) and a time-dependent x-ray magnetic circular dichroism (XMCD) technique. While time-dependent RIXS experiments probe the influence of electron-phonon coupling on the band structure and carrier dynamics in semiconductors, time-dependent XMCD experiments use element selectivity to probe the switching behavior of magnetic nanoparticles, clusters, and artificial nanostructures on a timescale from 100 ps to µsec. In 2003, basic instrumentation was installed, the proof of principle was demonstrated, and first theoretical modeling for both experiments was performed. The first presentations of results and concepts to the user community presented a strong and vital interest, resulting in various academic and industrial collaborations. The target of these collaborations is to improve the efficiency of light-emitting diodes and semiconductor-based lasers, as well as to increase the understanding of effects in order to allow an increase in the data density of magnetic storage media. (*Contact K. Attenkofer, klaus.attenkofer@anl.gov.*) ❍

Adaptive Optic, Bent-crystal Analyzer for X-ray Fluorescence Spectroscopy

An adaptive optic crystal bender being developed by BESSRC/XOR will improve the energy resolution of ultrafast laser-pump x-ray absorption/fluorescence probe spectroscopy. This device will resolve charge-carrier dynamics within the band structure of semiconductors, such as GaAs. The goal is to reach an x-ray energy resolution of better than 1 eV while collecting a large solid angle of fluorescent radiation under nonbackscattering conditions. So far, about 5 eV of resolution has been demonstrated, which is an improvement over the current state of the art (about 15 eV) for non-backscattering analyzers. The adaptive optic design permits the fine adjustment necessary for energy resolution and, at the same time, permits rapid configuration changes to select different fluorescent lines.

Although this optic was developed for the ultrafast spectroscopy project, the analyzer can benefit all x-ray absorption spectroscopy, particularly near-edge techniques for the measurement of chemical speciation. This applicability makes the analyzer an important instrumental development in its own right.

See: K. Attenkofer, B.W. Adams, and M.A. Beno, "Instrumentation for time-dependent, x-ray resonant Raman scattering," Proceedings of the SRI 2003 conference, to be published.

Author affiliation: Argonne National Laboratory ❍

A Fast CCD Camera for X-ray Photon Correlation Spectroscopy

Charge-coupled device (CCD) development and deployment at IMMY/XOR beamline 8-ID has proceeded on two fronts during the past year or so. A fast, direct-detection CCD camera based on a commercially available SMD (now Dalsa) CCD chip has been developed and deployed. The key feature of the fast CCD camera—the SMD1M60—as a detector for x-ray photon correlation spectroscopy (XPCS) experiments is that it permits the continuous acquisition of images, consisting of individual photon events, at full-frame data rates of up to 60 Hz and 1/16-frame data rates of up to 500 Hz. Thus, it is a simple matter to acquire data with a time resolution of as little as 2 ms, and data from a considerably larger solid angle can be collected if a time resolution of 17 ms is acceptable. In comparison to early-generation detectors, the much greater data rate possible with the SMD1M60 should permit a many-fold increase in the XPCS signal-to-noise ratio in cases where subsecond time steps are needed. In addition, the SMD1M60 is based on an inexpensive, commercially available CCD camera that is lightweight and conveniently transportable. Beyond XPCS, this detector may find application in time-resolved x-ray scattering experiments of all

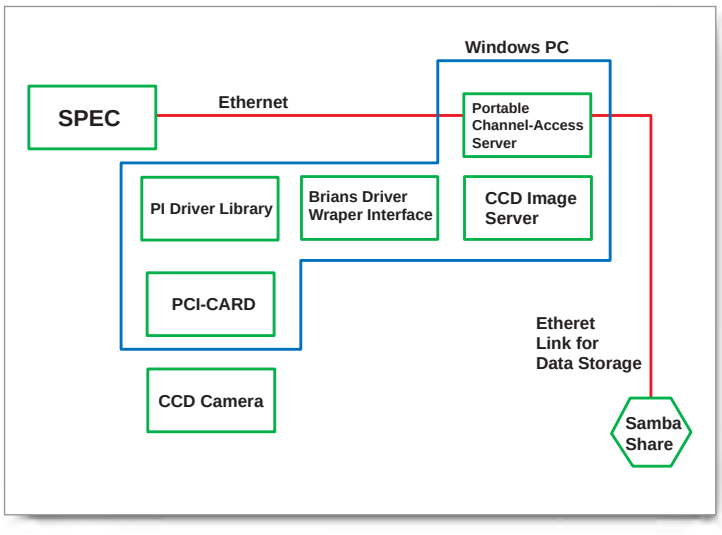

Fig. 1. CCD ImageServer-Yorick-spec control system schematic.

sorts. We have also found it capable of collecting superior small-angle x-ray scattering data. The original camera is available to general users in a collaborative mode. This camera is being duplicated so that it will be fully available to all users.

A Princeton Instruments deep-depletion, direct-detection CCD camera has been successfully integrated into the spec-based and Yorick-based beamline control and data acquisition and analysis system. A control schematic is shown in Fig. 1.

The controls and data acquisition of the CCD camera are implemented within a server-client model. The server software, CCD ImageServer, is a flexible means of acquiring CCD images within the Experimental Physics and Industrial Control System (EPICS) environment. The ImageServer application, running on a Windows-based PC, integrates all functionalities of the CCD camera into a simple API built on top of the EPICS Portable Channel Access Server. By wrapping the native camera-specific interface around a common device interface, the ImageServer application can transparently control cameras from many different manufacturers. On the client side, the beamline control software, Spec, fully controls the CCD camera through the EPICS PV interface and then integrates it into the full suite of 8-ID beamline controls for an experiment.

Data files generated by the CCD camera can be saved either directly to the server or to the (Linux-based) client through Samba-sharing of the directories. Spec provides a user interface to initialize and adjust the CCD parameters but not to display the live images. The EPICS extension EZCA library has been built into Yorick (an interpreted programming language for data analysis and image processing similar to IDL) so that Yorick displays real-time CCD images on the client. The Yorick user interface also provides image-processing utilities, such as camera contrast adjustments, image zooming, image dark subtraction, and image calculations. Since its deployment in late November 2003, the new camera control system has been used successfully by both IMMY/XOR members and general users. *(Contact S. Mochrie, simon.mochrie@yale.edu)* ❍

"Coherent" XPCS Analysis Code

A significant recent achievement has been the development and deployment of faster, more user-friendly x-ray photon correlation spectroscopy (XPCS) data reduction software, which is now installed at IMMY/XOR beamline 8-ID-I as a standard part of the XPCS package.

This GNU-public-licensed software package, called "coherent," includes several key features that greatly facilitate XPCS experiments and the 8-ID general-user program. Specifically, among many other features, it allows the graphic creation of masks for determining the data that should and should not be included in analysis; allows bad charge-coupled device frames to be dropped; automatically reads in relevant parameters based on the beamline configuration at the time of data acquisition (and allows them to be easily modified if necessary); and allows the experimentally determined autocorrelation decay functions to be fit to a variety of physically relevant functional forms. Perhaps most important, it achieves all of this in a manner that inexperienced users have found particularly easy to learn and experienced users have found straightforward to modify as needed for advanced analysis.

Outside of its use by IMMY/XOR members, the software—which has been subject to ongoing refinement since installation in July 2002 — has by now been employed by a number of research groups at universities (California, San Diego, Northern Illinois, SUNY Stony Brook) and user facilities Intense Pulsed Neutron Source, National Synchrotron Light Source) for their XPCS experiments at 8-ID. *(Contact A. Sandy, asandy@aps.anl.gov)* ❍

Zone-Plate Microfocusing for XPCS

Implementation of the IMMY/XOR 8-ID-E shutter has allowed development of the 8-ID-E side station without disturbing the fully operational general-user program at 8-ID-I. In this context, several important upgrades to 8-ID-E have been recently completed. One such improvement was vacuum integration of the 8-ID-E shutter with the transmission side-station monochromator. This significantly increased the flux delivered to station 8-ID-E. More significant has been the development and deployment at 8-ID-E of a micromotion xyz sample stage capable of submicron resolution. The stage motion is driven by Picomotors™ mounted on three orthogonal axes, each controlled in a feedback loop to laser optical position encoders. These encoders allow for absolute stage motion to submicron precision over several inches of travel. The design is simple, efficient, and less costly than comparable off-the-shelf units. However, relying on software feedback between two independent devices to achieve precise motion made integration of the setup into the control system nontrivial.

The stage was installed on a three-circle diffractometer to allow microprobe diffraction measurements with a zone-plate-focused x-ray beam. This geometry essentially makes possible independent crystallographic measurements of microstructures within a sample, retrieving information about local lattice constants, lattice orientation, and disorder.

Preliminary experiments mapping ferroelectric domains in $BaTiO_3$ indicate reliable stage motion to less than 0.1 μm, allowing users to successfully exploit the spatial resolution of the focused x-ray beam (vertical spot size ~0.8 μm). The stage has also been used recently by the collaborative general-user research groups of Y. Chu and I. McNulty. *(Contact M. Sutton, mark@physics.mcgill.ca)* ❍

Measuring the Microstructure of Processed Materials

The properties of many materials depend on microstructure as well atomic structure, which explains why so many materials processing methods focus on changing microstructure. Experimenters can study the microstructure of materials using dynamic light scattering, a method that uses coherent visible light. Information provided by this method, however, is limited by the wavelength of the light used. In order to study microstructure at shorter lengths, researchers from McGill University and UMR, Le Centre National de la Recherche Scientifique (CNRS), are extending the method into the x-ray regime, developing a scattering method called x-ray intensity fluctuation spectroscopy (XIFS). They show how it can be used to study systems that are not in equilibrium.

Although XIFS is new, other (incoherent) x-ray diffraction techniques have been used for decades for applications such as crystallography. XIFS, however, requires that the x-ray source be coherent and intense enough to provide a good diffraction "image" at the time scales of interest (which can be as short as milliseconds). Therefore, the researchers used the 8-ID beamline at IMMY/XOR sector 8 to demonstrate this method of studying microstructure.

XIFS exploits an effect of coherent radiation: speckle. When coherent light scatters diffusely off a disordered material, each spot in the image is the sum of many rays of scattered light, each with a different phase. Bright spots occur where the superposition of the rays is constructive, while dark spots occur where the rays add destructively. The entire image is speckled with a dark and light pattern.

This speckle pattern is a projection of the Fourier transform of the scattering volume. If the diffracting sample fluctuates over time, then the speckle intensities change as well. XIFS extracts information on the sizes and motions of light-scattering particles from the changes in time and space of the speckle pattern. Particles suspended in liquids undergo Brownian motion; hence, their position fluctuates over time and therefore so does the speckle pattern. The group measured the intensity fluctuations of the speckle pattern created by gold colloids in polystyrene (see Fig. 1). By measuring the way diffraction intensity changes over time, the researchers discerned changes in density over time.

This experiment demonstrates the possibility of measuring two-time correlation functions. Instead of averaging over time to obtain good statistics (as measurements of equilibrium systems often do), the researchers used an area detector to measure many speckles at the same time to obtain good statistics for a full two-time correlation function. For a system in equilibrium, such as the example mentioned above, the correlation between the measurement and density depends only on the difference in time between the measurements, as shown in the figure.

Many interesting materials, however, are not in equilibrium. A material that has undergone some sort of material processing in order to change its properties is not at equilibrium. Methods often used for measuring systems in equilibrium don't work for these materials, partly because they assume that the average scattered intensity remains constant.

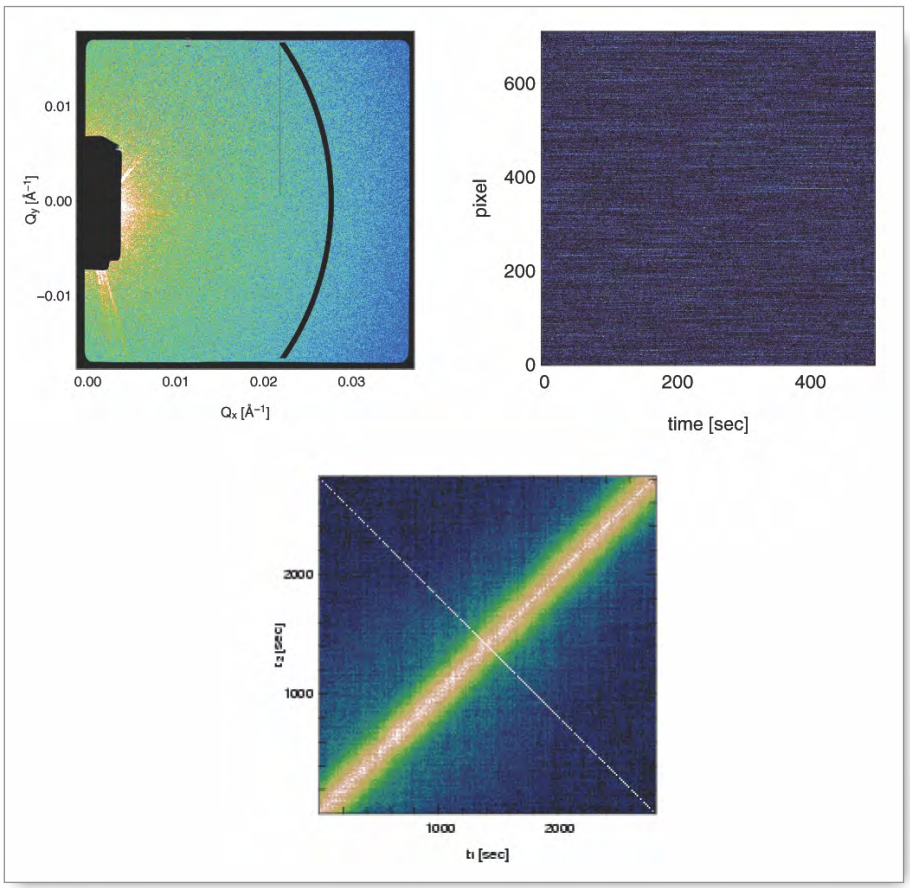

Fig. 1. Top left: Intensity of coherent x-ray small angle scattering from a system in equilibrium (6.0-nm Au particles in polystyrene). False color image uses brightness to indicate intensity. Black block on the left is the stop for the unscattered beam of x-rays. Black arc indicates the pixels sampled over time in the image at top right. Top right: Time evolution of an arc of pixels. Although all pixels share an average intensity, the intensity of the scattered x-rays at each individual pixel fluctuates over time due to the Brownian motion of the scattering particles. Bottom: By correlating the two rows in the top right image corresponding to the times t_1 and t_2, researchers obtained the two-time correlation function $C(t_1, t_2)$ for this particular wave vector. Because this system is in equilibrium, the correlation function depends only on t_1-t_2, as shown by the contours being parallel to the diagonal. The quality of the data demonstrate that this analysis can be used to measure two time correlation functions even for nonequilibrium systems.

This work demonstrates the method with an example: the phase separation of an aluminum-lithium alloy cooled to just below its critical temperature, where the microstructural changes that occur happen on a timescale that can be measured by this method. The sample was prepared by heating it above its critical temperature to mix the metals and then quickly cooling it from 475°C to room temperature, which "freezes in" this homogeneous structure. Then it was heated and held at 220°C, a temperature at which diffusion is significantly faster and the material starts to unmix. In this system, the two-time correlation function depends on both the time difference and the time since the temperature was raised. The good agreement between these measurements and a theoretical model of phase separation give more evidence of the validity of dynamical scaling. Work is in progress on using this technique for other systems. ❍

See: M. Sutton[1], K. Laaziri[1], F. Livet[2], and F. Bley[2], "Using coherence to measure two-time correlation functions," Opt. Express **11**, 2268-2277 (22 September 2003).
Author affiliations: [1]McGill University, [2]LTPCM-ENSEEG-INPG, UMR-CNRS

Use of the Advanced Photon Source was supported by the U.S. Department of Energy, Office of Science, Office of Basic Energy Sciences, under Contract No. W-31-109-Eng-38.

Mapping Microelectronic Circuits with X-rays

Thanks to the skill of chip designers in squeezing more and more components into every corner of a silicon wafer, microcircuits have historically been doubling in processing power nearly every 18 months. This trend has been made possible by photolithographic technologies capable of creating smaller and smaller structures. To reach the next generation of chip manufacturing, however, features smaller than 100 nm will have to be fabricated. Mass producing such structures also means rapidly measuring them and characterizing their quality. But current methods, such as electron microscopy and atomic force microscopy, all face profound challenges in sub-100-nm technological applications. Now, a team of researchers at the National Institute of Standards and Technology (NIST), ExxonMobil Research and Engineering, the Shipley Company, and Argonne National Laboratory are using x-ray scattering techniques to determine the shape and quality of photolithographic features with nanometer resolution.

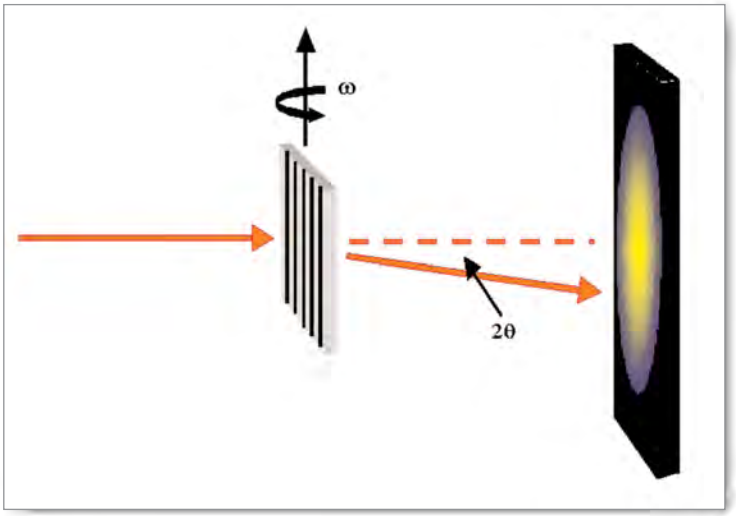

Fig. 1. Configuration of experiments for small-angle x-ray scattering. X-ray beam from the APS source hits the sample at normal incidence. Scattering x-rays are collected at 2θ downstream of beamline at different rotation angles ω.

Optical scattering has become an established tool in developing microfabrication methods as well as in characterizing structures on the process line. But as feature sizes decrease, the comparatively long wavelengths of light severely limit useful measurement. By moving to shorter x-ray wavelengths, the smaller structures envisioned for future generations of integrated circuits can be probed. In addition, the relatively weaker interaction of x-rays and most materials allows a wider range of materials (including metals) to be studied compared with the range available via light scattering.

To explore the possibility of employing x-ray scattering for feature dimension determination, the research team used samples of polymer photoresist arranged in a grating pattern on a silicon substrate. This kind of test pattern is a standard method of calibrating and evaluating photoresist quality and imaging conditions. The gratings used in these experiments were fabricated with a nominal line width of 180 nm. Small-angle x-ray scattering (SAXS) was carried out at the CMC-CAT beamline 9-ID at the APS, with the source beam directed onto the grating at normal incidence (Fig. 1). Transmission scattered x-rays were collected downstream of the source by means of a charge-coupled device camera 543 cm from the sample. The x-ray wavelength of 0.095 nm was selected to have sufficiently low absorption by the silicon substrate while maintaining a reasonable instrument resolution.

X-ray diffraction from the grating produced a linear pattern of spots on the detector for different rotation angles of the sample. This diffraction pattern is fitted to an expression based on a group of lines with a trapezoidal cross section. The width of the grating lines is then extracted from the data fit, as is the sidewall angle of the grating lines. For the three test gratings used (critical dimension ~180 nm), line widths of 171, 159, and 167 nm were measured with resolution (3 σ) on the order of 3 to 4 nm. Sidewall angles for the same specimens were 88.2°, 87.9°, and 88.5°. These results were in agreement with direct measurements made by scanning electron microscopy.

The results demonstrate the usefulness of SAXS in characterizing patterns created by photolithography. Data collection

for each sample was completed in a time on the order of seconds, making the method attractive from a processing standpoint. Through careful selection of x-ray wavelength, structures made from many different materials can be resolved, while future studies will examine samples with sub-100-nm feature sizes. With the extremely short wavelength x-rays available at third-generation synchrotrons such as the APS, SAXS could potentially become a valuable tool for the fabrication of next generation of microelectronics. ❍

See: R.L. Jones[1], T. Hu[1], E.K. Lin[1], W.-L. Wu[1], R. Kolb[2], D.M. Casa[3], P.J. Bolton[4], and G.G. Barclay[4], "Small angle x-ray scattering for sub-100 nm pattern characterization," Appl. Phys. Lett. **83** (19), 4059-4061 (10 November 2003).

Author affiliations: [1]NIST, [2]ExxonMobil Research and Engineering Company, [3]CMC-CAT, [4]Shipley Company, LLC

This work was funded in part by the Defense Advanced Research Projects Agency Advanced Lithography Program under Contract No. N66001-00-C-8083. Additional funding was provided by the NIST Office of Microelectronic Programs. R.L.J is supported by a NIST National Research Council postdoctoral fellowship. Use of the Advanced Photon Source was supported by the U.S. Department of Energy, Office of Science, Office of Basic Energy Sciences, under Contract No. W-31-109-Eng-38.

Advances in Quantitative X-ray Tomography

X-ray phase-contrast imaging—in which information about the structure and composition of an object is obtained from the refractive interaction of x-rays with matter—is advancing rapidly. One goal is to use x-ray phase tomography to create three-dimensional (3-D) images of an object with negligible absorption. Using the brilliant x-ray beams from the APS, researchers from the University of Melbourne and Argonne National Laboratory achieved that goal by making tomographic x-ray phase reconstructions of an atomic force microscope (AFM) tip at a spatial resolution of 900 nm. The resulting 3-D images yield a quantitative measurement of the real part of the refractive index. This work opens the door for full 3-D imaging of the complex refractive index with submicron spatial resolution.

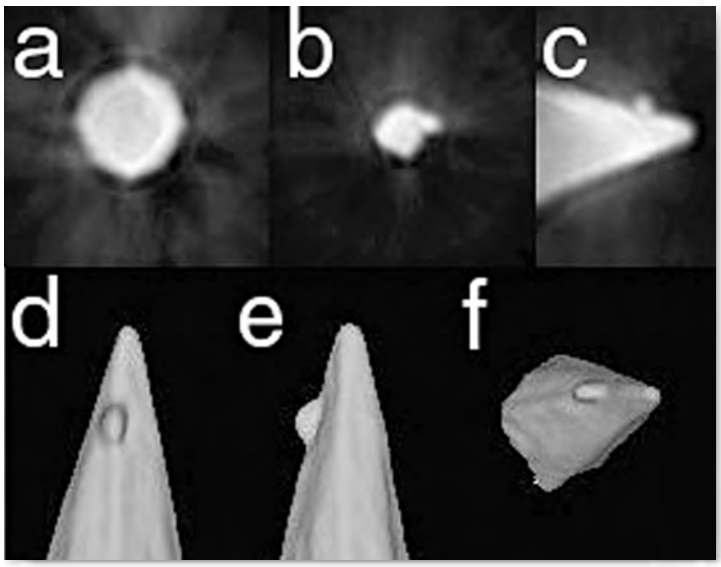

Fig. 1. Quantitative 3-D reconstructions of the real part of the refractive index of the AFM tip. (a) Horizontal slice through the tip. (b) Horizontal slice including the spherical bump. (c) Vertical slice. (d-f) Volume renderings.

Driving advances in this x-ray technology are third-generation synchrotrons, such as the APS, which offer significantly greater coherent x-ray flux. Researchers previously demonstrated quantitative phase two-dimensional imaging at the APS [1]. Building upon that research, they used the same arrangement for this tomographic study. The microscope was assembled at XOR beamline 2-ID-B at the APS. The sample was a commercially available AFM tip (Silicon-MDT Ltd., Moscow, Russia).

A highly coherent beam of 1.83-keV x-rays, defined by a 20-µm-diameter aperture, was passed through the sample. A 90-µm-diameter, 110-nm-thick Ni zone plate with an outer zone width of 45 nm was used to image the sample. The x-rays were propagated in vacuum to a backside-illuminated 1024 × 1024-pixel charge-coupled device camera with a 24 µm pixel size. The sample was magnified to approximately 160 times its actual size. Phase data for each projection were obtained, and the data were reconstructed into a 3-D image.

The absorption contrast of the silicon AFM tip sample was very small, yielding a very poor reconstruction by conventional x-ray microtomography reconstruction methods. The phase contrast is, however, significant at this key energy. The finest fringe structure visible in the projection data is consistent with an instrumental spatial resolution of 230 nm. Figure 1 shows examples of the resulting 3-D phase reconstructions. Figures 1(a) and 1(b) represent slices through the tip in the horizontal direction, whereas Fig. 1(c) depicts a slice of the reconstruction through the vertical direction.

In Figs. 1(b) and 1(f), a spherical bump, measuring 900 nm in diameter, is clearly visible. The faceted structure in Fig. 1(a) is even more evident in Figs. 1(d)–1(f). The AFM tip was not perfectly sharp, so it is possible that the actual resolution may be better than 900 nm, but no features at a smaller scale were seen. On the basis of sinograms taken from the tomographic data sets for both phases, the group was able to confirm that the facets are a genuine feature of the tip. In fact, such a structure is typical of the manufacturing process used to etch crystalline AFM tips [2]. The researchers also compared the known

composition of the AFM sample tip with the tabulated value at this energy. They found that the experimental value agreed with the tabulated value to well within the experimental error, confirming that a high-resolution quantitative map of the real part of the refractive index was obtained.

This work demonstrated quantitative imaging of the phase distribution of a weakly absorbing sample at a 3-D resolution of least 900 nm. It also yielded an accurate measurement of the real part of the sample refractive index. The next step is to obtain a full measurement of the 3-D complex refractive index. ❍

References

[1] B.E. Allman, P.J. McMahon, J.B. Tiller, K.A. Nugent, D. Paganin, A. Barty, I. McNulty, S.P. Frigo, Y.X. Wang, and C.C. Retsch, J. Opt. Soc. Am. A **17**, 1732 (2000).

[2] T.R. Albrecht, S. Akamine, T.E. Carver, and C.F. Quate, J. Vac. Sci. Technol. A **8**, 3386 (1990).

See: P.J. McMahon [1], A.G. Peele [1], D. Paterson [1], J.J.A. Lin [1], T.H.K. Irving [1], I. McNulty [2], and K.A. Nugent [1], "Quantitative X-ray phase tomography with sub-micron resolution," Opt. Comm. **217**, 53–58 (2003).

Author affiliations: [1]University of Melbourne, [2]Argonne National Laboratory

This work was supported by the Australian Synchrotron Research Program, which is funded by the Commonwealth of Australia under the Major National Research Facilities Program; by the Australian Research Council; and by the U.S. Department of Energy, Office of Science, Office of Basic Energy Sciences, under Contract No. W-31-109-Eng-38.

Full-field Imaging Methods

Fast X-ray Microtomography

The microtomography system at 2-BM offers near video-rate acquisition of tomographic data combined with automatic data acquisition, reconstruction, and visualization. Users can acquire up to 720 tomographic projections (1024 pixels × 1024 pixels) at 0.25° angular increments in less than 5 min. The data are reconstructed by a dedicated 32-node, 1-GHz Intel PIII computer cluster with 2 TB of distributed hard disk. Rendered three-dimensional (3-D) images of the sample are displayed on a workstation at the experimental station within 3 min of acquisition of the last projection. Low-resolution (512 pixels × 512 pixels) images are available within 50 s. The raw data are automatically backed up on tape and DVD, with the analyzed data ready for distribution within 15 minutes. At its maximum rate, the system can collect and analyze hundreds of samples in a 24-h experiment. This year, the charge-coupled device camera used to record the projections was mounted on a 1.2-m-long motorized rail aligned with the beam, enabling the sample-to-scintillator distance to be optimized for either absorption or phase contrast. A sample changer was also integrated into the system for automatic loading of up to 70 samples. The instrument is mounted on a dedicated, motorized, optical table that can easily slide in and out of the beam while keeping the components aligned. This configuration has greatly reduced the time required to switch between experiments at 2-BM.

See: S.R. Stock, K.I. Ignatiev, T. Dahl, A. Veis, and F. DeCarlo, "Three-dimensional microarchitecture of the plates (primary, secondary and carinar process) in the developing tooth of Lytechinus variegatus revealed by synchrotron x-ray absorption microtomography (microCT)," J. Struct. Biol. **144**, 282-300 (2003).

Structural Characterization of Combinatorial Materials

Combinatorial approaches play an increasingly important role in a wide range of disciplines as a method for high-throughput materials exploration. In particular, thin-film combinatorial samples can be fabricated with compositional profiles across a substrate so that phase diagrams and properties, especially phase boundaries and transitions, can be systematically mapped out and studied as a continuous function of composition. Reliable and rapid quantitative structural characterization has been a major bottleneck for this type of research, owing in part to the insufficient brilliance of laboratory x-ray sources. To eliminate this bottleneck, instrumentation and techniques have been developed at XOR 2 for combinatorial samples, in which x-ray diffraction and fluorescence measurements can be carried out in parallel using by Kirkpatrick-Baez focusing optics in a common sample coordinate system.

See: F. Tsui[1], L. He[1], L. Ma[1], A. Tkachuk[2], Y.S. Chu[2], K. Nakajima[3], and T. Chikyow[3], "Novel germanium-based magnetic semiconductors," Phys. Rev. Lett. **91**, 177203 (2003).

Time-resolved Full-field X-ray Diffraction Imaging

The high brilliance of APS bending magnet sources coupled with high-resolution CCD cameras make it possible to obtain time-resolved diffraction images down to submicrometer length scales. Since the diffraction contrast from the sample is obtained with a single exposure, the full-field imaging method is especially suited for investigation of dynamic systems. This technique was applied at XOR 2 to investigate nucleation and growth of ferroelectric domains in $BaTiO_3$ single crystals. *(Contact Y. Chu (ychu@aps.anl.gov)*

Scanning Fluorescence X-ray Microscopy

The x-ray fluorescence microprobes at XOR sector 2 operate in a mode in which full fluorescence spectra are acquired at every image position to maximize the amount of information extracted from the specimen. Dedicated software has also been developed for precise quantification of chemical elements in both single pixels and across whole images. Advanced procedures, such as cluster analysis and principal component analysis, can be applied to the acquired data sets to detect and visualize correlations that might not otherwise be apparent.

The beam stability during energy scans in hard x-ray absorption near-edge spectroscopy (XANES) experiments at 2-ID-D was improved considerably. By running the monochromator in channel-cut mode, beam drift was reduced to the size of the beam (0.25 µm). This made it possible to perform micro-XANES measurements on ultrafine (<50 nm) iron impurities in polysilicon solar cells, revealing that the precipitates are most likely $FeSi_2$.

See: T. Buonassisi, M. Heuer, O.F. Vyvenko, A.A. Istratov, E.R. Weber, Z. Cai, B. Lai, T.F. Ciszek, and R. Schindler, "Applications of synchrotron radiation x-ray techniques on the analysis of the behavior of transition metals in solar cells and single-crystalline silicon with extended defects," Physica B **340-342**, 1137-1141 (2003), and Z.H. Levine, S. Grantham, D.J. Paterson, I. McNulty, I.C. Noyan, and T.M. Levin, "Imaging material components of an integrated circuit interconnect," J. Appl. Phys. **95**, 405-407 (2004).

X-ray Nanodiffraction

Until recently, the reciprocal space characterization of nanomaterials with x-rays was limited to the measurement of their average properties because a large number of nano-objects had to be probed in order to produce a measurable signal. Improvements in hard x-ray sources, focusing optics, and diffraction techniques have recently enabled this limitation to be overcome. A new instrument at XOR beamline 2-ID-D integrates high-efficiency zone-plate lenses and a six-circle diffractometer to probe a broad range of reciprocal space with an intense, nanofocused x-ray beam. The necessary mechanical stability was achieved by use of vibration-isolation mechanisms and direct support of the diffractometer during data acquisition. The measured effective focal spot size is less than 200 nm. The typical measured photon flux density on the sample is 10^5 photons/s/nm^2/0.01% BW at x-ray energies of 6 keV to 12 keV, corresponding to 10^7 photons/s incident on 10 nm × 10 nm nano-object. *(Contact Z. Cai, cai@aps.anl.gov)*

Differential Phase-contrast Microscopy and On-the-Fly-Scanning

Thin, light specimens, such as biological cells and subcellular organelles, are nearly transparent to x-ray beams with photon energies above ~1 keV. However, at higher x-ray energies, the real part of the complex index of refraction can be several orders of magnitude larger than the imaginary part, especially for the light elements. This effect can be exploited to image low-density sample structures by differential phase contrast (DPC) x-ray microscopy. Differential phase-contrast can also be used in parallel with x-ray fluorescence detection for trace element mapping. Other advantages of this approach include simultaneous collection of bright field, dark field, and phase contrast signals; filtration of beam intensity variations; and compatibility with fast-scan methods. To develop DPC capability, an eight-element segmented detector was incorporated into the scanning x-ray microscopes at XOR beamlines 2-ID-B and 2-ID-E (Fig. 1). *(Contact D. Paterson (paterson@aps.anl.gov) and S. Vogt (vogt@aps.anl.gov)* ❍

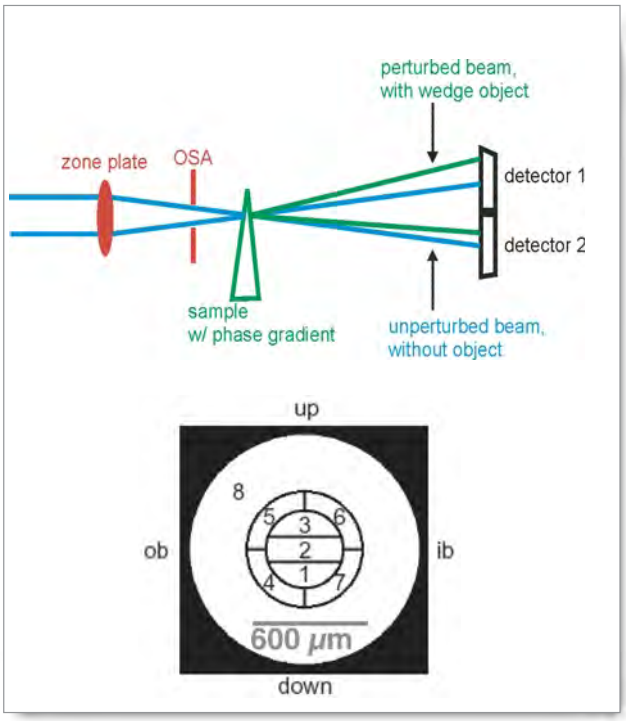

Fig. 1. Zone-plate scanning microscope (top) and segmented detector for DPC measurements.

X-ray Imaging Optics

Measurement of X-ray Beam Coherence

The availability of partially coherent x-ray beams at third-generation synchrotron sources and highly coherent x-ray beams at fourth-generation (linear coherent) x-ray sources is leading to significant new analysis capabilities. The coherence is often represented by a single number, such as the spatial coherence length. However, to fully understand x-ray experiments involving microfocusing, coherent diffraction, speckle, and interferometry, more detailed information about the coherence properties of the beam is required. A complete measurement by a series of Young's experiments is very time consuming. A much faster method, one that was developed for soft x-ray lasers, uses a complex mask known as a "uniformly redundant array" (URA) in which all aperture separations occur with equal frequency. A one-dimensional URA was prepared in gold using contact optical lithography and electroforming onto silicon nitride membranes. The overall width of the URA was 700 µm and the smallest feature size was 5 µm. The 1.6-µm-thick gold features transmitted 51% of the incident 7.9-keV x-rays, and imparted a π phase shift. The URA was used to measure the horizontal coherence of the x-ray beam at beamline 2-ID-D for a range of slit settings (Figs. 1a-1d).

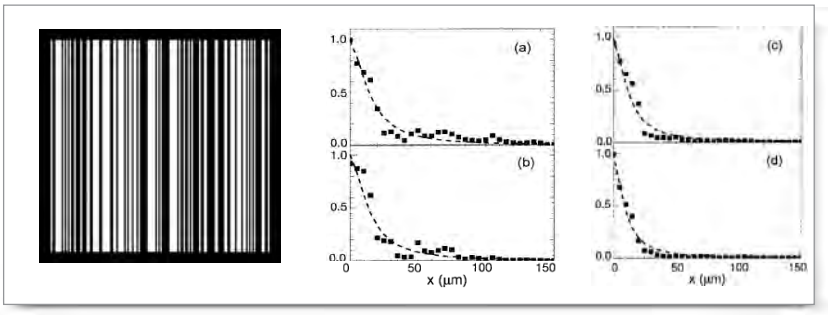

Fig. 1. One-dimensional URA (left) and measured modulus of the coherence factor with fits (right) for beamline slits of width (a) 10 µm, (b) 50 µm, (c) 90 µm, and (d) 170 µm.

See: J.J.A. Lin, D. Paterson, A.G. Peele, P.J. McMahon, C.T. Chantler, K.A. Nugent, B. Lai, N. Moldovan, Z. Cai, D.C. Mancini, and I. McNulty, "Measurement of the spatial coherence function of undulator radiation using a phase mask," Phys. Rev. Lett. **90**, 074801 (2003).

Kirkpatrick-Baez Microfocusing at 2-BM

A new Kirkpatrick-Baez (K-B) microfocusing mirror system (University of Chicago design with 10-cm vertical and 20-cm horizontal mirrors) was commissioned at XOR beamline 2-BM in 2003. The K-B system is configured to produce a moderately focused beam of 3 µm to 10 µm with a nominal focal length of ~0.5 m. This relatively long focal length allows convenient access to a large range of reciprocal space by using a four-circle diffractometer. At an incident angle of 3 mrad and working distance of 0.65 m, the focus size measured using knife-edge scans was 3 µm (vertical) × 4 µm (horizontal). The typical measured flux at the focus using 10-keV x-rays is 5×10^8 photons/s using a monochromatic ($\Delta E/E \sim 10^{-4}$) beam, 2×10^{10} photons/s using broadband monochromatic ($\Delta E/E \sim 10^{-2}$) beam, and 2×10^{11} photons/s with polychromatic beam (4 keV to 32 keV continuous spectrum). *(Contact Y. Chu, ychu@aps.anl.gov)*

Achromatic Fresnel Zone Plates

Zone-plate lenses produce among the smallest focal spots achieved in the x-ray region of the spectrum. The significantly lower chromaticity of this new optic opens up a larger portion of the x-ray spectrum for large-diameter, high-resolution focusing. Future applications include nanometer-scale x-ray microscopy, microanalysis, and next-generation lithography systems for the semiconductor industry.

A new type of high-resolution x-ray lens that combines a gold Fresnel zone plate (Fig. 2a) with a silicon refractive lens Fig. 2b) to achieve reduced chromatic aberration was recently demonstrated at XOR beamline 2-ID-B in collaboration with Xradia, Inc. When x-rays with energies of 1810 eV-1850 eV were used, it was found that the focal length of the achromatic lens remained constant within a depth of focus over a 12-eV range (Fig. 2c). Without the correcting refractive lens, the focal length was observed to change with a 2-eV change in the energy.

See: Y. Wang, W. Yun, and C. Jacobsen, "Achromatic Fresnel optics for wideband extreme-ultraviolet and X-ray imaging," Nature **424**, 50–53 (2003).

Fig. 2. (a) Scanning electron microscope (SEM) image of the zone plate, which is 160 µm in diameter and has a 50-nm finest zone. (b) An SEM image of the refractive lens. (c) Focal length of the achromatic lens as a function of photon energy in eV. Theoretical calculation (solid line) is shown plotted against the experimental data points.

Hard X-ray Zone Plates

The ability to focus an x-ray beam to an intense, nanometer-scale spot will open up a world of discovery at molecular length scales and beyond. Indeed, nanoscale hard x-ray focusing is the cornerstone for the Nanoprobe beamline currently under development at sector 26 of the APS. A spatial resolution of 60 nm to 80 nm at an x-ray energy of 10 keV was reproducibly demonstrated at XOR beamline 2-ID-D using a new Fresnel zone plate lens made of gold with a finest zone width of 50 nm. Until now, zone plates with 110-nm finest zones providing focal spot sizes of 150 nm were the workhorse optics in the 2-ID-D and 2-ID-E x-ray microprobes. With increased beam acceptance (these zone plates have a diameter of 160 µm, double that of previous ones used), the new optics significantly increase the focused x-ray flux density in addition to the spatial resolution. A second zone plate with a 100-nm finest zone but with four times the area was tested at 2-ID-E. This zone plate is now routinely used to provide experiments with greater flux at similar resolution. These results also demonstrate that the mechanical performance of the hard x-ray microprobe is capable of supporting sub-100-nm investigations. Continuing development in the optics and mechanical system should lead to even better spatial resolution. *(Contact B. Lai, blai@aps.anl.gov)*

Multilayer Spherical Grating Monochromator for 2-4-keV X-ray Beams

An x-ray monochromator for 2-keV to 4-keV x-rays was developed and tested at the XOR 2-ID-B beamline. The instrument uses multilayer-coated diffraction gratings instead of more traditional gratings or crystal optics, to select a narrow band of energies from the x-ray beam with much greater efficiency than is possible with single-layer-coated gratings. The energy resolution of the monochromator is typically 1 eV at 3 keV. This development solves a long-standing challenge of building an efficient monochromator for this difficult-to-access energy region, which includes the K-absorption edges of important elements such as silicon, sulphur, phosphorus, chlorine, and calcium. When the new multilayer grating monochromator is used, the time required to collect sulfur fluorescence images with the 2-ID-B scanning x-ray microscope was reduced from hours to minutes. *(Contact I. McNulty, mcnulty@aps.anl.gov)* ❍

High-energy X-ray Microfocusing

Microfocusing high-energy x-rays (E > 50 keV) poses severe technological challenges for commonly used microfocusing optics, such as multilayers or Fresnel lenses, due to the very short spatial periodicity that would be required. Perfect Si crystals provide an attractive alternative in that they are readily available and provide a spatial periodicity of a few angstroms. In Laue geometry, the x-ray beam is almost perpendicular to the crystal surface, resulting in a minimized footprint on the optical element. However, the periodicity cannot be tailored as a function of position, and Laue focusing in this manner requires a large energy bandwidth.

The Laue microfocusing principle is shown in Fig. 1. The crystal is bent to provide geometric focusing as described by the well-known lens equation. Broadening of the focal width by the crystal thickness can be prevented by an appropriate asymmetric cut. Tests at XOR 1 beamline 1-ID-B yielded a focused beam with a full-width, half-maximum size of 1.4 µm at 50 keV (see Fig. 2). The monochromator was placed on the same optical table as the sample to prevent focal degradation due to vibrations. *(Contact U. Lienert, lienert@aps.anl.gov.)* ❍

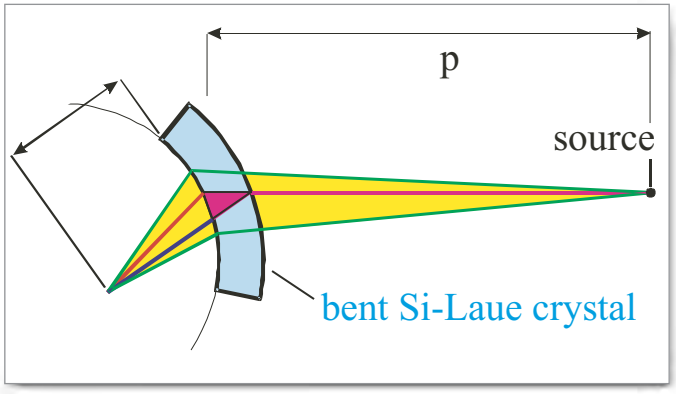

Fig. 1. Principle of the microfocusing bent Laue crystal setup. The focal lengths are p = 35 m and q = 1 m.

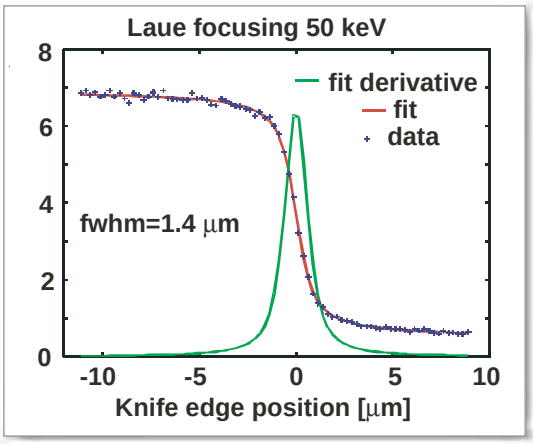

Fig. 2. Width of the focal line as measured by a Au fluorescence knife-edge scan.

Image-plate Data Collection and Processing for Protein Powder Diffraction

Protein powders present special difficulties for synchrotron diffraction data collection because of their sensitivity to the x-ray beam. For example, with the intensity available on XOR beamline 1-BM, even a relatively robust protein, such as hen egg white (HEW) lysozyme, does not retain crystalline integrity for more than 30 min. This time is insufficient for data collection by using a single-point diffraction scan with a crystal analyzer/detector system. To overcome this problem, a mar345 image-plate detector and data-processing techniques have been developed that give diffraction data of excellent quality.

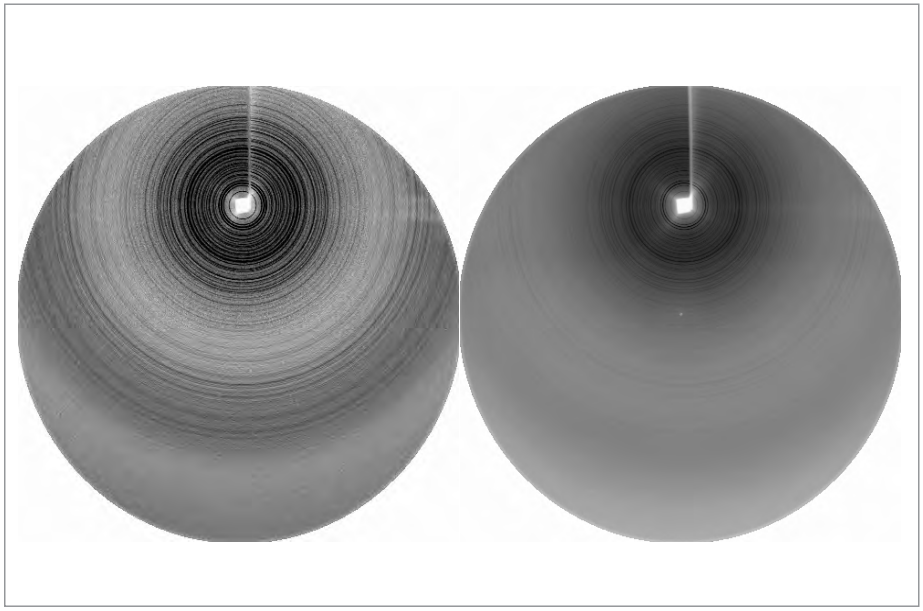

Fig. 1. mar345 image of HEW lysozyme powder obtained in 40-s exposure at beamline 1-BM at 20 keV (left), and image after background subtraction (right).

X-ray Operations and Research beamline 1-BM has focusing optics, and these are adjusted to set the beam focus at the surface of the mar345 detector positioned 50 cm-100 cm behind the sample position. The instrument thus operates in a Guinier camera focusing mode, thereby eliminating sample dimensions as a component of the diffraction line broadening. In addition, the mar345 image plate is displaced 10 cm vertically to give a wider 2Θ range than afforded by the usual centered position. Figure 1 (left) shows the image resulting from a 40-s exposure of tetragonal HEW lysozyme at $\lambda = 0.6193$ (~20 mar345 at 72.7 cm from the sample. Subtraction of a blank run to remove inherent image-plate flaws, an air-scatter run, a sample-holder run, and a solvent run yield the image shown in Fig. 5 (right). Each of these runs requires some scaling to account for different absorption effects, as well as the more obvious exposure times that may be employed in their collection. The resulting image has a relatively feature-free background that is easily modeled in subsequent Rietveld refinement. The "cake" option in FIT2D is used to integrate a 60°- 80° azimuthal region centered about the vertical direction of the image to give a powder pattern suitable for further analysis. Each point is assigned a "standard deviation" (as required for the Rietveld analysis) that is proportional to the square root of the intensity and $1/\sin 2\Theta$ to account for the variation in intensity statistics arising from the greater integration length over the image for higher-angle data points. The improvement in data quality from a single-point scan (from a consideration of sample size, data-collection time, and accessed azimuthal angle) is 10^4-10^6 for a single image-plate exposure. This can be higher if a series of exposures are summed to give a composite image for data analysis. At present, these powder patterns have about 2× poorer diffraction peak resolution than single-point detector scans of the same material. The smearing effects of the 300-µm "bleed over" on the mar345 image plate and the limit on focusing sharpness in the 1-BM optics account for most of this. *(Contact R.B. Von Dreele, vondreele@anl.gov.)* ❍

Conical Slit Cell

In high-energy x-ray experiments, focusing can provide spatial resolution perpendicular to the incident x-ray beam, but gaining spatial resolution in the direction along the incident beam is more challenging. One method that will provide such resolution is the crossed-beam technique using a conical slit cell. Figure 1 shows a setup that allows several complete diffraction rings to be observed simultaneously by using a conical slit cell and a two-dimensional large-area detector.

The conical slit cell was designed to accept seven reflections from samples of cubic symmetry. The slit openings are 20 µm. The device was fabricated by IMM in Mainz, Germany. A holder that provides the three translational and two rotational alignments was designed and built in-house. Commissioning results indicate that the slit cell meets the specified tolerance of 2 µm. *(Contact U. Lienert, lienert@aps.anl.gov.)* ❍

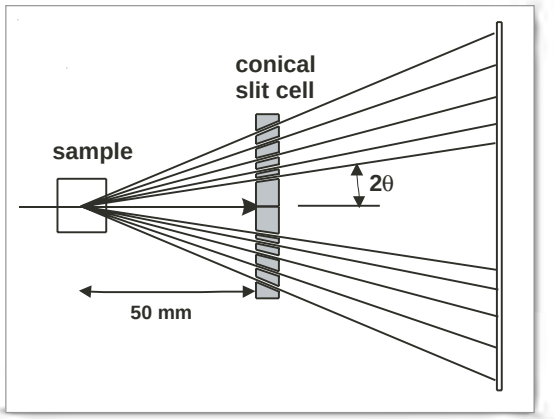

Fig. 1. Confinement of a longitudinal gauge length parallel to the beam by use of a conical slit cell. The cell is made of WC and is 2 mm thick.

Phase-enhanced Imaging

Phase-enhanced, real-time imaging of living insects is proving to be an important new tool for biologists. Recently, two major technical challenges associated with this technique have been tackled: increasing the survival time of the insects and increasing the time resolution of the images. Significant progress has been made on both fronts. Due to improved optics and an optimized setup, the efficiency of the XOR 1 detection system has been improved fivefold. Consequently, increasing the incident x–ray energy from 15 keV to 25 keV was possible, thereby reducing the dose absorbed in the insect. The per-frame exposure time was reduced from 1/60 s to 1/120 s, without altering the quality of the images. At present, the standard setup is limited to 30-Hz frame rates by the video camera.

As a result of these improvements, the survival of the insects increased from 10 minutes to more than 60 minutes. In addition, it is now possible to show that the x-ray beam has no significant impact on the insect. Figure 1 shows the respirometry data for a grasshopper taken with and without the x-ray beam. There is no difference in the 'beam on" and "beam off" respiration rates. In addition, no increases in the body temperatures of the insects were detected. This is a significant result because it allows insect physiologists to study insects in their normal state. This work was carried out in collaboration with K. Greenlee, S. Kirkton, and J. Harrison from Arizona State University.

In another study carried out with collaborators from The Field Museum (Chicago, Illinois), a high-speed camera was used at 1000 frames/s to film the escape-jump mechanism of a click beetle. It was found that the 10-µs exposure time was still not short enough to resolve the kinematics. Improvements in this direction are ongoing and will benefit many other applications. *(Contact W.-K. Lee, wklee@ aps.anl.gov; and K. Fezzaa, fezzaa@aps.anl.gov.)* ❍

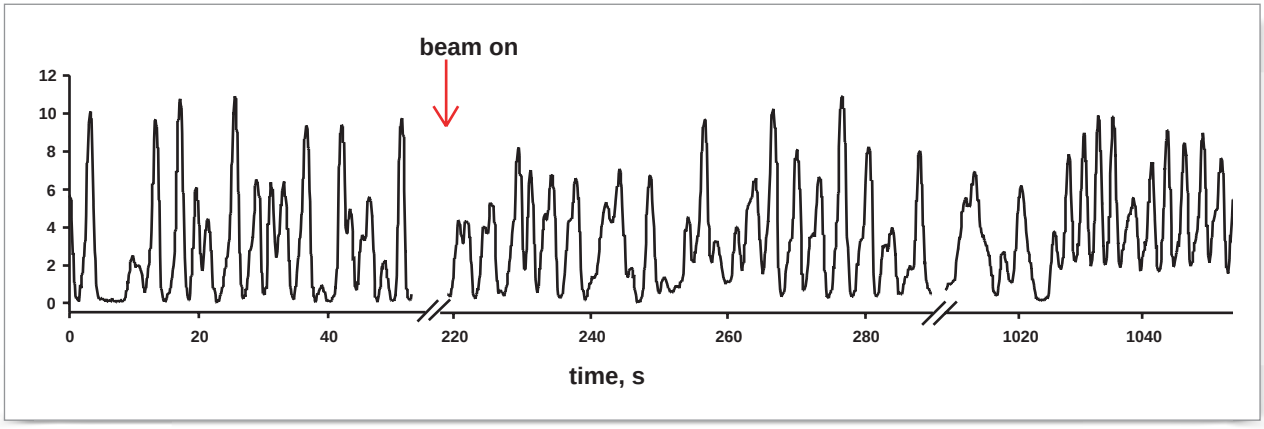

Fig. 1. Respirometry data for a grasshopper before and during the image recording. The vertical axis is CO_2 emissions in ppm. The mean frequency at rest is 0.29 Hz (literature average is 0.33 Hz). The mean frequency in the first minute is 0.27 Hz and in the 17th minute is 0.34 Hz.

General Electric Rad™ Detector

A large-area, high-energy x-ray detector from General Electric (GE) was evaluated at XOR beamline 1-ID. This detector, the GE Rad, was developed for medical imaging. It is very attractive for many synchrotron applications because it combines a large area (40 cm × 40 cm) with fast frame readout (tens of Hz). Several tests were performed using 80.7 keV x-rays. The results were compared directly to the widely used mar345 detector. The mar345 is comparable in size but has a much slower readout (~70 s).

For the given energy, the Rad sensitivity was approximately 400 e/x-ray photons. This is approximately 30% of the mar345 value. The signal/noise ratio was about half that of the mar345. The Rad point-spread function was measured to be 310 µm, which is slightly larger than the 200 µm pixel size and considerably lower than the point-spread function of the Mar345 (420 µm at a pixel size of 100 µm). The spatial distortion for both detectors was at or below 1×10^{-4} over the entire diameter, with the Rad detector exhibiting slightly larger but repeatable variations. It should be noted that the Rad detector was not precalibrated to account for spatial variations (as was the Mar345), and implementing such corrections should enhance its performance. In addition, a more recently developed GE detector (Angio™) offers similar specifications to the Rad but with a lower electronic noise, which should enhance performance for weak signals. Overall, the Rad performance was encouraging and showed that this "off-the-shelf" technology may find a niche in synchrotron applications. These tests were made with considerable technical support from GE Medical Systems (Milwaukee, Wisconsin). *(Contact J. Almer, almer@ aps.anl.gov; D. R. Haeffner, haeffner@aps.anl.gov)* ❍

A Rapid-acquisition, Pair-distribution-function Technique Using High-energy Synchrotron Radiation

The pair distribution function (PDF) method analyzes both diffuse scattering and Bragg scattering at the same time. It has emerged as a powerful technique for extracting structural information about complex and disordered materials, as well as materials that include a range of amorphous, nanocrystalline, and crystalline phases. Employing high-energy x-rays generated at the APS, high-quality, high-Q data can be obtained routinely. However, conventional PDF measurements that use a single energy-resolving detector are very time consuming, with typical measurements taking 6 to 8 hours.

In collaboration with colleagues from SUNY–Stony Brook, Michigan State University, and Brookhaven National Laboratory, a new data-acquisition technique was developed at XOR sector 1 for measuring PDF data with a two-dimensional (2-D) image-plate detector system. A PDF spectrum is collected in a few seconds of exposure. The detector readout time takes a couple of minutes.

To obtain high-quality PDF diffraction patterns, a number of issues were addressed. The most significant were the correction of the background signal from Compton scattering and from fluorescence, and the angle and energy dependencies of the image plate efficiency. With high-energy x-rays, a Q range of ~30 $Å^{-1}$ was achieved, and absorption by the sample and the environmental chamber was minimized.

Figure 1 shows a 2-D diffraction image of Ni powder. Figure 2 shows the spectrum after data reduction. The ability to measure PDF data in relatively short times (minutes instead of hours) opens the possibility of studying structural changes under *in situ* conditions and time-dependent chemical reactions. *(Contact P. Lee, pllee@aps.anl.gov.)* ❍

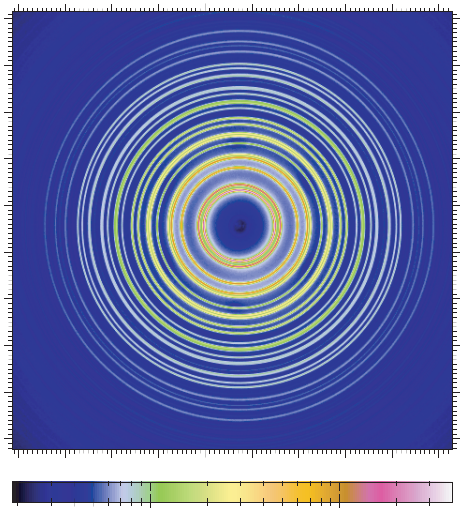

Fig. 1 Left: A two-dimensional diffraction pattern from Ni powder at room temperature with 97.972-keV x-rays was recorded on the mar345 image-plate detector system. Below: The reduced structure function F(Q) of Ni powder from Fig. 1. (b) The experimental G(r) (solid dots) and calculated PDF from the refined structural model (solid line).

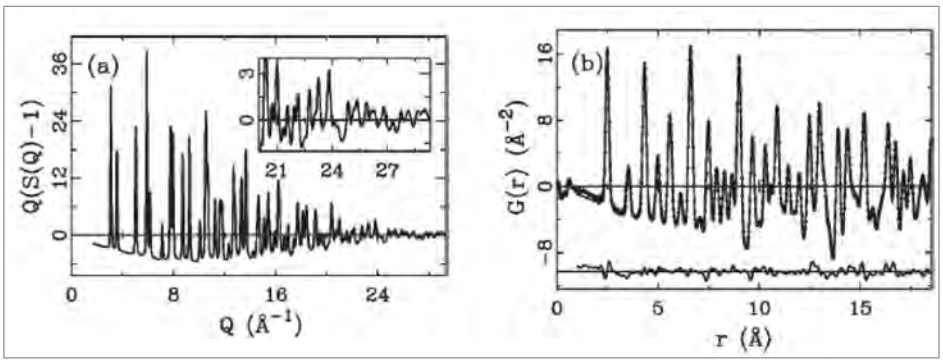

Phase-locked Detection Techniques for XMCD Measurements

X-ray Operations and Research sector 4 at the APS specializes in experiments that manipulate and analyze the x-ray beam polarization. This capability is particularly useful for measurements of the magnetic properties of materials. One of the primary techniques is x-ray magnetic circular dichroism (XMCD), which measures the difference in the absorption coefficient ($\mu_c = \mu^+ - \mu^-$) between opposite helicities of circularly polarized x-rays impinging on a magnetized sample near an absorption edge. Much like the Faraday and Kerr rotations of linearly polarized light used in magneto-optical techniques, this difference is proportional to the sample's magnetization, with the added advantage that the resonant process in the x-ray regime yields element-specific magnetization. The need to detect very small XMCD signals is essential in order to address problems of current scientific interest, such as detecting the small induced moments at magnetic/nonmagnetic interfaces or probing local magnetism by using helicity-dependent x-ray absorpton fine structure. Measuring XMCD signals smaller than ~10^{-3}, however, is difficult with conventional techniques because systematic errors in the data collection process, rather than simple counting statistics, are the dominant source of uncertainty in the measured spectra. At XOR beamline 4-ID-D, the limitations of conventional data collection have been overcome through the use of phase lock-in techniques to extend the sensitivity to signals as small as ~10^{-6}.

A sketch of the phase lock-in instrumentation is shown in Fig. 1. A monochromatic x-ray beam is incident on a diamond phase retarder, which converts the linearly polarized incident beam into either a right- or left-circularly-polarized transmitted beam. By rotating a thin (400 μm) diamond slightly below or above the Bragg angle through the use of a PZT rotation stage, the helicity of the transmitted beam can be reversed rapidly. The absorption of the sample is measured with two ion chambers, with the sample located in a cryostat/magnet between them. Conventional XMCD spectra measure the incident (V_o) and transmitted (V_t) intensity for each helicity across an absorption edge, then the difference is computed. On the basis of the number of absorbed photons, this measurement should, in principle, yield highly accurate XMCD data in relatively short integration times. Systematic errors, such as intrinsic electronic noise in the current amplifiers, ambient electronic noise in the experimental station, and minute changes in the beam position, however, limit the size of practically detectable XMCD difference signals. By using a phase-locked detection scheme, the effects of such electronic noise and beam instability can be eliminated and much smaller differences can be measured. This is achieved by rapidly switching (5 Hz-50 Hz) the helicity of the incident beam and using a lock-in amplifier to measure

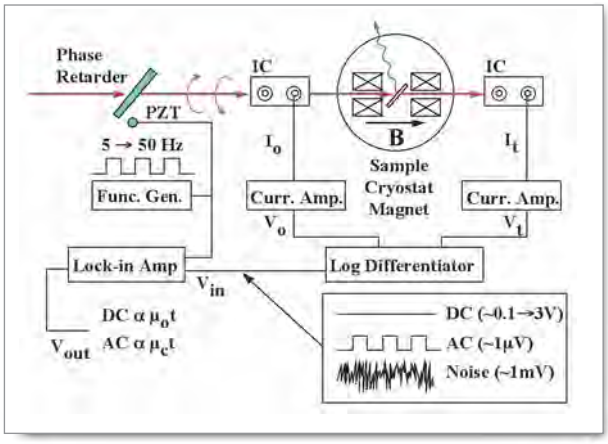

Fig. 1. Schematic of phase-lock setup along with the intensity and polarization of transmitted beam.

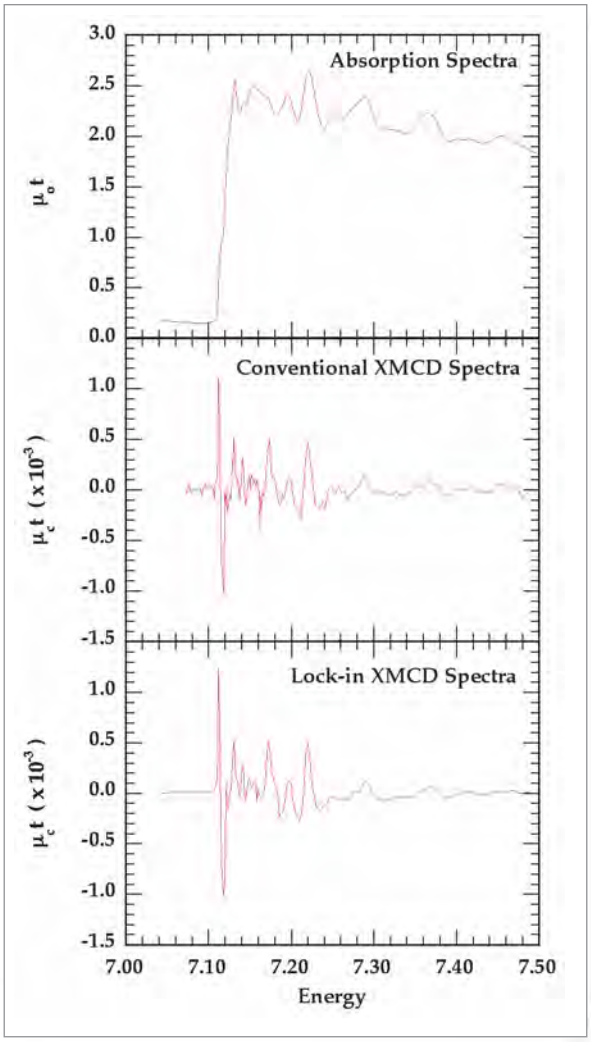

Fig. 2. Dichroic data at the Fe K edge using the normal collection method (middle) and the lock-in method (bottom). The latter was taken in ~1/10 the time.

the XMCD. The lock-in amplifier Fourier filters the absorption signal, isolating the differences at the "locked-in" frequency coincident with the frequency that is used to drive the phase-retarder oscillation.

Due to the asymmetric transmitted intensity through the phase retarder at the $\pm P_c$ positions, a specialized electronics module (the log differentiator in Fig. 1) must be used to properly normalize the signal while the phase retarder is oscillated during data acquisition. Using this technique, XMCD differences that are thousands of times smaller than the noise sources mentioned above can be extracted, because the spectral weight of white noise is negligible at the driving frequency and can, therefore, be effectively excluded in a lock-in measurement.

Two XMCD spectra taken over an extended energy range near the Fe K edge (7.11 keV) of an Fe foil are shown in Fig. 2. The spectrum measured by using standard techniques took approximately 8 h to collect, while the spectrum taken with lock-in detection was acquired in less than an hour. Furthermore, the signal-to-noise level in the "lock-in" spectrum is substantially less than in the spectrum taken using conventional techniques. *(Contact: Jonathan Lang, lang@aps.anl.gov)* ❍

Phase-Sensitive X-ray Diffraction Images of Microdefects in Biological Macromolecular Crystals

The most serious obstacle to determining the structures of proteins and other biological macromolecules by x-ray diffraction concerns the initial step of the process, which involves growing macromolecular crystals of suitable perfection. The effects of crystal microdefects on topological maps remain largely unknown because, until recently, dislocations and other microdefects could not be detected in the x-ray diffraction images under normal circumstances. The intrinsically weak scattering power of x-rays in protein crystals is one of the key factors responsible for the difficulty of x-ray imaging defects in these important systems.

In the last few years, however, substantial decreases in beam size and divergence offered by third-generation synchrotron x-ray sources have led to an upsurge in the development of various x-ray imaging and diffraction techniques that capitalize on the spatial coherence of these sources. The highly coherent hard x-ray beams have enabled researchers to observe phase-difference-based contrast effects in diffraction images that permit the detection and characterization of dislocations and other small lattice irregularities with unprecedented sensitivity.

Researchers from the NASA/Marshall Space Flight Center and the APS employed a phase-sensitive x-ray diffraction imaging approach that augmented the contrast of defects in bulk hen egg-white lysozyme (HEWL) and ferritin protein crystals. The experiments were carried out at the XOR beamline 2-BM

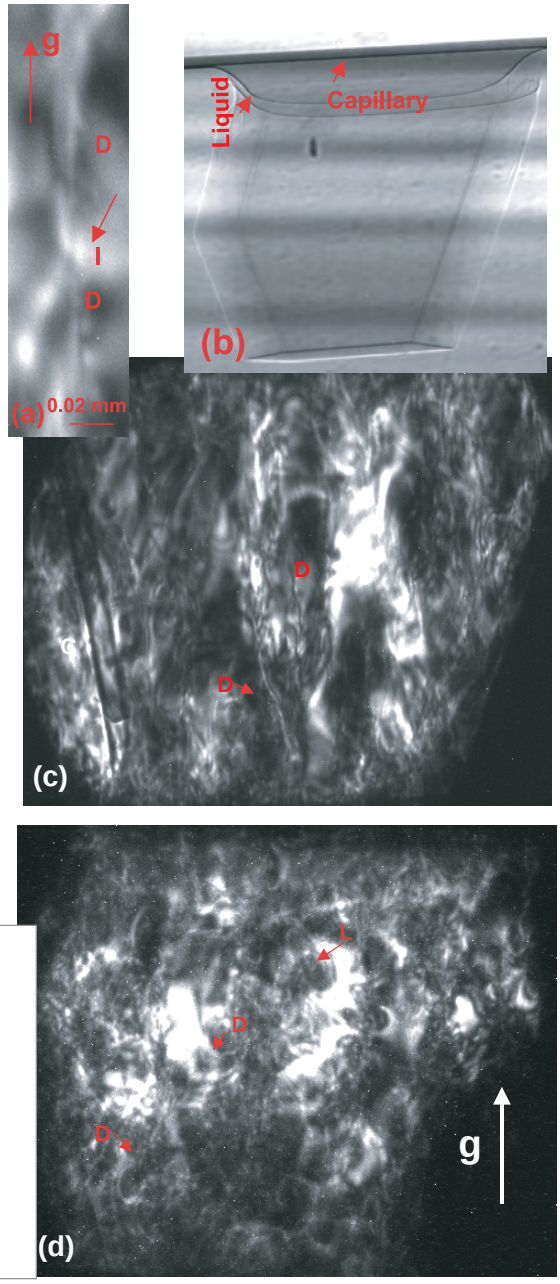

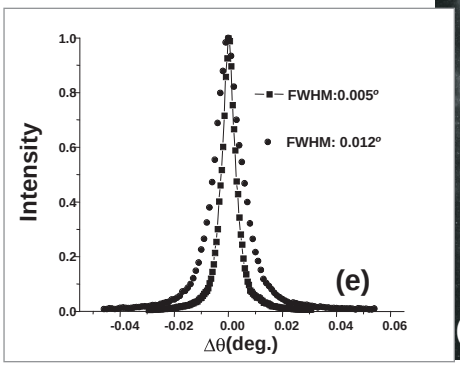

Fig. 1. (a) Phase-contrast x-ray diffraction image of a lysozyme crystal showing individual line defects (D), originating at the initial nucleus, and inclusions (I). (b) Phase-contrast x-ray image of the corresponding crystal. (c) and (d) reveal a dehydration-induced microstructural change. (e) 4 4 0 rocking curves; the square and round data points correspond to (c) and (d), respectively.

at the APS. A Si(111) double-bounce monochromator was used to deliver a "monochromatic" beam with DE/E ~0.01%; a six-circle Huber diffractometer was employed along with a scintillation detector and a charge-coupled-device camera to perform rocking-curve and imaging measurements.

Well-faceted and optically defect-free tetragonal HEWL and cubic ferritin crystals were loaded into quartz capillaries and fully bathed in the incident x-ray beam for the measurements. Reflections of choice were picked up for diffraction imaging using rays that had exited the crystal. By properly changing the object-to-detector distance, the researchers were able to optimize the phase contrast effects, which allowed a variety of defects to be observed in great detail for the first time. Sets of high-angular-sensitivity x-ray diffraction images of the HEWL crystals revealed defects such as dislocations, dislocation loops (or half loops), and additional structural features. The enhanced defect contrast resulted primarily from the strong phase contrast effects produced by "defocusing." Rich contrast structures were observed with uniformly grown ferritin crystals, as well. Not only were individual dislocations running in a specific orientation resolved, which originated at the central growth region of the protein crystal, but also a microstructural change induced by dehydration was mapped throughout the crystal (Fig. 1).

The work demonstrates that lattice defects and irregularities in weakly scattering protein crystals can be thoroughly mapped by simply incorporating the phase information of exiting x-rays into diffraction imaging. The direct mapping of the defect distribution and variations in intrinsic structural quality across an entire crystal can offer insights into macromolecular crystal perfection and growth, and have an impact on structural biology as well. Applying this approach to biological macromolecular systems could provide a new way to characterize structural defects, their properties, and the causes of lattice disorder in a wide spectrum of macromolecular crystals. ❍

See: Z.W. Hu[1], B. Lai[2], Y.S. Chu[2], Z. Cai[2], D.C. Mancini[2], B.R. Thomas,[1,3] and A.A. Chernov[1], "Phase Sensitive X-Ray Diffraction Imaging of Defects in Biological Macromolecular Crystals," Phys. Rev. Lett. **87**(14), 148101-1 to 148101-4 (1 October 2001).

Author affiliations: [1]NASA/Marshall Space Flight Center, [2]Argonne National Laboratory, [3]University of Alabama in Huntsville

This research was supported by NASA under NCC8-66-050 and an ITD award. Use of the Advanced Photon Source was supported by the U.S. Department of Energy, Office of Science, Office of Basic Energy Sciences, under Contract No. W-31-109-Eng-38.

Using Soft X-rays for Macromolecular Structure Determination

SER-CAT (APS sector 22) is currently testing procedures for the optimal use of soft x-rays for macromolecular structure determination. A focused Cr-radiation x-ray source (λ = 2.29 Å) at the University of Georgia is serving as a convenient test bed for handling data collection and structure determination techniques related to the use of longer-wavelength x-rays. For most elements, including calcium, sulfur, and many metal atoms, the anomalous scattering signal (delta F´´) using 6-7 keV x-rays is significantly larger than that observed using 12 keV x-rays. Soft x-rays could potentially enhance the use of these atoms and metal atoms as internal phasing probe(s) when they are naturally present in the crystal.

Using high-intensity chromium radiation (λ = 2.29 Å), a test bed for optimizing data collection with synchrotron soft x-ray beams has been developed, with the aim of advancing direct crystallography at SER-CAT, as well as at in-house facilities. Direct crystallography, structure determination from underivatized native protein crystals relies on the accurate detection of a single-wavelength anomalous scattering (SAS) signal from sulfur and/or metals present in the native protein crystals. Since the anomalous scattering signal strength for an atom depends on the energy of the x-rays used in the analysis and generally

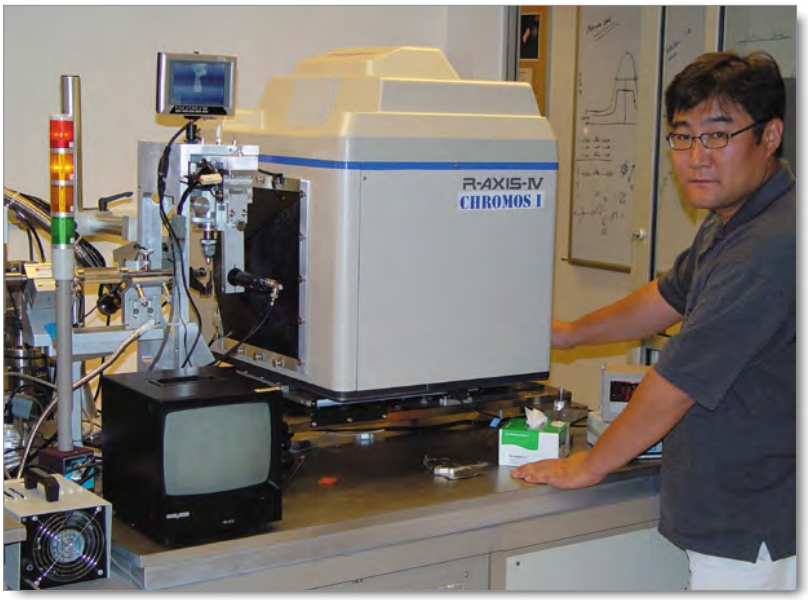

Fig. 1. University of Georgia researcher Doowon Lee sets up an experiment on the CHROMOS I soft x-ray test bed. The test bed consists of a chromium rotating anode, special chromium confocal focusing optics, and a commercial image-plated detector modified with a helium beam path and low absorbing windows.

increases with wavelength, soft x-rays ($\lambda \sim 2$ Å) should offer a means of increasing the sulfur anomalous scattering signal strength in the data, if absorption, which also increases with increasing wavelength, can be addressed.

An obvious source of soft x-rays is synchrotron radiation, because the wavelength of the x-rays produced is in the range of 0.6 to 2.3 Å, depending on beamline configuration. However, most modern beamlines are optimized for data collection near the selenium absorption edge at ~0.97 Å, dictated by the requirements of the selenomethionine multiple anomalous dispersion experiment. Little attention has been paid to optimizing performance in the 1.5- to 2-Å wavelength range required for successful sulfur SAS data collection. The CHROMOS I soft x-ray test bed shown in Fig. 1 will allow SER-CAT to develop and refine soft x-ray data collection strategies without using valuable synchrotron beam time. The CHROMOS I test bed will also be used to set initial benchmarks for beamline optimization using soft x-rays. *(Contact J. Chrzas, chrzas@ anl.gov)* ❍

Scanning Monochromatic DAXM as a Tool for Micron-resolution Lattice Dilatation and Curvature Measurements

The study of the interactions of large deflection bending strains and anticlastic curvature provides important clues for understanding the deformation of cylinders, cone-like structures, spheres, and shells under stress. Such knowledge is valuable for fundamental materials science as well as a wide range of technological design and construction applications. Although white beam differential-aperture x-ray microscopy (DAXM) has been used for the study and measurement of strain and anticlastic bending with micron resolution in three dimensions (3-D), it is not possible to determine dilatational strain, using white beams. Collaborators from Oak Ridge National Laboratory and Howard University have developed a scanning-monochromatic version of DAXM that makes µm-resolution 3-D studies of local lattice dilatations and tilts possible. Investigators from Oak Ridge National Laboratory and Howard University, using the MHATT/XOR (sector 7) and UNI-CAT (sector 34) microbeam capabilities at the APS, have demonstrated this new form of DAXM by measuring Poisson strain gradients and anticlastic curvature in strongly bent silicon.

The experimenters cylindrically bent a thin rectangular silicon plate, 25 µm in thickness by 10.6 mm in length by 8.74 mm in width, into an arch with a principal bend radius R = 3.06 ±0.02 mm at the center, giving a Searle parameter of $\beta = 1009$. In contrast to the 20-50 Bragg reflections that must be depth-profiled using white beam DAXM, the scanning monochromatic DAXM technique is more simple in that it uses only one Bragg reflection, which is profiled by a 50-µm platinum wire and a charge coupled device detector. To obtain the Bragg energy for each depth measured, a two dimensional scan of the x-ray microbeam energy versus the platinum wire position was performed with least-squares fitting to locate the center of the energy distribution.

White microbeam Laue diffraction measurements showed anticlastic rotations of nearly 0.3° at the edges of the silicon arch that decay in the middle of the arch to a series of approximately 0.01° to 0.02° oscillations that persist across the width of the arch.

Comparison of the anticlastic curvature measurements observed with those predicted by Fopl-Von Karman equations (using anisotropic, closed form solutions) yields some interesting results. At the edges of the silicon plate, the measured anticlastic rotations agree well with those predicted by the Fopl-Von Karman calculations, reaching the R/ν radius of curvature limit for distances of less than the plate thickness from the edge, where ν is the anisotropic Poisson's ratio. On the other

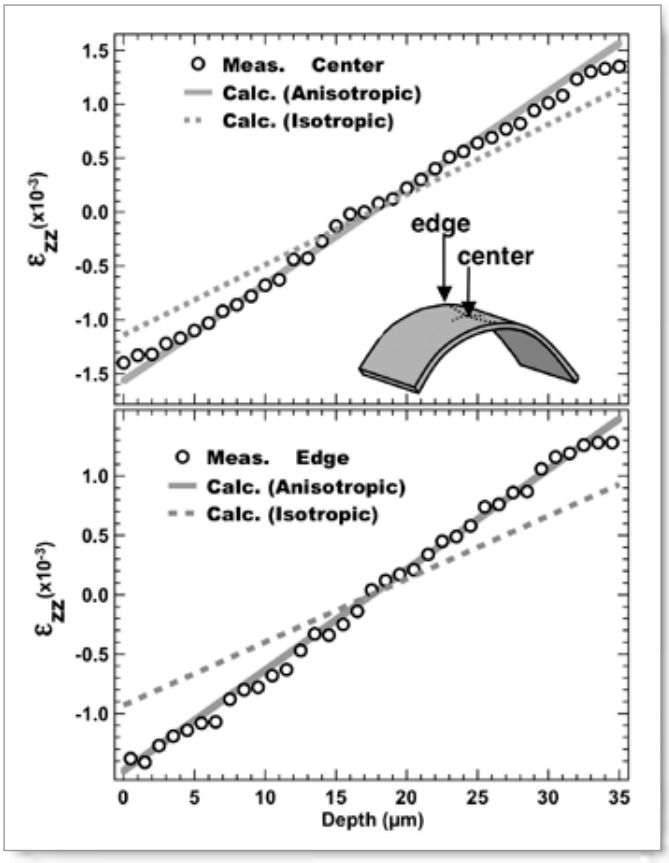

Fig. 1. Micron-resolution depth-resolved measurements and anisotropic calculations of Poisson strain as a function of depth in cylindrically bent silicon. The strain ε_{zz} is the fractional change in the lattice spacing normal to the surface.

hand, the small but persistent oscillations observed across the center of the arch are much larger than 100 times the amplitude predicted by linear elasticity and finite element calculations.

Micron-resolution depth-resolved Poisson dilatational strain was measured as a function of depth both at the center and the edge of the arch. As shown in Fig. 1, the depth-resolved dilatation measurements are consistent with the anticlastic curvature modified strain values predicted from anisotropic linear elasticity calculations, within the $\pm 10^{-4}$ measurement uncertainty.

This scanning-monochromatic extension of DAXM makes it possible to measure absolute lattice parameters with micron spatial resolution in three dimensions for the first time. Moreover, it has several advantages over white beam techniques: it requires profiling of only a single Bragg peak, it can provide local lattice tilts as well as dilatations, and, since energy scans are usually less than a few hundred electron volts, it is possible to use chromatic focusing optics such as Fresnel zone plates, as well as achromatic focusing mirrors. ❍

See: W. Yang[1], B.C. Larson[1], G.E. Ice[1], J.Z. Tischler[1], J.D. Budai[1], K.-S. Chung[1], and W. P. Lowe[2], "Spatially resolved Poisson strain and anticlastic curvature measurements in Si under large deflection bending," Appl. Phys. Lett. **82**(22) (2 June 2003).

Author affiliations: [1]Oak Ridge National Laboratory, [2]Howard University

This research was sponsored by the US Department of Energy, Basic Energy Sciences, Division of Materials Sciences under Contract No DE-AC05-00OR22725 with Oak Ridge National Laboratory, managed by UT-Battelle, LLC. Work performed on the MHATT/XOR beamline at the APS was supported in part by DOE Grant No. DE-FG02-99ER45743; UNI–CAT is operated by UIUC, ORNL, NIST, and UOP Research, Inc. Use of the Advanced Photon Source was supported by the U.S. Department of Energy, Office of Science, Office of Basic Energy Sciences, under Contract No. W-31-109-Eng-38.

A Deep Parabolic Refractive Lens for X-rays

A deep parabolic lens made from lithium has been demonstrated by researchers from the University of Michigan and the Experimental Facilities Division of the APS, together with a colleague from a small research and development company, Ecopulse. The first lithium-based x-ray optic was a multiprism collimator that was relatively easy to make and quite useful, thanks in part to its adjustable focal length, but it could not image. The lithium parabolic lenses have constant focal length and collimate x-rays very well, too, but they also are imaging devices. With future versions of these lenses, 6-keV to 12-keV x-rays can be used, as in conventional visible optics, for imaging, microscopy, etc. Refractive lenses from lithium are uniquely promising for future x-ray sources with very high power levels, such as the Linac Coherent Light Source at the Stanford Linear Accelerator Center in Palo Alto, California, and the Tesla high-gain, single-pass, free-electron laser at the DESY laboratory in Hamburg, Germany.

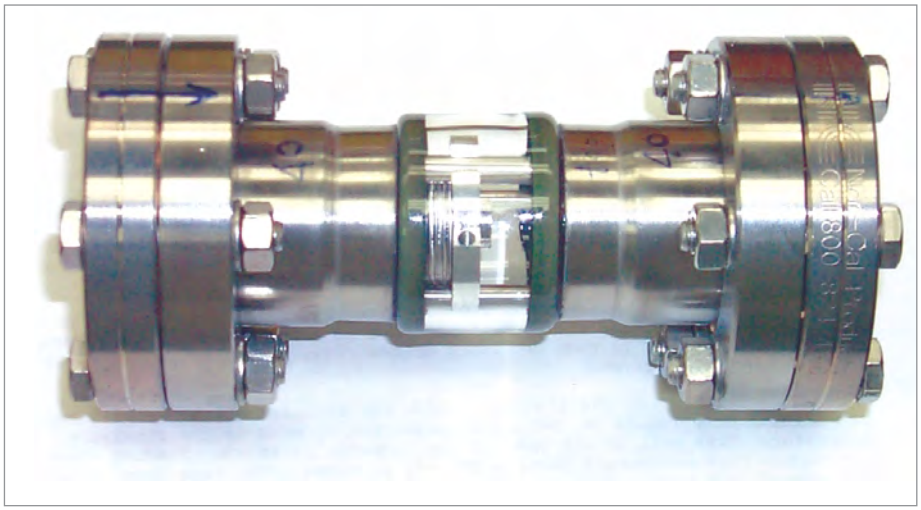

Fig. 1. Lithium lens package.

Lithium corrodes easily when it is in the open atmosphere, so the lithium lens is carefully packed in a hermetic enclosure with beryllium entrance and exit windows. The present package, as shown in Fig. 1, is simply a 2.75-in. conflat nipple that fits the standard manipulation stages. Alignment is easy, because the lens's optical axis is close to the nipple's symmetry axis. Figure 2 shows a 23-fold demagnified image of the (2-sigma) 680-µm-wide and 28-µm-high x-ray source at the MHATT/XOR 7-ID beamline. The width of the primary image is 30 µm, as it should be, but the height of the image should be 1 µm, not the 5 µm that is the resolution limit of the diagnostics (a scintillator screen observed through a microscope by a charge-coupled device camera). The 20-fold gain in intensity as measured by the diagnostics is largely consistent with the resolution-limited image and the 60% transmission of the x-rays, but it is many times lower than the 300-fold increase in intensity expected from an ideal image. Another problem is reflected in the image's imperfect shape: some x-rays end up next to the main image, and a few outliers even form a wide halo. These problems come from deviations of the ideal parabolic shape and should disappear with better manufacturing procedures.

The lens designs in this work are standard and were demonstrated earlier at the European Synchrotron Radiation Facility by refractive x-ray lens pioneers such as Snigirev, Lengeler, and colleagues (see, e.g., www.x-ray-lens.de). The

multiprism lens was suggested by Cederstrom (see, e.g., gluon.particle.kth.se/~ceder/). A group at Adelphi Technologies recently made lithium lenses, but of a different design (see www.adelphitech.com and Rev. Sci. Instrum. **74**, 2262 [2003]). ❍

See: N.R. Pereira[1], E.M. Dufresne[2], R. Clarke[2], and D.A. Arms[3], "Parabolic lithium refractive optics for x rays," Rev. Sci. Instrum. **75**(1), 37-41 (January 2004).
Author affiliations: [1]Ecopulse Incorporated, [2]University of Michigan, [3]Argonne National Laboratory

The work of N.R.P. was done with support from MDA through SBIR Contract No. N00178-02-C-3119 and is monitored by the Naval Surface Warfare Center, Dahlgren Division. Work supported in part by DOE Grant Nos. DE-FG02-03ER46023 and DE-FG02-00ER15031, and by the NSF FOCUS physics frontier center. Use of the Advanced Photon Source was supported by the U.S. Department of Energy, Office of Science, Office of Basic Energy Sciences, under Contract No. W-31-109-Eng-38.

Fig. 2. A 23-fold demagnified image of the (2-sigma) 680-μm-wide and 28- μm-high x-ray source on 7-ID.

Ultrafast X-ray Streak Camera

The shot-to-shot timing jitter of an x-ray streak camera developed at XOR 1 was reduced to close to 50 fs when it was triggered by a standard kilohertz laser with 1.2 % root-mean-square pulse energy fluctuation. This was achieved by improving the response time of deflection plates and the rise time of the ramp pulse generated by a photoconductive switch and by operating the photoconductive switch at optimum conditions. Furthermore, after reducing the angular distribution of an electron bunch, the temporal resolution of the x-ray streak camera operating in accumulation mode was better than 600 fs, as shown in Fig. 1 at right. An x-ray test of the streak camera has been performed at MHATT/XOR (sector 7), where a single shot of an APS single-bunch x-ray signal has been observed.

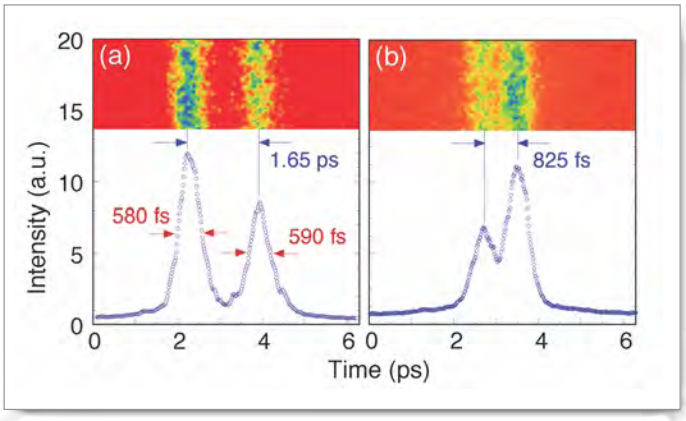

Fig. 1. Averaged lineout of the streak images with corresponding actual images (top) of two 30-fs ultraviolet pulses separated by 1650 fs (a) and 825 fs (b).

See: "An accumulative x-ray streak camera with sub-600-fs temporal resolution and 50-fs timing jitter," J. Liu[1], J. Wang[1], B. Shan[2], C. Wang[2], and Z. Chang[2], Appl. Phys. Lett. **82**(20), 3553-3555 (19 May 2003).
Author affiliations: [1]Argonne National Laboratory, [2]Kansas State University

This work was supported by the U.S. Department of Energy, Office of Science, Office of Basic Energy Sciences, under Contract No. W-31-109-Eng-38.

Dual-Canted Undulators at the GM/CA-CAT Insertion Device Beamlines

Requests for beam time at synchrotron radiation beamlines dedicated to macromolecular crystallography have increased significantly in the past several years, and it is anticipated that this trend will continue. In response to this growing demand, the General Medicine and Cancer Institutes Collaborative Access Team (GM/CA-CAT) was established by two partnering institutes at the National Institutes of Health (NIH). The National Institute of General Medical Sciences (NIGMS) and the National Cancer Institute (NCI) are funding the construction and operation of a national user facility for crystallographic structure determination of biological macromolecules by x-ray diffraction at sector 23 of the APS.

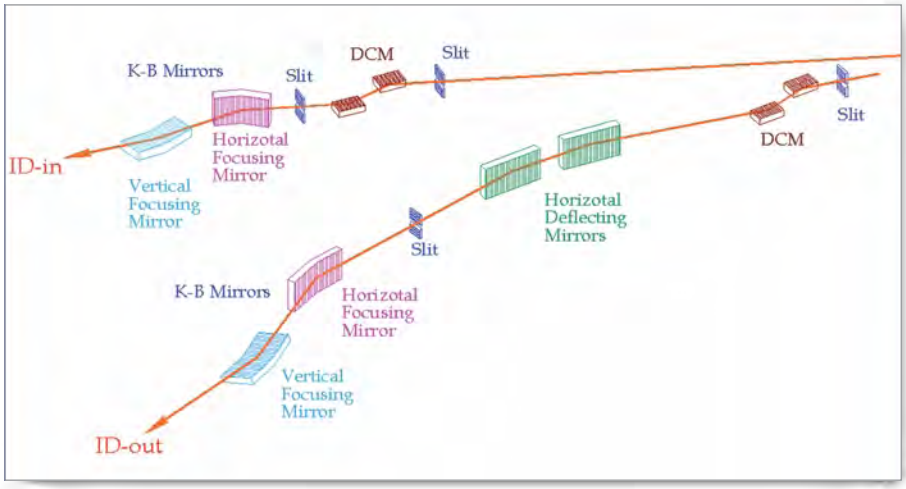

Fig. 1. Schematic view of the x-ray optics of the two ID beamlines.

Beam time will be available to users through the APS general user program and to grantees of the partnering institutes for special programs. The special program of the NIGMS is the Protein Structure Initiative in structural genomics was formed to study protein structural families and structural folds. This project will require the determination of a large number of protein structures in a high-throughput mode. The NCI has a special program for targeted drug design with the goal of transforming the process by which cancer therapeutics and preventatives are discovered, developed, and tested. Structural analyses will be necessary to determine how candidate drugs interact with their protein targets and to further refine drug design. In common with the structural genomics initiative, this will require the most advanced methods for rapid data collection and structure determination of the widest range of protein types at the highest available resolution.

In order to maximize the x-ray beam available to GM/CA-CAT users, the insertion device (ID) beamline at sector 23 has been equipped with the canted undulator configuration developed by the APS in response to the need for efficient use of APS sectors dedicated to macromolecular crystallography (see “Dual-canted Undulators” in the section, “The APS Light Source”). In the dual-canted undulator geometry [1], two hard x-ray insertion devices are placed co-linearly in the same straight section. The first successful implementation of the dual-canted undulator design was demonstrated in August 2003 at GM/CA-CAT sector 23.

Two insertion device beamlines in one sector can potentially double scientific throughput. But the design of the beamlines should allow them to operate independently while not compromising the performance characteristics of the two lines. The 1-mrad separation between the two beams will not accommodate a modern macromolecular crystallography experimental setup with a large-format mosaic charge-coupled device (CCD) detector. So the x-ray optical design must significantly increase the separation between the two beamlines.

In seeking a solution to this issue, GM/CA-CAT considered several possible designs, such as large-offset, double-crystal monochromators (DCMs) diffracting in the vertical or horizontal plane; pairs of white-beam mirrors; and pairs of vertical-deflecting monochromatic mirrors. Each of these designs was rejected for various reasons.

One design goal was minimizing the differences between the two beamlines for operational simplicity (Fig. 1). Each beamline employs a DCM to select the x-ray energy. Both the first and second crystals are indirectly cooled with liquid nitrogen, thereby removing potentially leaky cryogenic seals with the silicon. The outgoing monochromatic beam is maintained parallel to the incident white beam because the two crystals are at nearly the same temperature (77K), i.e., they have the same d-spacing. Dispersion of the Bragg angles of the first and second crystals as a function of energy (tuning error) is minimized by using a 160-mm-long second crystal and eliminating a Bragg parallel motion. The beam can be focused in both the vertical and horizontal plane with a pair of mirrors oriented in a Kirkpatrick-Baez (K-B) geometry [2]. These mirrors are constructed of modular piezoelectric bimorph materials [3]. The vertical focusing mirror has four segments, and each segment contains four electrodes. The horizontal focusing mirror has seven segments, each with two electrodes. The bimorph mirrors are shaped to focus the x-rays by applying a voltage to all the electrodes. By applying slightly different voltages to the various electrodes, one can control the detailed shape and minimize the slope error of the mirrors, resulting in a finely focused beam with minimal tails.

The major difference between the two ID beamlines is the location of the DCM and the addition of horizontal deflecting mirrors (HDMs) for the IDout beamline (Fig. 2). The DCM for IDout is positioned further upstream than the IDin DCM (29 m versus 62 m). The white IDin beam and the monochromatic IDout beam are separated by 30 mm in the vertical direction and 30 mm

in the horizontal direction at 30 m from the center of the two undulators. This allows the pair of HDMs to intercept the monochromatic beam sequentially and further deflect the beam horizontally. The mirrors have a unique "T"-shaped cross section to allow clearance for the neighboring white beam. The HDMs will be oriented at a fixed 4.0-mrad angle of incidence, thereby increasing the separation to 17.0 milliradians between the two beams. The resulting horizontal separation in the outboard experimental station, at approximately 56 m from the source, is ~500 mm. The performance characteristics of the two ID beamlines and the bending magnet beamline are summarized in Table 1. The energy of IDout is limited to 20 keV because of the high energy cut-off of the horizontal deflecting mirrors.

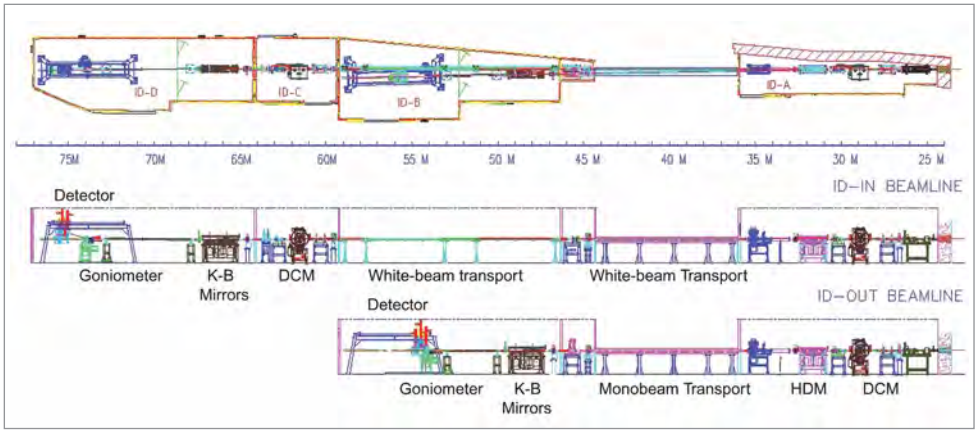

Fig. 2. Plan and elevation views of the two ID beamlines.

The end stations will be designed for streamlined, efficient throughput for a variety of crystal sizes and qualities, representing the cutting edge of structural biology research (Fig. 2). Each ID beamline will be independently tunable for multiwave anomalous dispersion experiments over a wide energy range. They will feature a variable sample-to-source distance, to enhance the control of beam convergence, and rapid-readout, large-format, multi-element CCD detectors, with achievable resolution up to 0.6 Å. Automation of sample mounting, beam alignment, and data collection is incorporated in the design. ❍

This work supported by the NIH National Institute of General Medical Sciences, and the National Cancer Institute. ACCEL Instruments, GmbH, Bergisch Gladbach, Germany has been responsible for the detailed design and fabrication of the beamline components. Use of the Advanced Photon Source was supported by the U.S. Department of Energy, Office of Science, Office of Basic Energy Sciences, under Contract No. W-31-109-Eng-38.

See: R.F. Fischetti[1], J.L. Smith[2], L.E. Berman[3], W. Diete[4], R. Signorato[4], R. Benn[1], S. Stepanov[1], R. Sanishvili[1], S. Xu[1], A. Urakhchin1, O. Makarov[1], and W.W. Smith[1], "Insertion Device Beamlines Based on the Dual-Canted Undulator Concept," in preparation.

Author Affiliations: [1]Argonne National Laboratory, [2]Purdue University, [3]Brookhaven National Laboratory, [4]ACCEL Instruments, GmbH

References

[1] P.K. Den Hartog, G.A. Decker, and L.J. Emery, "Dual Canted Undulators at the Advanced Photon Source," in *Proceedings of the 2003 Particle Accelerator Conference*, 833-835 (2003).

[2] P. Kirkpatrick and A.V. Baez, "Formation of Optical Images by X-rays," J. Opt. Soc. Am. **38** (9), 766-774 (1948).

[3] R. Signorato, O. Hignette, and J. Goulon, "Multi-Segmented Piezoelectric Mirrors as Active/Adaptive Optics Components," J. Synch. Rad. **5**, 797-800 (1998).

Table 1. ID and BM beamline characteristics.

	IDin and IDout	BM
Energy range (keV)	3.5–35, 3.5–20	3.5–35
Energy resolution (%, full vertical opening angle)	<0.02	<0.02
Flux @ 12 keV (photons/sec/100 mA/0.02% BW	>1.0 x 10^{13}	>1.0 x 10^{11}
Harmonic contamination (%)	<0.01	<0.01
Rate of energy change at 6.5 keV (eV/sec)	350	350
at 12.0 keV (eV/sec)	3500	3500
Beam position stability after 100-eV change (% of beam size (FWHM))	<5	<5
Beam position stability after 1000-eV change (% of beam size (FWHM))	<10	<10
Beam size at crystal (µm)	50 × 200 (V × H)	100 × 200 (V × H)
Beam divergence at crystal (mrad)	0.05 × 0.25 (V × H)	0.25 ×2.0 (V × H)

An Unprecedented Look at Rippled Surfaces and Interfaces of Liquids

Viewed with the naked eye, the mirror-like surface of a still liquid appears flat beyond measure. Yet, at atomic length scales, such a surface may be as wrinkled as the back of Methuselah's hand. Researchers rely on x-ray scattering to detect and measure such submicroscopic roughness. A team from the University of Chicago (UC) and the University of Illinois at Chicago (UIC) has developed a spectrometer that provides unprecedented spatial resolution of the features on liquid surfaces and liquid-liquid interfaces. With colleagues from Harvard University, and the University of Queensland, Australia, the researchers recently demonstrated the device's potential in a first series of measurements at the APS.

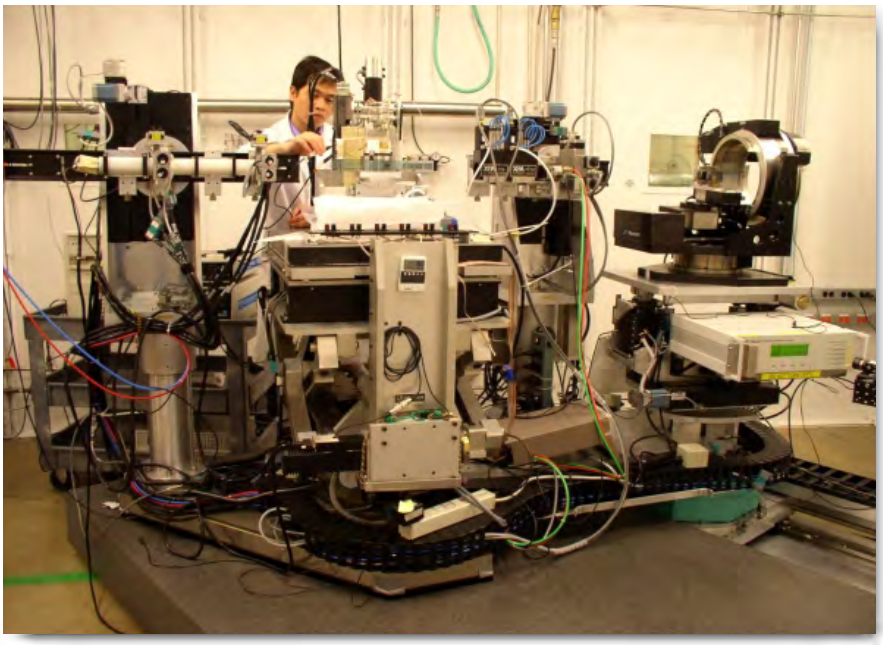

Fig. 1. The liquid surface/interface spectrometer at ChemMatCARS.

The liquid surface/interface spectrometer at the ChemMatCARS-CAT beamline 15-ID (Fig. 1) takes advantage of the high brilliance and wide energy range provided by the beamline. The beam scatters off a single-bounce steering crystal, which directs the x-rays down on to the sample. After scattering from the liquid surface or interface, the x-rays pass into an x-ray detector. Thanks to the beamline optics, the spectrometer can reach higher energies and momentum transfers than similar devices elsewhere. And that means the spectrometer can resolve smaller spatial features and handle a wider range of samples than rival devices.

For example, the researchers measured the specular reflectivity of the interface between a hydrocarbon known as 2-heptanone and underlying water (Fig. 2). Agitated by thermal motion and tugged by surface tension, the interface should ripple with capillary waves, which affect its reflectivity. According to theoretical calculations, those waves should have wavelengths of about 7 Å. By tracking how the reflectivity varied with the angle between the incident beam and the interface, the researchers confirmed the prediction. The beamline can pump out x-rays with energies up to 32 keV, which can penetrate an unusually wide variety of liquids, including water.

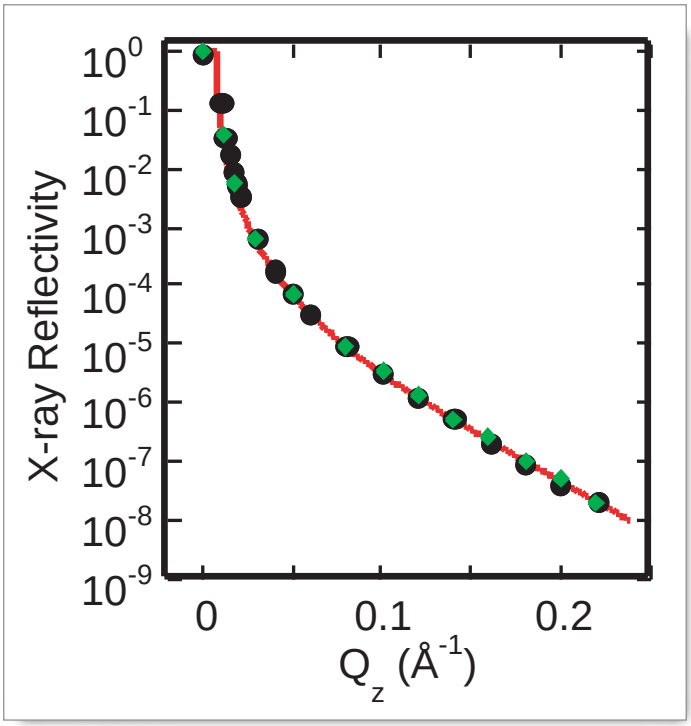

Fig. 2. Data and a fit for x-ray reflectivity from the 2-heptanone/water interface at 25°C. The measured interfacial width is 6.9 ± 0.2Å and can be compared to the value calculated from capillary wave theory of 7.3 Å. The interfacial width is smaller than the capillary wave value, but the discrepancy is only a 2-sigma effect.

The spectrometer's ability to reach high momentum transfer also makes it ideal for studying atomic-scale layering in liquids, such as liquid tin. Theoretical models suggest that, as with other liquid metals, the surface of liquid tin should have a layered structure, with the electron density varying from layer to layer. The structure should affect how the reflectivity of the surface varies with the angle of incidence. Measurements with the spectrometer confirmed these predictions.

The spectrometer can also accommodate bulky samples, such as large vacuum chambers to study liquid metals or Langmuir troughs for the study of single layers of molecules supported by a liquid's surface. For example, the researchers

studied the reflectivity of water covered with a monolayer of chain-like surfactant molecules, one end of which attracted water, and the other end of which repelled it. When compared with a theoretical model, the data indicated that the molecules stood out perpendicularly from the surface, like so many blades of grass in a thick lawn. Similarly, the team studied the reflectivity of disk-shaped porphyrin molecules on the surface of salt solutions. In this case, the data suggested that when the film was gently squeezed laterally with a specialized bar, the molecules began to tilt upward like snake scales, instead of lying flat like lily pads.

The researchers also studied the in-plane scattering from the surface of a dilute gallium-thallium alloy. In these measurements, the scattering changed not only the component of the x-ray's momentum perpendicular to the surface, but also the component of the momentum parallel to it. The scattering varies as a function of in-plane momentum transfer, and such variations revealed the structure of the monolayer of thallium on the surface of the alloy. The spectrometer allows experimenters to probe higher out-of-plane and in-plane momentum transfers than competing devices.

The first measurements only scratch the surface of the spectrometer's capabilities. The facility is open to general users, and future experiments are sure to add many new wrinkles to the science of liquid surfaces and interfaces. ❍

See: B. Lin[1], M. Meron[1], J. Gebhardt[1], T. Graber[1], M.L. Schlossman[2], and P.J. Viccaro[1], "The liquid surface/interface spectrometer at ChemMatCARS synchrotron facility at the Advanced Photon Source," Physica B **336**, 75-80 (2003).
Author affiliations: [1]ChemMatCARS, The University of Chicago, [2]University of Illinois at Chicago

ChemMatCARS is principally supported by a combined grant from the National Science Foundation and the U.S. Department of Energy, Basic Energy Sciences, under grant number CHE0087817. The Advanced Photon Source is supported by the U.S. Department of Energy, Office of Science, Office of Basic Energy Sciences, under contract No. W-31-109-Eng-38.

Demonstrating a Fabry-Pérot Interferometer for Hard X-rays

High-resolution optical devices, such as spectrometers and interferometers, are useful for making precise wavelength measurements in atomic spectroscopy, astrophysics, and many other physical and biological science applications, including use as interference filters and resonators in laser physics. The ability to use such devices when working with x-rays would be highly desirable. However, compared to visible light, x-ray photons have much higher energy and thus smaller wavelengths, making beams of x-rays difficult to reflect off surfaces. If the reflection obstacle could be overcome, x-ray interferometers could be extremely useful as interference filters having micro-eV spectral resolution to study the dynamics of solids, liquids, and macroscopic biological molecules.

Experimentalists from Hamburg University and Argonne National Laboratory, using XOR beamline 3-ID have succeeded in reflecting x-ray light directly backward and producing the first x-ray interference waves by means of a prototype x-ray Fabry-Pérot interferometer. This type of interferometer splits a beam and brings back together portions of the resulting multiple beams to a detector that can measure the interference between them. Since the interfering beams were split from the same initial beam, they were initially in phase. Their relative phase when they meet back at the detector depends on the difference in the lengths of their optical paths. By measuring the phase shifts of the beams, scientists can study the properties of extremely small-scale phenomena.

The primary components of the simplest Fabry-Pérot interferometer are two highly reflecting, low-absorbing parallel mirrors. A standing wave, or multiple reflections, of electromagnetic radiation can be created by adjusting the gap between the mir-

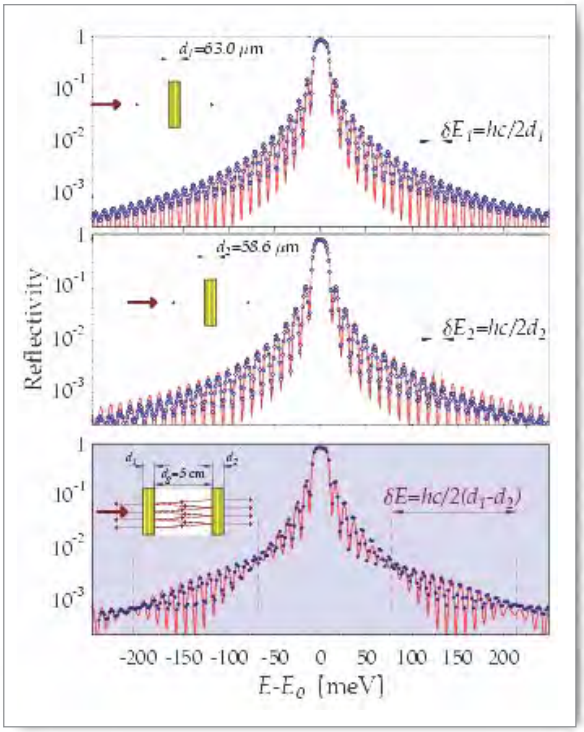

Fig. 1. Energy dependence of reflectivity from the sapphire x-ray mirrors(top) and from the x-ray Fabry-Pérot interferometer (bottom). Additional periodic "beat" modulation in the interferometer spectrum demonstrates a two-crystal interferometric effect (vertical dashed lines). Theoretical spectra (solid red lines) are overlaid on data.

rors to a distance that is one-half the radiation wavelength. Multiple reflections of x-rays had been previously reported in a system with two parallel silicon crystals, but the intensity of the reflected x-ray beams was too low to be useful for interferometry work.

Instead of using silicon crystals, the researchers employed sapphire crystals (α-Al_2O_3) that provided the necessary high reflectivity. The crystals were grown using a heat-exchange method. Dislocation-free samples were chosen after examining the grown crystals by white beam x-ray topography. The sapphire mirrors were placed at a distance of $d_g \approx 50$ mm and aligned parallel to each other to better than 0.3 microradians. Measurements were performed using x-rays monochromatized to a bandwidth of 2 meV before being directed normal to the mirrors with an accuracy of ± 5 microradians. The researchers measured the energy dependence of the interferometer reflectivity (Fig. 1) and the time dependence of the interferometer response to the excitation with 100-ps pulses of the incident x-ray photons.

As the x-ray energy approached the maximum reflectivity of the crystal mirrors, multiple-reflection signals reappeared every 358 picoseconds, with descending strength observed—the result of the x-rays bouncing back and forth between the mirrors. When the x-ray energy matched the maximum reflectivity, a train of more than 30 peaks was observed, produced by ≈ 60 reflections. This and other experimental data showed direct evidence that the prototype two-crystal x-ray Fabry-Pérot interferometer performed successfully. A set of 0.76 micro-eV broad Fabry-Pérot transmission resonances were measured by the time response of the interferometer. Interference patterns were observed directly in spectral dependences of reflectivity (Fig.1).

Future efforts will include (1) developing a combined optical/x-ray Fabry-Pérot interferometer (as sapphire is transparent to visible light, and optical sapphire mirrors can be fabricated using thin-film metalization) to directly link the wavelengths of optical photons and Mossbauer photons (in the x-ray part of the spectrum), and (2) developing interference filters with micro-eV spectral resolution for studying the dynamics of solids, liquids, and macroscopic biological molecules. ❍

See: Yu.V. Shvyd'ko[1], M. Lerche[1], H.-C.Wille[1], E. Gerdau[1], M. Lucht[1], H.D. Rüter[1], E.E. Alp[2], and R. Khachatryan[2], "X-Ray Interferometry with Microelectronvolt Resolution," Phys. Rev. Lett. **90**(1), 013904-1 to 013904-4 (10 January 2003).
Author affiliations: [1]Universität Hamburg, [2]XOR 3, Argonne National Laboratory

Use of the Advanced Photon Source was supported by the U.S. Department of Energy, Office of Science, Office of Basic Energy Sciences, under Contract No. W-31-109-Eng-38.

The Hard X-ray Nanoprobe Beamline at APS Sector 26

A hard x-ray nanoprobe with a spatial resolution of 30 nm is being constructed at APS sector 26. It uses x-rays with photon energies between 3 and 30 keV. This makes most elements in the periodic system accessible for x-ray fluorescence imaging using K and L atomic transitions at attogram sensitivity. Large penetration lengths (e.g., 140 µm in Si at a photon energy of 10 keV) allow imaging of buried features. Diffraction techniques will be used to probe local strain, structure, and orientation.

Two imaging modes, a scanning-probe mode and a full-field transmission mode, will be combined in a single instrument (Fig. 1). In the scanning probe mode, incident x-rays are focused into a small, diffraction-limited spot on the specimen. Photons from secondary processes, such as fluorescence and scattering, are used for image formation. In the full-field transmission mode, the specimen is illuminated by a condensor system, and a magnified image of the specimen in phase and/or absorption contrast is recorded by an area detector behind the specimen. In combination, these two modes fully use the radiation properties of an insertion device at a third-generation synchrotron source. In the *scanning probe mode*, the spatially coherent fraction of the undulator beam is used, taking advantage of the high brilliance provided by the APS. The *full-field transmission mode* uses the

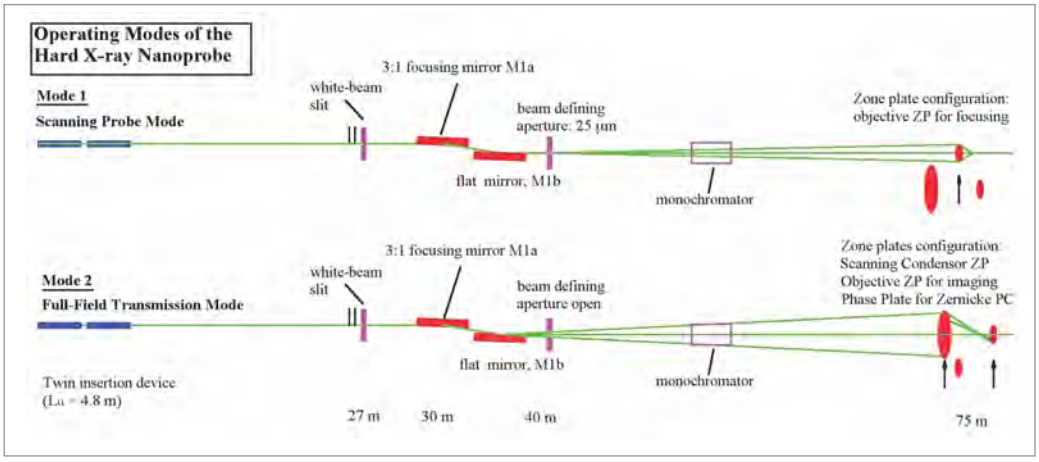

Fig. 1. Design concept for the nanoprobe beamline. An astigmatic beamline design provides spatial filtering in the horizontal direction to match the effective horizontal source size to the vertical beam size. A double-mirror layout provides a fixed exit and higher harmonics rejection. A double-crystal monochromator selects the desired energy. The change between scanning-probe mode and full-field transmission mode is achieved by moving the condensor zone plate, focusing zone plate, and objective zone in and out of the beam.

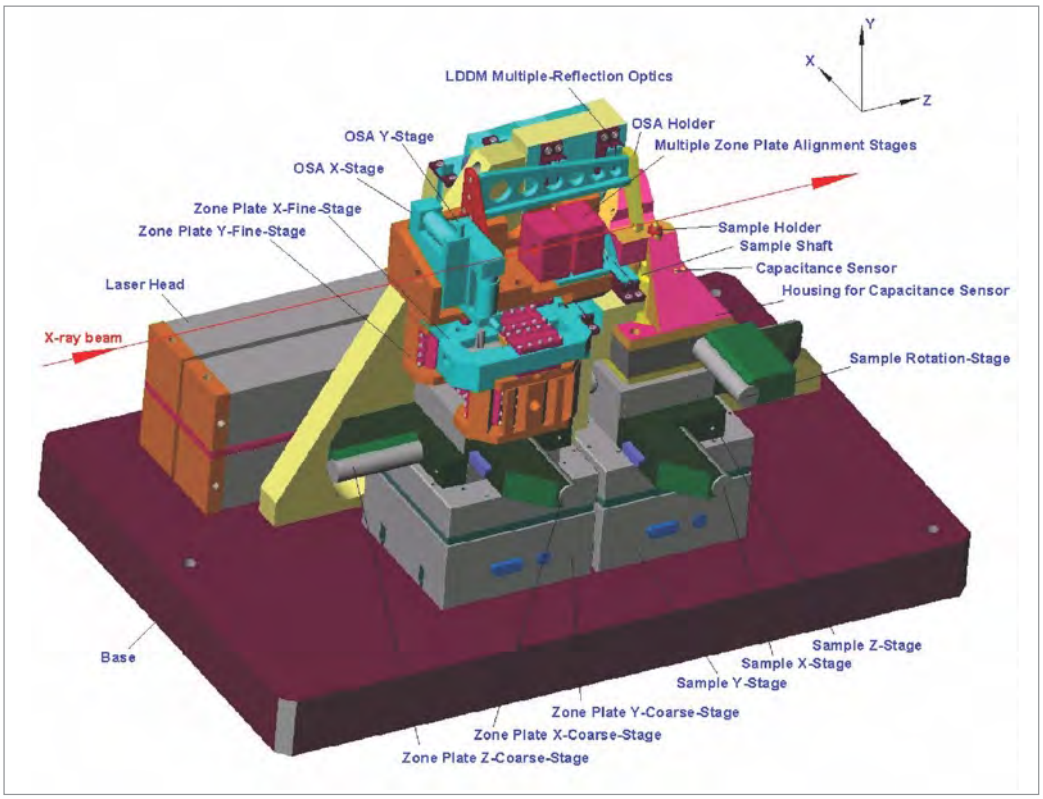

Fig. 2. Mechanical staging and laser Doppler feedback encoder for the hard x–ray nanoprobe prototype instrument.

entire, partially coherent undulator beam. To achieve the highest x-ray optical resolution, we plan to use Fresnel zone plates as focusing and imaging optics.

Two collinear APS undulators A with a period length of λ_u = 3.3 cm were chosen as the source of high-brilliance x-rays. This will maximize the brilliance and thereby the coherent flux in the existing APS ring layout. To provide spatially coherent illumination for the primary scanning probe mode, the beamline employs spatial filtering in the horizontal direction using a horizontally focusing mirror system at 30 m from the source and a horizontal slit (beam-defining aperture, BDA) at 40 m from the source. The mirror system consists of an elliptically bent, horizontally focusing mirror, M1a, and a plane mirror, M1b. This approach provides a fixed exit angle, improves higher harmonics rejection, and reduces the heat load on the components further downstream in the beamline. Using stripes of Pt, Cr, and Si, this double-mirror scheme allows us to tune the cutoff energy to any value between 3 keV and 30 keV. Because the beam-defining aperture is positioned downstream of the mirror, the mirror is always illuminated along its full length and minimizes thermally induced slope errors. A double-crystal monochromator using Si <111> crystals will be placed 65 m from the source. Since no spatial filtering is provided in the vertical direction, slope errors resulting from heat-induced strain on the first crystal are of concern, and cryogenic cooling will be implemented. Several additional auxiliary beamline components are planned, including a crystal polarizer, a large-bandpass monochromator, and a beam chopper.

The nanoprobe instrument will provide spectromicroscopy, nanospectroscopy, and diffraction contrast imaging as well as full-field imaging of two-dimensional (2-D) and three-dimensional specimens, at a spatial resolution of 30 nm. Critical to achieving these goals are the mechanical stability of the zone plate and specimen of 10 nm or better, zone plate motion along the beam axis with a transverse stability of 10 nm, and a single-axis rotation with a run-out of a few 100 nm. High stability is required to allow mapping and imaging at the resolution limit of the zone plates. Motion with high transverse stability is required to achieve nanospectroscopy at the resolution limit. Small run-out of the rotation stage is required to position a specimen for diffraction contrast imaging and to perform tomography in full-field transmission mode.

To provide high-spatial-resolution capabilities to users as rapidly as possible, a prototype instrument that provides these capabilities has been developed (Fig. 2). At the heart of the prototype is a 2-D differential laser Doppler displacement encoder system with a resolution of better than 1 nm. This system monitors the horizontal and vertical positions of the zone plate and specimen stages. The zone plate is mounted on a 2-D flexure stage with a range of 1.5 µm. Using the output of the encoder system, the flexure allows adjustment for changes in the transverse position of the zone plate and specimen at a rate of 100 Hz or better. The encoder system will be of particular use for nanospectroscopy, where the focal length of the zone plate needs to be changed in step with the incident energy. The flexure stage carrying the zone plate and specimen is mounted on commercial dc-motor-driven translation stages with 0.1-mm resolution and a range of 12 mm. A rotary encoder to provide feedback on run-out during specimen rotation is under development. *(Contact G.B. Stephenson, stephenson@anl.gov)* ❍

Using a Diamond Anvil Cell for Structural Investigations of Noncrystalline Materials at High Pressures

Learning how high pressures affect liquids and other noncrystalline materials at the atomic level would open the door to developing a theoretical understanding of their macroscopic properties—such as their viscosity and self-diffusion, electrical resistivity, compressibility, and thermal expansion—under such conditions. Significant progress became possible in this area with the advent of third-generation synchrotron sources, because their high-brightness x-ray beams enable researchers to use the weak x-ray scattering from these materials in deriving detailed atomic-level structural information about them.

A diamond anvil cell (DAC) is usually used in such experiments when very high pressures are sought. Such a cell essentially consists of a metal gasket placed between two diamond "anvils." A tiny hole in the gasket serves as a sample container. Pressure exerted on the diamonds forces them together, thus applying a magnified pressure on the gasket and the trapped sample. Diamond is used because it is the hardest material known and is transparent to x-rays and other forms of radiation. Typical DACs, however, are not suited for liquids and amorphous solids, so researchers from The University of Chicago developed and tested a modified DAC designed specifically for these materials.

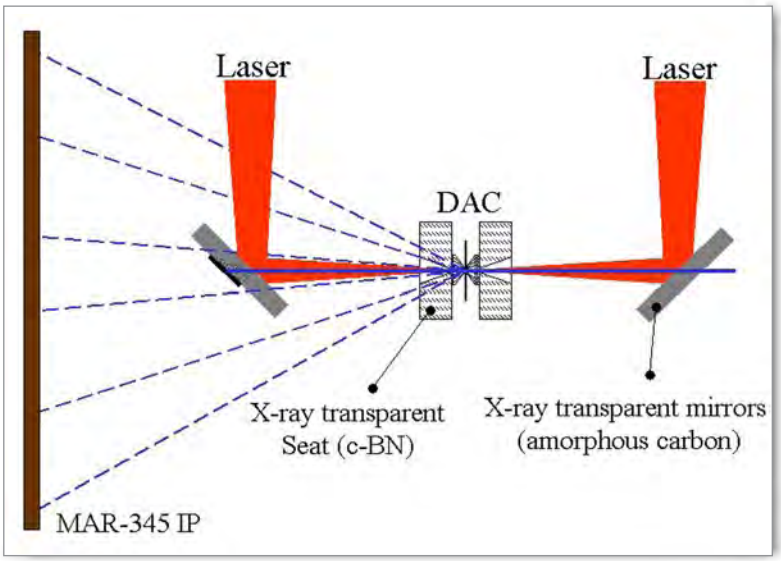

Fig. 1. Schematic of the experimental setup. Samples in the diamond anvil cell can be heated from both sides by a Nd:YLF laser. The laser heating and the x-ray diffraction/scattering and temperature measurements can be made simultaneously with the use of x-ray-transparent, carbon-based mirrors.

Diamond anvils are usually mounted on x-ray-absorbing tungsten carbide (WC) seats, which have conical apertures machined into them to provide x-ray access to and from the sample. A larger opening angle would increase coverage of momentum transfer, which is an essential factor for structural studies of noncrystalline materials. On the other hand, the larger opening angle would leave the seats structurally weakened, thus limiting the amount of pressure that can be applied.

To increase the radiation-admitting cone without machining a cone of larger opening angle, the researchers substituted cubic boron nitride (c-BN) for WC as the seat material (Fig. 1). Boron nitride is second only to diamond in hardness and, unlike WC, is transparent to x-rays. To increase the scattered x-ray signal even more, the researchers modified the gasket so that it would accept thicker samples. The modification involved drilling a relatively large hole in the gasket and filling it with boron epoxy. A much smaller hole was drilled at the center of the boron epoxy for sample loading.

This use of boron epoxy also greatly aided data analysis. Subjecting a DAC to an x-ray beam yields a strong x-ray signal from the DAC's components, in addition to the relatively weak signal from the sample. To isolate the sample's scattered x-rays, it is necessary to subtract the DAC's contribution. This is done by repeating the experiment without a sample in place.

For the signal from the empty DAC to serve as a background reference, all parts of the DAC must be identical to those used for high-pressure data collection. Among these parts, the metallic gasket is most critical. Since the metallic gasket hole serves as an aperture for x-ray scattering from the first diamond, great care must be taken to preserve the location, shape, and size of this aperture. Without the boron epoxy, the metallic gasket hole would inevitably deform under high pressures, making it impossible to have an identical aperture for a proper reference. By introducing amorphous boron (or another x-ray-transparent material) in the gasket, the large metallic hole outside the culet area is only weakly affected by high pressures, and deformations occur mainly in the transparent boron-filled area. This results in a metallic aperture close to that used in high-pressure data collection, thus providing a good background reference.

The utility of the modified DAC was demonstrated by using data for amorphous iron collected at 67 GPa at the GSECARS 13-BM beamline at the APS. The DAC's opening angle of 60° and the APS beamline energy of 37.44 keV (λ = 0.3311 Å) yielded a maximum momentum transfer of 98 nm^{-1}. By further tilting the DAC, the momentum transfer that can be covered was found to increase to 150 nm^{-1}. Researchers learned that the basic polyhedra forming the structure of amorphous iron remain unchanged with pressure.

Although the modified DAC was shown to be ideal for studying amorphous solids, it should be applicable to structural studies of liquids and crystalline materials as well. The large x-

ray access opening should benefit all DAC-based x-ray diffraction measurements, particularly those involving the angle dispersive technique, which is now widely used. The thicker sample capability should aid the study of low-Z materials (low x-ray scattering), while the combination of both of features promises to permit researchers to explore the properties of materials at ultrahigh pressures (>300 GPa), which is important to planetary science. ❍

See: G. Shen, V.B. Prakapenka, M.L. Rivers, and S.R. Sutton, "Structural investigation of amorphous materials at high pressures using the diamond anvil cell," Rev. Sci. Instrum. **74**, (6), 3021-3026 (June 2003).

Author affiliations: GSECARS, The University of Chicago

This work is supported by NSF-EAR 0001149 and 0229987. The GSECARS sector is supported by the National Science Foundation (Earth Sciences Instrumentation and Facilities Program) and Department of Energy-Basic Energy Sciences (Geoscience Program).

High-Temperature Triaxial Deformations at Pressures to 15 GPa

To date, knowledge of the physical and chemical processes taking place deep inside the Earth has come primarily from global-scale observations. Earth scientists have recognized, however, that gaining a full understanding of the structural and dynamic properties of the Earth's interior requires the integration of global-scale seismological and other geophysical observations with computer modeling based on laboratory simulations of high-pressure, high-temperature environments. Because of technical difficulties, the effects of high pressure on materials remain far less well studied than those of high temperature or changes in material composition. This situation is changing, however, thanks to new analytical techniques.

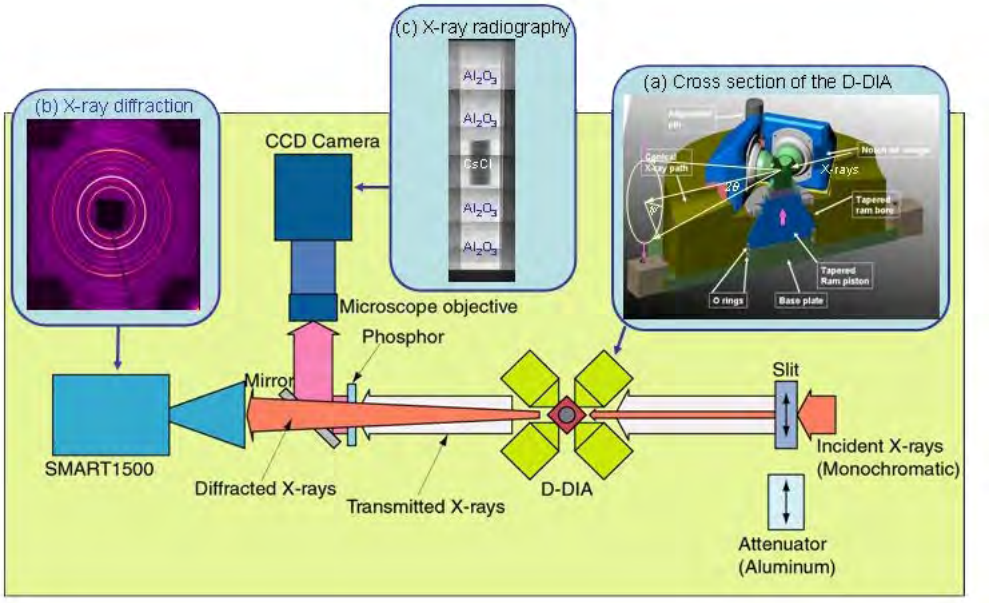

Fig. 1. Current GSECARS experimental setup for high-pressure, high-temperature deformation experiments. (a) The D-DIA, (b) Debye rings used in lattice strain analysis, and (c) x-ray absorption contrast image of sample converted to visible light by using a YAG single-crystal phosphor.

Researchers from The University of Chicago, Lawrence Livermore National Laboratory, the University of Colorado, and the State University of New York at Stony Brook collaborated in developing and testing a new high-pressure deformation apparatus that is capable of generating pressures up to 15 GPa at high temperatures (up to ~2000°C). This apparatus is a modification of the cubic-anvil apparatus known as the DIA, which is widely used in solid-media hydrostatic compression experiments that involve synchrotron x-ray diffraction. The apparatus takes advantage of recent developments in the use of synchrotron radiation, thus making it possible to perform quantitative deformation experiments under pressure and temperature conditions that extend down to the transition zone between the Earth's upper and lower mantle.

A DIA consists of six anvils. Four of the anvils face each other in the horizontal plane, while the other two face each other vertically. The square fronts of the anvils thus define a cubic volume at the center of the apparatus. The force of a single hydraulic actuator (or ram) applied along the vertical axis closes the DIA's guide blocks, thus compressing the cubic sample/furnace assembly.

The new apparatus, called the deformation-DIA (or D-DIA), features independent control of the displacements of one anvil pair, which is provided by two additional hydraulic actuators, called differential rams. The differential rams are located within the guide blocks of the D-DIA module and react against the platens driven by the main hydraulic ram that is responsible for hydrostatic pressurization. The unique capability of independently controlling the differential rams allows the imposition of a differential strain and stress field without simultaneously increasing the confining pressure. This capability overcomes a longstanding limitation of multi-anvil devices.

The researchers have successfully tested the D-DIA at both the National Synchrotron Light Source, using the SAM85 multi-anvil system, and at the APS, using the 250-ton hydraulic press at the GSECARS sector 13 bending magnet beamline. Tests with synchrotron x-rays have demonstrated that the D-DIA is capable of generating up to 30% axial strain on 1-2-mm-long samples under confining pressures up to 15 GPa at simultaneous high temperatures. Various compressive strain rates from 10^{-3} to ~2 x 10^{-6} s^{-1} have been achieved. Extensional experiments have also been successful. Strains are measured by using x-ray imaging, which has an ultimate length measurement precision of ~0.1 µm, while pressures are monitored by using standard materials with well established equations of state. X-ray-transparent anvils made of sintered polycrystalline cubic boron nitride have been successfully tested, by using a two-dimensional x-ray charge coupled device detector. Distortions in diffraction lines due to differential stress can be measured with a precision of about 20 MPa.

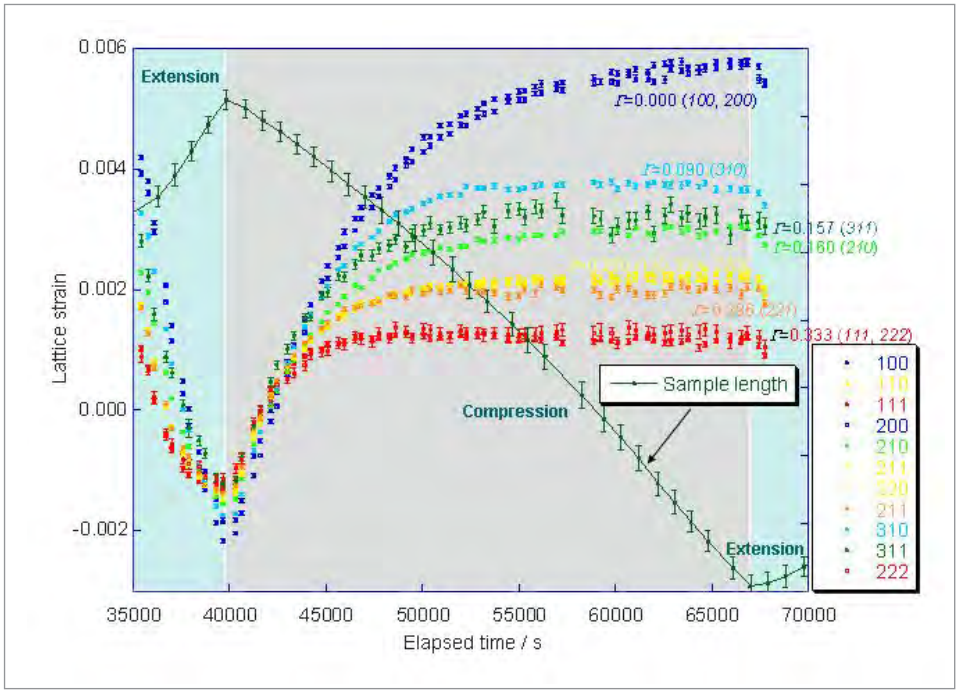

Fig. 2. Measurements of lattice strain in CsCl using 11 diffraction lines, plotted as a function of elapsed time during the first extension-compression deformation cycle. The x-ray wavelength was 0.19 Å (65 keV); spatial resolution in the length measurements was 1-2 µm. These lattice strains can be used to assess differential stress in the sample, through elasto-plastic modeling. Hysteresis loops have been measured by repeating the extension-compression cycles.

The D-DIA is open for general users at GSECARS (see Fig. 1), where several high-pressure deformation experiments have been performed. As an example, Fig. 2 shows lattice strains in CsCl (a body-centered-cubic material) determined from 11 reflections during both compression and extension, obtained by researchers from The University of Chicago. Saturation in lattice strain with plastic deformation is highly dependent on Miller indices, indicating strong yield anisotropy, even though the material is nearly isotropic elastically. ❍

See: Y. Wang[1], W.B. Durham[2], I.C. Getting[3], D.J. Weidner[4], "The deformation-DIA: A new apparatus for high temperature triaxial deformation to pressures up to 15 Gpa," Rev. Sci. Instrum. **74** (6), 3002-3011 (June 2003).

Author affiliations: [1]GSECARS, The University of Chicago, [2]Lawrence Livermore National Laboratory, [3]University of Colorado, Boulder, [4]State University of New York at Stony Brook

Work performed under the auspices of the U.S. Department of Energy by the Lawrence Livermore National Laboratory under Contract No. W-7405-Eng-48. Portions of this work were performed at GSECARS, Sector 13, APS. GSECARS is supported by the National Science Foundation-Earth Sciences, Department of Energy-Geosciences, W. M. Keck Foundation, and the U.S. Department of Agriculture. Use of the Advanced Photon Source was supported by the U.S. Department of Energy, Office of Science, Office of Basic Energy Sciences, under Contract No. W-31-109-Eng-38.

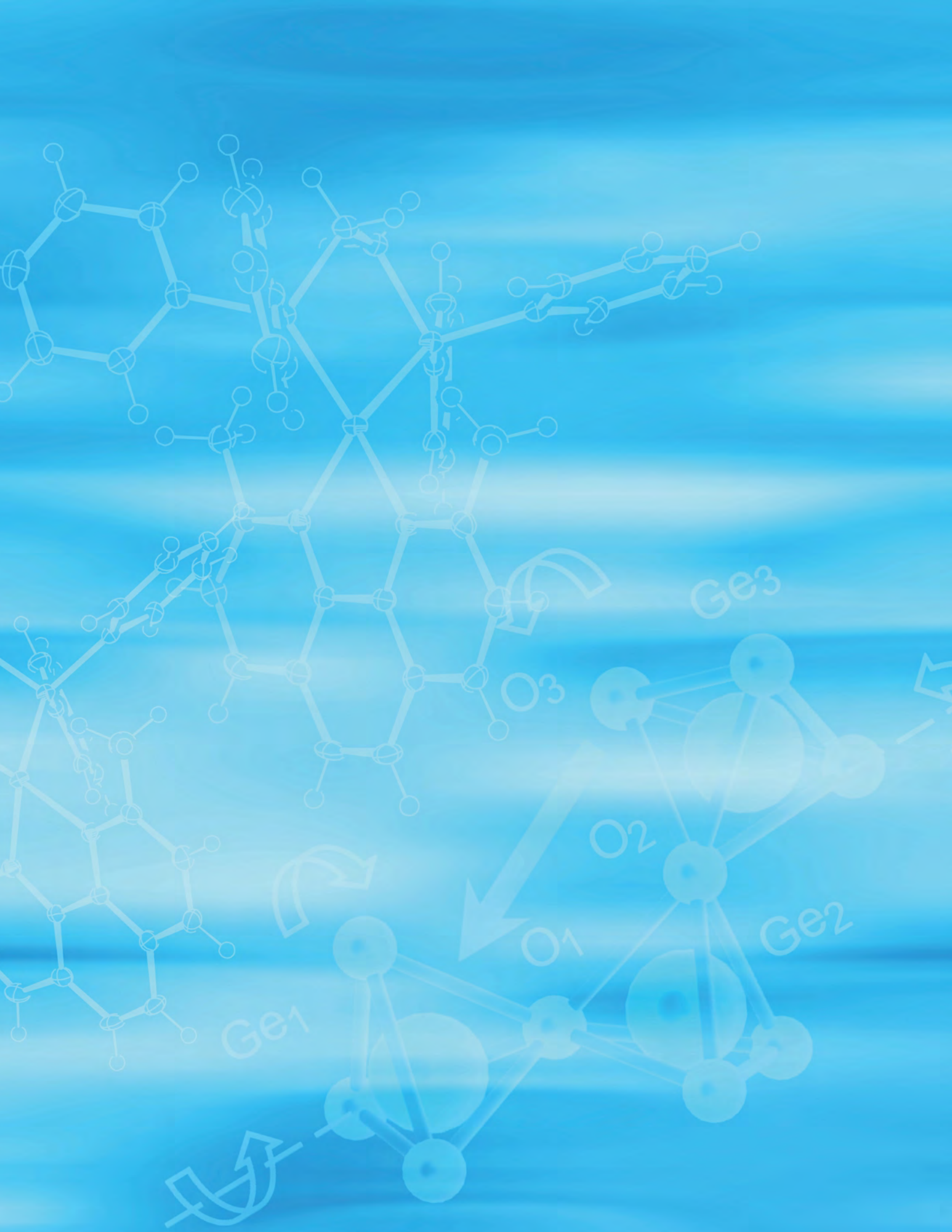
Ge3
O3
O2
Ge2
O1
Ge1

APS Users

APS Users

More than 5,000 members of the synchrotron radiation research community are users of the APS. As the number of APS users continues to increase, the APS facility and organization are evolving, finding new ways (and improving established practices) of serving the client base. Whether these changes involve reorganized groups or technological innovation, the goal is always to provide an environment where users can make the most of their time here. Reflecting the current reality of a maturing facility, a rapidly growing and evolving user community, and a greater facility role in operation of DOE-BES-supported sectors, APS ALD Murray Gibson committed an increased portion of the fiscal year 2003 budget to user support.

The APS User Program

User Access to the APS

Scientists and engineers who use the APS are granted access through several different scientific peer-review processes. Early APS users were all members of collaborative access teams (CATs)—groups who built, funded, managed, and used APS beamlines following scientific approval by a high-level peer-review body, the Program Evaluation Board, and administrative approval by the APS. In return, CAT members were allowed to use APS beamlines for 100% of the time during the first year of operation. Following that first year, they were allowed to use 75% of the beam time and required to provide the remaining 25% of the time to outside users (first called independent investigators, now general users [GUs]) who submit proposals for limited amounts of beam time. General users come to the APS to do their own research. Unlike CAT members, GUs do not pay for nor operate beamlines. As the APS has evolved, a number of beamlines have transitioned to APS funding and management. These beamlines now make up a much larger percentage of beam time (up to 80%) available to GUs.

In 2003, a new, more flexible, model was developed for users partnering with the APS. These “partner users” include

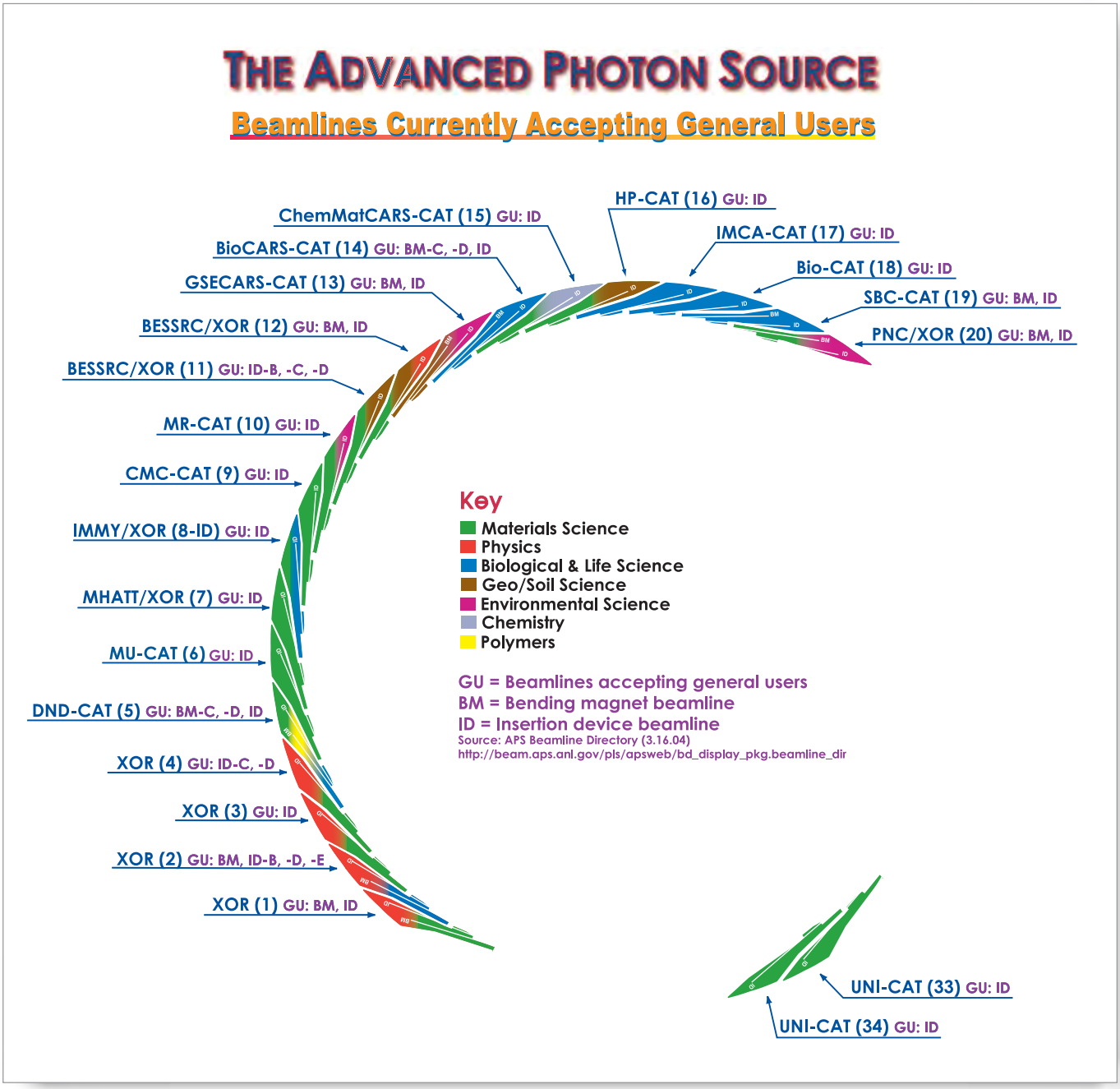

not only CATs and members of previous CATs but also groups involved in focused projects of smaller scope that make lasting improvements to the facility. For example, a CAT, which constructs, finances, and operates one or more beamlines, is considered the most comprehensive type of partner user. More limited partnerships involve the development of dedicated stations, instruments, or capabilities or the establishment of new user committees.

The APS General User Program

During 2003, the first complete year for the fully Web-based GU proposal submission, review, and allocation system (in which individual CAT programs were consolidated into an APS-managed central system), steady increases were seen in the numbers of new proposals and beam-time requests, as well as in the number of beamlines and shifts available to GUs (see Tables 1 and 2, next page).

Two types of GU proposals can be submitted: individual and program. Individual proposals are for single experiments and are valid only until scheduled, whereas program proposals, which are valid for a two-year period, describe research programs that require a series of visits to the APS over an extended period of time. In general, proposals are peer reviewed by one of eight scientific Proposal Review Panels before beam-time allocation and scheduling. However, in some cases, a proposal can be submitted with a rapid-access beam-time request for unallocated time during a current run, and then reviewed retrospectively.

During 2003, 830 new proposals were submitted. For Run 2003-1, the majority being individual proposals (Table 1).

Table 1. General-user requests for beam time during CY 2003.[1]

Run	New individual proposals	New program proposals	Beam-time requests on reviewed proposals	Rapid-access requests	Total beam time requests	Number of requests receiving approval
2003-1	130	100	90	20	340	210
2003-2	230	100	30	70	430	300
2003-3	230	100	100	80	510	320
Total	590	300	220	170	1280	830

[1] All numbers have been rounded. The 90 requests on previously reviewed proposals for 2003-1 represent legacy proposals from a previous system.

However, although the total number of new program proposals remained constant for the three cycles, program proposals remain active for two years, so by year's end, the number of active program proposals had increased significantly. The total number of beam-time requests for the year (1270, also shown in Table 1) provides the best measure of demand. (Beam-time requests must be submitted for each cycle in which a user wants to visit the APS.) Sixty-five percent of the submitted beam-time requests received time during 2003.

The APS Partner User Program

As described above, APS partner users, as differentiated from general users, contribute to the facility beyond performing excellent scientific research, and consequently, they require guaranteed access for longer periods and/or greater amounts of time than can be obtained through the general-user program. Although partner-user proposals for the development of a full beamline or sector can be submitted at any time for any unallocated areas on the APS experiment floor, proposals for developments of more limited scope can be entertained only for sectors where the APS provides full or partial operational support. The first call for partner user proposals of limited scope came in the summer of 2003 for beam time beginning with Run 2003-3. Seventeen proposals were received. Nine of these were approved for periods ranging from 1 to 3 years, with allocated beam time ranging from 5% to 30% per run. Figure 1 shows the six beamlines with approved partner users for Run 2003-3, as well as the percentage of beam time allocated to partner users on each.

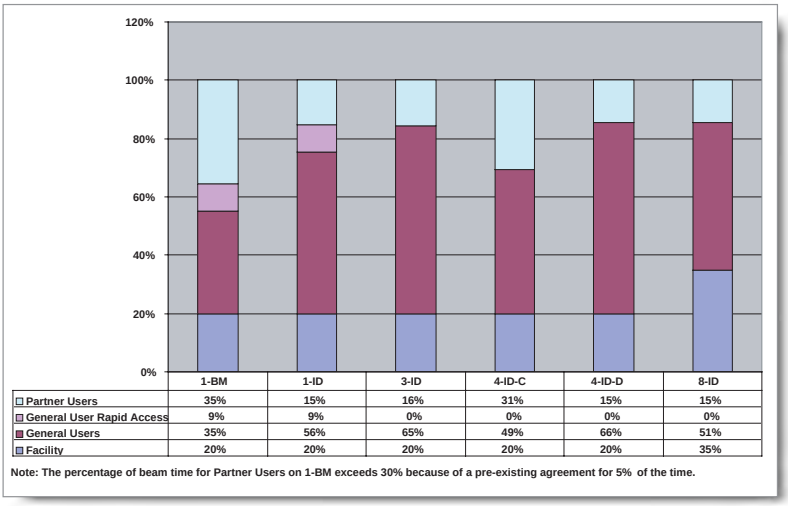

	1-BM	1-ID	3-ID	4-ID-C	4-ID-D	8-ID
Partner Users	35%	15%	16%	31%	15%	15%
General User Rapid Access	9%	9%	0%	0%	0%	0%
General Users	35%	56%	65%	49%	66%	51%
Facility	20%	20%	20%	20%	20%	35%

Note: The percentage of beam time for Partner Users on 1-BM exceeds 30% because of a pre-existing agreement for 5% of the time.

Fig. 1. Beam time by type of user on all beamlines with allocated partner user time for Run 2003-3 (the final run of Calendar Year 2003).

Outreach

To communicate the availability of GU beam time, and to expand the GU base, this year the APS instituted a GU outreach program, which involved the organization of exhibits at specific scientific meetings. These exhibits, staffed by beamline scientists and representatives of the APS User Office, were focused on the research interests specific to each meeting. For example, the first effort, at the American Crystallographic Association meeting in July 2003, highlighted research opportunities in structural biology (Fig. 2 shows the backdrop for the exhibit). At least one-third of the more than 800 meeting atten-

Table 2. Shifts and beamlines available for GUs in CY 2003.

Run	Beamlines available	Regular GU shifts	Rapid-access shifts	National user facility shifts (estimated)[1]	Approximate number of total shifts available
2003-1	32	1920	100	480	2500
2003-2	33	2140	140	720	3000
2003-3	34	2300	130	570	3000
Total		6360	370	1780	8500

[1] National user facility (NUF) shifts are those used and allocated by collaborative access teams that operate entirely on a general-user proposal basis. Proposals are received and reviewed by the APS, but only 25% of the time is allocated by the APS. Since the number of NUF shifts is estimated, the total number of available shifts is approximate.

Fig. 2. Display prepared for the 2003 American Crystallographic Society meeting

Fig. 3. Left to right: Jim Viccaro (Executive Director, Consortium for Advanced Radiation Sources; Principal Investigator, ChemMatCARS, APS sector 15; and Chair, APS Partner User Council), Pedro Montano (Program Manager for X-ray and Neutron User Facilities, DOE-BES), and Alec Sandy (XFD) meet at the APS exhibit at the fall 2003 Materials Research Society meeting.

dees stopped at the APS booth to pick up materials, discuss potential research opportunities, and learn how to use the online proposal submission system. An equally successful venture was an exhibit at the December 2003 Materials Research Society meeting in Boston, which had an attendance close to 5000. Figure 3 is a photo taken at the APS exhibit during that meeting. ❍

News from APS User Groups

The Inelastic X-ray Scattering Collaborative Development Team (IXS-CDT) and the Nanoprobe-CDT at the ANL Center for Nanoscale Materials (CNM) are the 22nd and 23rd research groups, respectively, to sign Memoranda of Understanding (MOUs) for construction of x-ray beamlines at the APS. (Collaborative development teams represent a new kind of partner-user arrangement at the APS. They are similar to the more traditional collaborative access team during the construction and commissioning phases but becomes an APS facility beamline during operations, open to competitive access by both general and partner users.)

IXS-CDT

With strokes from four ceremonial pens at a September 15, 2003, MOU signing ceremony (Fig. 4), the IXS-CDT became the 22nd research group to sign up for construction of x-ray beamlines at the APS. APS staff will construct the IXS-CDT beamline at sector 30 on the APS experiment hall floor. John Hill (Brookhaven National Laboratory) is the Executive Director of IXS-CDT; Ercan Alp (ANL/XFD) is the Managing Director.

Fig. 4. Pens at the ready, ANL Associate Laboratory Director and APS Director Murray Gibson (left); John Hill (BNL), Executive Director of IXS-CDT; ANL Deputy Laboratory Director Donald Joyce; and Miles Klein (U. of Illinois at Urbana-Champaign), IXS-CDT Executive Board Chairman, prepare to sign the IXS-CDT Memorandum of Understanding at a ceremony held at the APS.

The IXS sector intends to be the best in the world for inelastic x-ray scattering, a critical synchrotron x-ray application that takes full advantage of the brilliance from third-generation synchrotrons such as the APS. The IXS-CDT will have two specialized spectrometers: HERIX, a high-resolution inelastic x-ray scattering instrument for studies of lattice vibrations, and MERIX, a medium-resolution spectrometer for electronic structure measurements.

Members of IXS-CDT come both from the existing inelastic x-ray scattering community and from the broader scientific community that could benefit from access to such an instrument. Member institutions are the Massachusetts Institute of Technology; Northeastern University; Princeton University; the State University of New York, Stony Brook; Stanford University; the Universities of Akron (Ohio), California (San Diego), Illinois at Chicago and Urbana-Champaign, Tennessee, and Pennsylvania; and Western Michigan University; the Argonne, Brookhaven, and Oak Ridge national laboratories; the Carnegie Institute of Washington; the Albert Einstein College of Medicine; and Lucent Bell Laboratories.

Planners believe that the strength of IXS-CDT lies in a broad scientific program ranging from condensed matter physics to polymer science and biology, and the resources that members bring to the consortium. Understanding the dynamics of a material's molecular system is crucial from a number of perspectives. For researchers interested in hard condensed matter, a given system is completely described by the relaxed electronic state of molecules (called the "ground state") and the excitations from that ground state. From a soft condensed matter perspective, the propagation of sound waves and other density fluctuations determine the response of the system to time-varying probes—a key aspect of the properties of a material.

< Artist's rendering of the Center for Nanoscale Materials at Argonne National Laboratory.

Fig. 5. Construction of the Nanoprobe beamline officially begins with MOU signatures from (left to right): Derrick Mancini (CNM Project Manager), Eric Isaacs (CNM Director), Murray Gibson (ANL Associate Laboratory Director for the APS), Hermann A. Grunder (ANL Director), and G. Brian Stephenson (Director, CNM Nanoprobe Beamline).

Nanoprobe-CDT

On December 4, 2003, the MOU between the APS and the Center for Nanoscale Materials CDT was signed by principals from ANl, APS, and CNM (Fig. 5). The MOU allocated APS sector 26 to the CNM and authorized the CNM to begin construction and commissioning of the hard-x-ray Nanoprobe beamline.

The Nanoprobe beamline will be the centerpiece of the x-ray characterization facilities at the CNM, one of five Nanoscale Science Research Centers being constructed at the Department of Energy's national laboratories. The CNM is a $72 M federal/State-of-Illinois partnership for designing, synthesizing, fabricating, and characterizing materials at the nanoscale. The CNM user facility will provide the scientific community with a broad complement of tools, including the Nanoprobe and other advanced nanocharacterization, nanolithography, and synthesis tools. CNM users will be equipped to explore problems in nanophotonics, nanomagnetism, bioinorganic interfaces, nanocarbon, and complex oxides.

The Nanoprobe, which is being constructed by the CNM organization within ANL, is the CNM's premier nanocharacterization tool, designed to afford capabilities for fluorescence, diffraction, and transmission imaging at a spatial resolution of 30 nm or better. Funding for the Nanoprobe beamline is provided by DOE's Office of Basic Energy Sciences as part of the CNM equipment budget. The Nanoprobe is expected to advance the state of the art in nanoscience by providing the highest-spatial-resolution hard x-ray beamline in the world. With advanced zone plate optics and an optimized beamline

design, the performance goal is to provide a spatial resolution of 30 nm, a spectral range of 3 to 30 keV, and a working distance between the nanofocusing optics and the sample in a range of 10 to 30 mm. This unique instrument will not only be key to the specific research thrusts of the CNM but will be of very general utility to the broader nanoscience community.

The design and features of the Nanoprobe were developed with input from a broad user community, which met at several workshops. These included the workshop on "X-rays and Nanoscience" held in 2000; the "Workshop on Nanoscale Science using Synchrotron Techniques" held in 2001 concurrently with the APS Users Meeting; a separate workshop for the CNM in 2001; and a fourth workshop on "Institutes and Facilities for Nanoscience," held during the 2003 APS Users Meeting. All four workshops were well attended, attracting hundreds of potential users who provided valuable feedback.

The BioCARS BSL-2/BSL-3 Facility: A Resource for Solving Virus & Toxin Structures

The Biology Consortium for X-ray Research (BioCARS, APS sector 14) is a national user facility that fosters frontier research in the field of macromolecular crystallography. BioCARS provides state-of-the art facilities and scientific and technical support for structure determination of macromolecules by standard x-ray diffraction techniques (such as the multiple-wavelength anomalous diffraction technique). But the facility is also designed for two special tasks that set it apart from other centers for macromolecular crystallography at the APS and nationwide. The BioCARS beamline 14-ID can serve as both a monochromatic and polychromatic x-ray source. The polychromatic capability is essential for conducting time-resolved x-ray diffraction experiments that utilize the Laue technique. These experiments result in molecular movies depicting biologically important macromolecules as they perform their function. The other special feature of the BioCARS facility is that, as the result of planned substantial HVAC upgrades, all three experimental stations will be embedded in a Biosafety Level (BSL) 3 containment, unique at the APS and nationwide. This permits safe research with biohazardous materials classified as Biosafety Level 2 or 3 agents, such as human, animal, or plant viruses and toxins.

Agents classified as BSL-2 involve a broad range of indigenous moderate-risk agents that are present in the community and associated with human diseases of varying severity. Immunization or treatment for these agents is available. Examples include the measles and hepatitis B viruses, and *Salmonella.* Agents classified as BSL-3 are indigenous or exotic agents that may cause serious and potentially lethal human diseases as a result of exposure by the inhalation route. Examples of BSL-3 agents include *M. tuberculosis*, St. Louis encephalitis virus, and *Coxiella burnetii*. The guidelines for BSL-2 and BSL-3 facilities, described in the "Biosafety in Microbiological and Biomedical Laboratories" CDC/NIH publication (Fourth Edition, May 1999), require special safety equipment as well as a special facility design for the handling of BSL-2 and BSL-3 materials. Manipulation of all BSL-3 agents is done in a Class II biosafety cabinet (Fig. 6) that serves as the primary barrier. The facility is physically separated from access corridors and must be maintained under negative pressure with respect to the APS experiment hall while BSL-2 and BSL-3 experiments are being conducted. The air flows into the laboratory and is exhausted via a HEPA filter out of the APS building. Mandatory special operating procedures for BioCARS users and staff are being developed. They describe in detail the rules for conducting BSL-2 and BSL-3 experiments and responding to incidents and emergencies, as well as the safe disposal of any waste generated during such experiments.

Fig. 6. BioCARS biosafety cabinet in use.

The primary scientific and practical expertise for the work with BSL-2 and BSL-3 agents resides with BioCARS users. Many virus crystallographers nationwide already use the BioCARS facility for their research projects. In this expanding field of national importance, BioCARS is in a position to play an important role as the only synchrotron-based x-ray diffraction laboratory that can be used for the safe study of these samples. The facility is to be fully operational in 2004 *(Contact K. Brister, brister@cars.uchicago.edu.)*

Bio-CAT Helps Facilitate Fiber Diffraction Network

A number of Biophysics Collaborative Access Team (Bio-CAT) researchers, including Bio-CAT director Tom Irving, are helping to lead the newly formed, National Science Foundation-funded project "FiberNet," which coordinates the development of biological fiber diffraction methods, focusing particularly on computational methods. Activities will include the development and integration of software for biological fiber diffraction and exchange of information about fiber-diffraction methods through retreats, workshops, and a public Web site.

Perhaps the best-known achievement of fiber diffraction was the determination, 50 years ago, of the DNA structure by Crick and Watson, using the fiber diffraction data of Rosalind Franklin. Fiber diffraction continues to be an active and important area of structural biology, focusing on large biological assemblies, such as viruses and muscle fibers. The use of fiber diffraction in biological structure determination has been reviewed by Chandrasekaran and Stubbs (2001). Many biopolymers are long helical structures and have a natural tendency to form fibers. This tendency severely impedes the growth of single crystals. Even if crystals can be grown, the molecular interactions in the crystals rarely correspond to the biologically significant interactions in the fibers. Conventional crystallography is, therefore, often not applicable to these systems. Fiber diffraction is a powerful technique for determining the structural details of such polymers.

In the new network, software applications particularly concerned with structure determination and model refinement will be adapted to various platforms, integrated with the suite of programs available through the British Collaborative Computational Project for Fibre Diffraction (CCP13), and made available to the scientific community. New software will be developed where existing software is inadequate. The network software will be complementary to CCP13 software; together, they will eventually cover all aspects of biological fiber diffraction.

The network will also integrate U.S. fiber-diffraction groups with each other and with the world fiber-diffraction community, particularly with CCP13. This will be done through workshops organized by the core participants, including workshops at the Bio-CAT facility at the APS, and through partial sponsorship of sessions organized by the Fiber Diffraction Special Interest Group of the American Crystallographic Association (ACA SIG).

Membership in the network and participation in its activities will be open to all who are interested in the development of fiber diffraction. Through the ACA SIG, the user group of Bio-CAT, CCP13, and the network's own Web site, the group expects to reach virtually all interested parties. Network activities will directly impact the fiber diffraction community, particularly the biological fiber diffraction community, in the U.S. and internationally. They will also benefit the small-angle-scattering community and other groups using diffraction methods to study partially ordered molecular structures. Stay tuned for the release of the Web site address. More information on Bio-CAT can be found at http://www.bio.aps.anl.gov.

See: R. Chandrasekaran and G. Stubbs, "Fibre diffraction," *International Tables for Crystallography, Vol. F: Crystallography of Biological Macromolecules*, M.G. Rossman and E. Arnold, eds., 444-450 (Kluwer Academic Publishers, The Netherlands, 2001). *(Contact G. Stubbs (FiberNet Director), stubbs@vanderbilt.edu, or T. Irving, irving@iit.edu.)*

Nadia Leyarovska (left, the University of Georgia and SER-CAT) and Zhongmin Jin (the University of Georgia and SER-CAT) logging in crystal shipment for the Mail-In Crystallography Program.

Beamline Time Sharing at SER-CAT: Mail-in Crystallography & Remote User Participation

A major long-term goal for the Southeast Regional CAT (SER-CAT) is realizing the concept of providing its members with time-sharing of beam time. The purpose of this goal is to maximize the use of members' yearly allocated beam time (proportional to the shares that a member owns), increase the flexibility and frequency of a member's access to SER-CAT's beamlines, and reduce the travel expenses needed for data collection. Toward these ends, SER-CAT has initiated a mail-in crystallography program for members in order to work out the logistics of administering such a program. In the 2003-2 APS run (January-March 2003), a total of 24 h of beam time in five slots were allocated to the mail-in program, and SER-CAT staff collected data for nine research groups from seven institutions.

There is a disadvantage to mail-in crystallography because users cannot actively participate in the data collection. However, SER-CAT personnel are planning to test the feasibility of user remote participation through fast internet communication with resident scientists at SER-CAT's beamline. Once this program is implemented, a user sitting 10 feet or 1,200 miles from the experimental hutch can conduct research via actively participating in data collection and interacting with SER-CAT on-site personnel. This is one of several areas of research SER-CAT is pursuing to provide its members with the most effective use of available beam time for synchrotron macromolecular crystallography. *(Contact J. Chrzas, chrzas@anl.gov)*

UNI-CAT 34-ID Beamline Up & Running

The University-National Laboratory-Industry CAT has declared the sector 34 undulator beamline operational.

The 34-ID insertion device beamline is a dual-purpose beamline that supports coherent x-ray diffraction and x-ray microprobe techniques. This beamline is designed and constructed in a tandem configuration (not to be confused with the canted undulator configuration) based on a single APS undulator A and uses a horizontally deflecting mirror to split the beam into pink- and white-beam branches. The pink beam supplies a coherent x-ray diffraction (CXD) experiment with a general-purpose diffractometer. A diamond-crystal monochromator may be inserted to permit studies with monochromatic radiation. The white-beam branch provides a microfocus diffraction (MFD) experiment and includes an optional monochromator in the third optics enclosure. Both experiments are brilliance limited and can accept only a fraction of the divergence from the source. For this reason, the beam-splitting mirror, which divides the undulator beam, does not compromise the flux in either experiment.

The coherent x-ray diffraction experiment station, 34-ID-C, contains a specialized goniometer, which permits both vertical and horizontal scattering geometries and accommodates an ultrahigh-vacuum chamber to permit studies at clean surfaces.

Fig. 7. Wenjun Liu (University of Illinois) aligns a sample and prepares for a differential aperture scan in the 34-ID-E microbeam station.

A Kirkpatrick-Baez (K-B) focusing mirror system provides micron-scale beams that preserve the beam coherence.

The microbeam station at 34-ID-E, as shown in Fig. 7, produces x-ray beams that are routinely 0.4 µm x 0. 4 µm or better for use in diffraction or fluorescence techniques using K-B focusing mirrors. The specially designed micromonochromator allows the selection of either white or monochromatic conditions with a fixed focal spot on the sample. Diffraction techniques with this small spatial resolution permit careful examination of the stress-strain state of materials. Newly developed differential aperture microscopy techniques permit the microprobe to reveal diffraction information in order to determine the structure and/or orientation of small volumes within a solid sample and to provide spatial resolution of better than 1 µm in all three dimensions.

The development of the CXD instrument was funded by the Major Research Instrumentation program of the National Science Foundation, while the microbeam experimental capabilities were sponsored by the DOE Office of Basic Energy Sciences. In addition, through the Illinois Board of Higher Education, the State of Illinois has provided considerable support for construction and continuing operations. *(Contact P. Zschack, zschack@anl.gov.)* ❍

User Support

New User-Support Personnel

The **Beamline Technical Support Group (BTS)** works from the premise that each sector need not require its own complement of specialists. The BTS Group applies technical and administrative expertise to user instrument and facility engineering and design, the spare-equipment pool, and a dedicated material handler, and facilitates user access to a variety of APS resources, such as AutoCAD.

The **User Technical Interface** is the person empowered as the primary contact point between users and the three APS divisions in matters related to beamline technical information. This person assures the quality and availability of the huge storehouse of documentation needed by APS operations staff, as well as the users, for successful beamline operations in accordance with APS policies and procedures.

User Policy and Planning is the responsibility of the individual who works in close cooperation with users to establish the policies and procedures that govern researchers' access to the APS and their workplace activities while they're here. This person also coordinates user support activities that require interaction between APS organizations, including records and material handling; interdivisional beamline construction schedules; exchanges between users and APS technical staff regarding the installation of beamline shielding, utilities, personnel safety systems, front ends, and insertion devices; and reviews of beamline design and management and safety plans.

As the first APS ombudsman, this person is also a conduit to APS management for other issues raised by users.

Minimizing Beamline Downtime

Causes (and duration) of user-beam downtime at the APS due to accelerator equipment problems have been tracked and analyzed dating back to the inception of operations. Beginning in 2003, the Experimental Floor Operations (EFO) Group maintained statistics on downtime incurred by beamlines due to systems failures.

Floor coordinators catalog downtime as it occurs, recording details about each event and its resolution. Floor coordinators and systems personnel may access this information online while troubleshooting problems. Systems managers also analyze patterns in the data in order to preempt systems failures before they occur. Members of the EFO Group are also responsible for reviewing downtime events on a weekly basis and providing a report for APS management.

Minimizing the possibility of power interruptions at the APS beamlines was a priority in 2003. The first phase of emergency-power capability for the beamlines consisted of installing additional transformers and electrical panel boards for distribution of beamline-specific electricity throughout the experimental hall. During the second phase, each beamline's specific needs are assessed, and emergency power distributed accordingly.

Enhanced Sample Oversight & Experiment Capabilities

In order to allow users more freedom to study a wide variety of soils, the APS applied for and received a U.S. Department of Agriculture (USDA) permit to receive and manage regulated soil samples.

All foreign soils are regulated, as well as domestic soils from the Southeastern United States and a few other locations. Because of the many environmental dangers involved with transporting regulated soils and the organisms that they may contain, the USDA issues permits only to those organizations that can demonstrate safe handling, storage, and disposal of regulated soils. The APS has established protocols that meet and exceed the USDA standards.

There are presently 11 APS beamlines that have had and continue to schedule experiments involving radioactive samples. As the number of experiments at the APS involving radioactive samples continues to increase, the responsibilities of Material Balance Area (MBA) custodians, who track and monitor radioactive samples from arrival at the APS through use in an experiment and then removal from the facility, have been expanded to include all radioactive samples that arrive at the facility, not just those designated by DOE.

In order to expand APS experimental capabilities, beamline 10-ID was equipped with an exhaust system consisting of a roof-mounted chemical/radioisotope exhaust fan with and outside air bypass damper and intake, and HEPA filter. The exhaust system provides ventilation for the 10-ID-B experimental enclosure and for adjacent specialty gas cabinets. Experiments using flammable gasses such as 100% hydrogen and ethylene can now also be performed by making use of this exhaust system but bypassing the HEPA filters.

Computing

LOM Network Upgrade

The network switch/router providing network services to each laboratory/office module (LOM) was upgraded to a Cisco Catalyst 4507R switch/router, which provides redundant supervisor engines in case of hardware failure of the primary supervisor. This switch has a 64-Gbps switching fabric with a throughput of 48 Mpps. This configuration gives all ports gigabit connectivity and each sector now has an additional six copper ports and eight fiber ports. The gigabit uplinks to these switches are connected redundantly to a pair of core switches. If one core switch should fail, then the LOM switch will continue to operate from the other core switch with no downtime. The 4507R delivers integrated resiliency, and non-blocking Cisco Express Forwarding-based layer 2/3/4 switching is built in.

Cyber Security

Keeping the APS and its users in compliance with DOE and Argonne cybersecurity regulations and policy requires maintenance of security on more than 700 Windows-based workstations and servers, 200 Macintoshes, and nearly 400 Sun workstations and servers, plus 110 Linux workstations and servers. Toward this end, a new server was installed for patch monitoring and deployment. This server allows the latest patches to be pushed out to client machines outside normal work hours. This reduces downtime and keeps users' computing systems safe from attacks. Computing systems at APS sectors were configured to conform with network security requirements, and user access to APS servers and data was secured using encrypted connections such as VPN. Network security scans are continually reviewed, and new issues are resolved as they are discovered. Security for remote users is increased via patches, virus scanners, and firewalls so that accessing the ANL network does not compromise network security.

New Application Servers

The installation of three new Citrix MetaFrame servers replace the aging Carbon, Copper, and Calcium servers, and provide a new Web interface for secure access to APS Citrix servers. Users can access the Web Interface internally and externally. These servers will run the latest ANL-wide applications such as Paris, AMOS, Comet, and other business applications. The new servers provide users and sectors with more flexibility in accessing ANL business applications through a browser from anywhere by using secure channels with minimal configuration. The browser interface facilitates ease of use with any computing platform, allowing Apple, Sun, and Linux systems to run Windows applications as needed. The user sectors in the APS experiment hall will not be required to set up VPNs or other methods to traverse the APS firewall to access these systems.

Other upgrades during 2003 included SunFire 3800 servers for hardware redundancy and dynamic reconfiguration for central computing services, controls development work, accelerator operations, and ORACLE database services; and two Veritas NetBackup servers for remote Sun server backup.

XOR Computer & Network Support

As part of an ongoing program to keep XOR's computing technology current, and to anticipate future needs of the XOR user community, a number of XOR server computers were upgraded to new hardware during 2003. These servers, which provide a wide range of network services to XOR users including Web, printing, authentication, and other distributed data services and secure access to the XOR network for outside users, are new, low-profile, rack-mount computers that save valuable computer room floor space while providing better performance and higher reliability. At the same time, all XOR servers were moved to a new gigabit Ethernet network for improved performance. Also during 2003, Computer Support assumed responsibility for computer and network support for IMMY-CAT (now IMMY/XOR, sector 8). An ongoing effort to standardize computer configurations with the rest of XOR is under way in order to update computer and network management practices and procedures to accommodate IMMY/XOR and other user groups, as administrative responsibility is transferred to the APS Information Technology Group.

X-ray Optics Fabrication & Metrology

The Deposition Laboratory

The Optics Fabrication and Metrology (OFM) Group deposition laboratory has recently made multilayers of exceptional quality. Narrow-bandpass multilayers with bandpasses less than 1% are difficult to make because they require many thin layers stacked very reproducibly. Good interface abruptness is needed to yield good reflectivities. Multilayers and crystals are both Bragg-diffracting optics, but, whereas crystals have atomic lattices dictated by nature that do the diffracting, diffraction from multilayers occurs from a stack of sputtered layers that can be engineered.

Results for a theta-two-theta scan (i.e., for Q scanned along the surface normal) are shown in Fig. 8. These data were obtained with a Cu x-ray tube (8-keV x-rays) on a system designed to rapidly obtain such data for the deposition laboratory. The multilayer consisted of 300 periods of a WSi_2/Si bilayer and was grown in the large deposition chamber. This combination was chosen for study because the chemical interdiffusion at the interface is expected to be more stable than for W/Si multilayers. As obtained from these data, the tungsten silicide layers were 0.965-nm thick, and the silicon layers were 1.005-nm thick, yielding a period of only 1.970 nm. This same multilayer has been measured at beamlines, and the results shown were in reasonable agreement with these data. The bandpass was measured to be 0.55%, and reflectivity was measured at MHATT/XOR to be 50%.

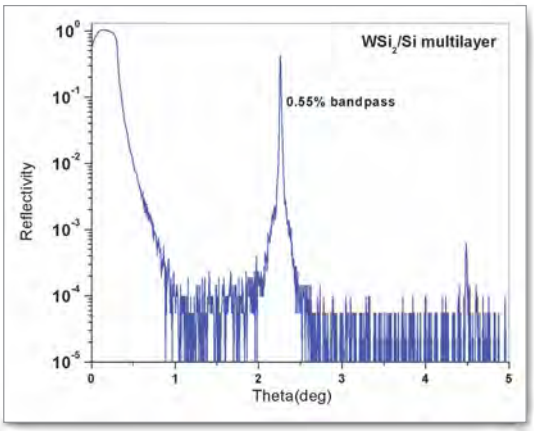

Fig. 8. Theta-two-theta scan of multilayer made with CuKα radiation.

Measurements at ChemMatCARS also confirmed these results.

Narrow-bandpass multilayers are useful in applications that require higher flux than can be obtained with a crystal monochromator but without an unacceptably large sacrifice in Q resolution (e.g., for small-angle scattering experiments).

The Metrology Laboratory

Stitching of interferometry data, using small-aperture, high-resolution phase-measuring interferometric systems, offers the potential for providing three-dimensional (3-D) measurements of the surfaces of long grazing-incidence mirrors with nanometer resolution over a range of spatial wavelengths much wider than that of a conventional long trace profiler (LTP). Obtaining a 3-D surface profile can be useful in many instances, such as selecting the best reflecting stripe on a mirror surface to be used. Thus, for undulator beams, the data can be used for simulating and predicting mirror performance under realistic conditions.

A stitching system using a standard 100-mm-aperture Fizeau interferometer is currently being developed at the APS metrology lab. Preliminary tests performed on a 460-mm-long flat float-glass substrate and on a 300-mm-long superpolished silicon substrate were encouraging. The stitched profiles showed no obvious overlap errors, and the results are in close agreement with those obtained by using the APS LTP. Figure 9 (next page) compares the power spectral density (PSD) profiles obtained from the LTP data and the corresponding stitched profile for the 460-mm float-glass substrate. The two profiles showed an overall agreement, despite the fact that the stitching measurements were performed in a nonideal environment.

At short spatial wavelengths (i.e., higher spatial frequencies) the PSD from LTP data showed a linear fall, while that from the stitched data exhibited a bump centered around the ~3.3-mm wavelength. The exact origin of the discrepancy is not known at this time. Efforts to improve the environment parameters (i.e., temperature stability and vibration) are currently under way. Finally, the high-frequency limit is set mainly by the interferometer charge-coupled device (CCD) detector resolution. The interferometer used in this work has only 256×256 pixels; a more modern interferometer can be equipped with a CCD detector that has as many as 1024×1024 pixels or more.

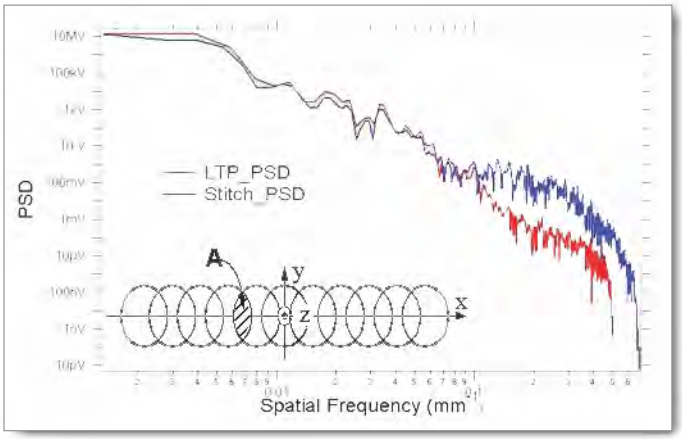

Fig. 9. Comparison of the power spectral density profiles obtained from the LTP data and the corresponding stitched profile for the 460-mm float-glass substrate. The overlap region for the stitched areas is labeled as "A."

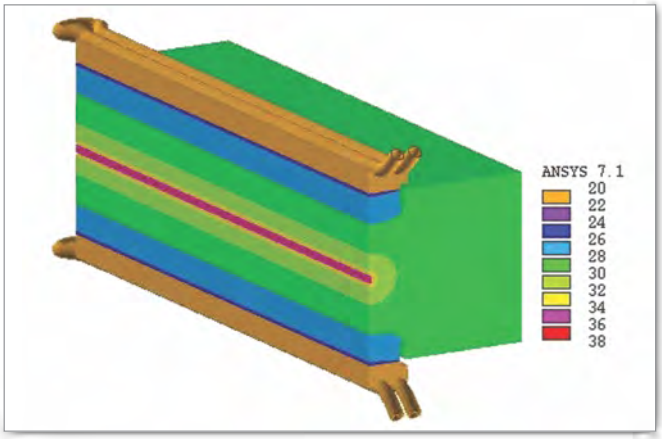

Fig. 11. Results of calculations for the temperature of the proposed Nanoprobe beamline side-cooled mirror. The calculations were made by using finite-element-analysis methods.

THE X-RAY CHARACTERIZATION LABORATORY

Crystalline diamond plates are quite attractive for use as monochromators for undulator radiation and are, in fact, used at several APS beamlines. Unlike Si, little work has been done in attempting to improve the diffraction properties of diamonds by polishing and etching the surface. To fill this technological void, a program to study the diffraction properties of the near-surface region of diamonds has been undertaken by the OFM Group. The study shows that rocking curves can be narrowed by as much as 17% by etching the diamond surface.

X-ray topography is a standard means to image lattice deformations. Conventional topographic images (i.e., those with the entire sample illuminated) are limited because the penetration depth varies over the surface. This occurs because the penetration depth is a sharp function of the differing diffraction angles of possible mosaic regions. To address this depth resolution issue, tomographical techniques have been employed in a topographic arrangement at XOR beamline 2-BM to limit the imaged region to within ~25 µm of the surface. A comparison of the two types of images is shown in Fig. 10. The tomographic-topographic image in Fig. 10(b) reveals linear features that appear to be crystallographically oriented.

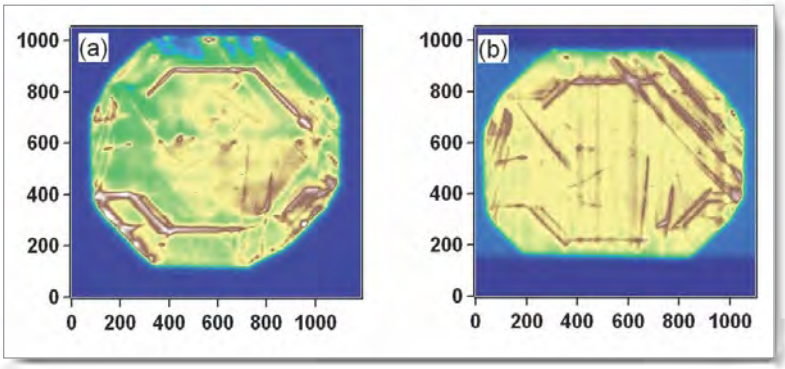

Fig. 10. (a) A (224) topographic image (with the entire sample illuminated at once) of a (001) oriented diamond plate at 12.0 keV with a two-theta angle of 90°. (b) A tomographically depth-limited topographic image for the same diamond under the same diffraction conditions, where the depth is limited to ~25 µm below the surface. (Data for a small portion of the sample are missing near the bottom of the figure.) The axes units are charge-coupled device pixel numbers; the diamond was 6 mm × 4 mm in area with a thickness of 0.5 mm.

OPTICS DESIGN

The Nanoprobe beamline will incorporate x-ray focusing optics to deliver soft and hard x-ray beams down to the nanoscale in size. In addition, high-resolution imaging, diffraction, coherent scattering, and high-throughput tomography are planned for the Nanoprobe. The beamline will have two collinear undulator A's (3.3-cm devices).

The first optics encountered by the combined x-ray beam from the two undulators is a high-heat-load focusing mirror (Fig. 11). This mirror is designed to handle the beam coming from both undulators together at closed gap, producing a normal heat flux of 340 W/mm^2 at the mirror location (i.e., 30 m away). The beam strikes the mirror at 0.15°-2.1°. The mirror is 500 mm long and 75 mm × 75 mm in cross section. The incident beam footprint is 500 mm long and 0.5-1.0 mm wide. The incident beam power can be as high as 600 W. The mirror must be cooled in such a way that the slope of any deformation along its length is under 1 µrad. The optimally side-cooled mirror shown in the figure meets this specification for a robust mirror, for which low maintenance and high reliability are the expected norms. Two water-cooled copper blocks in contact with the mirror remove the heat and, together with the two slots cut along the mirror length, suppress tangential errors to an acceptable level. As seen in the temperature contours shown in Fig. 11, the maximum temperature is under 40°C. The mirror material is single-crystal silicon. It will be polished to a roughness of less than 1 Å rms and a figure error of less than 1 µrad *(Contact: A. Macrander, atm@aps.anl.gov)*. ❍

Increase in APS users, by fiscal year

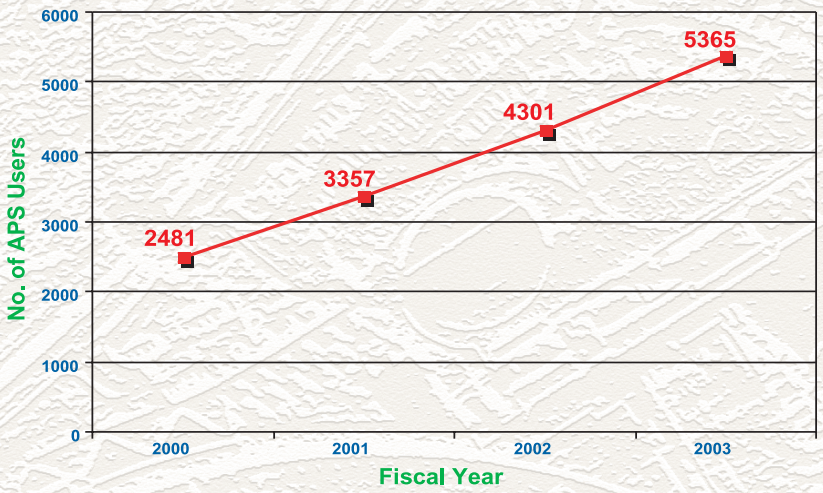

Users carrying out experiments at the APS, by fiscal year

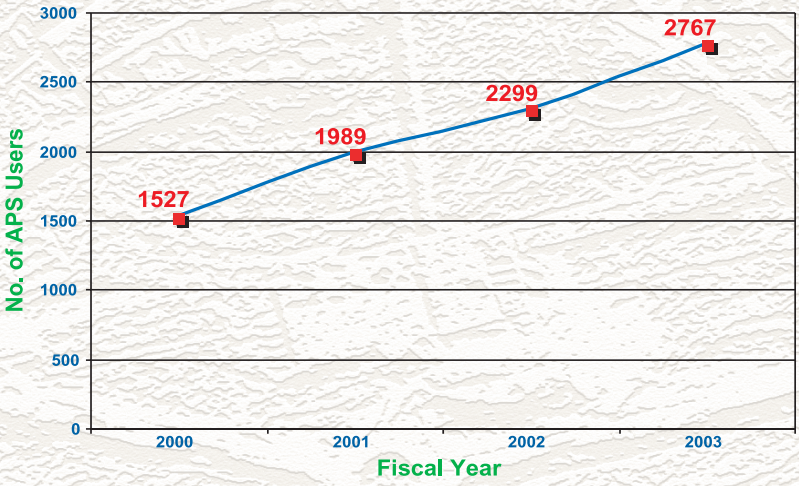

Visits by APS users, by fiscal year

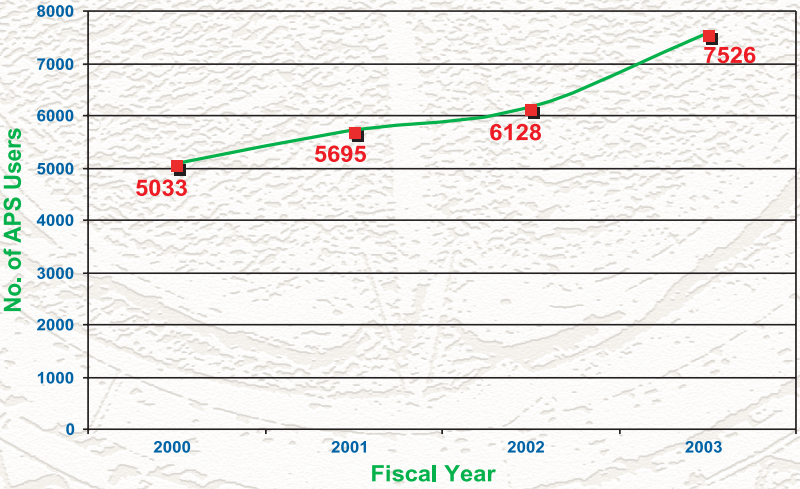

All U.S. APS users by state

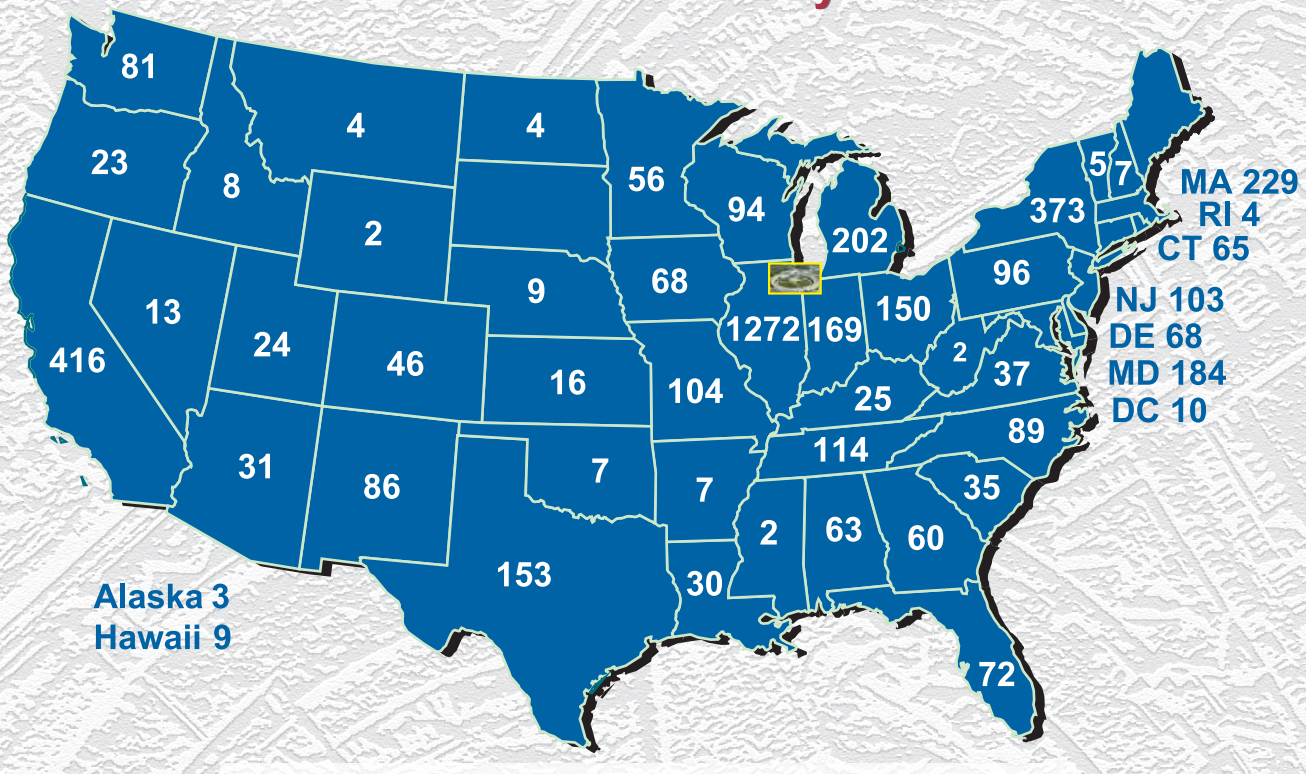

All APS users by geographic distribution

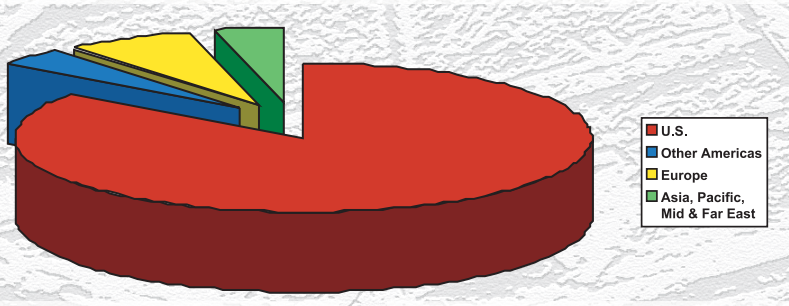

APS users by research interest

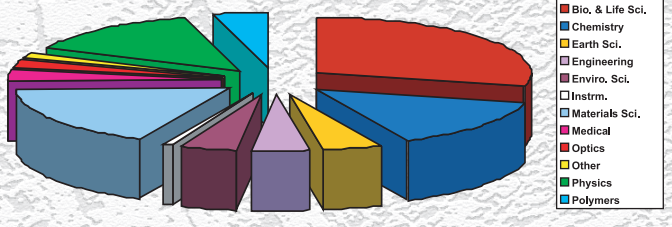

APS users by organization type

APS users by profession

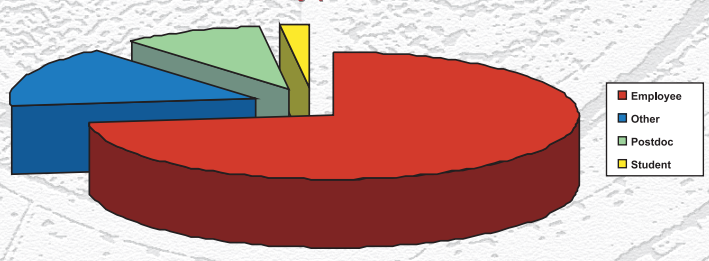

The APS Light Source

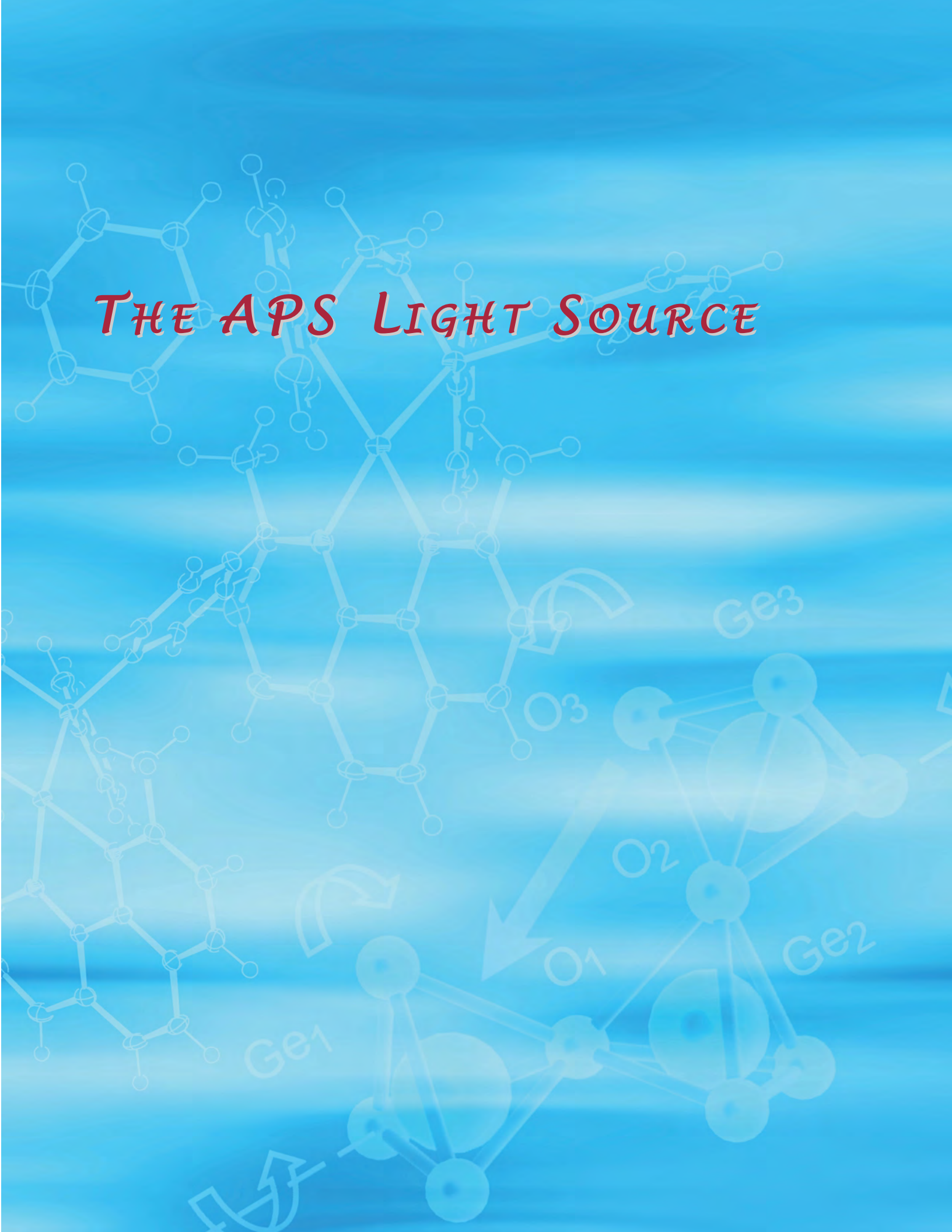

The APS Light Source

The APS continues its commitment to providing users with a reliable source of high-brilliance x-ray beams while innovating the future technologies that will keep x-ray science at the forefront of research.

Light Source Operations

In calendar year (CY) 2003, the APS scheduled 5,129 h for user operations and delivered 4,959.6 h. The emphasis continues to be on meeting established reliability goals of availability greater than 95% with a mean-time-between-faults (MTBF) rate of greater than 50 h. Orbit stability is also a very high priority, and this year progress was made in this area. The APS continues to utilize a schedule of three long runs and three extended maintenance periods, first employed in 2002.

Beam Availability & MTBF

During 2003, accelerator operations, as quantified by availability and MTBF, remained at the high levels achieved in 2002 (see Table 1). The APS has, since 2000, routinely exceeded the goal of 95% availability. Efforts have focused on maintaining this level of availability while reducing the number of faults. These efforts have resulted in two consecutive years of operation exceeding 40 h MTBF. Considerable improvements have been made to the radio-frequency (rf) and power-supply systems, traditionally high contributors to the fault rate. A significant factor in consistently meeting accelerator availability goals has been the high availability and MTBF of the high-power electrical systems (rf systems and magnet power supplies). The technical complexity and power levels of the rf systems and the large number of critical magnet power supplies in the storage ring (close to 1,400 individual units) present tremendous reliability challenges for the storage ring. Nevertheless, fault rates have improved considerably over recent years, and both rf and magnet power systems have consistently exceeded 99% availability (remarkably, the rf systems have exceeded 99% availability for the past *18 consecutive user runs*).

These improvements can be attributed in large part to the pragmatic and rigorous approach taken in analyzing and addressing problems and the proactive efforts to identify and resolve potential problems before they cause downtime. Causes (and duration) of user-beam downtime due to accelerator equipment problems have been tracked and analyzed dating back to the inception of operations. Beginning in 2003, the Experimental Floor Operations (EFO) Group began also main-

Table 1. Operations statistics—CY 2003.

	CY2002				CY2003
Run number		Run 03-1	Run 03-2	Run 03-3	
Start		1/29/03	5/28/03	10/01/03	
End		4/20/03	8/25/03	12/22/03	
Total hours scheduled (h)	5328	1647	1816	1666	5129
Beam available for users (h)	5208.7	1598.8	138.5	1622.3	4959.6
Beam availability (%)	97.8	97.1	95.7	97.4	96.7
Total downtime (h)	119.3	48.2	77.5	43.7	169.4
Average current (mA)	96.8	98.4	100.1	101.2	99.8
Number of faults	121	45	42	29	116
Mean time between faults (h)	43.0	35.5	41.4	55.9	42.8
Mean time to recovery (h)	0.99	1.07	1.85	1.51	1.46
Injector availability in top-up (%)	97.1	94.9	98.6	97.1	97.1

taining statistics on downtime incurred by beamlines due to systems failures [see: "Reducing Beamline Downtime" in the following section on APS Users]. To this end, the APS made increased use of periodic machine intervention periods for problem resolution. Examples of such rigor include detailed daily monitoring of rf system behavior to detect potential problems early and the automatic replacement of storage ring converters following transient trips so as to prevent recurring trips. A great deal of effort has also gone into identifying and replacing weak components, such as power-converter-control power supplies, and to reducing susceptibility to electromagnetic interference in the rf systems. As engineering improvements have been identified and implemented, they have been subjected to ever increasing quality assurance and workmanship standards, so as to minimize the chance of introducing new problems as old problems are resolved.

The local weather during the summer of 2003 was particularly stormy, leading to interruptions with longer than normal recovery times. This contributed to the increase in mean time to recovery during the summer 2003 run. The injector systems, needed every two minutes during top-up operation, were available 97.1% of the time, unchanged from 2002.

During 2003, user operations were scheduled for 5,129 h, and accelerator studies (including machine turn-on and operator training) for 1,315 h. The remaining 2,316 h were used for maintenance and scheduled machine repairs.

User Operation Fill Patterns

Various storage ring operation modes have been developed to meet different user-beam requirements. The operating modes used in 2003 were:

- Top-up, low emittance, 24 singlets fill pattern
- Top-up, low emittance, 1 + 7 x 8 hybrid (singlet) fill pattern
- Non-top-up, high emittance, 24 singlets fill pattern
- Non-top-up, low emittance, 324 multibunch

Top-up injection mode (injecting beam into the storage ring every two minutes) provides higher average photon flux and better beam stability for both the storage ring and the beamlines. Lower emittance and higher photon brightness can also be achieved without concerns about beam lifetime. Top-up mode is used for 75% of scheduled user beam time.

Non-top-up mode (refilling the storage ring twice every 24 hours) is mainly used to provide injector beam time for parasitic injector study, operator training, and injector maintenance and improvement. Early in 2003, the singlet fill pattern with the high-emittance lattice was used during non-top-up. This was changed in April to a 324-multibunch pattern, as explained in the next section.

The hybrid singlet pattern is used by the timing community to perform dynamical biological, chemical, and condensed matter/materials science studies.

Beam current is normally 100 mA for all modes, although incrementally higher beam currents are planned for the future.

The percentages of scheduled hours for each of the operation modes are shown in Fig. 1.

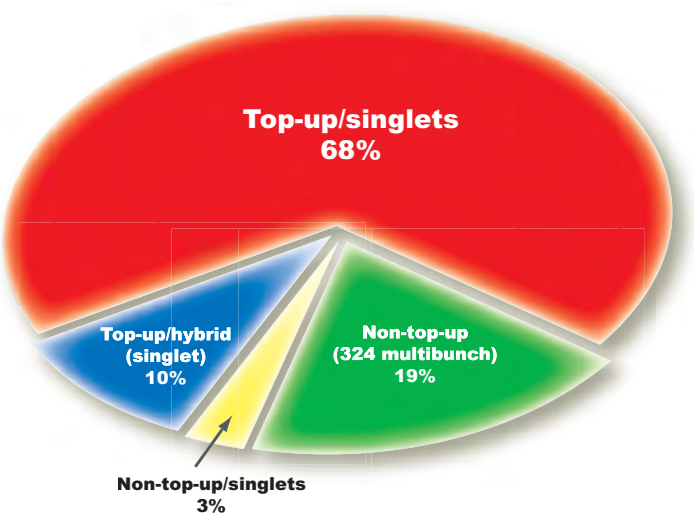

Fig. 1. Calendar year 2003 scheduled time for different operating modes.

The Storage Ring

(Tables 2 and 3 give main APS storage ring and storage ring beam parameters.)

A new, 324-bunch, low-emittance operational mode was introduced in April of 2003 for use during non-top-up periods. This mode has a long lifetime (60 h) due to small single-bunch charge and lower requirements for chromaticity correction. The 324-bunch fill pattern in this mode benefits experiments requiring high counting rate. Of benefit to both users and accelerator physicists is the fact that lattice changes are not needed when switching between these modes, resulting in more reproducible beam positions and efficient use of machine intervention time (i.e., repairs, studies, training). Lattice correction work also yielded benefits for the standard 24-bunch fill pattern. Previously, lifetime considerations and single-bunch instability thresholds had limited the single-bunch current in top-up mode to about 5 mA and linear coupling to 2.5%. The latest lattice improvements allowed us to lower the coupling to as low as 1%, further increasing the beam brightness. Furthermore, the improvements enabled stable operation for the first time with 8 mA in the singlet hybrid mode.

Beam-loss-induced radiation damage has been observed in the permanent undulator magnets, particularly those at IDs with a 5-mm vacuum chamber. There are two such chambers, representing the smallest physical apertures in the storage ring. (See section on "Radiation Effects on Insertion Devices" for remedies.) An alternate scheme would involve controlling beam losses to less sensitive locations. Preliminary calculations have been undertaken to analyze the beam losses and consider implementing a collimation concept.

Table 2. Main APS storage ring parameters.

Energy	7 GeV
Maximum current	102 mA
Natural emittance	2.5 nm
Vertical emittance	0.048 nm
Coupling	2%
Revolution frequency	272 kHz
Number of bunches	24 to 324
Time between bunches	153 to 11.3 ns
Momentum spread	0.96%

Table 3. APS beam parameters at radiation points, 2.5-nm horizontal emittance, 2% coupling.

		ID	BM
Horiz. beta function	(m)	19.5	2.00
Horiz. dispersion	(m)	0.172	0.056
Horiz. rms beam size	(μm)	275	89
Horiz. rms divergence	(mrad)	11.3	56
Vert. beta function	(m)	2.9	26.6
Vert. rms beam size	(μm)	12	36
Vert. rms divergence	(mrad)	4.1	1.7

Improved Storage Ring Orbit Stability

In 2003, orbit correction at 10 Hz was used on a routine basis, eliminating transients associated with insertion device (ID) gap changes. Data from front-end x-ray beam-position monitors (BPMs) at all 20 bending magnet (BM) beamlines and 15 ID beamlines were integrated with this fast orbit correction. The ability to compensate for residual gap-dependent systematic errors associated with ID x-ray BPMs (XBPMs) has now become commonplace.

The rms motions in the frequency band 0-to-30 Hz measured at the straight-section BPMs under ambient conditions remain at 1.3 μm in the horizontal plane and 0.8 μm in the vertical plane. A more meaningful measure of beam stability for many users, and one which has seen nearly an order of magnitude improvement for 2003, is the angular pointing stability. Prior to the inclusion of XBPMs in the global DC orbit correction algorithm, a typical beamline experienced long-term drift (48 h) at the level of up to 5 μrad, with fill-to-fill reproducibility at about this same level. This number has improved considerably, down to better than 0.5 μrad on a good day, and typically better than 1 microradian overall. These figures apply to BM beamlines vertically, and both horizontally and vertically to ID beamlines with active x-ray beam-position monitoring.

Impedance & Collective Effects

A complete impedance database has been constructed for the storage ring on the basis of wakefield analysis of all the accelerator components. These calculations were undertaken by using a finite-element code. A second, novel approach is a beam-based method of measuring the local transverse impedance through the use of the "response matrix analysis" method. This approach uses the fact that the transverse impedance acts to defocus the beam. By acquiring the response matrix as a function of bunch intensity, the strength of the effective defocusing can be obtained by using the storage ring model, and the impedance can be computed. The precision of this beam-based method is notable, and both complements and agrees well with the wakefield analysis. Preliminary simulations using the impedance database reproduce the measured single-bunch collective effects in the longitudinal plane: namely, bunch lengthening and energy-spread growth due to the microwave instability. The simulations also reproduce the observed single-bunch intensity limit and show that nonlinear coupling and vertical wakefields cause beam losses on the physical aperture in both the stored and injected beam. This leads to a threshold that prevents further accumulation in the single bunch. Various concepts to raise the single-bunch limit were studied that involve, for example, reducing the impedance or changing the injection scheme.

The main instability observed above 100 mA (many-bunch mode) is the longitudinal coupled bunch instability (CBI). This CBI is well understood and is typically stabilized with the standard technique of shifting the rf-cavity higher-order mode (HOM) driving frequency by either detuning the cavity or changing its temperature. However, operation at a different accelerating voltage or at a different current often requires readjustment of the cavity tune or temperature. In 2003, passive damping of

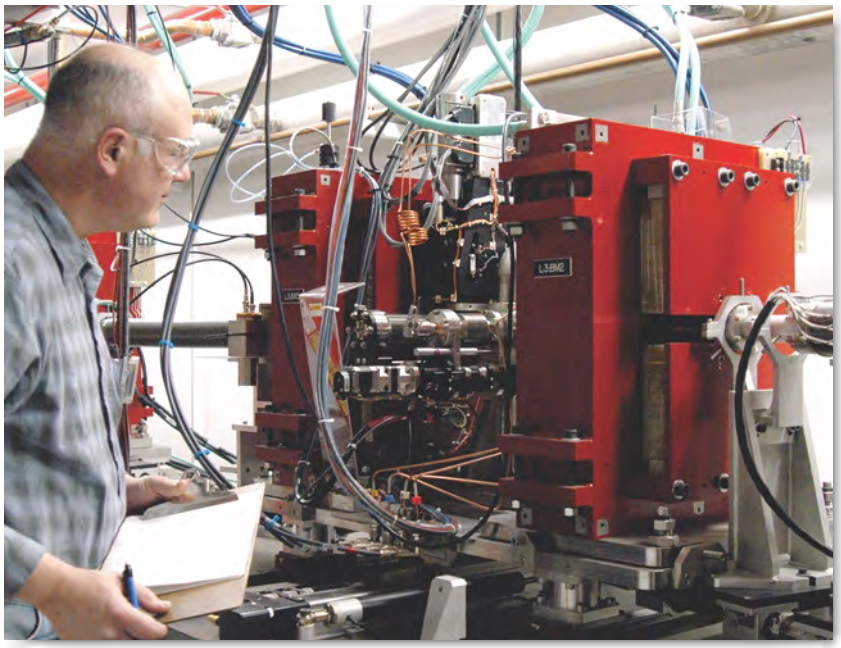

Bob Dortwegt (ASD-ME) inspects the APS linac bunch compressor diagnostics.

the HOMs to minimize this problem was investigated. During studies at and above 100 mA, the most dangerous HOMs were identified, as were those of the 16 rf cavities that were most responsible. A prototype HOM damper was developed and tested at high power in the rf test stand. A few of these dampers will be installed and tested in selected storage ring cavities during 2004.

The Linear Accelerator

2003 was a year of gradual improvements to the APS linear accelerator (or linac). The 35-MW klystrons are being incrementally upgraded to 45-MW klystrons, providing increased beam energy "overhead" and redundancy for user operations.

Over the course of the year, the linac water-flow monitoring system was upgraded from the old "go-no-go" flow trip switches to true water-flow sensors with no moving parts. This new system provides actual flow rates (useful for spotting problems before they become operation difficulties), incorporates no moving parts (for reduced maintenance requirements), and is far less susceptible to radiation damage than the old system.

Preparations have begun for a general linac BPM upgrade, which will consist mainly of new electronics. This will provide improved pulse-to-pulse monitoring capabilities and also include provisions for directly measuring the beam-to-rf phase. Both of these features will be important as the APS linac is called upon to perform higher single-bunch charge operation for direct booster injection, as well as various research tasks.

The Survey & Alignment Group, over the course of 2003, straightened the linac accelerator tank structures. Small deviations of the linac sectors from perfect straightness, typically on the order of less than .5 mm, are generally inconsequential for low-bunch charges but, as the bunch charge is increased, can start to degrade beam quality through wakefield effects. The procedure, first performed on the structures at the end of the linac, produced notable improvements in the transport of high-current beams through the linac. The final linac sector straightening took place during the December 2003 shutdown period.

The linac rf switching system has been more fully automated to facilitate rapidly redirecting linac rf power as required in the event of klystron failure. The system has proved very capable in practice and contributed to injector availability.

The Booster Synchrotron

Top-up operation, while important to APS users, places heavy demands on the particle-beam injectors, which are required to deliver reliable beam every 2 min., 24 h/day, 7 days/week. One difficulty is that APS accelerator operators have very little opportunity to "tune up" injector operation. Tuning up injection into the booster, for example, formerly required blocking the beam with viewing screens. A feedback system has been implemented that continuously controls the horizontal and vertical injection trajectory as well as the beam energy and rf system phase, eliminating the need for manual adjustments.

This automatic system calls for measuring the booster longitudinal and transverse injection transient turn-by-turn using several BPMs. These signals are Fourier-analyzed to find the six unique signals that give the oscillation amplitude and phase of the horizontal, vertical, and longitudinal motion. An existing feedback program has been configured to use these signals to control the injection transients. The horizontal and longitudinal loops are now in continuous operation.

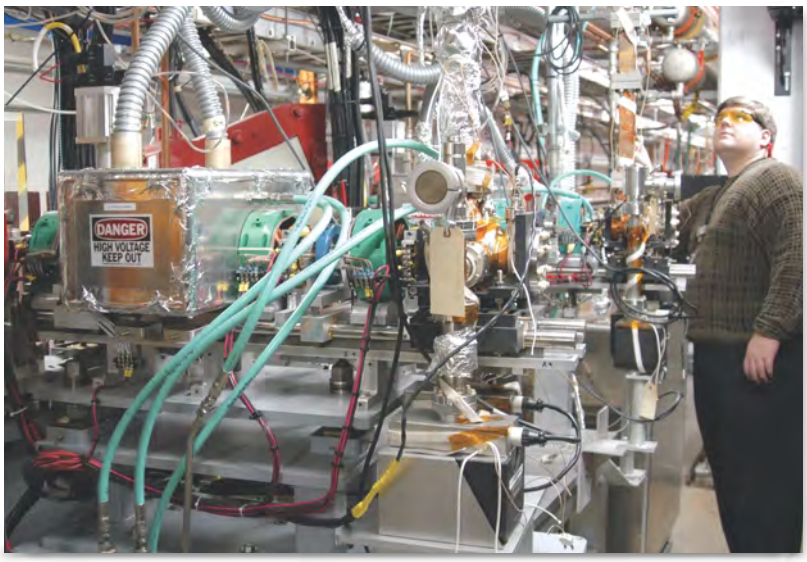

John Lewellen (ASD-PHY) in the APS linac injection region.

DUAL-CANTED UNDULATORS

Because of the increasing scarcity of unallocated beamline real estate at the APS, new ideas for enhancing productivity from the remaining storage ring straight sections have been considered. One of these ideas is the canted undulator (CU) straight section. In this configuration, a chicane is created with a trio of dipole magnets with an undulator in each leg (Fig. 2). The result is an angular separation between the x-ray beams that can be exploited downstream to create two independent beamlines from a single straight section.

CANTED-UNDULATOR COMPONENTS

The CU system consists of two shortened undulators, a special ID vacuum chamber, dipole magnets, a corrector magnet for the chicane, and a specialized front end.

Undulator: The standard undulator used at the APS is a 2.4-m-long, 3.3-cm-period hybrid planar magnetic structure mounted on a welded aluminum strongback. To make room for the chicane dipoles, five periods were removed from each end of the structure. The strongback is normally supported by a gap-separation mechanism at the Airy points (0.22315L from each end, where L is the total length) to minimize the distortion of the magnetic structure by equalizing the droop of the overhanging ends and of the sag at the midpoint between the two supports. The reduction in magnetic attraction force at the ends causes an increase in the overall amplitude of the droop. Finite-element calculations of the structure suggested that the deformation was within tolerances, which was confirmed by magnetic measurements.

ID Vacuum Chamber: The APS has designed a number of small-aperture ID vacuum chambers based on aluminum extrusions. A new extrusion has been developed that changes the chamber profile from an ellipse to an oval. This new profile was used for the CU straight section. A capacitive rf BPM is located at the center of the chamber.

Dipole and Corrector Magnets: In order to provide maximum flexibility for operation of the storage ring, electromagnets were chosen for the CU system dipoles. To maintain the symmetry of the chicane, the center dipole was designed to be twice as long as the end dipoles but with the same field. All three magnets are operated in series with a single power supply.

In order to maintain the independence of the two beamlines, an x-y corrector magnet was installed between the IDs that allows up to 30 μrad of steering correction. In this way, minor steering variations of the first undulator can be compensated with the APS feed-forward beam stabilization system so as to eliminate any effect on the trajectory of the inboard beam by the first undulator. All of the steering magnets, including the x-y corrector, were designed to be installed over an existing ID vacuum chamber. The two undulators, three dipoles, and corrector were measured magnetically as a group on the APS 6-m bench. No gap dependence of the magnetic

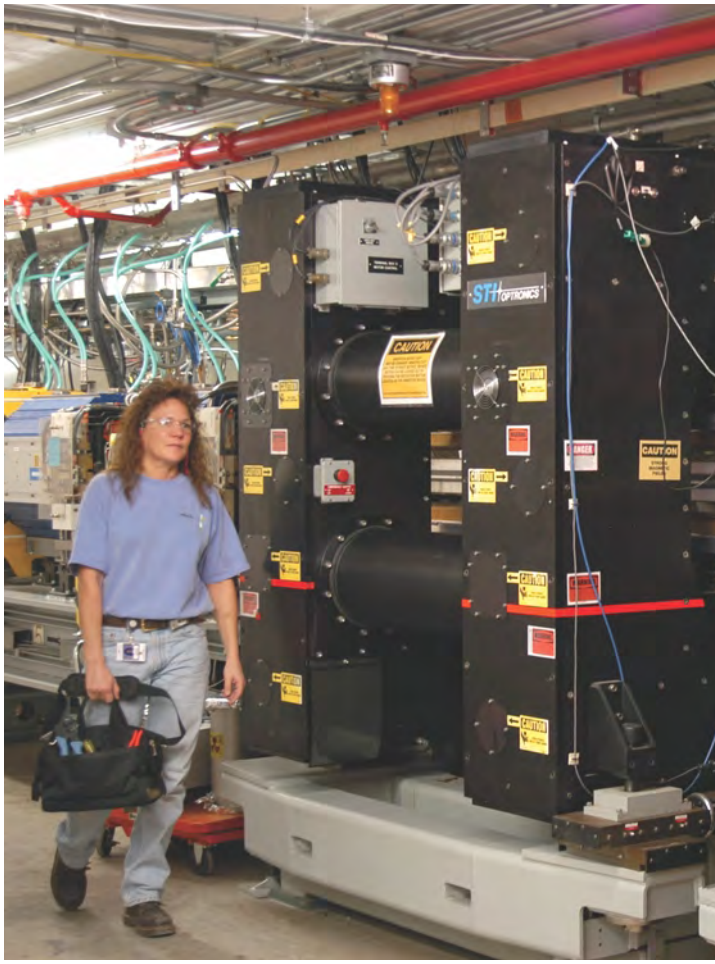

Cheryl Giacomi (ASD-VAC) passing by the dual-can

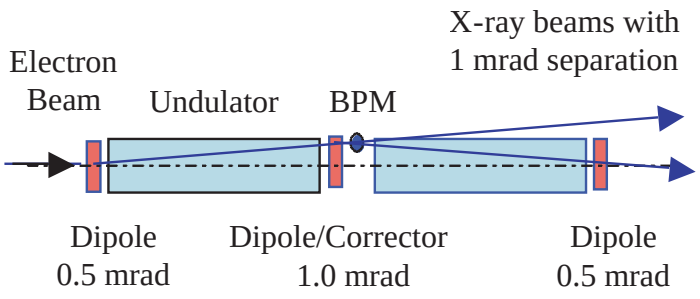

Fig. 2. Schematic layout of a CU straight section showing the angular separation of the x-ray beams produced by the three dipoles. The dipoles are placed symmetrically around the center of the straight section, and the BPM is displaced 113 mm downstream.

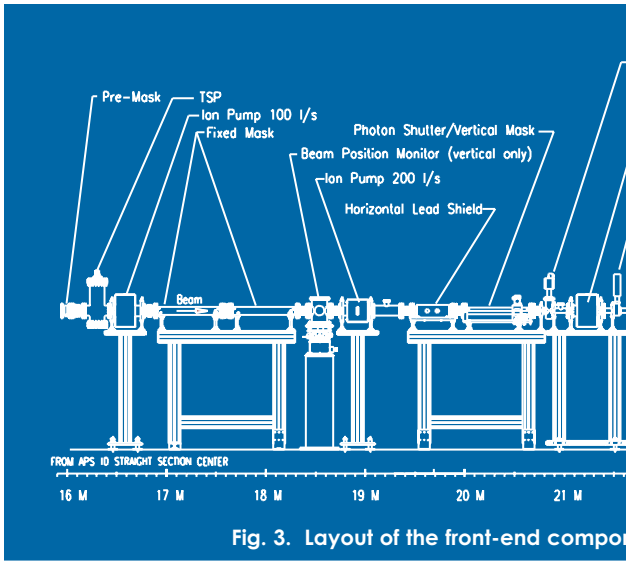

Fig. 3. Layout of the front-end compo

ted undulators installed at sector 23 on the APS storage ring.

Below: Thermalgram showing two beam spots from the GM/CA-CAT sector 23 canted undulator system, incident on a beam stop in the first optics enclosure.

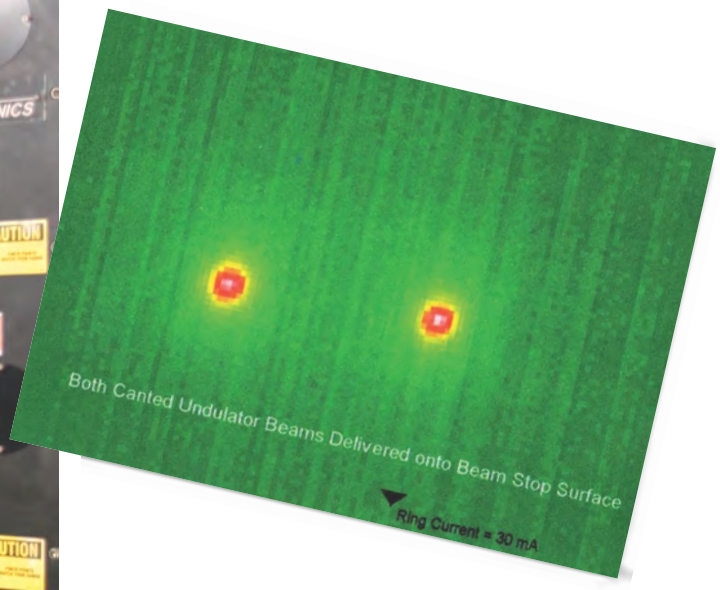

field was seen because of the proximity of the dipole magnets to the undulator magnetic structure.

Front End: A major challenge of the CU design was the thermal load on the front end. Because of the desire to increase the stored beam current at APS in the future, it was decided to design for a maximum allowable stored beam of 200 mA. This placed a severe constraint on the design of the first mask and first photon shutter. Also, the horizontal displacement of the two beams required that the glancing incidence surface of the photon shutters be horizontal rather than vertical, which would have been desirable from the standpoint of reducing the incident power density. The requirement to absorb two separate x-ray beams led to a unique design for the photon shutters. The chosen design intercepts the beams on a horizontal Glidcop® strike plate in the closed position and functions as a vertical mask in the open position. The relatively small separation of the beams at the entrance of the front end also contributed to a difficult thermal engineering challenge. Table 4 shows the thermal design limits for the system, the two photon shutters PS1 and PS2. Figure 3 shows a layout of the front end for a CU beamline.

Status: Two sectors (23 and 24) have had canted undulator systems installed and tested. In August of 2003, two beams were transported from the IDs at sector 23 on the first attempt.

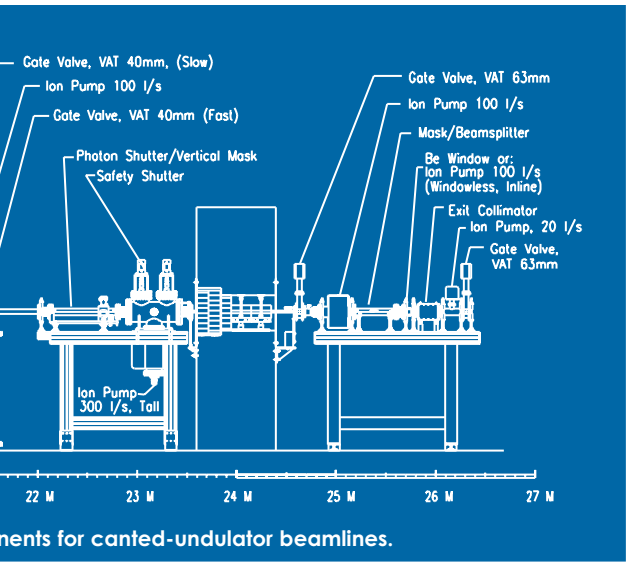

nents for canted-undulator beamlines.

Table 4. Canted undulator front-end parameters

Stored beam current (mA)	200	
Total power from two undulators (kW)	20.4	
Power density at normal incidence (kW/mrad^2)	281	
Temperature and equivalent stress for h = 0.015 W/mm^2°C, T_0 = 20 °C)	**PS1**	**PS2**
Incident angle	0.91°	0.91°
Peak normal incidence power density (kW/mm^2)	0.79	0.64
Peak incident power density (W/mm^2)	12.7	10.4

LIGHT SOURCE R&D

HIGH-BRIGHTNESS SOURCES

The performance of electron storage rings, thanks to the strong damping provided by synchrotron radiation, is not strongly dependent upon the performance of the electron-beam source. Over the course of many turns around the ring, the electron bunches are "damped down" into a configuration set by the ring itself, independently of the source parameters. Next-generation linac-based light sources, such as x-ray free-electron lasers and energy-recovery linacs, are essentially single-pass devices, and their performance depends almost entirely on the ability of the source to provide high-quality, high-peak-current electron beams, both at and beyond the present state of the art. The knowledge to be gained from designing these next-generation injectors also offers high promise for developing the ability to construct other devices, such as compact, high-powered THz radiation sources and multi-MV electron microscopes.

The APS has constructed a high-brightness injector test stand (ITS) at the gun end of the APS linac. Located in a separate accelerator enclosure and powered via the APS linac waveguide switching system, the ITS was first employed to characterize the new electron guns used for APS storage-ring injection several years ago. It has recently been upgraded to permit testing of new, high-brightness injector designs.

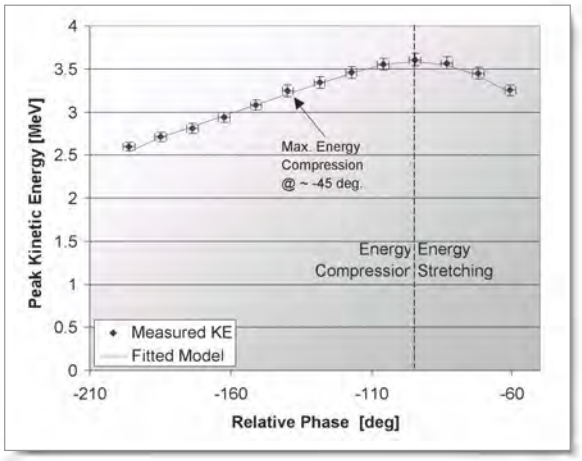

Fig. 4. Four-element CdTe detector, custom made by AMPTEK.

A ballistic-compression gun, intended to allow production of beams with very high peak currents and, more broadly, to explore longitudinal beam dynamics at low beam energies, is installed in the ITS. The initial benchmarking energy-compression experiments on the ballistic bunch compression gun have yielded results in very good agreement with theory (Fig. 4).

Provisions were also made for the installation in the injector test stand of a long-pulse drive, as well as a secondary beamline and rf shunt to allow two guns to be installed in the test area at the same time. This is being done partly to help expand the test stand's role in supporting ongoing APS operation (for instance, providing a gun specifically for operator training purposes), as well as to help prepare for the future requirements for the APS (for instance, testing ns-pulse lasers for direct booster injection applications).

Work has also continued on new injector designs, such as the higher-order mode rf gun, and novel focusing schemes to improve beam control and performance.

OPERATING STORAGE RING KLYSTRON RF SYSTEMS IN PARALLEL

352-MHz RF System Topology

The APS storage ring rf systems operate at a nominal rf frequency of 351.93 MHz and supply the necessary rf power to store up to 300 mA of electrons at 7 GeV. There are four 1.1-MW klystron-based continuous-wave (CW) rf systems dedicated to supplying power to the 16 storage ring rf cavities. A waveguide switching/combining system (Fig. 5) is utilized to direct and combine the outputs of the four rf systems to provide

Fig. 5. Doug Horan (left) and Geoff Pile (both ASD-RF) walking under the rf waveguide switch #1.

12 discrete operating modes. These modes allow single-ended or parallel operation of the storage ring rf systems. Parallel-klystron operation will be required to store more than 150 mA in the APS storage ring because the total amount of rf power required will exceed 2 MW CW.

The 16 single-cell rf cavities in the storage ring are grouped in 4 sectors of 4 cavities each. These four sectors are combined in pairs, with each pair being driven by either a single rf station or two rf stations operating in parallel. In both cases, WR2300 3-dB hybrids, are used as splitters in single-ended modes or as a combiner/ splitters in parallel modes. Motor-driven WR2300 phase shifters located after the hybrid output ports compensate for output phase changes that depend on whether the hybrids are being driven in single-ended or parallel fashion. The phase of the rf power that drives the storage ring cavity sectors must be kept within approximately 5° of optimum for stable beam operation, and the rf power must be equally divided between the sector-pairs to avoid stressing cavity components. The use of 3-dB, 90° hybrids to combine and then equally split the output of two rf systems requires that the output amplitude and phase of the parallel rf systems be controlled to within 6% and 2°, respectively. Low-level rf and high-voltage power supply controls are utilized to maintain these amplitude and phase tolerances.

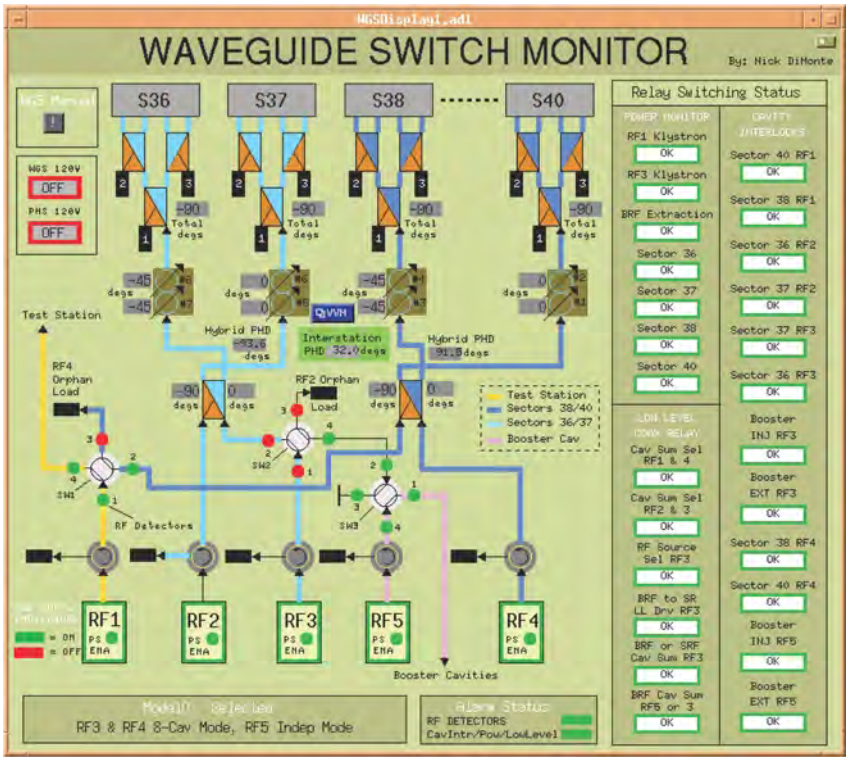

Fig. 6. APS rf waveguide switching and combining system.

Parallel-Klystron Phase and Amplitude Control

In the APS parallel klystron configuration, the rf power output from two 352-MHz rf systems is combined and then split by a 3-dB 90° WR2300 waveguide hybrid. Each of the two outputs of the hybrid supplies one-half of the combined rf power to one sector of rf cavities. Directional couplers installed in the straight waveguide sections just prior to the hybrid ports sample the signals at each port of the hybrid. All of these directional couplers are positioned at precisely the same distance from each hybrid port waveguide flange to establish accurate phase references.

The two rf stations are operated in parallel configuration utilizing a “master-slave” relationship. As shown in Fig. 6, RF1 is the master station and RF4 is the slave station. The phase-control loop maintains a constant phase relationship between the two stations at the input of the hybrid. A vector voltmeter is used as a phase detector to minimize amplitude-to-phase cross modulation, with the reference input of the voltmeter driven by the output of the master station. The setpoint of the phase-control proportional-integral-differential (PID) card is manually adjusted to maintain the power balance between the hybrid output ports.

The amplitude-control loop maintains a constant amplitude relationship between the two stations at the input of the hybrid, utilizing two envelope detectors and a PID amplifier to generate a slave-station amplitude control voltage.

Fast rf interlocking is used to prevent overpowering of the rf cavities, should the outputs of the two parallel rf stations drift appreciatively out of phase from one another at the input ports of the combining/splitting hybrid.

System Performance with Stored Beam

Initial no-beam tests of the parallel-klystron operating mode were performed in August 1999, with RF1 and RF4 configured in parallel mode. These tests demonstrated that the gap-voltage phase stability of the paralleled rf stations met the 1° peak-to-peak specification for the APS rf systems, with a static phase error of -3.5° between the output ports of the combining/splitting hybrid when the hybrid input powers were equal. In December 1999, 50 mA of beam was successfully stored using RF1 and RF4 operating in parallel mode and RF2 operating in single-ended mode. In the first high-current run that took place on September 30, 2001, 200 mA was stored using RF1 and RF4 operating in parallel mode and RF3 operating in single-ended mode.

Summary of the 225-mA Test Run

After the successful 200-mA run, the RF Group completed installation and testing of all final-version hardware required for full parallel operation of the storage ring rf systems. This operating mode (“mode 1”) configured RF1 and RF4 as one parallel pair, and RF2 and RF3 as a second parallel pair. This work was necessary to permit storage ring operation at currents higher than 200 mA.

On December 22, 2003, 225 mA was successfully stored with the rf systems operating in mode 1. This operating mode provided great flexibility in terms of uniform rf power require-

ment and distribution from each klystron. A main concern during the current ramp to 225 mA was the reaction of two independent storage ring rf gap voltage, automatic gain-control feedback loops due to a beam loss, and how quickly the rf power to the cavities would be reduced to safe levels. There were only two trips attributed to rf cavity pressure spikes, and the recovery from both events was quick. There were some elevated temperatures in the rf cavities as the stored beam current was increased, but none of the cavity-component temperatures reached their upper allowed limits. After each beam dump, RF Group personnel were on hand to manually reset the rf system parallel control loops in preparation for injection. This function will be automated in preparation for the next high-current run.

It is clear more than ever that keeping the rf cavities under vacuum for a long time increases their power-handling capability. This was evident during the 225-mA high-current run.

In summary, full parallel-mode operation of the storage ring rf systems made it possible to reach 225 mA without stressing klystrons and while staying within comfortable operational parameters. Long-term conditioning of the rf cavities with and without beam made a huge difference in high-power handling of the cavities and their performance.

The new stand-alone EPICS IOC is shown here in the hands of Eric Norum (Controls Group), one of the developers of the device. This low-cost module, which is essentially a PC running Linux, can be used to implement an EPICS control system with much of the capability as the entire control rack seen above Eric's left shoulder.

EPICS "iocCore"

The real-time accelerator and beamline control system at the APS is based on the Experimental Physics and Industrial Control System (EPICS) software toolkit, which was developed as a collaboration between Los Alamos National Laboratory and the APS Controls and Computing Group beginning in 1990 (see *APS Science 2002*). Since then, EPICS has grown in popularity among accelerator laboratories, telescope facilities, and even commercial applications and has become globally recognized as a capable, robust, and flexible platform upon which to build a control system. There are currently over 150 licensed users of the EPICS software, with many large Department of Energy facilities among them. Most beamlines at the APS and numerous beamlines at other light sources (14 at the National Synchrotron Light Source alone) use EPICS as the basis for beamline control. The APS continues to be a major contributor to the EPICS collaboration and is directly involved with EPICS development, documentation, distribution, and coordination.

Like all other accelerator technologies, EPICS must continually advance to stay current with emerging technology. A significant enhancement in the EPICS toolkit beginning with V.3.14.1 (December 2002) allows users of EPICS to take advantage of emerging computer platforms while significantly reducing the cost of EPICS implementation.

From its initial development, the real-time portion of EPICS (known as iocCore) was written to use a commercial real-time operating system (VxWorks® from Wind River Systems). Although VxWorks is extremely capable and robust, choosing it limited the selection of hardware that could be used for an input output controller (IOC). Almost all IOCs prior to V.3.14 consisted of a VME chassis, a VME single-board computer (for which VxWorks support was available), and a collection of VME modules for connections to the technical equipment. Many EPICS users found the "buy-in" cost to be as much as $10,000 to build their first IOC, an amount that was prohibitive for small projects.

However, thanks to EPICS V.3.14, EPICS iocCore can now be easily ported to different operating systems, greatly increasing the choices for implementing an IOC and reducing the buy-in cost. The standard distribution already supports numerous platforms, including Linux, Windows™, Solaris, Mac OS X, and RTEMS (an open source, real-time operating system). It is now possible to implement a stand-alone EPICS IOC for less than $500. This greatly increases the range of applications where EPICS is an attractive solution, suitable for even small projects.

Beamline Control Software

The Beamline Control and Data Acquisition (BCDA) Group has developed beamline software for APS-managed sectors 1 through 4, and has routinely made this software available to other facility sectors. With the expansion of the number of APS-managed sectors, BCDA interactions with sectors have increased even more. In particular, this accelerated activity has led to BCDA playing a key role in upgrading the beamline control system for IMMY/XOR.

Conversion of beamline-control software to work with the latest version of EPICS (V 3.14) allows beamline software to run on many more operating systems than possible under earlier versions of EPICS. The new operating systems include Linux and Windows. (We have noticed that Linux is becoming

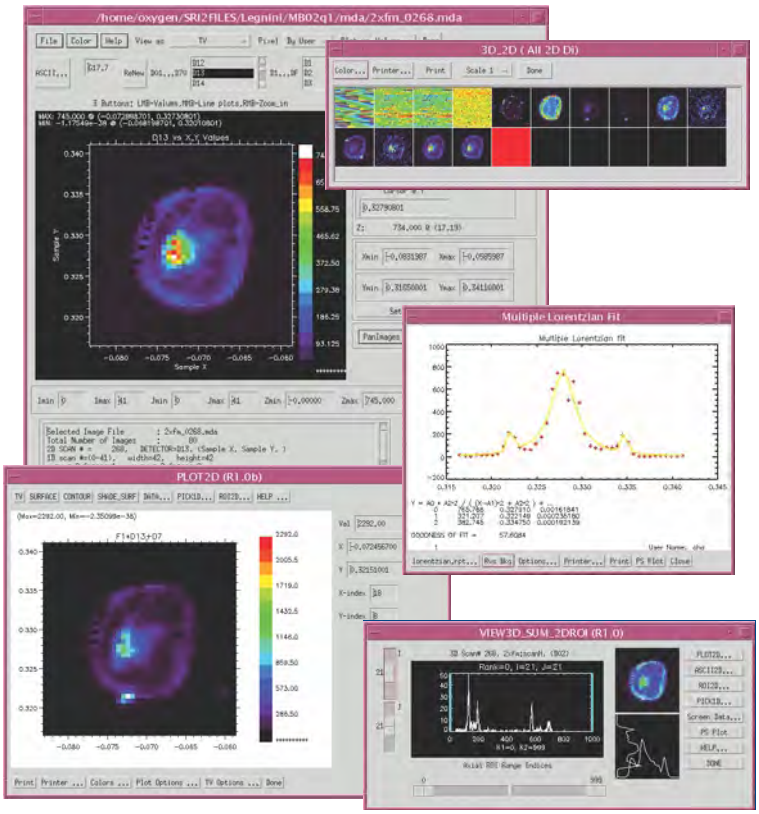

Fig. 7. Typical ScanSee display windows.

the most popular operating system among the APS user community.) Python, a powerful scripting language that has many advantages for use on beamlines, was used to write software to thoroughly test EPICS run-time calculation software. Python was also used for new modules to read and display scan data stored by beamline-control software.

EPICS plays a major role in another important BCDA initiative: data visualization. Using the RSI interactive display language (IDL), BCDA developed a flexible and easy-to-use visualization package. The EPICS/IDL visualization package includes a collection of general-purpose data visualization tools with simple analysis capabilities and several special-purpose scan-data visualization programs, such as catcher, viewer, and ScanSee (Fig. 7). They are written in the IDL programming language plus an interface layer of EPICS channel access function calls. All the visualization tools written in IDL are easily accessed by simple mouse clicks and are designed to be user friendly. The newly released IDL 6.0 also provides a new feature called the IDL virtual machine. This allows users to run previously compiled IDL programs without an IDL license. The BCDA took advantage of this fact by converting scan visualization tools to run on the IDL virtual machine. All visualization tools have been fully tested on both UNIX™ and Windows™ systems. They are available to users for free download from the BCDA web page (http://www.aps.anl.gov/aod/bcda/.

A new distribution system for beamline-control software has been introduced to make it easier for APS sectors to obtain BCDA software. By mirroring runable copies of most beamline software on APS-managed file servers, from which sector workstations and VME crates are permitted to read, the new distribution system enables sectors to use, and develop with, BCDA software without having to build or install it.

Streaming Video System

A streaming video (SV) system has been installed at the APS for operational and diagnostics use in the accelerator facility. The system is composed of multiple Apple® Xserves running QuickTime Broadcaster to encode and multicast video data onto the APS computer network for viewing on client computers using the open-source Mpeg4ip SV software (Fig. 8). A key feature of this setup is the low latency in the video that is viewed on a client computer. The latency of the video (the amount of time needed for a packet of data to go from one designated point to another) is 1 s or less. Latency is a critical factor in the real-time environment of accelerator controls. Most SV systems are set up to buffer at least 3 s, or more, of video. This would impose a challenge to accelerator operators who must respond to events that occurred several seconds ago.

The APS SV system is integrated into the site-wide video distribution system. This allows computer systems within the APS to access any of the video sources on site (diagnostic cameras, instruments with video outputs, etc.). Switching and routing of the video signals to the SV system are done with the integration of the video system components via EPICS. The system is also set up to allow remote access; authorized persons away from the facility can view the video streams by logging in to the APS via the virtual private network. This is a valuable tool for remote troubleshooting during user runs. Remote users employ Apple's QuickTime Player application (Fig. 8) on a Macintosh or Windows PC to access a low-bandwidth stream. Plans to provide video archiving of streamed video for training and other uses are also under way.

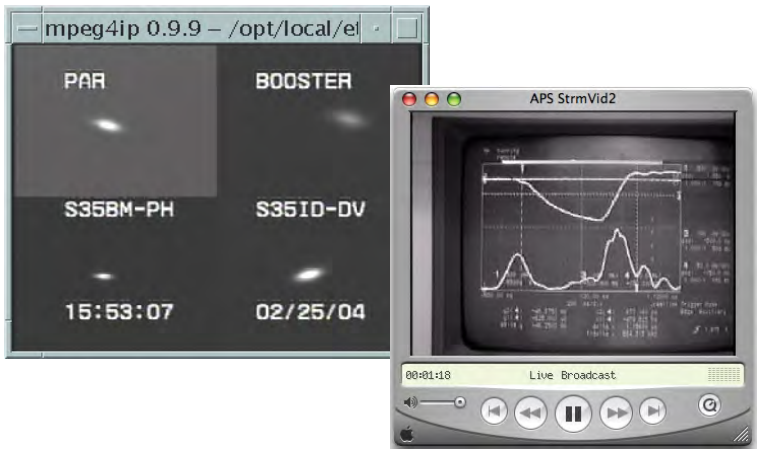

Fig. 8 (top). Mpeg4ip streaming video software shown running on a Solaris workstation. The software runs on Solaris, Linux, and Mac OS X. Bottom: QuickTime Player application showing a video stream from off site.

DIAGNOSTICS BEAMLINES AT SECTOR 35

X-ray beam brightness is next to beam stability as one of the most critical aspects of APS operations for users. Beam brightness is directly related to the quality of the electron beam. The key transverse parameter is source size, which is determined by beam emittance, energy spread, and lattice parameters. Sector 35 at the APS is dedicated to beam-diagnostics experiments designed to evaluate beam size, divergence, emittance, and bunch length, all with the goal of providing x-ray beams of the highest quality.

During user operations, beam sizes are acquired by x-ray pinhole cameras at the sector 35 BM and undulator, while the beam divergence at the straight sections is obtained by using the monochromatic undulator beam. The raw beam images are transmitted to users through the in-house cable TV at video rate (30 frames per second [fps]) and also through a fast web-image server (5 fps). The video images are also digitized and processed to extract horizontal and vertical beam sizes and beam divergences, which are available online as process variables, as shown in Table 5. The data are routinely archived during user operations and machine studies, and can be accessed through the use of tools developed by the APS Operations Analysis Group.

Two significant sector 35 diagnostics upgrades in 2003 were commissioning of the liquid nitrogen- (LN2) cooled monochromator at the 35-ID beamline and installation of the 4-m pinhole camera at the 35-BM beamline.

LN2-COOLED MONOCHROMATOR In August 2003, the single-crystal monochromator at 35-ID, which had been upgraded to LN2 cooling, began taking beam with a silicon-wafer assembly. During four months of operation, the heat-load limit of the assembly was tested, leading to increased confidence in the operation of the LN2 pump. Time-resolved imaging of the electron beam was also obtained. In two machine-study runs, single-bunch, single-pass images were captured at a resolution of 5 µrad, comparable to the vertical beam divergence (Fig. 9).

In December 2003, the cryocooled monochromator at 35-ID was used to support the high-current (225 mA) machine study. It was the only ID beamline approved to operate during the increased-current study period. Once again, the beamline was used to explore a new operating parameter space. Figure 10 shows the x-ray beam image and profile taken with the monochromator when a longitudinal instability was present.

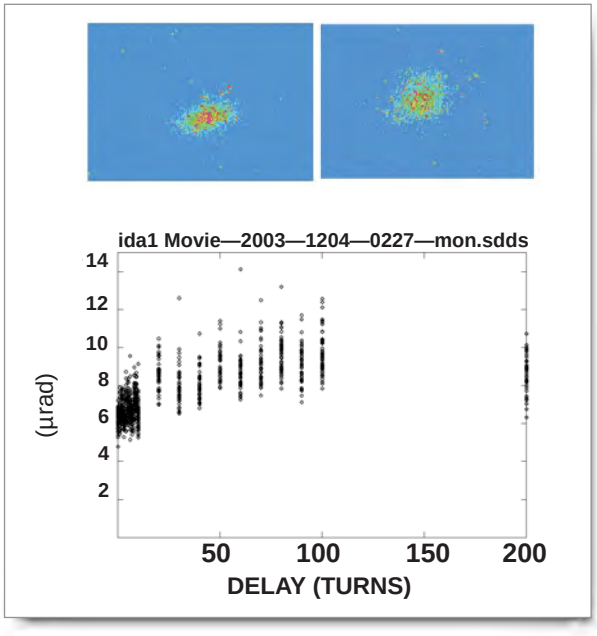

Fig. 9. Top: Single-turn ID x-ray beam images taken before firing the injection kicker (left) and 100 turns after the kicker pulse (right). Bottom: The rms vertical beam size (in µrad) as a function of turn numbers after the kicker firing.

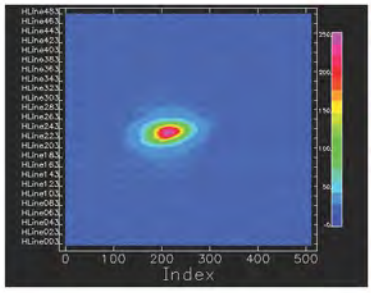

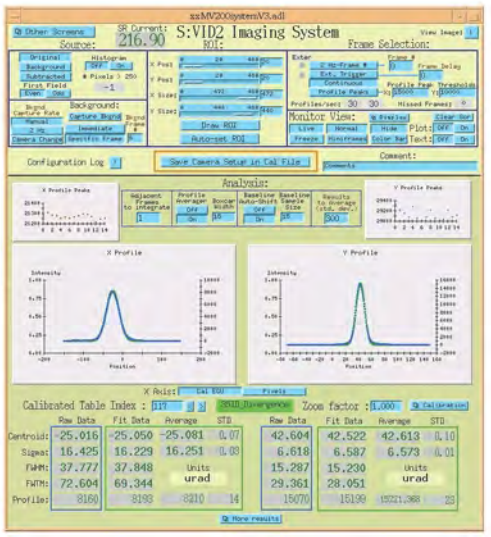

Fig. 10. X-ray beam image (above) and profile (right) taken with the LN2-cooled monochromator during the 225-mA run. A longitudinal instability was purposely induced for this part of the study.

Table 5. On-line beam information available during user operations.

Beam property	Process variable	Slow web display www.aps.anl.gov/asd/diagnostics/	Fast web display
BM beam size	S:VID1:x:fit:cal:sigmaM	image Data/S-VID1Data.html	axis35.aps.anl.gov
ID Divergence	S:VID2:x:fit:cal:sigmaM	image Data/S-VID2Data.html	axis35.aps.anl.gov
ID beam size	S:VID3:x:fit:cal:sigmaM	image Data/S-VID3Data.html	axis35.aps.anl.gov

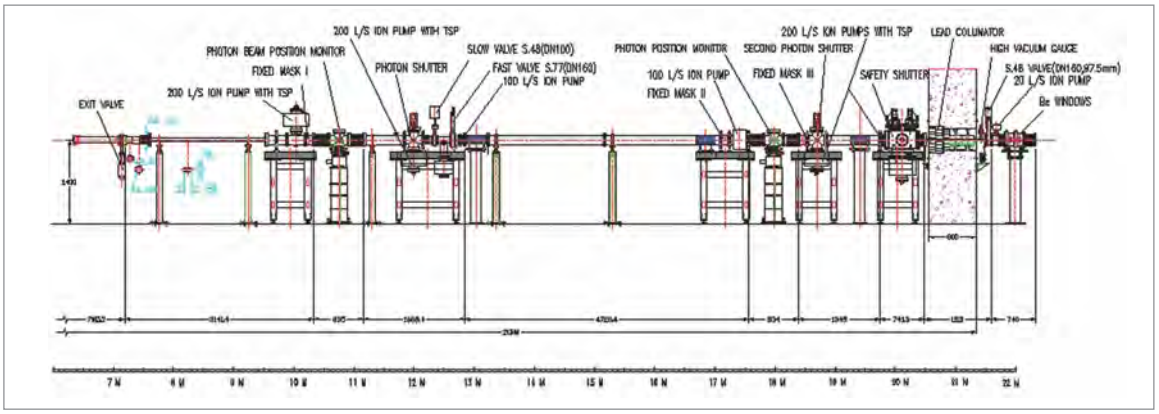

Fig. 11. General layout of the new BM front ends.

4-m Pinhole Camera The optimal spatial resolution of a pinhole camera is proportional to the square root of its object distance and the wavelength used for imaging. A new pinhole slits assembly located between two storage ring vacuum chambers was designed and fabricated, and then installed during the December 2003–January 2004 shutdown period. The pinhole is 4 m from the bend magnet source. When completed, the camera is expected to have a spatial resolution of 10 µm or less, compared to the current level of 22 µm. This resolution will dramatically improve the accuracy of measurements of the vertical beam size, which is less than 20 µm in some cases. Initial images of the beam have been obtained using a converter and a camera in the 35-BM-C station.

New Bending Magnet Front Ends

The APS has designed a new front end that will be used for BM beamlines. This new design builds upon the previous front-end design while implementing more recent fabrication techniques and lessons learned from eight years of operational experience. As before, the design is capable of handling the thermal load produced by a 300-mA stored beam in preparation for future accelerator improvements. Most components, such as fixed masks, photon shutters, safety shutters, and wall collimators, have been redesigned. The general layout of a BM front end is shown in Fig. 11.

Fixed masks confine the photon beam and protect the downstream components from a missteered beam. For manufacturing simplicity, the three oxygen-free, high-conductivity copper BM masks (Fig. 12) share a common design except for the aperture.

Photon shutters absorb the full power of the beam to isolate and protect downstream components. The new assembly (Fig. 13) is much less expensive to manufacture than the previous design and avoids some maintenance difficulties. The new actuator assembly allows cylinder changes without breaking vacuum.

The safety shutter has been redesigned with the same shielding features of current BM front-end safety shutters: a step labyrinth that avoids a direct line of sight, as shown in Fig. 14.

Fig. 12. Fixed masks.

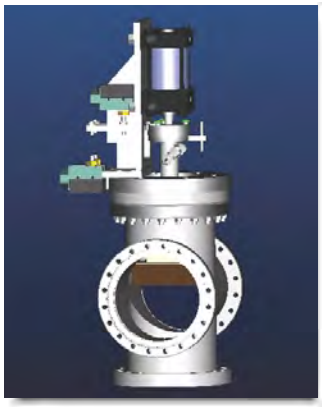

Fig. 13. The photon shutter.

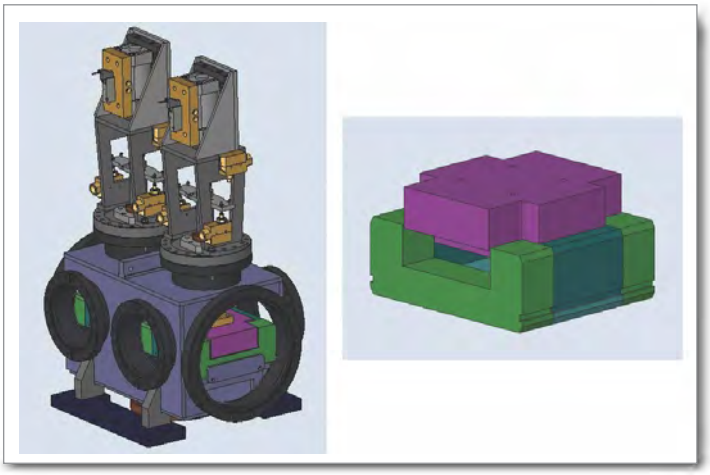

Fig. 14. The safety shutter and its tungsten blocks.

Several incidents involving movement of the lead shot in the existing BM front-end wall shielding led to a desire to replace the shot with lead bricks. Solid lead bricks will be stacked to fill the entire opening to a depth of 300 mm in the upstream area for maximum radiation protection. In the downstream area, the vacuum tube is enclosed by 50-mm-thick lead bricks (Fig. 15).

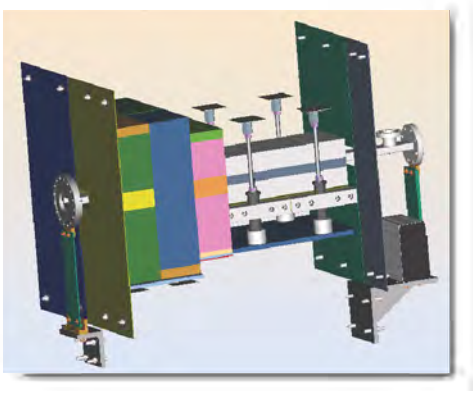

Fig. 15. The wall collimator.

Table 6. Optical apertures of the BM front-end components.

Component	Optical aperture (mm × mm)
Fixed mask 1	130 × 30 (in.) 62 × 8 (exit)
XBPM 1	90 × 24
Photon shutter 1	130 × 30
Slow valve	ϕ100
Fast valve	110 × 18
Lead collimator	94 × 20
Fixed mask 2	130 × 30 (in.) 104 × 8 (exit)
XBPM 2	125 × 18
Fixed mask 3	130 × 20 (in.) 111 × 5.2 (exit)
Photon shutter 2	130 × 30
Safety shutter	132 × 16
Wall collimator	141 × 16
Be window	145 × 8.8 (W) 145 × 12 (C)

Table 7. Bremsstrahlung shielding aperture or external size of shielding.

Component	Shielding aperture or external size of shielding
Lead collimator #1	100 × 26 300 (L) × 520 (W) × 100 (H)
Lead brick #2	300 (L) × 300 (W) × 100 (H)
Lead brick #3	300 (L) × 450 (W) × 100 (H) 300 (L) × 200 (W) × 100 (H)
Safety shutter	132 × 16
Wall collimator	151 × 26

In summary, the major design changes for the new BM front ends are:

- All fixed masks will have the same external size with one water-cooling loop.
- The slow-valve aperture is reduced to ϕ 4 in. from ϕ 6 in.
- Acoustic delay baffles in a transport pipe are removed.
- The photon shutters and safety shutter are newly designed.
- The wall collimator is newly designed, with lead bricks replacing lead shot.
- New support tables consist of a modular, lightweight, aluminum structure and a welded steel structure.

High-Heat-Load Front Ends

Two new APS beamlines (the Nanoprobe beamline at sector 26 and the Inelastic X-ray Scattering (IXS) beamline at sector 30) require two or three in-line undulators, respectively, to achieve the required high photon intensity. With the expectation of a future storage ring beam current that is higher, a new insertion device front end has been designed to handle a maximum total power of 21 kW and a maximum peak power density of 590 kW/mrad^2, which is approximately 3.8 times the heat load experienced with use of a single undulator at 100-mA stored beam current. This new front end will allow the operation of two in-line, 3.3-cm-period, 2.4-m-long undulators at k = 2.76 with 180 mA for the Nanoprobe beamline, or alternatively, three in-line undulators at k=2.0 with 150 mA for the IXS beamline. The new front ends are scheduled to be installed in September 2004 for IXS and January 2005 for the Nanoprobe beamline.

Front-End Layout & High-Heat-Load Management

The high-heat-load front ends for the Nanoprobe and IXS beamlines are almost identical in their design, except for the aperture of the exit mask and the Be window. The Nanoprobe beamline will use a window only for the commissioning phase, operating windowless during the mature phase. The exit mask aperture for the Nanoprobe beamline is to be 3 mm × 2 mm. The IXS beamline is to operate with a Be window. An exit mask aperture of 3 mm × 1 mm has been specified to reduce the total power on the downstream beamline components. The layout of the front end is shown in Fig. 16.

Front-End Component Analysis, Design, and Fabrication

Front-end fixed masks (FMs) and photon shutters (PSs) are used to confine and stop the intense synchrotron radiation inside the storage ring tunnel upstream from the first optical enclosure. The first fixed mask (FM1, the one closest to the storage ring) is exposed to a total power of 21.1 kW and a peak power density of 31.5 W/mm^2. The first photon shutter (PS1) absorbs as much as 14.6 kW, with a maximum power density of 24.6 kW/mm^2. The designs of FM1, FM2, FM4, PS1, and PS2 employ a common design concept. The fixed masks (FM1, FM2, and FM4) are horizontal masks, reducing the aperture in the horizontal direction only. At the open position, PS1 and PS2 are horizontal masks as well. An actuator installed at the down-

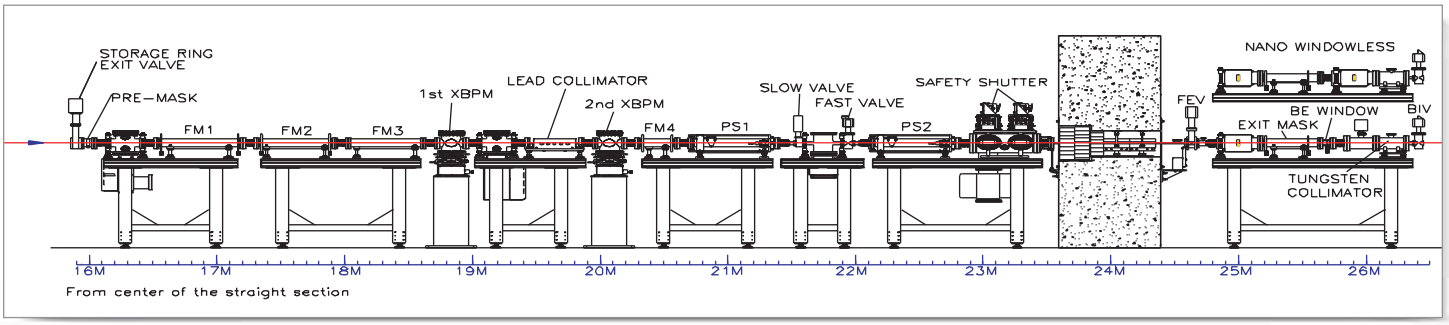

Fig. 16. Layout of the APS high-heat-load front end for the Nanoprobe and IXS beamlines.

stream end of PS1 and PS2 can actuate horizontally with an 8.5-mm stroke to make PS1 or PS2 pivot around a hinge near the inlet in order to shut off the beam; PS1 and PS2 are identical to each other.

A solid model of the mechanical design of PS1 is shown in Fig. 17. The thermal analysis of PS1 for the Nanoprobe beamline is shown in Fig. 18. The PS1 is made by brazing the left and right halves together. One half is OFHC copper only. The other half, which intercepts the beam at the closed position, is made of OFHC copper with an explosion-bonded Glidcop® face plate. The designs of FM3 and the exit mask use the same concept. Both are made by brazing the left and right halves together to form a V-shaped block. A slot is machined into each half before brazing to form the desired aperture size, such as 3 × 1 mm for the IXS device exit mask. All fixed masks and photon shutters are water cooled, with wire-coil inserts to enhance the cooling film coefficient.

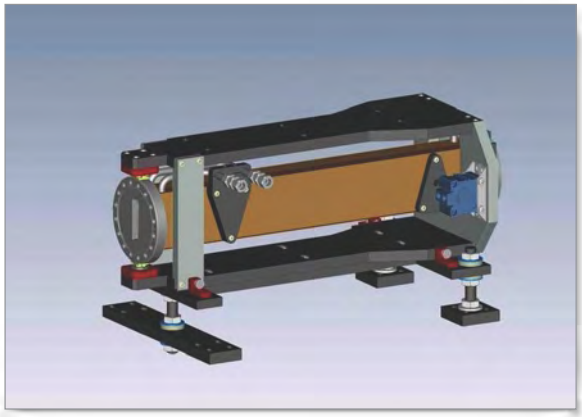

Fig. 17. Mechanical design of PS1.

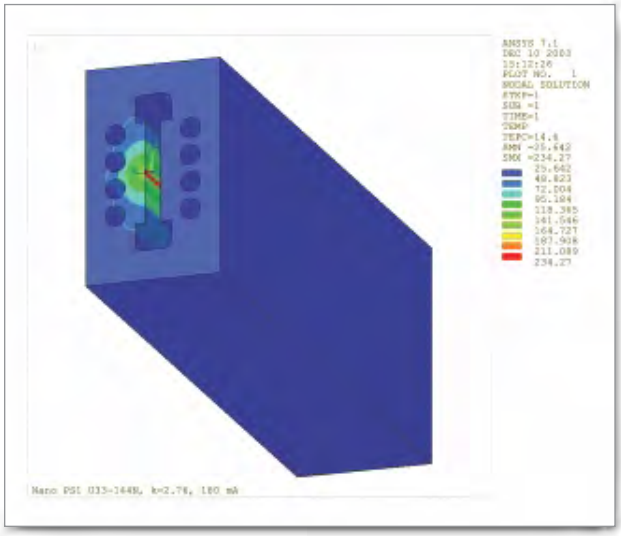

Fig. 18. Nanoprobe PS1 temperature (°C) plot.

ID Vacuum Chamber Development and Fabrication

Over the years, a family of ID vacuum chambers has been developed at the APS based on extruded-aluminum technology. In 2003, a new-style chamber was fabricated that features a new extrusion with a 7.5-mm aperture and a revised profile for greater clearance at the horizontal extremes of the aperture. This chamber helps reduce beam losses during injection while still providing a minimum undulator pole gap of 10.5 mm. This profile has been used in three canted-undulator sectors installed during 2003.

In past years, APS technology was extended to provide chambers for other synchrotron sources, including BESSY II, in Berlin, Germany; for the Deutsches Elektrononen-Synchrotron vacuum-ultraviolet free-electron laser; and for the Swiss Light Source at the Paul Scherer Institute. Recently, new designs were made for BESSY II and for the Canadian Light Source. Two of the BESSY II chambers were a repetition of an existing design, but four of the BESSY chambers were completely new designs with special BPM blocks and new end flanges. Water cooling was implemented in the body of these vacuum chambers and, for two of the four chambers, in the nose as well. Two of these four chambers also have an additional channel to allow the introduction of seed laser light for a femtosecond slicing experiment.

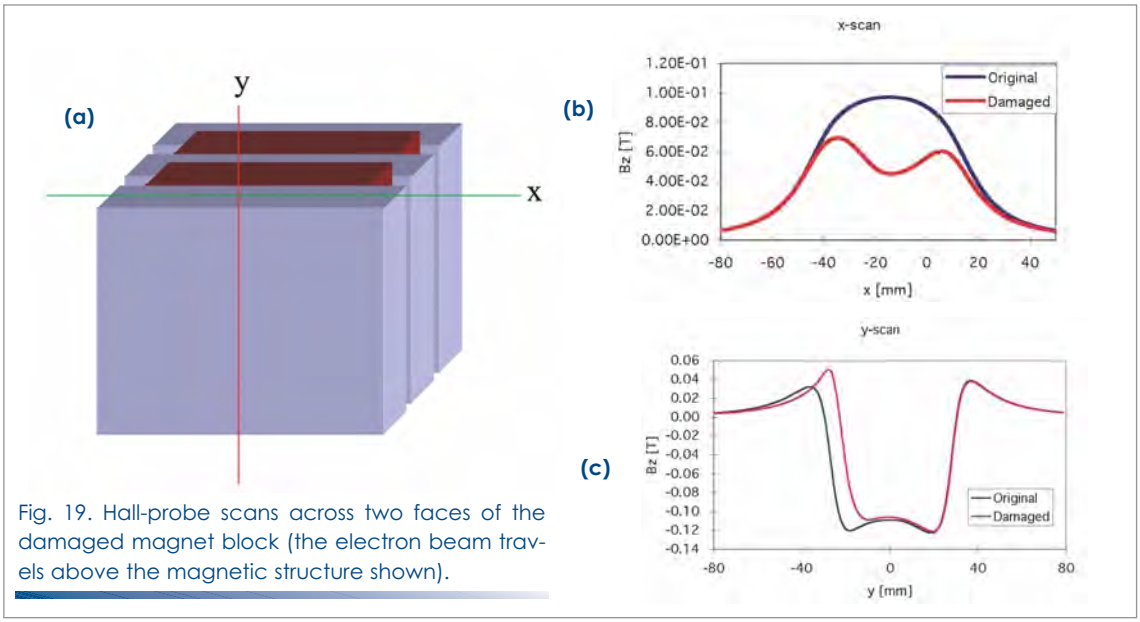

Fig. 19. Hall-probe scans across two faces of the damaged magnet block (the electron beam travels above the magnetic structure shown).

Radiation Effects on Insertion Devices

Radiation-induced demagnetization has been observed in a few IDs in the APS storage ring. To date, the IDs that suffered the most severe radiation damage are those located in sectors 3 and 4. Those are the only sectors in the storage ring equipped with small, 5-mm-aperture ID vacuum chambers.

Magnetic measurements of individual magnet blocks from the IDs located in these sectors showed that the damage is very localized. Hall-probe scans were performed over the faces of the magnet blocks, in both the x and y directions (Fig. 19a). The corresponding demagnetization profiles for magnet block #6 removed from the upstream end of the upstream undulator in sector 3 are shown in Fig. 19b-c. The transverse x-scan across the face of the magnet block showed that the magnet is primarily demagnetized directly under the beam (Fig. 19b). The vertical scan revealed demagnetization only in the top section of the magnet that is closest to the beam (Fig. 19c).

Since the magnet blocks are symmetric, they were able to be rotated in place. This placed the damaged region away from the beam, and the upstream undulator from sector 3 regained field strength. Standard tuning methods were then used to adjust the phase errors, and the device was reinstalled in the storage ring.

A pulsed magnetizer has also recently been purchased. Damaged magnet blocks removed from the upstream undulator in sector 3 and the sector 4 undulator were remagnetized to approximately the same total moment as the undamaged undulator magnets, as measured by Helmholtz coils. Figure 20 shows the difference in strength of each remagnetized magnet block from the average of all magnets in one undulator jaw of the sector 4 undulator. They all lie within a narrow band, as they did prior to their exposure in the radiation field of the storage ring. After remagnetization of the individual magnet blocks, the device was reassembled. The magnetic tuning proceeded smoothly, and the restored device from sector 4 was reinstalled.

Dose monitoring along the length of the damaged IDs in sectors 3 and 4 is continuing in order to allow comparisons with the demagnetization profiles. Alanine films were used for such measurements, because these dosimeters are thin enough to be placed directly in the magnet recess without affecting the minimum gap. The dose measurements revealed significant dose nonuniformities along the length of these IDs.

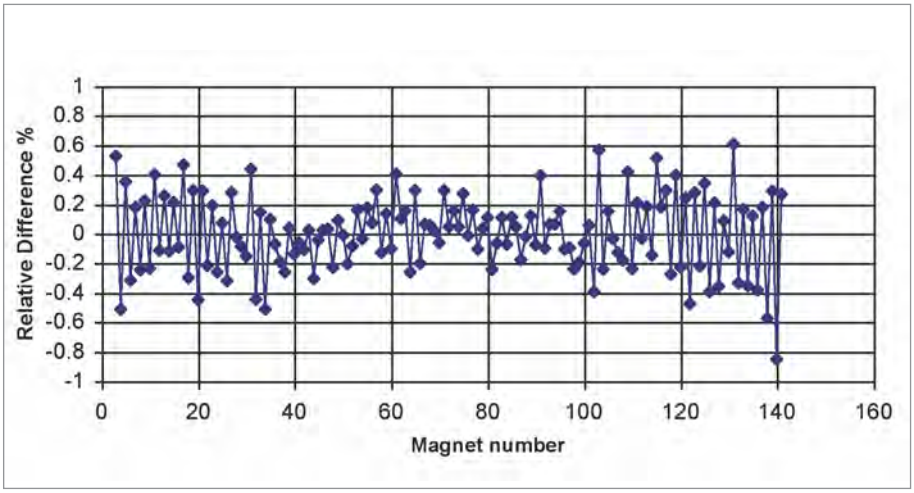

Fig. 20. Relative difference (%) between the magnetic moment of one magnet block and the average of the population of magnets for one jaw of the sector 4 undulator.

New Initiatives

New Initiatives

The APS provides its users with the brightest hard x-ray beams in the Western Hemisphere. This national research facility, which is funded by the U.S. Department of Energy, Office of Basic Energy Science, has been operating for user experimentation since 1996. The APS has proven to be a highly reliable source of brilliant x-ray beams for an ever-growing user population. It is APS management's responsibility to assure that this facility in particular, and x-ray science in general, continue to evolve to meet the needs of current and future users, who will bring synchrotron-technique science to new realms of scientific discovery.

Twenty Years on: A Vision for the Future of the APS

Over the past three decades, the brilliance of synchrotron x-ray sources has doubled every 10 months. Use of coherent flux, which is directly proportional to beam brilliance, has had major unforeseen benefits for work in the physical sciences, life sciences, and engineering. But improved performance will permit new uses of existing sources such as the APS.

Over the next 20 years, new and exciting x-ray sources are expected to appear on the x-ray science horizon. These sources will not be simple enhancements of existing third-generation sources. They will be a new breed of sources with new properties and the potential for new applications. Even as these new sources come into existence, the APS must remain at the cutting edge of third-generation synchrotron radiation technology, where the demand for x-rays will not decrease for the next 20 years or more. At the request of DOE, a 20-year upgrade plan for the APS has been developed. It is organized into four temporally overlapping phases:

• Phase I. Complete beamline installations on the remainder of the storage ring and maximize operations at existing beamlines. This phase, which has already begun, is expected to extend over the next eight years.

• Phase II. Optimize source characteristics. This phase will overlap Phase I and focus on upgrading of insertion devices and accelerator characteristics. It too, has already begun and will continue for a decade or more.

• Phase III. Develop the next-generation user facility by improving the efficiency and performance of beamlines and taking advantage of advanced detectors, robotics, and automation. This phase will start in full in approximately eight to ten years.

• Phase IV. Implement a major upgrade of the accelerator complex to develop a "super storage ring." Work on this final phase will begin about 10 years from now and will last for approximately 10 years.

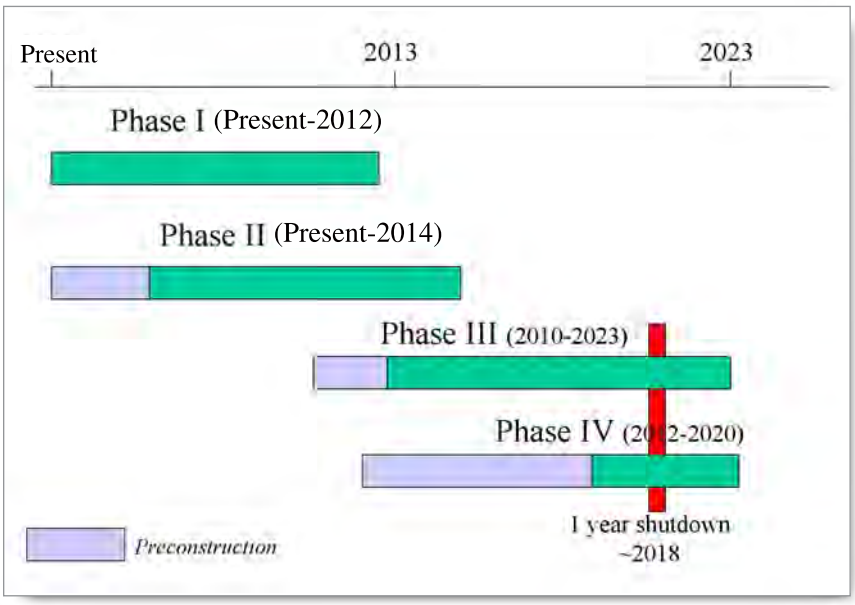

Fig. 1. Timeline for implementation of Phases I-IV.

Phase I

The appropriate focus for the first phase of a 20-year plan for APS upgrade (Fig. 1) is full utilization of the storage ring. It is expected that construction of approximately 10 new APS beamlines will occur from the present through FY 2012. This new construction will encompass the four remaining insertion device beamlines and the installation of several new bending magnet beamlines. These 10 new beamlines will not include three sectors dedicated to macromolecular crystallography, where construction has begun or is about to begin (General Medicine and Cancer Institutes Collaborative Access Team [CAT]), Northeastern CAT and Life Science CAT); the insertion device beamlines for two exciting proposals whose construction has been partially funded by DOE-BES (the inelastic x-ray scattering beamline and the nanoprobe beamline to be associated with the CNM); and a powder diffraction beamline on a bending magnet line, also funded (Fig. 2) by the Department of Energy's Office of Basic Energy Sciences.

Construction of the remaining available APS sectors is expected to continue through the next decade. In parallel with construction of new beamlines, we must contend with the aging of our existing beamlines. Ten years have passed since several APS beamlines were first designed, and they are in need of major refurbishments to take advantage of recent advances in optics and instrumentation. Development of state-of-the-art detectors is perhaps most urgent. In many cases, better detectors are already on the critical path to achieving faster data collection. Construction and refurbishment of some aging beamlines will be the responsibility of the APS, either alone or in collaboration with partner users. The proposed science to be performed at those beamlines will drive the new construction and upgrades.

The APS will rely heavily on guidance from its Scientific Advisory Committee in determining which beamlines will be built and upgraded. Future beamlines are expected to fall into two major categories: those used for "routine data collection," which need to be provided as "turn key" facilities (such as the powder diffraction line currently under construction); and cutting-edge beamlines optimized for "experiments," where constant innovation and tweaking are necessary for scientific success. The highly specialized beamlines in the second category are being designed for radiation properties optimized to particular types of research, such as inelastic x-ray scattering, high-energy x-ray scattering, or nanoprobe applications. Therefore, concurrent with development of new beamlines under Phase I, the aggressive source development specified in Phase II is also needed.

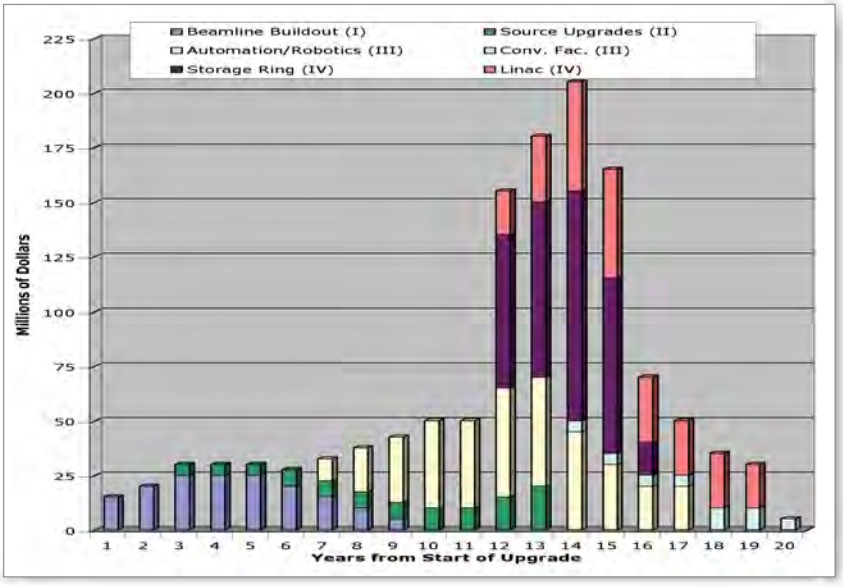

Fig. 2. Budget profile for Phases I-IV.

Phase II

Given the limitations imposed by the current magnetic lattice of the APS storage ring, further reductions in the natural emittance (presently better than the original design specification by a factor of almost three) can be only incremental. Therefore, without major reconstruction of the storage ring, significant increases in beam brilliance must come through the development of optimized insertion devices or increases in circulating beam current, as well as compatible front ends and optical components. These enhancements could improve effective brilliance by more than an order of magnitude.

Despite the common idea that high-energy, third-generation storage rings are associated with the production of hard x-rays, 6-8 GeV is, in fact, an ideal stored-beam energy for generating elliptically polarized soft x-rays. This fact, combined with the inherently superior stability of higher-energy beams, means that high-energy storage rings have considerable advantage in generating high-quality polarized soft x-ray beams. Insertion device development will push toward increased brightness at high energies with shorter-period devices capable of higher energies (20-45 keV) with the first harmonic. The most promising approach to this development will use superconducting undulators. Increased brilliance at high photon energies (25 keV and above) will improve inelastic x-ray scattering capabilities and provide an unequaled source of high-brilliance hard x-rays for high-energy elastic scattering. To improve beam brilliance further, the possibility of increasing the length of straight sections in the storage ring to accommodate longer or multiple insertion devices is being investigated. Longer straight sections would also allow installation of elliptically polarizing undulators optimized from 0.5 to 3 keV. The beam brilliance from these devices would result in a world-class beamline for photoemission and a photoemission electron microscope capable of spatial resolutions of a few nanometers, well suited to studying the magnetic properties of materials.

In addition to superconducting and polarizing undulators, Phase II work will also focus on solenoid-driven undulators. Insertion devices based on solenoids can have variable periods and variable fields (in contrast to present-day devices with fixed periods and variable fields), making them valuable for a host of scientific applications requiring optimization in several different energy ranges. As noted above, substantial reduction in the natural emittance of the APS is unlikely with its present lattice. However, the effective emittance delivered to users can be improved via enhanced beam stability. Phase II will continue the focus on this effort. Phase II will also focus on reducing the size and duration of perturbations of the stored beam during the top-up process, which will further enhance beam quality.

Phases III and IV

To adequately accommodate the estimated 10,000 researchers who will use the APS during the coming decade, Phase III enhancements will improve ease of access for users, beamline performance, and data-collection speed. Automation and robotics for sample alignment have already been implemented on some macromolecular crystallography beamlines at the APS and elsewhere. Many physical science beamlines could benefit from similar techniques. For instance, integration of automated sample changers into powder diffraction beamlines and small-angle-scattering beamlines seems to be a straightforward extension of the sample changers used for macromolecular crystallography. Moreover, automated alignment of optical components and diffractometers could substantially increase scientific productivity of some beamlines (particularly the turn key beamlines proposed for Phase I). A large class of experiments exists that could be performed effectively via remote access, if real-time communication of data, experimental conditions, and beamline control are achieved.

In Phase IV, significant improvements in the accelerator system are envisioned. As indicated above, maintaining the existing 40-fold symmetry of the storage ring implies that only incremental improvements in particle beam brilliance can be expected. Phase IV calls for a radical change in the storage ring magnetic lattice, from 40-fold symmetry to 80-fold, which will reduce beam emittance by a factor of eight. This 8-fold increase in beam brilliance— n combination with the increased brilliance achieved through optimized insertion devices, longer straight sections, and increased current—would put the APS near the limit of brilliance attainable with a storage ring of its dimensions and energy. The resulting super storage ring would significantly benefit the many important brilliance-related techniques. The obvious advantage of the Phase IV approach to a super storage ring is its use of existing beamlines. The novel concepts proposed would create new capabilities that would be qualitatively and quantitatively different, and considerable R&D would be required to verify the feasibility of the proposed alterations of the storage ring. Modification of the APS storage ring for reduced emittance would not be implemented until very late in the 20-year plan.

While Phases I and II, which were strongly supported by the BES Advisory Committee, will, in all likelihood, be funded through increased operational support, we are happy to report that our plans for Phases III and IV were strongly supported by DOE and the APS Upgrade (i.e., Phases III and IV) was recently included in DOE's 20-year plan, *Facilities for the Future of Science, A Twenty-Year Outlook*. ❍

The Argonne Linear Free-Electron Laser

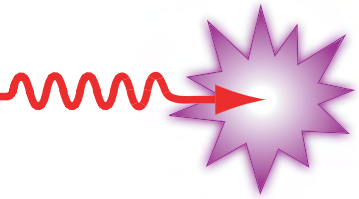

APS accelerator physicists have developed a high-gain free-electron laser (FEL) using the injector linear accelerator (linac) and the 20-m undulator in the low-energy undulator test line (LEUTL) tunnel. This is the first self-amplified spontaneous-emission (SASE) FEL to reach saturation at visible and ultraviolet wavelengths. (See *APS Science 2002*.) The LEUTL FEL allows experimental techniques hitherto not feasible in this wavelength region. Scientists at Argonne's Materials Science Division have installed a state-of-the-art spectrometer called SPIRIT (Single-Photon Ionization Resonant Ionization to Threshold) at the LEUTL end station to take advantage of the unique characteristics of the LEUTL FEL. An example is the first measurement of a nucleobase adduct by vacuum ultraviolet photoionization. Here, guanine was sputtered with an ion beam from a cinnamic acid matrix. The superior sensitivity of the LEUTL-SPIRIT combination over other methods in detecting adducts can be seen clearly in Fig. 1 (at least a factor of 100 in the case of the guanine-phenyl adduct). The result has important implications for measuring carcinogens and understanding the mechanisms by which they cause cancer.

The basic limitation of the LEUTL FEL is the severe lack of beam time available for experiments because the linac is normally exclusively used for running the APS in top-up mode. Even when the linac is available, it is shared by other activities.

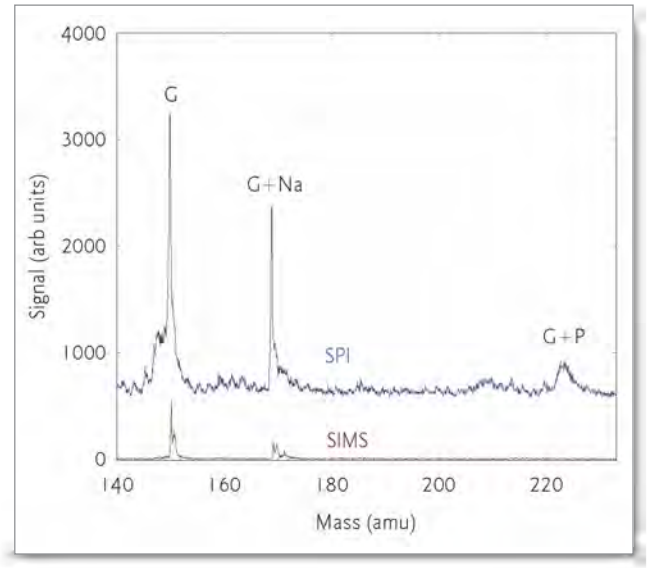

Fig. 1. Single photon ionization (SPI, blue) time-of-flight mass spectrum of guanine (G) with sodium (G+Na) and phenyl (G+P) adducts. The guanine was desorbed with an ion beam and photoionized with the LEUTL beam tuned near 157 nm. Notice the prominent G+P peak with SPI-LEUTL (in blue) compared to the barely visible corresponding peak with secondary ion mass spectrometry (SIMS, red). The SPI spectrum has been offset for clarity.

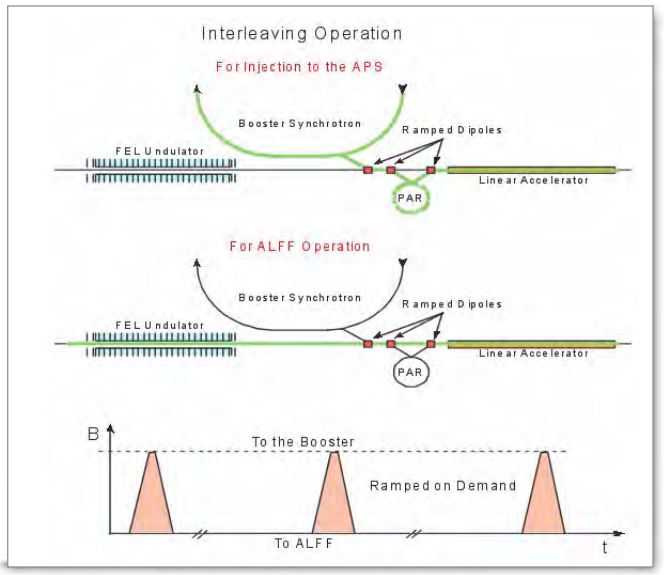

Fig. 2. Top: Electron beam path, shown in green, for injection into the booster synchrotron and APS storage ring. Middle: Beam path for ALF operations. Bottom: Timing diagram for the ramped dipoles used for interleaving.

Recently, APS submitted a proposal to the Department of Energy that would turn this one-of-a-kind FEL into a beamline capable of serving as a serious experimental program, which would be known as the Argonne Linear Free-Electron Laser, or ALF. The main improvements that need to be made for the ALF conversion are an upgrade of the linac and gun components for the interleaving operation and greater pulse stability. Interleaving, illustrated in Fig. 2, involves dynamically sharing the linac beams between top-up of the APS storage ring and servicing ALF; this will dramatically increase the availability of the FEL to 96%, compared to the current 3%. The operating wavelength region will be reoptimized by tuning the undulator gaps. The improvement project will take three years and cost about $5M.

Three scientific grand challenges are delineated in the ALF proposal: diagnosing the initial stages of cancer, evolution of our sun, and selective bond breaking. For a broader view on the potential scientific uses of the ALF, a workshop was held at Argonne on October 30-31, 2003. Over 60 scientists participated in four working groups: AMO (atomic, molecular, and optical sciences) and chemical physics, cosmochemistry and geosciences, material science, and biology and environmental science. The workshop confirmed that there is strong user interest the unique capabilities, not available from other sources, of the ALF beams in the combination of pulse energy (100 microjoules), duration (300 femtoseconds), and broad tunability. *(Contact K.-J. Kim, kwangje@aps.anl.gov)* ❍

There are a number of possible developments that may be attractive to new scientific users, including seeding to increase the temporal coherence, and related experiments with electron beams produced by the APS guns under development. They include ultrafast diffraction and microscopy. Given sufficient scientific interest, it is envisaged that the ALF and related activities can be incorporated as part of a new strategic initiative at Argonne.

Undulators for the Linac Coherent Light Source

The Linac Coherent Light Source (LCLS) at the Stanford Linear Accelerator Center (SLAC) will be the world's first x-ray free-electron laser (FEL). Compared to the APS, the peak brightness of the LCLS will be more than 9 orders of magnitude larger and the pulse length will be at least a factor of 500 shorter. These extreme properties will enable a broad range of new science and technologies.

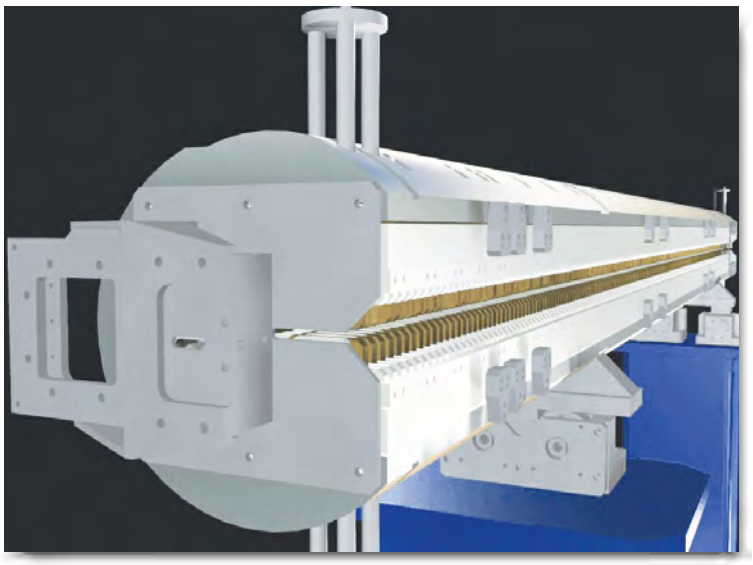

Fig. 1. A three-dimensional model of one of the 33 permanent magnet, fixed-gap, 3.4-m-long LCLS undulators.

The LCLS is scheduled to begin operation in 2009. Formal construction begins in fiscal year (FY) 2006, but a significant amount of construction will take place in FY05. Completion of LCLS construction is scheduled for the end of 2007, with commissioning to occur during 2008.

The x-ray FEL at the LCLS will initially operate much like the FEL at the APS (known as the LEUTL, for Low-Energy Undulator Test Line). A high-brightness electron beam will be accelerated by a linear accelerator. This beam will then be guided through a long, precision undulator magnet system. As the electron beam passes through the undulator magnetic field, the resulting light will generate x-rays, and these x-rays will interact back on the electron bunch. This process will conspire to create microbunching within the electron bunch, which will, in turn, radiate coherently and intensely at the resonant wavelength. An exponential runaway feedback process will develop and continue until the process reaches saturation. This self-amplified spontaneous emission FEL process generates an x-ray pulse that is transversely coherent and has a very high degree of temporal coherence. It is laser-like at x-ray wavelengths.

Much like the Spallation Neutron Source at Oak Ridge National Laboratory, the LCLS is a multilaboratory collaboration, the principal laboratory being SLAC, where the LCLS will be. Both the Argonne and Lawrence Livermore national laboratories are major collaboration participants.

Capitalizing on the precision undulator systems expertise at the APS, Argonne is responsible for the delivery of the approximately 130-m-long LCLS undulator system. This component includes the 33 permanent-magnet, fixed-gap undulators; the 33 focusing quadrupoles; all associated diagnostics, vacuum systems, and controls systems; and most supports. Advanced Photon Source scientists and engineers will also consult on the construction of a magnet measurement facility at SLAC.

For the LCLS contingent at APS, the year 2003 was a period of final transition from an R&D effort to the project engineering and design phase. In January 2003, Stephen Milton (milton@aps.anl.gov) was appointed ANL LCLS Project Director. An important LCLS milestone was achieved in May 2003 when the Department of Energy granted LCLS a Critical Decision 2a, giving approval to the request for long-lead procurements in FY05.

Throughout 2003, the ANL LCLS team concentrated on additional engineering and design issues and on completing tests on the first full-length undulator prototype magnet. This magnet, built in 2002, must achieve very exacting and critical tolerances. In particular, the normalized average field strength for this magnet must be correct to within 1.5×10^{-4}. This tolerance translates into an undulator gap constant to within 1 μm. The solution to this technical requirement came from an idea generated during the review of the undulator prototype in November 2003 and utilizes a "canted" pole concept: poles shimmed and tipped by 3 mrad relative to one another.

A complete work breakdown structure and an integrated cost and schedule for the ANL component of the LCLS project have been completed. These will be reviewed in May 2004 by an external, independent review committee, at which time formal baselines will be set for LCLS costs and schedules. ❍

LCLS

Stanford Linear Accelerator Center

Stanford Synchrotron Radiation Laboratory

Data

APS Data

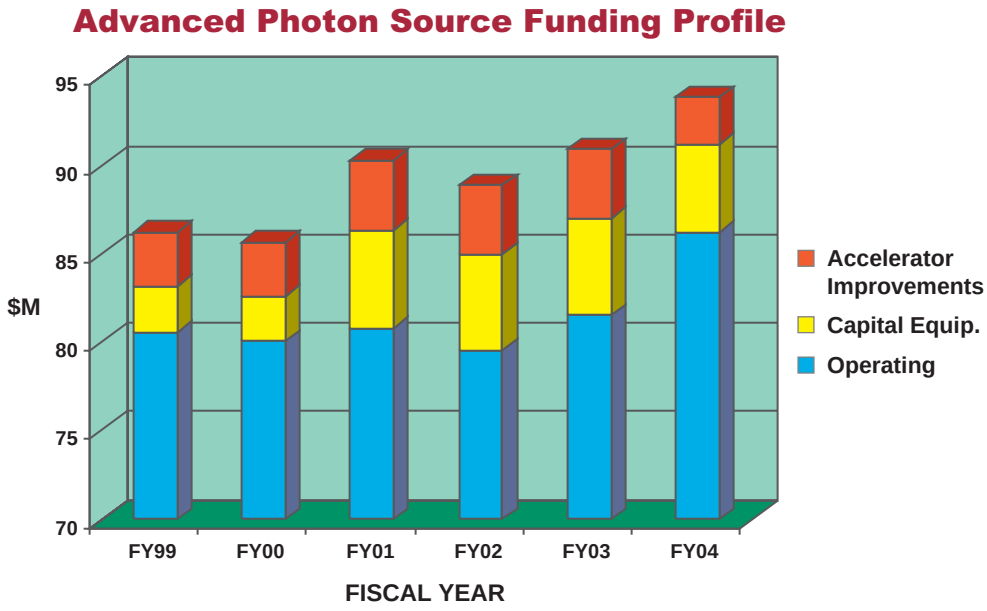

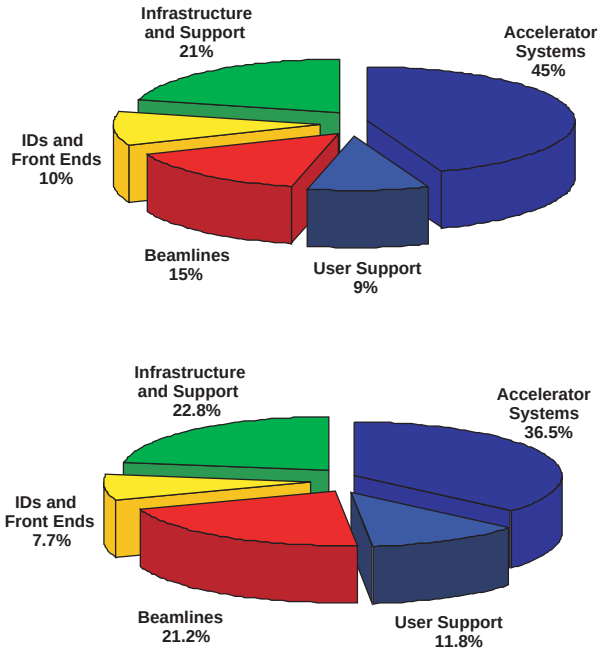

Comparison of APS spending, by function (top: FY 2001; bottom: FY 2003).

APS Organization

(3.31.04)

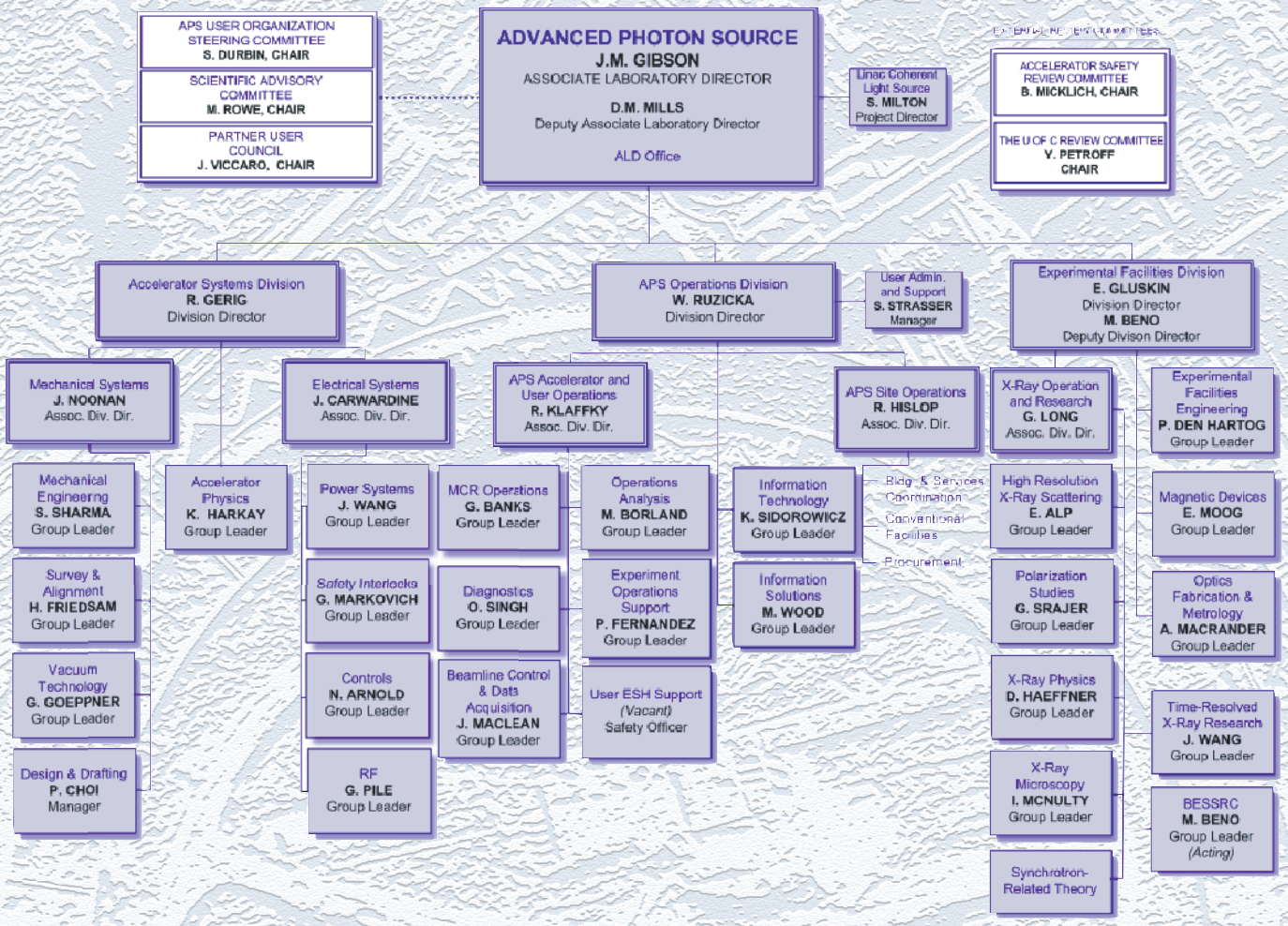

APS Staffing Profile

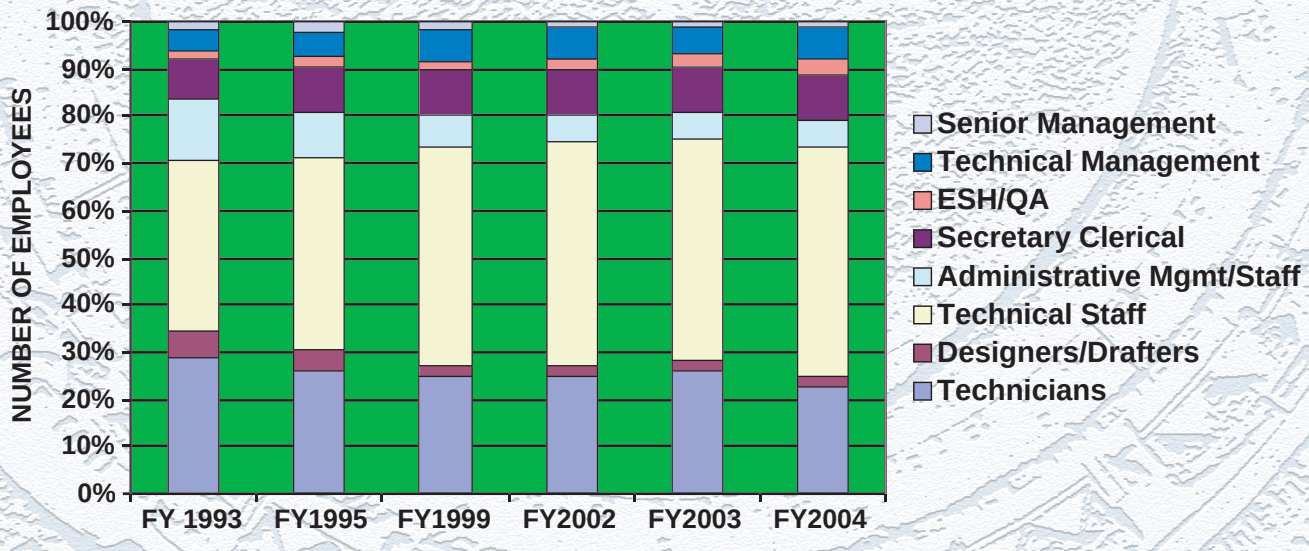

APS Source Parameters

Undulator A
Period: 3.30 cm
Length: 2.4 m
K_{max}: 2.74 (effective; at minimum gap)
Minimum gap: 10.5 mm
Tuning range: 3.0-13.0 keV (1st harmonic)
3.0-45.0 keV (1st-5th harmonic)
On-axis peak brilliance:
4.6 x 10^{19} ph/s/mrad^2/mm^2/0.1%bw at 7 keV
Source size and divergence at 8.0 keV:
Σ_x: 273 µm Σ_y: 10 µm
$\Sigma_{x'}$: 12.6 µrad $\Sigma_{y'}$: 6.6 µrad

2.70-cm Undulator (sector 3)
Period: 2.70 cm
Length: 2.4 m
K_{max}: 2.18 (effective; at minimum gap)
Minimum gap: 8.5 mm
Tuning range: 5.1-16.0 keV (1st harmonic)
5.1-60.0 keV (1st-5th harmonic)
On-axis peak brilliance:
6.4 x 10^{19} ph/s/mrad^2/mm^2/0.1%bw at 8 keV
Source size and divergence at 8.0 keV:
Σ_x: 273 µm Σ_y: 10 µm
$\Sigma_{x'}$: 12.6 µrad $\Sigma_{y'}$: 6.6 µrad

5.50-cm Undulator (sector 2)
Period length: 5.50 cm
Length: 2.4 m
K_{max}: 6.57 (effective; at minimum gap)
Minimum gap: 10.5 mm
Tuning range: 0.4-7.0 keV (1st harmonic)
0.4-25.0 keV (1st-5th harmonic)
On-axis peak brilliance:
1.9 x 10^{19} ph/s/mrad^2/mm^2/0.1%bw at 4 keV
Source size and divergence at 4.0 keV:
Σ_x: 273 µm Σ_y: 10 µm
$\Sigma_{x'}$: 13.8 µrad $\Sigma_{y'}$: 8.7µrad

APS Bending Magnet
Critical energy: 19.51 keV
Energy range: 1-100 keV
On-axis peak brilliance:
5.6 x 10^{15} ph/s/mrad^2/mm^2/0.1%bw at 16.3 keV
On-axis peak angular flux:
9.6 x 10^{13} ph/s/mrad^2/0.1%bw at 16.3 keV
On-axis peak horizontal angular flux:
1.6 x 10^{13} ph/s/mradh/0.1%bw at 5.6 keV
Source size and divergence at the critical energy:
Σ_x: 91 µm Σ_y: 30 µm
$\Sigma_{x'}$: 6 mrad $\Sigma_{y'}$: 47 µrad

Circularly Polarized Undulator (sector 4)
Period: 12.8 cm
Length: 2.1 m
Circular mode:
K_{max}: 2.65 (effective; for both horizontal and vertical fields at maximum currents 1.2 kA horizontal and 0.34 kA vertical)
B_{max}: 0.26 T (peak fields)
Tuning range: 0.5-3.0 keV (1st harmonic)
On-axis peak circular brilliance:
3.4 x 10^{18} ph/s/mrad^2/mm^2/0.1%bw at 1.8 keV
Linear mode:
K_{max}: 2.80 (effective; for both horizontal and vertical fields at maximum currents 1.4 kA horizontal and 0.40 kA vertical)
B_{max}: 0.29 T (peak fields)
Tuning range: 0.8-3.0 keV (1st harmonic)
0.8-10.0 keV (1st-5th harmonic)
On-axis peak linear brilliance:
2.5 x 10^{18} ph/s/mrad^2/mm^2/0.1%bw at 2.1 keV
Switching frequency: 0-5 Hz
Switching rise time: 20 ms
Source size and divergence at 1.5 keV:
Σ_x: 273 µm Σ_y: 10µm
$\Sigma_{x'}$: 17.9 µrad $\Sigma_{y'}$: 14.4 µrad

Elliptical Multipole Wiggler (sector 11)
Period length: 16.0 cm
Number of poles: 34 permanent magnets,
36 electromagnets
Length: 2.8 m
$K_{x\text{-}max}$: 1.3 (effective; at maximum current 1.15 kA)
$K_{y\text{-}max}$: 14.4 (peak; at minimum gap 24.0 mm)
Switching frequency: 0-10 Hz
Critical energy: 31.4 keV (at minimum gap)
Energy range: 5-200 keV
Source size and divergence at the critical energy:
Σ_x: 273 µm Σ_y: 10 µm
$\Sigma_{x'}$: 820 µrad (FWHM 1.9 mrad; non-Gaussian; linear mode)
$\Sigma_{y'}$: 47 µrad (linear mode)

TYPICAL APS MACHINE OPERATIONS PARAMETERS

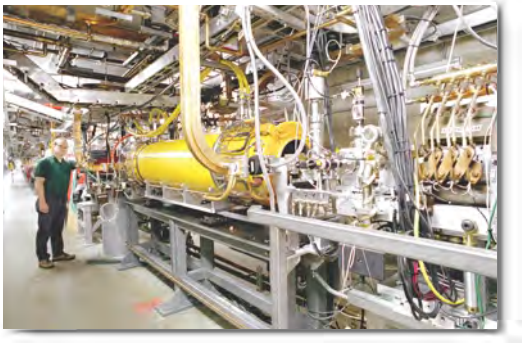

Linac

Frequency	2.856 GHz
Modulator pulse rep rate	30 Hz
Gun rep rate (1-5 pulses, 33.4 ms apart every .5 sec)	2-10 Hz
Beam pulse length	8-17 ns
Bunch length	1-10 ps FWHM
Output energy	325 MeV
Output beam charge	3 nC (max.)
Normalized emittance (mm mrad)	10 π nm mrad

Injector Synchrotron (Booster)

Circumference	368.0 m
Ramping rep rate	2 Hz
Radio frequency	351.930 MHz
Lattice structure	10 FODO cells/quadrant
Nominal extraction energy	7.0 GeV
Injection energy	325 MeV

Storage Ring System

Circumference	1104 m
Revolution frequency	272 kHz
Radio frequency	351.930 MHz
Nominal energy	7.0 GeV
Number of periods in lattice	40
Length available for insertion device	5.0 m
Nominal circulating current, multibunch	100 mA
Natural emittance	2.5 x 10^{-9} nm-rad

APS BEAMLINE GUIDE*

Source: http://beam.aps.anl.gov/pls/apsweb/bd_display_pkg.beamline_dir

(KEY: UA = 3.3 Undulator A; BM = Bending Magnet; CPU = Circularly Polarized Undulator; EMW = Elliptical Multipole Wiggler; GU = Accepting General Users)

Beamline		SCTR.	Discipline	Supported Techniques	Source	Status
1-BM	XOR	Physics, Materials Sci.	Powder diffraction Reflectivity	BM	Operational/GU	
1-ID	XOR	Materials Sci., Physics	Phase contrast imaging High-energy x-ray scattering	UA	Operational/GU	
2-BM	XOR	Physics, Life Sci.	Phase contrast imaging Tomography Microdiffraction General diffraction	BM	Operational/GU	
2-ID-B	XOR	Physics	Microfluorescence Phase contrast imaging Coherent x-ray scattering	5.5 Undulator	Operational/GU	
2-ID-D	XOR	Life Sci., Materials Sci.	Microfluorescence Microdiffraction Microprobe	UA	Operational/GU	
2-ID-E	XOR	Life Sci., Enviro. Sci.	Microfluorescence Imaging: X-ray fluorescence	UA	Operational/GU	
3-ID	XOR	Physics	Inelastic scattering Nuclear resonant scattering	2.7 Undulator	Operational/GU	
4-ID-C	XOR	Physics, Materials Sci.	Photoemission electron microscopy Photoemission spectroscopy X-ray magnetic circular dichroism Magnetic x-ray scattering	CPU	Operational/GU	
4-ID-D	XOR	Physics	X-ray magnetic circular dichroism Anomalous and resonant scattering Magnetic x-ray scattering	UA	Operational/GU	
5-BM-C	DND-CAT	Materials Sci., Polymer Sci.	Tomography Powder diffraction	BM	Operational/GU	
5-BM-D	DND-CAT	Materials Sci., Polymer Sci.	X-ray absorption fine structure High-energy x-ray scattering Polymer	BM	Operational/GU	
5-ID	DND-CAT	Materials Sci., Polymer Sci.	Macromolecular crystallography Powder diffraction Small-angle x-ray scattering X-ray optics development Polymer Inorganic crystallography	UA	Operational/GU	
6-ID	MU-CAT	Materials Sci.	Liquid scattering Magnetic x-ray scattering Powder diffraction Surface diffraction Liquid and solid surface scattering	UA	Operational/GU	
6-ID-D	MU-CAT	Materials Sci.	High-energy x-ray scattering Magnetic x-ray scattering Powder diffraction Time-resolved x-ray scattering	UA	Operational/GU	
7-ID	MHATT/XOR	Materials Sci.	Intensity fluctuation spectroscopy Time-resolved x-ray scattering Microprobe General diffraction	UA	Operational/GU	
8-BM	NE-CAT	Life Sci.	Macromolecular crystallography Multiwavelength anomalous dispersion	BM	Commissioning	

*As of 4.01.04

(KEY: UA = 3.3 Undulator A; BM = Bending Magnet; CPU = Circularly Polarized Undulator; EMW = Elliptical Multipole Wiggler;

GU = Accepting General Users)

Beamline		SCTR.	Discipline	Supported Techniques	Source	Status
8-ID	IMMY/XOR	Materials Sci.	Coherent x-ray scattering Small-angle x-ray scattering Time-resolved x-ray scattering Wide-angle x-ray scattering	UA	Operational/GU	
9-BM	CMC-CAT	Materials Sci.	X-ray absorption fine structure Surface diffraction General diffraction	BM	Commissioning	
9-ID	CMC-CAT	Materials Sci.	X-ray absorption fine structure Liquid scattering Magnetic x-ray scattering Small-angle x-ray scattering General diffraction	UA	Operational/GU	
10-ID	MR-CAT	Materials Sci., Enviro. Sci.	X-ray absorption fine structure microscopy X-ray absorption fine structure Diffraction anomalous fine structure	UA	Operational/GU	
11-ID-B	BESSRC/XOR	Materials Sci., GeoSci.	High-energy x-ray scattering	EMW	Operational/GU	
11-ID-C	BESSRC/XOR	Materials Sci., GeoSci.	High-energy x-ray scattering	EMW	Operational/GU	
11-ID-D	BESSRC/XOR	Materials Sci., GeoSci. General diffraction	X-ray absorption fine structure	EMW	Operational/GU	
12-BM	BESSRC/XOR	Materials Sci., GeoSci.	X-ray absorption fine structure Powder diffraction General diffraction	BM	Operational/GU	
12-ID	BESSRC/XOR	Materials Sci., Physics	Intensity fluctuation spectroscopy Photoemission spectroscopy Small-angle x-ray scattering	UA	Operational/GU	
13-BM	CARS-CAT	GeoSci., Enviro. Sci.	Tomography X-ray absorption fine structure Fluorescence spectroscopy Microprobe General diffraction Diamond anvil cell Multi anvil press	BM	Operational/GU	
13-ID	CARS-CAT	GeoSci., Enviro. Sci.	X-ray absorption fine structure Fluorescence spectroscopy Microdiffraction Surface diffraction Microprobe General diffraction Diamond anvil cell Multi anvil press	UA	Operational/GU	
14-BM-C	CARS-CAT	Life Sci.	Macromolecular crystallography Microdiffraction Time-resolved x-ray scattering	BM	Operational/GU	
14-BM-D	CARS-CAT	Life Sci.	Macromolecular crystallography Microdiffraction Time-resolved x-ray scattering	BM	Operational/GU	
14-ID	CARS-CAT	Life Sci.	Macromolecular crystallography Microdiffraction Multiwavelength anomalous dispersion Time-resolved x-ray scattering Laue crystallography	UA	Operational/GU	

(KEY: UA = 3.3 Undulator A; BM = Bending Magnet; CPU = Circularly Polarized Undulator; EMW = Elliptical Multipole Wiggler;

GU = Accepting General Users)

Beamline		SCTR.	Discipline	Supported Techniques	Source	Status
15-ID	CARS-CAT	Materials Sci., Chemistry	Anomalous and resonant scattering Liquid scattering Time-resolved x-ray scattering Wide-angle x-ray scattering Microcrystallography Liquid and solid surface scattering	UA	Operational/GU	
16-BM	HP-CAT	Materials Sci., GeoSci.	X-ray absorption fine structure Anomalous and resonant scattering Powder diffraction Single-crystal diffraction	BM	Construction	
16-ID-B	HP-CAT	Materials Sci., GeoSci.	X-ray absorption fine structure Compton scattering Inelastic scattering Microdiffraction Nuclear resonant scattering Powder diffraction Diamond anvil cell	UA	Operational/GU	
16-ID-D	HP-CAT	Materials Sci., GeoSci.	X-ray absorption fine structure Compton scattering Inelastic scattering Microdiffraction Nuclear resonant scattering Powder diffraction Diamond anvil cell	UA	Commissioning	
17-BM	IMCA-CAT	Life Sci.	Macromolecular crystallography Multiwavelength anomalous dispersion	BM	Commissioning	
17-ID	IMCA-CAT	Life Sci.	Macromolecular crystallography Multiwavelength anomalous dispersion	UA	Operational/GU	
18-ID	Bio-CAT	Life Sci.	X-ray absorption fine structure Fluorescence spectroscopy Small-angle x-ray scattering Time-resolved x-ray scattering General diffraction	UA	Operational/GU	
19-BM	SBC-CAT	Life Sci.	Macromolecular crystallography Multiwavelength anomalous dispersion	BM	Operational/GU	
19-ID	SBC-CAT	Life Sci.	Macromolecular crystallography Multiwavelength anomalous dispersion	UA	Operational/GU	
20-BM	PNC/XOR	Materials Sci., Enviro. Sci.	X-ray absorption fine structure Diffraction anomalous fine structure	BM	Operational/GU	
20-ID	PNC/XOR	Materials Sci., Enviro. Sci.	X-ray absorption fine structure microscopy Microfluorescence X-ray absorption fine structure Diffraction anomalous fine structure Microprobe General diffraction	UA	Operational/GU	
22-BM	SER-CAT	Life Sci.	Macromolecular crystallography	BM	Operational	
22-ID	SER-CAT	Life Sci.	Macromolecular crystallography Multiwavelength anomalous dispersion	UA	Operational	
31-ID	SGX-CAT	Life Sci.	Macromolecular crystallography	UA	Operational	
32-ID	COM-CAT	Materials Sci.	X-ray absorption fine structure Powder diffraction Single-crystal diffraction Small-angle x-ray scattering	UA	Operational	

(KEY: UA = 3.3 Undulator A; BM = Bending Magnet; CPU = Circularly Polarized Undulator; EMW = Elliptical Multipole Wiggler;

GU = Accepting General Users)

Beamline		SCTR.	Discipline	Supported Techniques	Source	Status
33-BM	UNI-CAT	Materials Sci.	Topography X-ray absorption fine structure General diffraction	BM	Operational	
33-ID	UNI-CAT	Materials Sci.	Anomalous and resonant scattering Inelastic scattering Small-angle x-ray scattering Surface diffraction Ultrasmall angle x-ray scattering General diffraction	UA	Operational/GU	
34-ID	UNI-CAT	Materials Sci.	Coherent x-ray scattering Microdiffraction Microprobe	UA	Operational/GU	

APS TECHNIQUES DIRECTORY*

Source: http://beam.aps.anl.gov/pls/apsweb/bd_display_pkg.technique_dir

Technique	Beamline
Absorption/Spectroscopy	
Fluorescence spectroscopy	13-BM, 13-ID, 18-ID
Intensity fluctuation spectroscopy	12-ID, 7-ID
Photoemission spectroscopy	12-ID, 4-ID-C
X-ray absorption fine structure	10-ID, 11-ID-D, 12-BM, 13-BM, 13-ID, 16-ID-B, 18-ID, 20-BM, 20-ID, 5-BM-D, 9-ID
X-ray magnetic circular dichroism	4-ID-C, 4-ID-D
High Pressure	
Diamond Anvil Cell	13-BM, 13-ID, 16-ID-B
Multi-Anvil Press	13-BM, 13-ID
Imaging	
X-ray absorption fine structure microscopy	10-ID, 20-ID
Microfluorescence	2-ID-B, 2-ID-D, 2-ID-E, 20-ID
Microprobe	13-BM, 13-ID, 2-ID-D, 20-ID, 34-ID, 7-ID
Phase contrast imaging	1-ID, 2-BM, 2-ID-B
Photoemission electron microscopy	4-ID-C
Tomography	13-BM, 2-BM, 5-BM-C
Protein Crystallography	
Macromolecular crystallography	14-BM-C, 14-BM-D, 14-ID, 17-ID, 19-BM, 19-ID, 5-ID
Multiwavelength anomalous dispersion	14-BM-D, 14-ID, 17-ID, 19-BM, 19-ID
Scattering	
Anomalous and resonant scattering	15-ID, 33-ID, 4-ID-D
Coherent x-ray scattering	2-ID-B, 34-ID, 8-ID
Compton Scattering	16-ID-B
Diffraction anomalous fine structure	10-ID, 20-BM, 20-ID
General diffraction	11-ID-D, 12-BM, 13-BM, 13-ID, 18-ID, 2-BM, 20-BM, 20-ID, 33-ID, 7-ID, 9-ID
High-energy x-ray scattering	1-ID, 11-ID-B, 11-ID-C, 5-BM-D, 6-ID-D
Inelastic scattering	16-ID-B, 3-ID, 33-ID
Liquid scattering	15-ID, 6-ID, 9-ID
Magnetic x-ray scattering	4-ID-C, 4-ID-D, 6-ID, 6-ID-D, 9-ID
Microdiffraction	13-ID, 14-BM-C, 14-BM-D, 14-ID, 16-ID-B, 2-BM, 2-ID-D, 34-ID
Nuclear resonant scattering	16-ID-B, 3-ID
Polymer	5-BM-D, 5-ID
Powder diffraction	1-BM, 12-BM, 16-ID-B, 5-BM-C, 5-ID, 6-ID, 6-ID-D
Reflectivity	1-BM
Small-angle x-ray scattering	12-ID, 18-ID, 33-ID, 5-ID, 8-ID, 9-ID
Surface diffraction	13-ID, 33-ID, 6-ID
Time-resolved x-ray scattering	14-BM-C, 14-BM-D, 14-ID, 15-ID, 18-ID, 6-ID-D, 7-ID, 8-ID
Ultrasmall-angle x-ray scattering	33-ID
Wide-angle x-ray scattering	15-ID, 8-ID
Miscellaneous	
X-ray optics development	

**as of 4.01.04*

APS Scientific Advisory Committee Members

William Bassett, *Director, Mineral Physics Laboratory, Cornell University*

Paul M. Bertsch, *Director, Savannah River Ecological Laboratory; Technical Director, Advanced Analytical Center for Environmental Sciences, University of Georgia*

Howard Birnbaum, *Director Emeritus, Materials Research Laboratory, University of Illinois at Urbana-Champaign*

John R. Helliwell, *Council for the Central Laboratory of the Research Councils Director of Synchrotron Radiation Science; Professor of Structural Chemistry, The University of Manchester*

Wayne Hendrickson, *Professor of Biochemistry and Molecular Biophysics, Columbia University College of Physicians and Surgeons; and Howard Hughes Medical Investigator, Columbia University of Biochemistry and Molecular Biophysics*

Peter Ingram, *Adjunct Professor of Pathology, Duke University Medical Center*

Denis McWhan, *Associate Laboratory Director (retired), Brookhaven National Laboratory*

Gerhard T. Materlik, *Director, Diamond Light Source Ltd., Rutherford Appleton Laboratory*

James R. Norris, *Chair, Department of Chemistry, The University of Chicago*

Paul Peercy, *Dean, College of Engineering, University of Wisconsin-Madison*

J. Michael Rowe (Chair, APS SAC), *Director, Center for Neutron Research, and Center for Neutron Research, National Institute of Standards & Technology*

Joachim Stöhr, *Professor and Deputy Director, Stanford Synchrotron Radiation Laboratory, Stanford Linear Accelerator Center*

Kathleen Taylor, *Director (retired), Materials and Processes Laboratory, General Motors Research & Development and Processing Center*

Pierre Wiltzius, *Director, Beckman Institute, and Professor, Departments of Materials Science and Engineering, and Physics, University of Illinois at Urbana-Champaign*

Source: http://www.aps.anl.gov/user/committees/sac/sac.html

APS Partner Users Council

Ercan Alp, XOR sector 3, *Argonne National Laboratory*

Wayne Anderson, LS-CAT, sector 21, *Northwestern University*

Mark Beno, BESSRC/XOR, sector 11, *Argonne National Laboratory*

Kent Blasie, CMC-CAT, sector 9, *University of Pennsylvania*

Bruce Bunker, MR-CAT, sector 10, *University of Notre Dame*

Malcolm Capel, NE-CAT, sector 24 and 8-BM, *Cornell University*

John Chrzas, SER-CAT, sector 22, *University of Georgia*

Roy Clarke, MHATT/XOR, sector 7, *University of Michigan*

Kevin D'Amico, SGX-CAT, sector 31, *Structural GenomiX, Inc.*

Bob Fischetti, GM/CA-CAT, sector 23, *Argonne National Laboratory*

Dean Haeffner, XOR, sector 1, *Argonne National Laboratory*

Tom Irving, Bio-CAT, sector 18, *Illinois Institute of Technology*

Andrzej Joachimiak, SBC-CAT, sector 19, *Argonne National Laboratory*

Lisa Keefe, IMCA-CAT, sector 17, *Illinois Institute of Technology*

David H. Mao, HP-CAT, sector 16, *Carnegie Institution of Washington*

Ian McNulty, XOR, sector 2, *Argonne National Laboratory*

Simon Mochrie, IMMY/XOR, sector 8, *Yale University*

Keith Moffat, BioCARS, sector 14, *The University of Chicago*

John Quintana, DND-CAT, sector 5, *Northwestern University*

Mark Rivers, GSECARS, sector 13, *The University of Chicago*

Doug Robinson, MU-CAT, sector 6, *Iowa State University*

George Srajer, XOR, sector 4, *Argonne National Laboratory*

G. Brian Stephenson, Nano-CDT, sector 26, *Argonne National Laboratory*

Ed Stern, PNC/XOR, sector 20, *University of Washington*

Jim Viccaro, ChemMatCARS, sector 15, *The University of Chicago*

Randy Winans, BESSRC/XOR, sector 12, *Argonne National Laboratory*

Paul Zschack, UNI-CAT, sectors 33 & 34, *University of Illinois at Urbana-Champaign*

APS Participants

Steven Davey, *Argonne National Laboratory*

Rod Gerig, *Argonne National Laboratory*

J. Murray Gibson, *Argonne National Laboratory*

Efim Gluskin, *Argonne National Laboratory*

Dennis Mills, *Argonne National Laboratory*

Bill Ruzicka, *Argonne National Laboratory*

Susan Strasser, *Argonne National Laboratory*

Jin Wang, *Argonne National Laboratory*

Source: http://www.aps.anl.gov/user/committees/puc/puc_list.htm

APS Users Organization Steering Committee

Malcolm Capel (sector 24), *Cornell University*

Lisa J. Keefe (sector 17), *Illinois Institute of Technology*

Lin X. Chen, Argonne National Laboratory

Mark Rivers (sector 13), *The University of Chicago*

David J. Cookson (sector 15), *The University of Chicago*

John P. Rose, *University of Georgia*

Julie Cross (sector 20), *University of Washington*

Sunil K. Sinha, *University of California, San Diego*

Stephen M. Durbin (APSUO Chair), *Purdue University*

Susan Strasser, *Argonne National Laboratory*

Stephan Ginell, *Argonne National Laboratory*

Carol Thompson, *Northern Illinois University*

Gene Ice, *Oak Ridge National Laboratory*

Paul Zschack (sectors 33 & 34), *University of Illinois*

Source: http://www.aps.anl.gov/user/committees/apsuo/members/home.html

Proposal Review Panels

Instrumentation

Eric Dufresne, *Chair*
Wilfried Schildkamp
Sarvjit Shastri

Imaging/Microbeam

Mark Rivers, *Chair*
George Cody
Barry Lai
John Miao
Al Thompson

Macromolecular Crystallography

Karl Volz, *Chair*
Craig Ogata
Amy Rosenzweig

Scattering/Applied Materials

Paul Fuoss, *Chair*
I. Cev Noyan
Carol Thompson
Robert A.Winholtz

Scattering/Condensed Matter

Joel Brock, *Chair*
Paul Evans
John Hill
Ben Larson
Young S. Lee
Guoyin Shen
Surendra Saxena
Haskell Taub

Scattering/Chemistry/Biology/Environmental Science

Neil Sturchio, *Chair*
Fred Stevens
David Tiede
Angus Wilkinson

Small-Angle Scattering

Larry Lurio, *Chair*
Andrew Allen
Jyotsana Lal
David Londono
Pappannan Thiyagarajan

Spectroscopy

Joe Woicik, *Chair*
Simon Bare
Lin X. Chen
Lisa M. Miller
Matt Newville

Source: http://www.aps.anl.gov/user/committees/prp/home.html

Beam Time Allocation Committees

Macromolecular Crystallography

Keith Brister
Robert Fischetti
Stephan Ginell
Andy Howard
Zdzislaw Wawrzak

All Other Science

Jon Tischler
Steve Heald
Brian Stephenson
Denis Keane

Source: http://www.aps.anl.gov/user/committees/bac/home.html

APS Publications—2003

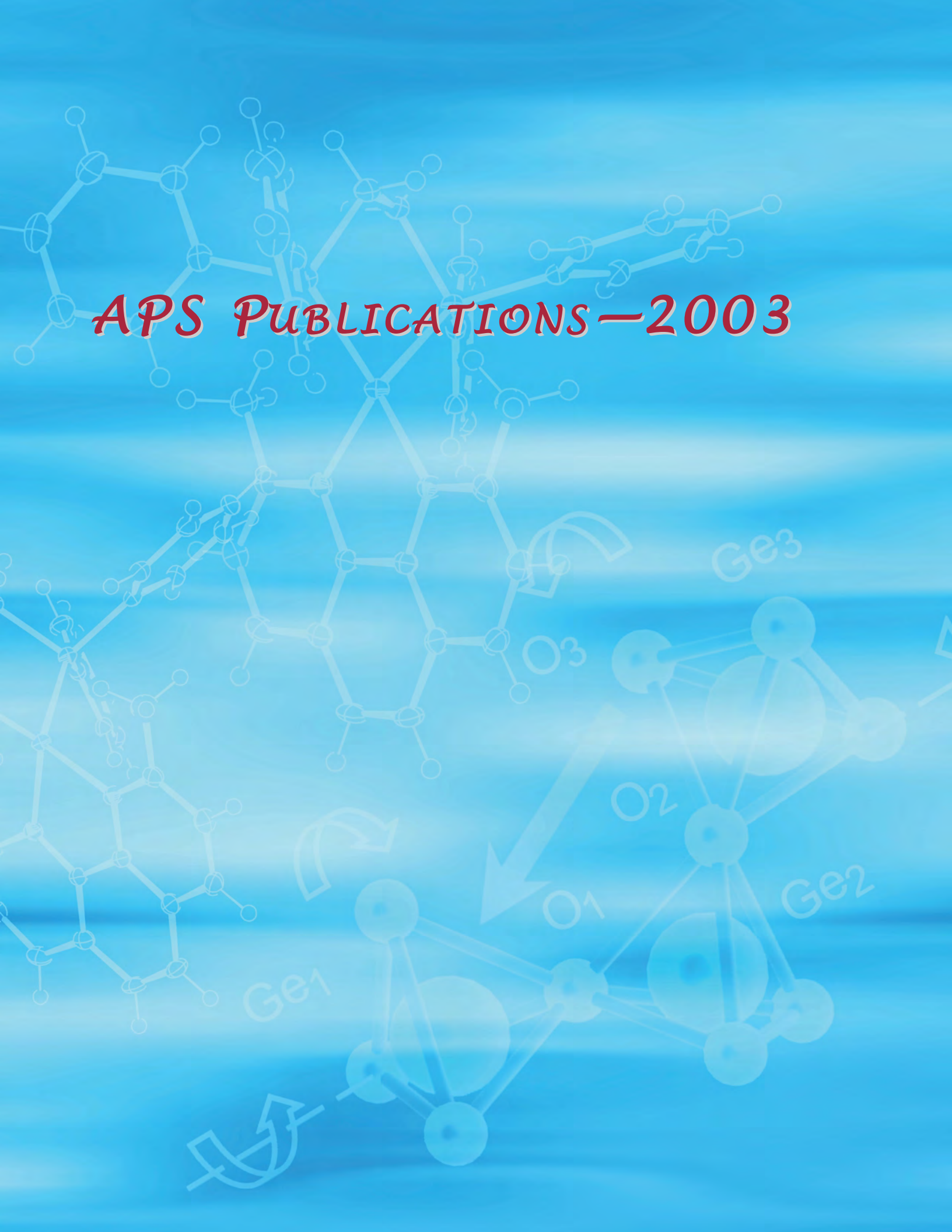

APS Publications—2003

The Advanced Photon Source (APS) maintains a searchable, publicly available database of all APS-related scientific and technical publications from APS users and personnel.

For access, go to: http://www.aps.anl.gov/aps/science-publications.html

Experimental Results: Journal Articles

H.A. Al-Khayat, L. Hudson, M.K. Reedy, T.C. Irving, J.M. Squire, "Myosin head configuration in relaxed insect flight muscle: X-ray modeled resting cross-bridges in a pre-powerstroke state are poised for actin binding," Biophys. J. **85**, 1063-1079 (2003).

B.W. Adams, "A time- and energy-resolving, multichannel event logger," Rev. Sci. Instrum. **74** (2), 1128-1134 (February 2003).

I. Agmon, T. Auerbach, D. Baram, H. Bartels, A. Bashan, R. Berisio, P. Fucini, H.A.S. Hansen, J. Harms, M. Kessler, M. Peretz, F. Schluenzen, A. Yonath, R. Zarivach, "On peptide bond formation, translocation, nascent protein progression and the regulatory properties of ribosomes," Eur. J. Biochem. **270**, 2543-2556 (February 2003).

I. Ahmad, J. C. Banar, J. A. Becker, T. A. Bredeweg, J. R. Cooper, D. S. Gemmell, A. Mashayekhi, D. P. McNabb, E. F. Moore, P. Palmer, R. S. Rundberg, J. P. Schiffer, S. D. Shastri, T. F. Wang, J. B. Wilhelmy, "Search for x-ray induced decay of the 31-yr isomer of ^{178}Hf at low x-ray energies," Phys. Rev. C **67**, 041305-1-041305-4 (2003).

K. Farid Ahmad, A. Melnick, S. Lax, D. Bouchard, J. Liu, C.-L. Kiang, S. Mayer, S. Takahashi, J.D. Licht, G.G. Privé, "Mechanism of SMRT corepressor recruitment by the BCL6 BTB domain," Molecular Cell **12** (6), 1551-1564 (2003).

V.E. Ahn, K.F. Faull, J.P. Whitelegge, J. Higginson, A.L. Fluharty, G.G. Privé, "Expression, purification, crystallization, and preliminary X-ray analysis of recombinant human saposin B," Protein Expres. Purif. **27** (1), 186-193 (2003).

S. Aich, F. Imabayashia, L.T.J. Delbaere, "Crystallization and preliminary X-ray crystallographic studies of phosphoenolpyruvate carboxykinase from Corynebacterium glutamicum," Acta Crystallogr. D **59** (9), 1640-1641 (2003).

M. Aittaleb, R. Rashid, Q. Chen, J.R. Palmer, C.J. Daniels, "Structure and function of archaeal box C/D sRNP core proteins," Nature Struct. Biol. **10** (4), 256-263 (2003).

J. Almer, U. Lienert, R. L. Peng, C. Schlauer, M. Oden, "Strain and texture analysis of coatings using high-energy x-rays," J. Appl. Phys. **94** (1), 697-702 (July 2003).

J.E. Amonette, R.K. Kukkadapu, E.E. Alp, W. Sturhahn, T.S. Toellner, "Heterogeneous electron-transfer kinetics with synchrotron ^{57}Fe Mossbauer spectroscopy," Geochim. Cosmochim. Acta **67** (12), 2109-2116 (June 2003).

J.E. Amonette, S.M. Heald, C.K. Russell, "Imaging the heterogeneity of mineral surface reactivity using Ag(I) and synchrotron X-ray microscopy," Phys. Chem. Miner. **30**, 559-569 (2003).

Y. Aria, A. Lanzirotti, S. Sutton, D.L. Sparks, J.A. Davis, "Arsenic speciation and reactivity in poultry litter," Environ. Sci. Technol. **37** (18), 4083-4090 (2003).

F. Arisaka, S. Kanamaru, P. Leiman, M.G. Rossmann, "The tail lysozyme complex of bacteriophage T4," Int. J. Biochem. Cell B. **35** (1), 16-21 (2003).

G.B. Armen, E.P. Kanter, B. Krässig, J.C. Levin, S.H. Southworth, L. Young, "Threshold krypton charge-state distributions coincident with K-shell fluorescence," Phys. Rev. A **67**, 042718-1-042718-12 (April 2003).

D.A. Arms, R.S. Shah, R.O. Simmons, "X-ray Debye-Waller factor measurements of solid ^{3}He and ^{4}He," Phys. Rev. B **67** (9), 094303-1-094303-11 (March 2003).

B.J. Baer, H. Cynn, V. Iota, C.-S. Yoo, G. Shen, “Phase diagram and equation of state of praseodymium at high pressures and temperatures,” Phys. Rev. B **67**, 134115-1-134115-7 (2003).

P. Balbo, M. Oliveira, “Crystallization and preliminary X-ray data of the $\alpha_2\varepsilon_2$ subcomponent of the acetyl-CoA decarbonylase/synthase multienzyme complex from Methanosarcina thermophila,” Acta Crystallogr. D **59** (4), 721-723 (2003).

D. Balch, E. Ustundag, D.C. Dunand, “Diffraction strain measurements in a partially crystallized bulk metallic glass composite containing ductile particles,” J. Non-Cryst. Solids **317** (1-2), 176-180 (2003).

D.K. Balch, E. Ustandag, D.C. Dunand, “Elasto-plastic load transfer in bulk metallic glass composites containg ductile particles,” Metall. Mater. Trans. A **34A**, 1787-1797 (2003).

R.I. Barabash, G.E. Ice, F.J. Walker, “Quantitative microdiffraction from deformed crystals with unpaired dislocations and dislocation walls,” J. Appl. Phys. **93** (3), 1457-1464 (February 2003).

D.P. Barondeau, C.D. Putnam, C.J. Kassmann, J.A. Tainer, E.D. Getzoff, “Mechanism and energetics of green fluorescent protein chromophore synthesis revealed by trapped intermediate structures,” Proc. Natl. Acad. Sci. **100** (21), 112111-12116 (2003).

A. Bashan, I. Agmon, R. Zarivach, F. Schluenzen, J. Harms, R. Berisio, H. Bartels, F. Franceschi, T. Auerbach, H. Hansen, E. Kossoy, M. Kessler, A. Yonath, “Structural basis of the ribosomal machinery for peptide bond formation, translocation, and nascent chain progression,” Molecular Cell **11**, 91-102 (2003).

A. Bellare, A. Gomoll, W. Fitz, R. Scott, T. Thornhill, “Improving the fatigue properties of poly(methyl methacrylate)orthopaedic cement containing radiopacifier nanoparticles,” Mater. Sci. Forum **426-432**, 3133-3138 (2003).

S. Bencharit, C.L. Morton, Y. Xue, P.M. Potter, M.R. Redinbo, “Structural basis of heroin and cocaine metabolism by a promiscuous human drug-processing enzyme,” Nature Struct. Biol. **10** (5), 349-356 (May 2003).

C.J. Benmore, J.K.R. Weber, S. Sampath, J. Siewenie, J. Urquidi, J.A. Tangeman, “A neutron and X-ray diffraction study of calcium aluminate glasses,” J. Phys. Condens. Matter **15**, S2413-S2323 (June 2003).

A.K. Bera, J. Zhu, H. Zalkin, J.L. Smith, “Functional dissection of the Bacillus subtilis pur operator site,” J. Bacteriol. **185** (14), 4099-4109 (2003).

U. Bergmann, W. Sturhahn, D.E. Linn Jr., F.E. Jenney Jr., M.W.W. Adams, K. Rupnik, B.J. Hales, E.E. Alp, A. Mayse, S.P. Cramer, “Observation of FE-H/D modes by nuclear resonant vibrational spectroscopy,” J. Am. Chem. Soc. **125** (14), 4016-4017 (March 2003).

U. Bergmann, H. Groenzin, O.C. Mullins, P. Glatzel, J. Fetzer, S.P. Cramer, “Carbon K-edge x-ray Raman spectroscopy supports simple, yet powerful description of aromatic hydrocarbons and asphaltenes,” Chem. Phys. Lett. **369** (1-2), 184-191 (February 2003).

R. Berisio, F. Schluenzen, J. Harms, A. Bashan, T. Auerbach, D. Baram, A. Yonath, “Structural insight into the role of the ribosomal tunnel in cellular regulation,” Nature Struct. Biol. **10** (5), 366-370 (March 2003).

R. Berisio, J. Harms, F. Schluenzen, R. Zarivach, H.A.S. Hansen, P. Fucini, A. Yonath, “Structural insight into the antibiotic action of telithromycin against resistant mutants,” J. Bacteriol. **185** (14), 4276-4279 (July 2003).

R.A. Bernal, S. Hafenstein, N.H. Olson, V.D. Bowman, P.R. Chipman, T.S. Baker, B.A. Fane, M.G. Rossmann, “Structural studies of Bacteriophage α3 Assembly,” J. Mol. Biol. **325** (1), 11-24 (2003).

J. Birrell, J.E. Gerbi, O. Auciello, J.M. Gibson, D.M. Gruen, J.A. Carlisle, “Bonding structure in nitrogen doped ultrananocrystalline diamond,” J. Appl. Phys. **93** (9), 5606-5612 (May 2003).

D.A. Bernstein, M.C. Zittel, J.L. Keck, “High-resolution structure of the E.coli RecQ helicase catalytic core,” EMBO J. **22** (19), 4910-4921 (2003).

J. Blanco, R.A. Moore, R.E. Viola, “Capture of an intermediate in the catalytic cycle of L-Aspartate-β-semialdehyde dehydrogenase,” Proc. Natl. Acad. Sci. **100**, 12613-12617 (2003).

J. Blanco, R.A. Moore, V. Kabaleeswaran, R.E. Viola, “A structural basis for the mechanism of Aspartate-β-semialdehyde dehydrogenase from Vibrio cholerae,” Protein Sci. **12**, 27-33 (2003).

A.B. Boraston, V.R. Notenboom, A.J. Warren, D.J. Kilburn, D.R. Rose, G. Davies, “Structure and ligand binding of carbohydrate-binding module Cs CBM6-3 reveals similarities with fucose-specific lectins and ‘galactose-binding’ domains,” J. Mol. Biol. **327** (3), 659-669 (2003).

C.E. Botez, W.C. Elliott, K. Li, E.D. Lu, P.F. Miceli, E.H. Conrad, P.W. Stephens, “Specular reflectivity from pyramidal surface morphologies,” Physica B **336**, 130-135 (2003).

C.E. Botez, K. Li, E. Lu, W.C. Elliott, P.F. Miceli, E. Conrad, P.W. Stephens, “Vacancy formation during low-temperature Ag(001) and Ag(111) homoepitaxy,” Adv. X Ray Anal. **46**, 167-172 (2003).

B.R. Bowman, M.L. Baker, F.J. Rixon, W. Chu, F.A. Quiocho, “Structure of the herpesvirus major capsid protein,” EMBO J. **22** (4), 757-765 (2003).

M.I. Boyanov, S.D. Kelly, K.M. Kemner, B.A. Bunker, J.B. Fein, A. Fowle, “Adsorption of cadmium to Bacillus subtilis bacterial cell walls: a pH-dependent x-ray absorption fine structure spectroscopy study,” Geochim. Cosmochim. Acta **67** (18), 3299-3311 (2003).

A. Braun, S. Shrout, A.C. Fowlks, B.A. Osaisai, S. Seifert, E. Granlund, E.J. Cairns, “Electrochemical in situ reaction cell for x-ray scattering, diffraction and spectroscopy,” J. Synchrotron Rad. **10**, 320-325 (July 2003).

S.C. Brooks, J.K. Fredrickson, S.L. Carroll, D.W. Kennedy, J.M. Zachara, A.E. Plymale, S.D. Kelly, K.M. Kemner, S. Fendorf, “Inhibition of bacterial U(VI) reduction by calcium,” Environ. Sci. Technol. **37** (9), 1850-1858 (2003).

J.S. Brunzelle, P. Shafaee, X. Yang, S. Weigand, Z. Ren, W.F. Anderson, “Automated crystallographic system for high-throughput protein structure determination,” Acta Crystallogr. D **59**, 1138-1144 (2003).

J.D. Budai, W. Yang, N. Tamura, J.-S. Chung, J.Z. Tischler, B. Larson, G.E. Ice, C. Park, D.P. Norton, “X-ray microdiffraction study of growth modes and crystallography tilts in oxide films on metal substrates,” Nature Materials **2** (7), 487-492 (July 2003).

T.E. Budarz, E.W. Prohofsky, S.M. Durbin, T. Sjodin, J.T. Sage, W. Sturhahn, E.E. Alp, “Determination of the complete set of iron normal modes in the heme model compound Fe^{III}(OEP)Cl from nuclear resonance vibrational spectroscopic data,” J. Phys. Chem. B **107**, 11170-11177 (2003).

T. Buonassisi, M. Heuer, O.F. Vyvenko, A.A. Istratov, E.R. Weber, Z. Cai, B. Lai, T.F. Ciszek, R. Schindler, “Applications of synchrotron radiation x-ray techniques on the analysis of the behavior of transition metals in solar cells and single-crystalline silicon with extended defects,” Physica B **340-342**, 1137-1141 (2003).

E. Burkel, R. Nicula, U. Ponkratz, H. Sinn, A. Alatas, E.E. Alp, “Lattice dynamics of Al-based quasicrystals studied by high-resolution inelastic x-ray scattering with synchrotron radiation,” Nucl. Instrum. Methods B **199**, 151-155 (2003).

W. Cai, C.F. Powell, Y. Yue, S. Narayanan, J. Wang, M.W. Tate, M.J. Renzi, A. Ercan, E. Fontes, S.M. Gruner, “Quantitative analysis of highly transient fuel sprays by time-resolved x-radiography,” Appl. Phys. Lett. **83** (8), 1671-1673 (August 2003).

Z. Cai, B. Lai, Y. Xiao, S. Xu, “An x-ray diffraction microscope at the Advanced Photon Source,” J. Phys. IV France **104**, 17-20 (2003).

E.A. Campbell, J.L. Tupy, T.M. Gruber, S. Wa, M.M. Sharp, C.A. Gross, S.A. Darst, “Crystal structure of Escherichia coli σ^E with the cytoplasmic domain of its anti-σ RseA,” Molecular Cell **11**, 1067-1078 (April 2003).

G. Cargill, L. Moyer, W. Yang, B. Larson, G. Ice, “X-ray microbeam strain measurements in polycrystalline films,” Mater. Sci. Forum **426-432**, 3945-3950 (2003).

S.R. Carino, R.S. Underhill, H.S. Tostmann, A.M. Skolnik, J.L. Logan, M.R. Davidson, J.T. Culp, R.S. Duran, “Grazing incidence synchrotron x-ray diffraction of polymerizing Langmuir monolayers,” Langmuir **19** (25), 10514-10522 (August 2003).

E.E. Carpenter, V. Cestone, G. Landry, V.G. Harris, K.M. Kemner, “Synthesis of Amorphous Lepidocrocite Thin Films via Spin-Spray Ferrite Plating,” Chem. Mater. **15** (6), 1235-1236 (2003).

S.A. Chambers, S.M. Heald, T. Droubay, “Local Co structure in epitaxial $Co_xTi_{1-x}O_{2-x}$ anatase,” Phys. Rev. B **67**, 100401-1-100401-4 (2003).

A. Changela, K. Chen, Y. Xue, J. Holschen, C.E. Outten, T.V. O'Halloran, A. Mondragon, “Molecular basis of metal-ion selectivity and zeptomolar sensitivity by CueR,” Science **301**, 1383-1387 (2003).

L.X. Chen, G.B. Shaw, I. Novozhilova, T. Liu, G. Jennings, K. Attenkofer, G.J. Meyer, P. Coppens, “MLCT State Structure and Dynamics of a Copper(I) Diimine Complex Characterized by Pump-Probe X-ray and Laser Spectroscopies and DFT Calculations,” J. Am. Chem. Soc. **125** (23), 7022-7034 (June 2003).

Y. Chen, P.A. Rice, “The role of the conserved Trp^{330} in Flp-mediated recombination: Functional and structural analysis,” J. Biol. Chem. **278** (27), 24800-24807 (2003).

L. Cheng, P. Fenter, M.J. Bedzyk, N.C. Sturchio, "Fourier-expansion solution of atom distributions in a crystal using x-ray standing waves," Phys. Rev. Lett. **90** (25), 255503-1-255503-4 (June 2003).

M.-H. Chiang, L. Soderholm, M.R. Antonio, "Redox chemistry of actinide ions in Wells-Dawson heteropolyoxoanion complexes," Eur. J. Inorg. Chem. **16**, 2929-2936 (June 2003).

M.-H. Chiang, C.W. Williams, L. Soderholm, M.R. Antonio, "Coordination of actinide ions in Wells-Dawson heteropolyoxoanion complexes," Eur. J. Inorg. Chem. **42**, 2663-2669 (July 2003).

R. Chiarizia, M.P. Jensen, M. Borkowski, J.R. Ferraro, P. Thiyagarajan, K.C. Littrell, "Third phase formation revisited: the U(VI), HNO_3-TBP, n-dodecane system," Solvent Extr. Ion Exc. **21** (1), 1-27 (March 2003).

Y. Cho, V. Sharma, J.C. Sacchettini, "Crystal Structure of ATP Phosphoribosyltransferase from Mycobacterium tuberculosis," J. Biol. Chem. **278** (10), 8333-8339 (2003).

J.-Y. Choe, C.V. Iancu, H.J. Fromm, R.B. Honzatko, "Metaphosphate in the active site of fructose-1,6-bisphosphatase," J. Biol. Chem. **278** (18), 16015-16020 (2003).

J.-Y. Choe, S.W. Nelson, H.J. Fromm, R.B. Honzatko, "Interaction of Tl^+ with product complexes of fructose-1,6-bisphosphatase," J. Biol. Chem. **278** (18), 16008-16014 (2003).

P.J. Chupas, X. Qiu, J.C. Hanson, P.L. Lee, C.P. Grey, S.J.L. Billinge, "Rapid acquisition pair distribution function (RA-PDF) analysis," J. Appl. Crystallogr. **36**, 1342-1347 (2003).

E.M. Ciszak, L.G. Korotchkina, P.M. Dominiak, S. Sidhu, M.S. Patel, "Structural basis for flip-flop action of thiamin pyrophosphate-dependent enzymes revealed by human pyruvate dehydrogenase," J. Biol. Chem. **278** (23), 21240-21246 (2003).

S.L. Colletti, J.L. Frie, E.C. Dixon, S.B. Singh, B.K. Choi, G. Scapin, C.E. Fitzgerald, S. Kumar, E.A. Nichols, S.J. O'Keefe, E.A. O'Neill, G. Porter, K. Samuel, D.M. Schmatz, C.D. Schwartz, W.L. Shoop, C.M. Thompson, J.E. Thompson, R. Wang, A. Woods, D.M. Zaller, J.B. Doherty, "Hybrid-designed inhibitors of p38 MAP kinase utilizing N-arylpyridazinones," J. Med. Chem. **46**, 349-352 (2003).

A.B. Conway, Y. Chen, P.A. Rice, "Structural plasticity of the Flp-Holliday junction complex," J. Mol. Biol. **326** (2), 425-434 (2003).

P. Coppens, "What can time-resolved diffraction tell us about transient species?: Excited-state structure determination at atomic resolution," Chem. Comm. **12**, 1317-1320 (2003).

M.K. Corbierre, N.S. Cameron, M. Sutton, S.G.J. Mochrie, L.B. Lurio, A. Rhum, R.B. Lennox, "Polymer-stablized gold nanoparticles and their incorporation into polymer matrices," J. Am. Chem. Soc. **123** (42), 10411-10412 (2003).

C.C. Correll, K. Swinger, "Common and disctinctive features of GNRA tetraloops based on a GUAA tetraloop structure at 1.4 Å resolution," RNA **9**, 355-363 (2003).

C.C. Correll, J. Beneken, M.J. Plantinga, M. Lubbers, Y.-L. Chan, "The common and the distinctive features of the bulged-G motif based on a 1.04 Å resolution RNA structure," Nucleic Acids Res. **31** (23), 6806-6818 (2003).

M.K. Crawford, R.L. Harlow, P.L. Lee, Y. Zhang, J. Hormadaly, R. Flippen, Q. Huang, J.W. Lynn, R. Stevens, B.F. Woodfield, J. Boerio-Goates, R.A. Fisher, "Structure and properties of the integer-spin frustrated antiferromagnet $GeNi_2O_4$," Phys. Rev. B **68**, 220408-1-220408-4 (December 2003).

A.R. Criswell, E. Bae, B. Stec, J. Konisky, G.N. Phillips Jr., "Structures of thermophilic and mesophilic adenylate kinases from the genus Methanococcus," J. Mol. Biol. **330** (5), 1087-1099 (2003).

S. Crosson, S. Rajagopal, K. Moffat, "The LOV domain family: Photoresponsive signaling modules coupled to diverse output domains," Biochemistry-US **42** (1), 2-10 (2003).

B. Cui, B. Lin, S.A. Rice, "Structure and phase transitions in confined binary colloid mixtures," J. Chem. Phys. **119** (4), 2386-2398 (July 2003).

J.J. Curry, H.G. Adler, S.D. Shastri, W.-K. Lee, "X-ray induced fluorescence measurement of density distributions in a metal-halide lighting arc," J. Appl. Phys. **93** (5), 2359-2368 (March 2003).

J.J. Curry, H.G. Adler, W.-K. Lee, S.D. Shastri, "Direct observation of de-mixing in a ceramic metal-halide arc lamp," J. Phys. D. Appl. Phys. **36**, 1529-1534 (2003).

M.L. Curtin, A.S. Florjancic, J. Cohen, W.-Z. Gu, D.J. Frost, S.W. Muchmore, H.L. Sham, "Novel and selective imidazole-containing biphenyl inhibitors of protein farnesyltransferase," Bioorg. Med. Chem. Lett. **13**, 1367-1371 (2003).

J. Cutler, N. Chen, D.T. Jiang, G.P. Demopoulos, Y. Jia, J.W. Rowson, "The nature of arsenic in uranium mill tailings by x-ray absorption spectroscopy," J. Phys. IV France **107**, 337-340 (2003).

P. Czoschke, H. Hong, L. Basile, T.-C. Chiang, "Quantum oscillations in the layer structure of thin metal films," Phys. Rev. Lett. **91** (22), 226801-1-226801-4 (November 2003).

R.A. Daines, I. Pendrak, K. Sham, G.S. Van Aller, A.K. Konstantinidis, J.T. Lonsdale, C.A. Janson, X. Qiu, M. Brandt, S.S. Khandekar, C. Silverman, M.S. Head, "First x-ray cocrystal structure of a bacterial FabH condensing enzyme and a small molecule inhibitor achieved using rational design and homology modeling," J. Med. Chem. **46**, 5-8 (2003).

R. Das, L.W. Kwok, I.S. Millet, Y. Bai, T.T. Mills, J. Maskel, G.S. Jacob, "The fastest global events in RNA folding: Electrostatic relaxation and tertiary collapse of the tetrahymena ribozyme," J. Mol. Biol. **332**, 311-319 (September 2003).

S. Datta, T. Ikeda, K. Kano, F.S. Mathews, "Structure of the phenylhydrazine adduct of the quinohemoprotein amine dehydrogenase from Paracoccus denitrificans at 1.7 Å resolution," Acta Crystallogr. D **59** (9), 1551-1556 (2003).

D.R. Davies, H. Interthal, J.J. Champoux, W.G. Hol, "Crystal structure of a transition state mimic for Tdpl assembled from Vanadate, DNA, and a Topoisomerase I-Derived Peptide," Chem. Biol. **10**, 139-147 (2003).

M.F. DeCamp, D.A. Reis, A. Cavalieri, P.H. Bucksbaum, R. Clarke, R. Merlin, E.M. Dufresne, D.A. Arms, A.M. Lindenberg, A.G. MacPhee, Z. Chang, B. Lings, J.S. Wark, S. Fahy, "Transient strain driven by a dense electron-hole plasma," Phys. Rev. Lett. **91** (16), 165502-1-165502-4 (October 2003).

J. Deng, Y. Xiong, P. Baocheng, S. Muttaiya, "Structure of an RNA dodecamer containing a fragment from SRP domain IV of Escherichia coli," Acta Crystallogr. D **59** (6), 1004-1011 (2003).

J. Diao, D.R. Cooper, D.A. Sanders, M.S. Hasson, "Crystallization of butyrate kinase 2 from Thermotoga maritima mediated by vapor diffusion of acetic acid," Acta Crystallogr. D **59** (6), 1100-1102 (2003).

M.L. Dietz, J.A. Dzielawa, I. Laszak, B.A. Young, M.P. Jensen, "Influence of solvent structural variations on the mechanism of facilitated ion transfer into room-temperature ionic liquids," Green Chem. **5** (6), 682-685 (October 2003).

C.T. Dillon, B.J. Kennedy, P.A. Lay, B. Lai, A.P.J. Stampfl, P. Ilinski, D. Legnini, J. Maser, W. Rodrigues, G. Shea-McCarthy, M. Chowela, "Implementation of x-ray microscopy and micro-XANES analysis for investigations of the cellular uptake and cellular metabolism of transition metals," J. Phys. IV France **104**, 293-296 (2003).

H. Ding, S. Qiu, R.J. Bunzel, D. Luo, A. Arabashi, S. Lu, J. Symersky, L.A. Nagy, L.J. DeLucas, S. Lib, M. Luo, "Purification, nanocrystallization and preliminary x-ray analysis of a C-terminal part of tropomodulin protein 1, isoform A, from Caenorhabditis elegans," Acta Crystallogr. D **59** (6), 1106-1108 (June 2003).

C.M. Doudna, M.F. Bertino, F.D. Blum, A.T. Tokuhiro, D. Lahiri, S. Chattopahyay, J. Terry, "Radiolytic synthesis of bimetallic Ag–Pt nanoparticles with a high aspect ratio," J. Phys. Chem. B **107**, 2966-2970 (2003).

R.W. Dunford, E.P. Kanter, B. Kraessig, S.H. Southworth, L. Young, P.H. Mokler, Th. Stöhlker, "Two-photon decay in gold atoms following photoionization with synchrotron radiation," Phys. Rev. A **67**, 054501-1-054501-4 (May 2003).

M. Egli, V. Tereshko, G.N. Murshudov, R. Sanishvili, X. Liu, F.D. Lewis, "Face-to-face and edge-to-face Pi-Pi interactions in a synthetic DNA with a Stilbenediether linker," J. Am. Chem. Soc. **125**, 10842-10849 (2003).

M. Egli, S. Sarkhel, G. Minasov, A. Rich, "Structure and function of the ribosomal frameshifting pseudoknot RNA from beet western yellow virus," Helv. Chim. Acta **86**, 1709-1727 (2003).

C. Eicken, M.A. Pennella, X. Chen, K.M. Koshlap, M.L. VanZile, J.C. Sacchettini, D.P. Giedroc, "A metal-ligand-mediated intersubunit allosteric switch in related SmtB/ArsR zinc sensor proteins," J. Mol. Biol. **333** (4), 683-695 (2003).

C. Eigenbrot, Y.G. Meng, R. Krishnamurthy, M.T. Lipari, L. Presta, B. Devaux, T. Wong, P. Moran, S. Bullens, D. Kirchhofer, "Structural insight into how an anti-idiotypic antibody against D3H44 (anti-tissue factor antibody) restores normal coagulation," J. Mol. Biol. **331**, 433-446 (2003).

O. El-Kabbani, P. Ramsland, C. Darmanin, R.P. Chung, A. Podjarny, "Structure of human aldose reductase holoenzyme in complex with Statil: An approach to structure-based inhibitor design of the enzyme," Proteins **50** (2), 230-238 (2003).

P.A. Elkins, J.M. Watts, M. Zalacain, A. van Thiel, P.R. Vatazka, M. Redlak, C. Andraos-Selim, F. Rastinejad, W.M. Holmes, "Insight into Catalysis by a Knotted TrmD tRNA Methyltransferase," J. Mol. Biol. **333**, 931-949 (September 2003).

D. Errandonea, M. Somayazulu, D. Häusermann, "Phase transitions and amorphization of $CaWO_4$ at high pressure," Phys. Status Solidi. b. **235** (1), 162-169 (2003).

D. Errandonea, M. Somayazulu, D. Häusermann, H .K. Mao, "Melting of tantalum at high pressure determined by angle dispersive x-ray diffraction in a double-sided laser-heated diamond-anvil cell," J. Phys. Condens. Matter **15**, 7635-7649 (2003).

D. Errandonea, Y. Meng, D. Hausermann, T. Uchida, "Study of the phase transformations and equation of state of magnesium by synchrotron x-ray diffraction," J. Phys. Condens. Matter **15**, 1277-1289 (February 2003).

G.A. Farnan, C.L. Fu, Z. Gai, M. Krcmar, A.P. Baddorf, Z.Y. Zhang, J. Shen, "Electronic Stability of Magnetic Fe/Co Superlattices with Monoatomic Layer Alternation," Phys. Rev. Lett. **91** (22), 226106-1-226106-4 (November 2003).

P. Fenter, C. Park, L. Cheng, Z. Zhang, M.P.S. Krekeler, N.C. Sturchio, "Orthoclase dissolution kinetics probed by in situ x-ray reflectivity: Effects of temperature, pH, and crystal orientation," Geochim. Cosmochim. Acta **67** (2), 197-211 (January 2003).

P. Fenter, L. Cheng, C. Park, Z. Zhang, N.C. Sturchio, "Structure of the Orthoclase (001) and (010)-Water Interfaces using High-Resolution X-ray Reflectivity," Geochim. Cosmochim. Acta **67** (22), 4267-4275 (November 2003).

A.A. Finch, N. Allison, S.R. Sutton, M. Newville, "Strontium in coral aragonite: 1. Characterization of Sr coordination by extended absorption X-ray fine structure," Geochim. Cosmochim. Acta **67** (7), 1189-1194 (2003).

R. Fischetti, A. Mirza, D.J. Rodi, T.C. Irving, E. Kondrashkina, L. Makowski, "Effect of beam dose on protein integrity," J. Synchrotron Rad. **10**, 398-404 (2003).

R. Fischetti, A.D. Mirza, J. Rodi., T.C. Irving, E. Kondrashkina, L. Makowski, "High resolution wide-angle x-ray scattering of protein solutions: Effect of beam dose on protein integrity," J. Synchrotron Rad. **10**, 398-404 (2003).

C.E. Fitzgerald, S.B. Patel, J.W. Becker, P.M. Cameron, D. Zaller, V.B. Pikounis, S.J. O'Keefe, G. Scapin, "Structural Basis for $p38_\alpha$ MAP kinase quinazolinone and pyridol-pyrimidine inhibitor specificity," Nature Struct. Biol. **10** (9), 764-769 (September 2003).

R.J. Fletcher, B.E. Bishop, R.P. Leon, R.A. Sclafani, C.M. Ogata, X.S. Chen, "The structure and function of MCM from archaeal M. thermoautotrophicum," Nature Struct. Biol. **10** (3), 160-167 (2003).

J.W. Freeland, D.J. Keavney, R. Winarski, P. Ryan, J.M. Slaughter, R.W. Dave, J. Janesky, "Grain boundary mediated oxidation and interlayer dipolar coupling in a magnetic tunnel junction structure," Phys. Rev. B **67** (13), 134411-1-134411-4 (April 2003).

C.J. Fromme, S.D. Bruner, W. Yang, M. Karplus, G.L. Verdine, "Product-assisted catalysis in base-excision DNA repair," Nature Struct. Biol. **10** (3), 203-211 (March 2003).

N. Fukuda, Y. Wu, G. Farman, T.C. Irving, H. Granzier, "Titin isoform variance and length dependence of activation in skinned bovine cardiac muscle," J. Physiol-London **51.1**, 147-154 (2003).

J.L. Fulton, S.M. Heald, Y.S. Badyal, J.M. Simonson, "Understanding the Effects of Concentration on the Solvation Structure of Ca^{2+} in Aqueous Solution. I. The Perspective on Local Structure from EXAFS and XANES," J. Phys. Chem. A **107**, 4688-4696 (May 2003).

L. Gan, M.R. Seyedsayamdost, S. Shuto, A. Matsuda, G.A. Petsko, L. Hedstrom, "The Immunosuppressive Agent Mizoribine Monophosphate Forms a Transition State Analogue Complex with Inosine Monophosphate Dehydrogenase," Biochemistry-US **42** (4), 857-863 (2003).

X. Gao, X. Wen, L. Esser, B. Quinn, L. Yu, C.-A. Yu, D. Xia, "Structural Basis for the Quinone Reduction in the bc1 Complex: A Comparative Analysis of Crystal Structures of Mitochondrial Cytochrome bc1 with Bound Substrate and Inhibitors at the Qi Site," Biochemistry-US **42** (30), 9067-9080 (2003).

A. Gardberg, L. Shuvalova, C. Monnerjahn, M. Konrad, A. Lavie, "Structural Basis for the Dual Thymidine and Thymidylate Kinase Activity of Herpes Thymidine Kinases," Structure **11** (10), 1265-1277 (2003).

S.M. Garrad, C.T. Capaldo, M.K. Rosen, I.G. Macara, D.R. Tomchick, "Structure of Cdc42 in a complex with the GTPase-binding domain of the cell polarity protein, Par6," EMBO J. **22** (5), 1125-1133 (2003).

K.S. Gautam, S. Kumar, D. Wermeille, D. Robinson, A. Dhinojwala, "Observation of Novel Liquid-Crystalline Phase above the Bulk-Melting Temperature," Phys. Rev. Lett. **90** (21), 215501-1-215501-4 (May 2003).

M.J. Giffin, J.C. Stroud, D.L. Bates, K.D. von Koenig, J. Hardin, L. Chen, "Structure of NFAT1 bound as a dimer to the HIV-1 LTR KB element," Nature Struct. Biol. **10** (10), 800-806 (2003).

B. Gilbert, B.H. Frazer, A. Belz, P.G. Conrad, K.H. Nealson, D. Haskel, J.C. Lang, G. Srajer, G. De Stasio, "Multiple scattering calculations of bonding and x-ray absorption spectroscopy of manganese oxides," J. Phys. Chem. A **107**, 2839-2847 (April 2003).

K. Gokulan, B. Rupp, M.S. Pavelka Jr., W.R. Jacobs Jr., J.C. Sacchettini, "Crystal Structure of Mycobacterium tuberculosis Diaminopimelate Decarboxylase, an Essential Enzyme in Bacterial Lysine Biosynthesis," J. Biol. Chem. **278** (20), 18588-18596 (2003).

J.A. Gomez, D. Guenzberger, D.E. Ellis, M.Y. Hu, E. Alp, E.M. Baggio-Saitovitch, E.C. Passamani, J.B. Ketterson, S. Cho, "Theoretical and experimental study of α-Sn deposited on CdTe(001)," Phys. Rev. B **67** (11), 115340-1-115340-11 (May 2003).

D.M. Goodner, D.L. Marasco, A.A. Escuadro, L. Cao, B.P. Tinkham, M.J. Bedzyk, "X-ray Standing Wave Study of the Sr/Si(0 0 1)-(2 ¥ 3) Surface," Surf. Sci. **547** (1-2), 19-26 (December 2003).

M.L. Gordon, D. Tulumello, G. Cooper, A.P. Hitchcock, P. Glatzel, O.C. Mullins, S.P. Cramer, U. Bergmann, "Inner-Shell Excitation Spectroscopy of Fused-Ring Aromatic Molecules by Electron Energy Loss and X-ray Raman Techniques," J. Phys. Chem. A **107** (41), 8512 -8520 (2003).

A.J. Goshe, I.M. Steele, B. Bosnich, "Supramolecular Recognition. Terpyridyl Palladium and Platinum Molecular Clefts and Their Association with Planar Platinum Complexes," J. Am. Chem. Soc. **125**, 444-451 (2003).

P. Graceffa, R. Dominguez, "Crystal structure of monomeric actin in the ATP state. Structural basis of nucleotide-dependent actin dynamics," J. Biol. Chem. **278** (36), 34172-34180 (2003).

V. Grum-Tokars, M. Milovanovic, J.E. Wedekind, "Crystallization and x-ray diffraction analysis of an all-RNA U39C mutant of the minimal hairpin ribozyme," Acta Crystallogr. D **59** (1), 142-145 (2003).

M. Guthrie, J. Urquidi, C.A. Tulk, C.J. Benmore, D.D. Klug, J. Neuefeind, "Direct structural measurements of relaxation processes during transformations in amorphous ice," Phys. Rev. B **68**, 184110-1-184110-5 (November 2003).

S.L. Gwaltney II, S.J. O'Connor, L.T.J. Nelson, G.M. Sullivan, H. Imade, W. Wang, L. Hasvold, Q. Li, J. Cohen, W.-Z. Gu, S.K. Tahir, J. Bauch, K. Marsh, S.-C. Ng, D.J. Frost, H. Zhang, S. Muchmore, C.G. Jakob, V. Stoll, C. Hutchins, S.H. Rosenberg, H.L. Sham, "Aryl tetrahydropyridine inhibitors of farnesyltransferase: Bioavailable analogues with improved cellular potency," Bioorg. Med. Chem. Lett. **13** (7), 1363-1366 (April 2003).

S.L. Gwaltney II, S.J. O'Connor, L.T.J. Nelson, G.M. Sullivan, H. Imade, W. Wang, L. Hasvold, Q. Li, J. Cohen, W.-Z. Gu, S.K. Tahir, J. Bauch, K. Marsh, S.-C. Ng, D.J. Frost, H. Zhang, S. Muchmore, C.G. Jakob, V.Stoll, C.Hutchins, S.H. Rosenberg, H.L. Sham, "Aryl tetrahydropyridine inhibitors of farnesyltransferase: Glycine, phenylalanine and histidine derivatives," Bioorg. Med. Chem. Lett. **13** (7), 1359-1362 (April 2003).

Y. Ha, D.J. Stevens, J.J. Skehel, D.C. Wiley, "X-ray structure of the hemagglutinin of a potential H3 avian progenitor of the 1968 Hong Kong pandemic influenza virus," Virology **309** (2), 209-218 (2003).

M.D. Hall, C.T. Dillon, M. Zhang, P. Beale, Z. Cai, B. Lai, A.P.J. Stampfl, T.W. Hambley, "The cellular distribution and oxidation state of platinum(II) and platinum(IV) antitumour complexes in cancer cells," J. Biol. Inorg. Chem. **8**, 726-732 (July 2003).

E.A. Hallinan, S.W. Kramer, S.C. Houdek, W.M. Moore, G.M. Jerome, D.P. Spangler, A.M. Stevens, H.S. Shieh, P.T. Manning, B.S. Pitzele, "4-Fluorinated L-lysine analogs as selective i-NOS inhibitors: methodology for introducing fluorine into the lysine side chain," Org. Biomol. Chem. **1** (2), 3527-3534 (January 2003).

A. Han, F. Pan, J.C. Stroud, H.-D. Youn, J.O. Liu, L. Chen, "Sequence-specific recruitment of transcriptional co-repressor Cabin1 by myocyte enhancer factor-2," Nature **422**, 730-734 (2003).

Z.H. Han, J.I. Budnick, M. Daniel, W.A. Hines, D.M. Pease, W.P. Klamut, B. Dabrowski, S.M. Mini, M. Maxwell, C.W. Kimball, "Nuclear Magnetic Resonance and Magnetization Studies of the Ferromagnetic Ordering Temperature Suppression in Ru Deficient $SrRuO_3$," Physica C **387** (1-2), 256-261 (May 2003).

J.C. Hanan, E. Üstündag, I.J. Beyerlein, G.A. Swift, J.D. Almer, U. Lienert, D.R. Haeffner, "Microscale damage evolution and stress redistribution in Ti-SiC fiber composites," Acta Mater. **51**, 4239-4250 (2003).

M.Z. Hasan, Y.-D. Chuang, Y. Li, P. Montano, M. Beno, Z. Hussain, H. Eisaki, S. Uchida, T. Gog, D.M. Casa, "Direct Spectroscopic Evidence of Holons in a Quantum Antiferromagnetic Spin-1/2 Chain," Int. J. Mod. Phys. B **17** (18,19,20), 3479-3483 (August 2003).

D. Haskel, J.W. Freeland, J. Cross, R. Winarski, M. Newville, F. Hellman, "XAFS study of local disorder in the α-Gd_xSi1-_x ammorphous magnetic semiconductor," Phys. Rev. B **67**, 115207-1-115207-7 (March 2003).

D. Haskel, Y. Choi, D.R. Lee, J.C. Lang, G. Srajer, J.S. Jiang, S.D. Bader, "Hard x-ray magnetic circular dichroism study of a surface-driven twisted state in Gd/Fe multilayers," J. Appl. Phys. **93** (10), 6507-6509 (May 2003).

D. Haskel, G. Srajer, Y. Choi, D.R. Lee, J.C. Lang, J. Meersschaut, J.S. Jiang, S.D. Bader, "Nature of inhomogeneous magnetic state in artificial Fe/Gd ferrimagnetic multilayers," Phys. Rev. B **67**, 180406-1-180406-4 (2003).

F.A. Hays, J.M. Vargason, P.S. Ho, "Effect of Sequence on the Conformation of DNA Holliday Junctions," Biochemistry-US **42** (32), 9586-959 (2003).

H. He, Y. Ding, M. Bartlam, F. Sun, Y. Le, X. Qin, H. Tang, R. Zhang, "Crystal Structure of Tabtoxin Resistance Protein Complexed with Acetyl Coenzyme A Reveals the Mechanism for Beta-Lactam Acetylation," Mol. Microbiol. **325**, 1019-1030 (2003).

J.P. Hessler, S. Seifert, R.E. Winans, "Spatially Resolved Small-Angle X-ray Scattering Studies of Soot Inception and Growth," P. Combust. Inst. **29** Pt. 2, 2743-2748 (2003).

D. Hibbs, P. Leverett, P. Williams, "Connellite-buttgenbachite from the Great Australia mine, Cloncurry: a crystal structural formula," Australas. J Miner. **9**, 39-42 (2003).

Q. Hoang, F. Sicheri, A. Howard, D. Yang, "Bone recognition mechanism of porcine osteocalcin from crystal structrure," Nature **425**, 977-980 (October 2003).

T. Holyoak, M.A. Wilson, T.D. Fenn, C.A. Kettner, G.A. Petsko, R.S. Fuller, D. Ringe, "2.4 Å Resolution Crystal Structure of the Prototypical Hormone-Processing Protease Kex2 in Complex with an Ala-Lys-Arg Boronic Acid Inhibitor," Biochemistry-US **42**, 6709-6718 (2003).

H. Hong, C.M. Wei, M.Y. Chou, Z. Wu, L. Basile, H. Chen, M. Holt, T.C. Chiang, "Alternating layer and island growth of Pb on Si by spontaneous quantum phase separation," Phys. Rev. Lett. **90**, 076104-1-076104-4 (2003).

M.Y. Hu, W. Sturhahn, T.S. Toellner, P. Mannheim, D.E. Brown, J. Zhao, E.E. Alp, "Measuring velocity of sound with nuclear resonant inelastic x-ray scattering," Phys. Rev. B **67** (9), 94304-1-94304-5 (March 2003).

M.Y. Hu, H. Sinn, A. Alatas, W. Sturhahn, E.E. Alp, H.-C. Wille, Yu. V. Shvy'ko, J.P. Sutter, J. Bandaru, E.E. Haller, V.I. Ozhogin, S. Rodriguez, R. Colella, E. Kartheuser, M.A. Villeret, "Effect of isotopic composition on the lattice parameter of germanium measured by x-ray scattering," Phys. Rev. B **67**, 113306-1-113306-11 (2003).

Y. Hu, L. Chen, S. Ha, B. Gross, B. Falcone, D. Walker, M. Mokhtarzadeh, S. Walker, "Crystal structure of the MurG:UDP-GlcNAc complex reveals common structural principles of a superfamily of glycosyltransferases," Proc. Natl. Acad. Sci. **100** (4), 845-849 (2003).

Q. Huai, H. Wang, Y. Sun, H.-Y. Kim, Y. Liu, H. Ke, "Three-Dimensional Structures of PDE4D in Complex with Roliprams and Implication on Inhibitor Selectivity," Structure **11**, 865-873 (2003).

Q. Huai, J. Colicelli, H. Ke, "The Crystal Structure of AMP-Bound PDE4 Suggests a Mechanism for Phosphodiesterase Catalysis," Biochemistry-US **42**, 113220-13226 (2003).

Y. Huang, M.J. Lemieux, J. Song, M. Auer, D.-N. Wang, "Structure and Mechanism of the Glycerol-3-Phosphate Transporter from Escherichia coli," Science **301**, 616-617 (August 2003).

P.A. Hubbard, X. Liang, H. Schulz, J.-J.P. Kim, "The Crystal Structure and Reaction Mechanism of Escherichia coli 2,4-Dienoyl-CoA Reductase," J. Biol. Chem. **278** (39), 37553-37560 (2003).

T.C. Hufnagel, F. Hellman, "Structural and magnetic length scales in amorphous $TbFe_2$," J. Magn. Magn. Mater. **256**, 322-327 (August 2003).

J. Huot, J.F. Pelletier, L.B. Lurio, M. Sutton, R. Schulz, "Investigation of dehydrogenation mechanism of MgH_2-Nb nanocomposites," J. Alloy Comp. **348**, 319-324 (2003).

K. Ignatiev, W.-K. Lee, K. Fezzaa, G.R. Davis, J.C. Elliott, S.R. Stock, "Three-dimensional mapping of fatigue crack position via a novel x-ray phase contrast approach," Adv. X Ray Anal. **46**, 314-319 (2003).

P. Ilinski, B. Lai, Z. Cai, W. Yun, D. Legnini, T. Talarico, M. Cholewa, L.K. Webster, G.B. Deacon, S. Rainone, D.R. Phillips, A.P.J. Stampfl, "The direct mapping of the uptake of platinum anticancer agents in individual human ovarian adenocarcinoma cells using a hard x-ray microprobe," Cancer Res. **63**, 1776-1779 (April 2003).

C.A. Impellitteri, K.G. Scheckel, J.A. Ryan, "Sorption of Arsenate and Arsenite on RuO_2xH_2O: A Spectroscopic and Macroscopic Study," Environ. Sci. Technol. **37** (13), 2936-2940 (2003).

N. Jakse, S. Krishnan, E. Artacho, T. Key, L. Hennet, B. Glorieux, A. Pasturel, D.L. Price, M.-L. Saboungi, "Structural Changes on Supercooling Liquid Silicon," Appl. Phys. Lett. **83** (23), 4734-4736 (December 2003).

A.J. James, C.R. Escalante, M. Yoon-Robarts, T.A. Edwards, R.M. Linden, A.K. Aggarwal, "Crystal Structure of the SF3 Helicase from Adeno-Associated Virus Type 2," Structure **11** (8), 1025-1035 (2003).

V. James, "False-Positive Results in Studies of Changes in Fiber Diffraction of Hair from Patients with Breast Cancer May Not Be False," J. Natl. Cancer I. **95** (2), 170-171 (2003).

V.J. James, "The traps and pitfalls inherent in the correlation of changes in the fibre diffraction pattern of hair with breast cancer," Phys. Med. Biol. **48** (2), L5-L9 (January 2003).

V.J. James, "Changes in the diffraction pattern of hair resulting from mechanical damage can occlude the changes that relate to breast cancer," Phys. Med. Biol. **48**, L37-L41 (July 2003).

V.J. James, "Fibre diffraction from a single hair can provide an early non-invasive test for colon cancer," Med. Sci. Mon. **9** (8), MT79-MT84 (2003).

J.H. Je, H. You, W.G. Cullen, V.A. Maroni, B. Ma, R.E. Koritala, M.W. Rupich, C.L.H. Thieme, "Microstructure of Re_2O_3 layers on cube textured Ni substrates," Physica C **384**, 54-60 (January 2003).

M.P. Jensen, J. Neuefeind, J.V. Beitz, S. Skanthakumar, L. Soderholm, "Mechanisms of metal ion transfer into room-temperature ionic liquids: the role of anion exchange," J. Am. Chem. Soc. **125** (50), 15466-15473 (December 2003).

X. Jin, J.H. Geiger, "Structures of NAD^+- and NADH-bound 1-L-myo-inositol 1-phosphate synthase," Acta Crystallogr. D **59**, 1154-1164 (2003).

C.S. Johnson, J.-S. Kim, A.J. Kropf, A.J. Kahaian, J.T. Vaughey, M.M. Thackeray, "Structural and Electrochemical Evaluation of $(1-x)Li_2TiO_3{\cdot}(x)LiMn_{0.5}Ni_{0.5}O_2$ as an Electrode Material for Lithium Batteries," J. Power Sources **119-121**, 139-144 (2003).

C.S. Johnson, J.-S. Kim, A.J. Kropf, A.J. Kahaian, J.T. Vaughey, M.M. Thackeray, L.M. L. Fransson, K. Edström, "Structural Characterization of Layered $Li_xNi_{0.5}Mn_{0.5}O_2$ ($0<x<2$) Oxide Electrodes for Li Batteries," Chem. Mater. **15**, 2313-2322 (2003).

J.A. Johnson, D. Holland, J. Urquidi, I.A. Gee, C.J. Benmore, C.E. Johnson, "Structure of Oxychloride Glasses by Neutron and X-ray "Difference" and XPS," J. Phys. Condens. Matter **15**, 4679-4693 (June 2003).

R.L. Jones, T. Hu, E.K. Lin, W.-L. Wu, R. Kolb, D.M. Casa, P.J. Boulton, G.G. Barclay, "Small angle x-ray scattering for sub-100 nm pattern characterization," Appl. Phys. Lett. **83** (19), 4059-4061 (2003).

Z.S. Juo, G.A. Kassavetis, J. Wang, P. Geldusche, P.B. Sigler, "Crystal structure of a transcription factor IIIB core interface ternary complex," Nature **422**, 534-539 (April 2003).

S.W. Kamtekar, W.D. Kennedy, J. Wang, C. Stathopoulos, D. Söll, T.A. Steitz, "The structural basis of cysteine aminoacylation of tRNAPro by prolyl-tRNA synthetases," Proc. Natl. Acad. Sci. **100** (4), 1673-1678 (2003).

A. Karlsson, J.V. Parales, R.E. Parales, D.T. Gibson, H. Eklund, S. Ramaswamy, "Crystal structure of naphthalene dioxygenase: Side-on binding of dioxygen to iron," Science **299**, 1039-1042 (2003).

B. Kauppi, C. Jakob, M. Farnegardh, J. Yang, H. Ahola, M. Alarcon, K. Calles, O. Engstrom, J. Harlan, S. Muchmore, A.-K. Ramqvist, S. Thorell, L. Ohman, J. Greer, J.-A. Gustafsson, J. Carlstedt-Duke, M. Carlquist, "The three-dimensional structures of antagonistic and agonistic forms of the glucocorticoid receptor ligand-binding domain: RU-486 induces a transconformation that leads to active antagonism," J. Biol. Chem. **278** (25), 22748-22754 (June 2003).

D.J. Keavney, D. Wu, J.W. Freeland, E. Johnston-Halperin, D.D. Awschalom, J. Shi, "Element resolved spin configuration in ferromagnetic manganese-doped gallium arsenide," Phys. Rev. Lett. **91** (18), 187203-1-187203-4 (October 2003).

S.D. Kelly, M.G. Newville, L. Cheng, K.M. Kemner, S.R. Sutton, P. Fenter, N.C. Sturchio, C. Spotl, "Uranyl incorporation in natural calcite," Environ. Sci. Technol. **37** (7), 1284-1287 (2003).

K.F. Kelton, G.W. Lee, A.K. Gangopadhyay, R.W. Hyers, T.J. Rathz, J.R. Rogers, M.B. Robinson, D.S. Robinson, "First X-ray Scattering Studies on Electrostatically Levitated Metallic Liquids: Demonstrated Influence of Local Icosahedral Order on the Nucleation Barrier," Phys. Rev. Lett. **90** (19), 195504-1-195504-4 (2003).

J.T.M. Kennis, S. Crosson, M. Gaudenvan, I.H.M. Stokkum, K. Moffat, R. van Grondelle, "Primary reactions of the LOV2 domain of phototropin, a plant blue-light photoreceptor," Biochemistry-US **42**, 3385-3392 (2003).

R. Khayat, R. Batra, C. Qian, T. Halmos, M. Bailey, L. Tong, "Structural and Biochemical Studies of Inhibitor Binding to Human Cytomegalovirus Protease," Biochemistry-US **42**, 885-891 (2003).

H.-S. Kim, P.A. Pasten, J.-F. Gaillard, P. C. Stair, "Nanocrystalline Todorokite-Like Manganese Oxide Produced by Bacterial Catalysis," J. Am. Chem. Soc. **125**, 14284-14285 (October 2003).

H. Kim, A. Ruhm, L.B. Lurio, J.K. Basu, J. Lal, S.K. Sinha, D. Lumma, S.G.J. Mochrie, "Surface Dynamics of Polymer Films," Phys. Rev. Lett. **90** (6), 068302-1-068302-4 (February 2003).

H. Kim, A. Rühm, L.B. Lurio, J.K. Basu, J. Lal, S.G.J. Mochrie, S.K. Sinha, "X-ray photon correlation spectroscopy on polymer films with molecular weight dependence," Physica B **336**, 211-214 (2003).

J.Y. Kim, J.A. Rodriguez, J.C. Hanson, A.I. Frenkel, P.L. Lee, "Reduction of CuO and Cu_2O with H_2: H embedding and kinetic effects in the formation of suboxides," J. Am. Chem. Soc. **125**, 10684-10692 (August 2003).

M.H. Kim, U. Derewendaq, Y. Devedjiev, Z. Dauter, Z.S. Derewenda, "Purification and crystallization of the N-terminal domain from the human doublecortin-like kinase," Acta Crystallogr. D **59**, 502-505 (2003).

L. Kjer-Nielsen, C.S. Clements, A.W. Purcell, A.G. Brooks, J.C. Whisstock, S.R. Burrows, J. McCluskey, J. Rossjohn, "Structural Basis for the Selection of Dominant Alpha-Beta T Cell Receptors in Antiviral Immunity," Immunity **18** (1), 53-64 (2003).

O. Kleifeld, A. Frenkel, J.M.L. Martin, I. Sagi, "Active site electronic structure and dynamics during metalloenzyme catalysis," Nature Struct. Biol. **10** (2), 98-103 (2003).

V.A. Klenchin, J.S. Allingham, R. King, Ju. Tanaka, G. Marriott, I. Rayment, "Trisoxazole macrolide toxins mimic the binding of actin-capping proteins to actin," Nature Struct. Biol. **10** (12), 1058-1063 (2003).

J. Kmetko, C. Yu, G. Evmenenko, S. Kewalramani, P. Dutta, "Organic-template-directed nucleation of strontium fluoride and barium fluoride: Epitaxy and strain," Phys. Rev. B **68**, 085415-1-085415-6 (August 2003).

Tzu-Ping Ko, Howard Robinson, Gao Yi-Gui, Chi-Hing C. Cheng, DeVries L. Arthur, Wang H. Andrew, "The Refined Crystal Structure of and Eel Pout type III Antifreeze Protein RD1 at 0.62-Å Resolution Reveals Structure Microheterogeneity of Protein and Solvation," Biophys. J. **84**, 1228-1237 (February 2003).

U. Koebler, A. Hoser, D. Hupfeld, "A complete description of the order parameter of Heisenberg-type magnets for $0 < T < Tc$," Physica B **328**, 276-282 (2003).

Y. Koh, H. Nakata, K. Maeda, H. Ogata, G. Bilcer, T. Devasamudram, J.F. Kincaid, P. Boross, Y.-F. Wang, Y. Tie, P. Volarath, L. Gaddis, R.W. Harrison, I.T. Weber, A.K. Ghosh, H. Mitsuya, "Novel bis-Tetrahydrofuranylurethane-Containing Nonpeptidic Protease Inhibitor (PI) UIC-94017 (TMC114) with Potent Activity against Multi-PI-Resistant Human Immunodeficiency Virus in Vitro," Antimicrob. Agents Ch. **47** (10), 3123-3129 (October 2003).

J.P. Konhilas, T.C. Irving, B.M. Wolska, E.E. Jweied, A.F. Martin, R.J. Solaro, P.P. de Tomb, "Troponin I in the murine myocardium: influence on length-dependent activation and interfilament spacing," J. Physiol.-London **547** (3), 951-961 (2003).

I.K. Koshelev, A.P. Paulikas, S. Uran, M.A. Beno, G. Jennings, J. Linton, B.W. Veal, "The Influence of a Reactive Element on the Growth of a Thermally Grown Chromia Scale: a Grazing Emission X-ray Fluorescence Study," Oxid. Met. **59** (5/6), 469-481 (June 2003).

R. Koynova, R.C. MacDonald, "Mixtures of Cationic Lipid O-Ethylphosphatidylcholine with Membrane Lipids and DNA: Phase Diagrams," Biophys. J. **85**, 2449-2465 (2003).

R. Koynova, R.C. MacDonald, "Cationic O-ethylphosphatidylcholines and their lipoplexes: phase behavior aspects, structural organization and morphology," Biochim. Biophys. Acta **1613**, 39-48 (2003).

M.J. Kramer, M.F. Besser, N. Yang, E. Rozhkova, D.J. Sordelet, Y. Zhang, P.L. Lee, "Devitrification studies of Zr-Pd and Zr-Pd-Cu metallic glasses," J. Non-Cryst. Solids **317**, 62-70 (February 2003).

A.S. Krasilnikov, X. Yang, T. Pan, A. Mondragon, "Crystal structure of the specificity domain of ribonuclease," Nature **421**, 760-764 (2003).

B. Krassig, J.-C. Bilheux, R.W. Dunford, D.S. Gemmell, S. Hasegawa, E.P. Kanter, S.H. Southworth, L. Young, L.A. LaJohn, R.H. Pratt, "Nondipole asymmetries of Kr 1s photoelectrons," Phys. Rev. A **67**, 022707-1-022707-7 (February 2003).

R. Kristelly, B.T. Earnest, L. Krishnamoorthy, J.J.G. Tesmer, "Preliminary structure analysis of the DH/PH domains of leukemia-associated RhoGEF," Acta Crystallogr. D **10**, 1859-1862 (2003).

A.J. Kropf, R.J. Finch, J.A. Fortner, S. Aase, C. Karanfil, C.U. Segre, J. Terry, G. Bunker, L.D. Chapman, "On a Bent Silicon Crystal in the Laue Geometry to Resolve X-ray Fluorescence for X-ray Absorption Spectroscopy," Rev. Sci. Instrum. **74**, 4696-4702 (November 2003).

M.R. Kuo, H.R. Morbidoni, D. Alland, S.F. Sneddon, B.B. Gourlie, M.M. Staveski, M. Leonard, J.S. Gregory, A.D. Janjigian, C. Yee, J.M. Musser, B. Kreiswirth, H. Iwamoto, R. Perozzo, W.R. Jacobs Jr., J.C. Sacchettini, D.A. Fidock, "Targeting Tuberculosis and Malaria through Inhibition of Enoyl Reductase: Compound Activity and Structural Data," J. Biol. Chem. **278** (23), 20851 -20859 (2003).

G. Kurisu, S.D. Zakharov, M.V. Zhalnina, S. Bano, V.Y. Eroukova, T.I. Rokitskaya, Y.N. Antonenko, M.C. Wiener, W.A. Cramer, "The structure of BtuB with bound colicin E3 R-domain implies a translocon," Nature Struct. Biol. **10** (11), 948-954 (2003).

G. Kurisu, H. Zhang, J.L. Smith, W.A. Cramer, "Structure of the Cytochrome b_6f Complex of Oxygenic Photosynthesis: Tuning the Cavity," Science **302**, 1009-1014 (2003).

T. Kwon, J.H. Chang, E. Kwak, C.W. Lee, A. Joachimiak, Y. C. Kim, J. Lee, Y. Cho, "Mechanism of histone lysine methyl transfer revealed by the structure of SET7/9-AdoMet," EMBO J. **22** (2), 292-303 (2003).

D. Lahiri, V. Subramanian, T. Shibata, E.E. Wolf, B. Bunker, P.V. Kamat, "Photoinduced Transformation at Semiconductor/Metal Interfaces: XAFS Investigation of Ultra Violet Irradiated TiO_2/Au Films," J. Appl. Phys. **93**, 2575-2581 (2003).

S.D. Lahiri, G. Zhang, D. Dunaway-Mariano, K.N. Allen, "The Pentacovalent Phosphorus Intermediate of a Phosphoryl Transfer Reaction," Science **299**, 2067-2071 (2003).

P. LeMagueres, H. Im, A. Dvorak, "Crystal Structure at 1.45 Å Resolution of Alanine Racemase from a Pathogenic Bacterium, Pseudomonas aeruginosa, Contains Both Internal and External Aldimine Forms,"
Biochemistry-US **42** (50), 114752-14761 (2003).

D.R. Lee, Y.S. Chu, Y. Choi, J.C. Lang, G. Srajer, S.K. Sinha, V. Metlushko, B. Ilic, "Characterization of the nanostructures of a lithographically patterned dot array by x-ray pseudo-Kossel lines," Appl. Phys. Lett. **82** (7), 982-984 (February 2003).

D.R. Lee, K. Shin, O.H. Seeck, H. Kim, Y.-S. Seo, M. Tolan, M.H. Rafailovich, J. Sokolov, S.K. Sinha, "X-ray Scattering from Freestanding Polymer Films with Geometrically Curved Surfaces," Phys. Rev. Lett. **90** (18), 185503-1-185503-4 (May 2003).

S. Lee, M.E. Sowa, Y. Watanabe, P.B. Sigler, W. Chiu, M. Yoshida, F.T.F. Tsai, "The Structure of ClpB: A Molecular Chaperone that Rescues Proteins from an Aggregated State.," Cell **115**, 229-240 (October 2003).

D.R. Lee, G. Srajer, M.R. Fitzsimmons, V. Metlushko, S.K. Sinha, "Polarized neutron scattering from ordered magnetic domains on a mesoscopic permalloy antidot array," Appl. Phys. Lett. **82** (1), 82-84 (January 2003).

Y.H. Lee, S. Nadaraia, D. Gu, D. Becker, J. Tanner, "Structure of the proline dehydrogenase domain of the multifunctional PutA flavoprotein," Nature Struct. Biol. **10**, 109-114 (January 2003).

C. Lehmann, K. Lim, V.R. Chalamasetty, W. Krajewski, E. Melamud, A. Galkin, A. Howard, Z. Kelman, P.T. Reddy, A.G. Murzin, O. Herzberg, "The HI0073/HI0074 protein pair from Haemophilus influenzae is a member of a new nucleotidyltransferase family: Structure, sequence analysis, and solution studies," Proteins **50** (2), 249-260 (2003).

P.G. Leiman, M.M. Shneider, V.A. Kostyuchenko, P.R. Chipman, V.V. Mesyanzhinov, M.G. Rossmann, "Structure and Location of Gene Product 8 in the Bacteriophage T4 Baseplate," J. Mol. Biol. **328** (4), 821-833 (2003).

Z.H. Levine, S. Grantham, C. Tarrio, D.J. Paterson, I. McNulty, T.M. Levin, A.L. Ankudinov, J.J. Rehr, "Mass absorption coefficient of tungsten and tantalum, 1450 eV to 2350 eV: Experiment, theory, and application," J. Res. Natl. Inst. Stan. **108** (1), 1-10 (January 2003).

D. Lexa, A.J. Kropf, "The Beam-Heating Effect in Simultaneous Differential Scanning Calorimetry/Synchrotron Powder X-ray Diffraction," Thermochim. Acta. **401** (2), 239-242 (2003).

D. Li, R. Zhao, W. Lilyestorm, D. Gai, R. Zhang, J.A. DeCaprio, E. Fanning, A. Joachimiak, G. Szakonyi, X.S. Chen, "Structure of the replicative helicase of the oncoprotein SV40 large tumour antigen," Nature **423**, 512-518 (May 2003).

J. Li, B. Sha, "Crystal Structure of the E. coli Hsp100 ClpB N-Terminal Domain," Structure **11**, 323-328 (2003).

J. Li, X. Qian, B. Sha, "The Crystal Structure of the Yeast Hsp40 Ydj1 Complexed with Its Peptide Substrate," Structure **11**, 1475-1483 (2003).

J. Li, B. Sha, "Preliminary X-ray crystallographic studies of yeast Hsp40 Ydj1 complexed with its peptide substrate," Acta Crystallogr. D **59** (7), 1317-1319 (2003).

Y. Li, M. Yasa, O. Pelletier, C.R. Safinya, E. Caine, E.E. Hu, P. Fernandez, "Metal layer Bragg-Fresnel lenses for diffraction focusing of hard x-rays," Appl. Phys. Lett. **82** (15), 2538-2540 (April 2003).

Z. G. Li, R.L. Harlow, F. Gao, P. Lin, R.Miao, L. Liang, "Crystalline characterization of an operational Li-ion battery by synchrotron radiation," J. Electrochem. Soc. **150** (9), A1171-A1175 (2003).

H.C. Lichtenegger, T. Schöberl, J.T. Ruokolainen, J.O. Cross, S.M. Heald, H. Birkedal, J.H. Waite, G.D. Stucky, "Zinc and mechanical prowess in the jaws of Nereis, a marine worm," Proc. Natl. Acad. Sci. **100**, 9144-9149 (August 2003).

R.L. Lieberman, D.B. Shrestha, P.E. Doan, B.M. Hoffman, T.L. Stemmler, A.C. Rosenzweig, "Bioinorganic Chemistry Special Feature: Purified particulate methane monooxygenase from Methylococcus capsulatus (Bath) is a dimer with both mononuclear copper and a copper-containing cluster," Proc. Natl. Acad. Sci. **100**, 3820-3825 (April 2003).

K. Lim, A. Tempczyk, N. Bonander, J. Toedt, A. Howard, E. Eisenstein, O. Herzberg, "A catalytic mechanism for D-Tyr-tRNAtyr deacylase based on the crystal structure of Hemophilus influenzae HI0670," J. Biol. Chem. **278** (15), 13496-13502 (April 2003).

B. Lin, M. Meron, J. Gebhardt, T. Graber, M.L. Schlossman, P.J. Viccar, "The liquid surface/interface spectrometer at ChemMatCARS synchrotron facility at the Advanced Photon Source," Physica B **336**, 75-80 (February 2003).

J.-F. Lin, V.V. Struzhkin, W. Sturhahn, E. Huang, J. Zhao, "Sound velocities of iron-nickel and iron-silicon alloys at high pressures," Geophys. Res. Lett. **30** (21), 2112 (2003).

J.J.A. Lin, D. Paterson, A.G. Peele, P.J. McMahon, C.T. Chantler, K.A. Nugent, B. Lai, N. Moldovan, Z. Cai, D.C. Mancini, I. McNulty, "Measurement of the spatial coherence function of undulator radiation using a phase mask," Phys. Rev. Lett. **90** (7), 074801-1-074801-4 (February 2003).

J.-F. Lin, J. Shu, H.-k. Mao, R. Hemley, G. Shen, "Amorphous boron gasket in diamond anvil cell research," Rev. Sci. Instrum. **74**, 4732-4736 (November 2003).

J.-F. Lin, D.L. Heinz, H.-k. Mao, R.J. Hemley, J.M. Devine, J. Li, G. Shen, "Stability of magnesiowustite in Earth's lower mantle," Proc. Natl. Acad. Sci. **100** (8), 4405-4408 (March 2003).

J.-F. Lin, A. Campbell, D. Heinz, G. Shen, "Static compression of iron-silicon alloys: Implications for silicon in the Earth's core," J. Geophys. Res. **108** (B1), 2045-2056 (2003).

T.E. Lister, Y.V. Tolmachev, Y. Chu, W.G. Cullen, H. You, R. Yonco, Z. Nagy, "Cathodic activation of RuO_2 single crystal surfaces for hydrogen-evolution reaction," J. Electroanal. Chem. **554-555**, 71-76 (September 2003).

C. Liu, L. Assoufid, R. Conley, A.T. Macrander, G.E. Ice, J.Z. Tischler, "Profile coating and its application for Kirkpatrick-Baez mirrors," Opt. Eng. **42** (12), 3622-3628 (December 2003).

C. Liu, R. Conley, L. Assoufid, A.T. Macrander, G.E. Ice, J.Z. Tischler, K. Zhang, "Profile coatings and their applications," J. Vac. Sci. Technol. A **21** (4), 1579-1584 (July 2003).

G. Liu, B.G. Szczepankiewicz, Z. Pei, D.A. Janowick, Z. Xin, P.J. Hajduk, C. Abad-Zapatero, H. Liang, C.W. Hutchins, S.W. Fesik, S.J. Ballaron, M.A. Stashko, T. Lubben, A.K. Mika, B.A. Zinker, J.M. Trevillyan, M.R. Jirousek, "Discovery and structure-activity relationship of oxalylarylaminobenzoic acids as inhibitors of protein tyrosine phosphatase 1B," J. Med. Chem. **46**, 2093-2103 (2003).

J. Liu, J. Wang, B. Shan, C. Wang, Z. Chang, "An accumulating x-ray streak camera with sub-600-fs temporal resolution and 50-fs timing jitter," Appl. Phys. Lett. **82** (20), 3553-3555 (May 2003).

P. Liu, Y.-F. Wang, H.E. Ewis, A. Abdelal, C.D. Lu, I.T. Weber, "Crystallization and preliminary X-ray diffraction data for the carboxylesterase Est30 from Bacillus stearothermophilus," Acta Crystallogr. D **59**, 1472-1473 (2003).

Y. Lui, Y. Xiong, O.V. Naidenko, J. Lui, R. Zhang, A. Joachimiak, M. Kronenberg, H. Cheroutre, E.L. Reinherz, J. Wang, "The Crystal Structure of a TL/CD8alphaalpha Complex at 2.1 Å Resolution. Implications for Modulation of TCell Activation and Memory," Immunity **18** (2), 205-215 (2003).

Y. Lui, X. Hong, J. Kappler, L. Jiang, R. Zhang, L. Xu, C.-H. Pan, W.E. Martin, R.C. Murphy, H.-B. Shu, S. Dai, G. Zhang, "Ligand-receptor binding revealed by the TNF family member TALL-1," Nature **423**, 49-56 (May 2003).

L.B. Lurio, H. Kim, A. Rühm, J.K. Basu, J. Lal, S.K. Sinha, S.G.J. Mochrie, "Surface Tension and Surface Roughness of Supported Polystyrene Films," Macromolecules **36**, 5704-5709 (2003).

T.W. Lynch, A. Mattis, J.F. Gardner, P.A. Rice, "Integration Host Factor: putting a twist on protein-DNA recognition," J. Mol. Biol. **330** (3), 493-502 (2003).

Q. Ma, R. A. Rosenberg, "Angle-resolved x-ray photoelectron spectroscopy study of the oxides on Nb surfaces for superconducting r.f. cavity applications," Appl. Surf. Sci. **206**, 209-217 (February 2003).

W.A. Macdonald, A.W. Purcell, N.A. Mifsud, L.K. Ely, D.S. Williams, L. Chang, J.J. Gorman, C.S. Clements, L. Kjer-Nielsen, D.M. Koelle, S.R. Burrows, B.D. Tait, R. Holdsworth, A.G. Brooks, G.O. Lovrecz, L. Lu, J. Rossjohn, J. McCluskey, "A Naturally Selected Dimorphism within the HLA-B44 Supertype Alters Class I Structure, Peptide Repertoire, and T Cell Recognition," J. Exp. Med. **198** (5), 679-691 (2003).

M.J. Maher, D.T.C. Huang, J.M. Guss, C.A. Collyer, R.I. Christopherson, "Crystallization of hamster dihydroorotase: Involvement of a disulfide-linked tetrameric form," Acta Crystallogr. D **59** (2), 381-384 (2003).

S. Majeed, G. Ofek, A. Belachew, C.-c. Huang, T. Zhou, P.D. Kwong, "Enhancing Protein Crystallization through Precipitant Synergy," Structure **11**, 1061-1070 (September 2003).

O.V. Makarova, D.C. Mancini, N. Moldovan, R. Divan, C.-M. Tang, D.G. Ryding, R.H. Lee, "Microfabrication of freestanding metal structures using graphite substrate," Sensor Actuat. A - Phys. **103**, 182-186 (January 2003).

O.V. Makarova, C.-M. Tang, D.C. Mancini, N. Moldovan, R. Divan, D.G. Ryding, R.H. Lee, "Development of a freestanding copper antiscatter grid using deep x-ray lithography," Microsystems Technologies **94**, 395-398 (2003).

M.E. Manley, G.H. Lander, H.Sinn, A. Alatas, W.L. Hults, R.J. McQueeney, J.L. Smith, J. Willit, "Phonon dispersion in uranium measured using inelastic x-ray scattering," Phys. Rev. B **67**, 052302-1-052302-4 (February 2003).

W.L. Mao, H.-K. Mao, P.J. Eng, T.P. Trainor, M. Newville, C.-C. Kao, D.L. Heinz, J.-F. Shu, Y. Meng, R.J. Hemley, "Bonding changes in compressed superhard graphite," Science **302**, 425-427 (October 2003).

W.L. Maoa, H.-k. Mao, "Generation of ultrahigh pressure using single-crystal chemical-vapor-deposition diamond anvils," Appl. Phys. Lett. **83** (25), 5190-5192 (December 2003).

G. Maris, Y. Ren, V. Volotchaev, C. Zobel, T. Lorenz, T.T.M. Palstra, "Evidence for orbital ordering in $LaCoO_3$," Phys. Rev. B **67**, 224423-1-224423-5 (June 2003).

B.L. Mark, D.J. Mahuran, M.M. Cherney, D. Zhao, S. Knapp, M.N.G. James, "Crystal Structure of Human Beta-Hexosaminidase B: Understanding the Molecular Basis of Sandhoff and Tay-Sachs Disease," J. Mol. Biol. **327** (5), 1093-1109 (2003).

J. Maser, D. Wagner, B. Lai, Z. Cai, D. Legnini, I. Moric, L. Bermudez, "Trace metals and their relation to bacterial infections studied by x-ray microscopy," J. Phys. IV France **104**, 283-288 (2003).

R.A. Mayanovic, S. Jayanetti, A.J. Anderson, W.A. Bassett, I.-M. Chou, "Relaxation of the Structure of Simple Metal Ion Complexes in Aqueous Solutions at up to Supercritical Conditions," J. Chem. Phys. **118** (2), 719-727 (January 2003).

P.J. McMahon, A.G. Peele, D. Paterson, J.J.A. Lin, T.H.K. Irving, I. McNulty, K.A. Nugent, "Quantitative x-ray phase tomography with submicron resolution," Opt. Commun. **217**, 53-58 (2003).

I. McNulty, D. Paterson, J. Arko, M. Erdmann, S.P. Frigo, K. Goetze, P. Ilinski, N. Krapf, T. Mooney, C.C. Retsch, A.P.J. Stampfl, S. Vogt, Y. Wang, S. Xu, "The 2-ID-B intermediate-energy scanning x-ray microscope at the APS," J. Phys. IV France **104**, 11-15 (2003).

S. Mehboob, J. Jacob, M. May, L. Kotula, P. Thiyagarajan, M.E. Johnson, L.W.-M. Fung, "Structural Analysis of the αN-Terminal Region of Erythroid and Nonerythroid Spectrins by Small-Angle X-ray Scattering," Biochemistry-US **42** (49), 14702-14710 (October 2003).

Y. Meng, M. Newville, S. Sutton, J. Rakovan, H.-K. Mao, "Fe and Ni impurities in synthetic diamond," Am. Mineral. **88**, 1555-1559 (2003).

D.J. Miller, N. Ouellette, E. Evodokimova, A. Savchenko, A. Edwards, W.F. Anderson, "Crystal complexes of a predicted S-adenosylmethionine-dependent methyltransferase reveal a typical AdoMet binding domain and a substrate recognition domain," Protein Sci. **12**, 1432-1442 (2003).

H. Mo, H. Taub, U.G. Volkmann, M. Pino, S.N. Ehrlich, F.Y. Hansen, E. Lu, P. Miceli, "A novel growth mode of alkane films on a SiO_2 surface," Chem. Phys. Lett. **377**, 99-105 (July 2003).

S.G.J. Mochrie, L.B. Lurio, A. Rühm, D. Lumma, M. Borthwick, P. Falus, H.J. Kim, J.K. Basu, J. Lal, S.K. Sinha, "X-ray photon correlation spectroscopy studies of colloidal diffusion and the capillary modes of polymer films," Physica B **336**, 173-176 (2003).

K. Moffat, "The frontiers of time-resolved macromolecular crystallography: movies and chirped X-ray pulses," Faraday Discuss. **122**, 65-77 (2003).

B.J. Moldovan, D.-T. Jiang, M.J. Hendry, "Mineralogical Characterization of Arsenic in Uranium Mine Tailings Precipitated from Iron-Rich Hydrometallurgical Solutions," Environ. Sci. Technol. **37**, 873-879 (2003).

M. Morais, S. Kanamaru, M.O. Badasso, J.S. Koti, B.A.L. Owen, C. McMurray, D.L. Anderson, M.G. Rossmann, "Bacteriophage ϕ29 scaffolding protein gp7 before and after prohead assembly," Nature Struct. Biol. **10** (7), 572-576 (2003).

C.M. Moure, F.S. Gimble, F.A. Quicho, "The Crystal Structure of the Gene Targeting Homing Endonuclease I-SceI Reveals the Origins of its Target Site Specificity," J. Mol. Biol. **334**, 685-695 (2003).

A.M. Mulichak, H.C. Losey, W. Lu, Z. Wawrzak, C.T. Walsh, R.M. Garavito, "Structure of the TDP-epi-Vancosaminyltransferase GtfA from the Chloroeremomycin Biosynthetic Pathway," Proc. Natl. Acad. Sci. **100**, 9238-9243 (2003).

G.A. Murphy, E.J. Spedale, S.T. Powell, L. Pillus, S.C. Schultz, L. Chen, "The Sir4 C-terminal Coiled Coil is Required for Telomeric and Mating Type Silencing in Saccharomyces cerevisiae," J. Mol. Biol. **334** (4), 769-780 (2003).

C.E. Murray, I.C. Noyan, P.M. Mooney, B. Lai, Z. Cai, "Mapping of strain fields about thin film structures using x-ray microdiffraction," Appl. Phys. Lett. **83** (20), 4163-4165 (November 2003).

N.G.D. Murray, C.A. Schuh, D.C. Dunand, "Solid-State Foaming of Titanium by Hydrogen-Induced Internal-Stress Plasticity," Scripta Mater. **49** (9), 879-883 (2003).

N. Muzet, B. Guillot, C. Jelsch, E. Howard, C. Lecomte, "Electrostatic complementarity in an aldose reductase complex from ultra-high-resolution crystallography and first-principles calculations," Proc. Natl. Acad. Sci. **100** (15), 8742-8747 (July 2003).

S.J. Naftel, R.R. Martin, T.K. Sham, B. Hart, M.A. Powell, "XANES of Chromium in Sludges Used as Soil Ameliorants," Can. J. Chem. **81**, 193 (2003).

M. Naghedolfeizi, J.- S. Chung, R. Morris, G.E. Ice, W.B. Yun, Z. Cai, B. Lai, "X-ray fluorescence microtomography study of trace elements in a SiC nuclear fuel shell," J. Nucl. Mater. **312**, 146-155 (2003).

I.V. Norozhilova, A.V. Volkov, P. Coppens, "Theoretical Analysis of the Triplet Excited State of the $[Pt_2(H_2P_2O_5)_4]^{4-}$ Ion and Comparison with Time-Resolved X-ray and Spectroscopic Results," J. Am. Chem. Soc. **125**, 1079-1087 (2003).

E.J. O'Loughlin, K.M. Kemner, D.R. Burris, "Effects of Ag^{I}, Au^{III}, and Cu^{II} on the Reductive Dechlorination of Carbon Tetrachloride by Green Rust," Environ. Sci. Technol. **37**, 2905-2912 (2003).

E.J. O'Loughlin, S.D. Kelly, R. Cook, R. Csencsits, K.M. Kemner, "Reduction of uranium(VI) by mixed Iron(II)/IronIII) Hydroxide (Green Rust): Formation of UO_2 Nanoparticles," Environ. Sci. Technol. **37**, 721-727 (2003).

E.J. O'Loughlin, S.D. Kelly, K.M. Kemner, R. Csencsits, R.E. Cook, "Reduction of Ag^{I}, Au^{III}, Cu^{II}, and Hg^{II} by Fe^{II}/Fe^{III} hydroxysulfate green rust," Chemosphere **53** (5), 437-591 (November 2003).

S. Orlicky, X. Tang, A. Willems, M. Tyers, F. Sicheri, "Structural basis for phospho-dependent substrate selection and orientation by the SCFCdc4 ubiquitin ligase," Cell **112** (2), 243-256 (2003).

E. Ortlund, L. Parker, S.F. Schreck, S. Ginell, W. Minor, J.M. Sodetz, L. Lebioda, "Crystal Structure of Human Complement Protein C8γ at 1.2 Å Resolution Reveals a Lipocalin Fold and a Distinct Ligand Binding Site," Biochemistry-US **41** (22), 7030-7037 (2003).

A.M. Orville, J.M. Studts, G.T. Lountos, K.H. Mitchell, B.G. Fox, "Crystallization and preliminary analysis of native and N-terminal truncated isoforms of toluene-4-monooxygenase catalytic effector protein," Acta Crystallogr. D **59**, 572-575 (2003).

J. Osipiuk, M.A. Walsh, A. Joachimiak, “Crystal structure of MboIIA methyltransferase,” Nucleic Acids Res. **31** (18), 5440-5448 (2003).

Z. Otwinowski, D. Borek, W. Majewski, W. Minor, “Multiparametric scaling of diffraction intensities,” Acta Crystallogr. A **59**, 228-234 (2003).

D. Paktunc, A. Foster, G. LaFlamme, “Speciation and characterization of arsenic in Ketza River mine tailings using x-ray absorption spectroscopy,” Environ. Sci. Technol. **37** (10), 2067-2074 (2003).

B. Pan, Y. Xiong, K. Shi, J. Deng, M. Sundaralingam, “Crystal Structure of an RNA Purine-rich Tetraplex Containing Adenine-Tetrads: Implications for Specific Binding in RNA Tetraplexes,” Structure **11** (7), 815-823 (2003).

B. Pan, Y. Xiong, K. Shi, M. Sundaralingam, “Crystal Structure of a Bulged RNA Tetraplex at 1.1 Å Resolution Implications for a Novel Binding Site in RNA Tetraplex,” Structure **11** (11), 1423-1430 (2003).

B. Pan, Y. Xiong, K. Shi, M. Sundaralingam, “An Eight-Stranded Helical Fragment in RNA Crystal Structure Implications for Tetraplex Interaction,” Structure **11** (7), 825-831 (2003).

S.S. Pang, L.W. Guddat, R.G. Duggleby, “Molecular Basis of Sulfonylurea Herbicide Inhibition of Acetohydroxyacid Synthase,” J. Biol. Chem. **278** (9), 7639-7644 (2003).

T. Paunesku, T. Rajh, G. Wiederrecht, J. Maser, S. Vogt, N. Stojicevic, M. Protic, B. Lai, J. Oryhon, M. Thurnauer, G. Woloschak, “Biology of TiO_2-oligonucleotide nanocomposites,” Nature Materials **2**, 343-346 (May 2003).

T. Paunesku, N. Stojicevic, S. Vogt, J. Maser, B. Lai, T. Rajh, M. Thurnauer, G. Woloschak, “Intracellualr localization of titanium dioxide-biomolecule nanocomposites,” J. Phys. IV France **104**, 317-319 (2003).

D. Peisach, P. Gee, K. Kent, Z. Xu, “The crystal structure of choline kinase reveals a eukaryotic protein kinase fold,” Structure **11**, 703-713 (2003).

E. Peisach, C.O. Pabo, “Constraints for Zinc Finger Linker Design as Inferred from X-ray Crystal Structure of Tandem Zif268–DNA Complexes,” J. Mol. Biol. **330** (1), 1-7 (2003).

E.F. Peltier, S.M. Webb, J.-F. Gaillard, “Zinc and lead sequestration in an impacted weltand system,” Adv. Environ. Res. **8**, 103-112 (2003).

S.J. Perez-Miller, T.D. Hurley, “Coenzyme Isomerization Is Integral to Catalysis in Aldehyde Dehydrogenase,” Biochemistry-US **42**, 7100-7109 (2003).

D.J. Plaut, S.M. Martin, K. Kjaer, M. Weygand, M. Lahav, L. Leiserowitz, I. Weissbuch, M. Ward, “Structural Characterization of Crystalline Ternary Inclusion Compounds at the Air-Water Interface,” J. Am. Chem. Soc. **125** (51), 15922-15934 (2003).

L.M. Podust, Y. Kim, M. Arase, B.A. Neely, B.J. Beck, H. Bach, D.H. Sherman, D.C. Lamb, S.L. Kelly, M.R. Waterman, “The 1.92-Å Structure of Streptomyces coelicolor A3(2) CYP154C1. A New Monooxygenase that Functionalizes Macrolide Ring Systems,” J. Biol. Chem. **278**, 12214-12221 (April 2003).

B. Pokroy, E. Zolotoyabko, “Microstructure of natural plywood-like ceramics: A study by high resolution electron microscopy and high energy electron diffraction,” J. Mater. Chem. **13** (4), 682-688 (2003).

G. Prag, S. Misra, E.A. Jones, R. Ghirlando, B.A. Davies, B.F. Horazdovshi, J.H. Hurley, “Mechanism of Ubiquitin Recognition by the CUE Domain of Vps9p,” Cell **113**, 609-620 (May 2003).

V.B. Prakapenka, L.S. Dubrovinsky, G. Shen, M. Rivers, S.R. Sutton, V. Dmitriev, H.-P. Weber, T. Le Bihan, “α-PbO_2-type high pressure polymorph of GeO_2,” Phys. Rev. B **67**, 132101-1-132101-4 (2003).

V. Prasad, S.-W. Kang, S. Kumar, “Novel examples of achiral bent-core azo compounds exhibiting B1 and anticlinic-antiferroelectric B2 mesophases,” J. Mater. Chem. **13**, 1259-1264 (2003).

M. Prhavc, T.P. Prakash, G. Minasov, M. Egli, M. Manoharan, “2'-O-[2-[2-(N,N-Dimethylamino)ethoxy]ethyl] Modified Antisense Oligonucleotides: Symbiosis of Charge Interaction Factors and Stereoelectronic Effects,” Org. Lett. **5**, 2017-2020 (2003).

L. Prunty, J. Bell, M. Rivers, “Synchrotron Radiation for Detecting Movement of a Volatile Soil Liquid,” J. Environ. Eng.-ASCE **129** (5), 479-482 (May 2003).

K.R. Purdy, Z. Dogic, S. Fraden, A. Rühm, L.B. Lurio, S.G.J. Mochrie, “Measuring the nematic order of suspensions of colloidal fd virus by x-ray diffraction and optical birefringence,” Phys. Rev. E **67**, 31708-1-31708-12 (2003).

N. Qafoku, C.C. Ainsworth, J.E. Szecsody, O. Qafoku, S.M. Heald, "Effect of coupled dissolution and redox reactions on $Cr(VI)_{aq}$ attenuation during transport in the sediments under hyperalkaline conditions," Environ. Sci. Technol. **37** (16), 3640-3644 (2003).

B.K. Rai, S.M. Durbin, E.W. Prohofsky, J.T. Sage, M.K. Ellison, A. Roth, W.R. Scheidt, W. Sturhahn, E.E. Alp, "Direct determination of the complete set of iron normal modes in a porphyrin-imidazole model for carbonmonoxy-heme proteins: [Fe(TPP)(CO)(1-MeIm)]," J. Am. Chem. Soc. **125** (23), 6927-6936 (May 2003).

S. Rajagopal, K. Moffat, "Crystal structure of a photoactive yellow protein from a sensor histidine kinase: Conformational variability and signal transduction," Proc. Natl. Acad. Sci. **100** (4), 1649-1654 (2003).

G. Rajan, G. Sur, J. Mark, D. Schaeffer, G. Beaucage, "Preparation and Characterization of Some Unusually Transparent Poly(dimethylsiloxane) Nanocomposites," J. Polym. Sci. Pol. Phys. **41**, 1897-1901 (2003).

Y. Ren, A. A. Nugroho, A. A. Menovsky, J. Strempfer, U. Rutt, F. Iga, T. Takabatake, C. W. Kimball, "Orbital-ordering-induced phase transition in $LaVO_3$ and $CeVO_3$," Phys. Rev. B **67**, 014107-1-014107-6 (January 2003).

C.K. Rhee, M. Wakisaka, Y.V. Tolmachev, C.M. Johnston, R. Haasch, K. Attenkofer, G.Q. Lu, H. You, A. Wieckowski, "Osmium nanoislands spontaneously deposited on a Pt(111) electrode: an XPS, STM and GIF-XAS study," J. Electroanal. Chem. **554-555**, 367-378 (September 2003).

S.A. Roberts, G.F. Wildner, G. Grass, A. Weichsel, A. Ambrus, C. Rensing, W.R. Montfort, "A Labile Regulatory Copper Ion Lies Near the T1 Copper Site in the Multicopper Oxidase CueO," J. Biol. Chem. **278** (34), 31958-31963 (2003).

I. Robinson, F. Pfeiffer, I. Vartanyants, Y. Sun, Y. Xia, "Enhancement of coherent X-ray diffraction from nanocrystals by introduction of X-ray optics," Opt. Express **11** (19), 2329-2334 (September 2003).

I.K. Robinson, C.A. Kenney-Benson, I.A. Vartanyants, "Sources of decoherence in beamline optics," Physica B **336**, 56-62 (February 2003).

W. Rodrigues, B.P. Tinkham, O. Sakata, T.-L. Lee, A. Kazimirov, M.J. Bedzyk, "X-ray standing wave study of Si/Ge/Si(0 0 1) heterostructures grown with Bi as a surfactant," Surf. Sci. **529** (1-2), 1-10 (March 2003).

Y. Romsicki, G. Scapin, V. Beaulieu-Audy, S. Patel, J.W. Becker, B.P. Kennedy, E. Asante-Appiah, "Functional characterization and crystal structure of the C215D mutant of protein-tyrosine phosphatase-1B," J. Biol. Chem. **278** (31), 29009-29015 (August 2003).

J.K. Rubach, B.V. Plapp, "Amino acid residues in the nicotinamide binding site contribute to catalysis by horse liver alcohol dehydrogenase," Biochemistry-US **42**, 2907-2915 (2003).

T.J. Rydel, J.M. Williams, E. Krieger, F. Moshiri, W.C. Stallings, S.M. Brown, J.C. Pershing, J.P. Purcell, M.F. Alibhai, "The crystal structure, mutagenesis, and activity studies reveal that patatin is a lipid acyl hydrolase with a Ser-Asp catalytic dyad," Biochemistry-US **42**, 6696-6708 (2003).

E. Sabini, S. Ort, C. Monnerjahn, M. Konrad, A. Lavie, "Structure of human dCK suggests strategies to improve anticancer and antiviral therapy," Nature Struct. Biol. **10**, 513-519 (2003).

A.H. Said, C.A. Burns, E.E. Alp, H. Sinn, A. Alatas, P. Giura, "Collective excitations in a metal-ammonia system as a function of electron density," Phys. Rev. B **68**, 104302-1-104302-8 (2003).

S. Sampath, C.J. Benmore, K.M. Lantzky, J. Neuefeind, K. Leinenweber, D.L. Price, J.L. Yarger, "Intermediate-Range Order in Permanently Densified GeO_2 Glass," Phys. Rev. Lett. **90** (11), 115502-1-115502-4 (March 2003).

S. Sampath, K.M. Lantzky, C.J. Benmore, J. Neuefeind, J. Siewenie, P.A. Egelstaff, J.L. Yarger, "Structural Quantum Isotope Effects in Amorphous Beryllium Hydride," J. Chem. Phys. **119** (23), 12499-12502 (December 2003).

G. Sandi, H. Joachin, R. Kizilel, S. Seifert, K.A. Carrad, "In Situ SAXS Studies of the Structural Changes of Polymer Nanocomposites Used in Battery Applications," Chem. Mater. **15**, 838-843 (February 2003).

G. Sandí, H. Joachin, R. Kizilel, S. Seifert, K.A. Carrado, "Studies of the Structural Changes of Polymer Nanocomposites Used in Battery," Chem. Mater. **15** (4), 838-843 (February 2003).

R. Sanishvili, A.F. Yakunin, R.A. Laskowski, T. Skarina, E. Evdokimova, A. Doherty-Kirby, G.A. Lajoie, J.M. Thornton, C.H. Arrowsmith, A. Savchenko, A. Joachimiak, A.M. Edwards, "Integrating Structure, Bioinformatics, and Enzymology to Discover Function," J. Biol. Chem. **278** (28), 26039-260445 (July 2003).

V. Saridakis, E.F. Pai, “Mutational, structural, and kinetic studies of the ATP-binding site of methanobacterium thermoautotrophicum nicotinamide mononucleotide adenylyltransferase,” J. Biol. Chem. **278**, 34356-34363 (2003).

G.N. Sarma, S.N. Savvides, K. Becker, M. Schirmer, R.H. Schirmer, P.A. Karplus, “Glutathione Reductase of the Malarial Parasite Plasmodium falciparum: Crystal Structure and Inhibitor Development,” J. Mol. Biol. **328** (4), 893-907 (2003).

P.V. Satyam, J. Kamila, S. Mohapatra, B. Satpati, D.K. Goswami, B.N. Dev, R.E. Cook, L. Assoufid, J. Wang, N.C. Mishra, “Crater formation in gold nanoislands due to MeV self-ion irradiation,” J. Appl. Phys. **93** (10), 6399-6401 (May 2003).

S.N. Savvides, H.-J. Yeo, M.R. Beck, F. Blaesing, R. Lurz, E. Lanka, R. Buhrdorf, W. Fischer, R. Haas, G. Waksman, “VirB11 ATPases are dynamic hexameric assemblies: New insights into bacterial type IV secretion,” Eur. Mol. Biol. **22** (9), 1969-1980 (2003).

G. Scapin, S.B. Patel, J.M. Lisnock, J.W. Becker, P.V. LoGrasso, “The Structure of JNK3 in Complex with Small Molecule Inhibitors: Structural Basis for Potency and Selectivity,” Chem. Biol. **10**, 705-712 (August 2003).

G. Scapin, S. Patel, Q. Wang, C. Desponts, D. Waddleton, K. Skorey, W. Cromlish, C. Bayly, M. Therien, J.Y. Gauthier, C.S. Li, . Ramachandran, B. Kennedy, E. Asante-Appiah, “The Structural Basis for the Selectivity of Benzotriazole Inhibitors of PTP1B,” Biochemistry-US **43** (39), 11451-11459 (September 2003).

D. Schaefer, J. Zhao, J. Brown, D. Anderson, D. Tomlin, “Morphology of dispersed carbon single-walled nanotubes,” Chem. Phys. Lett. **375**, 369-375 (June 2003).

S. Schaefer, J. Brown, D. Anderson, J. Zhao, K. Chokalingan, D. Tomlin, J. Ilavsky, “Structure and dispersion of carbon nanotubes,” J. Appl. Crystallogr. **36**, 553-557 (2003).

F. Schlunzen, J.M. Harms, F. Franceschi, H.A. Hansen, H. Bartels, R. Zarivach, A. Yonath, “Structural basis for the antibiotic activity of ketolides and azalides,” Structure **11**, 329-338 (March 2003).

M. Schmidt, S. Rajagopal, Z. Ren, K. Moffat, “Application of Singular Value Decomposition to the Analysis of Time-Resolved Macromolecular X-Ray Data,” Biophys. J. **84**, 2112-2129 (2003).

N. Schrader, K. Fischer, K. Theis, R.R. Mende, G. Schwarz, C. Kisker, “The Crystal Structure of Plant Sulfite Oxidase Provides Insights into Sulfite Oxidation in Plants and Animals,” Structure **11** (10), 1251-1263 (2003).

C.G. Schroer, M. Kuhlmann, T.F. Günzler, B. Lengeler, M. Richwin, B. Griesebock, D. Lützenkirchen-Hecht, R. Frahm, E. Ziegler, A. Mashayekhi, D. R. Haeffner, J.-D. Grunwaldt, A. Baiker, “Mapping the chemical states of an element inside a sample using tomographic x-ray absorption spectroscopy,” Appl. Phys. Lett. **82** (19), 3360-3362 (May 2003).

S. Shah, S. Ramakrishnan, Y. Chen, K. Schweizer, C. Zukoski, “Scattering Studies of the Structure of Colloid-Polymer Suspensions and Gels,” Langmuir **19**, 5128-5136 (May 2003).

S. Shah, Y. Chen, K. Schweizer, C. Zukoski, “Viscoelasticity and rheology of depletion flocculated gels and fluids,” J. Chem. Phys. **119** (16), 8747-8760 (October 2003).

S.A. Shah, Y.-L. Chen, S. Ramakrishnan, K.S. Schweizer, C. F. Zukoski, “Microstructure of dense colloid-polymer suspensions and gels,” J. Phys. Condens. Matter **15**, 4751-4778 (2003).

V. Sharma, A. Arockiasamy, D.R. Ronning, C.G. Savva, A. Hohlzenburg, M. Braunstein, W.R. Jacobs Jr., J.C. Sacchettini, “Crystal structure of Mycobacterium tuberculosis SecA, a preprotein translocating ATPase,” Proc. Natl. Acad. Sci. **100** (5), 2243-2248 (2003).

G. Shen, V.B. Prakapenk, M.R. Rivers, S.R. Sutton, “Structural investigation of amorphorous materials at high pressure using the diamond anvil cell,” Rev. Sci. Instrum. **74** (6), 3021-3026 (June 2003).

I.V. Shepotinovskaya, P.J. Focia, D.M. Freymann, “Crystallization of the GMPPCP complex of the NG domains of Thermus aquaticus Ffh and FtsY,” Acta Crystallogr. D **59** (10), 1834-1837 (2003).

T. Shibata, B. Bunker, J.F. Mitchell, “Local distortion of MnO_6 clusters in the metallic phase of $La_{1-x}Sr_xMnO_3$,” Phys. Rev. B **68**, 024103-1-024103-10 (July 2003).

B.H. Shilton, P.G. Telmer, “Insights into the Conformational Equilibria of Maltose-binding Protein by Analysis of High Affinity Mutants,” J. Biol. Chem. **278** (36), 34555-34567 (September 2003).

M. Shimaoka, T. Xiao, J.H. Lui, Y. Dong, C.D. Jun, A. McCormack, R. Zhang, A. Joachimiak, J. Takagi, J.H. Wang, T.A. Springer, Y. Yang, “Structures of the αL I domain and its complex with ICAM-1 reveal a shape-shifting pathway for integrin regulation,” Cell **112** (1), 99-111 (2003).

Yu. V. Shvyd'ko, M. Lerche, H.-C. Wille, E. Gerdau, M. Lucht, H.D. Rüter, E.E. Alp, R. Khachatryan, "X-ray interferometry with microelectronvolt resolution," Phys. Rev. Lett. **90** (1), 013904-1-013904-4 (January 2003).

H. Sinn, B. Glorieux, L. Hennet, A. Alatas, M. Hu, E.E. Alp, F.J. Bermejo, D.L. Price, M.-L. Saboungi, "Microscopic dynamics of liquid aluminum oxide," Science **299** (5615), 2047-2049 (March 2003).

S. Skanthakumar, C. W. Williams, L. Soderholm, "Incorporation of Am (Z=95) into the Superconductor-related Phase Pr_2CuO_4," Phys. Rev. B **68**, 064510-1-064510-7 (August 2003).

P. Sliz, S.C. Harrison, G. Rosenbaum, "How Does Radiation Damage in Protein Crystals Depend on X-Ray Dose?" Structure **11**, 13-19 (January 2003).

C.V. Smith, C.-C. Huang, A. Miczak, D.G. Russell, J.C. Sacchettini, K. Höner zu Bentrup, "Biochemical and Structural Studies of Malate Synthase from Mycobacterium tuberculosis," J. Biol. Chem. **278** (3), 1735-1743 (2003).

C.F. Snook, P.A. Tipton, L.J. Beamer, "Crystal structure of GDP-mannose dehydrogenase: A key enzyme of alginate biosynthesis in P. aeruginosa," Biochemistry-US **42** (16), 4658-4668 (2003).

K.L. Soldano, A. Jivan, C.V. Nicchitta, D.T. Gewirth, "Structure of the N-terminal domain of GRP94: Basis for ligand specificity and regulation," J. Biol. Chem. **278** (48), 48330-48338 (2003).

S.H. Southworth, E.P. Kanter, B. Krässig, L. Young, G. Armen, J.C. Levin, D.L. Ederer, M.H. Chen, "Double K-Shell Photoionization of Neon," Phys. Rev. A **67**, 062712-1-062712-6 (June 2003).

E. Specht, A. Rar, P. Zschack, H. Hong, J. Ilavsky, "Rapid structural and chemical characterization of ternary phase diagrams using synchrotron radiation," J. Mater. Res. **18** (10), 2522-2527 (October 2003).

W.A. Spieker, J. Liu, J.T. Miller, A.J. Kropf, J.R. Regalbuto, "An EXAFS study of the coordination chemistry of hydrogen hexachloroplatinate (IV) 2. Speciation of complexes adsorbed onto alumina," Appl. Catal. A-Gen. **243** (1), 53-66 (2003).

B. Spingler, D.A. Whittington, S.J. Lippard, "2.4 Å Crystal Structure of an Oxaliplatin 1,2-d(GpG) Intrastrand Cross-Link in a DNA," Inorg. Chem. **42** (2), 650-650 (2003).

J.E. Stelmach, L. Liu, S.B. Patel, J.V. Pivnichny, G. Scapin, S. Singh, C.E.C.A. Hop, Z. Wang, J.R. Strauss, P.M. Cameron, E.A. Nichols, S.J. O'Keefe, E.A. O'Neill, D.M. Schmatz, C.D. Schwartz, C.M. Thompson, D.M. Zaller, J.B. Doherty, "Design and synthesis of potent, orally bioavailable dihydroquinazolinone inhibitors of p38 MAP kinase," Bioorg. Med. Chem. Lett. **13**, 277-280 (2003).

S. Stemmer, Y. Li, B. Foran, P.S. Lysaght, S.K. Streiffer, P. Fuoss, S. Seifert, "Grazing-incidence small angle x-ray scattering studies of phase separation in hafnium silicate films," Appl. Phys. Lett. **83** (15), 3141-3143 (October 2003).

G.B. Stephenson, D.D. Fong, M.V. Ramana Murty, S.K. Streiffer, J.A. Eastman, O. Auciello, P.H. Fuoss, A. Munkholm, M.E.M. Aanerud, C. Thompson, "In Situ X-ray Studies of Vapor Phase Epitaxy of $PbTiO_3$," Physica B **336**, 81-89 (August 2003).

A.W. Stevenson, T.E. Gureyev, D. Paganin, S.W. Wilkins, T. Weitkamp, A. Snigirev, C. Rau, I. Snigierev, H.S. Youn, I.P. Dolbnya, W. Yun, B. Lai, R.F. Garrett, D.J. Cookson, K. Hyodo, M. Ando, "Phase-contrast x-ray imaging with synchrotron radiation for materials science applications," Nucl. Instrum. Methods B **199**, 427-435 (2003).

S.R. Stock, K.I. Ignatiev, T. Dahl, A. Veis, F. De Carlo, "Three-dimensional microarchitecture of the plates (primary, secondary, and carinar process) in the developing tooth of Lytechinus variegatus revealed by synchrotron X-ray absorption microtomography (microCT)," J. Struct. Biol. **144** (3), 282-300 (December 2003).

S.R. Stock, J. Barss, T. Dahl, A. Veis, J.D. Almer, F. De Carlo, "Synchrotron x-ray studies of the keel of the short-spined sea urchin Lytechinus variegatus: Absorption microtomography (microCT) and small beam diffraction mapping," Calcif. Tissue Int. **72**, 555-566 (2003).

S.R. Stock, K. Ignatiev, T. Dahl, J. Barss, K. Fezzaa, A. Veis, W.-K. Lee, F. De Carlo, "Multiple microscopy modalities applied to a sea urchin tooth fragment," J. Synchrotron Rad. **10**, 393-397 (2003).

V. Stoll, K.D. Stewart, C.J. Maring, S. Muchmore, V. Giranda, Y.-g.Y. Gu, G. Wang, Y. Chen, M. Sun, C. Zhao, A.L. Kennedy, D.L. Madigan, Y. Xu, A. Saldivar, W. Kati, G. Laver, T. Sowin, H.L. Sham, J. Greer, D. Kempf, "Influenza neuraminidase inhibitors: Structure-based design of a novel inhibitor series," Biochemistry-US **42**, 718-727 (2003).

J.C. Stroud, L. Chen, "Structure of NFAT Bound to DNA as a Monomer," J. Mol. Biol. **334** (5), 1009-1022 (2003).

B.-N. Su, E.J. Park, D. Nikolic, B.D. Santarsiero, A.D. Mesecar, J.S. Vigo, J.G. Graham, F. Cabieses, R.B.van Breemen, H.H.S. Fong, N.R. Farnsworth, J.M. Pezzuto, A.D. Kinghorn, "Activity-Guided Isolation of Novel Norwithanolides from Deprea subtriflora with Potential Cancer Chemopreventive Activity," J. Org. Chem. **68** (6), 2350-23621 (2003).

S. Suer, S. Misra, L.F. Saidi, J.H. Hurley, "Structure of the GAT comain of human GGA1: A syntaxin amino-terminal domain fold in an endosomal trafficking adaptor," Proc. Natl. Acad. Sci. **100** (8), 4451-4456 (April 2003).

C.N. Suryawanshi, P. Pakdel, D.W. Schaefer, "Effect of drying on the structure and dispersion of precipitated silica," J. Appl. Crystallogr. **36**, 573-577 (2003).

M. Sutton, K. Laaziri, F. Livet, F. Bley, "Using coherence to measure two-time correlation functions," Opt. Express **11** (19), 2268-2277 (September 2003).

K.K. Swinger, K.M. Lemberg, Y. Zhang, P.A. Rice, "Flexible DNA bending in HU–DNA cocrystal structure," EMBO J. **22** (14), 3749-3760 (2003).

B.G. Szczepankiewicz, G. Liu, P.J. Hajduk, C. Abad-Zapatero, Z. Pei, Z. Xin, T.H. Lubben, J.M. Trevillyan, M.A. Stashko, S.J. Ballaron, H. Liang, F. Huang, C.W. Hutchins, S.W. Fesik, M.R. Jirousek, "Discovery of a potent, selective protein tyrosine phosphatase 1B inhibitor using a linked-fragment study," J. Am. Chem. Soc. **125**, 4087-4096 (2003).

J. Takagi, Y. Yang, J.-h. Liu, J.-h. Wang, T.A. Springer, "Complex between nidogen and laminin fragments reveals a paradigmatic β-propeller interface," Nature **424**, 969 -974 (August 2003).

J.S. Taylor, T.S. Reid, K.L. Terry, P.J. Casey, L.S. Beese, "Structure of mammalian protein geranylgeranyltransferase type-I," EMBO J. **22**, 5963-5974 (2003).

A.S. Templeton, T.P. Trainor, A.M. Spormann, M. Newville, S.R. Sutton, A. Dohnalkova, Y. Gorby, G.E. Brown, "Sorption vs. biomineralization of Pb by Birkholderia cepacia biofilms," Environ. Sci. Technol. **37** (2), 300-307 (2003).

A. Teplyakov, G. Obmolova, S.Y. Chu, J. Toedt, E. Eisenstein, A.J. Howard, G. Gilliland, "Crystal structure of the ychF protein reveals binding sites for GTP and nucleic acid," J. Bacteriol. **185** (14), 4031-4037 (July 2003).

A. Teplyakov, G. Obmolova, P.P. Khil, A.J. Howard, R.D. Camerini-Otero, "Crystal Structure of the Escherichia coli YcdX Protein Reveals a Trinuclear Zinc Active Site," Proteins **51**, 315-318 (2003).

A. Teplyakov, G. Obmolova, N. Bir, P. Reddy, A.J. Howard, G.L. Gilliland, "Crystal structure of the YajQ protein from Haemophilus influenzae reveals a tandem of RNP-like domains," J. Struct. Funct. Geno. **4**, 1-9 (2003).

V. Tereshko, E. Skripkin, D.J. Patel, "Encapsulating Streptomycin within a Small 40-mer RNA," Chem. Biol. **10** (2), 175-187 (2003).

M. Terrak, G. Wu, W.F. Stafford, R.C. Lu, R. Dominguez, "Two distinct myosin light chain structures are induced by specific variations within the bound IQ motifs-functional implications," EMBO J. **22** (3), 362-371 (2003).

M.M. Thackeray, J.T. Vaughey, C.S. Johnson, A.J. Kropf, R. Benedek, L.M.L. Fransson, K. Edstrom, "Structural Considerations of Intermetallic Electrodes for Lithium Batteries," J. Power Sources **113**, 124-130 (2003).

D.L. Theobald, S.C. Schultz, "Nucleotide shuffling and ssDNA recognition in Oxytricha nova telomere end-binding protein complexes," EMBO J. **22** (16), 4314-4324 (2003).

P. Thiyagarajan, "Characterization of Materials of Industrial Importance Using Small-Angle Scattering Techniques," J. Appl. Crystallogr. **36**, 373-380 (June 2003).

C.B. Thomas, R.D. Scavetta, R.L. Gumport, M.E.A. Churchill, "Structures of Liganded and Unliganded RsrI N6-Adenine DNA Methyltransferase," J. Biol. Chem. **278** (28), 26094-26101 (July 2003).

T.B. Thompson, T.K. Woodruff, T.S. Jardetzky, "Structures of an ActRIIB:activin A complex reveal a novel binding mode for TGF-beta ligand:receptor interactions," EMBO J. **22**, 1555-1566 (2003).

R.E. Thorne, J.D. Brock, M. Sutton, "Comment on 'Motional Ordering of a Charge-Density Wave in the Sliding State'," Phys. Rev. Lett. **91** (4), 049703-1 (July 2003).

B.P. Tinkham, D.M. Goodner, D.A. Walko, M.J. Bedzyk, “X-ray studies of Si/Ge/Si(001) epitaxial growth with Te as a surfactant,” Phys. Rev. B **67**, 035404-1-035404-6 (January 2003).

V.R. Tirumala, G.T. Caneba, Y.Dar, H.-H. Wang, D.C. Mancini, “Nanoparticles from a controlled polymerization process,” Adv. Polym. Tech. **22** (2), 126-136 (June 2003).

J. Tischler, B. Larson, P. Zschack, P. Fleszar, A. Eguiluz, “Interplay between inelastic x-ray scattering and ab initio density-response calculations: Insight into the electronic correlations in aluminum,” Phys. Status Solidi. b. **237** (1), 280-288 (May 2003).

T. Tokunaga, J. Wan, M. Firestone, T. Hazen, K. Olson , J. Herman, S. Sutton, A. Lanzirotti, “Bioremediation and Biodegration,” J. Environ. Qual. **32**, 1641-1649 (2003).

T.K. Tokunaga, J.M. Wan, T.C. Hazen, E. Schwartz, M.K. Firestone, S.R. Sutton, M. Newville, K.R. Olson, A. Lanzirotti, W. Rao, “Distribution of chromium contamination and microbial activity in soil aggregates,” J. Environ. Qual. **32** (2), 541-549 (2003).

T.K. Tokunaga, K.R. Olson, J. Wan, “Moisture characteristics of Hanford gravels,” Vadose Zone J. **2**, 322-329 (2003).

T.K. Tokunaga, J. Wan, M.K. Firestone, T.C. Hazen, K.R. Olson, D.J. Herman, S.R. Sutton, A. Lanzirotti, “In Situ Reduction of Chromium(VI) in Heavily Contaminated Soils through Organic Carbon Amendment,” J. Environ. Qual. **32**, 1641-1649 (2003).

V.A. Tolhurst, D. Cookson, P. Turner, “A synchrotron study of m3-chloro-tri-m-chloro-m3-sulfido-hexakis(triphenyl- phospine)triruthenium(II)-tetrahydro-furan-water,” Acta Crystallogr. A **E59**, m218-m219 (2003).

P. Tortorelli, K. More, E. Specht, B. Pint, P. Zschack, “Growth stress - microstructure relationships for alumina scales,” Mater. High. Temp. **20** (3), 303-310 (November 2003).

P.N. Trikalitis, V. Petkov, M.G. Kanatzidis, “Structure of Redox Intercalated $(NH_4)_{0.5}V_2O_5{\cdot}mH_2O$ Xerogel Using the Pair Distribution Function Technique,” Chem. Mater. **15**, 3337-3342 (August 2003).

F. Tsui, L. He, L. Ma, A. Tkachuk, Y.S. Chu, K. Nakajima, T. Chikyow, “Novel germanium-based magnetic semiconductors,” Phys. Rev. Lett. **91** (17), 177203-1-177203-4 (October 2003).

T.C. Turek-Etienne, C.L. Strickland, M.D. Distefano, “Biochemical and structural studies with prenyl diphosphate analogues provide insights into isoprenoid recognition by protein farnesyl transferase,” Biochemistry-US **42**, 3716-3724 (2003).

J.F.C. Turner, S.E. McLain, T.H. Free, C.J. Benmore, K.H. Herwig, J.E. Siewenie, “On sample containment for neutron and high energy X-ray scattering,” Rev. Sci. Instrum. **74** (10), 4410-4417 (October 2003).

B.S. Twining, S.B. Baines, N.S. Fisher, J. Maser, S. Vogt, C. Jacobsen, A. Tovar-Sanchez, A. Sanudo-Wilhelmy, “Quantifying trace elements in individual aquatic protist cells with a synchrotron x-ray fluorescence microprobe,” Anal. Chem. **75**, 3806-3816 (August 2003).

B.S. Twining, S.B. Baines, N.S. Fisher, C. Jacobsen, J. Maser, “Quantification and localization of trace metals in natural plankton cells using a synchrotron x-ray fluorescence microprobe,” J. Phys. IV France **104**, 435-438 (2003).

M.P. Ulmer, R. Altkorn, M.E. Grahma, A. Madan, Y.S. Chu, “Production and performance of multilayer-coated conical x-ray mirrors,” Appl. Opt. **42** (34), 6945-6952 (December 2003).

J. Urquidi, C.J. Benmore, J. Neuefeind, B. Tomberli, “ISOMER-X: A new program for the analysis of high energy X-ray diffraction,” J. Appl. Crystallogr. **36**, 368-368 (April 2003).

J. Urquidi, C.J. Benmore, J. Neuefeind, B. Tomberli, C.A. Tulk, M. Guthrie, P.A. Egelstaff, D.D. Klug, “Isotopic Quantum Effects on the Structure of Low Density Amorphous Ice,” J. Phys. Condens. Matter **15**, 3657-3664 (May 2003).

A. Vahedi-Faridi, J. Porta, G.E. Borgstahl, “Improved three-dimensional growth of manganese superoxide dismutase crystals on the International Space Station,” Acta Crystallogr. D **59** (2), 385-388 (February 2003).

D. Vaknin, “Structure-Function Relations in Self-Assembled C18- and C20-Sphingosines Monolayers at Gas/Water Interfaces,” J. Am. Chem. Soc. **125** (5), 1313-1318 (2003).

D. Vaknin, P. Krueger, M. Loesche, “Anomalous X-Ray Reflectivity Characterization of Ion Distribution at Biomimetic Membranes,” Phys. Rev. Lett. **90** (17), 178102-1-178102-4 (2003).

J.M. Vargason, G. Szittya, J. Burgyan, T.M. Tanaka Hall, “Size Selective Recognition of siRNAby an RNA Silencing Suppressor,” Cell **115**, 799-811 (December 2003).

I.A. Vartanyants, I.K. Robinson, "Orgins of decoherence in coherent X-ray diffraction experiments," Opt. Commun. **222**, 29-50 (May 2003).

I.A. Vartanyants, I.K. Robinson, "Imaging of quantum array structures with coherent and partially coherent diffraction," J. Synchrotron Rad. **10**, 409-415 (2003).

A.V. Velentza, M.S. Wainwright, M. Zasadzki, S. Mirzoeva, J. Haiech, P.J. Focia, M. Egli, D.M. Watterson, "An Aminopyridazine Inhibitor of Death Associated Protein Kinase Attenuates Hypoxia-Ischemia Induced Brain Damage," Bioorg. Med. Chem. Lett. **13**, 3465-3470 (2003).

T.H. Venkataramaiah, B.V. Plapp, "Formamides Mimic Aldehydes and Inhibit Liver Alcohol Dehydrogenases and Ethanol Metabolism," J. Biol. Chem. **278** (38), 36699-36706, (September 2003).

A. Vertanessian, A. Allen, M. Mayo, "Agglomerate formation during drying," J. Mater. Res. **18** (2), 495-506 (February 2003).

A. Vila-Sanjurjo, W.K. Ridgeway, V. Seymaner, W. Zhang, S. Santoso, K. Yu, "X-ray crystal structures of the WT and a hyper-accruate ribosome from Escherichia coli," Proc. Natl. Acad. Sci. **100** (15), 8682-8687 (2003).

A.E. Visser, M.P. Jensen, I. Laszak, K.L. Nash, G.R. Choppin, R.D. Rogers, "Uranyl Coordination Environment in Hydrophobic Ionic Liquids: An in situ Investigation," Inorg. Chem. **42** (7), 2197-2199 (March 2003).

S. Vogt, J. Maser, C. Jacobsen, "Data analysis for x-ray fluorescence imaging," J. Phys. IV France **104**, 617-622 (2003).

S. Vogt, "MAPS: A set of software tools for analysis and visualization of 3D x-ray fluorescence data sets," J. Phys. IV France **104**, 635-638 (2003).

H. Walden, M.S. Podgorski, D.T. Huang, D.W. Miller, R.J. Howard, D.L. Minor Jr., J.M. Holton, B.A. Schulman, "The Structure of the APPB1-UBA3-NEDD8-ATP Complex Reveals the Basis for Selective Ubiquitin-like Protein Activation by an E1," Molecular Cell **12**, 1427-1437 (December 2003).

B. Wang, S.L. Alam, H.H. Meyer, M. Payne, T.L. Stemmler, D.R. Davis, W.I. Sundquist, "Structure and Ubiquitin Interactions of the Conserved Zinc Finger Domain Domain of Np14," J. Biol. Chem. **278** (22), 20225-20234 (2003).

W.K. Wang, V. Tereshko, P. Boccuni, D. MacGrogan, S.D. Nimer, D.J. Patel, "Malignant Brain Tumor Repeats: A Three-Leaved Propeller Architecture with Ligand/Peptide Binding Pocket," Structure **11** (7), 775-789 (2003).

X.-L. Wang, J. Almer, C.T. Liu, Y.D. Wang, J.K. Zhao, A.D. Stoica, D.R. Haeffner, W.H. Wang, "In situ synchrotron study of phase transformation behaviors in bulk metallic glass by simultaneous diffraction and small angle scattering," Phys. Rev. Lett. **91** (26), 265501-1-265501-4 (December 2003).

Y. Wang, W.B. Durham, I.C. Getting, D. Weidner, "The deformation-DIA: A new apparatus for high temperature triaxial deformation to pressures up to 15 GPa," Rev. Sci. Instrum. **74** (6), 3002-3011 (June 2003).

S.M. Webb, J.-F. Gaillard, L.Q. Ma, C. Tu, "XAS Speciation of Arsenic in a Hyper-Accumulating Fern," Environ. Sci. Technol. **37** (4), 754-760 (February 2003).

T.M. Weiss, P.-J. Chen, H. Sinn, E.E. Alp, S.-H. Chen, H. W. Huang, "Collective chain dynamics in lipid bilayers by inelastic x-ray scattering," Biophys. J. **84**, 3767-3776 (June 2003).

T.R. Welberry, D.J. Goossens, D.R. Haeffner, P.L. Lee, J. Almer, "High-energy diffuse scattering on the 1-ID beamline at the Advanced Photon Source," J. Synchrotron Rad. **10**, 284-286 (2003).

A.K. Wernimont, D.L. Huffman, L.A. Finney, B. Demeler, V.T. O'Halloran, A.C. Rosenzweig, "Crystal structure and dimerization equilibria of PcoC, a methionine-rich copper resistance protein from Escherichia coli," J. Biol. Inorg. Chem. **8**, 185-194 (2003).

M.W. Westneat, O. Betz, R.W. Blob, K. Fezzaa, W.J. Cooper, W.-K. Lee, "Tracheal respiration in insects visualized with synchrotron x-ray imaging," Science **299**, 558-560 (January 2003).

W.R. Wikoff, Z. Che, R.L. Duda, R.W. Hendrix, J.E. Johnson, "Crystallization and preliminary analysis of a dsDNA bacteriophage capsid intermediate: Prohead II of HK97," Acta Crystallogr. D **59**, 2060-2064 (2003).

C.J. Wilds, M.A. Maier, M. Manoharan, M. Egli, "Structural Basis for Recognition of Guanosine by a Synthetic Tricyclic Cytosine Analogue: Guanidinium G-Clamp," Helv. Chim. Acta **86**, 966-978 (2003).

D.S. Williams, P.M. Shand, T.M. Pekarek, R. Skomski, V. Petkov, D.L. Leslie-Pelecky, "Magnetic transitions in disordered $GdAl_2$," Phys. Rev. B **68**, 214404-1-214404-8 (December 2003).

G.J. Williams, M.A. Pfeifer, I.A. Vartanyants, I.K. Robinson, "Three-Dimensional Imaging of Microstructure in Au Nanocrystals," Phys. Rev. Lett. **90** (17), 175501-1-175501-4 (May 2003).

J.J. Wilson, O. Matsushita, A. Okabe, J. Sakon, "A bacterial collagen-binding domain with novel calcium-binding motif controls domain orientation," EMBO J. **22** (8), 1743-1752 (2003).

M.A. Wilson, J.L. Collins, Y. Hod, D. Ringe, G.A. Petsko, "The 1.1-Å resolution crystal structure of DJ-1, the protein mutated in autosomal recessive early onset Parkinson's disease," Proc. Natl. Acad. Sci. **100** (16), 9256-9261 (2003).

E.L. Wise, W.S. Yew, J.A. Gerlt, I. Rayment, "Structural Evidence for a 1,2-Enediolate Intermediate in the Reaction Catalyzed by 3-Keto-L-Gulonate 6-Phosphate Decarboxylase, a Member of the Orotidine 5'-Monophosphate Decarboxylase Suprafamily," Biochemistry-US **42** (42), 12133-12142 (2003).

E.L. Wise, D.E. Graham, R.H. White, I. Rayment, "The Structural determination of phosphosulfolactate synthase from Methanococcus jannaschii at 1.7 A Resolution: an enolase that isn't an enolase," J. Biol. Chem. **27**8, 45858-45863 (2003).

R.-Y. Wu, R.-G. Zhang, O. Zagnitko, I. Dementieva, N. Maltzev, J.D. Watson, R. Laskowski, P. Gornicki, A. Joachimiak, "Crystal Structure of Enterococcus faecalis SlyA-like Transcriptional Factor," J. Biol. Chem. **278** (22), 20240-20244 (May 2003).

Y. Xiao, F. Izumi, T. Graber, P.J. Viccaro, D. Wittmer, "Update in a Rietveld analysis program for x-ray powder spectro-diffractometry," Powder Diffr. **2003** (18), 32-35 (2003).

W. Xie, X. Liu, R.H. Huang, "Chemical trapping and crystal structure of a catalytic tRNA guanine transglycosylase covalent intermediate," Nature Struct. Biol. **10** (10), 781-788 (2003).

Z. Xin, T.K. Oost, C. Abad-Zapatero, P.J. Hajduk, Z. Pei, B.G. Szczepankiewicz, C.W. Hutchins, S.J. Ballaron, M.A. Stashko, T. Lubben, J.M. Trevillyan, M.R. Jirousek, G. Liu, "Potent, selective inhibitors of protein tyrosine phosphatase 1B," Bioorg. Med. Chem. Lett. **13**, 1887-1890 (2003).

Y. Xiong, F. Li, J. Wang, A.M. Weiner, T.A. Steitz, "Crystal Structures of an Archaeal Class I CCA-Adding Enzyme and Its Nucleotide Complexes," Molecular Cell **12**, 1165-1172 (2003).

G. Xu, D.E. Eastman, B. Lai, Z. Cai, I. McNulty, I.C. Noyan, C.K. Hu, "Nanometer precision metrology of submicron Cu/SiO_2 interconnects using fluorescence and transmission x-ray microscopy," J. Appl. Phys. **94** (9), 6040-6049 (November 2003).

Y. Xu, N. Yang, K.W. Dennis, R.W. McCallum, M.J. Kramer, Y. Zhang, P.L. Lee, "Processing induced changes in Curie temperature of $Nd_2Fe_{14}B$ melt-spun ribbons," J. Appl. Phys. **93** (10), 7993-7995 (May 2003).

Y. Xu, D.J. Weidner, J. Chen, M.T. Vaughan, Y. Wang, T. Uchida, "Flow-law for ringwoodite at subduction zone conditions," Phys. Earth Planet. In. **203**, 1-7 (2003).

Y. Yacoby, M. Sowwan, E. Stern, J. Cross, D. Brewe, R. Pindak, J. Pitney, E.B. Dufresne, R. Clarke, "Direct determination of epitaxial film and interface structure: GD_2O_3 on GaAs (100)," Physica B **336**, 39-45 (2003).

B. Yang, D. Li, S. Rice, "Two dimensional freezing of TI in the liquid-vapor interface of dilute TI in a Ga alloy," Phys. Rev. B **67**, 212103-1-212103-3 (2003).

H. Yang, P.D. Carr, Yu. McLoughlin, J.W. Liu, I. Horne, X. Qiu, C.M.J. Jeffries, R.J. Russell, J.G. Oakeshott, D.L. Ollis, "Evolution of an organophosphate-degrading enzyme: a comparison of natural and directed evolution," Protein Eng. **16** (2), 135-145 (2003).

N. Yang, K.W. Dennis, R.W. McCallum, M.J. Kramer, Y. Zhang, P.L. Lee, "Role of the Fe sublattice on the Invar anomaly in $R_2Fe_{14}B$ compounds," J. Appl. Phys. **93** (10), 7990-7992 (May 2003).

W. Yang, B.C. Larson, G.E. Ice, J.Z. Tischler, J.D. Budai, K.-S. Chung, W.P. Lowe, "Spatially resolved Poisson strain and anticlastic curvature measurements in Si under large deflection bending," Appl. Phys. Lett. **82** (22), 3856-3858 (June 2003).

K. Ye, L. Malinia, P.J. Dinshaw, "Recognition of small interfering RNA by a viral suppressor of RNA silencing," Nature **426**, 874-878 (2003).

A. Yilmazbayhan, O. Delaire, A.T. Motta, R.C. Birtcher, J.M. Maser, B. Lai, "Determination of the alloying content in the matrix of Zr alloys using synchrotron radiation microprobe x-ray fluorescence," J. Nucl. Mater. **321**, 221-232 (2003).

M.S. Yousef, S.A. Clark, P.K. Pruett, “Induced fit in guanidino kinases—comparison of substrate-free and transition state analog structures of arginine kinase,” Protein Sci. **12** (1), 103-111 (2003).

C.-J. Yu, G. Evmenenko, J. Kmetko, P. Dutta, “Effects of Shear Flow on Interfacial Ordering in Liquids: X-ray Scattering Studies,” Langmuir **19** (23), 9558-9561 (2003).

T.I. Zarembinsk, Y.-C. Kim, K. Peterson, D. Christendat, A. Dharamsi, C. Arrowsmith, A.M. Edwards, A. Joachimiak, “Deep trefoil knot implicated in RNA binding found in an archaebacterial protein,” Proteins **50**, 177-183 (2003).

X. Zhai, S. Peleshanko, N.S. Klimenko, K.L. Genson, D. Vaknin, M.Ya. Vortman, V.V. Shevchenko, V.V. Tsukruk, “Amphiphilic Dendritic Molecules: Hyperbranched Polyesters with Alkyl-Terminated Branches,” Macromolecules **36**, 3101-3110 (2003).

H. Zhang, B. Gilbert, F. Huang, J. Banfield, “Water-driven Structure Transformation in Nanoparticles at Room Temperature,” Nature **424**, 1025-1029 (August 2003).

H. Zhang, G. Kurisu, J.L. Smith, W.A. Cramer, “A defined protein-detergent-lipid complex for crystallization of integral membrane proteins: The cytochrome b_6f complex of oxygenic photosynthesis,” Proc. Natl. Acad. Sci. **100** (9), 5160-5163 (2003).

P. Zhang, P.S. Kim, T.K. Sham, “Electrochemical route for the fabrication of alkanethiolate-capped gold nanoparticles,” Appl. Phys. Lett. **82** (9), 1470-1472 (March 2003).

P. Zhang, T.K. Sham, “X-ray Studies of the Structure and Electronic Behaviour of Alkanethiolate-Capped Gold Nanoparticles: The interplay of Size and Surface Effects,” Phys. Rev. Lett. **90**, 245502-1-245502-4 (2003).

R.-G. Zhang, C.E. Andersson, A. Savchenko, S. Beasley, C.H. Arrowsmith, A. Edwards, A. Joachimiak, S.L. Mowbray, “Structure of Escherichia coli ribose-5-phosphate isomerase: an ubiquitous enzyme of the Calvin cycle,” Structure **11** (1), 31-42 (2003).

R.-G. Zhang, N. Duke, R. Laskowski, E. Evdokimova, T. Skarina, A. Edwards, A. Joachimiak, A. Savchenko, “Conserved Protein YecM from Escherichia coli Shows Structural Homology to Metal-Binding Isomerases and Oxygenases,” Proteins **51**, 311-314 (2003).

W. Zhang, G.N. Phillips Jr., “Crystallization and X-ray diffraction analysis of the sensor domain of the HemAT aerotactic receptor,” Acta Crystallogr. D **59** (4), 749-751 (2003).

W. Zhang, G.N. Phillips, “Structure of the Oxygen Sensor in Bacillus subtilis Signal Transduction of Chemotaxis by Control of Symmetry,” Structure **11** (9), 1097-1110 (2003).

X. Zhang, Z. Yang, S. I. Khan, J.R. Horton, H. Tamaru, E.U. Selker, X. Cheng, “Structural basis for the product specificity of histone lysine methyltransferases,” Molecular Cell **12**, 177-185 (2003).

Y. Zhang, A.P. Wilkinson, G.S. Nolas, P.L. Lee, J.P. Hodges, “Strategies for solving neighboring element problems: A case study using resonant x-ray diffraction and pulsed neutron diffraction to examine $Sr_8Ga_{16}Ge_{30}$,” J. Appl. Crystallogr. **36**, 182-1189 (2003).

A. Zhou, J.A. Huntington, N.S. Pannu, R.W. Carrell, R.J. Read, “How vitronectin binds PAI-1 to modulate fibrinolysis and cell migration,” Nature Struct. Biol. **10** (7), 541-544 (July 2003).

J. Zhou, Z. Xu, “Structural determinants of SecB recognition by SecA in bacterial protein translocation,” Nature Struct. Biol. **10** (11), 942-947 (2003).

X.E. Zhou, Y. Wang, M. Reuter, P. Mackeldanz, D.H. Kruger, E.J. Meehan, L. Chen, “A single mutation of restriction endonuclease EcoRII led to a new crystal form that diffracts to 2.1 Å resolution,” Acta Crystallogr. D **59**, 910-912 (2003).

G. Zhu, P. Zhai, X. He, S. Terzyan, R. Zhang, A. Joachimiak, J. Tang, X. C. Zhang, “Crystal Structure of the Human GGA1 GAT Domain,” Biochemistry-US **42**, 6392-6399 (2003).

M.v. Zimmermann, S. Grenier, C.S. Nelson, J.P. Hill, D. Gibbs, M. Blume, D. Casa, B. Keimer, Y. Murakami, C.-C. Kao, C. Venkataraman, T. Gog, Y. Tomioka, Y. Tokura, “Reply to ‘Comment on “X-ray resonant scattering studies of orbital and charge ordering in $Pr_{1-x}Ca_xMnO_3$”’,” Phys. Rev. B **68**, 127102-1-127102-2 (September 2003).

E. Zolotoyabko, J.P. Quintana, “Non-destructive microstructural analysis with depth resolution,” Nucl. Instrum. Methods B **200**, 32-38 (2003).

E. Zolotoyabko, J.P. Quintana, E.J. Townder, B.H. Hoerman, B.W. Wessels, “Nanosecond-scale domain dynamics in $BatiO_3$ probled by time-resolved x-ray diffraction,” Ferroelectrics **290**, 115-124 (2003).

Experimental Results: Conference Proceedings Articles

M.A. Anastasio, F. De Carlo, X. Pan, "Phase-contrast tomography and the local tomography problem," Proc. SPIE, Vol. **5030**, SPIE, (June 2003) 120-126.

C.E. Botez, K. Li, E.D. Lu, P.F. Miceli, E.H. Conrad, P.W. Stephens, "X-ray scattering studies of low-T Ag(001) and Cu(001) homoepitaxy: Vacancy trapping and surface morphology evolution," *Mat. Res. Soc. Symp. Proc.* **749**, Materials Research Society, (2003) W8.1.1-W8.1.6.

R. Divan, D.C. Mancini, N. Moldovan, L. Assoufid, Y.S. Chu, Q. Ma, R.A. Rosenberg, "X-ray patterned deposition of gold nanoparticles from solution," *26th Edition of the International Semiconductor Conf.*, IEEE, (2003) 39-42.

T.A. Dobbins, A.J. Allen, J. Ilavsky, G.G. Long, A. Kulkarni, H. Herman, P.R. Jemian, "Recent Developments in the Characterization of Anisotropic Void Populations in Thermal Barrier Coatings Using Ultra-Small-Angle X-Ray Scattering," *27th International Cocoa Beach Conference on Advanced Ceramics and Composites:* A **24**, American Ceramic Society, (2003) 517-524.

J. Fortner, C. Mertz, P. Jemian, S. Wolf, "Natural Ground Water Colloids from the USGS J-13 Well in Nye County, NV: A Study Using SAXS and TEM," *Science Basis for Nuclear Waste Management XXVI* **757**, Materials Research Society, (2003) 483-488.

J. Hertz, D. Ebel, W.K. Weisberg, "Tomographic study of shapes and metal abundances of Renazzo chondrules," *Lunar and Planetary Science XXXIV*, Lunar and Planetary Institute, (2003) 1959-1960.

J.M. Karner, S.R. Sutton, J.J. Papike, C.K. Shearer, M. Newville, "Oxidation state of vanadium in glass and olivine from terrestrial and Martian basalts: Implications for oxygen fugacity estimates," *Lunar and Planetary Science XXXIV*, Lunar and Planetary Institute, (March 2003) 1998-1999.

G.W. Lee, A.K. Gangopadhyay, K.F. Kelton, R.W. Hyers, T.J. Rathz, M.B. Robinson, J.R. Rogers, L. Hennet, S. Krishnan, "Undercooling and X-ray structural studies of Ti-Zr-Ni Liquids," *MRS Fall 2002 Conference Proceedings* **754**, Materials Research Society, (July 2003) 135-140.

Y. M. Liu, P. Zhang, T.K. Sham, "The Electronic Properties and L3 XANES of Au and Nano-Au," *NanoTech 2003, Technical Proceedings of the 2003 Nanotechnology Conference and Trade Show* **3**, Nano Science and Technology Institute, (2003) 183-186.

C. Morawe, J.-C. Peffen, E. Dufresne, Y. Chu, A.T. Macrander, "Double gradient multilayers for broadband focusing," *Crystals, Multilayers, and Other Synchrotron Optics*, Tetsuya Ishikawa, Albert T. Macrander, James L. Wood, eds., **5195**, SPIE, (December 2003) 1-11.

J. Murray, J.S. Boesenberg, D.S. Ebel, "Unambiguous voids in Allende chondrules and refractory inclusions," *Lunar and Planetary Science XXXIV*, Lunar and Planetary Institute, (March 2003) 1999-2000.

C.F. Powell, Y. Yue, S.-K. Cheong, S. Narayanan, R. Cuenca, S. Ciatti, D. Shu, J. Wang, "Effects of ambient pressure on fuel sprays as measured using x-ray absorption," *Proc. 16th Annual Conf. on Liquid Atomization and Spray Systems*, ILASS, (2003) CD ROM.

S.D. Shastri, A. Mashayekhi, J.T. Cremer, M.A. Piestrup, "X-ray optics for 50 - 100 keV undulator radiation using crystals and refractive lenses," Proc. SPIE, Vol. **5195**, SPIE, (2003) 63-75.

G.B. Stephenson, S.K. Streiffer, D.D. Fong, R. V.M. Murty, O. Auciello, P.H. Fuoss, J.A. Eastman, A. Munkholm, C. Thompson, "In-Situ Synchrotron X-ray Studies of the Processing and Physics of Ferroelectric Thin Films," *Reviews from Polar Oxides: Properties, Characterization, and Imaging*, POLECER, (June 2003) 135-144.

S.K. Streiffer, G.B. Stephenson, J.A. Eastman, C. Thompson, D.D. Fong, O. Auciello, P.H. Fuoss, "In Situ Studies of $PbTiO_3$ Thin Films," *Proc. of the 11th US-Japan Seminar on Dielectric and Piezoelectric Ceramics*, National Defense Academy, (September 2003) 171-178.

A. Tkachuk, H. Chen, "Anti-ferrodistortive Nanodomains in PMN Relaxor," *Fundamental Physics of Ferroelectrics* **677**, American Institute of Physics, (2003) 55-64.

J. Wong, M. Holt, H. Hong, M. Wall, A.J. Schwartz, P. Zschack, T.-C. Chiang, "Intensity Patterns of Diffuse X-Ray Scattering from Thermally Populated Phonons in fcc δ-Pu-Ga," *Plutonium Futures - The Science* **673**, American Institute of Physics, (2003) 221-223.

Y. Yacoby, M. Sowwan, R. Pindak, J. Cross, D. Walko, E. Stern, J. Pitney, R. MacHarrie, M. Hong, R. Clarke, "Direct Determination of the Stacking Order in Gd_2O_3 Epi-Layers on GaAs," *Symposium Z, Structure-Property Relationships of Oxide Surfaces and Interfaces II*, K. B. Alexander, C. B. Carter, R. W. Grimes, X. Pan, T. E. Wood, eds., **751**, Materials Research Society, (2003) Z4.5.1-Z4.5.6.

W. Yang, B.C. Larson, G.M. Pharr, G.E. Ice, J.G. Swadener, J.D. Budai, J.Z. Tischler, W. Liu, "Deformation Microstructure under Nanoindentations in Cu Using 3D X-ray Structural Microscopy," *Symposium Y, Surface Engineering 2002--Synthesis, Characterization*

and Applications, A. Kumar, W. J. Meng, Y.-T. Cheng, J. Zabinski, G. L. Doll, S. Veprek, eds., **750**, Materials Research Society, (2003) Y8.26.1-Y8.26.6.

Experimental Results:Books

B. W. Adams, P. H. Bucksbaum, M. F. DeCamp, E. M. Dufresne, M. E. Garcia, H. O. Jeschke, A. Lindenberg, D. A. Reis, P. Sondhauss, J. S. Wark, P. Zambianchi, "*Nonlinear Optics, Quantum Optics, and Ultrafast Phenomena with X-Rays: Physics with X-Ray Free-Electron Lasers,"* B. W. Adams,Kluwer Academic Publishers, 2003, 1-4020-7475-1.

Experimental Results: Book Chapters

B.W. Adams, M.F. DeCamp, E.M. Dufresne, D.A. Reis, "Laser Pump, X-ray Probe Spectroscopy on GaAs," *Nonlinear Optics, Quantum Optics, and Ultrafast Phenomena with X-Rays: Physics with X-Ray Free-Electron Lasers*, B. W. Adams, ed., Kluwer Academic Publishers, 2003, 159-174.

B.W. Adams, "Parametric Down Conversion," *Nonlinear Optics, Quantum Optics, and Ultrafast Phenomena with X-Rays: Physics with X-Ray Free-Electron Lasers*, B. W. Adams, ed., Kluwer Academic Publishers, 2003, 109-158.

M.F. DeCamp, D.A. Reis, P.H. Bucksbaum, "Seeing Sound: Measuring acoustic pulse propagation with x-rays," *Nonlinear Optics and Quantum Optics with X-rays: Physics with X-Ray Free-Electron Lasers*, B. W. Adams, ed., Kluwer Academic Publishers, 2003, 241-265.

M.L. Schlossman, A.M. Tikhonov, "X-ray Scattering Studies of Long-Chain Alkanol Monolayers at the Water-Hexane Interface," *Mesoscale Phenomena in Fluid Systems*, Fiona Case, ed., Oxford University Press, 2003, 81-95.

Experimental Results: Dissertations and Theses

Spencer Anderson, "Structural Changes in the Photocycle of the E46Q Mutant of Photoactive Yellow Protein," Ph.D., The University of Chicago, 2003.

Julio Blanco, "Structural Studies of Enzymes in the Aspartate Metabolic Pathway," Ph.D., University of Toledo, 2003.

Maxim Boyanov, "XAFS Studies of Metal-Ligand Interactions at Organic Suraces and in Solution," Ph.D., University of Notre Dame, 2003.

JungWan Cho, "Design and implementation of a testing apparatus for measurement of strain in ceramic composites using synchrotron radiation," Ph.D., Southern Illinois University at Carbondale, 2003.

Melissa Edeling, "A structural and functional investigation of a novel thiol disulfide oxidoreductase," Ph.D., University of Queensland, 2003.

Yejun Feng, "Exciton Spectroscopy Using Non-Resonant X-ray Raman Scattering," Ph.D., University of Washington, 2003.

Andrei Fluerasu, "Coherent X-ray Studies in Cu_3Au," Ph.D., McGill University, 2003.

Gabriela B. Gonzalez Aviles, "Studies on the Defect Structure of Indium-Tin Oxide Using X-ray and Neutron Diffraction," Ph.D., Northwestern University, 2003.

Thompson Gregory, "Predicting Polymorphic Phase Stability in Multilayered Thin Films," Masters, Ohio State University, 2003.

Ashfia Huq, "Structure and Properties of Alkali Fullerides and Structure Solution from Powder Diffraction," Ph.D., State University of New York at Stony Brook, 2003.

Sean Johnson, "Structural Mechanisms of DNA Replication Fidelity," Ph.D., Duke University, 2003.

C. Karanfil, "Bent Crystal X-Ray Optics for Synchrotron Radiation Research," Ph.D., Illinois Institute of Technology, 2003.

Debdutta Lahiri, "XAFS Studies of Nanocomposite Systems," Ph.D., University of Notre Dame, 2003.

Shinwoo Lee, "An XAFS Study of Zn and Cd Sorption Mechanisms on Montmorillonite and Hydrous Ferric Oxide Over Extended Reaction Times," Ph.D., Illinois Institute of Technology, 2003.

N. Leyarovska, "X-Ray Spectroscopy of Mn Based Single Molecule Magnets," Ph.D., Illinois Institute of Technology, 2003.

Matthew K. Miller, "Structural studies of the beta-lactum ring forming enzymes beta-lactam synthetase and carbapenam synthetase," Ph.D., Northwestern University, 2003.

Guinevere A. Murphy, "Crystallographic and functional characterization of the yeast Sri4p C-terminal coiled-coil domain," Ph.D., University of Colorado at Boulder, 2003.

Nagayoshi Sata, "High pressure studies on FexO: Quasi-isothermal compression experiments and applications to the Earth's core," Ph.D., Univeristy of Tokyo, 2003.

Syed Ali Shah, "Phase Behavior, Microstructure and Mechanics of Colloid-Polymer Mixtures," Ph.D., University of Illinois, 2003.

Chetan Suryawanshi, "Study of factors influencing structure of precipitated silica," Masters, University of Cincinnati, 2003.

V. Tirumala, "Reaction control in quiescent systems of free radical retrograde precipitation polymerization," Ph.D., Michigan Technological University, 2003.

Joerg Voigt, "Magnetische Strukturen in [Er/Tb]-Schichtsystemen: Einfluss der magnetischen Nachbarschaft und konkurrierender Anisotropien," Ph.D., Rheinisch-Westfaelische Technische Hochschule Aachen, 2003.

Amy K. Wernimont, "Crystallographic and biophyscial analyses of the human copper chaperone Hah1, its target protein the Wilson disease protein, and the bacterial copper chaperone, PcoC," Ph.D., Northwestern University, 2003.

Peng Zhang, "Synthesis, Structure and Bonding of Some Nanocrystalline Materials," Ph.D., University of Western Ontario, 2003.

Jian Zhao, "Dispersion and Morphology of Carbon Nanotubes," Masters, University of Cincinnati, 2003.

Accelerator & Beamline Technology & Theory: Journal Articles

C.J. Bocchetta, D. Bulfone, F. Cargnello, M. Danailov, G. D'Auria, B. Diviacco, M. Ferianis, A. Gambitta, E. Karantzoulis, G. Loda, M. Lonza, F. Mazzolini, D. Morelli, G. Pangon, V. Smaluk, M. Stefanutti, M. Svandrlik, L. Tosi, G. Tromba, A. Vascotto, R. Visintini, R. Bakker, W.A. Barletta, W.M. Fawley, R. Bonifacio, S.G. Biedron, M.D. Borland, S.V. Milton, S. De Silvestri, R.P. Walker, J.H. Wu, L.H. Yu, "Overview of FERMI@ELETTRA a Proposed Ultra Bright Coherent X-ray Source in Italy," Nucl. Instrum. Methods A **507**, 484-488 (July 2003).

K.C. Harkay, R.A. Rosenberg, "Properties of the electron cloud in a high-energy positron and electron storage ring," Phys. Rev. Spec. Top., Accel. Beams **6**, 034402-1-034402-12 (March 2003).

O. Hignette, P. Cloetens, W.-K. Lee, W. Ludwig, G. Rostaing, "Hard x-ray microscopy with reflecting mirrors: status and perspectives of the ESRF technology," J. Phys. IV France **104**, 267-270 (2003).

Z. Huang, K.-J. Kim, "Spontaneous and Amplified Radiation at the Initial Stage of a SASE FEL," Nucl. Instrum. Methods A **507**, 65-68 (July 2003).

Z. Huang, M. Borland, P. Emma, K.-J. Kim, "Theory and Simulation of CSR Microbunching in Bunch Compressors," Nucl. Instrum. Methods A **507**, 318-322 (July 2003).

O.H. Kapp, Y.-e Sun, K.-J. Kim, A.V. Crewe, "Attempt to Measure Smith-Purcell Radiation," Nucl. Instrum. Methods A **507**, II-65-II-66 (July 2003).

K.-J. Kim, "Notes on round-to-flat transformation of angular-momentum-dominated beams," Phys. Rev. Spec. Top., Accel. Beams **6**, 104002-1-104002-6 (October 2003).

J.W. Lewellen, C.A. Brau, "RF Photoelectric Injectors Using Needle Cathodes," Nucl. Instrum. Methods A **507**, 323-326 (July 2003).

Y. Li, S. Krinsky, J.W. Lewellen, K.-J. Kim, V. Sajaev, S.V. Milton, "Characterization of a chaotic optical field using a high-gain, self-amplified free-electron laser," Phys. Rev. Lett. **91** (24), 243602-1-243602-4 (December 2003).

Y. Li, J. Lewellen, Z. Huang, V. Sajaev, S.V. Milton, "Time-Resolved Measurement of a Self-Amplified Free-Electron Laser," Nucl. Instrum. Methods A **507**, 413-416 (July 2003).

A.H. Lumpkin, S.G. Biedron, R.J. Dejus, W. Berg, M. Borland, Y.C. Chae, M. Erdmann, Z. Huang, K.-J. Kim, Y. Li, J.W. Lewellen, S.V. Milton, E. Moog, V. Sajaev, B.X. Yang, "Observations of z-Dependent Microbunching Harmonic Intensities Using COTR in a SASE FEL," Nucl. Instrum. Methods A **507**, 246-249 (July 2003).

A.H. Lumpkin, Y.C. Chae, J.W. Lewellen, W.J. Berg, M. Borland, S.G. Biedron, R.J. Dejus, M. Erdmann, Z. Huang, K.-J. Kim, Y. Li, S.V. Milton, E.R. Moog, D.W. Rule, V. Sajaev, B.X. Yang, "Evidence for Transverse Dependencies in COTR and Microbunching in a SASE FEL," Nucl. Instrum. Methods A **507**, 200-204 (July 2003).

V. Mocella, W.-K. Lee, G. Tajiri, D. Mills, C. Ferrero, Y. Epelboin, “A new approach to the solution of the Takagi-Taupin equations for x-ray optics: Application to a thermally deformed crystal monochromator,” J. Appl. Crystallogr. **36**, 129-136 (January 2003).

M. Petra, P.K. Den Hartog, E.R. Moog, S. Sasaki, N. Sereno, I.B. Vasserman, “Radiation effects studies at the Advanced Photon Source,” Nucl. Instrum. Methods A **507**, 422-425 (2003).

V. Sajaev, Z. Huang, S.G. Biedron, P.K. Den Hartog, E. Gluskin, K.-J. Kim, J.W. Lewellen, Y. Li, O. Makarov, S.V. Milton, E.R. Moog, “Z-dependent Spectral Measurements of SASE FEL Radiation at APS,” Nucl. Instrum. Methods A **506**, 304-315 (2003).

V. Sajaev, Z. Huang, “Spectral Measurements of the Second Harmonic of the SASE FEL Radiation at APS,” Nucl. Instrum. Methods A **507**, 154-157 (July 2003).

G.K. Shenoy, “Impact of next-generation synchrotron radiation sources on materials research,” Nucl. Instrum. Methods B **199**, 1-9 (January 2003).

G.K. Shenoy, J.W. Lewellen, D. Shu, N.A. Vinokurov, “Variable-period undulators as synchrotron radiation sources,” J. Synchrotron Rad. 10 (3), 205-213 (March 2003).

I.B. Vasserman, S. Sasaki, R.J. Dejus, O.A. Makarov, E.R. Moog, E.M. Trakhtenberg, N.A. Vinokurov, “Magnetic measurements and tuning of the LCLS prototype undulator,” Nucl. Instrum. Methods A **507** (1-2), 191-195 (July 2003).

C.-x. Wang, K.-J. Kim, “Linear theory of transverse and longitudinal ionization cooling in a quadrupole channel,” Nucl. Instrum. Methods **503**, 401-408 (May 2003).

C.-x. Wang, “Dispersion in a bent-solenoid channel,” Nucl. Instrum. Methods A **503**, 409-413 (May 2003).

C.-x. Wang, V. Sajaev, C. Y. Yao, “Phase Advance and β Function Measurements using Model-Independent Analysis,” Phys. Rev. Spec. Top., Accel. Beams **6**, 104001-1-104001-10 (2003).

L. Zhang, W.-K. Lee, M. Wulff, L. Eybert, “Performance of a cryogenically cooled monochromator: FEA predictions compared with experimental measurements,” J. Synchrotron Rad. **10** (4), 313-319 (July 2003).

Accelerator & Beamline Technology & Theory: Conference Proceedings Articles

A. Alp, “Thermal-Stress Analysis of the High Heat-Load Crotch Absorber at the APS,” *Proceedings of MEDSI 2002*, Argonne National Laboratory, ANL-03/7, (2003) 427-432.

N.D. Arnold, D. Dohan, “Connection-Oriented Relational Database of the APS Control System Hardware,” *Proc. of the 2003 Particle Accelerator Conference*, Joe Chew, Peter Lucas, and Sara Webber, eds., IEEE, (2003) 2327-2329.

S. Berg, D. Bromberek, G. Goeppner, A. Haase, J. Hoyt, W. Michalek, T. Smith, “Development of the Low Return Loss 340-Size Ceramic Window for the APS Linac,” *Proceedings of MEDSI 2002*, Argonne National Laboratory, ANL-03/7, (2003) 50-57.

S. Berg, T. Barsz, D. Briddick, M. Givens, G. Goeppner, A.E. Grelick, W. Jansma, J. Lewellen, A. Lopez, M. Martens, W. Michalek, S. Wesling, “The Advanced Photon Source Injector Test Stand: Phase Two,” *Proc. of the 2003 Particle Accelerator Conference*, Joe Chew, Peter Lucas, and Sara Webber, eds., IEEE, (2003) 2029-2031.

S.W. Berg, D. Bromberek, J. Gagliano, A.E. Grelick, G. Goeppner, A. Nassiri, T. Smith, “Rebuilding WR-340 and WR-284 Waveguide Switches to Meet Higher Power at the Advanced Photon Source,” *Proc. of the 2003 Particle Accelerator Conference*, Joe Chew, Peter Lucas, and Sara Webber, eds., IEEE, (2003) 1416-1418.

M. Borland, “Coherent Synchrotron Radiation and Microbunching in Bunch Compressors,” *Proceedings of LINAC 2002*, Pohang Accelerator Laboratory, (May 2003) 11-15.

M. Borland, L. Emery, H. Shang, R. Soliday, “SDDS-Based Software Tools for Accelerator Design,” *Proc. of the 2003 Particle Accelerator Conference*, Joe Chew, Peter Lucas, and Sara Webber, eds., IEEE, (2003) 3461-3463.

B. Brajuskovic, P. Den Hartog, E. Trakhtenberg, "Mechanical analysis of the prototype undulator for the Linac Coherent Light Source," Proceedings of the 2003 Particle Accelerator Conference, J. Chew, P. Lucas, and S.Webber, eds., IEEE, (2003) 1017-1019.

Y.-C. Chae, K. Harkay, X. Sun, “Horizontal Coupling Impedance of the APS Storage Ring,” *Proc. of the 2003 Particle Accelerator Conference*, Joe Chew, Peter Lucas, and Sara Webber, eds., IEEE, (2003) 3011-3013.

Y.-C. Chae, K. Harkay, X. Sun, “Longitudinal Coupling Impedance of the APS Storage Ring,” *Proc. of the 2003 Particle Accelerator Conference*, Joe Chew, Peter Lucas, and Sara Webber, eds., IEEE, (2003) 3014-3016.

Y.-C. Chae, K. Harkay, X. Sun, “Vertical Coupling Impedance of the APS Storage Ring,” *Proc. of the 2003 Particle Accelerator Conference*, Joe Chew, Peter Lucas, and Sara Webber, eds., IEEE, (2003) 3008-3010.

Y.-C. Chae, “The Impedance Database and Its Application to the APS Storage Ring,” *Proc. of the 2003 Particle Accelerator Conference*, Joe Chew, Peter Lucas, and Sara Webber, eds., IEEE, (2003) 3017-3019.

G. Decker, X. Sun, “Observation of Coherent Microwave Transition Radiation in the APS Linac,” *Proc. of the 2003 Particle Accelerator Conference*, Joe Chew, Peter Lucas, and Sara Webber, eds., IEEE, (2003) 2688-2690.

P. Den Hartog, G.A. Decker, L.J. Emery, "Dual canted undulators at the Advanced Photon Source," Proceedings of the 2003 Particle Accelerator Conference, J. Chew, P. Lucas, and S.Webber, eds., IEEE, (2003) 833-835.

C. Doose, S. Sharma, “Investigation of Passive Vibration Damping Methods for the Advanced Photon Source Storage Ring Girders,” *Proceedings of MEDSI 2002*, Argonne National Laboratory, ANL-03/7, (2003) 133-139.

R. Dortwegt, C. Putnam, E. Swetin, “Mitigation of Copper Corrosion and Agglomeration in APS Process Water Systems,” *Proceedings of MEDSI 2002*, Argonne National Laboratory, ANL-03/7, (2003) 462-468.

R. Dortwegt, “Low-Conductivity Water Systems for Accelerators,” *Proc. of the 2003 Particle Accelerator Conference*, Joe Chew, Peter Lucas, and Sara Webber, eds., IEEE, (2003) 630-634.

L. Emery, “Measurement of Thermal Effects on the Advanced Photon Source Storage Ring Vacuum Chamber,” *Proceedings of MEDSI 2002*, Argonne National Laboratory, ANL-03/7, (2003) 140-146.

L. Emery, M. Borland, “Possible Long-Term Improvements to the Advanced Photon Source,” *Proc. of the 2003 Particle Accelerator Conference*, Joe Chew, Peter Lucas, and Sara Webber, eds., IEEE, (2003) 256-258.

L. Emery, M. Borland, H. Shang, “Use of a General-Purpose Optimization Module in Accelerator Control,” *Proc. of the 2003 Particle Accelerator Conference*, Joe Chew, Peter Lucas, and Sara Webber, eds., IEEE, (2003) 2330-2332.

L. Emery, “Application of Model Independent Analysis Using the SDDS Toolkit,” *Proc. of the 2003 Particle Accelerator Conference*, Joe Chew, Peter Lucas, and Sara Webber, eds., IEEE, (2003) 3464-3466.

L. Emery, I. Vasserman, O. Makarov, B. Deriy, S. Sasaki, R. Soliday, “Feedforward Correction of the Pulsed Circularly Polarizing Undulator at the Advanced Photon Source,” *Proc. of the 2003 Particle Accelerator Conference*, Joe Chew, Peter Lucas, and Sara Webber, eds., IEEE, (2003) 2261-2263.

H. Friedsam, J.M. Penicka, “Advanced Photon Source Upgrades and Improvements,” *Proc. of the 7th International Workshop on Accelerator Alignment*, SPring-8, (September 2003) 59-66.

A.E. Grelick, S. Berg, G. Goeppner, A. Nassiri, G. Pile, T. Smith, Y.W. Kang, A. Haase, D. Miller, “Testing and Operation of the WR340 Waveguide Window in the APS Linac,” *Proceedings of LINAC 2002*, Pohang Accelerator Laboratory, (May 2003) 713-715.

K.C. Harkay, L. Loiacono, R.A. Rosenberg, “Studies of a Generalized Beam-Induced Multipacting Resonance Condition,” *Proc. of the 2003 Particle Accelerator Conference*, Joe Chew, Peter Lucas, and Sara Webber, eds., IEEE, (2003) 3183-3185.

D. Horan, E. Cherbak, “Fast-Ferrite Tuner Operation on a 352-MHz Single-Cell RF Cavity at the Advanced Photon Source,” *Proc. of the 2003 Particle Accelerator Conference*, Joe Chew, Peter Lucas, and Sara Webber, eds., IEEE, (2003) 1177-1179.

M. Jaski, K. Thompson, S. Kim, H. Friedsam, W. Toter, J. Humbert, “Fabrication Techniques for Building Septum Magnets at the APS,” *Proceedings of MEDSI 2002*, Argonne National Laboratory, ANL-03/7, (2003) 89-96.

P.K. Job, J. Alderman, “Radiation Levels Experienced by the Insertion Devices during the Operation of Synchrotron Radiation Sources,” *Proc. of the 2nd International Workshop on Radiation Safety at Synchrotron Radiation Sources*, ESRF, (2003).

P.K. Job, “Experiences in Radiation Safety during Top-up Operation at the Advanced Photon Source,” *Proc. of the 2nd International Workshop on Radiation Safety at Synchrotron Radiation Sources*, ESRF, (2003).

A. Khounsary, S.D. Shastri, A. Macrander, “A Variable-Focus X-ray Compound Lens,” *Proceedings of MEDSI 2002*, Argonne National Laboratory, ANL-03/7, (2003) 58-64.

S.H. Kim, R. J. Dejus, C. Doose, R. L. Kustom, E. R. Moog, M. Petra, K. M. Thompson, "Development of a short-period superconducting undulator at APS," Proceedings of the 2003 Particle Accelerator Conference, J. Chew, P. Lucas, and S.Webber, eds., IEEE, (2003) 1020-1022.

S.-H. Lee, E. Trakhtenberg, P. Den Hartog, "Insertion device vacuum chamber for the Linac Coherent Light Source," Proceedings of the 2003 Particle Accelerator Conference, J. Chew, P. Lucas, and S.Webber, eds., IEEE, (2003) 824-826.

F. Lenkszus, L. Emery, R. Soliday, H. Shang, O. Singh, M. Borland, "Integration of Orbit Control with Real-time Feedback," *Proc. of the 2003 Particle Accelerator Conference*, Joe Chew, Peter Lucas, and Sara Webber, eds., IEEE, (2003) 283-287.

J. W. Lewellen, "Simulation of a Higher-Order Mode RF Photoinjector," *Proceedings of LINAC 2002*, Pohang Accelerator Laboratory, (May 2003) 671-673.

J.W. Lewellen, K. Beczek, S. Berg, D. A. Briddick, R. Dortwegt, M. Givens, A. Grelick, A. Nassiri, S. Pasky, T. L. Smith, "A Flexible Injector Test Stand Design," *Proc. of the 2003 Particle Accelerator Conference,* Joe Chew, Peter Lucas, and Sara Webber, eds., IEEE, (2003) 2038-2040.

J.W. Lewellen, S. Pasky, "An Operator Training Facility at the Advanced Photon Source," *Proc. of the 2003 Particle Accelerator Conference*, Joe Chew, Peter Lucas, and Sara Webber, eds., IEEE, (2003) 2333-2335.

J.W. Lewellen, "Energy-Spread Compensation of a Thermionic-Cathode RF Gun," *Proc. of the 2003 Particle Accelerator Conference*, Joe Chew, Peter Lucas, and Sara Webber, eds., IEEE, (2003) 2035-2037.

Y. Li, Z. Huang, J. Lewellen, S.V. Milton, V. Sajaev, K.-J. Kim, "Temporal Characteristics of a SASE FEL," *Proc. of the 2003 Particle Accelerator Conference*, Joe Chew, Peter Lucas, and Sara Webber, eds., IEEE, (2003) 905-907.

A.H. Lumpkin, C.Y. Yao, B.X. Yang, T. Toellner, "Bunch Purity Evolution during APS Storage Ring Top-up Operations," *Proc. of the 2003 Particle Accelerator Conference*, Joe Chew, Peter Lucas, and Sara Webber, eds., IEEE, (2003) 2411-2413.

A.H. Lumpkin, V. Scarpine, "The Feasibility of OTR Imaging of High-Intensity Proton Beams at FNAL," *Proc. of the 2003 Particle Accelerator Conference*, Joe Chew, Peter Lucas, and Sara Webber, eds., IEEE, (2003) 2414-2416.

A.H. Lumpkin, W.J. Berg, M. Borland, J. Lewellen, "Recent Characterizations of Electron Beams from the APS Linac," *Proc. of the 2003 Particle Accelerator Conference*, Joe Chew, Peter Lucas, and Sara Webber, eds., IEEE, (2003) 2417-2419.

A.H. Lumpkin, W.J. Berg, M. Borland, J.W. Lewellen, N.S. Sereno, "Initial CTR-based Bunch Length Measurements of Linac Beams Following the APS Bunch Compressor," *Proc. of the 2003 Particle Accelerator Conference*, Joe Chew, Peter Lucas, and Sara Webber, eds., IEEE, (2003) 2420-2422.

A.H. Lumpkin, B.X. Yang, C.Y. Yao, L. Emery, "X-ray Imaging of the APS Storage Ring Beam Stability Effects: From the Alaskan Earthquake to Undulator Field Changes," *Proc. of the 2003 Particle Accelerator Conference*, Joe Chew, Peter Lucas, and Sara Webber, eds., IEEE, (2003) 2423-2425.

R.J. Macek, A. Browman, M. Borden, D. Fitzgerald, T.S. Wang, T. Zaugg, K. Harkay, R. Rosenberg, "Electron cloud diagnostics in use at the Los Alamos PSR," *Proceedings of the 2003 Particle Accelerator Conference*, J. Chew, P. Lucas, S. Webber, eds., IEEE, (2003) 508-510.

E.R. Moog, "Novel insertion devices," Proceedings of the 2003 Particle Accelerator Conference, J. Chew, P. Lucas, and S.Webber, eds., IEEE, (2003) 156-160.

L.H. Morrison, S. Sharma, M. Given, "Storage Ring Injection Area Upgrade at the Advanced Photon Source (APS)," *Proceedings of MEDSI 2002*, Argonne National Laboratory, ANL-03/7, (2003) 34-41.

S. Pasky, M. Borland, "Dealing with Change while Maintaining Operational Reliability of the Advanced Photon Source Linear Accelerator," *Proceedings of LINAC 2002*, Pohang Accelerator Laboratory, (May 2003) 704-706.

S. Pasky, R. Soliday, "Conducting Research and Operator Training While Maintaining Top-up Reliability Using the Advanced Photon Source Linear Accelerator," *Proc. of the 2003 Particle Accelerator Conference*, Joe Chew, Peter Lucas, and Sara Webber, eds., IEEE, (2003) 1419-1421.

J.M. Penicka, H.W. Friedsam, "New Database Design for the APS Survey and Alignment Data," *Proc. of 7th International Workshop on Accelerator Alignment*, SPring-8, (September 2003) 549-557.

J.G. Power, W. Gai, J. Lewellen, S. Milton, K.-J. Kim, J. Simpson, H. Wang, D. Finley, H. Carter, "A compact wakefield measurement facility," Proceedings of the 2003 Particle Accelerator Conference, J. Chew, P. Lucas, and S.Webber, eds., IEEE, (2003) 1813-1815.

C. Putnam, R. Dortwegt, “Improved Temperature Regulation of Process Water Systems for the APS Storage Ring,” *Proceedings of MEDSI 2002*, Argonne National Laboratory, ANL-03/7, (2003) 454-461.

V. Sajaev, “Transverse Impedance Distribution Measurements using Response Matrix Fit Method at APS,” *Proc. of the 2003 Particle Accelerator Conference*, Joe Chew, Peter Lucas, and Sara Webber, eds., IEEE, (2003) 417-419.

N.S. Sereno, M. Borland, H. Shang, “Advanced Photon Source Booster Synchrotron Low-Emittance Lattice Commissioning Results,” *Proc. of the 2003 Particle Accelerator Conference*, Joe Chew, Peter Lucas, and Sara Webber, eds., IEEE, (2003) 247-249.

N.S. Sereno, F. Lenkszus, R.M. Lill, “Advanced Photon Source Booster Synchrotron Beam Position Monitor Upgrade and Applications,” *Proc. of the 2003 Particle Accelerator Conference*, Joe Chew, Peter Lucas, and Sara Webber, eds., IEEE, (2003) 2435-2437.

N.S. Sereno, “Advanced Photon Source Booster Synchrotron Subharmonic RF Capture Design,” *Proc. of the 2003 Particle Accelerator Conference*, Joe Chew, Peter Lucas, and Sara Webber, eds., IEEE, (2003) 827-829.

H. Shang, R. Soliday, L. Emery, M. Borland, “New Features in the SDDS-Compliant EPICS Toolkit,” *Proc. of the 2003 Particle Accelerator Conference*, Joe Chew, Peter Lucas, and Sara Webber, eds., IEEE, (2003) 3470-3472.

S. Sharma, C. Doose, E. Rotela, A. Barcikowski, “An Evaluation of Enhanced Cooling Techniques for High-Heat-Load Absorbers,” *Proceedings of MEDSI 2002*, Argonne National Laboratory, ANL-03/7, (2003) 398-408.

T.L. Smith, G. Waldschmidt, A. Grelick, S. Berg, “Bidirectional Coupler Optimization in WR284-Type Waveguide,” *Proc. of the 2003 Particle Accelerator Conference*, Joe Chew, Peter Lucas, and Sara Webber, eds., IEEE, (2003) 1422-1424.

R. Soliday, M. Borland, L. Emery, H. Shang, “New Features in the SDDS Toolkit,” *Proc. of the 2003 Particle Accelerator Conference*, Joe Chew, Peter Lucas, and Sara Webber, eds., IEEE, (2003) 3473-3475.

R. Soliday, M. Borland, L. Emery, H. Shang, “Use of a Simple Storage Ring Simulation for Development of Enhanced Orbit Correction Software,” *Proc. of the 2003 Particle Accelerator Conference*, Joe Chew, Peter Lucas, and Sara Webber, eds., IEEE, (2003) 3476-3478.

G. Swetin, M. Kirshenbaum, C. Putnam, “Cooling Water Systems for Accelerator Components at the Advanced Photon Source,” *Proceedings of MEDSI 2002*, Argonne National Laboratory, ANL-03/7, (2003) 445-453.

L.C. Teng, “Linear Coupling of RMS Emittances,” *Proc. of the 2003 Particle Accelerator Conference*, Joe Chew, Peter Lucas, and Sara Webber, eds., IEEE, (2003) 2895-2897.

E. Trakhtenberg, G. Wiemerslage, P. Den Hartog, B. Brajuskovic, "New insertion device vacuum chambers at the Advanced Photon Source," Proceedings of the 2003 Particle Accelerator Conference, J. Chew, P. Lucas, and S.Webber, eds., IEEE, (2003) 830-832.

C.-x. Wang, K.-J. Kim, “Linear Theory of Ionization Cooling and Emittance Exchange,” *Proceedings of LINAC 2002*, Pohang Accelerator Laboratory, (May 2003) 124-126.

C.-x. Wang, “Spatial-temporal Modes Observed in APS Storage Ring using MIA,” *Proc. of the 2003 Particle Accelerator Conference*, Joe Chew, Peter Lucas, and Sara Webber, eds., IEEE, (2003) 3410-3412.

C.-x. Wang, “Measurement and Application of Betatron Modes with MIA,” *Proc. of the 2003 Particle Accelerator Conference*, Joe Chew, Peter Lucas, and Sara Webber, eds., IEEE, (2003) 3407-3409.

C.Y. Yao, K. Harkay, L. Emery, “Tune System Applications at the APS,” *Proc. of the 2003 Particle Accelerator Conference*, Joe Chew, Peter Lucas, and Sara Webber, eds., IEEE, (2003) 2438-2440.

Accelerator & Beamline Technology & Theory: Book Chapters

B.W. Adams, “Nonlinear Optics of Free Electrons,” *Nonlinear Optics, Quantum Optics, and Ultrafast Phenomena with X-Rays: Physics with X-Ray Free-Electron Lasers*, B. W. Adams, ed., Kluwer Academic Publishers, 2003, 19-34.

B.W. Adams, “Dynamical Diffraction,” *Nonlinear Optics, Quantum Optics, and Ultrafast Phenomena with X-Rays: Physics with X-Ray Free-Electron Lasers*, B. W. Adams, ed., Kluwer Academic Publishers, 2003, 35-90.

B.W. Adams, “X-Ray Sources,” *Nonlinear Optics, Quantum Optics, and Ultrafast Phenomena with X-Rays: Physics with X-Ray Free-Electron Lasers*, B. W. Adams, ed., Kluwer Academic Publishers, 2003, 1-18.

B.W. Adams, “Ultrafast Diffractive X-Ray Optics,” *Nonlinear Optics, Quantum Optics, and Ultrafast Phenomena with X-Rays: Physics with X-Ray Free-Electron Lasers*, B. W. Adams, ed., Kluwer Academic Publishers, 2003, 91-108.

W.-K. Lee, P.F. Fernandez, D.M. Mills, “X-ray Crystal Optics,” *Undulator, Wiggler, and Their Applications*, H. Onuki and P. Elleaume, eds., Taylor & Francis, 2003, 369-420.

P. Zambianchi, “Nonlinear response functions for x-ray laser pulses,” *Nonlinear Optics, Quantum Optics, and Ultrafast Phenomena with X-Rays: Physics with X-Ray Free-Electron Lasers*, B. W. Adams, ed., Kluwer Academic Publishers, 2003, 287-326.

CONTRIBUTORS

The research highlights were written by:
David Voss (dvoss@nasw.org)
JR Minkel (j_r_minkel@hotmail.com)
Vic Comello (ANL-IPD)
Karen Fox (kfox@nasw.org)
Adrian Cho (hadriancho@yahoo.com)
David Appell (davidappell@comcast.net)
William Arthur Atkins (william.atkins@verizon.net)
Mona A. Mort (mamort@nasw.org)
Elise LeQuire (cygnete@mindspring.com)
Yvonne Carts-Powell (yvonne@nasw.org)
Mark Wolverton (exetermw@earthlink.net)
Kevin Brown (ANL-IPD)
Jane Andrew (XFD-UAS)
Paul Boisvert (ANL-IPD)

Additional writing, photographs, graphics, and other support from:
Ercan Alp (XFD-HRX), Ned D. Arnold (ASD-CTL), Cindy Chaffee (AOD-EFO), Judi Damm (Ranstad), Glenn A. Decker (AOD-AUO), Pat Den Hartog (XFD-XFE), Lisa Gades (AOD-EFO), Dean Haeffner (XFD-XRP), Douglas A. Horan (ASD-RF), Yifei Jaski (XFD-XFE), Kwang-Je Kim (ASD-ADM), Soon Hong Lee (XFD-XFE), Michelle Leighton (AOD-IS), John W. Lewellen (ASD-PHY), Alex Lumpkin (AOD-DIA), Jörg Maser (XFD-XMG), William P. Mc Dowell (AOD-IT), Ian McNulty (XFD-XMG), Stephen Milton (XFD-ADM), Elizabeth Moog (XFD-MD), Alireza Nassiri (ASD-RF), Marlene Nowotarski (APS-PA), Maria Petra (XFD-MD), Susan Picologlou (XFD-ADM), Geoffery Pile (ASD-RF), Steven Shoaf (ASD-CTL), George Srajer (XFD-PSG), Susan Strasser (AOD-UAS), Emil Trakhtenberg (XFD-XFE), Jeffrey Ullian (AOD-EFO), Wendy Vanwingeren (AOD-EFO), Gary Weidner (IPD-MED), William Wesolowski (AOD-EFO), Bingxin Yang (AOD-DIA)

Editorial advisors:
Mark A. Beno (XFD-ADM), Rodney Gerig (ASD-ADM), J. Murray Gibson (APS-PA), Efim Gluskin (XFD-ADM), Gabrielle G. Long (XFD-ADM), Dennis M. Mills, (APS-PA), William G. Ruzicka (AOD-ADM)

Technical and mechanical editing:
Marita Moniger (IPD-MED), Catherine Eyberger (ASD-ADM), Kelly Jaje (ASD-ADM), Susan Picologlou (XFD-ADM)
Cover design: Aaron Ashley (Ranstad)
Photography: ANL Photography Group (IPD-MED)
Project coordination, publication design, photography: Richard Fenner (APS-PA)
Our apologies to anyone inadvertantly left off this list. Your contributions are definitely appreciated.

Argonne National Laboratory, a U.S. Department of Energy Office of Science laboratory is operated by The University of Chicago.
The Advanced Photon Source is funded by the U.S. Department of Energy, Office of Science, Office of Basic Energy Sciences.